eman ta zabal zazu
UPV EHU

Universidad del País Vasco
Euskal Herriko Unibertsitatea
University of the Basque Country

ZTF-FCT

Dpto. Mineralogía y Petrología

DESARROLLO DE CAPAS DE CONTACTO PARA SU APLICACIÓN EN SOFC

DEVELOPMENT OF CONTACT COATINGS FOR SOFC

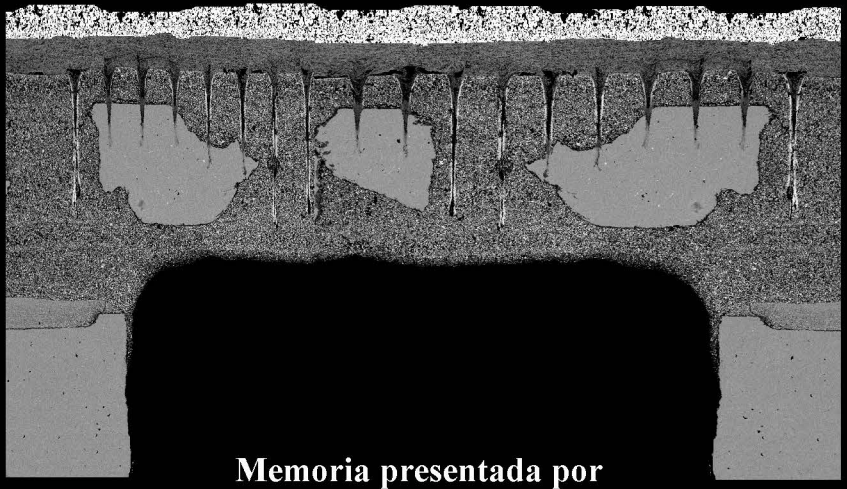

Memoria presentada por
Aroa Morán Ruiz
Para optar al grado de doctora por la UPV/EHU

Leioa, Junio 2015

“Si un sistema químico que está en equilibrio se somete a una perturbación que cambie cualquiera de las variables que determina el estado de equilibrio, el sistema evolucionará para contrarrestar el efecto de la perturbación”

Henri Louis Le Châtelier (1850-1936).

Agradecimientos

Son muchas las personas a las que quiero dar las gracias porque, de una manera u otra, me han ayudado a lo largo de esta etapa de mi vida.

En primer lugar, agradezco a mi directora, la Prof. Maribel Arriortua, la confianza depositada en mí y su continua disponibilidad y ayuda; espero no haberte defraudado. Doy las gracias a mi también director el Dr. Aitor Larrañaga; son muchos los recuerdos que me vienen a la cabeza, muchas horas de resultados comentados y de tiempo invertido; por todo ello gracias, pero sobre todo gracias por mostrarme tu lado más humano.

No olvido, a la Dra. Karmele Vidal, integrante del equipo de Pilas de Combustible del Departamento de Mineralogía y Petrología, y mi querida compañera de batalla. Gracias por tu dedicación, por tus conocimientos, y por esos buenos momentos que hemos compartido. Asimismo, agradezco a la Dra. Ana Écija y a la Dra. Verónica Miguel su ayuda y buena acogida durante este periodo de investigación.

Me gustaría mostrar también mi agradecimiento al personal técnico de los Servicios Generales de Investigación, SGIker, que han hecho posible realizar este trabajo. Agradezco, especialmente, al Dr. Sergio Fernandez toda su ayuda y consejos durante estos años, siempre dispuesto a reservarme un hueco para poder medir, ¡cuántas horas hemos pasado en el microscopio! No puedo olvidarme del Dr. Raúl Montero, gracias por todas tus aportaciones científicas a esta memoria y por tu siempre buen hacer en el uso del láser de femtosegundos. Gracias a la Dra. Belén Sánchez por su incansable disposición a resolver dudas relacionadas con la espectroscopia fotoelectrónica de rayos X (XPS).

Agradezco al personal del Centro Tecnológico Ikerlan, quienes me han permitido y ayudado a realizar mis primeras medidas electroquímicas y, en especial, a la Dra. Laida Otaegui por su constante ayuda siempre con una sonrisa.

Asimismo, doy las gracias al personal investigador del Instituto de Ciencia de Materiales de Aragón (ICMA) de la Universidad de Zaragoza, por haberme facilitado el llevar a cabo la formulación de las pastas presentadas en esta memoria así como su posterior análisis reológico, y por haberme dado la oportunidad de seguir con mis medidas electroquímicas. En especial agradezco al Dr. Miguel Ángel Laguna su sencillez, amabilidad y sus conocimientos, siempre útiles.

De forma especial, agradezco a la Universidad de Birmingham y, en especial, al grupo "Solid State Chemistry Group", dirigido por el Prof. Peter Raymond Slater su buena acogida, su ayuda en la realización de nuevas medidas electroquímicas, y su aporte a nivel personal. Gracias a todos y cada uno de ellos por hacerme sentir tan bien, ¡con vosotros gané en seguridad! No me puedo olvidar del Dr. Jose Manuel Porras, gracias, gracias y gracias, fue una experiencia muy reconfortante el tiempo compartido contigo, ¿cómo olvidar nuestras comidas en el Bella Italia?

Agradezco a los miembros del Tribunal el haber aceptado juzgar este trabajo de investigación.

Quisiera agradecer también a los doctores Luis Ortega y Xabi Montero el haber evaluado esta memoria como expertos internacionales.

Igualmente, quiero agradecer a todos mis compañeros de despacho en estos años, gracias a todos por lo que me habéis enseñado.

Mi manifiesta gratitud a la Universidad del País Vasco/Euskal Herriko Unibertsitatea, UPV/EHU, por la concesión de la beca de formación de personal investigador que he disfrutado durante estos cuatro años.

Por último, agradezco a todas las personas que llevo conmigo en todo lo que hago, estáis grabadas en mi alma por siempre y para siempre, personas que rozan la perfección, personas que quiero muchísimo.

Resumen

La investigación en materiales de contacto cátodo-interconector que mejoren el flujo de electrones, es necesaria en la generación de energía sostenible mediante celdas de combustible de óxido sólido (SOFC). De esta manera, este estudio aporta avances en una tecnología más atractiva para promover la transición hacia un sistema energético seguro, sostenible y competitivo, objetivo contemplado dentro del programa Horizonte 2020.

El uso de aleaciones metálicas como material interconector, permite reducir la temperatura de funcionamiento de las celdas SOFC, aumentando así su durabilidad y aplicabilidad; sin embargo, el empleo de este tipo de materiales presenta como nuevo reto el desarrollo de materiales de contacto con microestructuras y propiedades óptimas.

En este trabajo se recoge el desarrollo de estructuras multicomponente interconector-capa de contacto-cátodo. El uso de diferentes materiales de contacto, para la fabricación de estos sistemas, ha permitido la identificación y adaptación de las propiedades clave para obtener un material de contacto.

Los primeros ensayos se han realizado empleando soportes metálico planos Crofer22APU y cátodos cerámicos $La_{0.6}Sr_{0.4}FeO_3$ (LSF), utilizando como capas de contacto tres óxidos mixtos con estructura perovskita: $LaNi_{0.6}Fe_{0.4}O_{3-\delta}$ (LNF), $LaNi_{0.6}Co_{0.4}O_{3-\delta}$ (LNC) y $(La_{0.8}Sr_{0.2})_{0.95}Fe_{0.6}Mn_{0.3}Co_{0.1}O_3$ (LSFMC). La caracterización de los materiales de partida, y de los procesos de difusión y/o reacción que ocurren en las interfases interconector-capa de contacto-cátodo, a partir del estudio de las propiedades estructurales, microestructurales, espectroscópicas y electroquímicas, ha permitido seleccionar los materiales de contacto más apropiados.

El uso de interconectores acanalados, que permitan el flujo del gas oxidante en un sistema real, ha dado lugar a la preparación de una nueva configuración para optimizar el contacto interconector-cátodo. Así, se ha desarrollado un composite, formado por una malla Fe-22Cr recubierta por inmersión en una suspensión cerámica, formulada a partir de los óxidos seleccionados previamente.

Los ensayos de larga duración, así como la respuesta electroquímica a 800ºC, de las estructuras interconector-composite, han demostrado una adecuada integridad estructural del sistema, y una elevada conductividad eléctrica a través de la interfase interconector-composite.

Con objeto de simular la parte oxidante de un sistema operativo, garantizando el paso del gas oxidante a través del material de contacto, una vez optimizado el sistema interconector-composite, y utilizando un láser de femtosegundos, se ha micromecanizado el composite para, posteriormente, depositar el cátodo sobre el mismo, desarrollando así una nueva estructura interconector-capa de contacto-cátodo. En la última parte de la memoria presentada, se muestran los resultados más relevantes de los estudios de durabilidad, reproducibilidad y respuesta electroquímica de un sistema SOFC optimizado.

Summary

The investigation of cathode-interconnect contact materials to improve the electrons flow in a solid oxide fuel cell (SOFC), is necessary for sustainable energy production. This study can make these devices more attractive to Horizon 2020 program, the European Union Framework Programme for Research and Innovation (2014-2020).

The use of metallic alloys as interconnect material, reduces the operating temperature of SOFCs, increasing their durability and applicability. However, they present as a new challenge the development of contact materials with an adequate microstructure and properties.

This work shows the development of interconnect-contact coating-cathode type structures. Different contact layer starting materials, allowed the identification of key properties which determine the behaviour of the contact materials.

Starting experiments have been carried out using Crofer22APU metallic plane substrate, $La_{0.6}Sr_{0.4}FeO_3$ (LSF) ceramic cathode, and three perovskite-type mixed oxides as contact coatings: $LaNi_{0.6}Fe_{0.4}O_{3-\delta}$ (LNF), $LaNi_{0.6}Co_{0.4}O_{3-\delta}$ (LNC) and $(La_{0.8}Sr_{0.2})_{0.95}Fe_{0.6}Mn_{0.3}Co_{0.1}O_3$ (LSFMC). The most adequate contact layers have been selected based on the characterization of the initial materials, and the diffusion and/or reaction processes occurring at interconnect-contact coating-cathode interfaces, derived from the study of structural, microstructural, spectroscopic and electrochemical properties.

The use of a channel interconnect, which allows the transport of gases in a real system, has led to the development and optimization of a new interconnect-cathode contact system. Hence, previously selected contact materials were applied onto Fe-22Cr mesh squares by dipping them into the prepared ceramic slurries, thus obtaining a new metallic/ceramic contact composite.

Long-term stability tests as well as electrochemical behavior, at 800 ºC, of interconnect-composite structures, have shown an adequate structural integrity of the cell and high electrical conductivity through the interconnect-composite interface.

Femtosecond laser machined holes have been produced in the composite and then, cathode is deposited to form a new interconnect-contact coating-cathode structure. Thus, the development of a more real system is achieved, ensuring rapid oxidant gases transfer through interconnect-electrode interface, without compromising the contact resistance of the system. The last part of this work includes the most relevant results of the newly developed cell, emphasizing in the reproducibility of the final cell fabrication procedure and the durability and electrochemical behaviour.

Índice/Index

1. INTRODUCCIÓN / INTRODUCTION

- Contexto energético global / The global energy context
- Pilas de combustible / Fuel cells
- Pilas de combustible de óxido sólido / Solid oxide fuel cells
- Retos para las celdas SOFC / Challenges of SOFCs
  - Capas de contacto / Contact coatings
- Materiales empleados en este estudio / Materials used in this study
- Objetivos / Objetives
- Visión global de los hallazgos / Overview of findings

1.1. Contexto energético global / The global energy context

La elevada concentración de dióxido de carbono (CO_2) atmosférico está relacionada con el calentamiento global y el efecto invernadero. Las emisiones de CO_2, producidas principalmente a partir de la actividad humana, son actualmente más altas que en cualquier momento de nuestra historia. La Figura 1.1 muestra el crecimiento histórico de las emisiones de CO_2 en todo el mundo. En este sentido, a nivel mundial, el uso de combustibles fósiles ha sido la principal fuente de energía en el año 2013 (Figura 1.2a). Asimismo, la Figura 1.2b muestra los datos reales de consumo energético y el previsto hasta el 2040, evidenciando que continuará creciendo en un futuro cercano. Puesto que el consumo de combustibles fósiles sigue siendo la principal fuente de energía, mientras continúe incrementándose la demanda energética mundial, continuará el aumento de las emisiones de CO_2. Éste es un tema importante a tratar dentro del debate del cambio climático global[1-5].

Carbon dioxide (CO_2) emissions, which mainly reflect energy related human activities, are now higher than at any point in our history. Figure 1.1 shows the historical growth in CO_2 emissions throughout the world. The use of fossil fuels continues to dominate the global energy sector (Figure 1.2a). Thus, these global CO_2 emissions will continue to increase since world energy consumption is expected to rise (Figure 1.2b). Hence, energy consumption is an important issue of the global climate change debate[1-5].

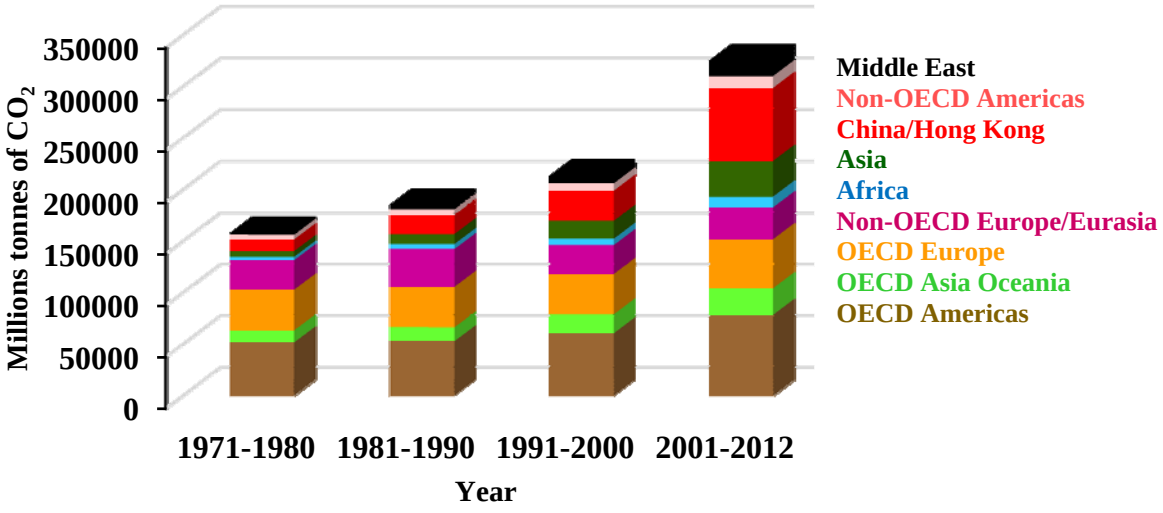

Figura 1.1. / Figure 1.1. Emisiones de CO_2 acumuladas entre 1971 y 2012[6]. / The cumulative CO_2 emissions from 1971 until 2012[6].

---

1 Singh S., Kennedy C. Estimating future energy use and CO_2 emissions of the world´s cities. *Environ. Pollut.* http://dx.doi.org/10.1016/j.envpol.2015.03.039.

2 Soimakallio S., Saikku L. CO_2 emissions attributed to annual average electricity consumption in OECD (the Organisation for Economic Co-operation and Development) countries. *Energy* 38(1) (**2012**) 13-20.

3 Akhmat G., Zaman K., Shukui T., Sajjad F. Does energy consumption contribute to climate change? Evidence from major regions of the world. *Renew. Sust. Energ. Rev.* 36 (**2014**) 123-134.

4 Azhar-Khan M., Zahir-Khan M., Zaman K., Naz L. Global estimates of energy consumption and greenhouse gas emissions. *Renew. Sust. Energ. Rev.* 29 (**2014**) 336-344.

5 Girod B., Van-Vuuren D.P., Hertwich E.G. Climate policy through changing consumption choices: Options and obstacles for reducing greenhouse gas emissions. *Global Environ. Chang.* 25 (**2014**) 5-15.

6 http://www.iea.org/publications/freepublications/publication/co2-emissions-from-fuel-combustion-highlights-2014.html. CO_2 Emissions from fuel combustion, IEA, **2014**.

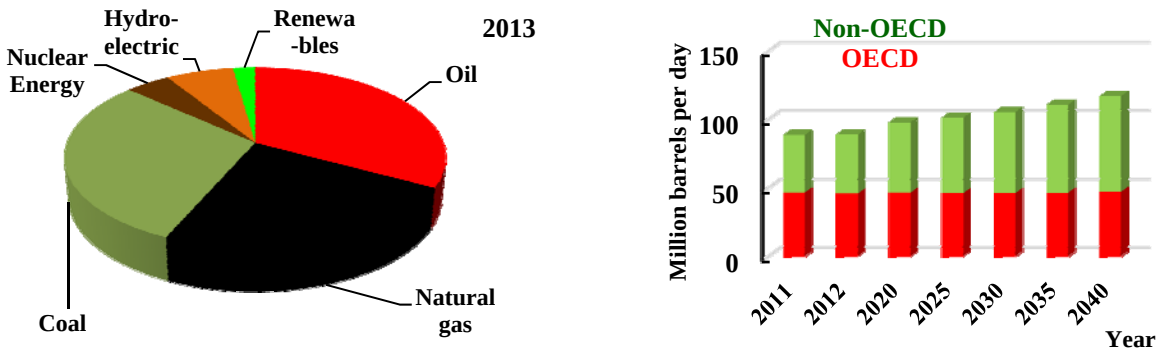

(a) (b)

Figura 1.2. / **Figure 1.2.** (a) Consumo global de energía primaria, en 2013, a partir del combustible utilizado[7], y (b) consumo de energía mundial entre 2011 y 2040[8]. / (a) World primary energy consumption by fuel type in 2013[7], and (b) global energy consumption between 2011 and 2040[8].

Se necesita un cambio a un modelo energético seguro y competitivo[9] que satisfaga nuestras futuras necesidades energéticas. En este sentido, los estudios realizados sobre las reservas de petróleo entre 2012 y 2013 (Figura 1.3) indican que, probablemente, estemos en el pico alto de extracción de petróleo, o al menos cerca. Este pico es el punto en el que la producción mundial de petróleo alcanza su nivel máximo a partir del cual su obtención disminuye (Hubbert 1971; Bowden 1985)[10].

Considering the expected energy growth trend, a secure and competitive energy supply will be a key challenge to meet our future energy requirements[9]. Moreover, the proved reserves of oil between 2012 and 2013 (Figure 1.3) indicate that we are probably in the peak oil today, or at least close. Peak oil is the point at which the global output of conventional oil reaches its maximum level and subsequently flow rates decrease (Hubbert 1971; Bowden 1985)[10].

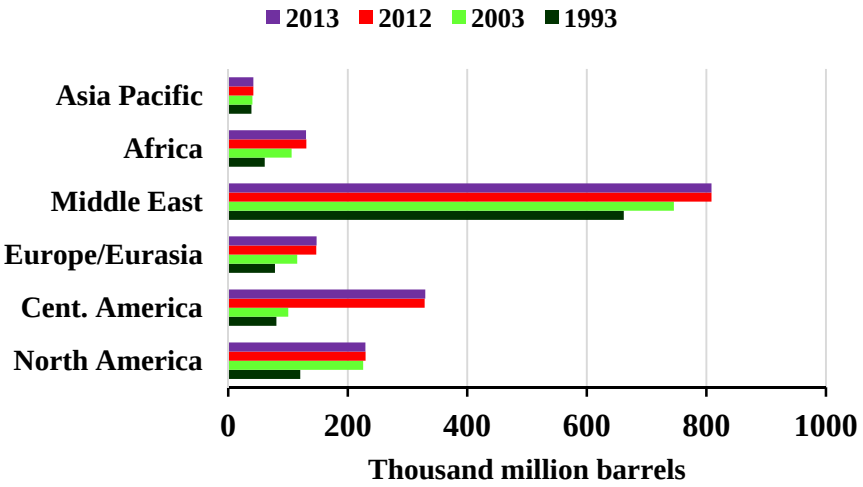

Figura 1.3. / **Figure 1.3.** Reservas de petróleo[7]. / Oil proved reserves[7].

[7] http://www.bp.com/statisticalreview. BP Statistical review of world energy June 2014.

[8] Conti J.J., Holtberg P.D. The *Annual Energy Outlook 2014* (AEO2014), U.S. Energy Information Administration (EIA).

[9] Abas N., Kalair A., Khan N. Review of fossil fuels and future energy technologies. *Futures*. doi:10.1016/j.futures.2015.03.003.

[10] Chapman I. The end of peak oil? Why this topic is still relevant despite recent denials. *Energ. Policy* 64 (**2014**) 93-101.

Para China, Irán y la India se ha registrado, en los últimos veintidós años, un aumento en las emisiones de CO_2 (Figura 1.4). Por el contrario, Rusia, Alemania y Reino Unido han mostrado una reducción del gas de efecto invernadero (GEI), debida, principalmente, a su política energética y el desarrollo de códigos de energía efectivos, tales como las altas inversiones realizadas en energías renovables[11]. En este contexto, se incluye la estrategia Europa 2020[12] (una estrategia para el crecimiento inteligente, sostenible e integrador) que, en el ámbito clima/energía, propone alcanzar, para el año 2020, los siguientes objetivos: (i) reducir las emisiones de gases de efecto invernadero en, al menos, un 20%, (ii) aumentar en un 20% el consumo total de fuentes energéticas renovables, (iii) alcanzar una eficiencia energética del 20%. Una de las principales vías para lograr los objetivos propuestos, es el programa "Horizonte 2020"[13,14], siendo éste, el mayor programa de investigación e innovación de la UE durante el periodo 2014 a 2020 [15].

Figure 1.4 depicts the increases in CO_2 emissions in the last twenty-two years of China, Iran and India. In contrast, Russia, Germany and the UK all had greenhouse-gas (GHG) reductions. The reason for this decrease are the energy policy and the effective building energy codes, such as high levels of investment in renewable energy[11]. In this context, according to the Europe 2020[12] program (a European strategy for smart, green and inclusive growth), the climate and energy aims that must be achieved, by 2020, are: (i) the reduction of greenhouse gas emissions by at least 20 %, (ii) a share of final energy consumption coming from renewable energy sources increased to 20 %, and (iii) an energy sufficiency of 20 %. One of the main instruments to achieve the aforementioned goals is the "Horizon 2020"[13,14] program, the biggest EU research and innovation program over the period 2014 to 2020 [15].

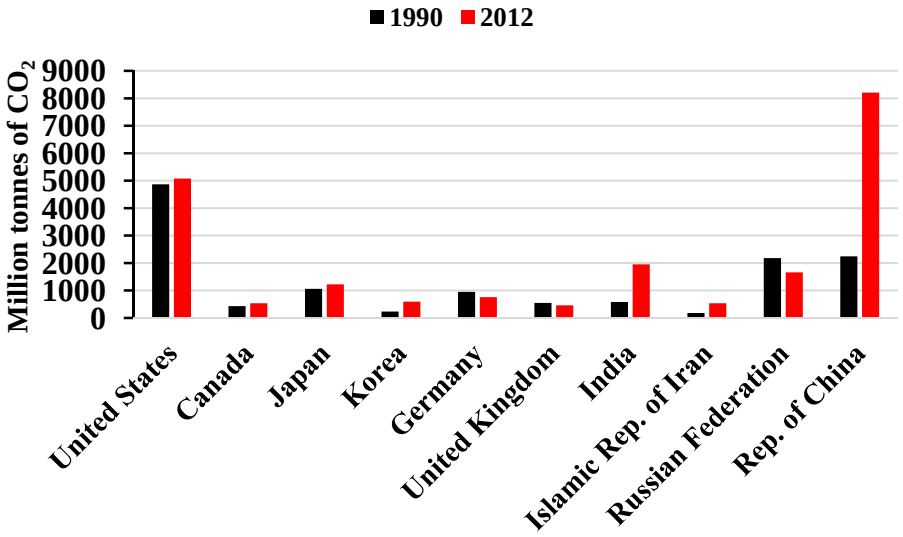

Figura 1.4. / Figure 1.4. Comparación entre los principales diez países emisores de CO_2, entre 1990 y 2012[16]**. /** Comparison of fuel combustion CO_2 emissions of the top ten emitters between 1990 and 2012[16].

[11] Nejat P., Jomehzadeh F., Taheri M.M., Gohari M., Majid M.Z. Abd. A global review of energy consumption, CO_2 emissions and policy in the residential sector (with an overview of the top ten CO_2 emitting countries). *Renew. Sust. Energ. Rev.* 43 (**2015**) 843-862.

[12] http://ec.europa.eu/europe2020/index_es.htm.

[13] http://www.eshorizonte2020.es/.

[14] http://ec.europa.eu/programmes/horizon2020/.

[15] Specchia S. Fuel processing activities at European level: A panoramic overview. *Int. J. Hydrog. Energ.* 39 (**2014**) 17953-17968.

[16] http://www.iea.org/publications/freepublications/publication/co2-emissions-from-fuel-combustion-highlights-2014.html. CO_2 Emissions from fuel combustion, IEA, **2014**.

A día de hoy, existen fuentes alternativas al petróleo, el gas y el carbón, entre las cuales se incluyen: plantas de energía hidroeléctrica y nuclear[17]; energía solar[18], eólica[19], biomasa[20], y las pilas de combustible de hidrógeno[21]; energía de las mareas[22] y geotérmica[23]. Para que se dé una posible transición de la economía actual basada en combustibles fósiles a la del hidrógeno, se necesitan dos elementos clave: (i) la captura y almacenamiento de CO_2 (CAC)[24], y (ii) el empleo de fuentes de energía, libres de carbón, para la producción de combustibles climáticamente neutros. En este sentido, las pilas de combustible y la producción del hidrógeno, a partir de portadores de energía, tienen un papel importante en la futura demanda energética, para aplicaciones móviles, portátiles y estacionarias[25].

There are many alternative sources to fossil fuels: e.g. hydroelectric and nuclear energy plants[17]; solar energy[18], wind power[19], biomass fuel[20] and hydrogen fuel cells[21]; tidal power[22] and geothermal heat[23]. The transition from current fossil-based to hydrogen economy includes two key elements: (i) CO_2 capture and sequestration (CCS)[24] with the utilization of solid carbon or new material alternatives, and (ii) production of carbon-neutral synthetic fuels from bio-carbon and hydrogen generated from water using carbon-free sources. On this point of view, fuel cell (FC) technology and fuel processing (the conversion of energy carriers to a hydrogen gas product) are playing a crucial role in the future energy generation systems for mobile, portable and stationary applications[25].

1.2. Pilas de combustible / Fuel cells

Enmarcada en este contexto, la memoria presentada se centra en las pilas de combustible (FCs), las cuales se basan en la conversión directa de energía química en eléctrica a partir de reacciones electroquímicas entre un combustible y un agente oxidante, sin que medie ningún proceso de combustión. Las relaciones entre los principios de operación de las pilas de combustible y sus principales características se resumen en la Tabla 1.1.

This work is focused on fuel cells (FCs), which are based on the direct conversion of chemical energy into electrical energy via electrochemical reactions between fuel and oxidant, without involving combustion. The relations between fuel cell´s principles of operation and features are summarized in Table 1.1.

---

17 Hong S., Bradshaw C.J.A., Brook B.W. Global zero-carbon energy pathways using viable mixes of nuclear and renewables. *Appl. Energ.* 143 (**2015**) 451–459.

18 Tsalikis G., Martinopoulos G. Solar energy systems potential for nearly net zero energy residential buildings. *Sol. Energy* 115 (**2015**) 743–756.

19 Tavner P. Wind power as a clean-energy contributor. *Energ. Policy* 36(12) (**2008**) 4397–4400.

20 Srirangan K., Akawi L., Moo-Young M., Chou C.P. Towards sustainable production of clean energy carriers from biomass resources. *Appl. Energ.* 100 (**2012**) 172–186.

21 Stambouli A.B. Fuel cells: The expectations for an environmental-friendly and sustainable source of energy. *Renew. Sust. Energ. Rev.* 15(9) (**2011**) 4507–4520.

22 Ramos V., Carballo R., Álvarez M., Sánchez M., Iglesias G. A port towards energy self-sufficiency using tidal stream power. *Energy* 71 (**2014**) 432–444.

23 Li K., Bian H., Liu C., Zhang D., Yang Y. Comparison of geothermal with solar and wind power generation systems. *Renew. Sust. Energ. Rev.* 42 (**2015**) 1464–1474.

24 Echevarria-Huaman R.N., Xiu-Jun T. Energy related CO_2 emissions and the progres son CCS projects: A review. *Renew. Sust. Energ. Rev.* 31 (**2014**) 368-385.

25 Lee Y.D., Ahn K.Y., Morosuk T., Tsatsaronis G. Environmental impact assessment of a solid-oxide fuel-cell-based combined-heat-and-power-generation system. *Energy* 79 (**2015**) 455-466.

Tabla 1.1. Resumen que relaciona los principios de las pilas de combustible con sus características[26] más relevantes.

Principios de operación	Características
Conversión de energía electroquímica en electricidad.	Alta eficiencia y alta densidad de energía; se reducen los GEI* y el ruido.
Mientras haya suministro de combustible y de un agente oxidante las pilas operan de manera continua.	Largos ciclos de operación.
Disposición de celdas formando un "stack".	Carácter modular.
Funcionan mejor con hidrógeno.	Se reducen los GEI.
Reformado interno de hidrocarburos.	Flexibilidad del combustible.

* Gases de efecto invernadero.

Table 1.1. Outline of the relations between a fuel cell´s principles of operation and features[26].

Principles of operation	Features
Electrochemical energy conversion.	High efficiency and energy density; reduced GHG* and noise.
Runs as long as fuel is supplied.	Long operational cycles.
Expansion by adding cells to a stack.	Modularity.
Runs best on pure hydrogen.	Reduced GHG.
Fuel reformation fuelling option.	Fuel flexibility.

* Greenhouse-gases.

La estructura básica de una pila de combustible consiste en un electrodo negativo (ánodo) y un electrodo positivo (cátodo) conectados a través de un circuito externo, y separados mediante un material aislante electrónico que permite el transporte de especies iónicas (electrolito). Los electrodos tienen una microestructura porosa y son permeables a los gases, con el fin de permitir la difusión de los reactivos. Tal y como se muestra en la Figura 1.5, en el ánodo, el combustible (hidrógeno molecular) se oxida dando lugar a protones (H^+) y electrones (e^-). Los iones hidrógeno migran a través del electrolito mientras que los electrones circulan a través del circuito externo hasta el cátodo. En éste, los electrones y los protones reaccionan en presencia del gas oxidante, y se produce agua y una cantidad importante de energía térmica[27,28].

The basic structure of a fuel cell consists of a fuel electrode (anode) and an oxidant electrode (cathode) which are connected via external circuit and are separated by an ion-conducting material (electrolyte). The electrodes have a porous structure and are gas permeable to allow diffusion of reactant. Molecular hydrogen (H_2) is delivered from a gas flow stream to the anode where it react electrochemically: the H_2 is oxidized to produce hydrogen ions (H^+) and electrons (e^-). These hydrogen ions migrate through electrolyte while the electrons are forced through an external circuit to cathode. At the cathode, the electrons and hydrogen ions react with the oxygen supplied from an external gas-flow stream to form water and heat[27,28], as shown in Figure 1.5.

[26] Sharaf O.Z., Orhan M.F. An overview of fuel cell technology: Fundamentals and applications. *Renew. Sust. Energ. Rev.* 32 (**2014**) 810-853.
[27] EG&G Technical Services, Fuel Cell Handbook, 7th ed., Morgantown, Department of Energy, USA, **2004**.
[28] Minh N.Q. Ceramic fuel cells. *J. Am. Ceram. Soc.* 76(3) (**1993**) 563-588.

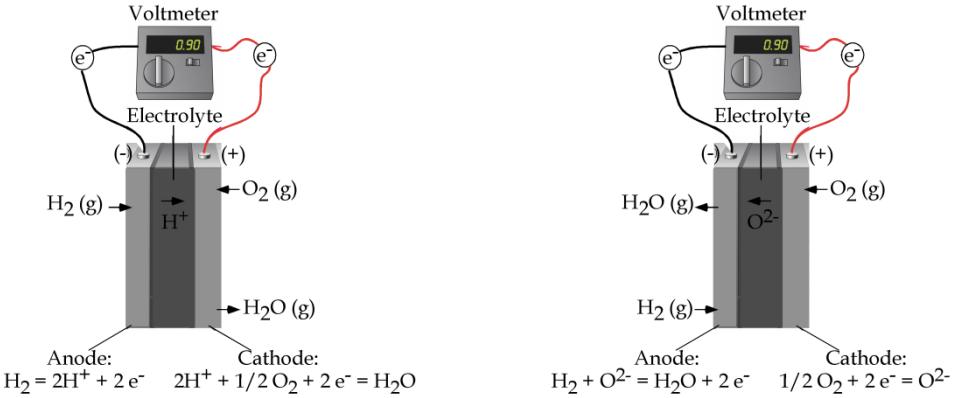

Figura 1.5. / **Figure 1.5.** Principios de funcionamiento de las celdas de combustible utilizando: (a) un electrolito ácido (conductor de iones positivos, H^+), y (b) un electrolito básico (conductor de aniones, OH^-, CO_3^{2-}, O^{2-}). / Working principle of fuel cell using: (a) a proton conducting electrolyte, and (b) an oxygen ion conducting electrolyte.

Termodinámica[29]**:** La reacción global en una pila de combustible produce agua, calor (Q_{heat}), y un trabajo eléctrico, W_{ele}, descrita en la ecuación 1.1:

Thermodynamics[29]**:** The overall reaction in the fuel cell produces water, heat (Q_{heat}), and electrical work (W_{ele}) as equation 1.1:

$$H_2 + ½\ O_2 \leftrightarrow H_2O + W_{ele} + Q_{heat} \qquad (1.1)$$

El trabajo eléctrico realizado por la celda corresponde a la cantidad de electricidad transferida cuando ocurre la reacción 1.2:

The electrical work being done by the cell correspond to the amount of electricity transferred when reaction (1.2) occurs:

$$-W_{ele} = N \cdot F \cdot E \qquad (1.2)$$

donde N es el número de electrones transferidos cuando el combustible se oxida, F es la constante de Faraday (96.6 kJ/mol), y E es el voltaje de la celda (la diferencia de potencial entre las terminales de una celda). El signo negativo indica que el sistema realiza el trabajo. Así, las reacciones son termodinámicamente favorables cuando existe una diferencia de potencial químico entre los reactivos y los productos, mientras que la difusión de iones óxido a través de la celda se da por la diferencia de presión parcial del oxígeno entre los dos lados de la celda. Esta diferencia de potencial químico se puede convertir en un potencial eléctrico E(V) mediante la ecuación de Nernst (1.3):

where N is the number of electrons transferred when fuel is oxidized, F is the Faraday constant (96.6 kJ/mol) and E is the cell voltage (the potential difference between the two electrode terminals of the operating cell). The negative sign indicates that work is being done by the system. Thus, the reactions are driven thermodynamically by the difference in chemical potential between the reactants and products, whereas the diffusion of oxide ions through the cell is driven by the

[29] http://www.springer.com/978-1-84996-027-4 (Chapter 2: Thermodynamics of Fuel Cells), **2011**.

difference in oxygen partial pressure between the two sides of cells. The difference in chemical potential can be converted into an electric potential by the Nernst equation (1.3):

$$E = E^{o} - (RT/NF)\cdot \ln [P_{H2O}/(P_{H2}\cdot P_{O2}^{1/2})] \qquad (1.3)$$

donde Eº es el potencial redox estándar, R es la constante de gases (8.31 J/kmol), F es la constante de Faraday, N es el número de electrones involucrados, T es la temperatura (K), y P es la presión parcial de cada uno de los gases (atm.): H_2O, O_2 y H_2 (productos y reactivos). A través de la ecuación de Nernst (1.3) se puede evaluar el efecto en el voltaje de la celda de: (i) cambios en las presiones parciales de cada componente, y (ii) cambios en la temperatura de funcionamiento. El potencial de Nernst, E, es el que corresponde al potencial ideal de una celda. Este potencial establece el límite o rendimiento máximo que se puede alcanzar con una celda de combustible. En general, nunca se llega a obtener el máximo ideal debido a las diferentes variables que intervienen en el sistema. La importancia de cada una de estas variables en una determinada celda, se puede determinar a partir de las denominadas curvas V-I en las que para diferentes densidades de corriente se evalúa la caída de voltaje (Figura 1.6). Estas caídas de tensión se clasifican en tres grupos: (i) las pérdidas por polarización de activación que se producen debido a reacciones electroquímicas que son muy lentas y requieren una cierta energía de activación para que se produzcan. Incluyen la actividad catalítica de los electrodos y de la resistencia a las reacciones electroquímicas, (ii) las pérdidas por polarización óhmica, las cuales se deben a resistencias eléctricas asociadas a los electrodos, electrolito e interconectores y a las resistencias de contacto en las intercapas correspondientes, y (iii) las pérdidas relacionadas con procesos de transporte, que se producen por limitaciones en los procesos de adsorción y desorción de los reactivos y productos. Están directamente relacionadas con la densidad de corriente, la actividad de los reactivos, y la microestructura de los electrodos. Dentro de estas pérdidas se incluyen los procesos de difusión o transporte de gas[30,31].

where Eº is standard cell potential, R is the gas constant (8.31 J/kmol), F is the Faraday constant, N is the number of electrons involved, T is the temperature (K) and P is the partial pressure (atm) of H_2O, O_2 and H_2 gases. The Nernst equation (1.3) is used to evaluate the effect of changes in reactant or product partial pressures and temperature, on the cell voltage. The Nernst potential, E, gives the ideal equilibrium cell potential, which sets the upper limit or maximum performance achievable by a fuel cell. A normal situation for fuel cells is shown in Figure 1.6, in which there is an initial exponential fall in voltage with current, followed by a linear decrease. These losses are so-called polarisation and result from three sources: (i) activation losses, (ii) ohmic losses and (iii) mass transport losses. The initial fall is associated with slow electrochemical reactions at the electrode surface that leads to activation polarisation and depends on the current density. The origin of the ohmic losses is the resistance to the flow of ions in the electrolytes and flow of the electrons in the electrodes and in their contact interfaces. The mass transport polarisation is related with the diffusion of the reactant species through the electrodes, inherent to the electrode materials and microstructure[30,31].

---

[30] Otaegui-Ameztegui L. Desarrollo de celdas de combustible tipo SOFC tubulares de soporte metálico. Ph.D. thesis work, Universidad de Navarra, **2013**.

[31] Vidal-Garcia K. Perovskitas $AFeO_3$ para cátodos SOFC. Efecto de los parámetros que controlan la posición A en sus propiedades. Ph.D. thesis work, UPV/EHU, **2008**.

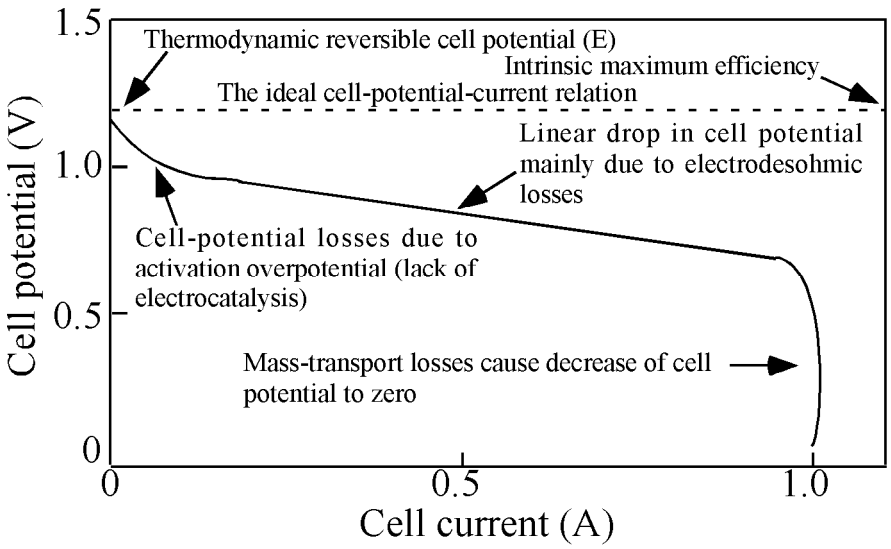

Figura 1.6. / **Figure 1.6.** Representación típica del voltaje de una pila de combustible con la variación de la densidad de corriente (Curva V-I)[32]. / Ideal situation in open-circuit voltage and voltage under current for a fuel cell[32].

Historia: El descubrimiento de las pilas de combustible se remonta al año 1839, cuando C.F. Schönbein (1799-1868) establece los primeros fundamentos de la reacción de electrolisis inversa, y ese mismo año, Sir William Grove (1811-1896) construyó un prototipo de pila de combustible, que él denomina, "batería de gas". En 1896, William W. Jacques (1855-1932) desarrolló la primera pila de combustible para uso doméstico. En 1900, Walther Nernst (1864-1941) dedujo la ley termodinámica que rige el principio de funcionamiento de las celdas de combustible, y fue el primero en usar zirconia como un electrolito sólido. Asimismo, en 1921, Emil Baur (1873-1944) construyó la primera pila de combustible de carbonato fundido (MCFC). Unos años más tarde, en 1937, E. Baur también desarrolló el primer dispositivo basado en una pila de combustible de óxido sólido (SOFC). Durante la Segunda Guerra Mundial (1939-1945), Francis Thomas Bacon (1904-1992) trabajó en pilas de combustible para submarinos de la Marina Real Británica. En 1960, la Administración Nacional de la Aeronáutica y del Espacio (NASA) empezó a utilizar las pilas de combustible alcalinas (AFC) para producir tres subproductos útiles en vuelos espaciales: (i) la electricidad para alimentar las naves espaciales, (ii) el agua para beber y para la refrigeración de los equipos, y (iii) el calor para evitar la congelación de los astronautas. Como consecuencia de la primera crisis del petróleo (1973), aumentó el interés en el desarrollo en pilas de combustible para aplicaciones industriales y domésticas. Hoy en día, las pilas de combustible tienen una amplia gama de aplicaciones. Éstas se pueden clasificar en tres grupos principales: (i) transporte (ii) estacionarias, y (iii) portátiles[33]. La Tabla 1.2 muestra un esquema cronológico de la historia de las pilas de combustible en los siglos XIX y XX.

[32] Hamnett A. The components of an electrochemical cell, in Handbook of Fuel Cells- Fundamentals, Technology and Applications (eds. Vielstich W., Lamm A, Gasteiger H.A.), John Wiley & Sons, New Jersey, USA, p. 3-12, **2003**.

[33] Perry M.L., Fuller T.F. A Historical perspective of fuel cell technology in the 20th century. *J. Electrochem. Soc.* 149(7) (**2002**) S59-S67.

History: Research and development that eventually led to a functional fuel cell goes back to the early 1800s. In 1839 the first fuel cell device was invented by Sir William Grove (1811-1896), which took hydrogen and oxygen, and produced small amounts of electricity as well as water. In 1896, William W. Jacques (1855-1932) developed the first fuel cell for household use. At the turn of the century, Wlather Nernst (1864-1941) deduced the thermodynamic law that describes principles of operation for a fuel cell, and he was also the first to use zirconia as a solid electrolyte. Additionally, in 1921, Emil Baur (1873-1944) constructed the first molten carbonate fuel cell (MCFC). A few years later, in 1937, E. Baur also developed the first device based on solid oxide fuel cell (SOFC). During World War II (1939-1945), Francis Thomas Bacon (1904-1992) worked on alkaline fuel cells for British Royal Navy submarines. In 1960, the USA National Aeronautics and Space Administration (NASA) started using alkaline fuel cells (AFC) to produce three useful by-products in spaceflight: i) electricity to power the spacecraft, ii) water for drinking and cooling equipment, and iii) heat to keep the astronauts from freezing. As a consequence of the oil crisis (1973), the impulsion for fuel cell development grew. Today, fuel cells are used in transportation, stationary and portable applications sectors, which are being gradually adopted by the public and private sectors[33]. Table 1.2 highlights the main milestones in the history of fuel cells.

Tabla 1.2. / **Table 1.2.** Los principales sucesos históricos de las pilas de combustible[34]. **/** Main milestones in the history of fuel cells[34].

Año(s) **Year(s)**	**Suceso Histórico** **Milestone**
1800	Sir A. Carliste y W. Nicholson describieron la electrolisis del agua. / Sir A. Carliste and W. Nicholson discovered the decomposition of water into hydrogen and oxygen using electricity (water electrolysis).
1839	Sir W.R. Grove inventó la primera pila de combustible (batería de gas) mientras que C.F. Schönbein descubrió los primeros fundamentos de las mismas. / Sir W.R. Grove invented the first fuel cell (gas battery) while C.F. Schönbein discovered the principle of a fuel cell.
1889	L. Mond y C. Langer desarrollaron una matriz para contener el electrolito líquido e introdujeron catalizadores de platino negro en polvo. / L. Mond and C. Langer developed a matrix that was able to contain the liquid electrolyte and introduced the platinum black catalysts.
1893	F.W. Ostwald describió el rendimiento teórico de una pila de combustible y determinó experimentalmente la interconexión de varios componentes de una pila. / F.W. Ostwald theoretically explained the processes taking place in a fuel cell and described the functions of different components.
1896	W.W. Jacques construyó la primera pila de combustible con aplicaciones prácticas. / W.W. Jacques builds the first fuel cell with a practical application.
1900	W. Nernst desarrolló electrolitos sólidos basados en zirconia. / W. Nernst developed zirconia-based solid electrolyte.
1921	E. Baur construyó la primera pila de combustible de carbonato fundido. / E. Baur built the first molten carbonate fuel cell.
1930s	E. Baur experimentó con electrolitos de óxido sólido a alta temperatura. / E. Baur experimented with solid oxide electrolytes at high temperature.
1933-1959	F.T. Bacon desarrolló la tecnología AFC. / F.T. Bacon developed AFC technology.

[34] Sharaf O.Z., Orhan M.F. An overview of fuel cell technology: fundamentals and applications. *Renew. Sust. Energ. Rev.* 32 (**2014**) 810-853.

Tabla 1.2 cont. / **Table 1.2 cont.** Los principales sucesos históricos de las pilas de combustible[34]. / Main milestones in the history of fuel cells[34].

Año(s) Year(s)	Suceso Histórico Milestone
1937-1939	E. Baur y H. Preis desarrollaron la tecnología SOFC. / E. Baur and H. Preis developed SOFC technology.
1955-1958	T. Grubb y L Niedrach de la General Electric desarrollaron la tecnología PEMFC. / T. Grubb and L. Niedrach developed PEMFC (Proton Exchange Membrane Fuel Cell) technology at General Electric.
1958-1961	G.H.J. Broers y J.A.A. Ketelaar desarrollaron la tecnología MCFC. / G.H.J. Broers and J.A.A. Ketelaar developed MCFC technology.
1960	La NASA utilizó la tecnología AFC, basada en el trabajo de Bacon, en el programa Apolo. /NASA used AFC technology based on Bacon´s work in its Apollo space program.
1961	G.V. Elmore y H.A. Tanner desarrollaron la tecnología PAFC. / G.V. Elmore and H.A. Tanner experimented with and developed PAFC (Phosphoric Acid Fuel Cell) technology.
1962-1966	Las PEMFC desarrolladas por General Electric se utilizaron en el programa Gemini (NASA). / The PEMFC developed by General Electric was used in NASA´s Gemini space program.
1992	Jet Propulsion Laboratory desarrolló la tecnología DMFC. / Jet Propulsion Laboratory developed DMFC (Direct Metanol Fuel Cell) technology.
1990s	Investigación, a nivel mundial, de las pilas de combustible, enfocado en las PEMFCs. / Worldwide researched on all fuel cell types with a focus on PEMFCs.
2000s	Comercialización de las pilas de combustible. / Early commercialization of fuel cells.

Tipos: La clasificación más común de las celdas de combustible se basa en el tipo de electrolito utilizado. En este sentido, las pilas de combustible se pueden clasificar en: (i) pilas de combustible alcalinas (AFM), (ii) pilas de combustible de membrana polimérica (PEMFC), (iii) pila de combustible de metanol directo (DMFC), (iv) pilas de combustible de carbonatos fundidos (MCFC), (v) pilas de combustible de ácido fosfórico (PAFC), y (vi) pilas de combustible de óxido sólido (SOFC)[35]. Las pilas de combustible de baja e intermedia temperatura (PEMFC, PAFC y AFC) muestran un rápido arranque, característica que hace interesante el uso de estas pilas en sistemas eléctricos móviles y portátiles. Sin embargo, éstas presentan, principalmente, dos inconvenientes: (i) el electrodo necesita que la electroactividad del catalizador sea estable con el tiempo, y (ii) el uso de metales preciosos como catalizador aumenta el coste de estos dispositivos. Las bajas temperaturas de operación, en estas celdas, contribuyen también a una baja tolerancia a las impurezas. Por otra parte, las pilas de combustible de carbonatos fundidos y de óxido sólido son de alta temperatura, apropiadas para sistemas de cogeneración y ciclos combinados (Tabla 1.3).

Types: Fuel cells are generally classified according to their electrolyte material; the principal ones include the alkaline fuel cell (AFC), proton exchange membrane fuel cell (PEMFC), direct methanol fuel cell (DMFC), molten carbonate fuel cell (MCFC), phosphoric acid fuel cell (PAFC), and solid oxide fuel cell (SOFC)[35]. Low- and medium-temperature operation fuel cells (PEMFC, PAFC and AFC) show a fast start-up time, which gives a great potential for mobile and portable electrical systems. However, the electrode requires a stable electroactivity of the catalyst with time, and in addition, the use of precious metal as catalyst raises the cost of the device. Moreover, they have low tolerance to impurities. On the other hand, molten carbonate and solid oxide fuel cells are high temperature fuel cells appropriate for cogeneration and combined cycle systems (Table 1.3).

[34] Sharaf O.Z., Orhan M.F. An overview of fuel cell technology: fundamentals and applications. *Renew. Sust. Energ. Rev.* 32 (**2014**) 810-853.

[35] Larminie J.C., Dicks A., Fuel Cell System Explained, John Wiley & Sons Ltd., New York, p. 1-24, **2003**.

Tabla 1.3. Características generales de los distintos tipos de pilas de combustible, clasificadas en función del electrolito[36].

Tipo de celda	PEMFC	AFC	PAFC	MCFC	DMFC	SOFC
Electrolito	Ácido sulfónico incorporado en una membrana polimérica.	• Disolución acuosa de KOH. • Membrana de intercambio iónico (AEM).	H_3PO_4 líquido en SiC.	Li_2CO_3,Na_2CO_3, K_2CO_3 líquido en $LiAlO_2$.	Ácido sulfónico incorporado en una membrana polimérica.	Zirconia estabilizada con itria (YSZ).
Ánodo/ cátodo/ interconector	Pt-carbón. Pt-carbón. Grafito.	Níquel. Ag-carbón. Hilos metálicos.	Pt-carbón. Pt-carbón. Grafito.	NiCr. Óxido de níquel litiado. Acero inoxidable.	Pt/Ru-carbón. Pt-carbón. Grafito.	Ni-YSZ. LSM. Cerámico/metálico.
Portador de carga	H^+	OH^-	H^+	CO_3^{2-}	H^+	O^{2-}
Temperatura de operación (ºC)	60-80	Bajo cero-230	160-220	600-700	25-110	500-1000
Ventajas	• Estructura compacta. • Arranque rápido. • Baja corrosion.	• Cinética de reducción rápida. • Flexibilidad de catalizador. • Amplio intervalo de temperaturas de operación.	• Buena tolerancia a contaminantes. • Cogeneración de alta eficiencia. • Gestión del agua simple.	• Flexibilidad de combustibles. • Posibilidad de reformado interno. • Alta tolerancia a contaminantes. • Cogeneración de alta eficiencia.	• Tamaño compacto. • Sistema simple. • Fácil almacenamiento y transporte de combustible.	• Alto rendimiento eléctrico. • Cogeneración de alta eficiencia. • Eliminación de problemas con el electrolito. • Flexibilidad de combustibles.
Retos	• Catalizadores caros. • Alta sensibilidad a contaminantes.	• Alta sensibilidad a contaminantes. • Baja densidad de energía. • Electrolito altamente corrosivo.	• Arranque lento. • Baja corriente y potencia. • Electrolito corrosivo. • Sistema voluminoso.	• Arranque lento. • Corrosión del electrolito y partes metálicas. • Requiere entrada de CO_2. • Cruce del aire.	• Cinética del ánodo lenta. • Falta de catalizadores para la oxidación directa de CH_3OH. • Cruce del agua y combustible.	• Arranque lento. • Requisitos estrictos para los materiales. • Alto estrés térmico. • Problemas de durabilidad.
Rendimiento eléctrico (%)	40-60	60-70	36-45	55-65	36-60	65-85

[36] Sharaf O.Z., Orhan M.F. An overview of fuel cell technology: Fundamentals and applications. *Renew. Sust. Energ. Rev.* 32 (**2014**) 810-853.

Table 1.3. Main characteristic of fuel cell types according to electrolyte[36].

Fuel cell type	PEMFC	AFC	PAFC	MCFC	DMFC	SOFC
Electrolyte	Sulphonic acid incorporated into a solid membrane.	• KOH water solution. • Anion exchange membrane (AEM).	Liquid H_3PO_4 in SiC.	Liquid Li_2CO_3,Na_2CO_3, K_2CO_3 in $LiAlO_2$.	Sulphonic acid incorporated into a solid membrane.	Solid yttria-stabilized zirconia (YSZ).
Anode/ cathode/ interconnect	Pt-carbon. Pt-carbon. Graphite.	Nickel. Ag-carbon. Metallic wires.	Pt-carbon. Pt-carbon. Graphite.	NiCr. Lithiated NiO. Stainless steel.	Pt/Ru-carbon. Pt-carbon. Graphite.	Ni-YSZ. LSM. Ceramic/metallic.
Charge carrier	H^+	OH^-	H^+	CO_3^{2-}	H^+	O^{2-}
Operation temperature (ºC)	60-80	Below zero-230	160-220	600-700	Ambient-110	500-1000
Advantages	• Compact structure. • Rapid start-up. • Low corrosion.	• Fast reduction reaction kinetics. • Catalyst flexibility. • Wide range of operation temperature.	• Good tolerance to contaminants. • High-grade heat. • Simple water management.	• Fuel flexibility. • Possibility of internal reforming. • High tolerance to contaminants. • High-grade heat.	• Compact size. • Simple system. • Easy fuel storage and delivery.	• High electrical efficiencies. • High-grade heat. • Eliminated electrolyte issues. • Fuel flexibility.
Challenges	• Expensive catalyst. • High sensitivity to contaminants.	• High sensitivity to contaminants. • Low power density. • Highly corrosive electrolyte leads to sealing issues.	• Slow start-up. • Low power density and electrical efficiencies. • Electrolyte acid loss.	• Slow start-up. • Electrolyte and metallic parts corrosion. • CO_2 injection requirement. • Air crossover.	• Poor anode kinetics. • Lack of efficient catalysts for direct oxidation of methanol. • Fuel and water crossover.	• Slow start-up. • Strict material requirements. • High thermal stresses. • Sealing and durability issues.
Electrical efficiency (%)	40-60	60-70	36-45	55-65	36-60	65-85

1.3. Pilas de combustible de óxido sólido / Solid oxide fuel cells

Este trabajo se centra en las pilas de combustible de óxido sólido (SOFCs). Las altas temperaturas de funcionamiento (600-1000 ºC), disminuyen las limitaciones cinéticas en el cátodo, y hacen posible el uso de materiales cerámicos como conductores de iones óxido. Éstos aumentan su conductividad con la temperatura. Además, las SOFCs permiten la conversión de una amplia gama de combustibles y producen una gran cantidad de calor que puede aprovecharse en un proceso de cogeneración, obteniendo un rendimiento del sistema ≥ 80 %. En este sentido, estos dispositivos se utilizan para sistemas de producción combinada de calor y electricidad (CHP) [37].

This work is focused on solid oxide fuel cells (SOFCs). In these devices, operating at a sufficiently high temperature (600-1000 ºC), all kinetics limitations at the cathode disappear, and it also becomes possible to use solid ceramic oxide-ion conductors that show high conductivities with temperature. Moreover, SOFCs operate on a wide variety of fuels and, the generation of high-quality heat and its application in combined heat and power (CHP) co-generation system allow that the overall system efficiency reaches ≥ 80 % [37].

Electrolito: El electrolito es el componente que separa las reacciones anódica y catódica, y transporta los iones de oxígeno del cátodo al ánodo. En las últimas décadas, se han propuesto diversas formulaciones de óxidos como electrolito, con objeto de conseguir materiales que cumplan los siguientes requisitos: (i) elevada conductividad iónica y aislante electrónico; (ii) compatibilidad química y mecánica con los componentes adyacente; (iii) químicamente estable en ambientes oxidantes y reductores; (iv) completamente denso e impermeable al paso de gas; y (v) fabricable en forma de películas delgadas para reducir pérdidas óhmicas y flexibilizar la temperatura de operación[37,38].

Electrolyte: The electrolytes are oxygen ion conductors, in which current flow occurs by the movement of oxygen anions through the crystal lattice. During the past decades, many oxide formulations have been studied into improved electrolytes, which must: (i) show high oxygen ion conductivity and minimum electronic conductivity; (ii) have good chemical stability with respect to the electrodes and inlet gases; (iii) be able to be formed into a thin, high density strong film with no gas leaks; and (iv) have a thermal expansion coefficient compatible with the other components[37,38].

Hasta la fecha, el electrolito más utilizado para las SOFCs, que operan a temperaturas ≥ 800 ºC, ha sido la zirconia estabilizada con itria, (YSZ, $(ZrO_2)_{1-x}(Y_2O_3)_x$, ($x \approx 0.08–0.1$)), que presenta una estructura tipo fluorita. Este tipo de estructura favorece la migración de los iones óxido y facilita la creación de vacantes de oxígeno. Asimismo, se han utilizado otros conductores iónicos que muestran también esta estructura, como es la ceria (Ce_2O_3) dopada, que posee una conductividad iónica elevada a temperaturas de operación más bajas (500-700 ºC). Los principales óxidos utilizados como elementos dopantes son el Gd_2O_3, Sm_2O_3 e Y_2O_3 (GDC, SDC e YDC, respectivamente), aumentando la conductividad de los sistemas. Por ultimo, tambien son buenos

[37] Singhal S.C., Kendall K. Introduction to SOFCs, in High temperature solid oxide fuel cells fundamentals, design and applications (eds. Singhal S.C., Kendall K.), Elsevier, Oxford, UK, p. 1-19, **2003**.

[38] Yamamoto O. Low temperature electrolytes and catalysts, in Handbook of Fuel Cells- Fundamentals, Technology and Applications (eds. Vielstich W., Lamm A, Gasteiger H.A.), John Wiley & Sons, New Jersey, USA, p. 1002-1014, **2003**.

conductores de iones de oxígeno, algunos tipos de perovskitas como el galato de lantano, $LaGaO_3$, dopado con Sr y Mg ($La_{1-x}Sr_xGa_yMg_{1-y}O_{3-\delta}$, LSGM) que ha sido más extensamente estudiado. El LSGM, presenta mayor conductividad iónica que la zirconia estabilizada con itria, pero en atmósferas reductoras, se produce la evaporación del galio y los productos formados son incompatibles con el níquel que forma parte del ánodo. Las principales tres regiones de temperatura de operación para las SOFCs son: 500-650 ºC, 650-800 ºC y 800-1000 ºC, correspondientes a electrolitos basados en CeO_2, LSGM y ZrO_2, respectivamente. Cada una de estas regiones requiere el desarrollo de electrodos especificos, optimizados para la temperatura de funcionamiento de la celda[39].

Until now, yttria-stabilised zirconia, ZrO_2 with 8-10 mol %Y_2O_3 (8-10YSZ), possessing the fluorite structure, has been the most favoured electrolyte for SOFCs at temperatures above 800 ºC. Other fluorite structure oxide ion conductors, such as doped ceria (Ce_2O_3), has been proven to operate at reduced temperatures (500-700 ºC) with ionic conductivity values comparable with YSZ at much higher temperatures. Commonly the CeO_2 host is substituted with either Sm, Gd or Y ($Ce_{1-x}Sm_xO_{2-\delta}$, CSO, $Ce_{1-x}Gd_xO_{2-\delta}$, CGO or $Ce_{1-x}Y_xO_{2-\delta}$ CYO), creating significant vacancy concentrations. The final class of `conventional´ electrolyte is based upon the perovskite structures, such as $LaGaO_3$ doped with Sr and Mg ($La_{1-x}Sr_xGa_yMg_{1-y}O_{3-\delta}$, LSGM). Levels of conductivity reported for these materials were higher than the YSZ, in the 600-750 ºC temperature range. There are three main operating conditions for SOFCs: 500-650 ºC, 650-800 ºC and 800-1000 ºC, corresponding to CeO_2-based, LSGM-based and ZrO_2-based electrolytes, respectively. Each of these ranges required the development of specific electrodes optimised for the operating temperature[39].

Ánodo: En el ánodo o “electrodo de combustible”, es donde el combustible es oxidado por los iones óxido para liberar los electrones que pasan a través de un circuito externo. Los principales requisitos para los materiales ánodo son: (i) elevada actividad electrocatalítica, (ii) elevada conductividad iónica y eléctrica, (iii) estabilidad en atmósferas reductoras, (iv) coeficientes de expansión térmica semejantes con el electrolito y el resto de componentes de la celda, (v) estructura física adecuada para el transporte de combustible, (vi) estabilidad química y mecánica, especialmente en celdas de soporte anódico, (vii) capacidad de producir el reformado de hidrocarburos (si procede), y (viii) estabilidad en presencia de compuestos de azufre[40]. El ánodo más empleado es el cermet Ni/YSZ (mezcla entre una cerámica y un metal); la red cerámica permite adecuar el TEC del ánodo al del electrolito YSZ, y evita la aglomeración de las partículas de níquel. Asimismo, el níquel presenta excelentes propiedades catalíticas para la oxidación del combustible. Además, su microestructura porosa permite extender el TPB (puntos triples de reacción donde se encuentran la molécula O_2, el electrodo y electrolito) en todo el volumen del ánodo (Figura 1.7). En general, el ánodo consiste en un material composite formado por una parte metálica y una cerámica con composición similar al electrolito. Así, como ejemplo, las celdas de soporte electrolito de CGO y LSGM suelen presentar Ni-CGO y Ni-LSGM como materiales ánodo, respectivamente[41].

---

[39] Skinner S.J., Laguna-Bercero M.A. Advanced inorganic materials for solid oxide fuel cells, in Energy Materials (eds. Bruce D.W., O'Hare D., Walton R.I.), John Wiley & Sons, Ltd, Chichester, UK. doi:10.1002/9780470977798. ch2. **2011**.

[40] Brett D.J.L., Atkirson A., Brandon N.P., Skinner S.J., *Chem. Soc. Rev.* 37 (**2008**) 1568-1578.

[41] Wincewicz K.C., Cooper J.S. Taxonomies of SOFC materials and manufacturing alternatives. *J. Power Sources* 140 (**2005**) 280-296.

Anode: The anode requirements are: (i) effective oxidation catalyst, (ii) high electronic conductivity, (iii) stability in the reducing environment, (iii) thermal expansion compatible with the electrolyte and other fuel cell components, (iv) a physical structure offering low fuel transport resistance, (v) chemical and mechanical stability, and (vi) tolerance to sulphur contaminants. The typical anode is Ni/YSZ cermet (i.e., mixture of ceramic and metal), in which the role of zirconia is structural and Ni gives the catalytic activity. Moreover, the porous microstructure of the anode provides the electro-active sites for the electrochemical reactions at the triple phase boundaries (TPBs: meeting point of gas phase, ionic phase and electronic phase) as shown in Figure 1.7. In general, the anode is a composite material consisting of a metallic component mixed with the ceramic electrolyte composition. Hence, for YSZ-based cells the anode material would typically be of Ni-YSZ composite type. Similarly, for CGO- and LSGM-based cells the composite materials are of the Ni-CGO and Ni-LSGM type, respectively[41].

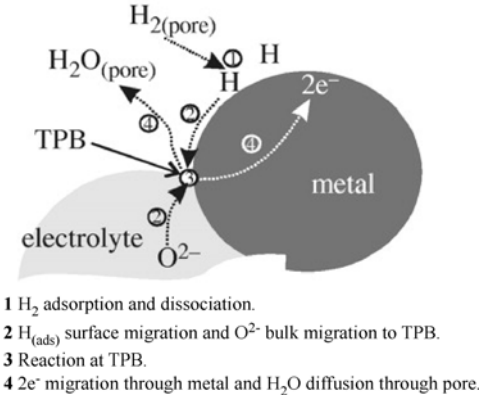

Figura 1.7. / **Figure 1.7.** Representación esquemática del punto triple de reacción en el ánodo (TPB)[42]. / Schematic view of reaction pathway at close-up of anode cermet TPB[42].

Cátodo: En el cátodo o "electrodo de aire", el oxígeno reacciona con los electrones procedentes del exterior, pasando a iones óxido que migran a través del electrolito. Los principales requerimientos de los materiales cátodo son: (i) alta actividad electrocatalítica para la reducción del oxígeno, (ii) elevada conductividad iónica y eléctrica, (iii) estabilidad en atmósferas oxidantes, (iv) estabilidad mecánica, especialmente en celdas de soporte catódico, y (v) compatibilidad química y térmica con el resto de componentes de la celda. Análogamente al ánodo, el cátodo también debe poseer una elevada concentración de puntos triples de reacción (TPB) activos, para que las reacciones electroquímicas no estén únicamente limitadas a la región frontera de tres fases electrolito-gas-electrodo, y así, éstas se extiendan a la estructura interna del cátodo. En este sentido, el cátodo, además de ser un buen conductor mixto, actúa como catalizador para la disociación del oxígeno; su microestructura y composición afecta al tamaño y distribución de los TPB. Diversos autores han recopilado las diferentes perovskitas utilizadas como cátodo hasta la fecha, haciendo hincapié en su conductividad electrónica, y compatibilidad con los componentes adyacentes[43]. En este contexto, las series $Ln_{1-x}M_xMnO_3$, $Ln_{1-x}M_xCoO_3$ y $Ln_{1-x}M_xFeO_3$ han suscitado gran interés debido a su aplicación potencial como materiales cátodo para SOFCs[44].

---

[42] Brandon N.P., Brett D.J. Engineering porous materials for fuel cell applications. *Phil. Trans. R. Soc. A* 364 (**2006**) 147-159.

[43] Sun C., Hui R., Roller J. Cathode materials for solid oxide fuel cells: a review. *J. Solid State Electrochem.* 14 (**2010**) 1125-1144.

[44] Ecija-Verdejo A. Óxidos mixtos tipo perovskita $Ln_{0.5}M_{0.5}FeO_{3-\delta}$ (Ln=La, Sm, Nd, Gd; M=Ba, Sr) para su aplicación como cátodos en pilas SOFC. Ph.D. thesis work, UPV/EHU, **2012**.

Cathode: The cathodes have to possess many properties including: (i) high electrocatalytic activity for oxygen reduction; (ii) high electronic conductivity; and (iii) compatibility with other cell components. The chemical reactions between the electrode, electrolyte and gas phase take place at a limited area (TPB) within the cathode structure. Thus, the electrode material is working as an electronic conductor and oxygen reduction catalyst. Microstructure and composition affects the size and distribution of the TPBs. Several authors have summarised the range of perovskites investigated up to date, focusing on the conductivity, ion transport and compatibility of these materials[43]. In this context, $Ln_{1-x}M_xMnO_3$, $Ln_{1-x}M_xCoO_3$ and $Ln_{1-x}M_xFeO_3$ series have attracted attention due to their potential application as cathode materials for SOFCs[44].

Uno de los materiales más empleados en celdas con electrolito de YSZ, y que operan a temperaturas superiores a 800 ºC, es la manganita de lantano ($LaMnO_3$) dopada con estroncio, así el catión La^{3+} se sustituye por Sr^{2+} generándose el sistema $La_{1-x}Sr_xMnO_3$ (LSM). Estas perovskitas son conductoras electrónicas tipo p, con propiedades eléctricas determinadas, principalmente, por la relación La/Sr. Debido a que éstas son pobres conductoras iónicas, las reacciones electroquímicas están limitadas a la región frontera de tres fases electrolito-gas-electrodo (TPB). La composición exacta de la perovskita también influye en las propiedades químicas del cátodo, afectando, de manera importante, a la compatibilidad química con el electrolito YSZ. Los principales productos de reacción recogidos en la bibliografía, son $La_2Zr_2O_7$ y $SrZrO_3$ [45] para composiciones con bajo y alto contenido en estroncio, respectivamente. La formación de ambos óxidos bloquea la reacción de reducción del cátodo. En este contexto, se utilizan barreras de ceria dopada con samaria, por ejemplo $Ce_{0.8}Sm_{0.2}O_{1.9}$ (SDC), entre el cátodo y electrolito para prevenir las reacciones químicas entre ambos materiales[46].

For high temperature cells, such as those based on YSZ, the most commonly used cathode is Sr doped $LaMnO_3$, forming $La_{1-x}Sr_xMnO_3$ (LSM) system. These perovskites are p-type electronic conductors, and their electrical properties are mainly determined by the La/Sr ratio. Since LSM is a poor ionic conductor, the electrochemical reactions can only occur at electrolyte/cathode interphase. The exact composition of the perovskite also influences on the chemical properties of the cathode, affecting to the chemical compatibility with YSZ electrolyte. Hence, the reactivity of LSM with YSZ to form pyrochlore type products, $La_2Zr_2O_7$ and $SrZrO_3$ [45] for low and high Sr content compositions, respectively, blocks the cathode reduction reactions. Doped ceria barrier layers, such as samarium doped ceria ($Ce_{0.8}Sm_{0.2}O_{1.9}$, SDC), have been widely used between the cathode and electrolyte to prevent the formation of these poorly conducting secondary phases[46].

Aunque el LSM clásico tiene un rendimiento adecuado, a 1000 ºC muestra baja conductividad iónica, lo que conduce a resistencias altas del cátodo a temperaturas inferiores. La conductividad mixta (MIEC), se consigue mediante la mezcla de un material conductor iónico con uno electrónico para crear un composite, o reemplazando el átomo de la posición B (Mn) de la perovskita por

---

[44] Ecija-Verdejo A. Óxidos mixtos tipo perovskita $Ln_{0.5}M_{0.5}FeO_{3-\delta}$ (Ln=La, Sm, Nd, Gd; M=Ba, Sr) para su aplicación como cátodos en pilas SOFC. Ph.D. thesis work, UPV/EHU, **2012**.

[45] Martínez-Amesti A., Larrañaga A., Rodríguez-Martínez L.M., Aguayo A.T., Pizarro J.L., Nó M.L., Laresgoiti A., Arriortua M.I. Reactivity between La(Sr)FeO_3 cathode, doped CeO_2 interlayer and yttria-stabilized zirconia electrolyte for solid oxide fuel cell applications. *J. Power Sources* 185 (**2008**) 401-410.

[46] Martínez-Amesti A. Celdas de combustible de óxido de sólido. Estudios de reactividad y optimización de la intercapa cátodo-electrolito. Ph.D. thesis work, UPV/EHU, **2009**.

elementos que proporcionan conductividad mixta como son el cobalto, el hierro, y el níquel[47]. Las perovskitas que presentan conductividad mixta son prometedoras en su aplicación como cátodos ya que extienden la superficie de reacción TPB (Figura 1.8), mejorando el comportamiento electroquímico, incluso a temperaturas por debajo de 800 ºC. Otros candidatos prometedores para su uso como cátodos, a temperaturas de operación intermedias, son los compuestos conocidos como cobaltitas, donde B=Co, por analogía con las manganitas. En este contexto, destacan los compuestos de la serie $La_{1-x}Sr_xCoO_{3-\delta}$ (LSC), que presentan alta conductividad iónica y electrónica en un amplio intervalo térmico. En comparación con el resto de los metales de transición (Cr, Mn, Fe, Ni), el cobalto muestra los menores sobrepotenciales catódicos. Sin embargo, los principales problemas de estas cobaltitas son el alto TEC (coeficiente de expansión térmica) y su tendencia a reaccionar con el YSZ, por encima de 900 ºC. Con el fin de lograr materiales más estables que el LSC se ha sustituido el La por Gd, Sm, Pr y Dy. Sin embargo, el óxido mixto $Gd_{1-x}Sr_xCoO_{3-\delta}$ presenta menor conductividad que el LSC y reacciona también con el YSZ. Por otra parte, el $Sm_{1-x}Sr_xCoO_{3-\delta}$ se ha utilizado en celdas de combustible de temperatura intermedia (500 ºC), siendo éste un gran avance para la tecnología SOFC. Por último, la fase $Dy_{1-x}Sr_xCoO_{3-\delta}$ es estable para $x > 0.6$, presentando un comportamiento similar al del LSC[48].

In the case of the LSM perovskite, the mixed ionic-electronic conductivity (MIEC) might be achieved in two ways: (i) mixing an electronic conductor with an ionic conducting oxide to form a composite, or (ii) replacing perovskite B position atom (Mn) by elements which provide mixed conductivity, such as Co, Fe or Ni[47]. Thus, MIEC perovskites extends the active oxygen reduction site from the typical TPB (electrolyte/cathode interphase) to the entire cathode surface (Figure 1.8), improving cathode electrochemical behaviour even at temperatures below 800 ºC. Therefore, on reducing the operation temperature, it finds that cobaltites, $La_{1-x}Sr_xCoO_{3-\delta}$ (LSC), show both high electronic and fast ion conductivities in a wide operating temperature range. Compared to other transition metals (Cr, Mn, Fe, Ni), cobalt shows the lowest cathodic polarization overpotential. However, the thermal properties of these cobaltites result in cracking and delamination of the cathode due to their high thermal expansion coefficient (TEC) values. Moreover, replacement of lanthanum with Gd, Sm, Pr or Dy in LSC has been investigated to improve the stability of the initial LSC. However, $Ga_{1-x}Sr_xCoO_{3-\delta}$ shows lower conductivity than LSC and, like LSC, it also reacts with YSZ. On the other hand, $Sm_{1-x}Sr_xCoO_{3-\delta}$ has been used in intermediate temperature fuel cells (500 ºC), contributing to a breakthrough of SOFC technology. Finally, $Dy_{1-x}Sr_xCoO_{3-\delta}$ is stable for $x>0.6$, and shows a similar behaviour to that observed for LSC[48].

---

47 Qiu L., Hirano A., Imanishi N., Takeda Y. $Ln_{1-x}Sr_xCo_{1-y}Fe_yO_{3-\delta}$ (Ln=Pr, Nd, Gd; x=0.2, 0.3) for the electrodes of solid oxide fuel cells. *Solid State Ionics* 158 (**2003**) 55-65.

48 Skinner S.J. Recent advances in perovskite-type materials for solid oxide fuel cell cathodes. *Int. J. Inorg. Mater.* 3 (**2001**) 113-121.

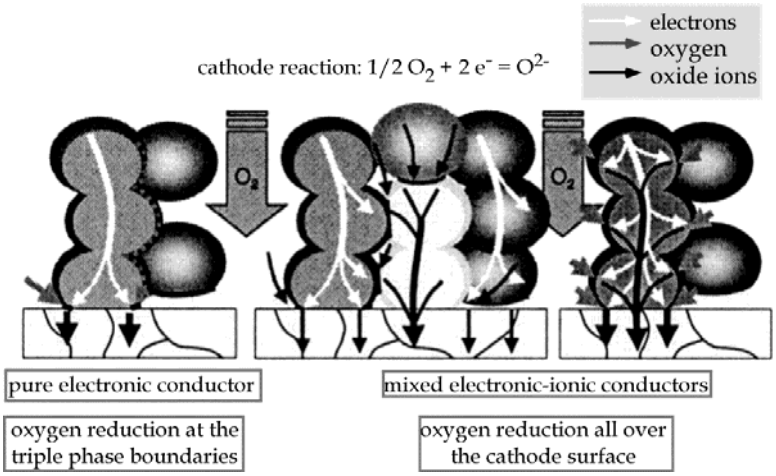

Figura 1.8. / **Figure 1.8.** Reducción de oxígeno en los TPBs para un cátodo conductor electrónico puro, y en toda la superficie para cátodo composite y conductor mixto[49]. / Oxygen reduction at a pure electronic, composite and mixed conducting cathode[49].

Por otra parte, con objeto de minimizar la problemática del TEC, se han estudiado las ferritas-cobaltitas, $La_{1-x}Sr_xCo_{1-y}Fe_yO_{3-\delta}$ (LSCF)[50], mostrando resultados positivos. En este sentido, las perovskitas de hierro, donde B=Fe, con fórmula general $La_{1-x}Sr_xFeO_3$ (LSF) también son compuestos atractivos en el área de los cátodos[51]. Se ha observado que para ciertos valores de x, estas fases poseen buenas propiedades catalíticas y conductoras entre 600 y 800 ºC. En comparación con las cobaltitas, esta serie muestra menor TEC y superior compatibilidad con el YSZ y electrolitos basados en cerio. En cuanto a la resistencia superficial específica (ASR), el comportamiento de las manganitas es inferior al del resto de compuestos, siendo las perovskitas de hierro las que muestran la menor ASR. Por lo tanto, los compuestos basados en $La_{1-x}Sr_xFeO_{3-\delta}$ son candidatos prometedores como cátodos para pilas de combustible de óxido sólido de temperatura intermedia (IT-SOFCs)[52].

On the other hand, to overcome high TEC issue a substitution of Co for Fe was performed to form cathodes of $La_{1-x}Sr_xCo_{1-y}Fe_yO_{3-\delta}$ (LSCF)[50], which show a lower thermal expansion coefficient (TEC). Recent attempts have focused on iron perovskites, $La_{1-x}Sr_xFeO_3$ (LSF), since they possess good catalytic and conductive properties between 600 and 800 ºC[51]. Compared to cobaltites, this serie shows a small TEC and a high compatibility with YSZ and ceria based electrolytes. As far as the area specific resistance (ASR) is concerned, the manganites show higher resistance than other compounds, exhibiting iron perovskites the lowest area specific resistance. Therefore, $La_{1-x}Sr_xFeO_3$ compounds are promising candidates as cathodes for intermediate solid oxide fuel cells (IT-SOFCs)[52].

---

[49] Ivers-Tiffée E., Weber A., Herbstritt D. Materials and technologies for SOFC-components. *J. Eur. Ceram. Soc.* 21 (**2001**) 1805–1811.

[50] Kawada T. Perovskite oxide for cathode of SOFCs, in perovskite oxide for solid oxide fuel cells (eds. T. Ishihara), p. 147-166, **2009**.

[51] Vidal K., Rodríguez-Martínez L.M., Ortega-San Martín L., Martínez-Amesti A., Nó M. L., Rojo T., Laresgoiti A., Arriortua M.I. The effect of doping in the electrochemical performance of $(Ln_{1-x}M_x)FeO_{3-\delta}$ SOFC cathodes. *J. Power Sources* 192 (**2009**) 175-179.

[52] Ecija-Verdejo A. Óxidos mixtos tipo perovskita $Ln_{0.5}M_{0.5}FeO_{3-\delta}$ (Ln=La, Sm, Nd, Gd; M=Ba, Sr) para su aplicación como cátodos en pilas SOFC. Ph.D. thesis work, UPV/EHU, **2012**.

Interconector: Individualmente, una celda SOFC, puede producir un voltaje o potencial alrededor de 1 V; sin embargo, para aplicaciones que requieren de un mayor voltaje, estas celdas operan como un conjunto de unidades conectadas a través de interconectores. Éstos proporcionan la conexión eléctrica entre ánodo de una celda y el cátodo de la celda adyacente, asegurando así que el flujo de electrones llega a todas las celdas individuales. Además, actúan como barrera física para evitar cualquier contacto entre el combustible y el oxidante. Los típicos requerimientos para los materiales interconector son: (i) alta conductividad eléctrica bajo atmósfera reductora y oxidante, (ii) ser impermeable a los gases, (iii) estabilidad química y microestructural, a la temperatura de operación de la celda, y en atmósfera reductora y oxidante, (iv) compatibilidad térmica y química con los materiales adyacentes, (v) alta resistencia mecánica, (vi) alta conductividad térmica y (vii) elevada densidad. Se han estudiado los materiales tipo cermet como posibles interconectores. Mezclas de cromo metálico con cromita de lantano (5-25 % en volumen), $LaCrO_3$, sinterizado a 1500 ºC, han posibilitado buenos resultados para su aplicación en SOFC. Sin embargo, los interconectores cerámicos y metálicos son los más empleados. Los materiales tipo perovskita, basados en $LaCrO_3$, dopados con Ca o Sr y Mg en las posiciones A y B, respectivamente, $La_{1-x}Ca_xCrO_3$, $La_{1-x}Sr_xCrO_3$ y $LaCr_{1-x}Mg_xO_3$, son los más utilizados para la interconexión de una SOFC con aplicaciones en alta temperatura. De acuerdo a varias investigaciones, el dopaje de los metales alcalinotérreos en estas perovskitas es necesario para mejorar la conductividad eléctrica de las mismas. En este contexto, el dopaje con metales de transición, por ejemplo $La_{0.8}Sr_{0.2}Cr_{0.97}V_{0.03}O_3$ y $LaCr_{0.78}Mg_{0.05}Al_{0.16}O_3$, puede ajustar el TEC así como disminuir su temperatura de sinterizado[53].

Interconnect: For SOFC applications where high voltage and potency are required, solid oxide fuel cells are connected through interconnectors. It constitutes a barrier, separating the fuel feed and the oxidant between two adjacent cells, and works as current collector, ensuring that the electron flow reach all the single cells. Typical requirements for the interconnector materials are: (i) high electronic conductivity with low ionic conductivity, (ii) chemical stability in both fuel and air atmospheres, (iii) thermal expansion match to other cell components, (iv) high mechanical strength, (v) high thermal conductivity, and (vi) chemical stability with regard to other cell components. Cermet-type materials have been proposed as interconnect, e. g. mixtures of metallic chromium with 5-25 vol % lanthanum chromite, $LaCrO_3$, by sintering at 1500 ºC, have obtained good results for interconnect applications in SOFC technology. Other typical compounds as $LaCrO_3$ doped with Sr or Ca on A-site or Mg on B-site, i. e. $La_{1-x}Ca_xCrO_3$, $La_{1-x}Sr_xCrO_3$ and $LaCr_{1-x}Mg_xCrO_3$, are the most common candidate ceramic interconnect materials for use at high temperatures. In these perovskites, the alkaline earth metals are necessary to obtain sufficient electrical conductivity. In addition, transition metal dopants can also be added to adjust the thermal expansion or to reduce the sintering temperature necessary for the required gas tightness; for example, $La_{0.80}Sr_{0.20}Cr_{0.97}V_{0.03}O_3$ or $LaCr_{0.78}Mg_{0.05}Al_{0.16}O_3$ [53].

Por otra parte, la reducción de la temperatura de trabajo (≤ 800 ºC) ha permitido el desarrollo de interconectores metálicos, obteniendo una mejora en el rendimiento de las SOFC con soporte de

[53] Hilpert K., Quadakkers J., Singheiser L. Interconnects, in Handbook of Fuel Cells- Fundamentals, Technology and Applications (eds. Vielstich W., Lamm A., Gasteiger H.A.), John Wiley & Sons, New Jersey, USA, p. 1037-1051, **2003**.

electrolito[54]. Teniendo en cuenta la resistencia a la corrosión a alta temperatura, las aleaciones formadoras de alúmina basadas en Ni-Al, muestran buenas propiedades protectoras debido a la formación de una capa fina y adherente de Al_2O_3; sin embargo, este óxido de aluminio presenta una baja conductividad electrónica. A pesar de que el óxido de cromo, Cr_2O_3, ofrece menor resistencia a la oxidación/corrosión que la alúmina, este óxido posee una mayor conductividad eléctrica. No obstante, a largos tiempos de operación, las aleaciones basadas en cromo forman una excesiva capa de Cr_2O_3 que empeora la estabilidad de las mismas (por ejemplo, el Ducrolloy, Cr-5Fe-Y_2O_3), limitando así el uso de estos materiales a temperaturas de operación intermedias (< 700 ºC). Sin embargo, las aleaciones formadoras de óxido de cromo son comúnmente estudiadas, en particular, las de cromo-hierro (aceros inoxidables ferríticos). Éstos poseen un alto contenido en cromo (12-28 %), son magnéticos, y presentan una baja concentración de carbón. Teniendo en cuenta que la mayoría de los aceros inoxidables están basados en sistemas Fe-Cr-C y Fe-Cr-Ni-C, los elementos carbón, cromo, y níquel se añaden a la aleación para estabilizar la estructura de la misma. En este sentido, los aceros inoxidables se dividen en cuatro grupos: (i) martensíticos, (ii) ferríticos (α-Fe), (iii) austenoferríticos (dúplex), y austeníticos (γ-Fe).

On the other hand, the reduction of operating temperature (≤ 800 ºC) allowed the development of metallic interconnects to get around the difficulties in the electrolyte-supported SOFC[54]. Considering resistance to high temperature corrosion, alumina-forming alloys based on Ni-Al shows excellent protective properties; however, the formed alumina scale presents a low electronic conductivity. In spite of the fact that chromia provides less oxidation/corrosion protection than alumina it gives more electronic conductivity. But, the application of chromium-based alloys (such as, Ducrolloy, Cr-5Fe-Y_2O_3), as interconnect materials in SOFCs, is still limited to intermediate temperature operation (< 700 ºC) due to their long-term stability problem related with the thickness of oxide scale, which is considered to be too thick for reliable operation. However, chromia-forming alloys, particularly, chromium-iron systems (ferritic stainless steels) are widely used as interconnect materials. They are high chromium magnetic steels that have low carbon content. The chromium content of these metals varies from 12 to 28 %. Since most of the stainless steels are based on the Fe-Cr-C and Fe-Cr-Ni-C systems, carbon, chromium and nickel alloying elements are used to stabilize stainless steel structure. Hence, stainless steels can be divided into four groups: (i) martensitic, (ii) ferritic (α-Fe), (iii) ferritic-austenitic (duplex) and (iv) austenitic (γ-Fe).

En comparación con las aleaciones Fe-Cr, las aleaciones Ni-Cr (por ejemplo, los aceros austeníticos Fe-Cr-Ni y las superaleaciones de Ni-Cr), han demostrado mayor resistencia a la oxidación, así como conductividad eléctrica satisfactoria. Sin embargo, la mayoría de las aleaciones con base níquel, tienen el TEC más alto, comparado con los demás componentes de celda. Este factor favorece la formación de grietas en la interfase interconector/electrodo. Entre los aceros que contienen níquel, la aleación comercial Haynes 230 (Ni-Cr-W-Mo), muestra la mejor resistencia a la oxidación, y forma una capa delgada, compuesta principalmente de Cr_2O_3 y espinelas tipo $(Mn,Cr,Ni)_3O_4$, al exponerse a altas temperaturas[55]. En comparación con la capa de óxido de cromo pura, Cr_2O_3, ésta (óxido/espinela) presenta una mayor conductividad eléctrica. La composición óptima para el interconector dependerá del diseño de la celda y de las condiciones de

[54] Zhu W.Z., Deevi S.C. Development of interconnect materials for solid oxide fuel cells. *Mat. Sci. Eng. A* 348 (**2003**) 227-243.

[55] Alvarado-Flores J. Avances en el desarrollo de interconectores metálicos de celdas SOFC. *Boletín de la Sociedad Española de Cerámica y Vidrio* 52 (**2013**) 194-206.

funcionamiento de la misma. Así, los aceros ferríticos con bajo contenido en cromo se suelen usar para celdas de soporte de electrolito basado en ceria, o de soporte de ánodo basado en un cermet de níquel. Sin embargo, estos metales pueden tener una mayor cantidad de cromo para las celdas de soporte de electrolito basado en zirconia.

In this way, nickel-containing steels are also studied as interconnects, such as austenitic stainless steels (Fe-Cr-Ni) and Ni-based superalloys (Ni-Cr), however, the mismatch in thermal expansion with the other cell components leads to cracks at the interconnect/electrode interfaces. Among the Ni-containing steels, the Haynes 230 (Ni-Cr-W-Mo) showed the best oxidation resistance and the oxide scale composed of Cr_2O_3 and outer spinel, $(Mn,Cr,Ni)_3O_4$, might have better electronic conductivity than a pure chromia scale[55]. The optimum steel composition will depend on the cell design used and operating conditions. Thus, in Ni-cermet anode-based or ceria electrolyte-supported cells, lower Cr content ferritic steels are preferred than that using zirconia electrolyte-based concepts.

Comparadas con las cerámicas basadas en cromitas de lantano, las aleaciones formadoras de óxido de cromo tienen ventajas tales como alta conductividad eléctrica y térmica. Sin embargo, la formación de la capa sólida Cr_2O_3, en la superficie de los interconectores, tiene principalmente dos inconvenientes[56,57]: (i) este óxido reacciona con aire y vapor de agua para dar lugar a la formación de especies gaseosas como el CrO_3 (g) y $CrO_2(OH)_2$ (g), respectivamente. Estas especies gaseosas de cromo se transportan hacia el cátodo, bloqueando los sitios activos como Cr (III), aumentando así la polarización del cátodo, y (ii) el crecimiento de esta capa de óxido, poco conductora, entre los interconectores metálicos y los electrodos, da lugar a una falta de contacto entre ellos, produciendo pérdidas óhmicas en la celda. Además, el crecimiento anómalo del óxido de cromo, a largos tiempos de operación de una SOFC, puede acelerar el proceso de corrosión del interconector, disminuyendo su durabilidad[58]. Por otra parte, los interconectores cerámicos y el cátodo se sinterizan a 1300 ºC, obteniendo así un fuerte enlace entre ambos materiales. Sin embargo, el uso de interconectores metálicos limita la temperatura de sinterizado, reduciendo de este modo la adherencia de éstos con el cátodo. En este sentido, debido a la alta resistencia de contacto entre electrodo-colector de corriente, investigaciones recientes indican la necesidad de distinguir esta resistencia de la total de la celda.

Compared to the La-chromite-based ceramics, chromia-forming alloys possess higher electrical and thermal conductivities than ceramic materials. However, since an oxide layer inevitably forms on their surfaces, they have two main disadvantages[56,57]: i) vaporization of Cr_2O_3 as volatile Cr(VI) species (CrO_3 (g), $CrO_2(OH)_2$ (g), CrO_2OH (g)) are transported with the oxidant gas and block the electrochemically active sites with solid Cr (III), increasing the cathode polarization, and ii) the formation of oxide scales that leads ohmic losses of the cell. Moreover, the anomalous growth of oxide scales under SOFC interconnect operating conditions can accelerate the corrosion, affecting the stability of the metallic interconnects[58]. On the other hand, compared to ceramic interconnect, in which a solid bond with cathode is achieved by sintering at 1300 ºC, metallic interconnect shows a

[56] Zhu W.Z., Deevi S.C. Development of interconnect materials for solid oxide fuel cells. *Mat. Sci. Eng. A* 348 (**2003**) 227-243.

[57] Yang Z., Xia G., Singh P., Stevenson J.W. Electrical contacts between cathodes and metallic interconnects in solid oxide fuel cells. *J. Power Sources* 155 (**2006**) 246-252.

[58] Miguel-Pérez V., Martínez-Amesti A., Nó M.L., Larrañaga A., Arriortua M.I. Oxide scale formation on different metallic interconnects for solid oxide fuel cells. *Corros. Sci.* 60 (**2012**) 38-49.

poor adherence with electrode. Hence, recent investigations indicate the necessity to distinguish experimentally the resistance associated with the electrode coating/current collector contact from the total cell resistance due to the high value of the contact resistance associated with it.

El cromo se oxida selectivamente para formar la capa protectora superficial de Cr_2O_3 debido a que, dentro de los constituyentes que componen la aleacion, el cromo es el metal menos noble. Sin embargo, el hecho de que ocurra esta oxidación selectiva también depende de: (i) la concentracion del componente activo de la aleación (las aleaciones formadoras de óxido de cromo necesitan al menos un 17-20 % de Cr), (ii) la temperatura, y (iii) la presión parcial del oxígeno[59].

Since chromium is the least noble constituent of an alloy, Cr is selectively oxidized to form an outer protective oxide layer. However, the occurrence of selective oxidation also depends on the concentration of the active alloying component (chromia-forming alloys require a chromium content of approximately 17-20 %), on the temperature, and on the partial oxygen pressure[59].

Los elementos que contienen los aceros presentan diferentes afinidades con el oxígeno, y los átomos de reacción no difunden a la misma velocidad a través de las fases de óxido o metálicas. Cuando un material metálico (M) reacciona con el oxígeno (O_2), se forma un óxido de este material en la superficie metálica, según la ecuación 1.4. Asimismo, si el oxígeno se disuelve dentro de la aleación, el componente menos noble puede oxidarse dentro de la aleación (oxidación interna).

The elements included in the alloys have different affinities for oxygen, and the reacting atoms do not diffuse at the same rates either in the oxide or the alloy phases. The oxidation reaction of a metal (M) with an oxidizing environment (O_2) leading to the formation of a metal oxide on its surface can be expressed as equation 1.4. Moreover, if the oxygen dissolves in the alloy phase, the least noble alloy component also forms oxide inside the alloy (internal oxidation).

$$xM\ (s) + y/2O_2\ (g) \leftrightarrow M_xO_y\ (s) \qquad (1.4)$$

Termodinámicamente, la formación de M_xO_y es favorable cuando la presión parcial del oxígeno, en el ambiente, es mayor que la presión de disociación del óxido. Por lo tanto, cuando más baja sea la presión de disociación, el óxido formado será termodinámicamente más estable. Sin embargo, el proceso de oxidación depende tanto de factores termodinámicos como cinéticos.

Thermodynamically, the formation of the oxide M_xO_y is only possible if the oxygen partial pressure in the environment is higher than the dissociation pressure of the oxide. Thus, the lower dissociation pressure, the more thermodynamically stable is the oxide. The oxidation process of a metal surface is not only determined by thermodynamics, also kinetic aspects have to be considered.

Según la teoría de oxidación de Wagner[60], los sistemas sometidos a alta temperatura y controlados por procesos de difusión, a través de la red de la capa de óxido, siguen una tendencia parabólica, de acuerdo con la ecuación 1.5:

---

[59] Kofstad P. Oxidation of alloys, in High-temperature oxidation of metals. John Wiley & Sons, INC, New York, p. 264-299, **1966**.

[60] Wagner C. Theoretical analysis of the diffusion processes determining the oxidation rate of alloys. *J. Electrochem. Soc.* 99 (**1952**) 369-380.

Based on the classical Wagner oxidation theory[60], the chromia scale growth follows parabolic time dependence if oxidation is controlled by the diffusion of metal and/or oxygen ions through the oxide lattice (equation 1.5):

$$x^2 = k \cdot t \qquad (1.5)$$

donde x es el espesor de óxido (cm), t (s) el tiempo de oxidación, y k es la constante parabólica de velocidad de oxidación ($g \cdot cm^{-4} \cdot s^{-1}$). Sin embargo, la ley de Wagner no tiene en cuenta la formación de microcracks y la densidad del óxido de cromo, ambos factores dependientes del tiempo. La conductividad eléctrica del óxido de cromo a 800-1000 ºC es de $1\text{-}5 \cdot 10^{-2}$ $S \cdot cm^{-1}$, y la misma puede aumentarse con el dopaje. La velocidad de difusión en los óxidos con estructura espinela suele ser menor que en los óxidos simples; en este sentido, la pasivación de las aleaciones interconnector suele consistir en la formación de una doble capa superficial. Así, la capa de óxido formada a partir de la oxidación de los sistemas Fe-Cr-Mn, como el sustrato tipo Crofer22, está compuesta principalmente por una capa interna de óxido de cromo, Cr_2O_3 (cromia) y una capa externa con estructura espinela, M_3O_4 ($M=Mn^{3+/4+}$ y Cr^{6+})[61,62].

in which x (cm) is the scale thickness, t (s) the time, and k ($g \cdot cm^{-4} \cdot s^{-1}$) the parabolic oxidation rate constant. However, both the time-dependent density of chromia scale and the formation of microvoids and microcracks contribute to the scale growth process. The electrical conductivity of chromia at 800-1000 ºC has been reported to be $1\text{-}5 \cdot 10^{-2}$ $S \cdot cm^{-1}$, which could be enhanced by doping. Since diffusion rates in spinels are often smaller than in the single oxides, protective scales on high-temperature oxidation-resistant interconnects usually consist of complex oxides. Thus, oxidation of Fe-Cr-Mn system, such as commercial Crofer22 interconnect, provides the formation of chromia oxide, Cr_2O_3, and a dense M_3O_4 ($M=Mn^{3+/4+}$ y Cr^{6+}) spinel top layer on the surface of the alloy[61,62].

Capa protectora: El uso de capas protectoras, entre el cátodo e interconector, puede disminuir la cinética de oxidacion y mejorar la adhesión de la capa de óxido sobre los sustratos, y prevenir la difusión de cromo. Estos materiales deben cumplir, entre otros, los siguientes requisitos: (i) alta conductividad eléctrica, (ii) adecuada compatibilidad química y un coeficiente de expansión térmico similiar a los materiales adyacentes, (iii) baja difusividad de los cationes cromo, y (iv) estabilidad química y estructural en aire a la temperatura de operación de la celda SOFC[63].

Protective coating: Using a coating that acts as a protective layer can avoid the migration of chromium to the cathode and improve oxide growth resistance of interconnects. The coatings must have adequate conductivity, matching thermal expansion, low chromium cation and oxygen anion diffusivity, and be chemically compatible with adjacent components and stable in air[63].

---

60 Wagner C. Theoretical analysis of the diffusion processes determining the oxidation rate of alloys. *J. Electrochem. Soc.* 99 (**1952**) 369-380.

61 Fontana S., Amendola R., Chevalier S., Piccardo P., Caboche G., Viviani M., Molins R., Sennour M. Metallic interconnects for SOFC: Characterisation of corrosion resistance and conductivity evaluation at operating temperature of differently coated alloys. *J. Power Sources* 171 (**2007**) 652–662.

62 Yang Z., Guan-Guang X., Maupin G.D., Stevenson J.W. Conductive protection layers on oxidation resistant alloys for SOFC interconnect applications. *Surf. Coat. Tech.* 201(7) (**2006**) 4476–4483.

63 Miguel-Pérez V., Martínez-Amesti A., Nó M.L., Larrañaga A., Arriortua M.I. The effect of doping $(Mn,B)_3O_4$ materials as protective layers in different metallic interconnects for solid oxide fuel cells. *J. Power Sources* 243 (**2013**) 419-430.

Los posibles materiales para la utilización como capa protectora en SOFC se pueden clasificar en cuatro grupos principales[64]: (i) óxidos de elementos reactivos (La_2O_3, CeO_2, Nd_2O_3 y Y_2O_3), (ii) óxidos con fórmula general MAlCrYO (M=Co,Mn,Ti,Ni), (iii) perovskitas conductoras, tales como $La_xSr_{1-x}CoO_3$, $La_{1-x}Sr_xCrO_3$ y $La_xSr_{1-x}MnO_3$, y (iv) espinelas conductoras, $(Mn,Co)_3O_4$, Co_3O_4 y $(Cu,Mn)_3O_4$, por ejemplo. Dentro de todos estos materiales, los óxidos mixtos con estructura espinela son los más utilizados debido a su sinterabilidad y, además, presentan una conductividad eléctrica mayor que la capa de óxido superficial (Cr_2O_3, $(Mn,Cr)_3O_4$) característica del interconector metálico en condiciones SOFC. A pesar de que las espinelas $Mn_{1-\delta}Co_{2-\delta}O_4$ (MC) son las más estudiadas[65,66], algunos trabajos indican que, teniendo en cuenta las medidas ASR realizadas a largos tiempos de operación, la adherencia de estas capas sobre aleaciones tipo Crofer22 puede ser un factor a mejorar para su posterior aplicación en sistemas SOFC[67]. En este sentido, la presencia de cerio, como elemento reactivo en la capa protectora, aumenta su adherencia al substrato. Como ejemplo, los estudios realizados sobre la composición $Ce_{0.05}Mn_{1.475}Co_{1.475}O_4$ mostraron una capa de óxido bien adherida al interconector[68,69]. Asimismo, otros grupos de investigación han estudiado espinelas Mn-Co dopadas con Fe, Ti, y/o Cu[70,71], obteniendo mejoras en la densificación del material y una mayor conductividad electrica con respecto a la capa $MnCo_2O_4$. Trabajos previos, realizados en nuestro grupo[72], concluyen que la capa de $MnCo_{1.9}Fe_{0.1}O_4$ (MCF) es más efectiva como barrera para el cromo que la $MnCo_2O_4$ (MC), debido a que MCF muestra mejores resultados electroquímicos para una microestructura similar; la presencia de hierro en la espinela mejora la estabilidad de estos óxidos. Además, debido al bajo coste del níquel, también se han estudiado las espinelas $NiMn_2O_4$ y $NiFe_2O_4$ como capas protectoras, obteniendo interesantes resultados ya que éstas proporcionan una adecuada conductividad sobre el subtrato[73].

Basically, SOFC protective coatings fall into four main categories[64]: (i) reactive element oxides (REOs) such as La_2O_3, CeO_2 and Y_2O_3, (ii) MAlCrYO (M represents a metal, e.g., Co, Mn, Ti or Ni), (iii) conductive perovskites such as $La_xSr_{1-x}CoO_3$ and $La_{1-x}Sr_xCrO_3$ and $La_xSr_{1-x}MnO_3$ and (iv) conductive spinels, such as $(Mn,Co)_3O_4$, Co_3O_4 and $(Cu,Mn)_3O_4$. Several studies have concluded that spinel oxides have higher electrical conductivity than oxide scale phases (Cr_2O_3, $(Mn,Cr)_3O_4$)

---

64 Shaigan N., Qu W., Ivey D.G., Chen W. A review of recent progress in coatings, Surface modifications and alloy developments for solid oxide fuel cell ferritic stainless steel interconnects. *J. Power Sources* 195 (**2010**) 1529-1542.

65 Magdefrau N.J. Evaluation of solid oxide fuel cell interconnect coatings: reaction layer microstructure, chemistry and formation mechanisms, Ph.D. thesis work, University of Connecticut, **2013**.

66 Zhang H., Wu J., Liu X., Baker A. Studies on elements diffusion of Mn/Co coated ferritic stainless steel for solid oxide fuel cell interconnects application. *Int. J. Hydrogen Energ.* 38 (**2013**) 5075-5083.

67 Akanda S.R., Walter M.E., Kidner N.J., Seabaugh M.M. Lifetime prediction for manganese cobalt spinel oxide coatings on metallic interconnects. *Thin Solid Films* 565 (**2014**) 237-248.

68 Yang Z., Xia G., Nie Z., Templeton J.D., Stevenson J.W. Ce-modified $(Mn,Co)_3O_4$ spinel coatings on ferritic stainless steels for SOFC interconnect applications. *Electrochem. Solid St.* 11(8) (**2008**) B140-B143.

69 Chou Y.S., Stevenson J.W., Choi J.P. Long-term evaluation of solid oxide fuel cell candidate materials in a 3-cell generic stack test fixture, part III: stability and microstructure of Ce-(Mn,Co)-spinel coating, AISI441 interconnect, alumina coating, cathode and anode. *J. Power Sources* 257 (**2014**) 444-453.

70 Hosseini N., Abbasi M.H., Karimzadeh F., Choi G.M. Development of $Cu_{1.3}Mn_{1.7}O_4$ spinel coating on ferritic stainless Steel for solid oxide fuel cell interconnects. *J. Power Sources* 273 (**2015**) 1073-1083.

71 Puranen J., Pihlatie M., Lagerbom J., Bolelli G., Laakso J., Hyvärinen L., Kylmälahti M., Himanen O., Kiviaho J., Lusvarghi L., Vuoristo P. Post-mortem evaluation of oxidized atmospheric plasma sprayed Mn-Co-Fe oxide spinel coatings on SOFC interconnects. *Int. J. Hydrogen Energ.* 39(30) (**2014**) 17284-17294.

72 Miguel-Pérez V., Martínez-Amesti A., Nó M.L., Larrañaga A., Arriortua M.I. The effect of doping $(Mn,B)_3O_4$ materials as protective layers in different metallic interconnects for solid oxide fuel cells. *J. Power Sources* 243 (**2013**) 419-430.

73 Liu Y., Chen D.Y. Protective coatings for Cr_2O_3-forming interconnects of solid oxide fuel cells. *Int. J. Hydrogen Energ.* 34 (**2009**) 9220-9226.

formed under SOFC conditions. The $Mn_{1-\delta}Co_{2-\delta}O_4$ (MCO) spinels have been the most extensively studied[65,66]. However, ASR test of MCO coated Crofer22 showed that the adhesion of these coatings may be an issue for long-term applications[67]. For this reason Ce was added to the coating as reactive element in order to increase oxide scale and coating adherence to the metal substrate. A composition of $Ce_{0.05}Mn_{1.475}Co_{1.475}O_4$ was used and the obtained results have looked promising[68,69]. Moreover, other research groups have also studied Mn-Co spinels doped with Fe, Ti or Cu which exhibit higher electrical conductivity and better densifications than $MnCo_2O_4$ due to a partial substitution of Co by Fe, Ti and/or Cu[70,71]. Previous works, which are performed in our group, also concluded that[72] $MnCo_{1.9}Fe_{0.1}O_4$ was a more effective barrier than $MnCo_2O_4$, resulting in better electrochemical results with similar microstructure. The presence of low iron content in $MnCo_{1.9}Fe_{0.1}O_4$ improved the stability of coating. In addition, $NiMn_2O_4$ and $NiFe_2O_4$ spinels were also studied as protective coatings due to the low cost of nickel, providing effective conducting path to metallic substrate[73].

Capa de contacto: Sin embargo, a pesar de la utilidad del empleo de capas protectoras, la velocidad de degradación para los *stacks* (apilamientos), de celdas de combustible de óxido sólido, es aún mayor que la necesaria para la comercialización de estos dispositivos. En este sentido, el contacto interconector-cátodo juega un papel importante en resistencia eléctrica de la celda[74], como se ha indicado anteriormente. Así, el uso de una capa de contacto, entre el interconector (o capa protectora) y el cátodo, puede aumentar la conductividad eléctrica interfacial y disminuir también las interacciones entre ambos materiales. Estudios previos muestran que como consecuencia de la inserción de una malla de platino como material de contacto del cátodo, la resistencia superficial específica (ASR) de la celda estudiada, a 800 ºC, disminuye de 1.43 a 0.19 $\Omega \cdot cm^2$ mientras que el área eficaz de contacto aumenta del 4.6 al 27.2 % [75,76]. Una discusión más detallada sobre capas de contacto se incluye en el apartado 1.4.1. Los materiales típicos utilizados en las SOFC se recogen en la Figura 1.9[77-79].

Contact coating: However, despite the usefulness of protective coatings, the stack degradation rates are still higher than the required ones for SOFC commercialization. The interconnect-cathode interface plays an important role in the electrical resistance of the cell[74], as it has already pointed out. Thus, the use of a conductive contact layer between interconnect and cathode could reduce electron transmission resistance as well as the interaction between both materials. Thus, according to other authors, the area specific resistance (ASR) of the unit cell decreased from 1.43 to 0.19 $\Omega \cdot cm^2$ at 800 ºC, when the effective contact area was increased from 4.6% to 27.2% by adding platinum mesh on the cathode side[75,76]. Thus, electrical contact resistance between interconnect and cathode layer, in solid oxide fuel cells, has attracted much attention since it is one significant part of the total contact resistance, which plays an important role in the fuel cell performance. A detailed discussion of contact coatings is given in Section 1.4.1. As a summary, Figure 1.9 contains[77-79] the

---

74 Guan W.B., Zhai H.J., Jin L., Li T.S., Wang W.G. Effect of contact between electrode and interconnect on performance of SOFC stacks. *Fuel Cells* 11(3) (**2011**) 445–450.

75 Wang G., Guan W., Miao F., Wang W.G. Factors of cathode current-collecting layer affecting cell performance inside solid oxide fuel cells stacks. *Int. J. Hydrogen Energ.* 39 (**2014**) 17836-17844.

76 Guan W.B., Jin L., Ma X., Wang W.G. Investigation of impactors on cell degradation inside planar SOFC stacks. *Fuel Cells* 12(6) (**2012**) 1085-1094.

77 Singh P., Minh N.Q. Solid oxide fuel cells: technology status. *Int. J. Appl. Ceram. Technol.* 1(1) (**2004**) 5-15.

78 Orera A., Slater P.R. New chemical systems for solid oxide fuel cells. *Chem. Mater.* 22 (**2010**) 675-690.

79 Mahato N., Banerjee A., Gupta A., Omar S., Balani K. Progress in material selection for solid oxide fuel cell technology: A review. *Prog. Mater. Sci.* (**2015**), doi:10.1016/j.pmatsci.2015.01.001.

typical materials used in SOFCs. Nevertheless, the correct material selection will depend on the final operating conditions.

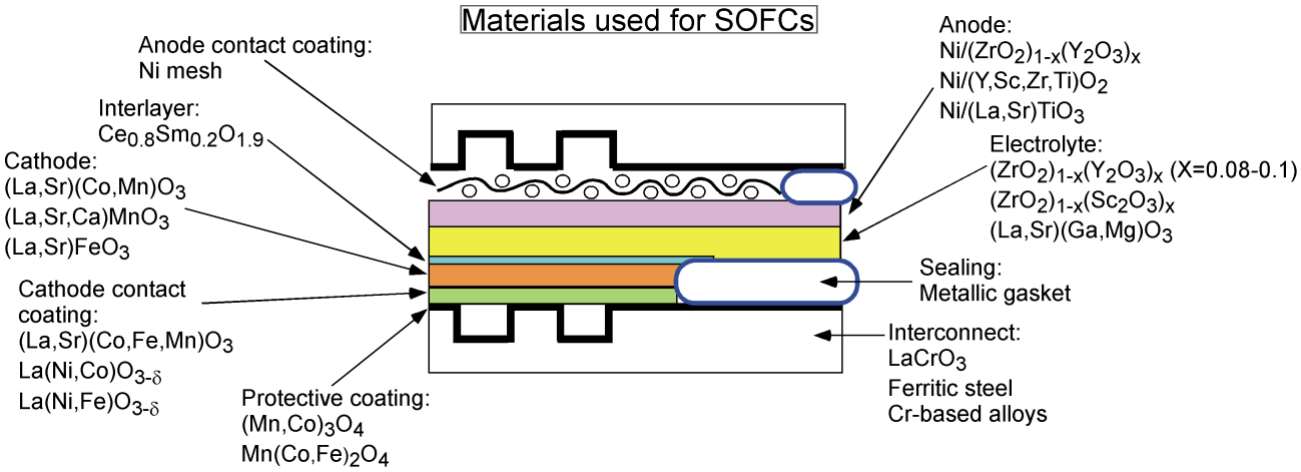

Figura 1.9. / **Figure 1.9.** Materiales con aplicación en celdas de combustible de óxido sólido. / Some of the most typical materials used for solid oxide fuel cell applications.

Geometría: Las configuraciones geométricas más utilizadas para las celdas SOFC son: (i) la planar y (ii) la tubular[80]. Las primeras celdas SOFC desarrolladas por la compañía Westinghouse Electric, en 1980, presentaban un diseño tubular, debido a que el apilamiento de celdas en esta configuración garantiza la estanqueidad de los conductos por los que circula el gas, no siendo necesario el empleo de sellantes[81] entre cada celda, a diferencia de lo que ocurre con la configuración planar. Sin embargo, los *stacks* planares se caracterizan por tener mayor densidad energética que los tubulares ya que estos últimos presentan una mayor resistencia eléctrica, debido a que el camino a recorrer por los electrones generados en la geometría tubular, es más largo[82] (Figura 1.10).

Geometry: A single SOFC can be shaped into tubular or planar structures[80]. Westinghouse Electric Corporation proposed tubular SOFC configuration in 1980, because such a single may be assembled into a cell stack without using seal between each cell. Gas-tight sealing is required for planar SOFC along the edges of the electrodes, electrolyte and interconnect as well as between individual cells to bond the cell stacks, prevent intermixing and leakage of gases in the anode and the cathode compartments, and provide electrical insulation to avoid electrical shorting[81]. On the other hand, the planar SOFC may possess higher performance[82], but the main hurdle that needs to overcome is the high temperature sealant (Figure 1.10).

[80] Stöver D., Buchkremer H.P., Huijsmans J.P.P. MEA/cell preparation methods: Europe/USA, in Handbook of Fuel Cells- Fundamentals, Technology and Applications (eds. Vielstich W., Lamm A., Gasteiger H. A.), John Wiley & Sons, New Jersey, USA, p. 1015-1032, **2003**.

[81] Singh R.N. Sealing technology for solid oxide fuel cells (SOFC). *Int. J. Appl. Ceram. Technol.* 4(2) (**2007**) 134-144.

[82] Otaegui-Ameztegui L. Desarrollo de celdas de combustible tipo SOFC tubulares de soporte metálico. Ph.D. thesis work, Universidad de Navarra, **2013**.

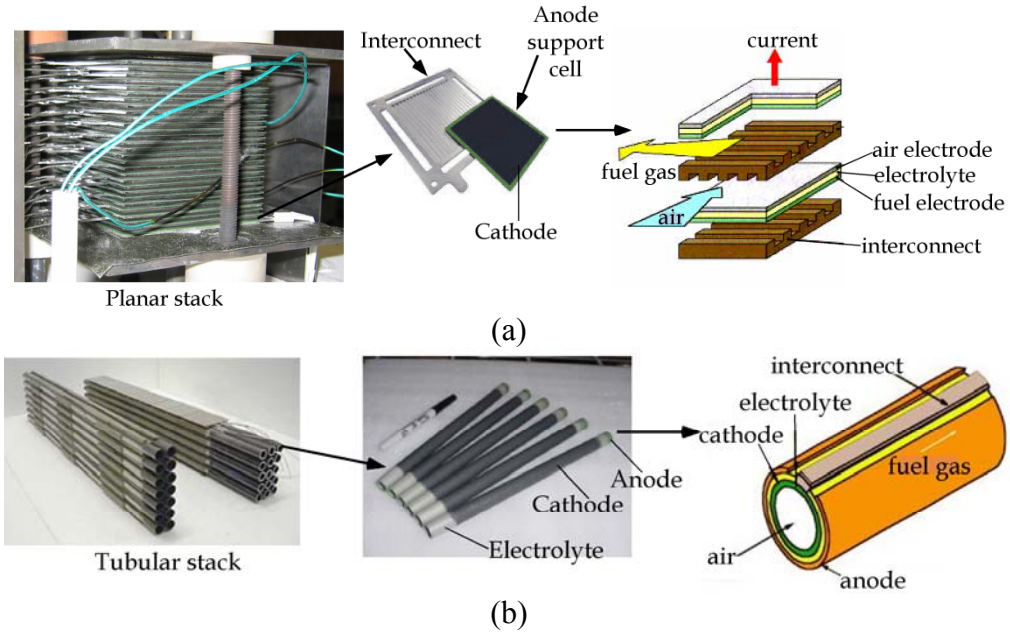

Figura 1.10. / **Figure 1.10.** Diseños para la celda de combustible de óxido sólido: configuración (a) planar y (b) tubular. / (a) Planar and (b) tubular designs for solid oxide fuel cells.

Dependiendo del material que aporta el soporte mecánico de cada celda, éstas se pueden clasificar en[83]: (i) celdas de soporte de electrolito, (ii) celdas de soporte catódico, (iii) celdas de soporte anódico, y (iv) celdas de soporte metálico. Las celdas de soporte de electrolito garantizan la estabilidad mecánica del dispositivo. Sin embargo, el elevado espesor del electrolito (0.1-0.2 mm) requiere de temperaturas de operación entre 850 y 1000 ºC para minimizar las pérdidas internas. El uso de celdas de soporte catódico o anódico permiten disminuir el espesor del electrolito y, como consecuencia, se reduce también la temperatura de operación. Sin embargo, cuanto menor sea el espesor del electrolito más difícil será la producción del mismo. Por otra parte, las celdas de soporte metálico reducen los costes del sistema al reducir las partes cerámicas e introducir aleaciones metálicas más baratas[84,85].

Moreover, these single cells can be designed as electrolyte-supported, anode-supported, cathode-supported, or metallic-supported, where the thickest layer acts as the cell structural support[83]. The electrolyte-supported configuration possesses a relatively strong structure; however, it also has higher resistance due to the thicker electrolyte layer, so higher operating temperatures are required to reduce internal ohmic losses. Lower operating temperatures may be achieved by using anode-supported or cathode-supported configurations with a thin electrolyte, but production of electrolyte layers becomes more difficult with decreasing thickness; on the other hand, metallic-supported design reduces the cell cost[84,85].

Aplicaciones: A día de hoy, se han identificado diferentes mercados para los sistemas SOFC, entre los que se incluyen: (i) aplicaciones estacionarias (generadores eléctricos), en sistemas combinados de calor y energía (Combined Heat and Power, CHP) para uso residencial, comercial e

---

83 Minh N.Q. Solid oxide fuel cell technology-features and applications. *Solid State Ionics* 174 (**2004**) 271-277.

84 Yokokawa H., Sakai N., Horita T., Yamaji K. Recent developments in solid oxide fuel cell materials. *Fuel cells* 1(2) (**2001**) 117-131.

85 Szabo P., Ansar A., Franco T., Gindrat M., Kiefer T. Stack tests of metal-supported plasma-sprayed SOFC, 10th European SOFC Forum, Lucerne, *European Fuel Cell Forum Proceedings*, **2012**.

industrial, (ii) aplicaciones de transporte como unidades auxiliares de energía, y (iii) energía portátil[86]. La principal aplicación se centra en sistemas SOFC-CHP para uso residencial, suministrando la electricidad y calor requerido (intervalo de potencias de 1 a 10 kW) (Figura 1.11). La Tabla 1.4 muestra una comparación tecnoeconómica entre una de las más prometedoras aplicaciones de las SOFCs para el futuro, el sistema híbrido SOFC/turbina de gas, y sus competidores, cuando se emplean como generadores de energía, con cogeneración. Se observa que las celdas de combustible de óxido sólido poseen una alta eficiencia y factor de capacidad con respecto al resto de tecnologías.

Applications: Several markets for SOFC systems have been identified including residential, commercial and industrial CHP (combined heat and power) as stationary power, auxiliary power units for transportation sector, and portable power[86]. A major application is perceived, at the 1-10 kW power level, for the large residential block basis CHP generation sector. A residential SOFC-CHP (SOFC cogeneration system combining heat and power) system provides electrical power, space heating, and domestic water heating requirements (Figure 1.11). Table 1.4 shows technoeconomic comparison between SOFC in combination with a gas turbine (SOFC/gas turbine hybrid), which is one of the most promising SOFCs applications for the future, and their competitors in the stationary power/CHP sector. The comparison reveals that with respect to competing technologies, the solid oxide fuel cell system has a high efficiency and capacity factor.

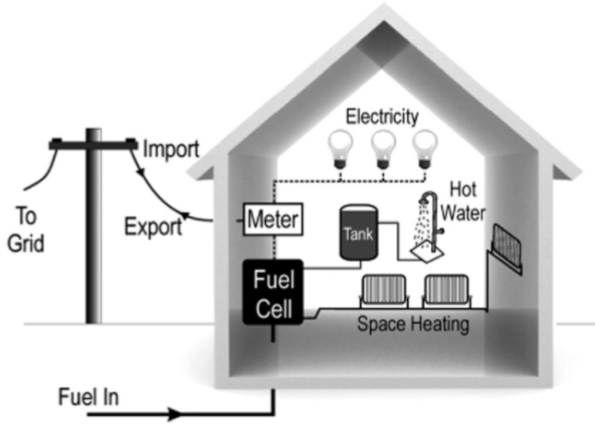

Figura 1.11. / **Figure 1.11.** Micro-CHP de celdas de combustible para uso doméstico[87]. / Fuel cell micro CHP in a domestic home[87].

[86] Gerwen R.J.F. Systems and Applications, in High temperature solid oxide fuel cells fundamentals, design and applications (eds. Singhal S.C., Kendall K.), Elsevier, Oxford, UK, p. 363-392, **2003**.

[87] Elmer T., Worall M., Wu S., Riffat S.B. Fuel cell technology for domestic built environment applications. State of-the-art review. *Renew. Sust. Energ. Rev.* 42 (**2015**) 913-931.

Tabla 1.4. / **Table 1.4.** Comparación tecnoeconómica entre el sistema híbrido SOFC/turbina de gas y sus competidores[88]. / Technoeconomic comparison between SOFC and their competitors in the stationary power/CHP sector[88].

Energía estacionaria-Tecnología CHP/Stationary power-CHP technology	Energía/Power level (MW)	Eficiencia[a]/ Efficiency[a] (%)	Durabilidad/ Lifetime (years)	Factor de capacidad/Capacity factor (%)
Híbrido SOFC-turbina de gas/SOFC-gas turbine hybrid	**0.1-100**	**55-65**	**5-20**	**Up to 95**
Ciclo de vapor (carbón)/ Steam cycle (coal)	10-1000	33-40	> 20	60-90
Ciclo de turbina de gas (gas natural)/Gas turbine cycle (natural gas)	0.03-1000	30-40	> 20	Up to 95
Nuclear/Nuclear	500-1400	32	> 20	70-90
Hidroeléctrica/Hydroelectric	0.1-2000	65-90	> 40	40-50
Turbina de viento/Wind turbine	0.1-10	20-50	20	20-40
Geotérmica/Geothermal	1-200	5-20	> 20	Up to 95
Solar fotovoltaica/Solar photovoltaic	0.001-1	10-15	15-25	<25

[a] Desde la entrada de energía a la salida eléctrica. / [a] From energy input to electrical output.

La tecnología SOFC ha dado un gran avance con respecto a años anteriores. No obstante, se necesita realizar más investigación en nuevos materiales, y técnicas de fabricación y de diseño de las celdas SOFC, para lograr su comercialización a gran escala.

SOFC technology has been advancing fast over the past years. However, further research in new materials and, SOFC cells fabrication and design techniques, is necessary for their large-scale commercialization.

1.4. Retos para las celdas SOFC / Challenges of SOFCs

La durabilidad de las celdas SOFC, debe de estar dirigida a la maximización de su rendimiento, y así alcanzar la comercialización de estos dispositivos. Algunos de los procesos de degradación están relaciones con: (i) problemas de contacto entre los componentes de la celda, y (ii) deterioro microestructural y disminución de la actividad catalítica de los electrodos. Los principales problemas que afectan a la estabilidad y durabilidad de la celda se muestran en la Figura 1.12[89-92].

[88] Sharaf O.Z., Orhan M.F. An overview of fuel cell technology: Fundamentals and applications. *Renew. Sust. Energ. Rev.* 32 (**2014**) 810-853.

[89] Barelli L., Barluzzi E., Bidini G. Diagnosis methodology and technique for solid oxide fuel cells: A review. *Int. J. Hydrogen Energ.* 38 (**2013**) 5060-5074.

[90] Yousfi Steiner N., Hissel D., Moçotéguy P., Candusso D., Marra D., Pianese C. Sorrentino M. Application of fault tree analysis to fuel cell diagnosis. *Fuel Cells* 12(2) (**2012**) 302-309.

[91] Yokokawa H., Tu H., Iwanschitz B., Mai A. Fundamental mechanisms limiting solid oxide fuel cell durability. *J. Power Sources* 182 (**2008**) 400-412.

[92] Hsiao Y.C., Selman J.R. The degradation of SOFC electrodes. *Solid State Ionics* 98 (**1997**) 33-38.

The long-term stability of SOFC must be addressed to maximize the performance and thus to reach the commercial status of these devices. Examples of degradation mechanisms include contact problems between adjacent cell components, microstructural deterioration of the porous electrodes, and blocking of the reaction sites within the electrodes. Figure 1.12 shows the main issues that affect the cell stability and durability[89-92].

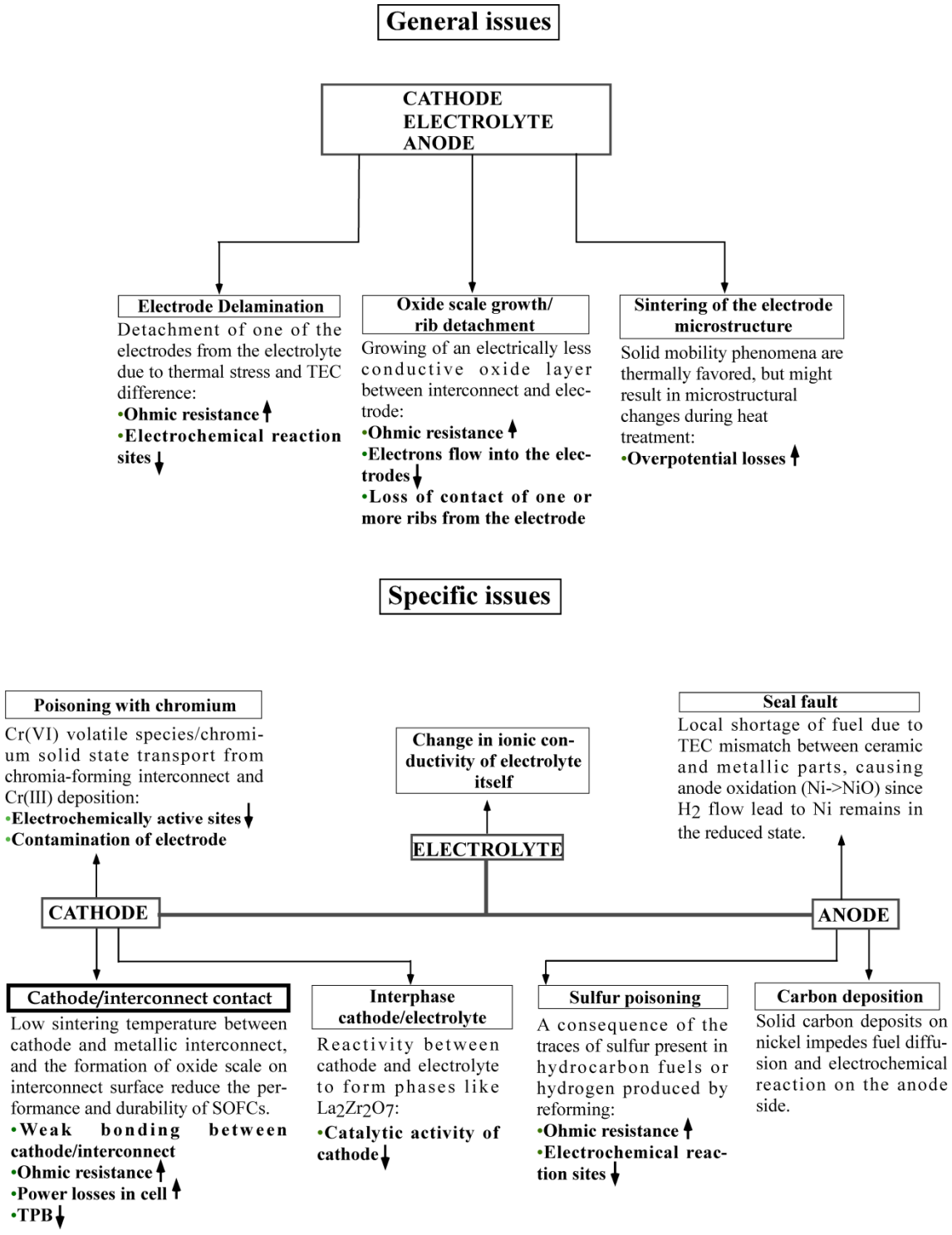

Figura 1.12. / Figure 1.12. Esquema de los principales retos de las celdas de combustible de óxido sólido. / Scheme of the main issues of solid oxide fuel cells at the present.

Los principales factores que causan la degradación microestructural son los largos tiempos de operación a temperaturas elevadas, y el envenenamiento de los electrodos debido a la presencia de contaminantes, tales como el azufre y cromo. El envenenamiento del cátodo se produce por la volatilización de las especies de cromo, CrO_3 (g), $CrO_2(OH)_2$ (g) y $CrO_2(OH)$ (g)), provenientes de la capa pasivadora Cr_2O_3 (s), formada en la superficie del interconector. Estos compuestos de Cr(VI) (g) se reducen a Cr(III) (s) y se depositan en los sitios activos electroquímicos de la TPB bloqueando los mismos, e interaccionan con el material cátodo, dando lugar a fases de baja conductividad eléctrica, que hacen que el rendimiento de las celdas sea menor. La inestabilidad termodinámica, de la capa superficial de óxido formada, es la principal causa para que se dé la formación de especies volátiles, ya que el proceso de oxidación/reducción del cromo es reversible. La formación de las diferentes especies volátiles depende de la presión parcial del oxígeno y del vapor de agua. Así, en la medida que la presión de vapor sea más alta en el aire, es más probable que ocurra el envenenamiento en el cátodo. La vaporización del cromo también se ve afectada por la velocidad de flujo de los gases, la temperatura, y la composición de la capa pasivadora[93]. La deposición de cromo sobre el electrodo puede entenderse a través de mecanismos electroquímicos y/o químicos[94,95]. Así, las especies de vapor que contienen cromo pueden reducirse de forma electroquímica en los puntos triples gas-iones-electrones (TPB). Sin embargo, hay una explicación alternativa basada en la teoría de nucleación, en donde la deposición de cromo ocurre a través de la disociación química de las especies Cr (VI) (g), facilitada por la reacción entre las especies gaseosas y los agentes nucleantes. Por lo tanto, no es necesaria la presencia de TPBs para que también se dé la deposición de especies de cromo.

Long periods of operation at elevated temperature and the electrode poisoning by contaminants, such as chromium and sulfur, are responsible for microstructural degradation. The poisoning of the cathode microstructure with volatile chromium (Cr (VI) (g), such as CrO_3 (g), $CrO_2(OH)_2$ (g) and $CrO_2(OH)$ (g) species) from the interconnect chromia scale leads to the chromium rich compound deposits (Cr (III) (s)) on the cathode electrochemically active sites, affecting cathode active area. Since this process is reversible, the basic reason for chromium volatility is the thermodynamic instability of the formed chromia scales. These volatile chromium species depend on the partial oxygen pressure and water content, being vapor pressure higher in air side than that in the fuel side. Chromium vaporization also is affected by flow rate, temperature and scale composition[93]. The chromium deposition has been attributed to both electrochemical and chemical mechanisms[94,95]. For an electrochemical reaction, deposition occurs at the three phase gas-ions-electrons interface (TPB) which enlarge into the electrode since it shows mixed conducting properties. However, there is an alternative explanation based on a chemical reaction, rather than electrochemical reduction, consists of the nucleation theory, in which chromium deposition is dominated by the chemical dissociation reaction of the high valent gaseous chromium species, facilitated by the nucleation reaction between the gaseous chromium species and nucleation agents.

---

93 Jiang S.P., Chen X. Chromium deposition and poisoning of cathodes of solid oxide fuel cells-A review. *Int. J. Hydrogen Energ.* 39(1) (**2014**) 505-531.

94 Chen X., Zhang L., Liu E., Jiang S.P. A fundamental study of chromium deposition and poisoning at $(La_{0.8}Sr_{0.2})_{0.95}(Mn_{1-x}Co_x)O_{3\pm\delta}$ ($0.0 \leq x \leq 1.0$) cathodes of solid oxide fuel cells. *Int. J. Hydrogen Energ.* 36 (**2011**) 805-821.

95 Park E., Taniguchi S., Daio T., Chou J.-T., Sasaki K. Influence of cathode polarization on the chromium deposition near the cathode/electrolyte interface of SOFC. *Int. J. Hydrogen Energ.* 39 (**2014**) 1463-1475.

Por otra parte, los principales problemas de contacto entre los componentes de estas celdas incluyen la delaminación del electrodo o separación entre electrolito-electrodo debido a la formación de fases secundarias entre cátodo-electrolito y la escasa compatibilidad del coeficiente de expansión térmica de ambos materiales. Este fenómeno también suele ser una consecuencia de los ciclos térmicos o los de oxidación-reducción (ciclados redox), que degradan progresivamente la unión de las dos capas adyacentes. Asimismo, el crecimiento de una capa poco conductora de óxido entre el interconector y el electrodo disminuye el contacto eléctrico entre ambos componentes. En este sentido, la falta de contacto entre las interfases interconector-electrodo y electrodo-electrolito impide el transporte de los electrones y especies iónicas, respectivamente, necesario para extender la superficie de reacción TPB y lograr un buen rendimiento de la celda.

On the other hand, contact problems include delamination of an electrode from the electrolyte, and the growth of a poorly conductive oxide layer between metallic interconnect ribs and the electrode, which favours a lack of contact between both materials. These contact problems have severe consequences on the performance, since they increase the ohmic resistance of the cell, which hinders the transport of electrons and ionic species between interconnect-electrode, and electrode-electrolyte, respectively. Hence, this loss of electrochemically active surface area in a porous electrode has a negative impact on the cell performance because it causes a decrease in the amount of reaction sites (TPB) available within the electrode volume.

Como consecuencia de la reducción de los sitios electroquímicos activos de la TPB, el *rib* del interconector adyacente a una delaminación contiene menos corriente que cuando éste está próximo a una zona libre de delaminación, ya que el área del cátodo afectada es electroquímicamente inactiva y no genera demanda de portadores de carga. Por otra parte, como ya se ha indicado anteriormente, la oxidación del interconector obstaculiza también el paso de electrones hacia el cátodo. En este sentido, la pérdida de contacto eléctrico entre *rib*-cátodo hace que los electrones no puedan cruzar esta interfase, y busquen otra zona por donde puedan acceder al cátodo. De ahí que los ribs del interconector próximos a interfases "intactas" de interconector-cátodo y cátodo-electrolito sufran un aumento de su densidad de corriente, lo cual conlleva un sobrecalentamiento localizado, aumentando la velocidad de oxidación en dicha zona[96] (Figura 1.13).

Electrode delamination consist of a detachment of one of the electrodes from the electrolyte. This phenomenon is usually a consequence of thermal or redox cycling, which progressively degrades the bonding of the two adjacent layers at the interphase. Thus, the rib adjacent to the delamination carries less current than it does when the entire cell is intact, because the cathode segment affected by delamination is electrochemically inactive and does not generate any demand for charge carriers. Moreover, as it has said before, the interconnect oxidation is another important degradation mode affecting contact resistance due to the formed chromium oxide layer hinders the electrons flow into the cathode coating. Therefore, electron conduction can also be interrupted because of the loss of contact of one or more ribs from the cathode material. So, the electronic current cannot go from the interconnect to the cathode through the affected ribs. Consequently, the electronic current density increases at the first intact rib adjacent to the group of detached ribs, since the cell below the interconnect detachment is still electrochemically active. This increased local

[96] Gazzarri J.I., Kesler O. Short-stack modeling of degradation in solid oxide fuel cells Part I. Contact degradation. *J. Power Sources* 176 (**2008**) 138-154.

current density could lead to further degradation becouse of localized overheating, such as an increase in chromia growth rate[96] (Figure 1.13).

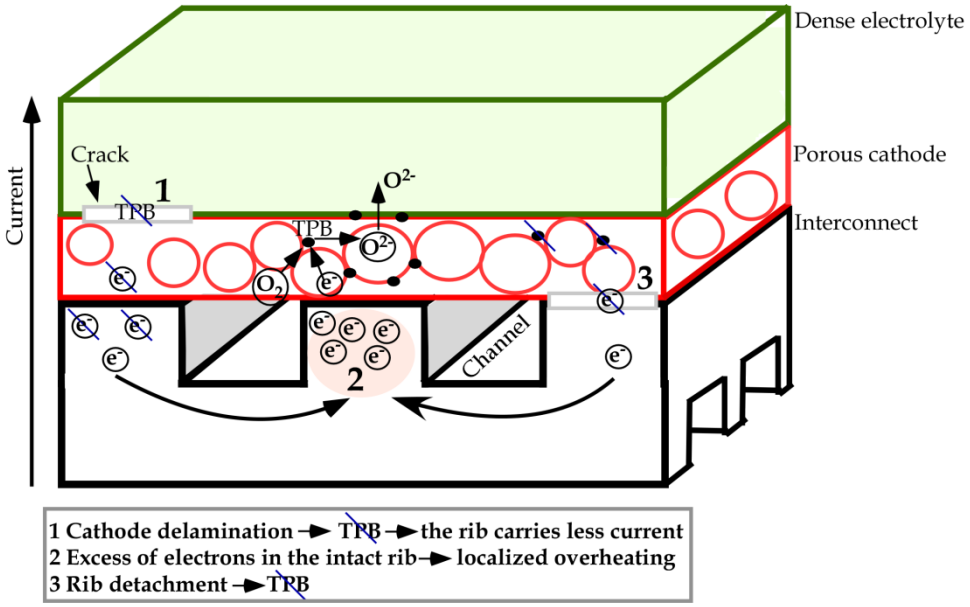

Figura 1.13. / **Figure 1.13.** Principales procesos de degradación debidos a la falta de contacto entre cátodo-electrolito y cátodo-interconector. / The main degradation processes due to lack of contact between cathode/electrolyte and cathode/interconnect.

Son muchas las estrategias seguidas para disminuir los procesos de degradación mostrados en este apartado. En este contexto, esta memoria se centra en la aplicación de capas de contacto que actúen como adhesivo eléctrico para conectar catodo-interconector, y disminuir así las pérdidas óhmicas que se producen en las celdas SOFC a día de hoy.

A number of different strategies might be applied to reduce the identified main degradation processes. In this context, this thesis is focused on the application of conductive coatings acting as an electric adhesive to connect the cathode with the substrate, which could increase the performance of SOFCs.

1.4.1. Capas de contacto / Contact coatings

Mantener una adecuada adhesión entre el interconector y electrodo es muy importante para asegurar la durabilidad de los stacks de SOFCs. En las celdas de combustible de óxido sólido de alta temperatura (HT-SOFCs), el enlace entre el cátodo y el interconector $LaCrO_3$ se consigue, normalmente, mediante el sinterizado a 1300 ºC. Este tratamiento asegura un enlace fuerte entre ambos componentes y, por lo tanto, no se requiere del empleo de materiales de contacto. Sin embargo, el uso de interconectores metálicos en sustitución de materiales cerámicos para las SOFC de temperatura intermedia (IT) limita la temperatura de sinterizado de la celda[97,98]. En este sentido,

[97] Wu J., Liu X. *J. Mater. Sci. Technol.* 26(4) **(2010)** 293-305.
[98] Sun C., Hui R., Roller J. Cathode materials for solid oxide fuel cells: a review. *J. Solid State Electrochem.* 14 **(2010)** 1125-1144.

se hace necesario el empleo de capas de contacto que proporcionen un enlace homogéneo y eviten las pérdidas óhmicas entre dichos materiales[99]. Así, en las IT-SOFCs, la conexión entre cátodo e interconector se lleva a cabo mediante la compresión de los *stack* al aplicar una presión y, además, se añaden materiales de contacto que actúen como colector de corriente entre el cátodo y el sustrato metálico[100] (Figura 1.14).

Interconnect-electrode interfacial adhesion is very important for the durability of the SOFC stacks. In HT-SOFCs, the bond between the cell and the $LaCrO_3$ interconnect is typically realized by sintering at 1300 ºC. A solid bond with good electrical contact is obtained and no other contact material is then required. However, the use of chromium-containing ferritic stainless steels interconnects limits the sintering temperature of IT-SOFCs[97,98], thus, the use of a contact material between metallic interconnect and porous electrode could provide a homogeneous bonding, avoiding power losses between both materials[99]. Hence, connection of the cathode to the interconnect is usually accomplished by compression of the stack using an external load frame, and is helped by using a contact layer, which acts as current collecting layer between the interconnect and electrode. Figure 1.14 shows the concept of cathode contact layer when catalyst layer or cathode is an electronic-ionic composite material[100].

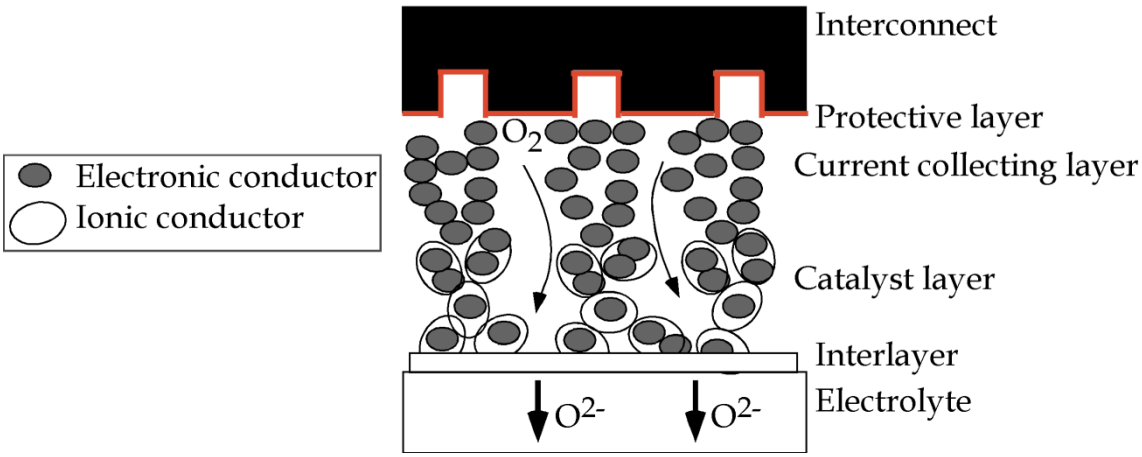

Figura 1.14. / Figure 1.14. Representación esquemática de las intercapas electrolito-interconector en una celda SOFC. / Schematic representation of contact-cathode layers for SOFCs.

Los materiales empleados como capa de contacto entre interconector y cátodo deben cumplir los siguientes requisitos[101-103]: (i) alta conductividad eléctrica para reducir la propia resistencia del material, (ii) estabilidad química y estructural en atmósfera oxidante, a la temperatura de operación de la celda, (iii) apropiada actividad de sinterización para mantener un compromiso entre un grado

[99] Mat A., Timurkutluk B., Timurkutluk C., Kaplan Y. Effects of ceramic based pastes on electrochemical performance of solid oxide fuel cells. *Ceram. Int.* 40 (**2014)** 8575-8583.

[100] Tao Y. Nishino H., Ashidate S., Kokubo H., Watanabe M., Uchida H. Polarization properties of $La_{0.6}Sr_{0.4}Co_{0.2}Fe_{0.8}O_3$-based double layer-type oxygen electrodes for reversible SOFCs. *Electrochim. Acta* 54 (**2009**) 3309-3315.

[101] Yang Z., Xia G., Singh P., Stevenson J.W. Electrical contacts between cathodes and metallic interconnects in solid oxide fuel cells. *J. Power Sources* 155 (**2006**) 246-252.

[102] Wang F., Yan D., Zhang W., Chi B., Pu J., Jian L. $LaCo_{0.6}Ni_{0.4}O_{3-\delta}$ as cathode contact material for intermediate temperature solid oxide fuel cells. *Int. J. Hydrogen Energ.* 38 (**2013)** 646-651.

[103] Tucker M.C., Cheng L., DeJonghe L.C. Selection of cathode contact materials for solid oxide fuel cells. *J. Power Sources* 196 (**2011)** 8313-8322.

de compactación que aporte las propiedades eléctricas necesarias a la capa de contacto, sin acelerar el proceso de corrosión del metal y, además, que permita una elevada área de contacto, (iv) compatibilidad química con los materiales adyacentes y coeficientes de expansión térmica semejantes al resto de componentes que garanticen la compatibilidad termomecánica, y (v) una adecuada permeabilidad a los gases, manteniendo la integridad estructural necesaria de la capa.

The cathode contact materials compositions should fulfill the following requirements[101-103]: i) high electrical conductivity to minimize the resistance of the contact layer itself ii) high sinterability to ensure high mechanical strength and good bonding with the adjacent components, iii) chemically compatible and appropriate thermal expansion behavior with the adjacent materials, iv) high thermochemical and structural stability in the oxidizing cathode environment, and v) an adequate gas permeability, maintaining the mechanical integrity of the formed layer.

Son muchos los tipos de materiales de contacto estudiados en la bibliografía, entre los cuales se incluyen: (i) metales nobles (Ag) o composites de metales nobles-perovskitas (Ag-$(La_{0.6}Sr_{0.4})(Co_{0.8}Fe_{0.2})O_3$, Ag-$La_{0.8}Sr_{0.2}MnO_3$), (ii) óxidos mixtos con estructura perovskita, utilizados como cátodos convencionales[104] ($La_{0.8}Sr_{0.2}Co_{0.75}Fe_{0.25}O_3$, $La_{0.8}Sr_{0.2}FeO_3$), (iii) óxidos mixtos con estructura espinela, M_3O_4 (M=Ni,Mn,Co,Cu,Fe), (iv) nuevos óxidos como $Ni_{0.33}Co_{0.67}O$, y (v) capas metálicas-cerámicas, como la doble capa compuesta por $Ni_{80}Cr_{20}$ / $(La_{0.75}Sr_{0.25})_{0.95}MnO_3$, la cual podría proporcionar un "puente" de unión entre el interconector y cátodo, aumentando la conductividad y adhesión de dicha interfase, sin el empleo de tratamientos de sinterizado a alta temperatura[105].

Cathode/interconnect contact materials in SOFCs include many type of compounds: i) noble metals (Ag) or noble metal-perovskite composites (Ag-$(La_{0.6}Sr_{0.4})(Co_{0.8}Fe_{0.2})O_3$, Ag-$La_{0.8}Sr_{0.2}MnO_3$), ii) conventional perovskite cathode materials[104] (such as, $La_{0.8}Sr_{0.2}Co_{0.75}Fe_{0.25}O_3$, $La_{0.8}Sr_{0.2}FeO_3$), iii) oxides with a spinel structure, M_3O_4 (M=Ni, Mn, Co, Cu, Fe), or iv) recently developed oxides like $Ni_{0.33}Co_{0.67}O$, or v) metallic-ceramic coatings, such as $Ni_{80}Cr_{20}/(La_{0.75}Sr_{0.25})_{0.95}MnO_3$ dual-layer, which could bridge the gap between interconnect and electrode, increasing the conductivity and adhesive ability of the interface between both materials, without using a high temperature sintering process[105].

---

[101] Yang Z., Xia G., Singh P., Stevenson J.W. Electrical contacts between cathodes and metallic interconnects in solid oxide fuel cells. *J. Power Sources* 155 (**2006**) 246-252.

[102] Wang F., Yan D., Zhang W., Chi B., Pu J., Jian L. $LaCo_{0.6}Ni_{0.4}O_{3-\delta}$ as cathode contact material for intermediate temperature solid oxide fuel cells. *Int. J. Hydrogen Energ.* 38 (**2013**) 646-651.

[103] Tucker M.C., Cheng L., DeJonghe L.C. Selection of cathode contact materials for solid oxide fuel cells. *J. Power Sources* 196 (**2011**) 8313-8322.

[104] Skinner S.J., Laguna-Bercero M.A. Advanced Inorganic Materials for Solid Oxide Fuel Cells, in Energy Materials (eds. Bruce D.W., O'Hare D., Walton R.I.), John Wiley & Sons, Ltd, Chichester, UK, **2011**. doi: 10.1002/9780470977798.ch2.

[105] Wu W., Guan W., Wang G., Liu W., Zhang Q., Chen T., Wang W.G. Evaluation of $Ni_{80}Cr_{20}/(La_{0.75}Sr_{0.25})_{0.95}MnO_3$ dual layer coating on SUS 430 stainless steel used as metallic interconnect for solid oxide fuel cells. *Int. J. Hydrogen Energ.* 39 (**2014**) 996-1004.

Sin embargo, los óxidos con estructura perovskita se han estudiado especialmente como materiales de contacto del cátodo[106-108]. Las composiciones con B=Co, Ni se han utilizado debido a su alta conductividad eléctrica, mientras que los óxidos con B=Cr, Fe, Mn son característicos por su estabilidad a elevadas temperaturas[109-111]. La introducción de metales alcalinotérreos como Ca, Ba o Sr aumentan la actividad de sinterizado y la conductividad. Estudios realizados con la fase $(La_{1-x}Sr_x)MnO_3$ han demostrado que esta composición cambia el comportamiento de oxidación y mejora la durabilidad de los interconectores metálicos[112]. Cuando se han utilizado las fases $(La,Sr)CoO_3$, $(La,Sr)(Co,Fe)O_3$ y $La(Ni,Fe)O_3$, como capas de contacto, sobre diferentes aleaciones ferríticas (Crofer22APU, E-Brite y 430), se ha observado[113] una difusión de los cationes B de la perovskita (Ni,Fe,Co), hacía la fase con estructura espinela, formada a partir de los metales de transición presentes en la aleación, que proporciona una mayor conductividad eléctrica a la capa de óxido. Además, algunos estudios[114-117] han puesto de manifiesto que en comparación a las fases Ruddlesden-Popper ($Nd_{1.8}Ce_{0.2}CuO_4$, $La_{1.2}Sr_{0.8}NiO_4$), las perovskitas como $La(Ni,Co)O_{3-\delta}$, $La(Ni,Fe)O_{3-\delta}$ y/o $LaSr(Fe,Co)O_3$ muestran una menor reactividad con la espinela protectora $MnCo_2O_4$.

However, the perovskite structure oxides have been widely investigated for cathode contact applications[106-108]. Compositions with B=Co, Ni have been used because of their high conductivity, while the oxides with B=Cr, Fe, Mn are known to be stable at high temperatures[109-111]. Moreover, the introduction of alkali-earth elements, such as Sr, increases the sintering activity and the conductivity. Other authors indicated that $(La_{1-x}Sr_x)MnO_3$ coatings change the oxidation behaviour and enhance the long term stability of metallic interconnects[112]. In other works, $(La,Sr)CoO_3$, $(La,Sr)(Co,Fe)O_3$ and $La(Ni,Fe)O_3$ coated ferritic alloys (Crofer22APU, E-Brite and 430) were studied[113], concluding that perovskite B-site cations (Ni, Fe, Co) diffuse to form stable spinel with

---

106 Tietz F., Sebold D. Interface reactions between electrically conductive ceramics and ferritic steel-I. The system Cr-22Fe-0.5Mn/Mn_2O_3/(La,Ca)(Cr,Co,Cu)O_3. *Mater. Sci. Eng. B* 150 (2008) 135-140.

107 Sharma V.I., Yildiz B. Degradation mechanism in $La_{0.8}Sr_{0.2}CoO_3$ as contact layer on the solid oxide electrolysis cell anode. *J. Electrochem. Soc.* 157(3) (**2010**) B441-B448.

108 Montero X., Tietz F., Stöver D., Cassir M., Villarreal I. Comparative study of perovskites as cathode contact materials between an $La_{0.8}Sr_{0.2}FeO_3$ cathode and a Crofer22APU interconnect in solid oxide fuel cells. *J. Power Sources* 188 (**2009**) 148-155.

109 Millar L., Taherparvar H., Filkin N., Slater P., Yeomans J. Interaction of $(La_{1-x}Sr_x)_{1-y}MnO_3$-$Zr_{1-z}Y_zO_{2-\delta}$ cathodes and $LaNi_{0.6}Fe_{0.4}O_3$ current collecting layers for solid oxide fuel cell application. Proceedings of the Conference for the Engineering Doctorate in Enviromental Technology, University of Surrey, **2008**.

110 Basu R.N., Tietz F., Teller O., Wessel E., Buchkremer H.P., Stöver D. $LaNi_{0.6}Fe_{0.4}O_3$ as a cathode contact material for solid oxide fuel cells, *J. Solid State Electrochem.* 7 (**2003**) 416-420.

111 Konysheva E., Laatsch J., Wessel E., Tietz F., Christiansen N., Singheiser L., Hilpert K. Influence of different perovskite interlayers on the electrical conductivity between $La_{0.65}Sr_{0.3}MnO_3$ and Fe/Cr based steels. *Solid State Ionics* 177 (**2006**) 923-930.

112 Conceiçao L.D., Dessemond L., Djurado E., Souza M.M.V.M. $La_{0.7}Sr_{0.3}MnO_3$-coated SS444 alloy by dip-coating process for metallic interconnect supported solid oxide fuel cells. *J. Power Sources* 241 (**2013**) 159-167.

113 Lacey R., Pramanick A., Lee J.C., Jung J.I., Jiang B., Edwards D.D., Naum R., Misture S.T. Evaluation of Co and perovskite Cr-blocking thin films on SOFC interconnects. *Solid State Ionics* 181 (**2010**) 1294-1302.

114 Wang F., Yan D., Zhang W., Chi B., Pu J., Jian L. $LaCo_{0.6}Ni_{0.4}O_{3-\delta}$ as cathode contact material for intermediate temperature solid oxide fuel cells. *Int. J. Hydrogen Energ.* 38 (**2013**) 646-651.

115 Zhang W., Wang F., Wang K., Pu J., Chi B., Jian L. Chemical compatibility and electrical contact between Ni–Cr–Mo alloy and $LaCo_{0.6}Ni_{0.4}O_{3-\delta}$ in intermediate temperature solid oxide fuel cells. *Int. J. Hydrogen Energ.* 37 (**2012**) 17253-17257.

116 Guan W.B., Zhai H.J., Jin L., Li T.S., Wang W.G. Effect of contact between electrode and interconnect on performance of SOFC stacks. *Fuel Cells*, 11 (3) (**2011**) 445-450.

117 Tucker M.C., Cheng L., De Jonghe L.C. Inorganic binder-containing composite cathode contact materials for solid oxide fuel cells. *J. Power Sources* 224 (**2013**) 174-179.

transition metals from the interconnect. Moreover, some studies[114-117] have concluded that perovskite oxides such as $La(Ni,Co)O_{3-\delta}$, $La(Ni,Fe)O_{3-\delta}$ and/or $LaSr(FeCo)O_3$ have lower reactivity with spinel protective layers ($MnCo_2O_4$) than Ruddlesden-Popper structure phases ($Nd_{1.8}Ce_{0.2}CuO_4$, $La_{1.2}Sr_{0.8}NiO_4$).

A pesar de las interacciones, entre este tipo de materiales y las aleaciones formadoras de óxido de cromo, que causan la formación de fases como $SrCrO_4$, Cr-espinelas y/o Cr-perovskitas, el empleo de materiales de contacto, en la mayoría de los casos, sigue siendo eficaz para mejorar el contacto eléctrico entre cátodo e interconector metálico.

Despite the interactions of these kind of materials with Cr-containing steel interconnects, due to their susceptibility to form phases like $SrCrO_4$, Cr-spinels or Cr-perovskites, the use of those materials, in most of the cases, are effective for improving the electrical contact between the cathodes and metallic interconnects.

1.5. Materiales empleados en este estudio / Materials used in this study

Este trabajo se centra en la parte oxidante de una pila de combustible de óxido sólido (SOFC) (Figura 1.15).

This work focuses on the oxidizing side of a solid oxide fuel cell (SOFC) (Figure 1.15).

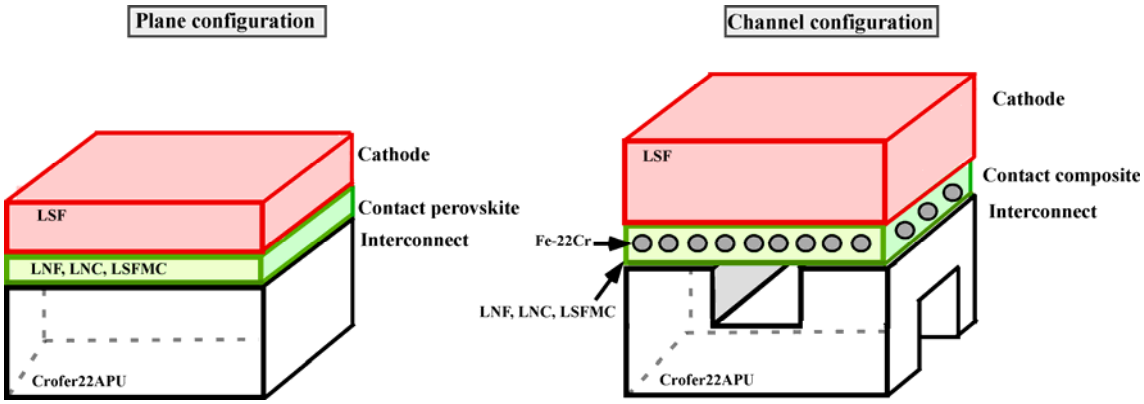

Figura 1.15. / **Figure 1.15.** Materiales y configuraciones empleadas en este trabajo. / Materials and configurations used in this study.

Para la construcción de las celdas, presentadas en esta memoria, se ha utilizado como cátodo la ferrita $La_{0.6}Sr_{0.4}FeO_3$ (LSF), como interconector un acero inoxidable ferrítico (Crofer22APU) plano y mecanizado formando canales, y como capas de contacto de partida tres óxidos mixtos con estructura perovskita $LaNi_{0.6}Fe_{0.4}O_{3-\delta}$ (LNF), $LaNi_{0.6}Co_{0.4}O_{3-\delta}$ (LNC) y $(La_{0.8}Sr_{0.2})_{0.95}Fe_{0.6}Mn_{0.3}Co_{0.1}O_3$ (LSFMC), a partir de los cuales se ha desarrollado un nuevo material de contacto: un composite formado por una malla metálica Fe-22Cr recubierta por inmersión (dip coating) en las suspensiones o pastas formuladas a partir de las cerámicas iniciales.

The cells presented in this Thesis have been built using: $La_{0.6}Sr_{0.4}FeO_3$ (LSF) ferrite as cathode, Crofer22APU ferritic stainless steel, with and without machining channels, as interconnect, and three perovskite-type mixed oxides, $LaNi_{0.6}Fe_{0.4}O_{3-\delta}$ (LNF), $LaNi_{0.6}Co_{0.4}O_{3-\delta}$ (LNC) and $(La_{0.8}Sr_{0.2})_{0.95}Fe_{0.6}Mn_{0.3}Co_{0.1}O_3$ (LSFMC), as initial contact coatings. Starting from these coatings it has developed a new contact composite: a Fe-22Cr metallic mesh coated by dipping into the pastes, which are made based on the initial ceramics.

1.6. Objetivos / Objetives

El principal objetivo de este trabajo consiste en el desarrollo de capas de contacto como solución a las pérdidas óhmicas interconector-cátodo, existentes en las celdas de combustible de óxido sólido (SOFC) a día de hoy.

En este aspecto, se plantean nuevos retos a los que es necesario dar solución. Entre otros, resulta imprescindible obtener un material de contacto de gran conductividad electrónica, relativamente denso que permita el flujo del gas oxidante, y con un fuerte enlace al interconector metálico y cátodo cerámico. No obstante, otro de los retos que se plantea es obtener una capa con una adecuada integridad mecánica, para que ésta pueda ser depositada sobre el interconector, sin limitar el flujo del gas oxidante por los canales. Se pretende, también, analizar los procesos de reacción que se producen en las interfaces interconector-cátodo e interconector-capa de contacto-cátodo, que alteran las propiedades electroquímicas.

En primer lugar, la estrategia seguida para abordar estos retos ha consistido en estudiar los sistemas interconector-cátodo e interconector-capa de contacto-cátodo, utilizando como interconector una placa metálica plana, lo cual ha facilitado la deposición de la capa de contacto así como el posterior análisis de los sistemas. Este estudio, ha permitido caracterizar los materiales de partida, además de identificar diferentes procesos de degradación, permitiendo sustituir la configuración inicial de la celda por una configuración de canales, obtenida a través del uso de un interconector acanalado, formado a partir de la placa metálica inicial. Así, además de simular una celda SOFC más real, también ha permitido el desarrollo de un composite como capa de contacto, formado por una malla metálica Fe-22Cr recubierta por inmersión de los óxidos de contacto seleccionados previamente.

La aplicación de largos tiempos de operación sobre esta nueva estructura, interconector de canales-composite de contacto, para su posterior estudio a partir de sus propiedades estructurales, microestructurales, espectroscópicas y electroquímicas, ha permitido una caracterización detallada de este sistema.

Una vez optimizada esta nueva estructura, con objeto de garantizar el flujo del gas oxidante a través del material composite, mediante un láser de femtosegundos, se han realizado microperforaciones sobre el composite y, posteriormente, se ha depositado el cátodo sobre el mismo. Este trabajo finaliza con el estudio de esta nueva estructura, interconector de canales-composite de contacto micromecanizado-cátodo, en base a su respuesta electroquímica y estabilidad a largos tiempos de operación.

Nowadays, interconnect-cathode contact, in a solid oxide fuel cell (SOFC), is dependent on contact layers to ensure adequate application lifetime. The main goal of this work is to develop contact coating materials to promote ohmic contact formation between interconnect and the electrode. Respecting this, new challenges arise out that need resolving.

The principal subobjectives of this work include: find a relatively dense and high electrical conductive contact material, which acts as strong adhesive bond between metallic interconnect and ceramic cathode, facilitates gas distribution to cathode, and provides mechanical support to be a continuous layer without sacrificing the flow of the air through the channels. It also aims at analyzing the reaction processes that occur at interconnect-contact coating-cathode interfaces, which change electrochemical behavior of the cell.

Firstly, to address these challenges, interconnect-cathode and interconnect-contact coating-cathode systems have been studied, using a metallic sheet as interconnect, in order to facilitate the contact layer deposition as well as the subsequent analysis. Thus, the characterization of starting materials and identification of the cell degradation processes have been carried out. From the obtained results, starting cell configuration has changed from flat to channel one. The initial alloys were machined to form a channel structure. Hence, this structure allowed to simulate a more realistic SOFC cell, and has also led the process for the development of a new composite material as contact coating which is formed by: a Fe-22Cr mesh dip coated with a ceramic slurry based on previously selected contact perovskites.

A detailed characterization of this new structure, channeled interconnect-contact composite, has performed through long-term stability tests and the post analysis from structural, microstructural, spectroscopic and electrochemical measurements.

Being the channeled structure optimized, in order to ensure rapid oxidant gases transfer through the composite, femtosecond laser machined holes are performed in the ceramic/metallic composites and then, cathode is deposited to form a new interconnect-contact coating-cathode structure. The reproducibility of the developed cell fabrication methodology and its durability and electrochemical behavior have been studied, giving a final discussion of the obtained results.

1.7. Visión global de los hallazgos / Overview of findings

Los resultados más relevantes de este trabajo, se presentan siguiendo un orden cronológico, y se recogen en las secciones 2, 3 y 4 de esta memoria.

En buen acuerdo con la bibliografía consultada sobre pilas de combustible de óxido sólido (SOFCs), la necesidad de emplear un material de contacto que actúe como "pegamento conductor" entre el interconector y el cátodo, se hace cada vez más latente. Así, el punto de partida de esta memoria comienza con la comprobación experimental de la problemática planteada. Para ello, se han seleccionado tres óxidos mixtos de estructura perovskita, con fórmulas $LaNi_{0.6}Fe_{0.4}O_{3-\delta}$ (LNF), $LaNi_{0.6}Co_{0.4}O_{3-\delta}$ (LNC) y $(La_{0.8}Sr_{0.2})_{0.95}Fe_{0.6}Mn_{0.3}Co_{0.1}O_3$ (LSFMC), como materiales de contacto. LNF, LNC y LSFMC destacan por su alta estabilidad, su alta conductividad, y adecuado coeficiente de expansión térmico, respectivamente. Con objeto de simular los sistemas interconector-cátodo e interconector-capa de contacto-cátodo, se han seleccionado $La_{0.6}Sr_{0.4}FeO_3$ (LSF) y Crofer22APU como cátodo e interconector, respectivamente.

La sección 2 de esta memoria (*Characterization of the starting materials. Evaluation of the system in plane configuration*) tiene como objetivo principal caracterizar los materiales de partida, y los procesos químicos que ocurren en las interfases interconector-cátodo e interconector-capa de contacto-cátodo, mediante el estudio estructural, microestructural, espectroscópico y electroquímico. Los resultados obtenidos confirman una reducción en la resistencia entre Crofer22APU-LSF al añadir un material de contacto entre ambos. La resistencia al flujo de electrones entre las interfases interconector-capa de contacto-cátodo, en las primeras horas de ensayo a 800ºC (temperatura de funcionamiento de una celda SOFC), viene dada por la conductividad intrínseca del material de contacto, obteniendo una gran densidad de corriente en el sistema Crofer22APU-LNC-LSF. Sin embargo, a largos tiempos, además de la conductividad del material de contacto, su compatibilidad estructural y química con los materiales adyacentes, comienzan a tener relevancia en la adecuada respuesta electroquímica de estos sistemas. En este sentido, se ha considerado que los materiales LNF y LNC son los más prometedores debido a su adecuada compatibilidad estructural y química con el cátodo e interconector, y su alta capacidad de conducción de electrones.

- *J. Power Sources* 248 (**2014**) 1067-1076.
- *Fuel Cells* 13(3) (**2013**) 398-403.
- *Mater. Charact.*, sent (MTL-15064), **2015**.

En este primer estudio, con objeto de facilitar el proceso de deposición del material de contacto sobre el interconector, así como su estudio posterior, se ha empleado como interconector una placa metálica de Crofer22APU, evaluando así el sistema en una configuración plana. Sin embargo, en las secciones 3 y 4 de este trabajo, con el fin de adaptar la celda estudiada a un sistema más real, se ha adecuado el interconector a una placa acanalada, sin cambiar la composición química del mismo.

El segundo reto de esta investigación tiene como objetivo formar una capa de contacto que posea las características, ya destacadas, para un buen material de contacto, y una integridad estructural que permita la continuidad de la misma sobre el interconector, sin interferir en el flujo de los canales. En este contexto, se ha creado un composite metálico-cerámico a través de la técnica de dip coating: la parte metálica está formada por una malla de Fe-22Cr y, la cerámica, por una suspensión de los materiales de contacto seleccionados en el bloque anterior: LNF y LNC, obteniendo así un

composite para cada material cerámico. Se ha estudiado la viabilidad de este nuevo material como material de contacto, haciendo hincapié en sus propiedades físicas, químicas y eléctricas. Asimismo, se ha observado su estabilidad a largos tiempos a 800ºC, y su adherencia y compatibilidad estructural-química con el interconector acanalado. Los resultados de estos estudios se recogen en la sección 3 (*Formation and characterization of a new composite contact material. Evaluation of the system in channel configuration*). Se observan resultados satisfactorios en ambos materiales, obteniendose una menor resistencia al paso de corriente en el sistema interconector-malla/LNC. Además, se ha incluido un primer estudio de la posible mejora del composite si se recubre la malla metálica con la espinela $MnCo_{1.9}Fe_{0.1}O_4$ (MCF) como capa protectora.

- *J. Power Sources* 269 (**2014**) 509-519.
- *Int. J. Hydrogen Energ.* 40 (**2015**) 4804-4818.

En la sección 4 de esta memoria *(Real system evaluation: channeled interconnect-laser micromachined composite contact coating-cathode structure)*, se propone el empleo de una configuración final interconector-capa de contacto-cátodo y para ello, una vez formado el sistema interconector-composite, mediante el empleo de un láser de femtosegundos, se ha micromecanizado el composite empleado como capa de contacto, garantizando así el flujo del gas oxidante hasta el cátodo. En primer lugar, se ha definido los parámetros óptimos empleados para el láser y los daños causados por el mismo. Una vez caracterizada la interacción láser-composite, se ha evaluado el sistema interconector acanalado-composite micromecanizado-cátodo a través de estudios de estabilidad y respuesta electroquímica. Se ha demostrado una adecuada reproducibilidad del proceso, y resistencias bajas al paso de corriente a través de estas estructuras.

- *J. Power Sources*, under review (D-15-02057), **2015**.
- *Int. J. Hydrogen Energ.,* in press (doi: 10.1016/j.ijhydene.2015.04.134), **2015**.

The relevant results of this work are presented in a chronological order and collected in the second, third and fourth thesis sections.

It becomes increasingly important to use contact materials that act as "conductive adhesive" between interconnect and cathode, in good agreement with reported solid oxide fuel cells (SOFCs) literature. Thus, three perovskite-type mixed oxides, $LaNi_{0.6}Fe_{0.4}O_{3-\delta}$ (LNF), $LaNi_{0.6}Co_{0.4}O_{3-\delta}$ (LNC) and $(La_{0.8}Sr_{0.2})_{0.95}Fe_{0.6}Mn_{0.3}Co_{0.1}O_3$ (LSFMC), have been selected as contact materials to check experimentally the issue raised. LNF, LNC and LSFMC are characterized by their high stability, metallic conductivity, and adequate thermal expansion coefficient, respectively. $La_{0.6}Sr_{0.4}FeO_3$ (LSF) cathode and Crofer22APU interconnect are selected to simulate interconnect-cathode and interconnect-contact coating-cathode structures.

The goal of the second section of this work (*Characterization of the starting materials. Evaluation of the system in plane configuration*) has been to describe interconnect-cathode and interconnect-contact coating-cathode structures, in a plane configuration, focusing on structural, microstructural, spectroscopic and electrochemical analyses of these cells. Physical, chemical and electrical properties of the starting cell components are also included. The obtained results confirm that the contact resistance at the Crofer22APU-LSF interface is reduced as result of adding a contact coating between both materials. The initial area specific resistance of interconnect-contact coating-cathode interfaces depends on electrical conductivity of the contact perovskites. For Crofer22APU-LNC-LSF system, a high current density has been registered. However, long-term electrochemical response of these kinds of systems, under operating conditions, also depends on the interaction between the contact material and adjacent components. In this context, LNF and LNC are considered the most promising materials due to their adequate structural integrity, low reactivity between the applied layers, and high electrical conductivity.

- *J. Power Sources* 248 (**2014**) 1067-1076.
- *Fuel Cells* 13(3) (**2013**) 398-403.
- *Mater. Charact.*, sent (MTL-15064), **2015**.

The use of flat and channel designs of Crofer22APU interconnect has led to evaluate the system in plane and channel configurations. The second section of this work has focused on the evaluation of the system in plane configuration to facilitate deposition of the cell components, and posterior analysis process. However, the used flat configuration can be adapted to a more real system using a channelled interconnect, as has been described in the third and fourth sections of this work.

The second challenge of this investigation is to develop a contact material, which has the characteristics already highlighted, and adequate structural integrity without sacrificing the flow of the air through the channels. In this context, the development of a new metallic-ceramic contact composite has been carried out: previously selected contact materials, LNF and LNC, were applied onto Fe-22Cr mesh squares by dipping them into the prepared ceramic slurries. The electrical resistance, chemical compatibility and adherence between ceramic and metallic parts of the composite, under long term operating conditions at 800 ºC, are determined. Results of electrical performance and stability of interconnect-composite structure are also presented. All of these results are shown in the third section (*Formation and characterization of a new composite contact material. Evaluation of the system in channel configuration*). Satisfactory results have been observed for both materials, obtaining the lowest resistance to current flow in interconnect-mesh/LNC system. An initial study of a possible improvement in the developed composite

properties if the mesh is coated with $MnCo_{1.9}Fe_{0.1}O_4$ (MCF) spinel as a protective layer has also included.

- *J. Power Sources* 269 (**2014**) 509-519.
- *Int. J. Hydrogen Energ.* 40 (**2015**) 4804-4818.

In the fourth section of this work (*Real system evaluation: channeled interconnect-laser micromachined composite contact coating-cathode structure*), the use of a final interconnect-contact layer-cathode configuration is proposed. Being interconnect-composite structure formed, microholes are performed on contact composite coating, using a femtosecond laser, thus, ensuring rapid oxidant gas transfer up to the cathode. Firstly, the optimum laser parameters and the effect of drilling on the initial sample elemental composition are discussed. After the laser-composite interaction has been characterized, the channeled interconnect-micromachined contact composite-cathode system has been analysed in terms of stability and electrochemical behaviour. An adequate reproducibility of the process and low contact resistance through the studied structure interfaces is observed.

- *J. Power Sources*, under review (D-15-02057), **2015**.
- *Int. J. Hydrogen Energ.,* in press (doi: 10.1016/j.ijhydene.2015.04.134), **2015**.

2. CHARACTERIZATION OF THE STARTING MATERIALS. EVALUATION OF THE SYSTEM IN PLANE CONFIGURATION

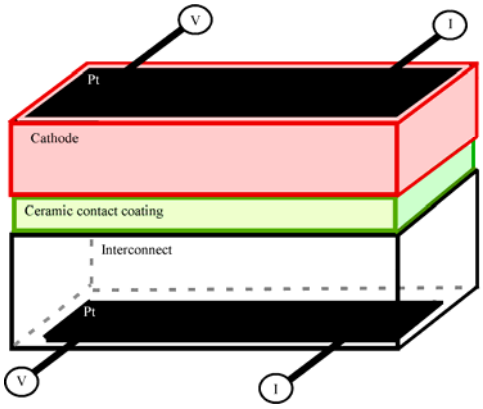

2.1. Effects of using $(La_{0.8}Sr_{0.2})_{0.95}Fe_{0.6}Mn_{0.3}Co_{0.1}O_3$, $LaNi_{0.6}Fe_{0.4}O_{3-\delta}$ and $LaNi_{0.6}Co_{0.4}O_{3-\delta}$ as contact materials on solid oxide fuel cells. *J. Power Sources* 248 (**2014**) 1067-1076.

2.2. Chemical compatibility and electrical contact of $LaNi_{0.6}Co_{0.4}O_{3-\delta}$ (LNC) between Crofer22APU interconnect and $La_{0.6}Sr_{0.4}FeO_3$ (LSF) cathode for IT-SOFC. *Fuel Cells* 13(3) (**2013**) 398-403.

2.3. Solid oxide fuel cell improvement using a ceramic contact material between Crofer22APU interconnect and $La_{0.6}Sr_{0.4}FeO_3$ cathode. *Mater. Charact.*, sent (MTL-15064), **2015**.

Resultados más relevantes*

*** Se muestra un resumen de los resultados más relevantes registrados en las publicaciones contenidas en la presente sección.**

La alta conductividad observada para $LaNi_{0.6}Fe_{0.4}O_{3-\delta}$ (LNF) y $LaNi_{0.6}Co_{0.4}O_{3-\delta}$ (LNC), y el buen ajuste entre los valores del coeficiente de expansión térmico (TEC) de $(La_{0.8}Sr_{0.2})_{0.95}Fe_{0.6}Mn_{0.3}Co_{0.1}O_3$ (LSFMC) y el interconector Crofer22APU, permiten el uso de estos materiales como capas de contacto. Los estudios de difracción de rayos X (XRD) han demostrado que estos materiales presentan una adecuada estabilidad térmica a la temperatura de sinterizado en celda, 1050 ºC, así como después de ser tratados a 800 ºC durante 1000 h, en aire. Sin embargo, el cátodo $La_{0.6}Sr_{0.4}FeO_3$ (LSF) presenta una menor estabilidad a largos tiempos de operación, dando lugar a la formación de fases como $LaSrFeO_4$ (P*nma*) y $SrFe_{12}O_{19}$ (P6_3/*mmc*). Diferentes mezclas cátodo LSF-capa de contacto (1:1 en peso) se han sometido a 800 ºC durante 1000 h, y se han analizado mediante el método Rietveld, observándose que existe una adecuada compatibilidad química entre los materiales de contacto y el cátodo; los tratamientos a alta temperatura favorecen la formación de la solución sólida $(LSF)_x$(LNC,LNF o LSFMC)$_{1-x}$.

Las celdas estudiadas se han preparado a partir de la deposición de sus componentes, mediante spray manual coloidal. A través de las medidas iniciales de voltamperometría a 800 ºC, se ha analizado el comportamiento electroquímico de las celdas interconector plano Crofer22APU-capa de contacto LNF, LNC, LSFMC o LSF-cátodo LSF. Se ha utilizado el cátodo como capa de contacto para observar el efecto de añadir un material de contacto en la estructura interconector-cátodo. Los resultados electroquímicos iniciales muestran que la resistencia eléctrica, en este tipo de celdas, depende de la conductividad de la capa de contacto empleada. Así, los valores de resistencia superficial especifica (ASR) disminuyen siendo de 0.018(1), 0.015(1), 0.010(1) y 0.006(1) $\Omega \cdot cm^2$ para LSFMC, LSF, LNF y LNC, respectivamente. Después de 100 h, las celdas LSF y LSFMC muestran la mayor resistencia al paso de corriente, mientras que para la celda-LNF y –LNC la señal de ASR 0.054(7) y 0.041(2) $\Omega \cdot cm^2$, respectivamente, se mantiene estable hasta 1300 h.

Se han realizado análisis EDX de las secciones transversales de cada celda para determinar la microestructura y la distribución de los elementos después de las medidas electroquímicas. Además, se han llevado a cabo medidas de XRD, sobre celdas tratadas a 800 ºC durante 1000 h, para identificar las fases formadas de los procesos de reacción, que se producen en las intercapas interconector-capa de contacto-cátodo e interconector-cátodo. En este sentido, las medidas de espectroscopia fotoelectrónica de rayos X (XPS), llevadas a cabo sobre celdas interconector-capa de contacto, tras ser sometidas a largos tiempos de operación, han permitido la identificación de las fases secundarias presentes en la superficie del material de contacto.

Según los resultados morfológicos y microestructurales, las capas de óxido formadas a partir de las combinaciones con LSFMC y LNF son más homogéneas que las observadas para las celdas en las que se usa LNC y LSF como material de contacto. Esta diferencia puede estar relacionada con los siguientes factores: (i) distribución de los aditivos minoritarios dentro del interconector, (ii) relación del TEC entre materiales adyacentes, y/o (iii) composición química del material de

contacto. Sin embargo, la estructura Crofer22APU-LSFMC-LSF sufre una degradación importante después de 100 h de medida ASR, a 800 ºC.

Para todos los casos, la capa de óxido formada en la interfase interconector-capa de contacto, está compuesta por dos zonas: una interna, constituida por un óxido de cromo, Cr_2O_3, y una capa externa, formada por un óxido mixto con estructura espinela M_3O_4 ($M=Fe^{3+/4+}$, Cr^{6+}, $Mn^{3+/4+}$). La presencia de manganeso, cobalto y hierro, en las perovskitas de contacto, favorece la formación de espinelas de diferente composición en la interfase entre la aleación y el material de contacto. En este contexto, estas espinelas de manganeso, cobalto y hierro pueden mejorar la conductividad de la celda, especialmente las espinelas de cobalto. Las líneas de barrido, así como los mapas de distribución de elementos EDX indican, en todos los casos, que existe una difusión de cromo. Esta volatilización de cromo, procedente del interconector, da lugar a la formación de fases como $SrCrO_4$ ($P2_1/n$) y perovskitas de cromo ($Pbnm$), esta última presente también en la superficie de la capa de contacto.

La adecuada compatibilidad estructural-química y la baja resistencia al flujo de corriente, a largos tiempos de operación, observadas en la celda-LNF y celda-LNC, respectivamente, han permitido la selección de ambos materiales para continuar el estudio y abordar una configuración real.

Relevant results*

*** A brief summary of the research papers results, which are included in the present section, is shown.**

The observed high conductivity values for $LaNi_{0.6}Fe_{0.4}O_{3-\delta}$ (LNF) and $LaNi_{0.6}Co_{0.4}O_{3-\delta}$ (LNC) and, the good fit between TECs values of $(La_{0.8}Sr_{0.2})_{0.95}Fe_{0.6}Mn_{0.3}Co_{0.1}O_3$ (LSFMC) and the interconnect make the use of these materials as contact coatings interesting. X-ray diffraction (XRD) measurements revealed that these materials are thermally stable at real cell processing sintered temperature, 1050 ºC, and after treated at 800 º C for 1000 h, in air. However, the partial degradation of $La_{0.6}Sr_{0.4}FeO_3$ (LSF) cathode occurs after long-term operating conditions, resulting in the formation of secondary phases like $LaSrFeO_4$ (P*nma*) and $SrFe_{12}O_{19}$ (P6_3/*mmc*). Powder mixtures of each contact material with LSF cathode (1:1 in weight) were aged at 800 ºC for 1000 h. The Rietveld refinements of these treated mixtures indicated an adequate chemical compatibility between the contact and cathode materials; high temperature treatments provide the formation of a solid solution of $(LSF)_x(LNC, LNF \text{ or } LSFMC)_{1-x}$.

The studied cells were prepared by colloidal spay deposition technique. The electrochemical behaviour of {Crofer22APU interconnect-LNF, LNC, LSFMC or LSF contact coating-LSF cathode} cells was analysed using voltammetry measurements over short-term periods. Lanthanum strontium ferrite cathode is used instead of contact material to evaluate the effect of adding a contact perovskite on interconnect-cathode structure. The obtained results showed that the initial area specific resistance (ASR) mainly depends on electrical conductivity of the measured contact perovskite. Thus, the ASR values were 0.018(1), 0.015(1), 0.010(1) and 0.006(1) $\Omega \cdot cm^2$ when LSFMC, LSF, LNF and LNC contact coatings are used, respectively. Moreover, the ASR of LNF and LSFMC cells increased after testing for100 h at 800 ºC, whereas for LNF and LNC systems the ASR values of 0.054(7) and 0.041(2) $\Omega \cdot cm^2$, respectively, remained stable up to 1300 h.

In order to determine the microstructure and estimate the extent of element interdiffusion across assembly interfaces, EDX analysis was performed on cross-sections of the different cells after ASR measurements. In addition, the identification of the formed reaction phases at interconnect-contact coating-cathode and interconnect-cathode interfaces, after they are treated at 800 ºC for 1000 h, was carried out using X-ray diffraction measurements (XRD). In this context, X-ray photoelectron spectroscopy was also used to determine the chemical state of the elements and surface composition of these aged structures.

According to morphological and microstructural analyses, the thickness of oxide scale observed for the combination with LSFMC and LNF is reasonable homogeneous in contrast with systems with LNC and LSF in which this oxide scale is not uniform. This effect can be related to: (i) the distribution of minor additives within interconnect (ii) the difference in thermal expansion coefficients (TECs) between adjacent materials, and/or (iii) the contact material compositions. However, Crofer22APU-LSFMC-LSF structure undergoes a significant degradation after ASR test at 800 ºC for 100 h, in air.

For all cases, oxide scale is composed of two layers: Cr_2O_3 bonded to the metal substrate followed by spinel layer M_3O_4 ($M=Fe^{3+/4+}$, Cr^{6+}, $Mn^{3+/4+}$). The Mn-, Co- and Fe-containing contact perovskites lead to the formation of spinels with different compositions, which can improve electrical conductivity of the cell, particularly, spinels of cobalt. In additions, EDX elemental linescans and maps show chromium enrichment in contact and cathode layers. Thus, this chromium volatilization from FeCr interconnect allows the formation of phases like $SrCrO_4$ ($P2_1/n$) and Cr-containing perovskites (P*bnm*).

Since LNF- and LNC-cells showed an adequate structural-chemical compatibility and low area specific resistance values at long-term operating conditions, respectively, LNF and LNC contact perovskites have been selected to continue the study, in which a more real configuration is addressed.

2.1. Effects of using $(La_{0.8}Sr_{0.2})_{0.95}Fe_{0.6}Mn_{0.3}Co_{0.1}O_3$, $LaNi_{0.6}Fe_{0.4}O_{3-\delta}$ and $LaNi_{0.6}Co_{0.4}O_{3-\delta}$ as contact materials on solid oxide fuel cells

J. Power Sources 248 **(2014)** 1067-1076.

Abstract

Three lanthanum-based perovskite ceramic compounds were studied as contact materials, $(La_{0.8}Sr_{0.2})_{0.95}Fe_{0.6}Mn_{0.3}Co_{0.1}O_3$ (LSFMC), $LaNi_{0.6}Fe_{0.4}O_{3-\delta}$ (LNF) and $LaNi_{0.6}Co_{0.4}O_{3-\delta}$ (LNC), between a Crofer22APU interconnect and a $La_{0.6}Sr_{0.4}FeO_3$ (LSF) cathode. The layers were deposited using in all cases wet colloidal spray technique. Phase structures of materials were checked by X-Ray Diffraction (XRD) measurements. Electrical conductivity and thermal expansion coefficient (TEC) for these selected compounds were also determined.

The important properties of the resulting {interconnect/contact layer/cathode} systems; including area specific resistance (ASR), reactivity, and adhesion of contact materials to the interconnect and to the cathode were investigated. Moreover, the electrical resistance and reactivity of the system without a contact layer, {steel/LSF/LSF} system, was measured for comparison. The contact resistance is strongly influenced by the conductivity of selected contact materials, showing the lowest ASR values for {Crofer22APU/LNC/LSF} assembly. The point microanalysis on cross-section of the systems, after ASR measurements, reveals that there is chromium enrichment in the contact and cathode layers which allows the formation of phases like $SrCrO_4$ and Cr-containing perovskite in short exposure times. An adequate integrity and low reactivity is achieved when LNF contact coating is applied between Crofer22APU and LSF cathode without compromising the contact resistance of the system.

Keywords: SOFC, interconnect, contact perovskite, ohmic resistance losses, electrical contact.

Highlights

- Lanthanum-based perovskite ceramic contact materials were studied.
- Contact resistance of $La_{0.6}Sr_{0.4}FeO_3$/contact layer/Crofer22APU is evaluated.
- Contact resistance of contact materials studied depends on their conductivity.

2.1.1. Introduction

Despite IT-SOFCs advantages, lacks of contact between interconnect ribs and electrode is still unsolved. The interfacial adhesion between the oxide scale and electrode is very important for the durability of the cell[1]. To solve this problem, cathode contact layers are used between interconnect an electrode, and is often accomplished by compression of the stack using and external load frame[2-3]. In practice, however, adhesion between contact material/interconnect needs even to be improved. Cathode contact materials, apart from providing electrical contact between adjacent components, can also serve to improve in-plane conduction over the area of the cathode. In this case, contact material acts as a layer of the electrocatalyst used in the cathode[4-5].

Earlier studies have concluded that the use of cathode contact layers improves electrons transfer through the contact interface from interconnect to activate cathode layer[6]. Therefore, the oxygen reduction reaction in the cathode tripe-phase boundaries has more electrons from the interconnect, resulting in a substantial increase in cell performance. It was also found that cell degradation inside the stack, is principally dependent on the interfacial contact between the cathode current collecting layer and the interconnect[7].

The cathode contact material composition is required to possess high electrical conductivity and appropriate sintering activity to minimize the resistance of the contact layer itself and to protect the steel substrate from excessive oxidation. Besides, it must be chemically compatible with both the protective materials or chromia-forming interconnects and the perovskite cathodes. The contact material, as well as, its reaction products should demonstrate an appropriate thermal expansion behavior and high thermochemical and structural stability in the oxidizing cathode environment[8-9].

As pointed out before, cathode/interconnect contact materials in SOFCs include many type of compounds: i) noble metals (Ag) or noble metal-perovskite composites (Ag-$(La_{0.6}Sr_{0.4})(Co_{0.8}Fe_{0.2})O_3$, Ag-$La_{0.8}Sr_{0.2}MnO_3$), ii) conventional perovskite cathode materials[10] (such as, $La_{0.8}Sr_{0.2}Co_{0.75}Fe_{0.25}O_3$, $La_{0.8}Sr_{0.2}FeO_3$), iii) oxides with a spinel structure, M_3O_4 (M=Ni, Mn,

---

1 Jiang S.P. Resistance measurement in solid oxide fuel cells. *J. Electrochem. Soc.* 148(8) (**2001)** A887-A897.

2 Tucker M.C., Cheng L., DeJonghe L.C. Selection of cathode contact materials for solid oxide fuel cells. *J. Power Sources* 196 (**2011**) 8313-8322.

3 Montero X., Tietz F., Stöver D., Cassir M., Villarreal I. Comparative study of perovskites as cathode contact materials between an $La_{0.8}Sr_{0.2}FeO_3$ cathode and a Crofer22APU interconnect in solid oxide fuel cells. *J. Power Sources* 188 (**2009**) 148-155.

4 Tucker M.C., Cheng L., De-Jonghe L.C. Inorganic binder-containing composite cathode contact materials for solid oxide fuel cells. *J. Power Sources* 224 (**2013**) 174-179.

5 Tao Y. Nishino H., Ashidate S., Kokubo H., Watanabe M., Uchida H. Polarization properties of $La_{0.6}Sr_{0.4}Co_{0.2}Fe_{0.8}O_3$-based double layer-type oxygen electrodes for reversible SOFCs. *Electrochim. Acta* 54 (**2009**) 3309-3315.

6 Guan W.B., Zhai H.J., Jin L., Li T.S., Wang W.G. Effect of contact between electrode and interconnect on performance of SOFC stacks. *Fuel Cells* 11(3) (**2011**) 445-450.

7 Guan W.B., Jin L., Ma X., Wang W.G. Investigation of impactors on cell degradation inside planar SOFC stacks. *Fuel Cells* 12(6) (**2012**) 1085-1094.

8 Yang Z., Xia G., Singh P., Stevenson J.W. Electrical contacts between cathodes and metallic interconnects in solid oxide fuel cells. *J. Power Sources* 155 (**2006**) 246-252.

9 McCarthy B.P., Pederson L.R., Chou Y.S., Zhou X.D., Surdoval W.A., Wilson L.C. Low-temperature sintering of lanthanum strontium manganite-based contact pastes for SOFCs. *J. Power Sources* 180 (**2008)** 294-300.

10 Skinner S.J., Laguna-Bercero M.A. Advanced Inorganic Materials for Solid Oxide Fuel Cells, in Energy Materials (eds. Bruce D.W., O'Hare D., Walton R.I.), John Wiley & Sons, Ltd, Chichester, UK. doi:10.1002/9780470977798.ch2. **2011**.

Co, Cu, Fe), or iv) recently developed oxides like $Ni_{0.33}Co_{0.67}O$. Despite the interactions of these kind of materials with Cr-containing steel interconnects, due to their susceptibility to form phases like Ag_2CrO_4, $AgCrO_2$, $SrCrO_4$, Cr-spinels or Cr-perovskites, the use of those materials, in most of the cases, are quite effective for improving the electrical contact between the cathodes and metallic interconnects[11-15]. In this study, $(La_{0.8}Sr_{0.2})_{0.95}Fe_{0.6}Mn_{0.3}Co_{0.1}O_3$ (LSFMC), $LaNi_{0.6}Fe_{0.4}O_{3-\delta}$ (LNF) and $LaNi_{0.6}Co_{0.4}O_{3-\delta}$ (LNC) were selected for their use as contact layers, for intermediate cell operation temperature (IT-SOFC, 600-800 ºC), due to their adequate sintering activity, electrical conductivity and thermal expansion coefficient (TEC). To carry out this study, lanthanum strontium ferrite, $La_{0.6}Sr_{0.4}FeO_3$ (LSF), has been chosen as cathode due to its acceptable electric and ionic conductivity, relative control of the porosity and enough catalytic activity that allows the reduction of the oxidant gas (air or oxygen) at low operating temperatures[16]. As interconnect Crofer22APU was selected due to its good workability, high corrosion resistance and cost-effectiveness[17].

In the present research, three perovskites, LSFMC, LNF and LNC were investigated as contact materials. Phase structure using XRD, electrical conductivity and TEC values of selected materials were determinated. Results of electrical performance and chemical stability of cathode contact materials in combination with Crofer22APU and $La_{0.6}Sr_{0.4}FeO_3$ as interconnect and cathode, respectively, are presented and discussed. In addition, the system {steel/LSF/LSF} without a contact layer was also studied for comparison. The use of different perovskites as contact materials based on its properties and, on contacting resistance and chemical compatibility of each system will be discussed.

2.1.2. Experimental

Powders of $(La_{0.8}Sr_{0.2})_{0.95}Fe_{0.6}Mn_{0.3}Co_{0.1}O_3$ (LSFMC), $LaNi_{0.6}Fe_{0.4}O_{3-\delta}$ (LNF), $LaNi_{0.6}Co_{0.4}O_{3-\delta}$ (LNC) and $La_{0.6}Sr_{0.4}FeO_3$ (LSF) were purchased from NexTech, Fuel Cell Materials, and Crofer22APU was obtained from ThyssenKrupp VDM. X-Ray Diffraction (XRD) at room temperature, using a Philips X'Pert PRO diffractometer equipped with Cu K_α radiation (λ = 1.5418 Å), was used to check phase structures of the commercial materials. The power generator has been provided at 40 kV and 40 mA. The patterns were recorded in 2θ steps of 0.026º in the 18-90º range.

---

[11] Wilkinson L.T., Zhu J.H. Ag-Perovskite composite materials for SOFC cathode-interconnect contact. *J. Electrochem. Soc.* 156(8) (**2009**) B905-B912.

[12] Lu Z., Xia G., Templeton J.D., Li X., Nie Z., Yang Z., Stevenson J.W. Development of $Ni_{1-x}Co_xO$ as the cathode/interconnect contact for solid oxide fuel cells. *Electrochem. Commun.* 13 (**2011**) 642-645.

[13] Tucker M.C., Cheng L., DeJonghe L.C. Glass-containing composite cathode contact materials for solid oxide fuel cells. *J. Power Sources* 196 (**2011**) 8435-8443.

[14] Wang F., Yan D., Zhang W., Chi B., Pu J., Jian L. $LaCo_{0.6}Ni_{0.4}O_{3-\delta}$ as cathode contact material for intermediate temperature solid oxide fuel cells. *Int. J. Hydrogen Energ.* 38 (**2013**) 646-651.

[15] Zhang W., Wang F., Wang K., Pu J., Chi B., Jian L. Chemical compatibility and electrical contact between Ni–Cr–Mo alloy and $LaCo_{0.6}Ni_{0.4}O_{3-\delta}$ in intermediate temperature solid oxide fuel cells. *Int. J. Hydrogen Energ.* 37 (**2012**) 17253-17257.

[16] Vogt U.F., Holtappels P., Sfeir J., Richter J., Duval S., Wiedenmann D., Züttel A. Influence of A-site variation and B-site substitution on the physical properties of (La, Sr)FeO_3 based perovskites. *Fuel Cells* 6 (**2009**) 899-906.

[17] Miguel-Pérez V., Martínez-Amesti A., Nó M.L., Larrañaga A., Arriortua M.I. Oxide scale formation on different metallic interconnects for solid oxide fuel cells. *Corros. Sci.* 60 (**2012**) 38-49.

The diffraction data of the samples were fitted in all the cases by Rietveld method using the FULLPROF program[18-20].

For bulk conductivity and TEC measurements, pellets of powders were sintered at the temperatures shown in Table 2.1 to achieve full density. Then, sintered pellets were cut in ~1 x 3 x 7 mm bars; the conductivity measurements were carried out with the standard dc four-point method on the rectangular sintered bars, from room temperature to 1000 ºC in air with a heating rate of 2 ºC·min^{-1}, using a power source controlled by PC using Lab Windows/CVI field point system. The measured conductivity values were corrected taking into account the porosity of the samples[21]. Thermal expansion measurements (TEC) for the contact layers, cathode and interconnect were carried out from room temperature to 1000 ºC in air with a heating rate of 5 ºC·min^{-1} by using a Unitherm Model 1161 dilatometer.

Table 2.1. Sintering procedure used for fabrication of rectangular bars for electrical conductivity and the degree of compactation (%) obtained for each material.

Composition	Sintering procedure	Relative density (%)*
LNF	1350 ºC, 5h	90
LSFMC	1250 ºC, 10 h	98
LNC	1200 ºC, 5h	79
LSF	1150 ºC, 5 h	93

* Theoretical density was calculated from the results obtained in Rietveld analysis. Experimental density was determinated geometrically from the volume and weight of the samples.

The contact evaluation of the studied material layers between Crofer22APU interconnect and LSF cathode was carried out with the interconnect preoxidized at 800 ºC for 100 h in air in a Carbolite furnace. Prior to the oxidation, the sheets were cut into 10 x 10 mm squares with 1 mm thickness, and also were polished using #800 grit SiC, cleaned with acetone in an ultrasonic bath and dried. As observed in other studies, preoxidation of interconnect may reduce Cr and Fe transport into the contact coating, after long oxidation times. In addition, preoxidized samples developed thin coating which may decrease interfacial stress over time between the contact layer and interconnect[22]. The deposition of the contact materials was carried out using wet colloidal spray deposition technique, as was described in Ref. 23, and sintered at 1050 ºC for 2h to obtain a rather dense coating. LSF cathode was deposited on contact layers using the same deposition technique and sintered at 950 ºC for 2h to produce a porous layer. The suspensions were made mixing in a ball mill during 1 hour the powders, ethanol and ZrO_2 cylinders as grinding media. For the area specific resistance (ASR) measurements a dc four-point method was used and, samples were prepared

[18] Rietveld H.M. A profile refinement method for nuclear and magnetic structures. *J. Appl. Crystallogr.* 2 (**1969**) 65-71.

[19] Rodríguez-Carvajal J. Recent advances in magnetic structure determination by neutron powder diffraction. *Physica B* 192 (**1993)** 55-69.

[20] Rodríguez-Carvajal J. Fullprof program: Rietveld pattern matching analysis of powder patterns, Grenoble, **2011**.

[21] Vidal K., Rodríguez-Martínez L.M., Ortega-San-Martín L., Nó M.L., Rojo T., Arriortua M.I. Effect of the A cation size disorder on the properties of an iron perovskite series for their use as cathode for SOFCs. *Fuel Cells* 11 (**2011)** 51-58.

[22] Hoyt K.O., Gannon P.E., White P., Tortop R., Ellingwood B.J., Khoshuei H. Oxidation behavior of $(Co,Mn)_3O_4$ coatings on preoxidized stainless steel for solid oxide fuel cell interconnects. *Int. J. Hydrogen Energ.* 37 (**2012**) 518-529.

[23] Martínez-Amesti A., "Celdas de combustible de óxido sólido. Estudios de reactividad y optimización de la intercapa cátodo-electrolito", Ph.D. thesis work, UPV/EHU, **2009**.

according to the geometries shown in Fig. 2.1. Electrical contact between the sandwich structure and external measuring circuit were obtained with two Pt wires welded to the Pt mesh at interconnect and cathode side, in combination with Pt paste onto the surface of interconnect and cathode. The overall ASR of {Crofer22APU/contact material/cathode} setup was measured at 800 ºC for up to 16 h to evaluate the starting point stability of the obtained contact resistance values, and it was estimated by the voltage value measured by cronoamperometry applying a current of 300 mA, using a VSP Potentiostat/Galvanostat (Princeton Applied Research, Oak Ridge, US).

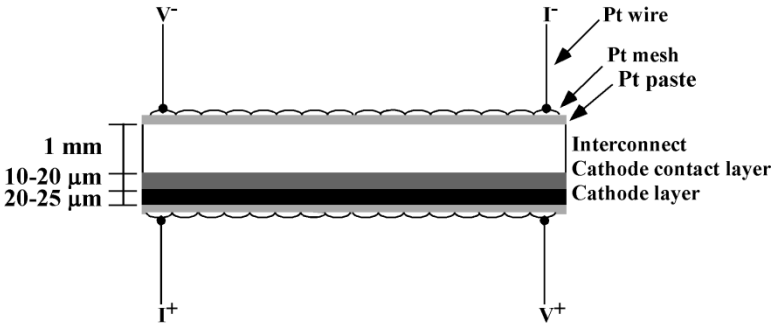

Figure 2.1. Sample setup for contact ASR measurement of {Crofer22APU/contact layer/LSF} system.

Cross-section of the sandwich structures, after contact resistance measurements, were then metallographically prepared and investigated with scanning electron microscope (SEM, JEOL LSM-6400) equipped with an Oxford Pentafet energy dispersive X-ray analyzer (EDX) to study the microstructure of the systems and, to determinate extend of interdiffusion between materials. The composition analysis on the samples cross-section was made using back-scattered electrons (BSE) at 20 kV accelerating voltage, $1 \cdot 10^{-9}$ A current density and 15 mm working distance. Due to the overlap of the emission lines for the studied elements (Table 2.2), the INCA 350 software from Oxford was used to reconstruct the spectra and it was compared with the measured one to confirm the presence or absence of these elements.

Table 2.2. Main emission lines for the analyzed elements.

Element	K_α (keV)	K_β (keV)	L_α (keV)	L_β (keV)
La			4.650	5.041
Cr	5.411	5.946		
Mn	5.894	6.489		
Fe	6.398	7.057		
Co	6.924	7.648		
Ni	7.471	8.263		

2.1.3. Results and discussion

2.1.3.1. Phase characterization

The phase structures of studied commercial materials (LNC, LNF, LSFMC, LSF and Crofer22APU) were refined by the Rietveld method, as shown in Fig. 2.2. All the perovskite phases

showed a rombohedral structure with R-*3c* space group; however, steel has a cubic arrangement and it crystallizes in space group I*m-3m*, as expected.

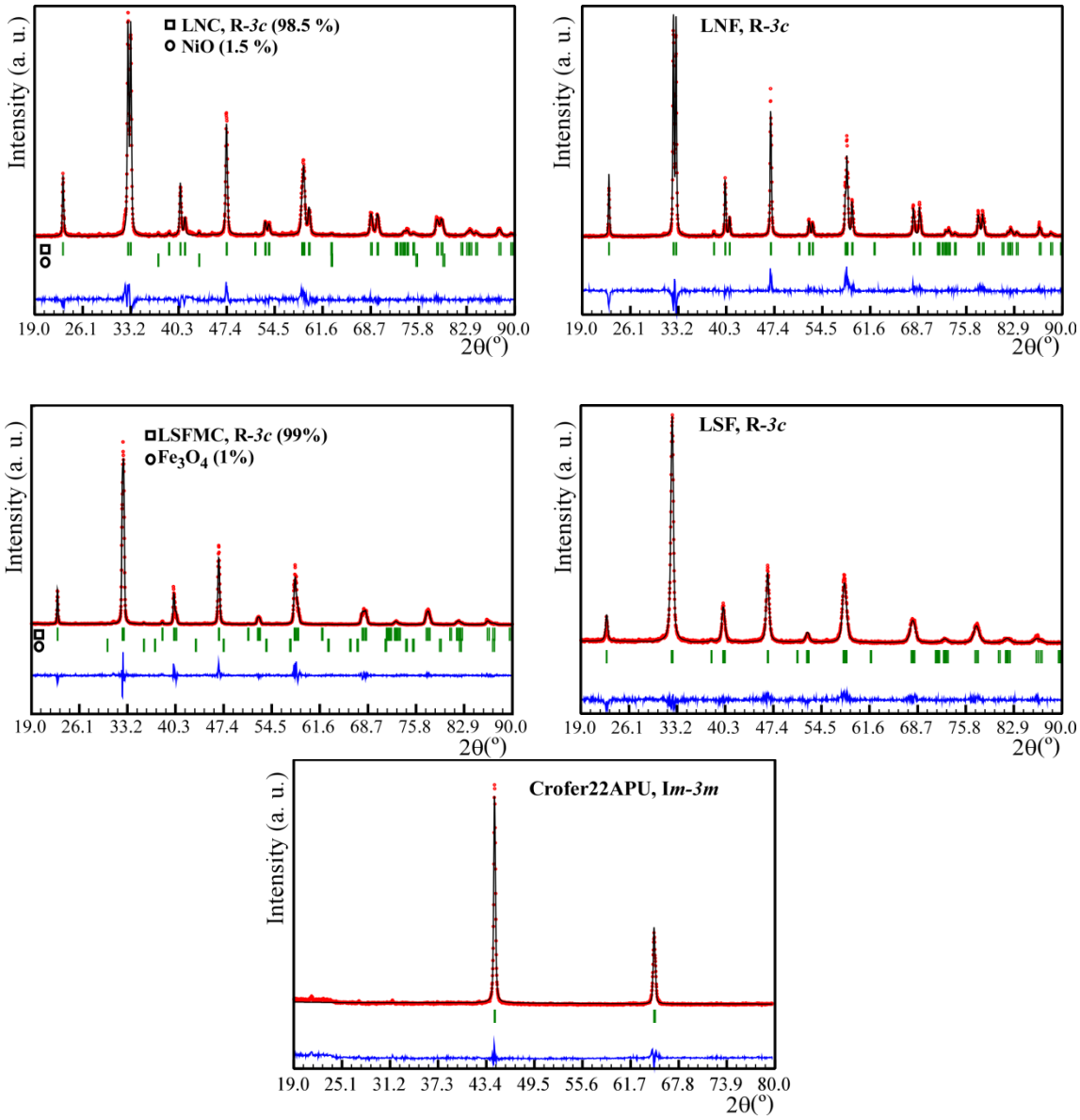

Figure 2.2. Rietveld X-Ray diffraction pattern refinements for commercial LSF, LSFMC, LNF, LNC and Crofer22APU materials. Circles denote experimental points; upper solid line the calculated profile. Theoretical peak positions (vertical sticks) and difference lines are shown in the bottom of each pattern.

The refined cell parameters and unit cell volumes are summarized in Table 2.3. The quantitative analysis demonstrates that the studied materials were pure except LSFMC and LNC. For LNC two very weak peaks corresponding to NiO were found (1.5 % in weight) and for LSFMC, Fe_3O_4 phase (2 % in weight) was quantified.

Table 2.3. General structural parameters obtained from the Rietveld analysis.

Material	Space group	Lattice parameters a (Å) / c (Å)	V (Å^3)	χ^2
LNC	R-*3c*	5.459(1)/13.137(1)	339.04(1)	3.29
LNF	R-*3c*	5.513(1)/13.272(1)	349.33(1)	3.77
LSFMC	R-*3c*	5.522(1)/13.412(1)	354.22(1)	3.33
LSF	R-*3c*	5.528(1)/13.451(2)	355.93(1)	2.03
Crofer22APU	I*m-3m*	2.881(1)	23.91(1)	7.31

The dependence of conductivity of each perovskite on temperature and the Arrhenius plot for the electrical conductivity in air is shown in Figures 2.3 and 2.4, respectively. The conductivity increases with increasing temperature up to a maximum and then decreases due to the lattice oxygen loss, for the LSFMC, LSF and LNF perovskites, implying a small semiconductor behavior[21]. For the LNC material, however, the conductivity decreases continuously with increasing temperature, implying a metallic behavior[24].

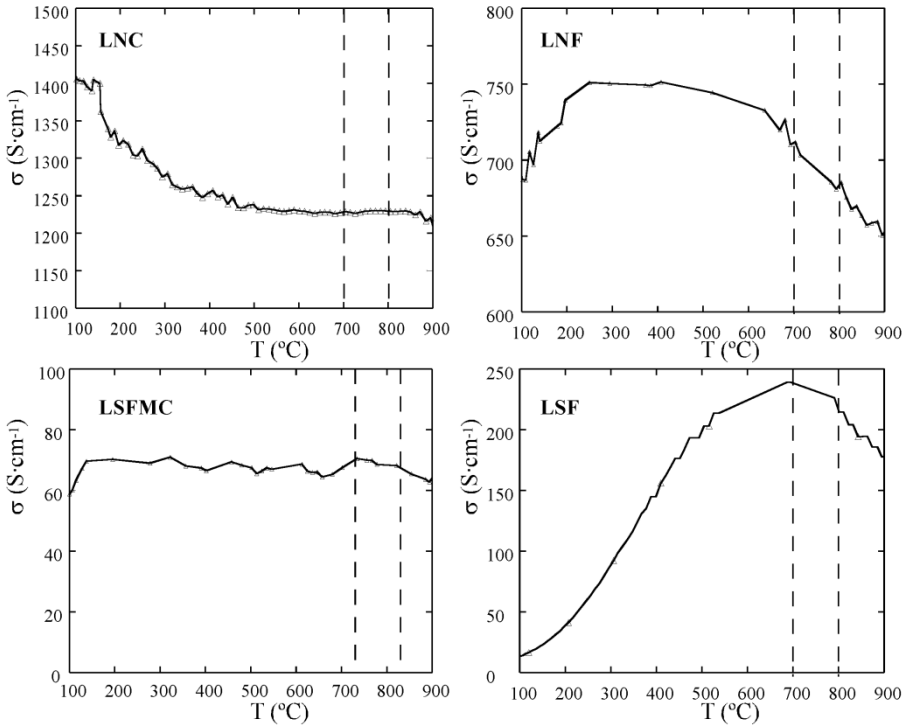

Figure 2.3. Electrical conductivity of $(La_{0.8}Sr_{0.2})_{0.95}Fe_{0.6}Mn_{0.3}Co_{0.1}O_3$, $LaNi_{0.6}Fe_{0.4}O_{3-\delta}$, $LaNi_{0.6}Co_{0.4}O_{3-\delta}$ and $La_{0.6}Sr_{0.4}FeO_3$ perovskites as a function of temperature.

For the compositions with semiconducting behavior, the temperature dependence of the conductivity can be described by the small polaron hopping mechanism[25] as it shown in Equation 2.1:

[24] Huang A., Yao K., Wang J. Conducting perovskite $LaNi_{0.6}Co_{0.4}O_3$ ceramics with glass additions. *J. Electroceram.* 16 (**2006)** 313-319.

[25] Cox P.A., The Electronic Structure and Chemistry of Solids, Oxford Science Publications, Oxford, UK, **1987**.

$$\sigma = \frac{A}{T}\exp\left(\frac{-Ea}{KT}\right) \quad (2.1)$$

Where A is the pre-exponential factor, T is the temperature, k is the Boltzmann constant, and E_a is the activation energy for the hopping of the small polarons.

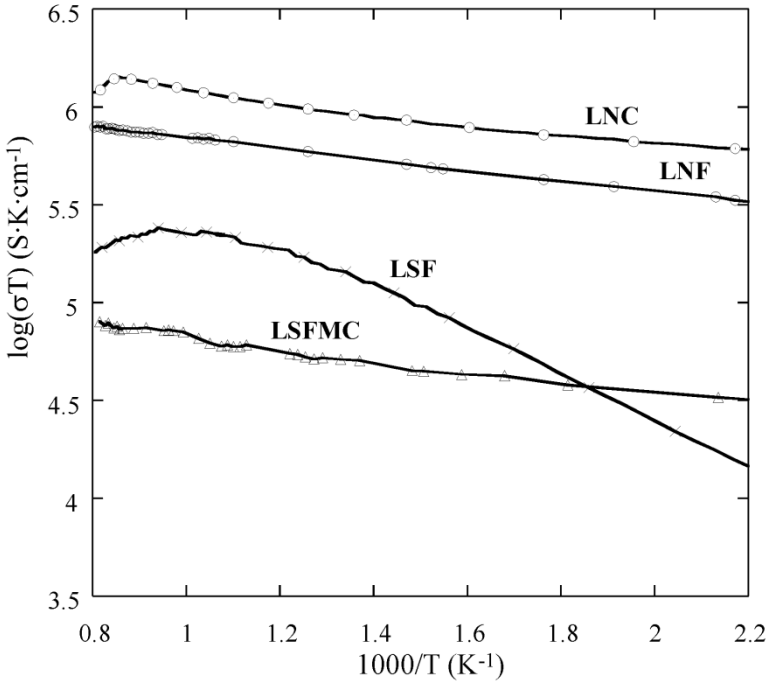

Figure 2.4. Arrhenius plot of selected perovskites as a function of temperature.

The activation energy obtained from the Arrhenius plots (for LSFMC, LSF and LNF samples) and the maximum in conductivity and at 800 ºC for all compounds are given in Table 2.4.

Table 2.4. Maxima in conductivity, conductivity values at 800 ºC and activation energy obtained from the Arrhenius plots for all the compounds.

Composition	σ_{Max} (S·cm^{-1}), T_{Max} (ºC)	$\sigma_{800ºC}$ (S·cm^{-1})	E_a (RT-T_{Max}) (eV)
$LaNi_{0.6}Co_{0.4}O_{3-\delta}$ (LNC)*	1405.9	1229	—
$LaNi_{0.6}Fe_{0.4}O_{3-\delta}$ (LNF)	751.4	685	0.02
$(La_{0.8}Sr_{0.2})_{0.95}Fe_{0.6}Mn_{0.3}Co_{0.1}O_3$ (LSFMC)	71.3	65	0.08
$La_{0.6}Sr_{0.4}FeO_3$ (LSF)	239.7	214	0.11

* For LNC sample the activation energy was not calculated due to it exhibit metallic electrical conduction in every range of temperature.

The obtained conductivity values of the samples are in good agreement with other studies for these types of compounds[14,26-29]. As observed, at 800 ºC the LNC and LNF show higher conductivity than

[26] Huang K., Lee H.Y., Goodenough J.B. Sr- and Ni-doped $LaCoO_3$ and $LaFeO_3$ perovskites-new cathode materials for solid oxide fuel cells. *J. Electrochem. Soc.* 145(9) (**1998**) 3220-3227.

[27] Bevilacqua M., Montini T., Tavagnacco C., Vicario G., Fornasiero P., Graziani M. Influence of synthesis route on morphology and electrical properties of $LaNi_{0.6}Fe_{0.4}O_3$. *Solid State Ionics* 177 (**2006)** 2957-2965.

LSFMC, whose conductivity value is smaller than the one obtained for the cathode material (LSF). It is known that conductivity of contact materials is one of the most important properties for ensuring acceptable ASR. However, the selection of contact material also depends on mechanical integrity of the Crofer22APU/contact layer/LSF interfaces and on its stability. Thus, in terms of conductivity LNF and LNC are appropriate to use as contact layer and, LSFMC is a suitable choice according to its mechanical integrity[3] and also because its TEC value is closely matched with that of the interconnect, as shown below.

Figure 2.5 shows the thermal expansion curves of the five materials obtained upon heating from 200 to 1000 ºC. The TEC results present close to linear dependence in the temperature range of 30-1000 ºC for the Crofer22APU and LNC samples. For the other materials, however, the curves become steeper above the temperature at which each compound shows the maximum in conductivity, corresponding probably to a lattice oxygen loss giving rice to the lattice expansion. As it has been discussed in other works[29-31], this lattice expansion, associated with the formation of oxygen vacancies, can be attributed to: (i) the repulsion force arised between those mutually exposed cations when oxygen ions are extracted from the lattice; and/or (ii) the increase in cation size due to the reduction of Co and Fe ions from higher to lower valences, which must occur concurrently with the formation of oxygen vacancies in order to maintain the electrical neutrality.

The average TECs at different temperatures for all the components studied are listed in Table 2.5. As expected, Co based perovskite shows higher TEC values than obtained for Co-free perovskites, such as manganites, nickelites and ferrites[32-35]. As can be observed, for LNF and LNC, the $\alpha_{30\text{-}800\ ^oC}$ and $\alpha_{30\text{-}1000\ ^oC}$ values are comparables to those obtained for the cathode, respectively. For LSFMC, however, these TEC values are smaller showing intermediate values between LSF cathode and Crofer22APU interconnect.

---

[28] Ullmann H., Trofimenko N., Tietz F., Stöver D., Ahmad-khanlou A. Correlation between thermal expansion and oxide ion transport in mixed conducting perovskite-type oxides for SOFC cathodes. *Solid State Ionics* 138 (**2000)** 79-90.

[29] Ralph J.M., Kilner J.A., Steele B.C.H. Improving Gd-doped ceria electrolytes for low temperature solid oxide fuel cells. *Mater. Res. Soc. Symp. Proc*. 575 (**2001)** 309-314.

[30] Li S., Lü Z., Huang X., Su W. Thermal, electrical, and electrochemical properties of Nd-doped $Ba_{0.5}Sr_{0.5}Co_{0.8}Fe_{0.2}O_{3-\delta}$ as a cathode material for SOFC. *Solid State Ionics* 178 (**2008)** 1853-1858.

[31] Li Z., Wei B., Lü Z., Huang X., Su W. Structure, electrical and thermal properties of $(Ba_{0.5}Sr_{0.5})_{1-x}Gd_xCo_{0.8}Fe_{0.2}O_{3-\delta}$ perovskite as a solid-oxide fuel cell cathode. *Solid State Ionics* 207 (**2012)** 38-43.

[32] Gao Z., Mao Z., Wang C., Liu Z. Preparation and characterization of $La_{1-x}Sr_xNi_yFe_{1-y}O_{3-\delta}$ cathodes for low-temperature solid oxide fuel cells. *Int. J. Hydrogen Energ*. 35 (**2010)** 12905-12910.

[33] Lv H., Zhao B-Y., Wu Y-J., Sun G., Chen G., Hu K-A. Effect of B-site doping on $Sm_{0.5}Sr_{0.5}M_xCo_{1-x}O_{3-\delta}$ properties for IT-SOFC cathode material (M=Fe, Mn) *Int. Mater. Res. Bull*. 42(12) (**2007)** 1999-2012.

[34] Lee K.T., Manthiram A. Synthesis and characterization of $Nd_{0.6}Sr_{0.4}Co_{1-y}Mn_yO_{3-\delta}$ ($0\leq y\leq 1.0$) cathodes for intermediate temperature solid oxide fuel cells. *J. Power Sources* 158 (**2006)** 1202-1208.

[35] Taguchi H., Komatsu T., Chiba R., Nozawa K., Orui H., Arai H. Characterization of $LaNi_xCo_yFe_{1-x-y}O_3$ as a cathode material for solid oxide fuel cells. *Solid State Ionics* 182 (**2011)** 127-132.

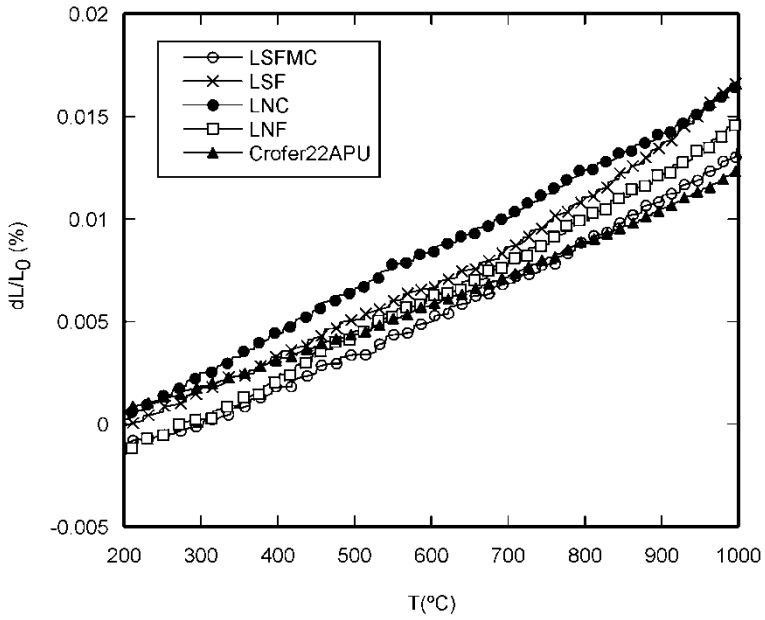

Figure 2.5. Thermal expansion curves of the materials that compose the studied systems, obtained upon heating from 200 to 1000 ºC in air.

The measured average TECs are higher than the ones reported in other works[16, 36-38] for this type of compositions. Those small differences can be attributed to the influence of the sample preparation method and different sintering temperatures[39].

Table 2.5. Thermal expansion coefficients for the studied materials.

Component	Material	$\alpha_{30\text{-}800\,^{\circ}C}$ (K^{-1})	$\alpha_{30\text{-}1000\,^{\circ}C}$ (K^{-1})
Interconnect	Crofer22APU	$11.8\cdot10^{-6}$	$12.8\cdot10^{-6}$
Contact layer	LNC	$17.9\cdot10^{-6}$	$17.5\cdot10^{-6}$
Contact layer	LNF	$16.1\cdot10^{-6}$	$16.0\cdot10^{-6}$
Contact layer	LSFMC	$14.5\cdot10^{-6}$	$14.6\cdot10^{-6}$
Cathode	LSF	$16.1\cdot10^{-6}$	$17.5\cdot10^{-6}$

The TEC values obtained for the interconnect material is smaller than for the other components of the cell, especially for the LNC and LNF compositions. Although the TEC values are not exactly the same, they present an obvious concern for integrity of the contact layers and interfaces during thermal cycling. It is necessary to remark that for the cell preparation, the contact layer will be relatively thin with a certain porosity to ensure the flow of oxygen, properties that are expected to reduce thermal stress. In the preparation of the cells, all of these materials have been successfully employed as contact layer between cathode and interconnect, despite having larger TEC than Crofer22APU material.

---

[36] Sukpirom N., Iamsaard S., Charojrochkul S., Yeyongchaiwat J. Synthesis and properties of $LaNi_{1-x}Fe_xO_{3-\delta}$ as cathode materials in SOFC. *J. Mater. Sci.* 46 (**2011)** 6500-6507.

[37] Kumar R., Yi E., Hang Y., Myung C. Thermal, micro-structural, and electrical properties of a $La_{1-x}Sr_xMn_{0.85}Fe_{0.05}Co_{0.05}Ni_{0.05}O_{3+\delta}$ (x=0-0.4 mole) cathode system. *Met. Mater. Int.* 15 (**2009)** 1055-1060.

[38] Tietz F., Raj I-A., Zahid M., Stöver D. Electrical conductivity and thermal expansion of $La_{0.8}Sr_{0.2}(Mn,Fe,Co)O_{3-\delta}$ perovskites. *Solid State Ionics* 177 (**2006)** 1753-1756.

[39] Dutta A., Mukhopadhyay J., Basu R.N. Combustion synthesis and characterization of LSCF-based materials as cathode of intermediate temperature solid oxide fuel cells. *J. Eur. Ceram. Soc.* 29 (**2009)** 2003-2011.

From these results, it can be concluded that: (i) LNC and LNF compounds present the highest conductivity values and their TECs values are comparables to those obtained for the cathode and, (ii) despite the fact that LSFMC showed the lowest conductivity, the TEC results obtained for this perovskite presents the best fit with the TEC values obtained for the interconnect.

2.1.3.2. ASR measurements and post-test analysis

Figure 2.6 shows that ASR values (Table 2.6) of the different contact perovskites tested are stable during the contact resistance measurements. The contact made by LNC, which has the lowest electrical resistance among the three selected perovskites, gives the lowest ASR, while the contact made by LSFMC, which present a lower electrical conductivity, leads to a higher contact resistance. The value of the electrical resistance for the system with only LSF amounts to 0.015 $\Omega \cdot cm^2$, and it was relatively constant during the experiment. The ASR values for the systems with the LNC and LNF contact layers are 0.006 and 0.010 $\Omega \cdot cm^2$, respectively. These values are lower than that for the system with LSF only, as was expected for LSFMC this value is higher and amounts to 0.018 $\Omega \cdot cm^2$.

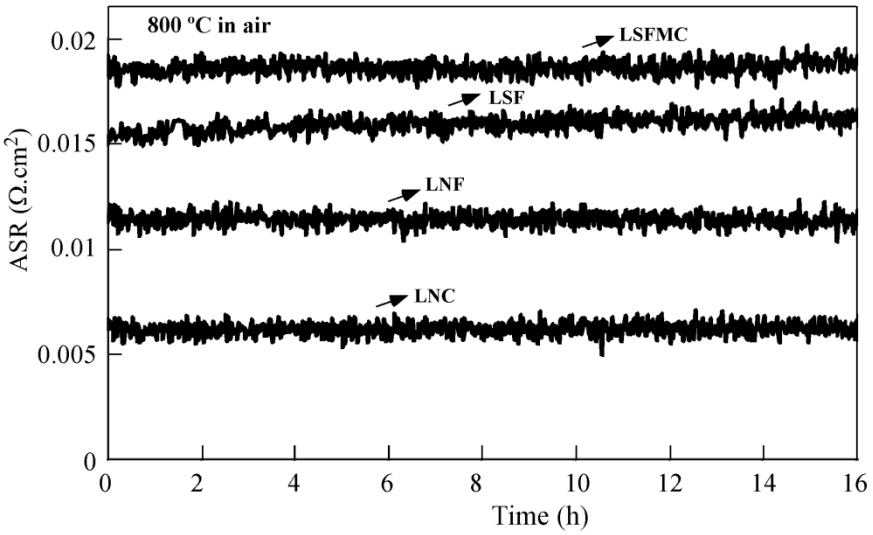

Figure 2.6. ASR for {Crofer22APU/contact layer/LSF} interfaces as a function of time with different contact materials and for the {Crofer22APU/LSF/LSF} system.

The achieved contact resistance values are considerably lower than that of previously reported results for this kind of materials[3]. However, it has been published for {interconnect: AISI441/contact layer: $Ni_{0.33}Co_{0.67}O$/cathode: $La_{0.8}Sr_{0.2}MnO_3$} combination and for {interconnect: 441SS/protective coating: $Mn_{1.5}Co_{1.5}O_4$/contact layer: $La_{0.7}Sr_{0.3}CoO_3$/cathode: $La_{0.6}Sr_{0.4}Co_{0.8}Fe_{0.2}O_3$} assemblies the same order of ASR values[2, 12]. The significantly low ASR was probably due to the microstructure and thickness of the different layers, and/or due to the good bonding of the interfaces between contact layer and cathode, and contact layer and interconnect.

Table 2.6. Area specific resistance values for the different tested contact perovskites measured at 800 ºC in air.

System: Crofer22APU/contact layer/LSF	≈ ASR ($\Omega \cdot cm^2$)
LNC	0.006(1)
LNF	0.010(1)
LSF	0.015(1)
LSFMC	0.018(1)

It is known[40] for this kind of systems that the initial area specific resistance mainly depends on electrical conductivity of the measured perovskites while the time evolution of the ASR depends on the interactions between the contact materials and adjacent components. For this reason it is difficult to assert that the reaction products between ferritic steel and contact or cathode layers exhibit sufficiently high electronic conductivity not to increasing the contact resistance.

The polished cross-sections of different systems after ASR measurements at 800 ºC are shown in Figure 2.7. Five layers can be distinguished in all the samples, including: the interconnect, the oxide scale, the contact layer, the cathode and the Pt paste. The thicknesses of the contact materials can be estimated to be between 10-20 μm, respectively. In addition, in all cases, the thickness of the cathode is about 20-25 μm. The total thickness of the oxide scale for the combination with LSFMC is similar to the system with LNF, which is about 1.5 μm. The oxide layers formed at the LNC/ and LSF/Crofer22APU interfaces are not completely homogeneous in thickness. It is likely that the protective chromia scale growth rate, depends on the contact material composition. This effect can be also related to the amount and distribution of minor alloying additions in Crofer22APU, such as reduction of Si and Al additives, leading to an increase of oxidation rates during the preoxidation of the interconnect[41].

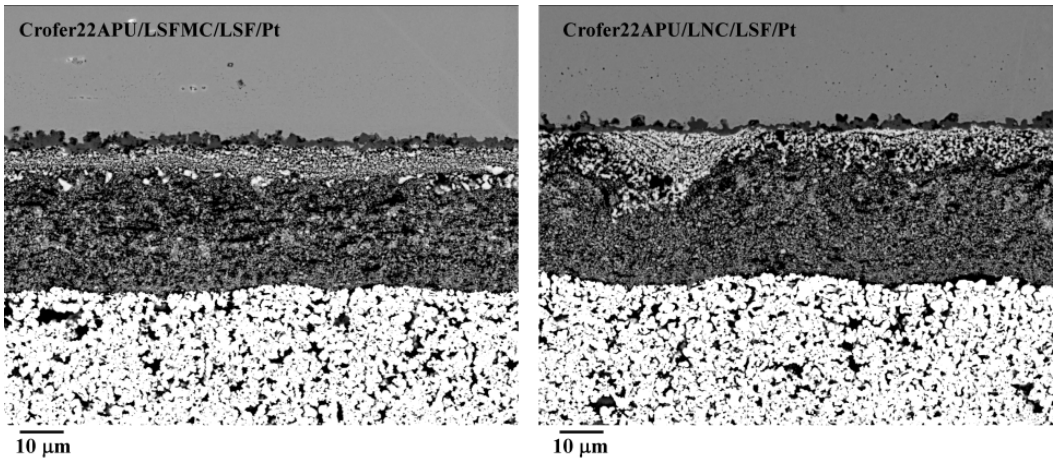

Figure 2.7. Metallographic cross-sections (back-scattered electron image) of the different {Crofer22APU/contact layer/ LSF} systems after ASR measurements at 800 ºC in air.

[40] Shong W.J., Liu C.K., Chen C.Y., Peng C.C., Tu H.J., Fey G.T.K., Lee R.Y., Kao H.M., Effects of lanthanum-based perovskite coatings on the formation of oxide scale for ferritic SOFC interconnect. *Mater. Chem. Phys.* 127 (**2011**) 45-50.

[41] Huczkowski P., Quadakkers W.J., Effect of geometry and composition of Cr steels on oxide scale properties relevant for interconnector applications in solid oxide fuel cells (SOFCs), Forschungszentrum Jülich, **2007**.

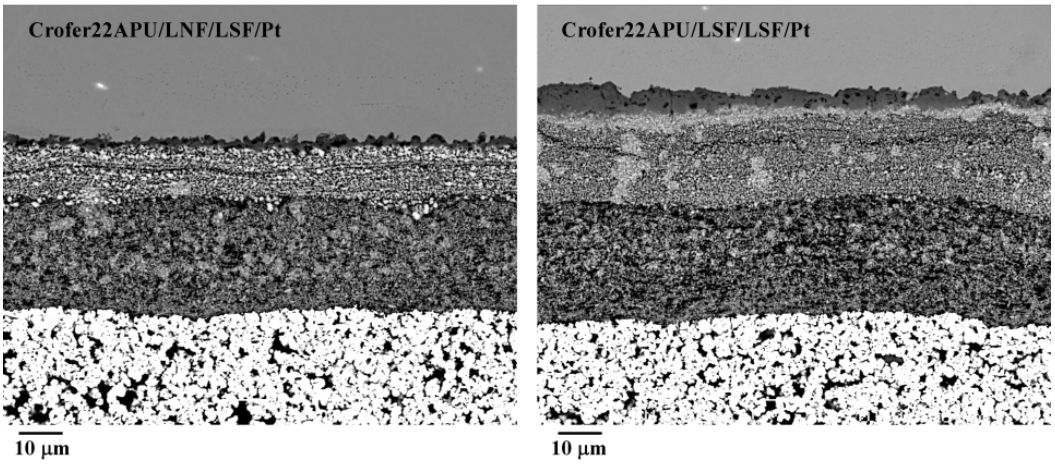

Figure 2.7. cont. Metallographic cross-sections (back-scattered electron image) of the different {Crofer22APU/contact layer/ LSF} systems after ASR measurements at 800 ºC in air.

The microstructure of the cathode layer in all the samples is similar, revealing open porosity with a pore size of approximately 0.5-2 μm. The pore size distribution of the contact pastes depends on the reactivity undergone by each system after ASR measurements. The pores over the contact layer cross-sections for LNF, LNC and LSFMC have a diameter of about 1 μm, whereas for LSF is about 0.5-1 μm. Compared to other three contact materials, LSF has fewer pores and it shows a quite uniform distribution of the pores. In all the samples the contact layers were well bonded to the metallic substrate. However, during the preoxidation process of the interconnect, the formation of voids at the interface between the oxide scale and the steel can be detected. According to other studies[41] insufficient La in the steel melt can lead to void formation. The cathode and contact layer are well attached especially when LSF was used as contact material and also for LNF combination. For LNC and LSFMC systems the cathode is not so properly attached to the contact layer, probably due to the mismatch between TECs values.

To estimate the extent of interfacial interdiffusion, in the starting hours, for the contact material and the interconnect, or the contact material and the cathode, linescans were performed using EDX analysis along the samples as shown in Figure 2.8. For all the cases, oxide scale is composed of two layers: Cr_2O_3 bonded to the metal substrate followed by $(B)_3O_4$ spinel layer (B= Cr, Co, Fe, Ni, Mn) in good agreement with the literature[42]. The growth of chromia is governed by an outward and inward diffusion of Cr and O, respectively[43].

[42] Fontana S., Chevalier S., Caboche G. Metallic interconnects for solid oxide fuel cell: performance of reactive element oxide coating during 10, 20 and 30 months exposure. *Oxid. Met.* 78 (**2012**) 307-328.

[43] Zhao Y., "Oxidation behavior of ferritic alloys as interconnect of solid oxide fuel cell (SOFC)" Ph.D. thesis work, Auburn University, **2012**.

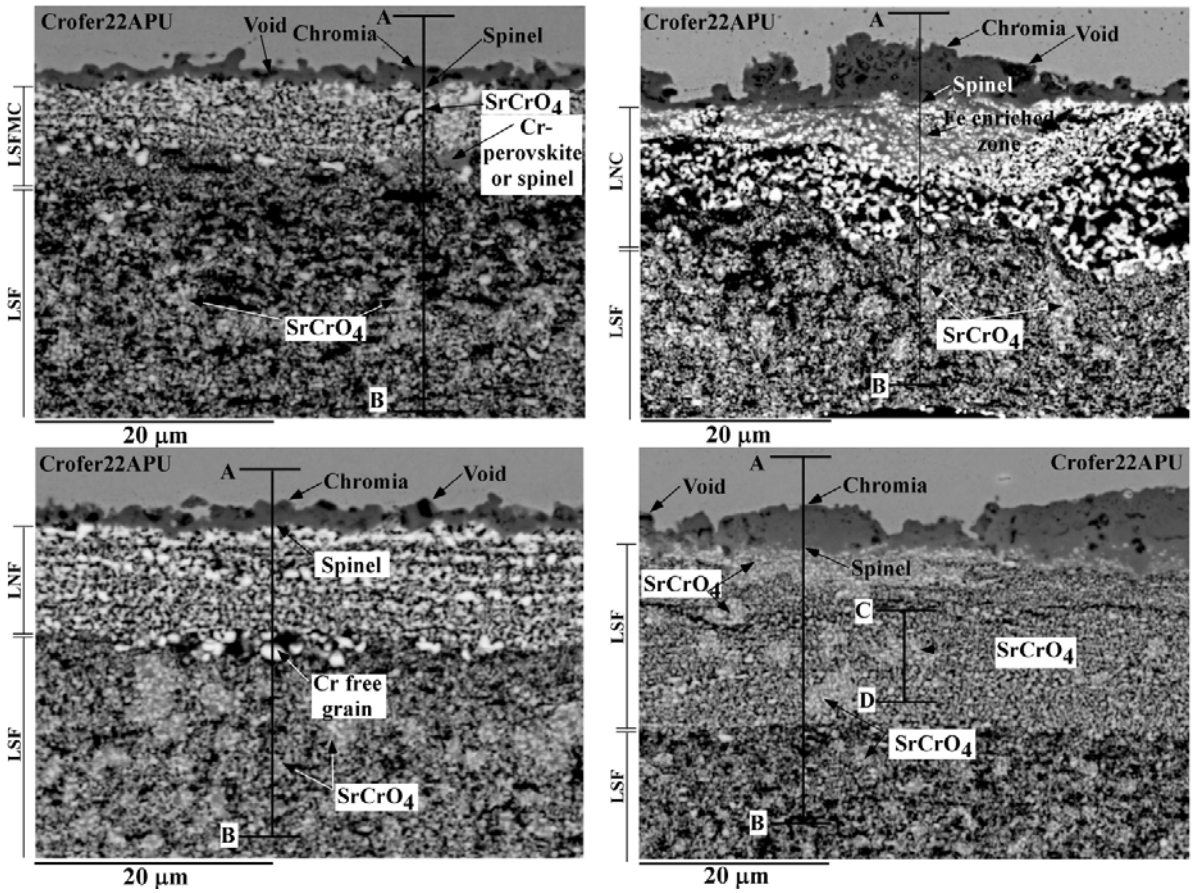

(a)

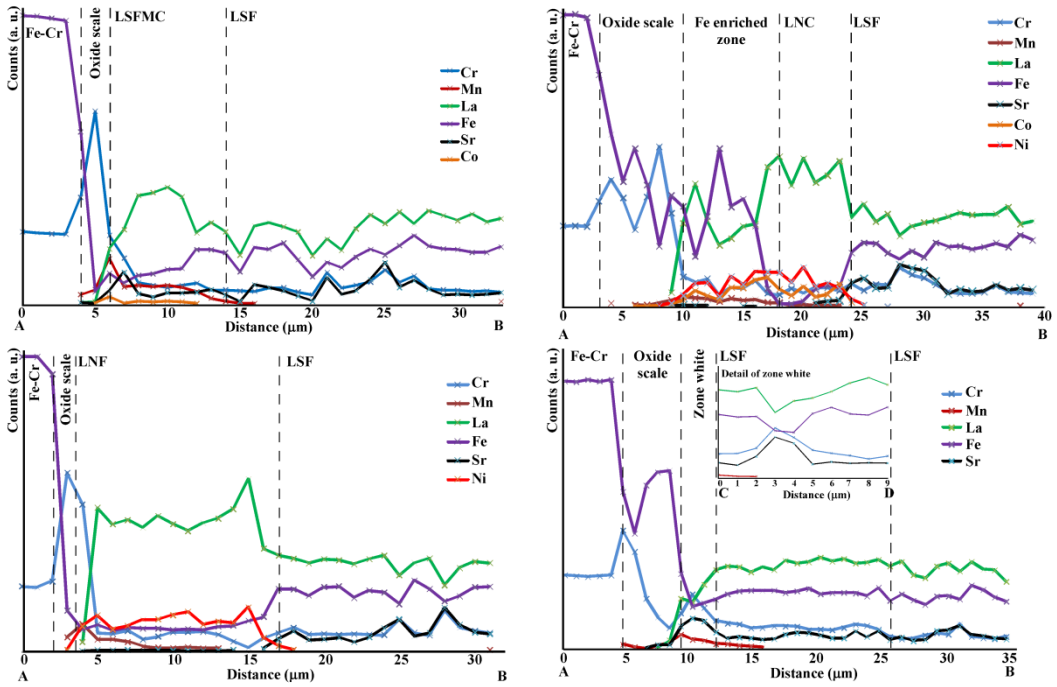

(b)

Figure 2.8. a) Details of SEM cross-sections of studied systems after contact resistance measurements, b) representative results to estimate the extent of interdiffusion at the different systems interfaces from EDX point analysis.

The addition of manganese as additive in the alloy enhances the formation of the spinel formed under the Cr_2O_3 layer and, it improves the scale conductivity which prevents chromium migration and formation of Cr(VI) oxide and oxy-hydroxide species. Thus, the reduction in the rate of cathode degradation by Cr poisoning is given. Therefore, Mn-containing perovskites like LSFMC can also facilitate the formation of Cr-Mn spinels. For Co- and Fe- containing perovskites, such as LNC and LNF, the cobalt and iron released from the perovskite lattice can react with the Cr and Mn from the oxide scale to form $(Cr,Mn,Co,Fe)_3O_4$ spinels. The existence of Fe or Co ions in the spinel grains might improve considerably the electrical conductivity of the coated sample.

For all the systems, the element interdiffusion between cell components is mainly concentrated on Fe, Cr and Mn which released from the interconnect. In the cross-section imagenes grey coloured zones can be detected within the contact and cathode material probably associated to the formation of Cr-containing perovskites[44-46]. The presence of some cracks through the ceramic layers, specially observed for LNC, and the chromium enrichment zones observed for all the systems, can contribute to a higher densification of coating causing in some of the systems cracks. In addition, the cracks can be explained by interactions between contact material and oxide scale, leading to expanded volume of the layer.
Due to the mobility of Sr in cathode environment, large regions enriched with Cr and Sr are observed within the LSF and LSFMC layers owing to $SrCrO_4$ precipitation[47], which is detected[3] as "white zones" in the images.

When LNC contact material is used, a Fe enriched zone with many different compositions was formed between chromia scale and LNC coating (Fig. 2.9). Considering that denser contact layer retains better Cr, it can be deduced that a decrease in the degree of compaction of the layer makes increasing in chromia evaporation, thereby leading to the low concentration of Cr_2O_3 in Crofer22APU/LNC interface. Thus, the increase in the concentration of Fe oxides like Fe_2O_3 is given. This oxide is less dense than Cr_2O_3 and may facilitate cation diffusion of Cr^{3+}, Mn^{3+} and Fe^{3+} to the surface, resulting in a reaction with the contact coating[48]. Despite the open porosity of the contact layer, LNC gives the lower ASR due to its higher conductivity.

---

44 Stodolny M.K., Boukamp B.A., Blank D.H.A., Van Berkel F.P.F. $La(Ni,Fe)O_3$ stability in the presence of chromia-A solid-state reactivity study. *J. Electrochem. Soc.* 158(2) (**2011**) B112-B116.

45 Morán-Ruiz A., Vidal K., Larrañaga A., Arriortua M.I. Chemical compatibility and electrical contact of $LaNi_{0.6}Co_{0.4}O_{3-\delta}$ (LNC) between Crofer22APU interconnect and $La_{0.6}Sr_{0.4}FeO_3$ (LSF) cathode for IT-SOFC. *Fuel Cells* 13(3) (**2013**) 398-403.

46 Badwal S.P.S., Deller R., Foger K., Ramprakash Y., Zhang J.P. Interaction between chromia forming alloy interconnects and air electrode of solid oxide fuel cells. *Solid State Ionics* 99 (**1997**) 297-310.

47 Ardigò M.R., Perron A., Combemale L., Heintz O., Caboche G., Chevalier S. Interface reactivity study between $La_{0.6}Sr_{0.4}Co_{0.2}Fe_{0.8}O_{3-\delta}$ (LSCF) cathode material and metallic interconnect for fuel cell. *J. Power Sources* 196 (**2011**) 2037-2045.

48 Miguel-Pérez V., Martínez-Amesti A., Nó M.L., Larrañaga A., Arriortua M.I. The effect of doping $(Mn,B)_3O_4$ materials as protective layers in different metallic interconnects for solid oxide fuel cells. *J. Power Sources* 243 (**2013**) 419-430.

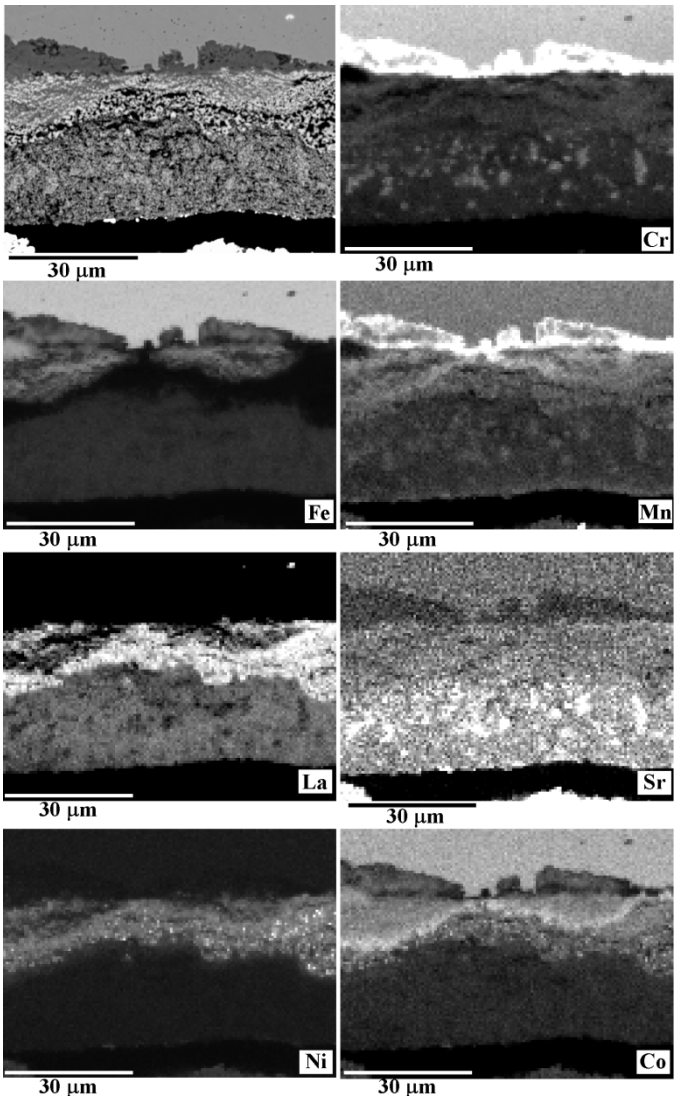

Figure 2.9. EDX mapping of the cross-section of {Crofer22APU /LNC/LSF} combination after ASR measurements in air at 800 ºC.

2.1.4. Conclusions

Direct contact between interconnect and cathode in IT-SOFC stack generally leads to electrical losses. They can be diminished by appropriate contact layers. Three lanthanum-based perovskite ceramic compounds, $(La_{0.8}Sr_{0.2})_{0.95}Fe_{0.6}Mn_{0.3}Co_{0.1}O_3$ (LSFMC), $LaNi_{0.6}Fe_{0.4}O_{3-\delta}$ (LNF) and $LaNi_{0.6}Co_{0.4}O_{3-\delta}$ (LNC) were selected as contact materials for this study. The observed high conductivity values for LNF and LNC and, the good fit between TECs values of LSFMC and the interconnect make the use of these materials as contact layers interesting.

The thickness of oxide scale observed for the combination with LSFMC and LNF is reasonable homogeneous in contrast with systems with LNC and LSF in which this oxide scale is not uniform. This effect can be related to the distribution of minor additives within interconnect which produces differences in scale growth or, it can be also associated to the contact material compositions. For all cases, oxide scale is composed of two layers: Cr_2O_3 bonded to the metal substrate followed by spinel layer. The Mn-, Co- and Fe-containing perovskites used in this study lead to the formation of

spinels with different compositions which can improve electrical conductivity of coated samples. In the four systems the chromium enrichment observed in contact and cathode layers allowed the formation of phases like $SrCrO_4$ and Cr-containing perovskite in short exposure times. When LNC contact material is used, a Fe enriched zone with many different compositions is formed between chromia scale and contact coating probably due to the open porosity of the contact layer which prevents the formation of protective coating of chromia. The obtained contact resistance values are strongly influenced by the conductivity of the selected contact material. The ASR contribution of all the systems is fairly acceptable for the performance of a SOFC stack operating in the intermediate temperature range.

The selection of the best contact layer is based on a compromise between mechanical integrity of the Crofer22APU/contact layer/LSF interfaces and, contact resistance and chemical compatibility of the system. In the present case, LNF coating can be a suitable choice as contact coating due to the adequate integrity and low reactivity between the applied layers without compromising the contact resistance of the system. Future work will include long-term stability of {Crofer22APU/LNF/LSF} system in terms of contact resistance and chemical compatibility.

2.1.5. Supplementary material

Long-term durability of SOFCs has become an important issue in recent years. The interfacial adhesion between interconnect and electrode is important for the durability of the cell so, the development on materials, by improving long-term durability of the cell, is increasing. In order to know the behaviour of the selected contact materials under long-term conditions, {Crofer22APU interconnect/contact layer/LSF cathode} structures are prepared using spray deposition technique. These systems are tested at 800 ºC up to 100 h. The cross-section of these samples show no degradation for the systems in which LNC and LNF are used as contact materials, nevertheless a high instability is observed when LSFMC material is tested (Fig. S1). Considering the ASR measurements, for {Crofer22APU/LSFMC/LSF} 50 % degradation per 100 h is observed, being the ASR value constant in the other two systems. These starting results show the necessity to continue working on the microstructure optimization of the {Crofer22APU/LSFMC/LSF} multilayer structure. System degradation analysis of LNF and LNC with interconnect and cathode are continued at 800 ºC up to 1300 h. After 1300 h, {Crofer22APU/LNC/LSF} shows no meaningful degradation in contrast to {Crofer22APU/LNF/LSF} which presents degradation of 20 %. SEM cross-sections of the treated systems (Fig. S1) show poor sinterability between particles and large holes are detected in the contact layers. Nevertheless, in both samples, the contact layers present good adherence to the cathode and to the interconnect. EDX is used to estimate the extent of element interdiffusion across assembly interfaces. For both systems amounts of Cr are detected all around the contact materials. For {Crofer22APU/LNC/LSF} structure no chromium is detected within the cathode neither Ni nor Co; a small white layer between LNC and LSF is detected. However, for {Crofer22APU/LNC/LSF} assembly Cr is detected through the cathode in the first 40μm. In order to improve the obtained results it would be necessary to optimize the thickness and sintering temperature of the ceramic coatings.

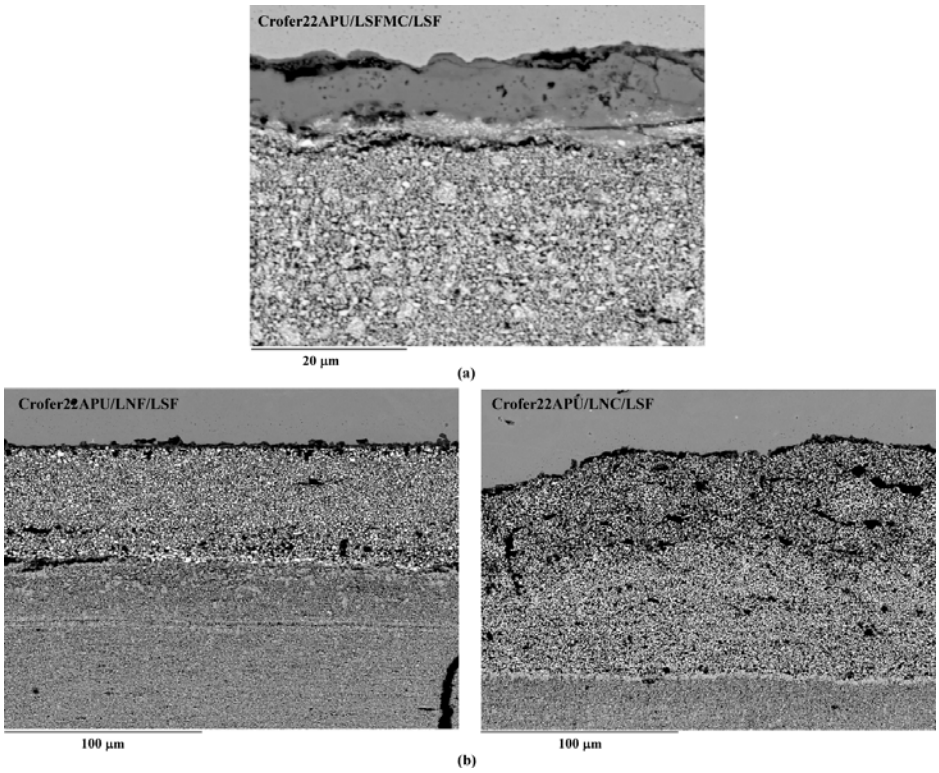

Figure S1 SEM observations of a) {Crofer22APU/LSFMC/LSF} structure after treated at 800 ºC up to 100 h in air and, b) {Crofer22APU/LNF or LNC/LSF} systems after heated at 800 ºC for 1300 h in air.

2.2. Chemical compatibility and electrical contact of $LaNi_{0.6}Co_{0.4}O_{3-\delta}$ (LNC) between Crofer22APU interconnect and $La_{0.6}Sr_{0.4}FeO_3$ (LSF) cathode for IT-SOFC

Fuel Cells 13(3) **(2013)** 398-403.

Abstract

In order to simulate the contact situation of interconnect/contact layer/cathode in SOFC stacks, contact resistance and chemical compatibility of $LaNi_{0.6}Co_{0.4}O_{3-\delta}$ (LNC) as contact layer between Crofer22APU interconnect and $La_{0.6}Sr_{0.4}FeO_3$ (LSF) cathode was investigated at 800 ºC in air for more than 1300 h using X-ray diffraction (XRD), scanning electron microscopy (SEM) set-up equipped with an energy dispersive X-ray analyser (EDX) and area specific resistance (ASR) measurements. The XRD analysis reveals that multiple phases were formed during ASR test. The point microanalysis on cross-section of Fe-Cr/LNC/LSF system, after ASR measurements, shows chromium within the porous contact material mainly concentrated close to interconnect, but no Cr, Ni or Co was detected in the cathode. It was found between LNC and LSF cathode, a thin and uniform layer which contains Sr, La, Cr, Co, Ni and Fe. The contact between layers could act as a physical barrier for element migration and thus can suppress degradation of the cathode for these systems. The area specific resistance slope depends on the interactions between the contact material and/or cathode and the interconnect. Co-containing spinels formed during ASR test can be responsible of the resistance decrease of the system, related to the low degradation of the cell.

Keywords: solid oxide fuel cells, LNC contact material, interconnect, chemical compatibility, area specific resistance.

Highlights

- Long-term contact resistance of $La_{0.6}Sr_{0.4}FeO_3$/LNC/Crofer22APU is evaluated.
- LNC/LSF contact interface acts as a physical elements diffusion barrier.
- Co-spinel as reaction phase could reduce the ASR of the system.

2.2.1. Introduction

In recent years, great efforts have been dedicated to develop low or intermediate temperature solid oxide fuel cells (IT-SOFC) operating at 500-800 ºC. Lowering the operating temperature will improve cell durability and reduce the system final cost[49]. Thus, it can suppress degradation of components and extend the range of acceptable material selection, such as metallic interconnects like Crofer22APU[50]. However, there always exists a ceramic/metallic interface, which potentially contributes to a high contact resistance and thus to power losses[51-53]. Recent investigations[54] indicate the necessity to distinguish experimentally the resistance associated with the electrode coating/current collector contact from the total cell resistance due to the high value of the contact resistance associated with it.

Connection of the cathode to the interconnect is usually accomplished by compression of the stack using an external load frame, and is helped by use of a contact material layer between the porous ceramic cathode and metallic interconnect. Thus, a suitable cathode contact material minimises the interfacial electrical resistance and maximises the power output of SOFC stacks.

A number of different compounds used as contact materials, in SOFC systems, and their requirements have been already described in introduction section 2.1.1[55-62].

In the present study, LNC contact layer is symmetrically sandwiched between Crofer22APU metallic interconnect and LSF ceramic cathode, following Crofer22APU/LNC/LSF /Pt/LSF/LNC/Crofer22APU configuration, to measure the contact area specific resistance (ASR).

---

[49] Brett D.J.L., Atkirson A., Brandon N.P., Skinner S.J. Intermediate temperatura solid oxide fuel cells. *Chem. Soc. Rev.* 37 (**2008**) 1568-1578.

[50] Miguel-Pérez V., Martínez-Amesti A., Nó M.L., Larrañaga A., Arriortua M.I. Oxide scale formation on different metallic interconnects for solid oxide fuel cells. *Corros. Sci.* 60 (**2012**) 38-49.

[51] Guan W.B., Zhai H.J., Jin L., Li T.S., Wang W.G. Effect of contact between electrode and interconnect on performance of SOFC stacks. *Fuel Cells* 11(3) (**2011**) 445-450.

[52] Jiang S.P., Love J.G., Apateanu L. Effect of contact between electrode and current collector on the performance of solid oxide fuel cells. *Solid State Ionics* 160 (**2003)** 15-26.

[53] Tucker M.C., Cheng L., DeJonghe L.C. Selection of cathode contact materials for solid oxide fuel cells. *J. Power Sources* 196 (**2011**) 8313-8322.

[54] Jiang S.P. Resistance measurement in solid oxide fuel cells. *J. Electrochem. Soc.* 148(8) (**2001)** A887-A897.

[55] Yang Z., Xia G., Singh P., Stevenson J.W. Electrical contacts between cathodes and metallic interconnects in solid oxide fuel cells. *J. Power Sources* 155 (**2006**) 246-252.

[56] McCarthy B.P., Pederson L.R., Chou Y.S., Zhou X.D., Surdoval W.A., Wilson L.C. Low-temperature sintering of lanthanum strontium manganite-based contact pastes for SOFCs. *J. Power Sources* 180 (**2008)** 294-300.

[57] Wilkinson L.T., Zhu J.H. Ag-Perovskite composite materials for SOFC cathode-interconnect contact. *J. Electrochem. Soc.* 156(8) (**2009)** B905-B912.

[58] Montero X., Tietz F., Stöver D., Cassir M., Villarreal I. Comparative study of perovskites as cathode contact materials between an $La_{0.8}Sr_{0.2}FeO_3$ cathode and a Crofer22APU interconnect in solid oxide fuel cells. *J. Power Sources* 188 (**2009**) 148-155.

[59] Lu Z., Xia G., Templeton J.D., Li X., Nie Z., Yang Z., Stevenson J.W. Development of $Ni_{1-x}Co_xO$ as the cathode/interconnect contact for solid oxide fuel cells. *Electrochem. Commun.* 13 (**2011**) 642-645.

[60] Tucker M.C., Cheng L., DeJonghe L.C. Glass-containing composite cathode contact materials for solid oxide fuel cells. *J. Power Sources* 196 (**2011)** 8435-8443.

[61] Wang F., Yan D., Zhang W., Chi B., Pu J., Jian L. $LaCo_{0.6}Ni_{0.4}O_{3-\delta}$ as cathode contact material for intermediate temperature solid oxide fuel cells. *Int. J. Hydrogen Energ.* 38 (**2013**) 646-651.

[62] Zhang W., Wang F., Wang K., Pu J., Chi B., Jian L. Chemical compatibility and electrical contact between Ni–Cr–Mo alloy and $LaCo_{0.6}Ni_{0.4}O_{3-\delta}$ in intermediate temperature solid oxide fuel cells. *Int. J. Hydrogen Energ.* 37 (**2012)** 17253-17257.

Long time chemical compatibility of the system was tested after 1300 h at 800 ºC in air. Previously the feasibility of combining LNC as contact material and LSF as cathode was checked.

2.2.2. Experimental

The Crofer22APU alloy used in the present study is a Fe-Cr based alloy that was developed for application of metallic interconnects in intermediate temperature SOFCs. It was provided by Thyssenkrupp VDM, and its chemical composition, given by the supplier, is listed in Table 2.7. The powder materials used were: $LaNi_{0.6}Co_{0.4}O_{3-\delta}$ (LNC) (NexTech, Fuel Cell Material) as contact material, and $La_{0.6}Sr_{0.4}FeO_3$ (LSF) (NexTech, Fuel Cell Material) as cathode material.

Table 2.7. Composition of the steel in wt%.

	Cr	Fe	Mn	Ti	Si	Al	Mo	Others
Crofer22APU	22	Bal.*	0.5	0.1	0.25	0.25	-	La 0.15

* Balance.

For conductivity measurements, to achieve full density, as has been described in experimental section 2.1.2, LNC and LSF were sintered at 1200 ºC and 1150 ºC for 5 h, respectively. The electrical conductivity was measured with the standard dc four-point method on rectangular bars of approximate dimensions 1 x 3 x 7 mm. Two Pt electrodes were utilized for conducting current along the length, and two Pt electrodes were used for measuring voltage across the section at a certain distance (Figure 2.10). Conductivity measurements were performed from room temperature to 900 ºC in air using a heating rate of 2 ºC·min^{-1} using a power source controlled by PC using Lab Windows/CVI field point system.

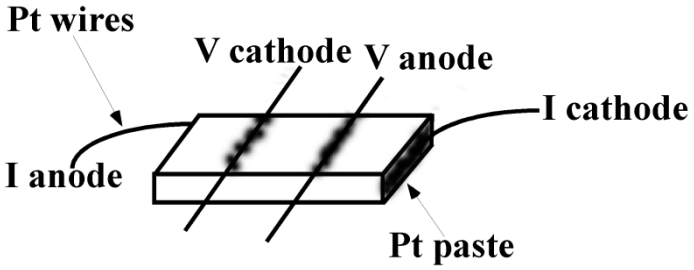

Figure 2.10. Schematic representation for conductivity measurements by the four-probe dc method of LNC and LSF.

In order to understand the chemical compatibility between the contact material and cathode, both materials were thoroughly mixed (50:50 wt. %). 10 g of each sample with 220 g of zirconia balls and 25 ml of acetone were milled during 8 h and then, the solvent was evaporated. The starting materials and the powders mixture, were sintered at 950 ºC for 2h and then treated at 800 ºC for 1080 h in air.

The contact and compatibility evaluation of contact layer between a Crofer22APU interconnect and LSF cathode was carried out with the interconnect pre-oxidized at 800 ºC for 100 h. Prior to the oxidation, the sheets were cut into 10 x 10 mm squares with 1 mm thicknesses. Metals were polished using #800 grit SiC and cleaned with acetone in an ultrasonic bath and dried. It was necessary to pre-oxidized interconnect to reduce interfacial stress over time between the contact

material and the interconnect[63]. The deposition of the contact materials was carried out using wet colloidal spray deposition technique on interconnects and sintered at 1050 ºC for 2h to obtain a rather dense coating. LSF cathode was deposited on contact layer using the same deposition technique and sintered at 950 ºC for 2h to produce a porous layer. The suspensions were made mixing in a ball mill during 1 hour the powders, ethanol and ZrO_2 cylinders as grinding media. An assembly of Crofer22APU/LNC/LSF was symmetrically sandwiched following the configuration showed in Figure 2.11. In order to achieve a better mechanical contact during measurement a 1 Kg/cm^2 weight is placed on top of the layer system. The overall ASR of the Crofer22APU/LNC/LSF setup was measured by four-point method at 800 ºC for up to 1316 h. Pt wires were spot-welded on the opposite side to the interconnect and the area was painted by Pt paste. Area specific resistance (ASR) was estimated by the voltage value measured after applying a current of 300 mA.

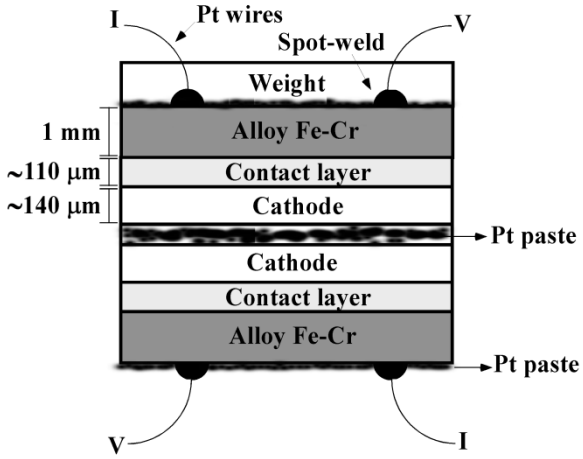

Figure 2.11. Sample setup for contact ASR measurement of the Crofer22APU/LNC/LSF symmetrical system.

X-ray diffractometer (XRD, X´Pert PRO) with Cu k_α radiation (λ= 1.5418 Å) was used to identify the commercial materials, to study the evolution of the LNC, LSF and the LNC-LSF mixture after they prolonged heating at 800°C, and to analyze the possible chemical process after the ASR test. The power generator has been provided at 40 kV and 40 mA. The patterns were recorded in 2θ steps of 0.026º in the 15-95º range, counting for 181 second per step. In addition, scanning electron microscope (SEM, JEOL LSM-6400) equipped with an Oxford Pentafet energy dispersive X-ray analyzer (EDX) was used for cross-sectional microstructure examination and composition analysis. The composition analysis on the sample cross-section was made using back-scattered electrons (BSE) at 20 kV accelerating voltage, $1 \cdot 10^{-9}$ A current density and 15 mm working distance. Due to the overlap of the emission lines for the studied elements, the INCA 350 software from Oxford was used to reconstruct the spectra and it was compared with measured one and to confirm the presence or absence of these elements.

[63] Hoyt K.O., Gannon P.E., White P., Tortop R., Ellingwood B.J., Khoshuei H. Oxidation behavior of $(Co,Mn)_3O_4$ coatings on preoxidized stainless steel for solid oxide fuel cell interconnects. *Int. J. Hydrogen Energ.* 37 (**2012**) 518-529.

2.2.3. Characterization and results

The crystal structure given by technical specifications of studied materials (LNC, LSF, and Crofer22APU) were checked by XRD. Figure 2.12 shows the X-ray full-profile refinement of starting materials fitted by the Rietveld method. The quantitative analysis shows that the analyzed materials are pure except LNC in which two very weak peaks corresponding to NiO were found (1.5 % in weight).

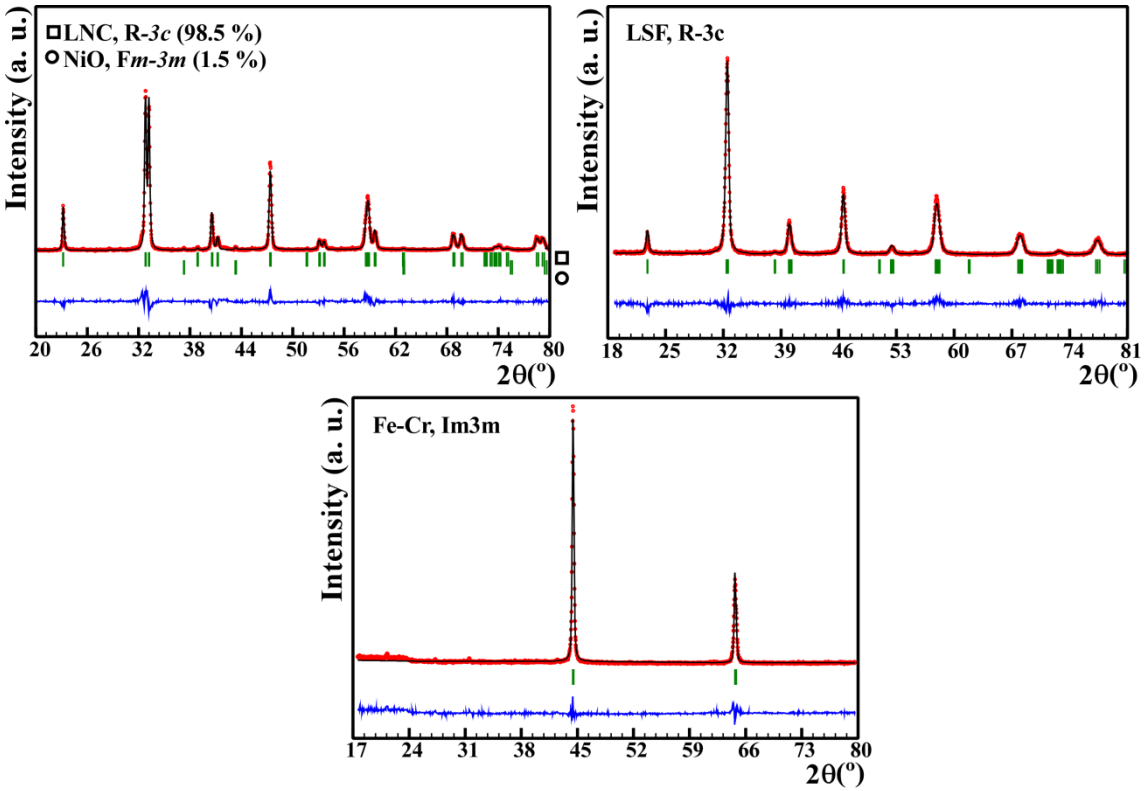

Figure 2.12. Rietveld X-ray diffraction patters for commercial LNC, LSF and Crofer22APU materials.

Figure 2.13 presents full-profile refinements of contact and cathode materials and the mixture of both (50:50 wt. %) after been sintered at 950 ºC for 2h and been treated at 800 ºC for 1080 h in air. The resulting Rietveld analysis demonstrates that LNC remains stable after prolonged heating in air, but the cathode degrades to LSF phase (91.8 %), $LaSrFeO_4$ (7 %), Fe_3O_4 (1 % in weight), and $SrFe_{12}O_{19}$ (<1% in weight). Nevertheless, for the treated mixture no main reactions products were identified; only the starting NiO corresponding to the contact material, and traces of La_2O_3 and SrO, so it can be concluded that the use of LNC/LSF might avoid the formation of decomposition phases from the cathode.

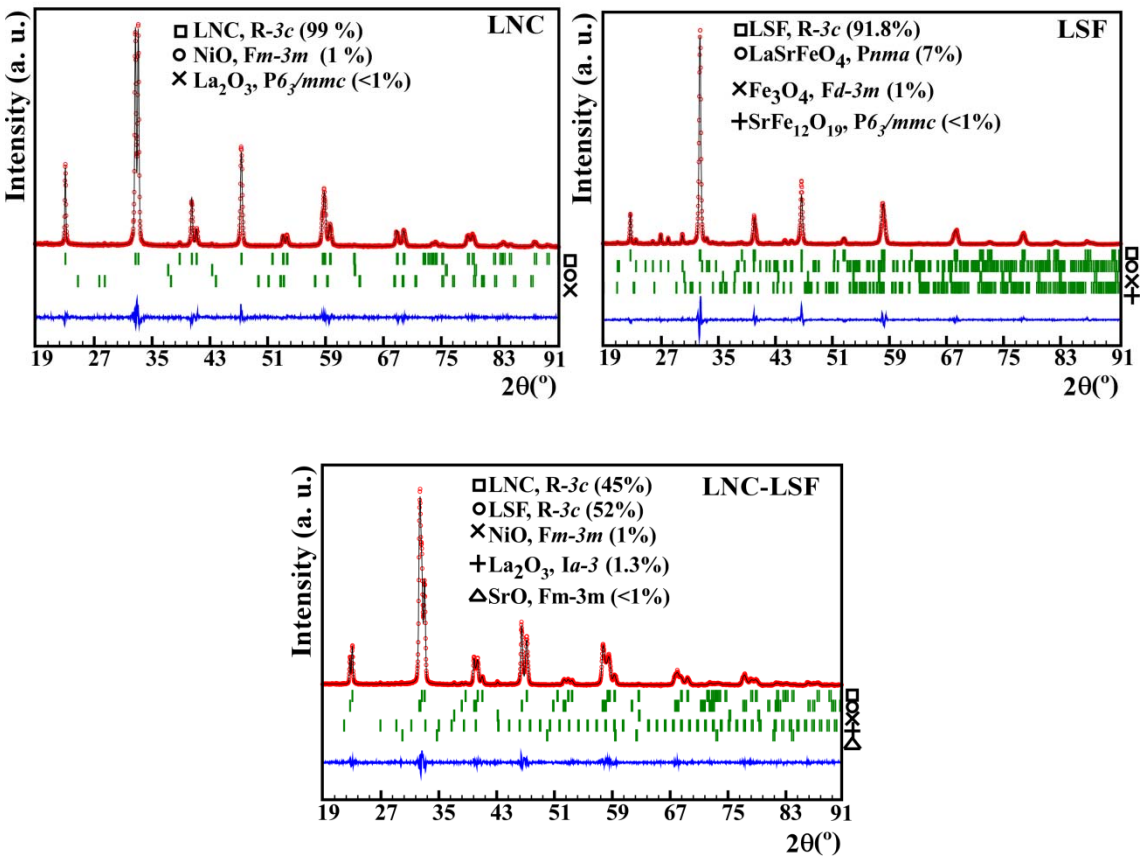

Figure 2.13. Rietveld analysis of LNC, LSF and LNC-LSF mixture after heated at 800 ºC for 1080 h in air.

The conductivity of LNC and LSF was measured in the temperature range from room temperature to 900 ºC, as shown in Figure 2.14. The electronic conductivity of LNC is mainly carried by the narrow itinerant conduction band of the Ni-arrays[64] so this material exhibits metallic like conductivity. For LSF material the electrical conduction occurs by thermally activated of small polarons hopping as was shown in previous researches[65-67].

[64] Huang A., Yao K., Wang J. Conducting perovskite $LaNi_{0.6}Co_{0.4}O_3$ ceramics with glass additions. *J. Electroceram.* 16 (**2006**) 313-319.

[65] Sogaard M., Hendriksen P.V., Mogensen M. Oxygen nonstoichiometry and transport properties of strontium substituted lanthanum ferrite. *J. Solid State Chem.* 180 (**2007**) 1489-1503.

[66] Vidal K., Rodríguez-Martínez L.M., Ortega-San-Martín L., Nó M.L., Rojo T., Arriortua M.I. Effect of the A cation size disorder on the properties of an iron perovskite series for their use as cathode for SOFCs. *Fuel Cells* 11 (**2011**) 51-58.

[67] Écija Verdejo A., "Óxidos mixtos tipo perovskita $Ln_{0.5}M_{0.5}FeO_{3-\delta}$ (Ln=La,Sm,Nd,Gd; M=Ba,Sr) para su aplicación como cátodos en pilas SOFC". Ph. D. thesis work, UPV/EHU, **2012**.

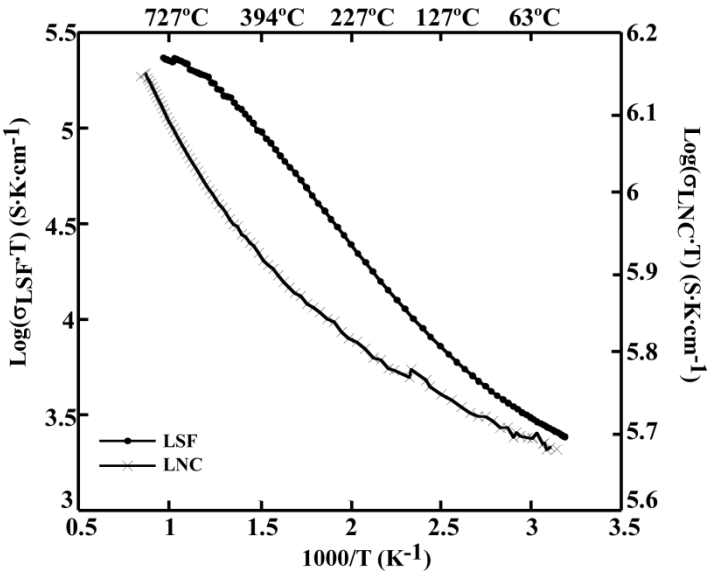

Figure 2.14. Arrhenius plot of $LaNi_{0.6}Co_{0.4}O_{3-\delta}$ and $La_{0.6}Sr_{0.4}FeO_3$ perovskites as a function of temperature.

The conductivity values of LNC and LSF at 800 ºC are ≈1200 and ≈200 $S \cdot cm^{-1}$, respectively, in good agreement with the observed in other works for these type of compounds[68,69]. Those values are appropriated to use LNC as contact material in solid oxide fuel cells.

The chemical compatibility of LNC with LSF at 800 ºC after 1080 h and their appropriate values of conductivity make possible to use these materials.

2.2.3.1. ASR measurements and post-test analysis

The XRD results of the Crofer22APU/LNC/LSF system after ASR test at 800 ºC in air for 1080 h, presented in Figure 2.15, reveal that the main and secondary phases are (La,Sr)(Ni,Co,Fe)O_3 (rhombohedral, space group: R-*3c*), (La)(Ni,Co,Cr)O_3 (rhombic, space group: P*bnm*) and $SrCrO_4$, NiO, respectively. Apart from those compounds, $SrNiO_3$, Cr_2O_3 and the M_3O_4 (M= Fe,Mn,Ni,Co or Cr) spinel can be observed in smaller amount. The original Fe-Cr substrate was identified indicating that the X-ray penetration was enough to observe the signal of all the formed layers. Due to the similarity of the ionic radio of Cr, Mn, Ni, Co and/or Fe, it is difficult to determine the exact chemistry of the M_3O_4 spinel using the XRD technique.

[68] Sun C., Hui R., Roller J. Cathode materials for solid oxide fuel cells: a review. *J. Solid State Electrochem.* 14 (**2010**) 1125-1144.

[69] Huang A., Yao K., Wang J. Conducting perovskite $LaNi_{0.6}Co_{0.4}O_3$ ceramics with glass additions. *J. Electroceram.* 16 (**2006**) 313-319.

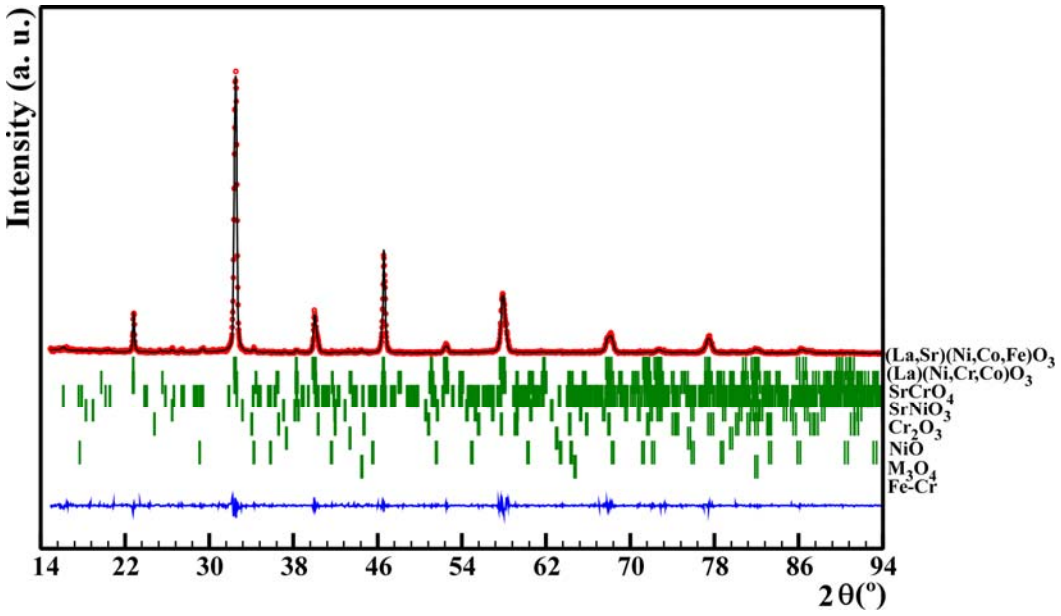

Figure 2.15. Full-profile refinement without structural model (Pattern matching) of Crofer22APU/LNC/LSF system after heated at 800 ºC in air for 1080 h.

The formation of $(La)(Ni,Co,Cr)O_3$ can be understood through two possible mechanism, according to the following equations[70].

$1.5Cr_2O_3(s) + 3(La)(Ni,Co)O_3 = 3(La)(Ni_yCo_xCr_{1-x-y})O_3 + (Cr_{1-x-y}Co_xNi_y)_3O_4 + 0.25O_2$
$3CrO_3(g) + 3(La)(Ni,Co)O_3 = 3(La)(Ni_yCo_xCr_{1-x-y})O_3 + (Cr_{1-x-y}Co_xNi_y)_3O_4 + 2.5O_2$

The structure of Cr-containing perovskite is rhombic in contrast to LNC which is rhombohedral. The deconvolution of doublet peak (in the range of 39-42º in 2θ) provides the option to detect the rhomboedral and rhombic phases (Figure 2.16), this procedure was described in previous studies[71]. For the pure LNC, heated at 800 ºC in air for 1080 h, two single peaks can be indexed as (202) and (006) of the rhomboedral phase. In the sample Crofer22APU/LNC/LSF after heated in the same conditions, two single peaks begin evolving into a double peak with additional two reflections of the rhombic phase indicating the presence of both rhombohedral and rhombic perovskite phases.

[70] Badwal S.P.S., Deller R., Foger K., Ramprakash Y., Zhang J.P. Interaction between chromia forming alloy interconnects and air electrode of solid oxide fuel cells. *Solid State Ionics* 99 (**1997**) 297-310.

[71] Stodolny M.K., Boukamp B.A., Blank D.H.A., Van Berkel F.P.F. $La(Ni,Fe)O_3$ stability in the presence of chromia-A solid-state reactivity study. *J. Electrochem. Soc.* 158(2) (**2011**) B112-B116.

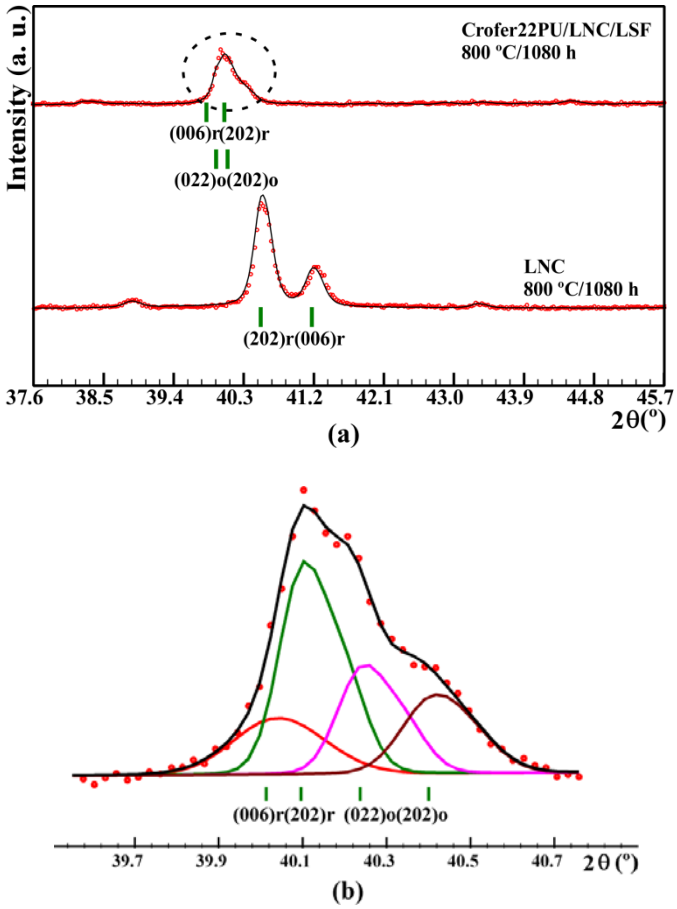

Figure 2.16. a) X-ray diffraction peaks variation of LNC and Crofer22APU/LNC/LSF system after heated at 800 ºC in air for 1080 h, in the 2θ range ≈37-45º, and b) deconvolution of formed signal of system.

The cross-section back-scattered electron image of the Crofer22APU/LNC/LSF interface after ASR measurements (Figure 2.17(a)) shows poor sinterability between particles and large holes were detected in the contact layer. Their presence could be an accidental effect due to a surface inhomogeneity in the steel. Nevertheless, the contact layer looks adherent to the cathode.

Throughout the contact layer can be observed differences in the emission of the backscattered electrons from different regions. High average atomic number layers were close to the cathode material. In addition, a white coloured thin and uniform layer was formed between the contact layer and the cathode. The surface of Crofer22APU was covered by a thin and discontinuous oxide scale. EDX was used to estimate the extent of element interdiffusion across assembly interfaces. Linescans were produced from a points analysis along the sample, representative results are shown in Figure 2.17(b). Large amounts of Cr were detected all around the contact material, especially in the first 45 μm, but no chromium was detected within the cathode neither Ni nor Co. The small white layer between the contact material and the cathode contains La, Sr, Cr, Co, Ni and Fe, so the contact itself could act as a barrier for element diffusion.

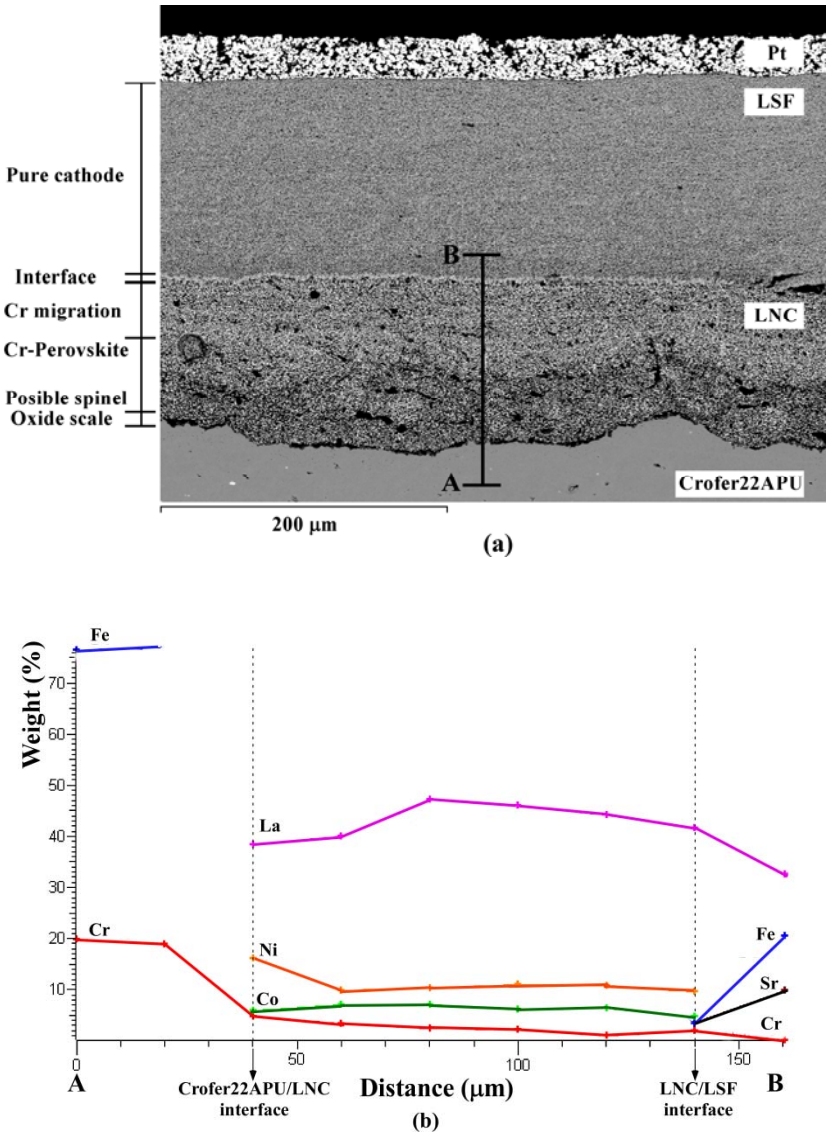

Figure 2.17. a) SEM cross-section (back-scattered electron image) of Crofer22APU/LNC/ LSF system after heated at 800 ºC for 1300 h in air with b) representative results to estimate the extent of interdiffusion at the system interfaces from EDX points analysis.

Figure 2.18 shows variation of ASR of Crofer22APU/LNC/LSF contact with testing time at 800 ºC in air. The obtained signal was relatively stable near 0.04 Ω cm^2 until the end of the test. Different studies, point out the relative initial ASR follows the trend of the conductivity of the contact layer[58]. After 1300 h, the low degradation of ASR is likely due to small element migration between interconnect and contact materials to form Co-containing spinels, which protects the Cr poisoning and improves the scale conductivity of the system.

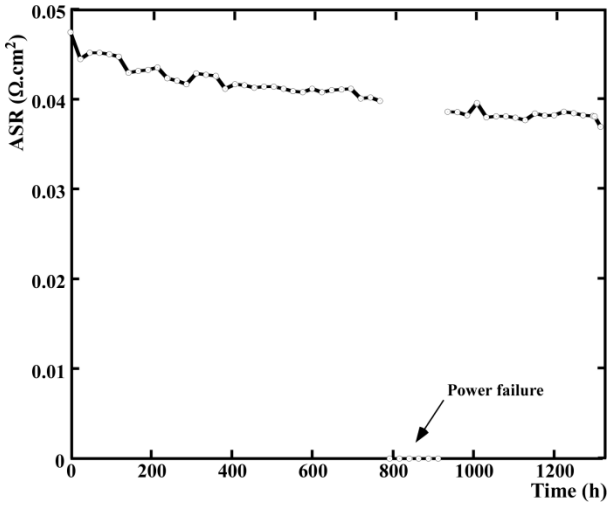

Figure. 2.18. Area specific resistance (ASR) for Crofer22APU/LNC/LSF system as a function of time.

The aim of this work was to simulate the contact situation of Crofer22APU/LNC/LSF in IT-SOFC conditions. After prolonged heating at 800 ºC in air, $SrCrO_4$ might have been formed between contact layer and the cathode. The presence of NiO and $SrNiO_3$ might mean that Ni was practically extracted from LNC perovskite lattice, whereas Cr was incorporated to form a rhombic $La(Ni,Co,Cr)O_3$ phase, which was mainly concentrated in the first 50 μm of contact layer. The use of LNC as contact layer with thicknesses of 110 μm might avoid migration of elements toward the cathode. In addition, the low presence of Cr_2O_3 suggests that this element presents diffusion to be incorporated to the spinel phase, or that the growth rate of created metal oxides on the metal surface, under oxidation atmosphere, could be lowered if a conductive layer, such as LNC coated, is applied on the surface of interconnect.

2.2.4. Conclusions

After checked the feasibility of LNC as contact material using LSF as cathode, the contact situations of LNC between Crofer22APU interconnect and LSF was studied after prolonged heating at 800 ºC in air. From the results obtained, the following conclusions could be extracted.

The combination of LNC contact layer and LSF cathode with Crofer22APU interconnect leads to the formation of, principally, $(La,Sr)(Ni,Co,Fe)O_3$, $La(Ni,Co,Cr)O_3$, $SrCrO_4$, and NiO phases. Therefore, this result demonstrates the intrinsic instability of the LNC and LSF when Cr-containing metallic interconnect is in direct contact with them.

LNC/LSF contact interface acts as physical elements diffusion barrier. Thus prevents the migration of Cr, Ni, Co toward the cathode. The ASR contributed by the Crofer22APU/LNC/LSF contact, around 0.04 Ω cm^2, is acceptable for the performance of a SOFC stack operated in the intermediate temperature range (600-800 ºC). Co-containing spinels formed during the ASR test reduce the resistance of the system.

Taking into account the previous points, LNC material would seem to offer promising opportunities as a Cr-resistant contact coating.

2.3. Solid oxide fuel cell improvement using a ceramic contact material between Crofer22APU interconnect and $La_{0.6}Sr_{0.4}FeO_3$ cathode

Mater. Charact., sent (MTL-15064), **2015**.

Abstract

$LaNi_{0.6}Co_{0.4}O_{3-\delta}$ (LNC), $LaNi_{0.6}Fe_{0.4}O_{3-\delta}$ (LNF) and $(La_{0.8}Sr_{0.2})_{0.95}Fe_{0.6}Mn_{0.3}Co_{0.1}O_3$ (LSFMC) were used as cathode contact coatings. The long-term stability of these materials was tested by X-ray diffraction (XRD). Thermo X-ray diffractometry (TDX) analyses revealed that the studied three perovskites present a reversible transition from rhombohedral to cubic structure with increasing temperature. X-ray photoelectron spectroscopy (XPS) indicated the presence of La_2O_3 and/or SrO as surface impurities on initial oxides. Long-term treatment at 800 ºC of powder mixtures of each contact material with $La_{0.6}Sr_{0.4}FeO_3$ (LSF) cathode (1:1 wt.) allowed the formation of a complete solid solution of $(LSF)_x(LNC,LNF \text{ or } LSFMC)_{1-x}$. The {Crofer22APU interconnect/contact coating} systems, were exposed at 800 ºC for 1000 h, showing a low degradation rate of contact coatings. XPS and XRD analyses performed on top of the three coated samples reveal the presence of Cr-perovskite when LNC and LNF are used. XRD, scanning electron microscopy with energy dispersive X-ray spectroscopy (SEM-EDX), and area specific resistance (ASR) measurements were used to evaluate the long-term behaviour of {interconnect/contact coating/cathode} structures, in presence and absence of contact coating. The contact resistance of cells decreases using contact layers; after 1300 h at 800 ºC the {Crofer22APU/ LNC/LSF} setup showed stable ASR value of 0.041(2) $\Omega \cdot cm^2$.

Keywords: SOFC; cathode contact coating; contact resistance; chromium poisoning; degradation.

Highlights

- XRD reveals structural changes in $LaNi_{0.6}B_{0.4}O_{3-\delta}$ (B=Co,Fe) by Cr^{3+} substitution.
- Using a perovskite contact coating on alloy interconnect the ASR of the system decreases.
- ASR for {Crofer22APU/LNC/LSF} was 0.041(2) $\Omega \cdot cm^2$ after 1300 h at 800 ºC, in air.

2.3.1. Introduction

In recent years, the increasing concentrations of greenhouse gases in the atmosphere due to the use of fossil fuels is causing average temperatures to rise all over the world. To deal with these needs, solid oxide fuel cells (SOFCs) have been introduced as an alternative to conventional methods of energy production[72,73]. The long-term durability of SOFC must be addressed to maximize the performance and thus to reach the commercial status of these devices. The main degradation processes in SOFC are due to the faults between the layers, producing the increase in cell ohmic resistance and, the electrode microstructural degradation. These "SOFC faults" can be understood in terms of deterioration of single components and interactions between cell components. The electrode delamination, oxide layer growth and rib detachment make an increase in cell ohmic resistance. Furthermore, long periods of operation at elevated temperature and the electrode poisoning by contaminants, such as chromium, are responsible for microstructural degradation. Therefore, these issues affect the cell stability and durability[74,75].

Interconnect oxidation is an important degradation mode affecting contact resistance due to the formed chromium oxide layer hinders the electrons flow into the contact coating. Moreover, electron conduction can also be interrupted because of the loss of contact of one or more ribs from the contact material. So, the electronic current cannot go from the interconnect to the cathode through the affected ribs. However, it can travel laterally across the cathode because of the relatively high mobility of the electrons. This results in a current density arose at the first intact rib adjacent to the group of detached ribs. Such a current increase may cause localized overheating and thereby rise the oxidation rate of the affected zone. In common with the oxide layer growth, also this malfunction situation causes an increase in total resistance of the cell[74,76,77]. On the other hand, the poisoning of the cathode microstructure with chromium from the interconnect leads to the chromium rich compound deposits on contact coating and on cathode electrochemically active sites. Thus, the electrical conductivity of contact coating and cathode active area could be affected.

The interaction between metallic interconnect and perovskite type oxides for SOFC has been investigated extensively in[78-83]. Different authors indicate that a degradation factor of strontium

---

72 Al-Qattan A., Elsherbini A., Al-Ajmi K. Solid oxide fuel cell application in district cooling. *J. Power Sources* 257 (**2014**) 21-26.

73 Specchia S. Fuel processing activities at European level: A panoramic overview. *Int. J. Hydrogen Energ.* 39 (**2014**) 17953-17968.

74 Barelli L., Barluzzi E., Bidini G. Diagnosis methodology and technique for solid oxide fuel cells: A review. *Int. J. Hydrogen Energ.* 38 (**2013**) 5060-5074.

75 Jiang S.P., Chen X. Chromium deposition and poisoning of cathodes of solid oxide fuel cells – A review. *Int. J. Hydrogen Energ.* 39(1) (**2014**) 505-531.

76 Gazzarri J.I., Kesler O. Short-stack modeling of degradation in solid oxide fuel cells Part I. Contact degradation. *J. Power Sources* 176 (**2008**) 138-154.

77 Grolig J.G., Froitzheim J., Svensson J.E. Coated stainless steel 441 as interconnect material for solid oxide fuel cells: oxidation performance and chromium evaporation. *J. Power Sources* 248 (**2014**) 1007-1013.

78 Shaigan N., Qu W., Douglas G.I., Chen W. A review of recent progress in coatings, surface modifications and alloy developments for solid oxide fuel cell ferritic stainless steel interconnects. *J. Power Sources* 195 (**2010**) 1529-1542.

79 Shong W.J., Liu C.K., Chen C.Y., Peng C.C., Tu H.J., Fey G.T.K., Lee R.Y., Kao H.M., Effects of lanthanum-based perovskite coatings on the formation of oxide scale for ferritic SOFC interconnect. *Mater. Chem. Phys.* 127 (**2011**) 45-50.

80 Conceição L.D., Dessemond L., Djurado E., Muccillo E.N.S. $La_{0.7}Sr_{0.3}MnO_{3-\delta}$ barrier for Cr_2O_3-forming SOFC interconnect alloy coated by electrostatic spray deposition. *Surf. Coat. Tech.* 254 (**2014**) 157-166.

doped ferrite, manganite, cobaltite and/or nickelite compositions, in presence of chromium, was the formation of $SrCrO_4$ at the grains of the materials; besides, the deposition of Cr_2O_3 or $(Mn,Cr)_3O_4$ spinel is given. In fact, as was indicated in[84-86], $La(Cr,B)O_3$ (B=Ni,Co,Fe) is formed when a transition element of perovskite is extracted from the initial oxide lattice.

Using interconnect protective coating in combination with contact layer can avoid the migration of chromium to the cathode, improve the oxide growth resistance and reduce the power losses in cell[83,87-89]. The contact coatings must have adequate conductivity, appropiate thermal expansion coefficient, be chemically compatible with adjacent components and stable in air[90]. Some studies[91,92] have concluded that perovskite oxides such as $La(Ni,Co)O_{3-\delta}$, $La(Ni,Fe)O_{3-\delta}$ and/or $LaSr(FeCo)O_3$ have lower reactivity with spinel protective layer ($MnCo_2O_4$) than Ruddlesden-Popper structure phases ($Nd_{1.8}Ce_{0.2}CuO_4$, $La_{1.2}Sr_{0.8}NiO_4$), and are good candidates to be used as contact layers.

The purpose of this paper is to analyse the long-term behaviour of {Crofer22APU interconnect/contact coating/LSF cathode} systems, using three different compositions of perovskite $LaNi_{0.6}Co_{0.4}O_{3-\delta}$ (LNC), $LaNi_{0.6}Fe_{0.4}O_{3-\delta}$ (LNF) and $(La_{0.8}Sr_{0.2})_{0.95}Fe_{0.6}Mn_{0.3}Co_{0.1}O_3$ (LSFMC) as cathode current collectors. Moreover, the effectiveness of each contact coating is also studied.

---

81 Pyo S.S., Lee S.B., Lim T.H., Song R.H., Shin D.R., Hyun S.H., Yoo Y.S. Characteristic of $(La_{0.8}Sr_{0.2})_{0.98}MnO_3$ coating on Crofer22APU used as metallic interconnects for solid oxide fuel cells. *Int. J. Hydrogen Energ.* 36 (**2011**) 1868-1881.

82 Wang F., Yan D., Zhang W., Chi B., Pu J., Jian L. $LaCo_{0.6}Ni_{0.4}O_{3-\delta}$ as cathode contact material for intermediate temperature solid oxide fuel cells. *Int. J. Hydrogen Energ.* 38 (**2013**) 646-651.

83 Montero X., Tietz F., Stöver D., Cassir M., Villarreal I. Comparative study of perovskites as cathode contact materials between an $La_{0.8}Sr_{0.2}FeO_3$ cathode and a Crofer22APU interconnect in solid oxide fuel cells. *J. Power Sources* 188 (**2009**) 148-155.

84 Stodolny M.K., Boukamp B.A., Blank D.H.A., Van Berkel F.P.F. $La(Ni,Fe)O_3$ stability in the presence of chromia-A solid-state reactivity study. *J. Electrochem. Soc.* 158(2) (**2011**) B112-B116.

85 Stodolny M.K., Boukamp B.A., Blank D.H.A., Berkel F. P. F.V. Impact of Cr-poisoning on the conductivity of $LaNi_{0.6}Fe_{0.4}O_3$. *J. Power Sources* 196 (**2011**) 9290-9298.

86 Morán-Ruiz A., Vidal K., Larrañaga A., Arriortua M.I. Chemical compatibility and electrical contact of $LaNi_{0.6}Co_{0.4}O_{3-\delta}$ (LNC) between Crofer22APU interconnect and $La_{0.6}Sr_{0.4}FeO_3$ (LSF) cathode for IT-SOFC. *Fuel Cells* 13(3) (**2013**) 398-403.

87 Montero X., Jordán N., Pirón-Abellán J., Tietz F., Stöver D., Cassir M., Villarreal I. Spinel and perovskite protection layers between Crofer22APU and $La_{0.8}Sr_{0.2}FeO_3$ cathode materials for SOFC interconnects. *J. Electrochem. Soc.* 156(1) (**2009**) B188-B196.

88 Seabaugh M.M., Day M., Beachy M., McCormick B.E., Ibanez S. Materials development for SOFC applications. *ECS Trans.* 25(2) (**2009**) 619-628.

89 Wu W., Guan W., Wang G., Liu W., Zhang Q., Chen T., Wang W.G. Evaluation of $Ni_{80}Cr_{20}/(La_{0.75}Sr_{0.25})_{0.95}MnO_3$ dual layer coating on SUS 430 stainless steel used as metallic interconnect for solid oxide fuel cells. *Int. J. Hydrogen Energ.* 39 (**2014**) 996-1004.

90 Morán-Ruiz A., Vidal K., Larrañaga A., Laguna-Bercero M.A., Porras-Vázquez J.M., Slater P.R., Arriortua M.I. $LaNi_{0.6}Co_{0.4}O_{3-\delta}$ dip-coated on Fe-Cr mesh as a composite cathode contact material on intermediate solid oxide fuel cells. *J. Power Sources* 269 (**2014**) 509-519.

91 Morán-Ruiz A., Vidal K., Laguna-Bercero M.A., Larrañaga A., Arriortua M.I. Effects of using $(La_{0.8}Sr_{0.2})_{0.95}Fe_{0.6}Mn_{0.3}Co_{0.1}O_3$ (LSFMC), $LaNi_{0.6}Fe_{0.4}O_{3-\delta}$ (LNF) and $LaNi_{0.6}Co_{0.4}O_{3-\delta}$ (LNC) as contact material on solid oxide fuel cells. *J. Power Sources* 248 (**2014**) 1067-1076.

92 Tucker M.C., Cheng L., DeJonghe L.C. Selection of cathode contact materials for solid oxide fuel cells. *J. Power Sources* 196 (**2011**) 8313-8322.

2.3.2. Experimental

Three perovskite, $LaNi_{0.6}Co_{0.4}O_{3-\delta}$ (LNC), $LaNi_{0.6}Fe_{0.4}O_{3-\delta}$ (LNF) and $(La_{0.8}Sr_{0.2})_{0.95}Fe_{0.6}Mn_{0.3}Co_{0.1}O_3$ (LSFMC) were used as contact coatings (NexTech, Fuel cell Materials). Lanthanum strontium ferrite (NexTech, Fuel Cell Materials), $La_{0.6}Sr_{0.4}FeO_3$, and Crofer22APU steel (ThyssenKrupp VDM) were used as cathode and interconnect, respectively. The chemical composition of Fe-Cr based alloy is reported in previous study of our group[93]. The electrical conductivity values at 800 ºC and average thermal expansion coefficients (TECs,$\alpha_{30\text{-}800\ ^oC}$) of used materials are listed in Table 2.8 [91].

Table 2.8. Conductivity and thermal expansion coefficient values (TECs) at 800 ºC for $LaNi_{0.6}Co_{0.4}O_{3-\delta}$ (LNC), $LaNi_{0.6}Fe_{0.4}O_{3-\delta}$ (LNF), $(La_{0.8}Sr_{0.2})_{0.95}Fe_{0.6}Mn_{0.3}Co_{0.1}O_3$ (LSFMC), $La_{0.6}Sr_{0.4}FeO_3$ (LSF) and Crofer22APU materials [91].

Composition	σ_{800^oC} (S/cm)	$\alpha_{30\text{-}800^oC}$ (K^{-1})
$LaNi_{0.6}Co_{0.4}O_{3-\delta}$ (LNC)	1229	$17.9\cdot10^{-6}$
$LaNi_{0.6}Fe_{0.4}O_{3-\delta}$ (LNF)	685	$16.1\cdot10^{-6}$
$(La_{0.8}Sr_{0.2})_{0.95}Fe_{0.6}Mn_{0.3}Co_{0.1}O_3$ (LSFMC)	65	$14.5\cdot10^{-6}$
$La_{0.6}Sr_{0.4}FeO_3$ (LSF)	214	$16.1\cdot10^{-6}$
Interconnect	Metallic	$11.8\cdot10^{-6}$

The particle size of the contact coatings was analysed by laser dispersion analyser using a Malvern MasterSizerX. The equipment is based on the angular distribution of forward scattered light, operates with a collimated helium-neon laser beam at 640 nm and is able to provide the particle size distribution from 0.1 to 1000 μm range. Spherical particle shape analysis mode was used to estimate the particle sizes. Initial powders (refractive index: 2.34) were ultrasonically dispersed for 5 min using ethanol (refractive index: 1.39) as dispersant. Thermodiffractometry (TDX) analysis of the initial contact powders was carried out in a Bruker D8 Advance Theta-Theta diffractometer with Cu K_α radiation (λ = 1.5418 Å) and HTK2000 chamber with a Pt sample holder. The powder generator was set to 30 kV and 20 mA. The patterns were recorded from room temperature to 1200 ºC each 20 ºC, which were scanned with 2 s ranging from 19-90 º with 0.03º steps. The suggested contact powders were compacted under uniaxial pressure (press, Specac) with a 13 mm diameter. Pellets were sintered, in a conventional Carbolite furnace, at 1050 ºC for 2 h, contact coating sintering temperature in cell[86,91], and at 950 ºC for 2h to treated at 800 ºC for 1000 h, in air. Furthermore, powder mixtures of each contact material with $La_{0.6}Sr_{0.4}FeO_3$ cathode were prepared with a weight ratio of 1:1, according to the procedure in Ref. [86]. The mixtures were pressed into 13 mm diameter pellets, using 1 g of each sample, finally sintered at 950 ºC for 2h to heat treated at 800 ºC up to 1000 h, in air.

On the other hand, the interconnect was preoxidized in air at 800 ºC for 100 h, as described in Ref. [91], to reduce Cr and Fe transport into the contact coating after long oxidation times and to

[93] Miguel-Pérez V., Martínez-Amesti A., Nó M.L., Larrañaga A., Arriortua M.I. Oxide scale formation on different metallic interconnects for solid oxide fuel cells. *Corros. Sci.* 60 (**2012**) 38-49.

lower interfacial stress over time between the contact material and the interconnect. The deposition of the contact materials on interconnect was performed using wet colloidal spray deposition technique, as was described in Ref. [96]. The suspensions were made mixing in a ball mill (LABMILL 8000) during 1 hour the powders, ethanol and ZrO_2 cylinders (diameter: 9.5 mm) as grinding media. These samples were sintered at 1050 ºC for 2h to obtain a rather dense coating and then, they aged at 800 ºC for 1000 h in air. In order to obtain {Crofer22APU interconnect/contact coating/LSF cathode} and {Crofer22APU interconnect/cathode} systems, the cathode was deposited on sintered contact coatings or on preoxidized Fe-Cr substrate, using the same deposition technique, and then sintered at 950 ºC for 2h to allow a porous cathode. These structures were treated at 800 ºC for 1000 h in air.

For area specific resistance (ASR) measurements, a half-cells {interconnect/contact coating/cathode} and {Crofer22APU interconnect/cathode} were symmetrically sandwiched following the configuration showed in Figure 2.19. In order to achieve a better mechanical contact during measurements a weight load of 1 kg was placed on top of the system. The electrical conductivity of symmetrical cells was measured using a dc four-point method[97], in air, at 800 ºC up to 1300 h. The electronic contacts were made using platinum wire and platinum paste. To ensure good contact between cathode of one side half-cell with the cathode side of the adjacent half-cell, the surface of cathodes was painted with a platinum paste (Figure 2.19). Area specific resistance was estimated by the voltage value measured by cronoamperometry applying a current of 300 mA[83], using a Solartron 1260 Frequency Response Analyzer.

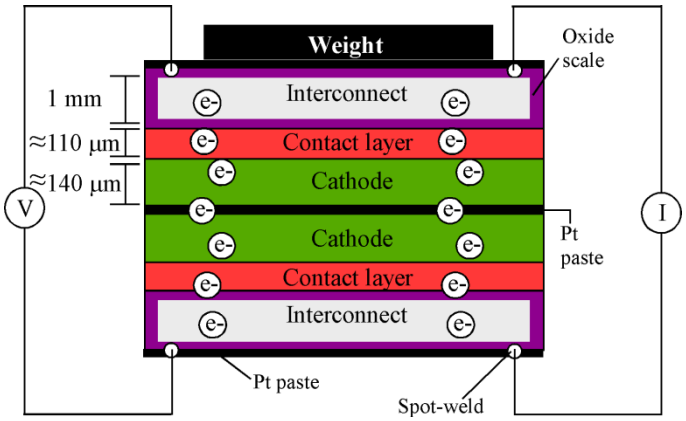

Figure 2.19. Scheme of the setup for ASR measurements.

The crystalline phases from all of heated samples were characterized by X-ray diffraction (XRD) recorded at room temperature, using a Philips X`Pert PRO diffractometer equipped with Cu K_α radiation (λ = 1.5418 Å). The power generator has been provided at 40 kV and 40 mA. The

[94] Hoyt K.O., Gannon P.E., White P., Tortop R., Ellingwood B.J., Khoshuei H. Oxidation behavior of $(Co,Mn)_3O_4$ coatings on preoxidized stainless steel for solid oxide fuel cell interconnects. *Int. J. Hydrogen Energ.* 37 (**2012**) 518-529.

[95] Ou D.R., Cheng M. Effect of pre-oxidation on the oxidation resistance of spinel-coated Fe–Cr ferritic alloy for solid oxide fuel cell applications. *J. Power Sources* 247 (**2014**) 84-89.

[96] Charpentier P., Fragnaud P., Schleich D.M., Gehain E. Preparation of thin film SOFCs working at reduced temperature. *Solid State Ionics* 135 (**2000**) 373-380.

[97] Schroder D.K.. Semiconductor material and device characterization, 3rd edition, John Wiley & Sons, New York, p. 149-156, **1998**.

patterns were recorded in 2θ steps of 0.026º in the 18-90º range. The preliminary evaluation of the composition of the samples was performed using the X`Pert HighScore Software based on Powder Diffraction File (PDF) database[98]. Having identified the phases, full-profile refinements were performed using the FullProf program[99] to get % in weight of each phase in the samples. The compositions of the initial contact material surfaces, and the contact coatings in long-term contact with Fe-Cr interconnect were obtained from X-ray photoelectron spectroscopy (XPS) survey scans (step energy 1 eV, dwell time 0.1 s, pass energy 80 eV), using a SPECS (Berlin, Germany) system equipped with a Phoibos 150 1D-DLD analyser and monochromatic Al K_α radiation ($h\cdot\nu$= 1486.6 eV). The chemistries of selected elements were taken from higher energy resolution scans of the appropriate peaks (step energy 0.1 eV, dwell time 0.1 s, pass energy 20 eV) with an electron take-off angle of 90º. The binding energies (BEs) were calibrated against the surface carbon contamination at 284.6 eV. The spectra were fitted by CasaXPS 2.3.16 software, modelling properly weighted sum of Gaussian and Lorentzian component curves, after background subtraction according to Shirley.

The microstructure, composition and phase distribution of all the samples were analysed using a JEOL LSM-6400 scanning electron microscope (SEM) equipped with an Oxford Pentafet energy dispersive X-ray analyzer (EDX). Surface microstructure was observed using secondary electrons (SE) at an accelerating voltage of 20 KV, a current of $1.1\cdot10^{-11}$ A and a working distance of 15 mm. The backscattered electron signal (BSE) at 20 kV and a current intensity of $1\cdot10^{-9}$ A were used for EDX microanalyses (the live time is set to 100 s). Samples for cross-section analysis were embedded in an epoxy resin, polished using standard metallographic techniques, and coated with a coal graphite layer (10 nm) deposited by evaporation (Quorum Q150T Sputter Coater) to provide electrical conductivity. Taking into account the EDX resolution was approximately 133 eV and the overlap of the emission lines of the elements involved in this study[86,93,100], the INCA 350 software (Oxford Instrument) was used to reconstruct the spectra and they were compared with the measured ones to confirm the presence or absence of these elements. This software considers the theoretical emission lines of the elements and the theoretical intensity ratio (Ik_α/Ik_β) lines of the analysed elements. The emission lines used for the analysis were K_α and K_β for Cr, Co, Fe, Ni and Mn, L_α for Sr and La and, L_β for La.

2.3.3. Results and discussion

2.3.3.1. Characterization of contact materials

In good agreement with Table 2.9 the properties of the used contact materials depend on doping/modifying A and B perovskite sites, as well as, the applied processing conditions. Thus, the A- and/or B-site cations can partly be replaced in order to improve properties such as the electrical conductivity, interconnect-contact coating compatibility, sinterability and/or thermal- and mechanical stability, which can lead to modifications in the crystallographic structure[101,102].

---

[98] National institute of standards and technology gaithersburg: Inorganic crystal structure database ICSD realease 2001/1. Fachinformationszentrum Karlsruhe.

[99] Rodríguez-Carvajal J. Fullprof program: Rietveld pattern matching analysis of powder patterns, Grenoble, **2011**.

[100] Introduction to energy dispersive X-ray spectroscopy (EDS), http://micron.ucr.edu/public/manuals/EDX-intro.pdf.

[101] Ullmann H., Trofimenko N. Composition, structure and transport properties of perovskite-type oxides. *Solid State Ionics* 119 (**1999**) 1-8.

The metallic like conductivity of $LaNiO_3$ [103] gives to $LaNi_{0.6}BO_{3-\delta}$ (B=Fe,Co) coatings a high electrical conductivity whereas that $LaFeO_3$, $LaCoO_{3-\delta}$ and $LaMnO_3$ perovskites show p-type conductivity by transfer of charge carries via B-O-B (M=Fe,Co) bonds[104-106]. However, $LaCoO_3$ undergoes a semiconductor-metallic transition at ~750 ºC [103,107]. The thermal stability of lanthanum nickelate ($LaNiO_{3-\delta}$) is limited to 980-1000 ºC [108-110], while lanthanum orthoferrite ($LaFeO_3$) is stable in air up to its melting point (~1900 ºC)[108,111]. The phase diagram of nominal $LaCoO_3$ as function of temperature and oxygen partial[112,113] shows that lanthanum cobaltite ($LaCoO_3$) is stable under an oxidizing atmosphere but the reduction of cobalt takes place with increasing temperatures and decreasing oxygen partial pressures. However, the reduction behaviour of Ni^{3+} at high temperature or low P_{O2} is higher than Co^{3+}. Nevertheless, the thermodynamic stability range of $LaCoO_3$ is narrow compared to the lanthanum manganite ($LaMnO_3$). The thermal expansion coefficient (TEC) is about $22{\cdot}10^{-6}$, $10{\cdot}10^{-6}$, $10.8{\cdot}10^{-6}$ and $11.2{\cdot}10^{-6}$ K^{-1} for $LaCoO_3$ $LaNiO_3$, $LaFeO_{3-\delta}$ and $LaMnO_3$, respectively[103,106,114-116]. Moreover, the reactivity for lanthanum perovskites could be estimated to decrease in the following order: $LaCoO_3$ > $LaMnO_3$ > $LaFeO_3$, meaning that $LaCoO_3$ is the most reactive at any given temperature[117]. It is interesting to note that the ionic conductivities also increase in the same order since the ionic migration requires weakly bonded ions. Thus, cobalt-containing perovskites show the highest ionic conductivity, which should result in high oxygen ionic mobility. For $LaNi_{0.6}Fe_{0.4}O_{3-\delta}$ composition, the iron doping decreases the electrical conductivity and increases both thermal stability and thermal expansion coefficient.

---

[102] Vogt U.F., Holtappels P., Sfeir J., Richter J., Duval S., Wiedenmann D., Züttel A. Influence of A-site variation and B-site substitution on the physical properties of (La, Sr)FeO_3 based perovskites. *Fuel Cells* 6 (**2009**) 899-906.

[103] Hjalmarsson P., Sogaard M., Hagen A., Mogensen M. Structural properties and electrochemical performance of strontium- and nickel-substituted lanthanum cobaltite. *Solid State Ionics* 179 (**2008**) 636-646.

[104] Kharton V.V., Figueiredo F.M., Kovalevsky A.V., Viskup A.P., Naumovich E.N., Yaremchenko A.A., Bashmakov I.A., Marques F.M.B. Processing, microstructure and properties of $LaCoO_{3+\delta}$ ceramics. *J. Eur. Ceram. Soc.* 21 (**2001**) 2301-2309.

[105] Nagde K.R., Bhoga S.S. Effect of Sr contento n structure and electrical properties of $La_{1-x}Sr_xMnO_3$ from ITSOFC cathode view point. *Ionics* 15 (**2009**) 571-578.

[106] Ruiz-Morales J.C., Canales-Vázquez J., Marrero-López D., Peña-Martínez J., Pérez-Coll D., Núñez P., Savaniu C., Rodríguez-Placeres C., Dorta-Martín V.I., Ballesteros B. Pilas de combustible de óxido sólido (SOFC). Centro de la cultura popular canaria, p. 127-141, **2008**.

[107] Lal B., Raghunandan M.K., Gupta M., Singh R.N. Electrocatalytic properties of perovskite-type obtained by a novel stearic acid sol-gel method for electrocatalysis of O_2 evolution in KOH solutions. *Int. J. Hydrogen Energ.* 30 (**2005**) 723-729.

[108] Kiselev E.A., Cherepanov V.A. p (O_2)-stability of $LaFe_{1-x}Ni_xO_{3-\delta}$ solid solutions at 1100 ºC. *J. Solid State Chem.* 183 (**2010**) 1992-1997.

[109] Bannikov D.O., Cherepanov V.A. Thermodynamic properties of complex oxides in the LaNiO system. *J. Solid State Chem.* 179 (**2006**) 2721-2727.

[110] Nakamura T., Petzow G., Gauckler L.J. Stability of the perovskite phase $LaBO_3$ (B=V, Cr, Mn, Fe, Co, Ni) in reducing atmosphere I. Experimental results. *Mater. Res. Bull.* 14 (**1979**) 649-659.

[111] Moruzzi V.L., Shafer M.W. Phase equilibria in the system La_2O_3-iron oxide in air. *J. Am. Ceram. Soc.* 43 (**1960**) 367-372.

[112] Petrov A.N, Cherepanov V.A., Zuev A.Y. Thermodynamics, defect structure, and charge transfer in doped lanthanum cobaltites: an overview. *J. Solid State Electrochem.* 10 (**2006**) 517-537.

[113] Hjalmarsson P. Strontium and nickel substituted lanthanum cobaltite as cathode in solid oxide fuel cells. Ph. D. Thesis, Technical University of Denmark, **2008**.

[114] Huang K., Lee H.Y., Goodenough J.B. Sr- and Ni-doped $LaCoO_3$ and $LaFeO_3$ perovskites-new cathode materials for solid oxide fuel cells. *J. Electrochem. Soc.* 145(9) (**1998**) 3220-3227.

[115] Dasgupta N., Krishnamoorthy R., Jacob K.T. Crystal structure and thermal and electrical properties of the perovskite solid solution $Nd_{1-x}Sr_xFeO_{3-\delta}$ ($0 \le x \le 0.4$). *Solid State Ionics* 149 (**2002**) 227-236.

[116] Badwal S.P.S., Foger K. Materials for solid oxide fuel cells. *Mater. Forum* 21 (**1997**) 187-224.

[117] Hrovat M., Katsarakis N., Reichmann K., Bernik S., Kuscer D., Holc J. Characterization of $LaNi_{1-x}Co_xO_3$ as a possible SOFC cathode material. *Solid State Ionics* 83 (**1996**) 99-105.

Nevertheless, for $LaNi_{0.6}Co_{0.4}O_{3-\delta}$ perovskite, cobalt doping increases ionic conductivity, thermal expansion coefficient and stability problems at high temperatures.

Studying the effect of the La:Sr ratio was also found to have a marked effect on the performance of these kind of materials; the increase of Sr content improves electrical conductivity[106,118]. The conductivity in $(La_{0.8}Sr_{0.2})_{0.95}Fe_{0.6}Mn_{0.3}Co_{0.1}O_3$ is due to the polaron hopping after substitution of divalent strontium for trivalent lanthanum. The introduction of an A-site deficiency in this system could improve the processing of the coating[118,119]. Moreover, the thermal expansion coefficients were found to be lowest for the compositions with greatest A-site deficiency thus TEC values of LSFMC is close to that of the metallic interconnects.

The characterization of contact coatings starts with Figure 2.20, which shows the room temperature X-ray diffraction patterns of the initial samples ($LaNi_{0.6}Co_{0.4}O_{3-\delta}$ (LNC), $LaNi_{0.6}Fe_{0.4}O_{3-\delta}$ (LNF) and $(La_{0.8}Sr_{0.2})_{0.95}Fe_{0.6}Mn_{0.3}Co_{0.1}O_3$ (LSFMC)), and after two heat treatments, both in air: (i) sintered at 1050 ºC for 2h, contact coating sintered temperature in the processing of a real cell, and (ii) sintered at 950 ºC for 2 h to be treated at 800 ºC up to 1000 h.

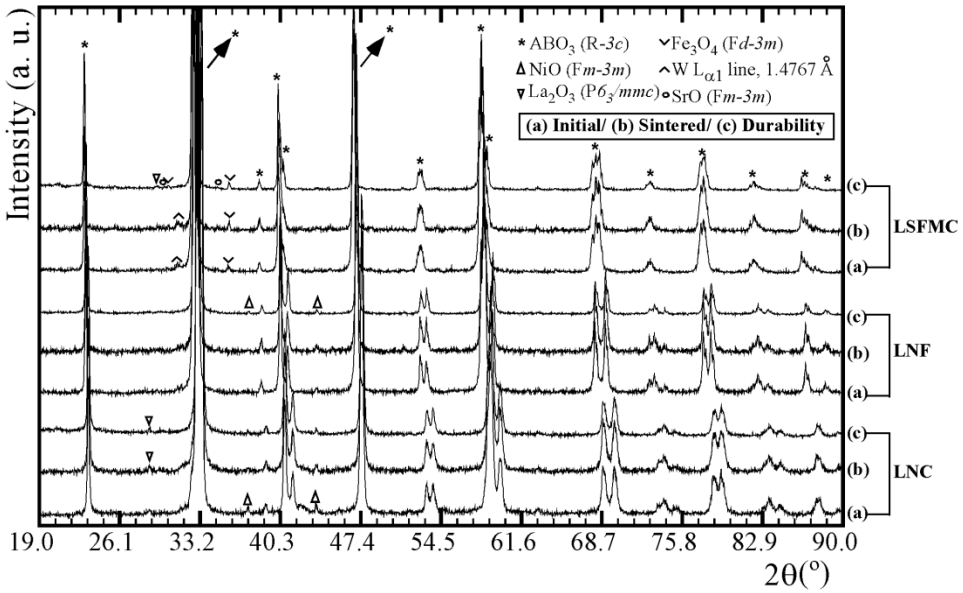

Figure 2.20. XRD patterns, obtained at room temperature in air, for $LaNi_{0.6}Co_{0.4}O_{3-\delta}$ (LNC), $LaNi_{0.6}Fe_{0.4}O_{3-\delta}$ (LNF) and $(La_{0.8}Sr_{0.2})_{0.95}Fe_{0.6}Mn_{0.3}Co_{0.1}O_3$ (LSFMC) powders at different time and temperature conditions: (a) initial material, (b) after sintered at 1050 ºC for 2h and (c) after 1000 h at 800 ºC, in air. The arrows point out the symbol of the corresponding phase based on the diffraction peaks positions.

In Ref. [91] the coexistence of the initial LNC and LSFMC perovskite phase with several impurities has already been reported. The X-ray diffraction analyses reveal the formation of La_2O_3 and SrO for LSFMC after a 1000 h treatment at 800 ºC. For LNC coating the intensity of the diffraction peak of La_2O_3 indicates that the proportion of formed lanthanum oxide is reduced over time. LNF material shows two very weak peaks corresponding to NiO after both treatments.

---

[118] Skinner S.J. Recent advances in perovskite-type materials for solid oxide fuel cell cathodes. *Int. J. Inorg. Mater.* 3 (**2001**) 113-121.

[119] Kostogloudis G.-Ch., Ftikos Ch. Properties of A-site deficient $La_{0.6}Sr_{0.4}Co_{0.2}Fe_{0.8}O_{3-\delta}$ based perovskite oxides. *Solid State Ionics* 126 (**1999**) 143-151.

Table 2.9 shows the X-ray full-profile refinement results made by the Rietveld method for the initial contact materials and after different treatments. The results of the quantitative analysis of initial contact powders are presented in our previous work[91].

Table 2.9. Quantitative Rietveld analysis results; % in weight of the phases which are in initial $LaNi_{0.6}Co_{0.4}O_{3-\delta}$ (LNC), $LaNi_{0.6}Fe_{0.4}O_{3-\delta}$ (LNF) and $(La_{0.8}Sr_{0.2})_{0.95}Fe_{0.6}Mn_{0.3}Co_{0.1}O_3$ (LSFMC) contact materials[91] and, the formed phases in three coatings after sintered at 1050 ºC for 2h and after treated 1000 h at 800 ºC, in air.

Sample	ABO_3	NiO	La_2O_3	Fe_3O_4	SrO	χ^2
Initial LNC	98.5(1)	1.5(2)	-	-	-	3.32
LNC 1050ºC	98.8(4)	1.0(1)	0.2(1)	-	-	2.25
Long term LNC	99.2(4)	0.8(1)	< 0.2	-	-	2.30
Initial LNF	100.0	-	-	-	-	3.95
LNF 1050ºC	99.1(6)	0.9(2)	-	-	-	2.24
Long term LNF	99.2(5)	0.8(1)	-	-	-	3.97
Initial LSFMC	98.7(5)	-	-	1.3(2)	-	3.65
LSFMC 1050ºC	97.7(7)	-	-	2.3(3)	-	3.05
Long term LSFMC	97.4(5)	-	0.2(1)	2.2(2)	0.2(1)	4.23

Figures 2.21 and 2.22 show the XRD analysis of LNC and LNF, LSFMC coatings, respectively, after different treatments. Full-profile refinements were performed starting from the atomic coordinates of each phase, as taken from the Inorganic Crystal Structure Database (ICSD)[120]. The quantitative analysis shows that after sintered at 1050 ºC for 2h or long term treatment the amount of starting impurities keep quite constant and a small amount of new oxides, like SrO, in LSFMC coating, are formed. For all of contact powders the % in weight of the starting perovskite structure, with R-*3c* group, remains almost unchanged, thus the coatings show low degradation at high temperature (1050 ºC) or long-term conditions.

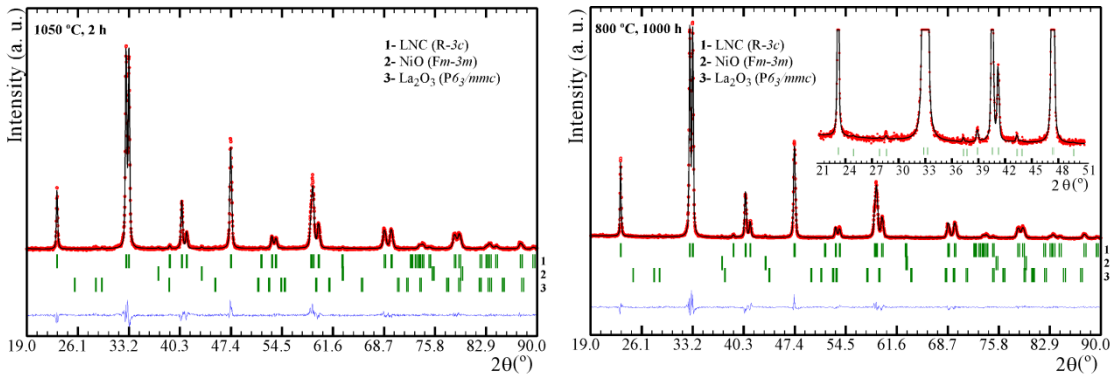

Figure 2.21. Full-profile X-ray refinements of $LaNi_{0.6}Co_{0.4}O_{3-\delta}$ (LNC) material after sintered at 1050 ºC for 2 h (left) and after 1000 h at 800 ºC (right) in air.

[120] Allmann R., Hinek R., Bergerhoff G., Brown I.D. ICSD-Inorganic Crystal Structure Database, FIZ Karlsruhe, National Institute of Standards and Technology (NIST), **2009**.

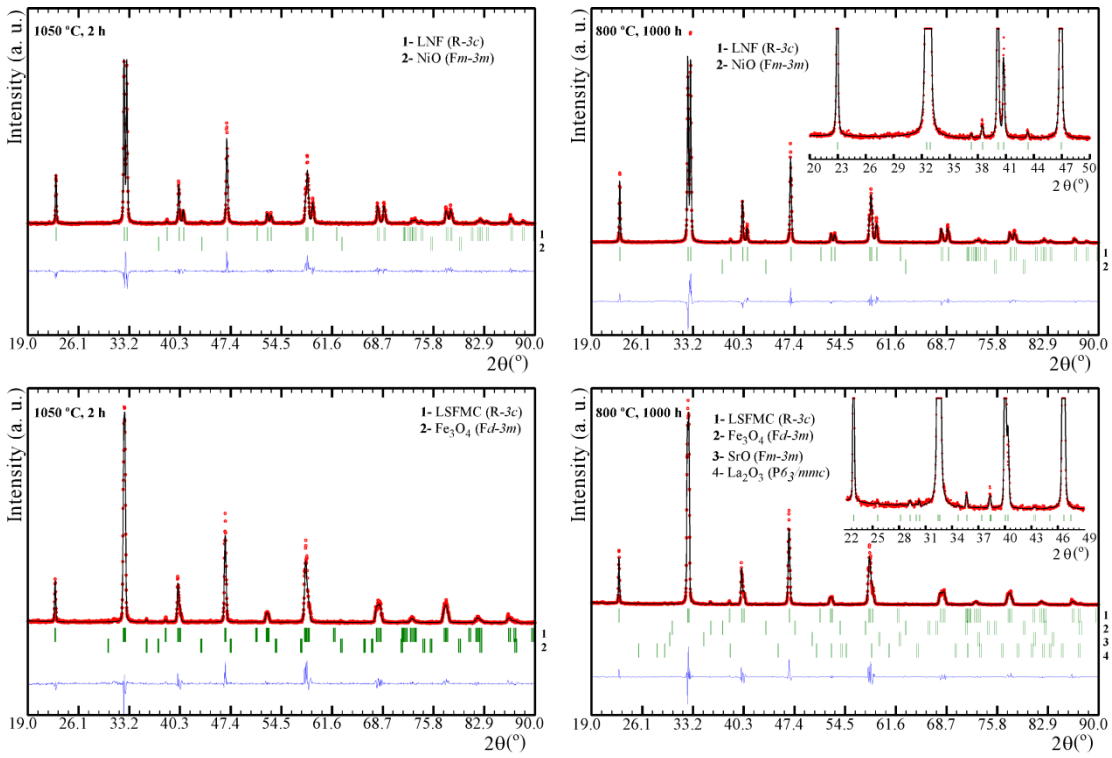

Figure 2.22. Full-profile X-ray refinements of $LaNi_{0.6}Fe_{0.4}O_{3-\delta}$ (LNF) and $(La_{0.8}Sr_{0.2})_{0.95}Fe_{0.6}Mn_{0.3}Co_{0.1}O_3$ (LSFMC) contact materials after sintered at 1050 ºC for 2 h and after 1000 h at 800 ºC, in air.

Thermo X-ray diffractometry (TDX) analyses revealed that LNC, LNF and LSFMC present a reversible transition from rhombohedral (R-*3c*) to cubic (P*m-3m*) structure with increasing temperature, according to Figure 2.23. The rhombohedral distorsion of the perovskite is characterized by the splitting of the principal reflection, which appears as a double peak in the 2θ=32-34 º range. In the three coatings, the splitting of the reflection gradually decreases at temperatures above 400 ºC. Notice that at 800 ºC the principal peak shows an asymmetrical shape (Figure 2.23). This indicates that the cell parameters of both samples are getting closer. The normalized unit cell volumes of the perovskite phases with rhombohedral and cubic symmetries are very close, indicating a high probability of a reversible phase transformation, at high temperatures.

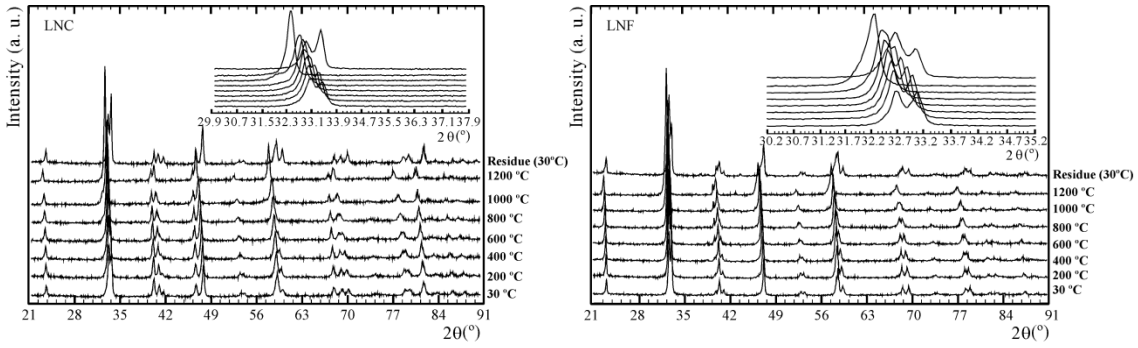

Figure 2.23. Diffraction patterns of $LaNi_{0.6}Co_{0.4}O_{3-\delta}$ (LNC), $LaNi_{0.6}Fe_{0.4}O_{3-\delta}$ (LNF) and $(La_{0.8}Sr_{0.2})_{0.95}Fe_{0.6}Mn_{0.3}Co_{0.1}O_3$ (LSFMC) measured from room to high temperature, as a dynamic process.

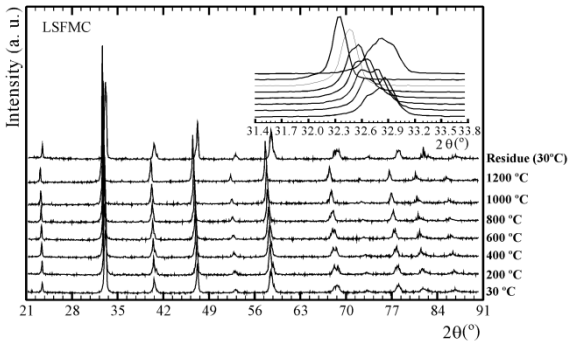

Figure 2.23. cont. Diffraction patterns of $LaNi_{0.6}Co_{0.4}O_{3-\delta}$ (LNC), $LaNi_{0.6}Fe_{0.4}O_{3-\delta}$ (LNF) and $(La_{0.8}Sr_{0.2})_{0.95}Fe_{0.6}Mn_{0.3}Co_{0.1}O_3$ (LSFMC) measured from room to high temperature, as a dynamic process.

The results provided from the Rietveld refinements performed at 1200 ºC and in the obtained residue of each coating are summarized in Table 2.10. The quantitative analysis shows that the composition of LNC and LNF coatings at 1200 ºC consist primarily of P*m-3m* perovskite with small amounts of nickel oxide. However, the proportion of ABO_3 cubic phase in LSFMC, at high temperature, is decreased considerably, showing R-*3c* perovskite as main phase with Fe_3O_4 as impurity.

Table 2.10. Quantitative % in weight of the formed phases in LNC, LNF and LSFMC contact coatings at 1200 ºC and in its residues after TDX analysis.

Sample	ABO_3 (R-*3c*)	ABO_3 (P*m-3m*)	ABO_3 (P*bnm*)	$La_2NiO_{4+\delta}$ (F*mmm*)	NiO (F*m-3m*)	Fe_3O_4 (F*d-3m*)	χ^2
LNC 1200ºC	-	97.8(9)	-	-	2.2(4)	-	2.61
Residue LNC	95.1(5)	3.6(2)	-	0.2(1)	1.1(1)	-	3.44
LNF 1200ºC	-	97.4(9)	-	-	2.6(4)	-	3.72
Residue LNF	54.7(7)	13.0(5)	29.3(5)	-	3.0(3)	-	2.42
LSFMC, 1200ºC	81.9(8)	15.3(5)	-	-	-	2.8(5)	1.92
Residue LSFMC	92.7(8)	3.5(3)	-	-	-	3.8(6)	2.02

The quantified minor oxides, which were presented in the coatings at 1200 ºC, have already identified in the initial materials (Table 2.9). Figure 2.24 shows X-ray diffraction pattern refinements carried out in LNC coating at 1200 ºC and in its residue at room temperature. The corresponding Rietveld refinements for LNF and LSFMC coatings are presented in Figure 2.25.

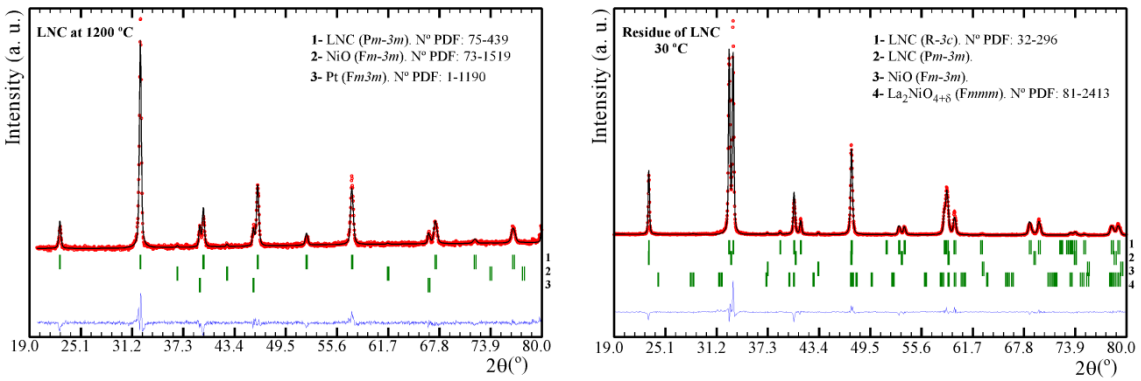

Figure 2.24. Rietveld refinement XRD patterns of $LaNi_{0.6}Co_{0.4}O_{3-\delta}$ (LNC) at 1200 ºC (left) and for the residue obtained at room temperature after X-ray thermodiffractometry (TDX) (right).

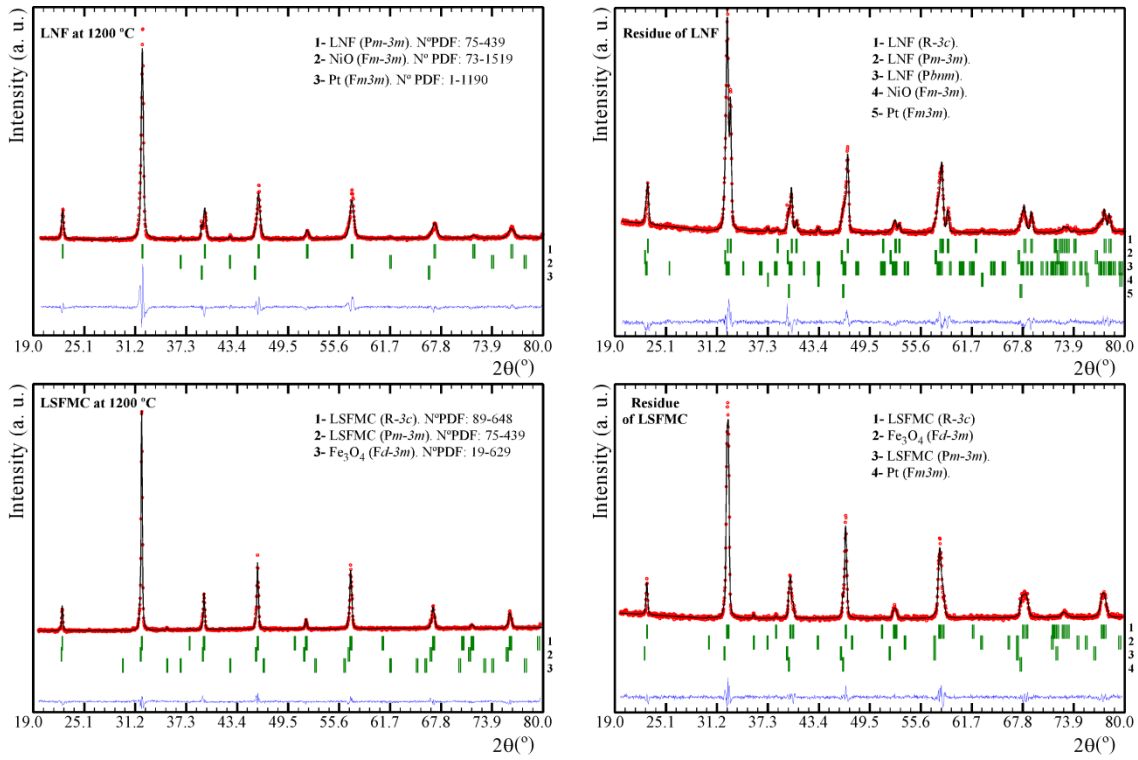

Figure 2.25. Rietveld refinement XRD patterns of $LaNi_{0.6}Fe_{0.4}O_{3-\delta}$ (LNF) and $(La_{0.8}Sr_{0.2})_{0.95}Fe_{0.6}Mn_{0.3}Co_{0.1}O_3$ (LSFMC) at 1200 ºC and of its residues obtained at room temperature after X-ray thermodiffractometry (TDX) analysis.

According to other authors[103,121], the high electrical conductivity of contact coatings could also be associated with an increase in the perovskite structure symmetry which is coupled to the R-*3c* → P*m-3m* transition. Residue of LNF shows mixture of rhombohedral (R-*3c*), orthorhombic (P*bnm*) and cubic (F*m-3m*) symmetries that might be due to local displacements of the structure. In the residues of the other two contact coatings mixture of rhomboedral and cubic symmetry is given, and besides in LNC residue a small amount of a new orthorhombic phase, $La_2NiO_{4+\delta}$ (F*mmm*) is detected.

For all contact coatings XPS survey (Figure 2.26) and high resolution spectra of the La3d, Sr 3d, Ni 2p, Co 2p, Fe 2p and Mn 2p were obtained. Table 2.11 gives the binding energies (BEs) of main peaks and relative atomic percentage concentration of detected elements. The chemical composition (% at. conc.) of the powder surfaces is based on the high resolution XPS analyses. Figure 2.27 provides LNC high resolution spectra of analysed zones; the XPS analyses performed on LNF and LSFMC surfaces are given as supplementary material *(section A, Figures S1 and S2*).

[121] Mizusaki J., Tabuchi J., Matsuura T., Yamauchi S., Fueki K. Electrical conductivity and seebeck coefficient of nonstoichiometric $La_{1-x}Sr_xCoO_{3-\delta}$. *J. Electrochem. Soc.* 136 (**1989**) 2082-2088.

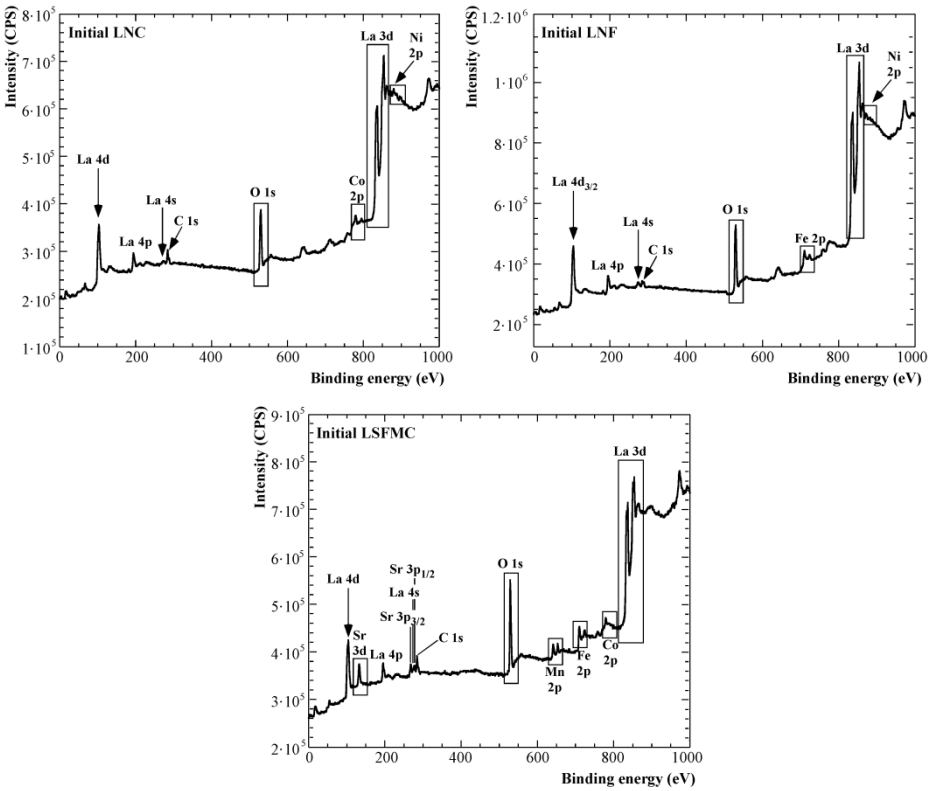

Figure 2.26. X-ray photoelectron spectroscopy (XPS) survey spectrums taken from $LaNi_{0.6}Co_{0.4}O_{3-\delta}$ (LNC), $LaNi_{0.6}Fe_{0.4}O_{3-\delta}$ (LNF) and $(La_{0.8}Sr_{0.2})_{0.95}Fe_{0.6}Mn_{0.3}Co_{0.1}O_3$ (LSFMC) initial materials.

Table 2.11. XPS analysis results of the detected elements for the surface of the initial contact coatings (LNC, LNF and LSFMC).

Peak	Initial LNC		Initial LNF	
	Binding Energy (eV)	% at. Conc.	Binding Energy (eV)	% at. Conc.
La $3d_{5/2}$ in ABO_3	832.61	9.8	832.81	10.8
La $3d_{5/2}$ in La_2O_3	834.46	13.5	834.57	12.4
Sr 3d in ABO_3	-	-	-	-
Sr 3d in SrO	-	-	-	-
Ni $2p_{1/2}$ in ABO_3	871.90	5.9	871.98	6.4
Co $2p_{3/2}$ in ABO_3	779.50;781.47	3.7	-	-
Fe $2p_{3/2}$ in ABO_3	-	-	709.55;711.38	4.2
Mn $2p_{3/2}$ in ABO_3	-	-	-	-
O 1s	528.09;528.85; 530.55;531.33	67.1	528.22;529.14; 530.65;531.29	66.2

Table 2.11. cont. XPS analysis results of the detected elements for the surface of the initial contact coatings (LNC, LNF and LSFMC).

Peak	Initial LSFMC	
	Binding Energy (eV)	% at. Conc.
La $3d_{5/2}$ in ABO_3	833.15	9.8
La $3d_{5/2}$ in La_2O_3	834.57	8.0
Sr 3d in ABO_3	132.01;133.76	2.4
Sr 3d in SrO	132.84;134.45	1.9
Ni $2p_{1/2}$ in ABO_3	-	-
Co $2p_{3/2}$ in ABO_3	779.55;781.34	1.3
Fe $2p_{3/2}$ in ABO_3	709.59;711.29	8.1
Mn $2p_{3/2}$ in ABO_3	641.73	3.8
O 1s	528.74;529.22; 530,69;531.81	64.7

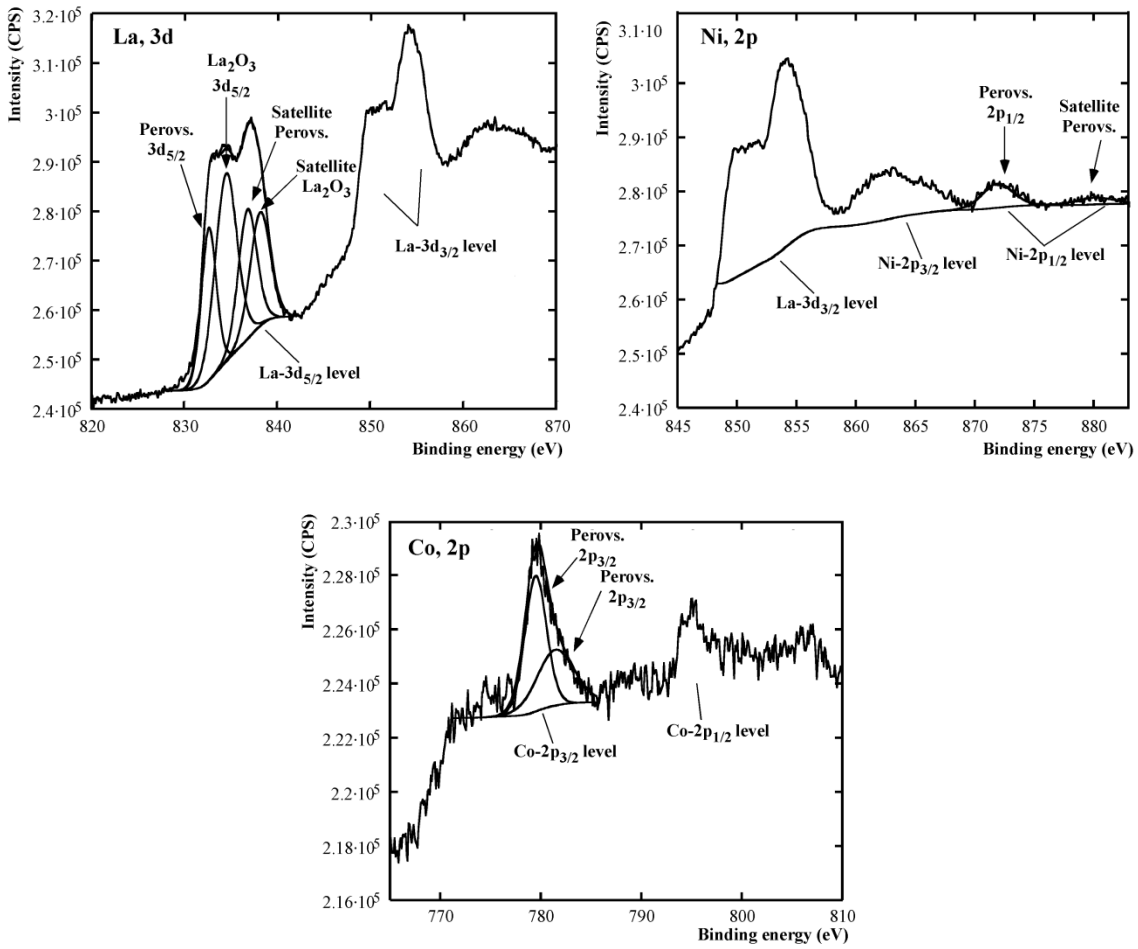

Figure 2.27. La $3d_{5/2}$, Ni $2p_{1/2}$ and Co $2p_{3/2}$ spectral regions of the surface of initial $LaNi_{0.6}Co_{0.4}O_{3-\delta}$ (LNC) powder.

In the three samples, for La, there are two peaks, one at ≈833 eV which correspond to La^{3+} in perovskite[122] and, another at ≈834 eV which is assigned to La^{3+} in La_2O_3 [90]. The peaks appearing at ≈131 eV and ≈133 eV (Sr $3d_{5/2}$) could be assigned to Sr^{2+} in perovskite and in SrO, respectively[123-125]. According to other authors[126-129], the elements identified from the peaks at ≈780 eV (Co $2p_{3/2}$), ≈872 eV (Ni $2p_{3/2}$), ≈710 eV (Fe $2p_{3/2}$), ≈711 eV (Fe $2p_{3/2}$) and ≈642 eV (Mn $2p_{3/2}$) were found in the perovskite structure. The atomic concentrations of these elements, which form contact perovskites, are in good agreement with ABO_3 structure (Table 2.11).

Figure 2.28 shows the typical scanning electron microscopy images of contact material powders. The shape of LNC powder particles is different from the LNF and LSFMC ones.

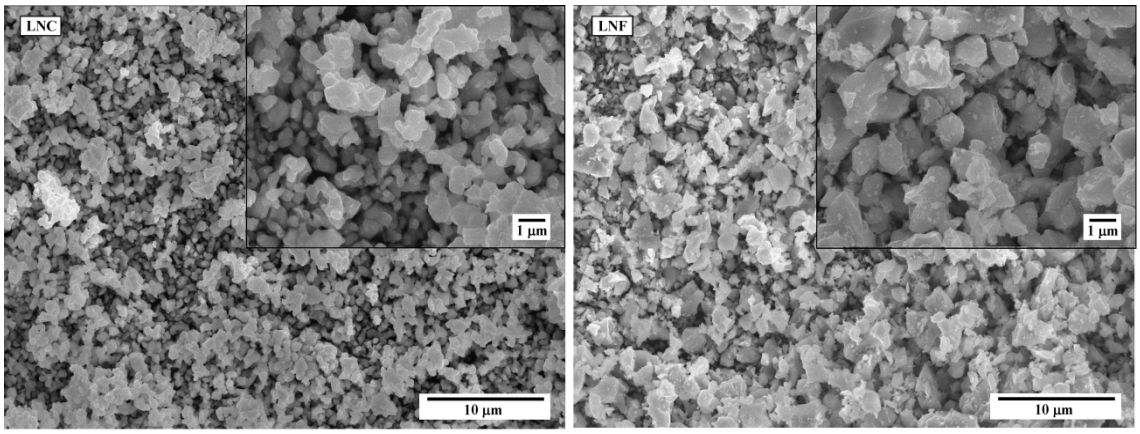

Figure 2.28. Scanning electron microscope (SEM) micrographs of the surface of $LaNi_{0.6}Co_{0.4}O_{3-\delta}$ (LNC), $LaNi_{0.6}Fe_{0.4}O_{3-\delta}$ (LNF) and $(La_{0.8}Sr_{0.2})_{0.95}Fe_{0.6}Mn_{0.3}Co_{0.1}O_3$ (LSFMC) powders.

[122] Bin F., Song C., Lu G., Song J., Gong C., Huang Q. $La_{1-x}K_xCoO_3$ and $LaCo_{1-y}Fe_yO_3$ perovskite oxides: preparation, characterization, and catalytic performance in the simultaneous removal of NO_x and diesel soot. *Ind. Eng. Chem. Res.* 50 (**2011**) 6660-6667.

[123] Tabata K., Matsumoto I., Kohiki S. Surface characterization and catalytic properties of $La_{1-x}Sr_xCoO_3$. *J. Mater. Sci.* 22 (**1987**) 1882-1886.

[124] Liu B., Zhang Y., Tang L. X-ray photoelectron spectroscopic studies of $Ba_{0.5}Sr_{0.5}Co_{0.8}Fe_{0.2}O_{3-\delta}$ cathode for solid oxide fuel cells. *Int. J. Hydrogen Energ.* 34 (**2009**) 435-439.

[125] Crumlin E.J., Mutoro E., Liu Z., Grass M.E., Biegalski M.D., Lee Y.L., Morgan D., Christen H.M., Bluhm H., Shao-Horn Y. Surface strontium enrichment on highly active perovskites for oxygen electrocatalysis in solid oxide fuel cells. *Energ. Environ. Sci.* 5 (**2012**) 6081-6088.

[126] Lima S.M.D., Peña M.A., Fierro J.L.G., Assaf J.M. $La_{1-x}Ca_xNiO_3$ perovskite oxides: characterization and catalytic reactivity in dry reforming of methane. *Catal. Lett.* 124 (**2008**) 195-203.

[127] Konysheva E., Irvine J.T.S. Evolution of conductivity, structure and thermochemical stability of lanthanum manganese iron nickelate perovskites. *J. Mater. Chem.* 18 (**2008**) 5147-5154.

[128] Kim J.H. X-ray photoelectron spectroscopy analysis of $(Ln_{1-x}Sr_x)CoO_{3-\delta}$ (Ln: Pr, Nd and Sm). *Appl. Surf. Sci.* 258 (**2011**) 350-355.

[129] Ghaffari M., Shannon M., Hui H., Tan O.K., Irannejad A. Preparation, surface state and band structure studies of $SrTi_{(1-x)}Fe_{(x)}O_{(3-\delta)}$ (X=0-1) perovskite-type nano structure by X-ray and ultraviolet photoelectron spectroscopy. *Surf. Sci.* 606 (**2012**) 670-677.

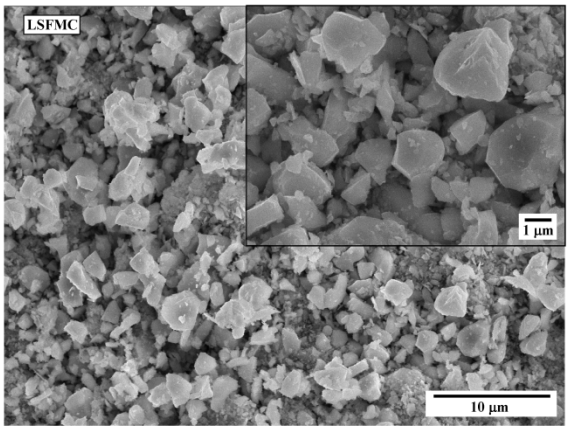

Figure 2.28. cont. Scanning electron microscope (SEM) micrographs of the surface of $LaNi_{0.6}Co_{0.4}O_{3-\delta}$ (LNC), $LaNi_{0.6}Fe_{0.4}O_{3-\delta}$ (LNF) and $(La_{0.8}Sr_{0.2})_{0.95}Fe_{0.6}Mn_{0.3}Co_{0.1}O_3$ (LSFMC) powders.

On average, these contact materials show similar grain sizes, between 1-2 µm, in good agreement with the homogeneity of the starting powders, which exhibit similar morphology in terms of unimodal particle size distribution (Figure 2.29). The average particle size (d_{50}) for LNC, LNF and LSFMC was 2.37, 2.17 and 2.44 µm, respectively. There is some particle agglomeration in all cases, which can explain the observed average grain size in the range of 2-5 µm, in good agreement with observed agglomerates in Figure 2.28.

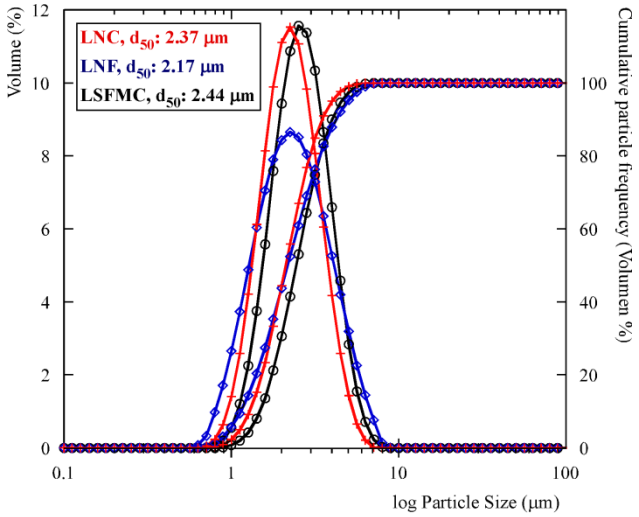

Figure 2.29. Particle size distribution of contact powders, including d_{50} value for each material.

Since the obtained d_{50} value depends on which technique was used to measure it (there are methods which only consider the smallest particles), technical specification d_{50} values were lower than observed experimental values, being 1 and 0.66 µm for LNC and LNF, respectively.

2.3.3.2. Compatibility between $La_{0.6}Sr_{0.4}FeO_3$ and contact materials after 1000 h at 800 ºC

Figure 2.30 shows the Rietveld refinements of the cathode-contact coating mixtures after long heat treatment in air. The refinements allow the quantification of the phases (Table 2.12). These XRD analyses reveal that the initial perovskite structure (rhombohedral, space group R-*3c*) of the

cathode and contact coating remains after treatment. However, according to previous study of our group[130] a possible $(LSF)_x(LNC, LNF \text{ or } LSFMC)_{1-x}$ phase might form, which could explain the desviation of quantified rhombohedral phases from the expected value (50 % in weight of each phase). But, the similarity of cell parameters of initial perovskite phases as well as of possible solid solution intermediate compounds make difficult to determine the number of R-*3c* phases present in each mixture. So, this overlapping of Bragg peaks in the diffraction patterns of the initial phases can also hinder the quantification of main perovskite phases.

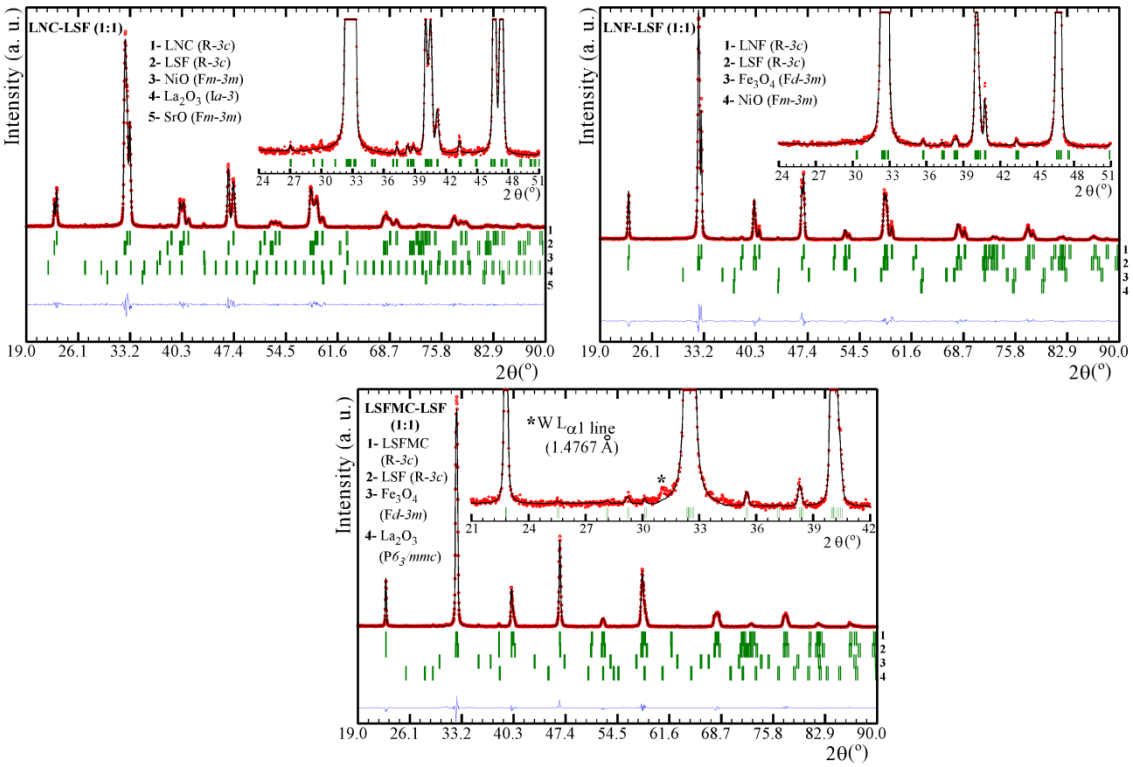

Figure 2.30. Rietveld refinements X-ray diffraction patterns, obtained at room temperature in air, for the three contact material-cathode (1:1) mixture after 1000 h at 800 ºC in air.

Table 2.12. % in weight, obtained from the Rietveld refinements, for the formed phases in contact coating (LNC, LNF or LSFMC)-cathode (LSF) 1:1 mixture after 1000 h at 800 ºC, in air.

Sample	**ABO_3** R-*3c* contact coating	**ABO_3** R-*3*c cathode	**NiO** F*m-3m*	**La_2O_3** I*a-3*	**La_2O_3** P*6₃/mmc*	**SrO** F*m-3m*	**Fe_3O_4** F*d-3m*	χ^2
LNC-LSF	44.8(2)	52.9(3)	1.0(1)	1.3(3)	-	< 0.2	-	1.85
LNF-LSF	43.1(3)	55.2(4)	0.9(1)	-	-	-	0.8(1)	3.05
LSFMC-LSF	80.4(6)	18.1(3)	-	-	0.2(1)	-	1.3(1)	2.26

In the case of LNC-LSF mixture XRD analysis reveals the formation of La_2O_3 (I*a-3*) instead of lanthanum oxide with P*6₃/mmc* space group, and small amount of SrO is formed[86]. Over time the intensity of La_2O_3 (P*6₃/mmc*) diffraction peaks get smaller, indicating that the proportion of formed

[130] Martínez-Amesti A., Larrañaga A., Rodríguez-Martínez L.M., Nó M.L., Pizarro J.L., Laresgoiti A., Arriortua M.I. Chemical compatibility between YSZ and SDC sintered at different atmospheres for SOFC applications. *J. Power Sources* 192(1) (**2009**) 151-157.

oxide decrease (Table 2.9). In our previous studies[86] the X-ray profile of LSF material after long-term heat treatment revealed the formation of $LaSrFeO_4$ (P*nma*), Fe_3O_4 (F*d-3m*) and $SrFe_{12}O_{19}$ (P6_3/*mmc*) phases, which could explain the additional Fe_3O_4 appearance in LNF-LSF mixture. The formation of secondary phases in LSFMC-LSF mixture are in good agreement with the result obtained in X-ray full-profile refinement for LSFMC powder after long-term heat treatment in air (Table 2.9).

2.3.3.3. Study of {interconnect/contact layer/cathode} systems and effectiveness of contact coatings after 1000 h at 800 ºC

The room temperature X-ray diffraction patterns of the top of the {Crofer22APU interconnect/contact coating} and {Crofer22APU interconnect/contact coating/ $La_{0.6}Sr_{0.4}FeO_3$ cathode} systems were obtained, in air, and in presence and absence of contact coating, {interconnect/cathode}, at 800 ºC for 1000 h (Figure 2.31).

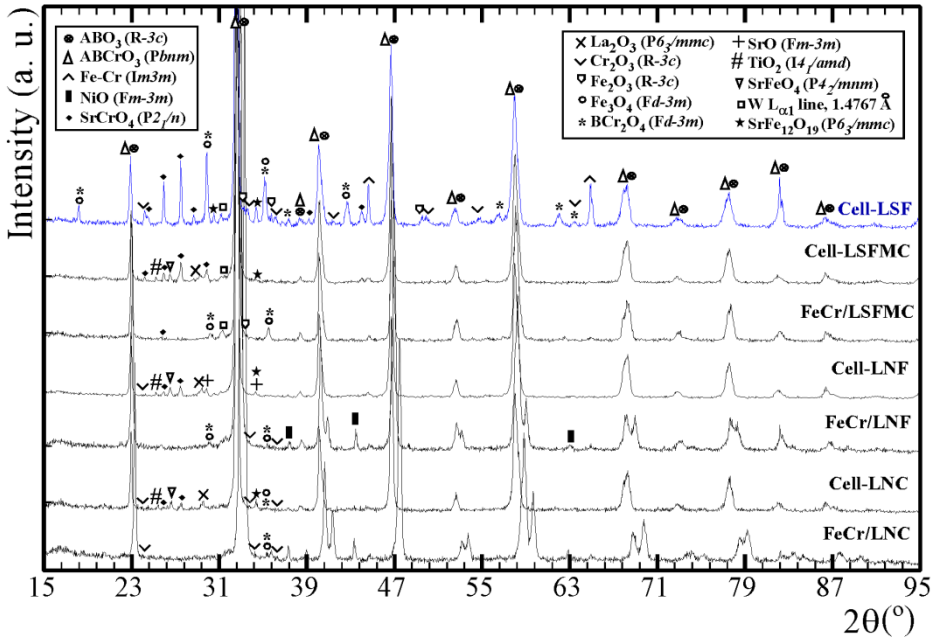

Figure 2.31. X-ray patterns obtained at room temperature in air for {interconnect/contact coating} (FeCr/LNC, FeCr/LNF, FeCr/LSFMC) and, for {interconnect/cathode} (Cell-LSF) as well as {interconnect/contact coating/cathode} (Cell-LNC, Cell-LNF, Cell-LSFMC). All of them after 1000 h at 800 ºC in air.

The results made by the Rietveld method are provided in Table 2.13 and Figures 2.32 and 2.33. The Fe-Cr interconnect was identified, in all the samples, indicating that the X-ray penetration was enough to observe the signal of all the formed layers.

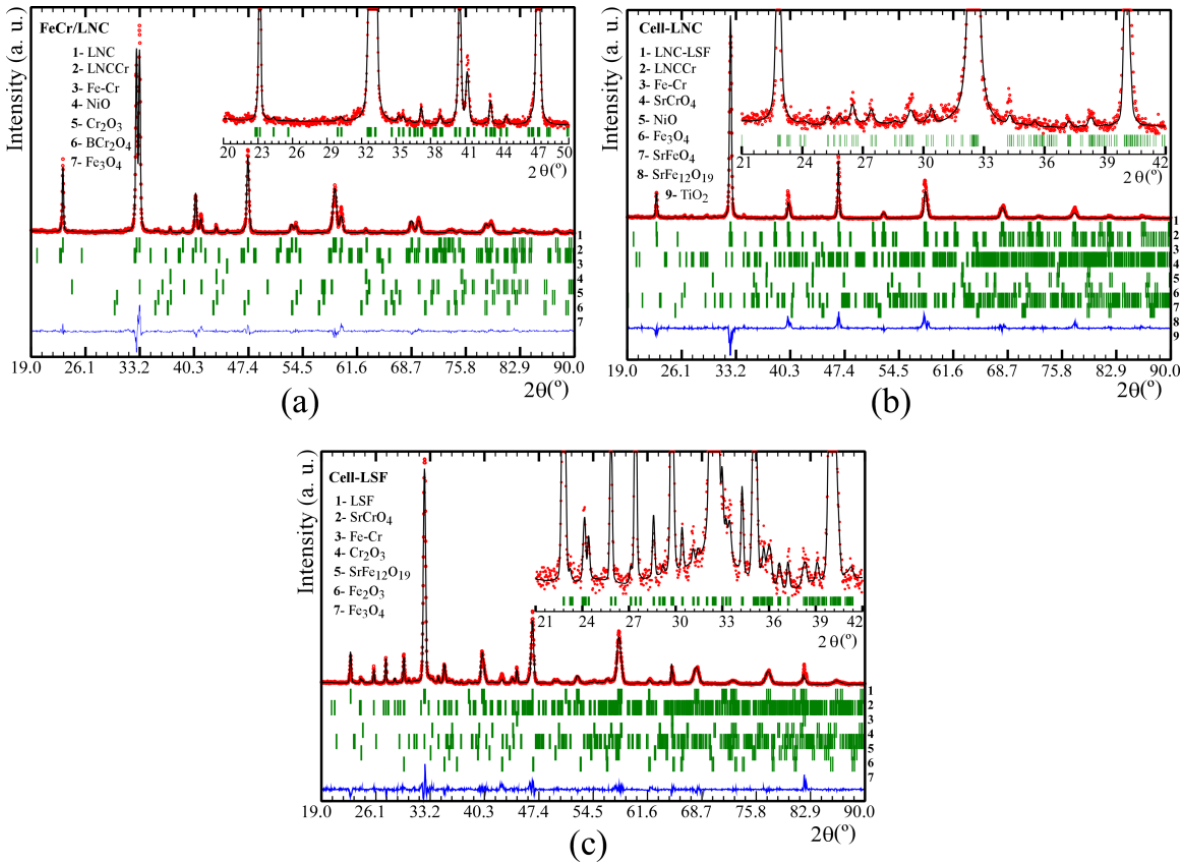

Figure 2.32. Rietveld refinements performed at room temperature for: (a) {Crofer22APU interconnect/LNC contact coating}, (b) {Crofer22APU interconnect/LNC contact coating/LSF cathode} and (c) {Crofer22APU interconnect/LSF cathode}, after 1000 h at 800 ºC in air.

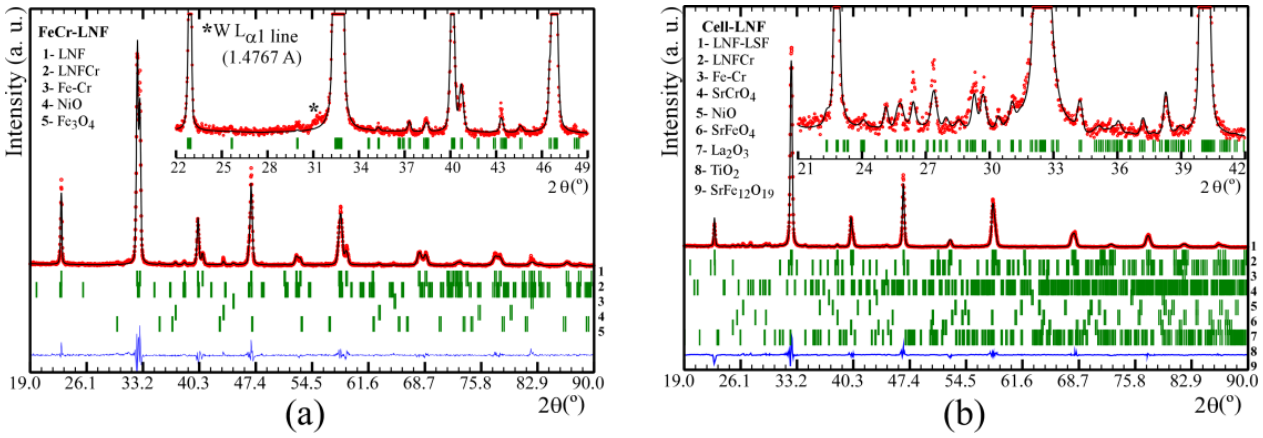

Figure 2.33. Rietveld refinements performed at room temperature in air for: (a) {Crofer22APU interconnect/LNF contact coating}, (b) {Crofer22APU interconnect/LNF contact coating/LSF cathode}, (c) {Crofer22APU interconnect/LSFMC contact coating} and (d) {Crofer22APU interconnect/LSFMC contact coating/LSF cathode}, after 1000 h at 800 ºC in air.

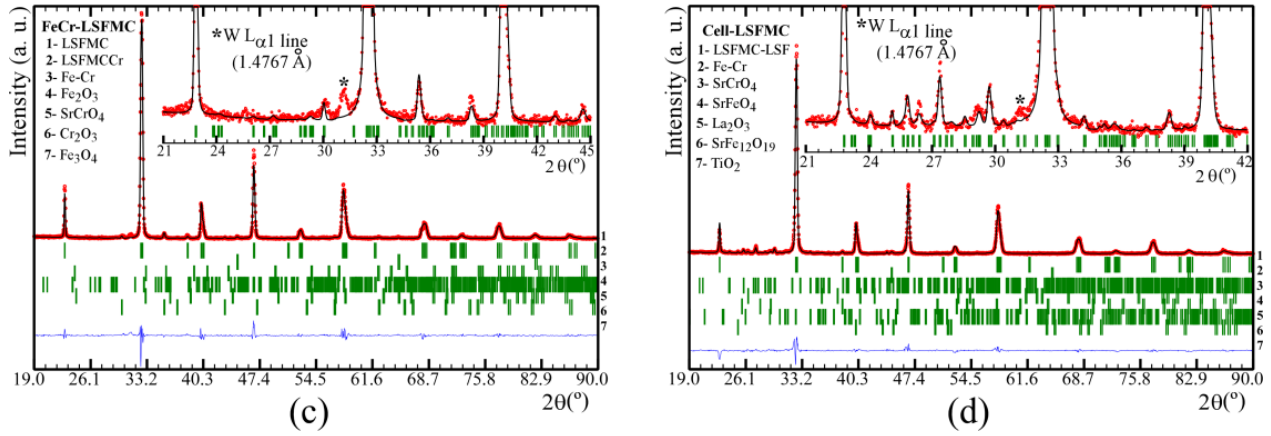

Figure 2.33. cont. Rietveld refinements performed at room temperature in air for: (a) {Crofer22APU interconnect/LNF contact coating}, (b) {Crofer22APU interconnect/LNF contact coating/LSF cathode}, (c) {Crofer22APU interconnect/LSFMC contact coating} and (d) {Crofer22APU interconnect/LSFMC contact coating/LSF cathode}, after 1000 h at 800 ºC in air.

Table 2.13. Rietveld results, % in weight of the formed phases in the coating surface of {interconnect/contact coating} (FeCr/LNC, FeCr/LNF, FeCr/LSFMC) and, for {interconnect/cathode} (Cell-LSF) as well as {interconnect/contact coating/cathode} (Cell-LNC, Cell-LNF and Cell-LSFMC). All of them after 1000 h at 800 ºC, in air.

Identification of phases			*Samples (after 1000 h at 800 ºC in air)*		
Phases	**Space group**	**Nº PDF**	**Cell-LSF**	**FeCr/LNC**	**Cell-LNC**
ABO_3	R-*3c*	82-1961	56.5(5)	92.2(6)	49.6(12)
$ABCrO_3$	P*bnm*	24-1016	-	1.2(1)	27.4(8)
Fe-Cr	I*m3m*	34-396	4.0(1)	< 1	< 1
NiO	F*m-3m*	73-1519	-	3.6(2)	2.0(9)
$SrCrO_4$	P$2_1/n$	15-368	18.7(4)	-	15.8(15)
La_2O_3	P$6_3/mmc$	83-1355	-	-	-
Cr_2O_3	R-*3c*	85-730	1.8(1)	0.7(1)	-
Fe_2O_3	R-*3c*	73-2234	1.8(2)	-	-
Fe_3O_4	F*d-3m*	19-629	12.5(4)	1.1(2)	0.4(2)
BCr_2O_4	F*d-3m*	31-630	-	< 0.2	-
TiO_2	I$4_1/amd$	71-1169	-	-	1.1(3)
$SrFeO_4$	P$4_2/mnm$	81-911	-	-	0.9(2)
$SrFe_{12}O_{19}$	P$6_3/mmc$	79-1411	4.7(2)	-	1.8(2)
χ^2			3.03	2.21	3.61

Table 2.13. cont. Rietveld results, % in weight of the formed phases in the coating surface of {interconnect/contact coating} (FeCr/LNC, FeCr/LNF, FeCr/LSFMC) and, for {interconnect/cathode} (Cell-LSF) as well as {interconnect/contact coating/cathode} (Cell-LNC, Cell-LNF and Cell-LSFMC). All of them after 1000 h at 800 ºC, in air.

Identification of phases			*Samples (after 1000 h at 800 ºC in air)*			
Phases	**Space group**	**Nº PDF**	**FeCr/LNF**	**Cell-LNF**	**FeCr/LSFMC**	**Cell-LSFMC**
ABO_3	R-*3c*	82-1961	80.1(8)	87.5(5)	91.9(6)	80.5(6)
$ABCrO_3$	P*bnm*	24-1016	16.6(4)	2.4(2)	-	-
Fe-Cr	I*m3m*	34-396	< 1	< 1	< 1	< 1
NiO	F*m-3m*	73-1519	1.9(1)	0.5(1)	-	-
$SrCrO_4$	P$2_1/n$	15-368	-	3.6(2)	0.8(1)	14.4(5)
La_2O_3	P$6_3/mmc$	83-1355	-	0.4(1)	-	0.3(1)
Cr_2O_3	R-*3c*	85-730	-	-	< 0.2	-
Fe_2O_3	R-*3c*	73-2234	-	-	0.9(3)	-
Fe_3O_4	F*d-3m*	19-629	0.5(2)	-	5.2(2)	-
BCr_2O_4	F*d-3m*	31-630	-	-	-	-
TiO_2	I$4_1/amd$	71-1169	-	0.6(1)	-	0.6(1)
$SrFeO_4$	P$4_2/mnm$	81-911	-	1.8(2)	-	1.7(2)
$SrFe_{12}O_{19}$	P$6_3/mmc$	79-1411	-	2.2(2)	-	1.5(2)
χ^2			2.51	3.68	2.45	3.27

The X-ray diffraction pattern of {interconnect/cathode} (Cell-LSF) confirms the interaction between the LSF perovskite and the uncoated metallic interconnect. As main phases were identified: $La_{0.6}Sr_{0.4}FeO_3$ % 56.5(5), $SrCrO_4$ % 18.7(4), Fe_3O_4 % 12.5(4); and as secondary phases: $SrFe_{12}O_{19}$ % 4.7(2), Cr_2O_3 % 1.8(1), Fe_2O_3 % 1.8(2). The reaction between Sr from the cathode and Cr from the alloy allows the formation of strontium chromate. According to our studies and other authors[93,131] Fe_2O_3, Fe_3O_4 and Cr_2O_3 appear in the oxide scale formed on Crofer22APU after 1000 h at 800 ºC in air. However, in our previous work[86] the study of long-term stability of initial LSF powder at 800 ºC for 1000 h, in air, reveals that cathode is partially degraded due to the formation of $LaSrFeO_4$ (P*nma*), Fe_3O_4 (F*d-3m*) and $SrFe_{12}O_{19}$ (P$6_3/mmc$), which could be explain the difference between the amount of Fe_3O_4 formed in Cell-LSF and in the rest of systems in which a contact coating was applied. The study of {interconnect/contact coating} assemblies reveals the formation of Cr-containing perovskites, basically in {FeCr/LNF}, in agreement with other studies[84,132]. The presence of NiO and Fe_3O_4 as impurity in initial LNC and LSFMC powders, respectively, could explain that the highest amount of these oxides was detected in systems in which LNC or LSFMC was used as contact coating (Table 2.13). The presence of NiO might also mean that Ni was practically extracted from LNC perovskite lattice, whereas Cr was incorporated to form rhombic Cr-perovskite[86,132]. The amount of the hematite phase quantified only in {FeCr/LSFMC} could significate that Fe^{3+} comes from the perovskite lattice instead of the oxide scale of the interconnect. A small amount of chromia was detected in {FeCr/LNC} and {FeCr/LSFMC} systems, indicating the possibility of Cr_2O_3 comes from the vapour phase transport of Cr (VI) volatile species (e. g., CrO_3 (g), $CrO_2(OH)_2$ (g)) and/or solid state diffusion of Cr (III) ions to

[131] Fontana S., Chevalier S., Caboche G. Metallic interconnects for solid oxide fuel cell: performance of reactive element oxide coating during 10, 20 and 30 months exposure. *Oxid. Met.* 78 (**2012**) 307-328.

[132] Stodolny M.K.. Cr-tolerance of the IT-SOFC La(Ni,Fe)O_3 material. Ph. D. thesis work, University of Twente, **2012**.

deposit as chromia in contact coating[75,133]. The low presence of Cr_2O_3 suggests that the formation of secondary phases with chromium inhibit the formation of this oxide[84].

The introduction of LSF cathode in the coated systems allows the formation of solid solution between contact and cathode material. In this case, the formation of Cr-perovskite is favoured in Cell-LNC. The observed La_2O_3, in Cell-LNF and Cell-LSFMC, could indicate that Sr of the cathode is introduced in A position of contact perovskite whereas La is released. In the case of Cell-LNC the amount of formed solid solution is not enough to form lanthanum oxide, in good agreement with LNC reaction to form $La(Ni,Co,Cr)O_3$. The formation of $SrFeO_4$ is related with the introduction of LSF cathode in the coated systems[134]. Titanium oxides could be formed as internal oxides for this alloy at the alloy/scale interface. Ti is a minor reactive element in Crofer22PU and is known to oxidise internally when exposed to high temperatures, reducing the volatility of Cr [135]. The second sintered treatment of the cathode at 950 ºC 2h in {interconnect/contact coating/cathode} structure could make TiO_2 detectable for XRD.

In order to determine the microstructure and to estimate the extent of element interdiffusion across assembly interfaces, EDX line scan analysis was performed on the cross-section of {interconnect/contact coating/cathode} structures following heat treated in air at 800 ºC for 1000 h (Figure 2.34). The SEM analysis confirms that LNF and LSFMC porous contact coatings are well enough bonded to the Crofer22APU interconnect and cathode. However, for LNC system the contact coating is not so properly attached to interconnect, probably due to the mismatch between TEC values, in good agreement with our previous results[91]. For all of the samples some cracks are observed through the contact coating, probably due to the stress caused by heating/cooling processes, which undergone the sample in sintered and long-term heat treated conditions.

[133] Jiang S.P., Zhen Y. Mechanism of Cr deposition and its application in the development of Cr-tolerant cathodes of solid oxide fuel cells. *Solid State Ionics* 179 (**2008**) 1459-1464.

[134] Vidal K. Perovskitas $AFeO_3$ para cátodos SOFC. Efecto de los parámetros que controlan la posición A en sus propiedades. Ph. D. thesis work, UPV/EHU, **2008**.

[135] Montero X., Tietz F., Stöver D., Cassir M., Villarreal I. Evaluation of commercial alloys as cathode current collector for metal-supported tubular solid oxide fuel cells. *Corros. Sci.* 51(1) (**2009**) 110-118.

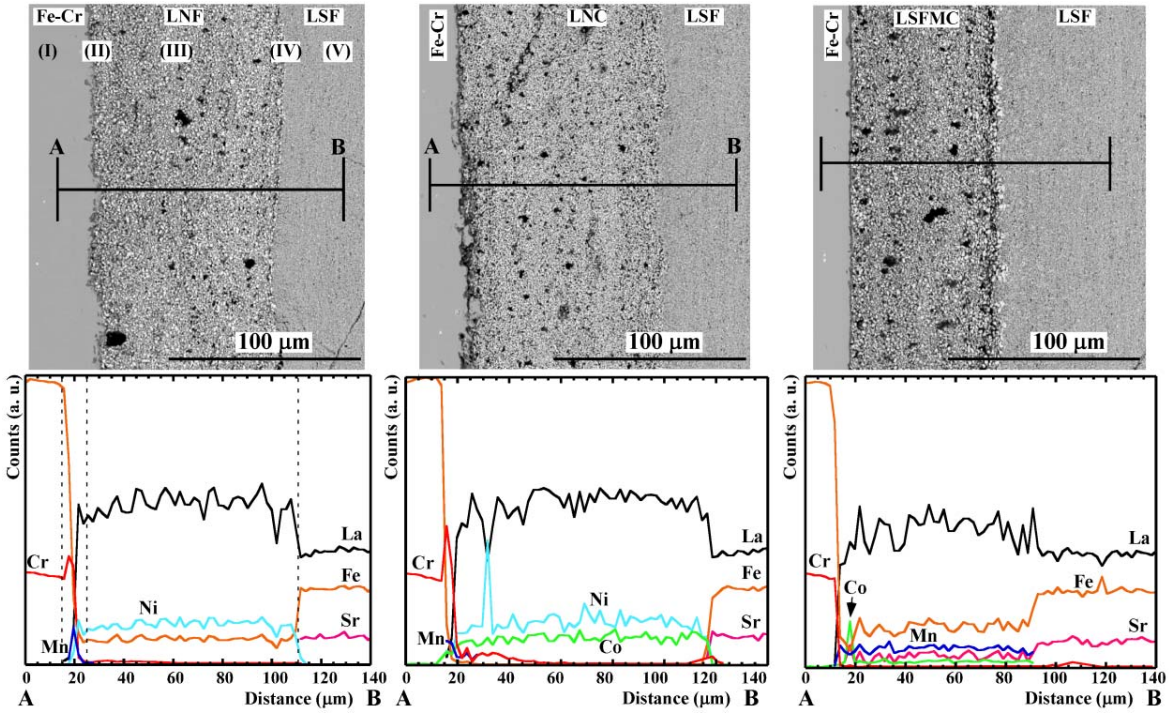

Figure 2.34. Cross-sectional backscattered electron (BSE) images and the corresponding energy dispersive X-ray spectroscopy (EDX) elemental line scan of Cell-LNF, Cell-LNC and Cell-LSFMC after treated at 800 ºC in air for 1000 h.

Five layers can be distinguished in the analyzed systems, including: metallic interconnect (I), the oxide scale (II), the contact coating (III), the contact coating/cathode interface (IV) and the cathode (V). The EDX line scans revealed that zone II was enriched mainly of Cr and some Mn. This analysis provided no evidence for Cr penetration through the contact coatings. But, for LNC coating chromium was detect in the first ≈30 µm of coating, being this layer more permeable to Cr probably because is not properly bonded to the substrate to protect the interconnect. Besides, for LNC and LSFMC an increase in content of chromium is observed in layer IV.

The chemical state of the elements and surface composition of {interconnect/contact material} assemblies were revealed by photoelectron spectroscopy. Figure 2.35 shows the survey spectra of the top of the surface of the {metallic/contact coating} systems after treated at 800 ºC for 1000 h, in air. As an example, the high resolution XPS spectra of different zones for {Crofer22APU/LNC} system is given in Figure 2.36. The corresponding high resolution XPS spectra of the analyzed zones in {Crofer22APU/LNF} and {Crofer22APU/LSFMC} assemblies are displayed as Supplementary material *(Section C, Figures S5 and S6)*. The binding energies (BEs) and relative atomic percentage concentration of O 1s, La $3d_{5/2}$, Sr 3d, Mn $2p_{3/2}$, Co $2p_{1/2}$, Fe $2p_{3/2}$ and Cr $2p_{3/2}$ core-levels of samples, are summarized in Table 2.14.

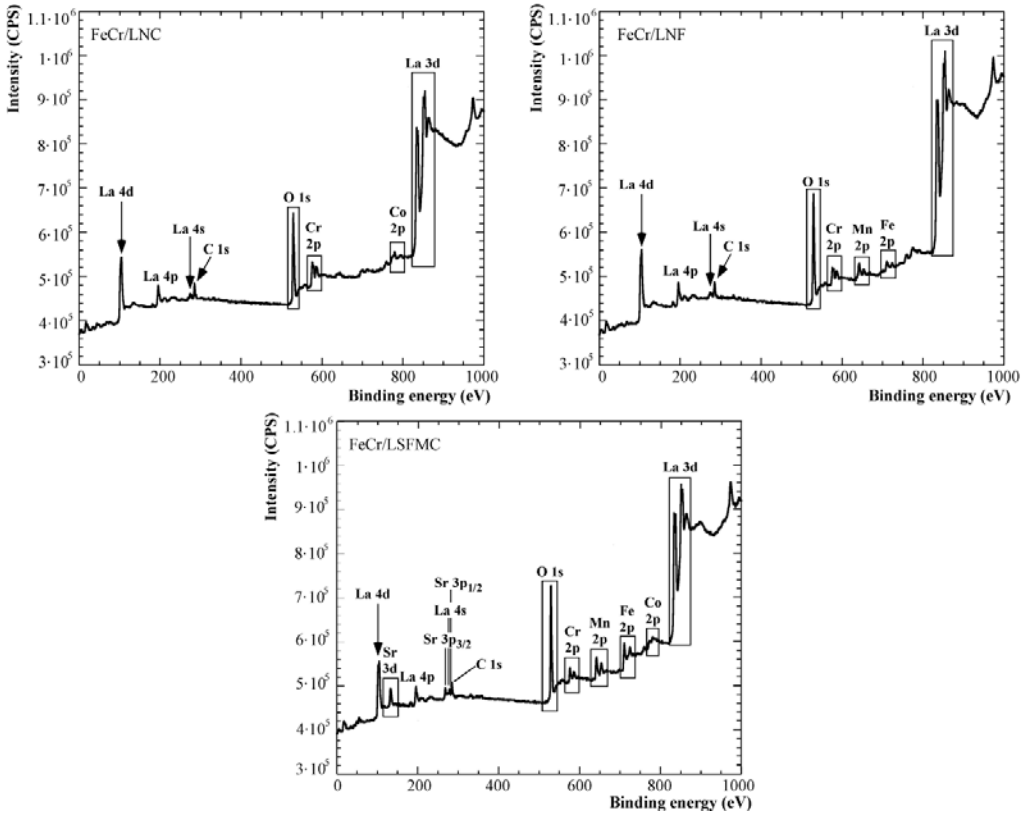

Figure 2.35. XPS survey spectrums of the surface of the {Crofer22APU interconnect/contact coating} system, using $LaNi_{0.6}Co_{0.4}O_{3-\delta}$ (LNC), $LaNi_{0.6}Fe_{0.4}O_{3-\delta}$ (LNF) or $(La_{0.8}Sr_{0.2})_{0.95}Fe_{0.6}Mn_{0.3}Co_{0.1}O_3$ (LSFMC) as contact coating, after 1000 h at 800 ºC in air.

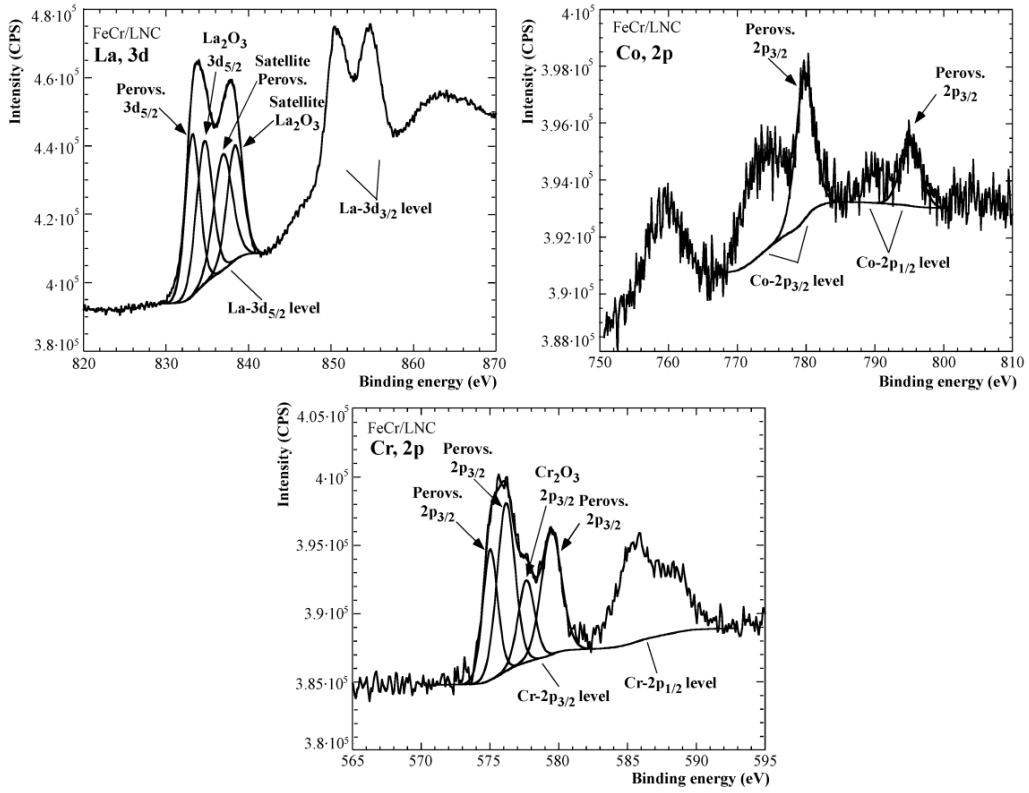

Figure 2.36. La 3d, Cr 2p and Co 2p spectral regions of the surface of {Crofer22APU interconnect/LNC contact coating} system after 1000 h at 800 ºC in air.

Table 2.14. XPS analysis results of the detected elements for the surface of FeCr/LNC, LNF or LSFMC assemblies, after heat treated at 800 ºC for 1000 h in air.

Peak	FeCr/LNC		FeCr/LNF	
	Binding Energy (eV)	% at. Conc.	Binding Energy (eV)	% at. Conc.
La $3d_{5/2}$ in ABO_3	833.22	10.1	833.18	10.2
La $3d_{5/2}$ in La_2O_3	834.67	9.5	834.51	9.6
Sr 3d in ABO_3	-	-	-	-
Sr 3d in SrO	-	-	-	-
Ni $2p_{1/2}$ in ABO_3	-	-	-	-
Co 2p in ABO_3	779.8;795.19	1.9	-	-
Fe $2p_{3/2}$ in ABO_3	-	-	710.02;712.87	3.2
Mn $2p_{3/2}$ in ABO_3	-	-	-	-
Mn $2p_{3/2}$	-	-	642.01;644.81	4.2
Cr $2p_{3/2}$ in ABO_3	575.02;576.17;579.47	8.5	575.01;576.32;579.28	5.1
Cr $2p_{3/2}$ in Cr_2O_3	577.65	1.5	578.00	0.7
Cr $2p_{3/2}$	-	-	580.66	0.2
O 1s	528.87;530.31; 531.51;533.21	68.5	528.83;529.83; 531.39;532.82	66.8

Peak	Fe/CrLSFMC	
	Binding Energy (eV)	% at. Conc.
La $3d_{5/2}$ in ABO_3	833.17	7.4
La $3d_{5/2}$ in La_2O_3	834.42	6.8
Sr 3d in ABO_3	132.09;134.00	3.1
Sr 3d in SrO	133.47;135.50	1.1
Ni $2p_{1/2}$ in ABO_3	-	-
Co 2p in ABO_3	-	-
Fe $2p_{3/2}$ in ABO_3	709.99;712.11	7.3
Mn $2p_{3/2}$ in ABO_3	641.43	3.8
Mn $2p_{3/2}$	643.94	1.4
Cr $2p_{3/2}$ in ABO_3	-	-
Cr $2p_{3/2}$ in Cr_2O_3	-	-
Cr $2p_{3/2}$	574.97;576.19;578.13	3.6
O 1s	528.75;529.48; 530.87;532.58	65.5

According to XPS analyses performed on top of the three coated system surfaces, for La, there are two peaks, one at ≈833 eV which corresponds to La^{3+} in perovskite phase and, another at ≈834 eV which is assigned to La^{3+} in La_2O_3, in good agreement with the starting material surface XPS results. Moreover, the peaks appearing at ≈132 eV and ≈133.5 eV (Sr $3d_{5/2}$) indicates de existence of Sr^{2+} in ABO_3 structure and in SrO, respectively. Taking into account the fact that the atomic concentration of elements assigned to the A and B site of perovskite have to remain a ratio of 1:1, the peaks appearing at ≈575 eV, ≈576 eV and ≈579 eV (Cr $2p_{3/2}$) could be assigned to chromium in perovskite[90,136]. In addition, the binding energy of ≈578 eV (Cr $2p_{3/2}$) is detected in LNC and LNF contact coatings, which is in good agreement with Cr_2O_3 superficial oxide[137,138].

[136] Stojanovic M., Haverkamp R.G., Mims C.A., Moudallal H., Jacobson A.J. Synthesis and characterization of $LaCr_{1-x}Ni_xO_3$ perovskite oxide catalysts. *J. Catal.* 165 (**1997**) 315-323.

[137] Battistoni C., Dormann J.L., Fiorani D., Paparazzo E., Viticali S. An XPS and Mössbauer study of the electronic properties of $ZnCr_xGa_{2-x}O_4$ spinel solid solutions. *Solid State Commun.* 39(4) (**1981**) 581-585.

Apart of the detected Cr-perovskite and Cr_2O_3, the XPS results suggest that there are more Cr species in LNF and LSFMC coatings. For LSFMC layer the absence of Cr-perovskite is in good agreement with XRD analysis (Table 2.13). Besides, for LNC and LNF the peaks corresponding to Ni 2p were not observed, which could indicate that Ni was extracted to introduce chromium in ABO_3 structure, in good agreement with the observed NiO by XRD.

Moreover, the binding energies of ≈710 eV, ≈712-713 eV (Fe $2p_{3/2}$), ≈780eV, ≈795 eV (Co 2p) and ≈641 eV (Mn $2p_{3/2}$) suggesting the presence of iron, cobalt, and manganese respectively, in the perovskite structure. Additionally, another kind of manganese is concentrated on LNF and LSFMC surface, in good agreement with the observed signals of about ≈642 eV, ≈645 eV and ≈644 eV (Mn $2p_{3/2}$), respectively[139], which could be related with the formation of a low thickness Mn-spinel barrier layer. On the contrary, for FeCr/LNC system Mn is more concentrated in the bulk of the structure, allowing XRD detection.

2.3.3.4. ASR measurements and post-test analysis

The degradation of the {interconnect/contact coating/cathode} systems was evaluated using ASR measurements in air at 800 ºC. Figure 2.37 shows the contact ASR as a function of time, for the assembly formed by {Crofer22APU/contact coating/LSF}. To evaluate the effectiveness of using contact coating in these systems, the ASR values obtained were compared with ASR values obtained for {Crofer22APU/LSF cathode} cell. Reference values of system without contact coating area are also shown in Figure 2.37. The obtained ASR values for different tested systems are summarized in Table 2.15.

The ASR values of the cell without contact coating were higher (0.31(1) $\Omega \cdot cm^2$) than those of the stacks with interconnect coated with LNC, LNF and LSFMC. This might be due to the formation of secondary phases such as $SrCrO_4$ between cathode and uncoated Crofer22APU, which increase the contact resistance of the cell.

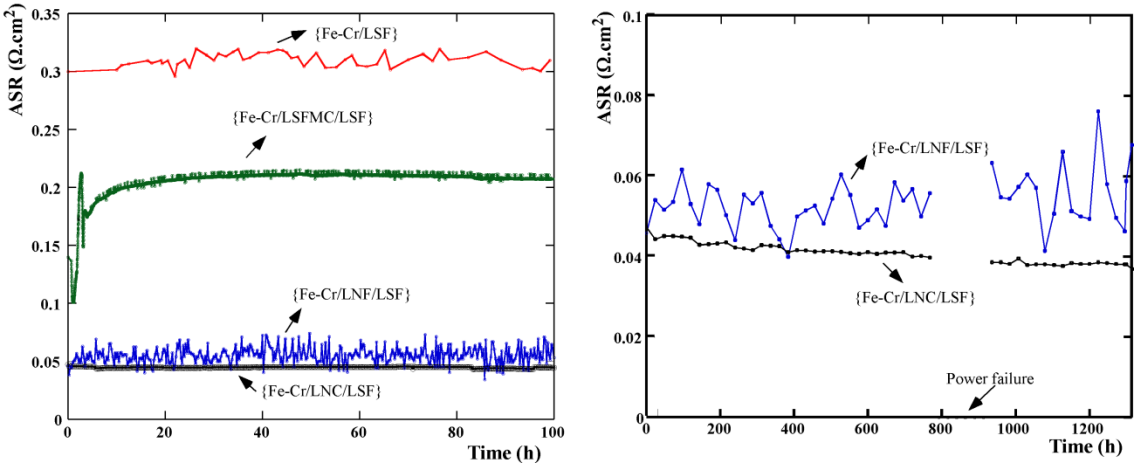

Figure 2.37. Area specific resistance values, at 800 ºC in air, for different interfaces tested in the {interconnect/cathode} and {interconnect/contact coating/cathode} systems for the first 100 h (left) and for the systems up to 1300 h (right).

---

[138] Mandrino Dj., Donik C. Chemical-state information obtained by AES and XPS from thin oxide layers on duplex stainless steel surfaces. *Vacuum* 86 (**2011**) 18-22.

[139] Wei Z.X., Xiao C.M., Zeng W.W., Liu J.P. Magnetic properties and photocatalytic activity of $La_{0.8}Ba_{0.2}Fe_{0.9}Mn_{0.1}O_{3-\delta}$ and $LaFe_{0.9}Mn_{0.1}O_{3-\delta}$. *J. Mol. Catal. A-Chem.* 370 (**2013**) 35-43.

Table 2.15. Area specific resistance values for the different tested systems measured at 800 ºC in air.

Sample	Cell-LSF	Cell-LSFMC	Cell-LNF		Cell-LNC	
Time (h)	100	100	100	1300	100	1300
≈ ASR (Ω·cm^2)	0.31(1)	0.21(2)	0.055(7)	0.054(7)	0.045(1)	0.041(2)

The ASR values as a function of time were different depending on the contact perovskite. As expected, the initial resistance is influenced by the electrical conductivity of the perovskites[83,91]. However, the instability of the measurement over the time could be related with material interactions or interfacial contact loose effects. Several studies have shown[140-142] that the phase transformation in the oxide scale is related to the formation of BCr_2O_4 spinels reaction products, in which B is a transition metal coming from the perovskite contact coating. Since $MnCoCrO_4$ spinel shows a higher conductivity than both Cr_2O_3 and $MnCr_2O_4$ phases, the use of LNC could offer a more effective reduction in contact resistance[143]. However, its higher ionic conductivity could lead to a higher growth rate of the scale beneath the contact layer[144]. Furthermore, in order to prevent cracking of the oxide scale, the thermal expansion coefficients of the formed new spinels should also take into account. According to other authors, the chromium spinels have the lowest TECs and the mismatch of TEC with alloys increases with increasing chromium content. Thus, $(Mn,Co,Fe)_3O_4$ has the closest match with Crofer22APU[143].

Since the Cr deposition process is kinetically limited by nucleation reactions between the gaseous Cr species and nucleation agents, the deposition process of Cr species depends on the nature of the contact materials[145-149]. The contact materials, which are free of nucleation agents (such as Mn-, Sr-, Ba-containing species), would be more tolerant toward the Cr deposition. In the case of LSFMC, the nucleation agents is Sr^{2+} to form $SrCrO_4$ deposits. The formation of $(Cr,Mn)_3O_4$-type spinel would be enhanced if there is sufficient supply of Mn^{2+} ions, which is

[140] Yang P., Liu C.K., Wu J.Y., Shong W.J., Lee R.Y., Sung C.C. Effects of pre-oxidation on the microstructural and electrical properties of $La_{0.67}Sr_{0.33}MnO_{3-\delta}$ coated ferritic stainless steels. *J. Power Sources* 213 (**2012**) 63-68.

[141] Fujita K., Hashimoto T., Ogasawara K., Kameda H., Matsuzaki Y., Sakurai T. Relationship between electrochemical properties of SOFC cathode and composition of oxide layer formed on metallic interconnects. *J. Power Sources* 131 (**2004**) 270-277.

[142] Fang Y., Wu C., Duan X., Wang S., Chen Y. High-temperature oxidation process analysis of $MnCo_2O_4$ coatings on Fe-21Cr alloy. *Int. J. Hydrogen Energ.* 36(9) (**2011**) 5611-5616.

[143] Wang K., Liu Y., Fergus J.W. Interaction between SOFC interconnect coating materials and chromia. *J. Am. Ceram. Soc.* 94(12) (**2011**) 4490-4495.

[144] Wei W., Chen W., Ivey D.G. Oxidation resistance and electrical properties of anodically electrodeposited Mn-Co oxide coatings for solid oxide fuel cell interconnect applications. *J. Power Sources* 186 (**2009**) 428-434.

[145] Sun C., Hui R., Roller J. Cathode materials for solid oxide fuel cells: a review. *J. Solid State Electrochem.* 14 (**2010**) 1125-1144.

[146] Jiang S.P., Zhen Y. Mechanism of Cr deposition and its application in the development of Cr-tolerant cathodes of solid oxide fuel cells. *Solid State Ionics* 179 (**2008**) 1459-1464.

[147] Zhen Y.D., Tok A.I.Y., Jiang S.P., Boey F.Y.C. La(Ni, Fe)O_3 as a cathode material with high tolerance to chromium poisoning for solid oxide fuel cells. *J. Power Sources* 170 (**2007**) 61-66.

[148] Zhen Y.D., Tok A.I.Y., Boey F.Y.C., Jiang S.P. Development of Cr-tolerant cathodes of solid oxide fuel cells. *Electrochem. Solid-state Lett.* 11 (**2008**) B42-B46.

[149] Jiang S.P., Zhen Y.D. Mechanism of Cr deposition and its application in the development of Cr-tolerant cathodes of solid oxide fuel cells. *Solid State Ionics* 179 (**2008**) 1459-1464.

related with the cathodic polarization[150,151]. Thus, in this study the formation of BCr_2O_4 (B=Mn) is not favoured.

The absence of nucleation agents in LNF and LNC compositions reduces the Cr deposits, being more stable in the presence of a Fe-Cr alloy interconnect. Further, considering that denser contact layer retains better Cr, the chromium poisoning behaviour also depends on the microstructure of the contact coating[91].

For {Crofer22APU/LSFMC/LSF} structure, initially the ASR increased quickly and then more slowly, the observed values are near 0.21(1) $\Omega \cdot cm^2$ for 100 h. The contact resistance value of the {Crofer22APU/LNF/LSF} cell, remains unchanged at 0.055(7) $\Omega \cdot cm^2$ up to 100 h, similar behaviour to that of the stack formed by LNC. Nevertheless, the lowest and the most constant ASR value was obtained when LNC was used as contact coating, obtaining an ASR value of 0.045(1) $\Omega \cdot cm^2$ up to 100 h.

The system degradation analysis of LNC and LNF with interconnect and cathode is continued at 800 ºC in air up to 1300 h (Figure 2.37, Table 2.15). The {Crofer22APU/LNC/LSF} assembly shows no meaningful degradation in contrast to {Crofer22APU/LNF/LSF} which presents a little increase of the resistance. However, the ASR contributed by Crofer22APU/LNF/LSF contact, 0.054(7) $\Omega \cdot cm^2$ at 1300 h, is acceptable for the performance of SOFC stacks[152]. For LNC contact coating the obtained signal was relatively stable near 0.041(2) $\Omega \cdot cm^2$ until the end of the test. In our previous work[86] it has been shown that the formation of Co-containing spinels could be related to the low degradation of ASR in {interconnect/LNC/cathode} system. The obtained ASR values for all the studied systems are higher if they are compared with the electrical resistance values obtained in our other study[91], in which, the thicknesses of contact coating and cathode were about, 10-20 μm and 20-25 μm, respectively. Besides in Ref. 91, the overall ASR of {interconnect/contact coating/cathode} setup was measured for the starting operation time up to 16 h, which could change over time.

To determine the composition and microstructure of the interconnect/contact coating/cathode interfaces after ASR measurements up to 1300 h, the cross section of the samples were evaluated using backscattered electron (BSE) detector (Figure 2.38). Moreover, the microanalyses at different points of studied systems were acquired using EDX (Figure 2.38). In both samples the chemical interaction between materials is based on the gaseous diffusion of Cr species (Cr(VI)) or solid state diffusion of chromium ions. According to other authors[75] the direct contact of coating with Fe-Cr interconnect facilitates the solid state diffusion of Cr and accelerates the Cr deposition. However, in both samples, the microstructure of the contact material revealed open porosity, allowing vapor phase transport of volatile Cr-species throughout the contact coatings[90].

---

[150] Jiang S.P., Zhang J.P., Apateanu L., Foger K. Deposition of chromium species at Sr-doped $LaMnO_3$ electrodes in solid oxide fuel cells I. Mechanism and kinetics. *J. Electrochem. Soc.* 147 (**2000**) 4013-4022.

[151] Jiang S.P., Zhang S., Zhen Y.D. Early interaction between Fe-Cr alloy metallic interconnect and Sr-doped $LaMnO_3$ cathodes of solid oxide fuel cells. *J. Mater. Res.* 20 (**2005**) 747-758.

[152] Miguel-Pérez V. Interconectores metálicos y capas protectoras para su aplicación en pilas SOFC. Ph.D. thesis work, UPV/EHU, **2013**.

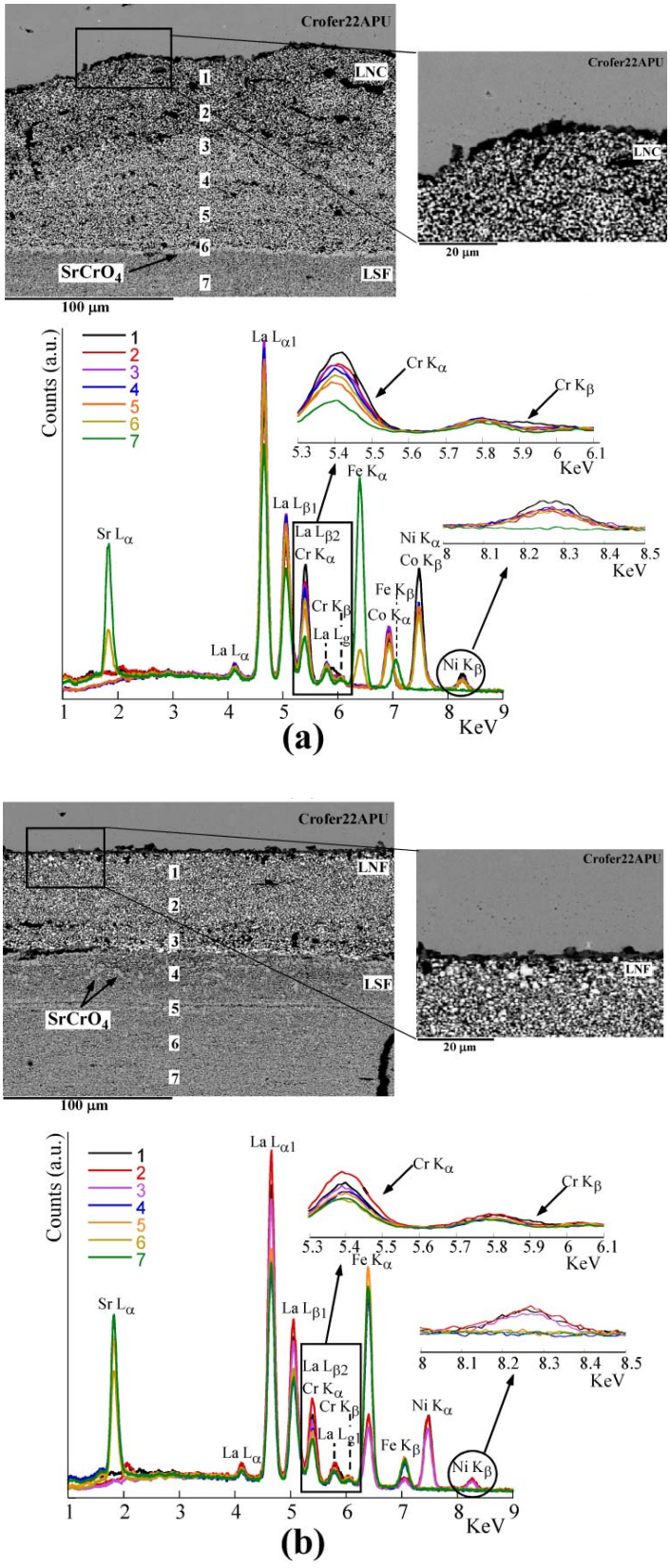

Figure 2.38. BSE images and EDX analysis on different points for: (a) {Crofer22APU interconnect/LNC contact coating/LSF cathode} and (b) {Crofer22APU/LNF/LSF} assemblies after long-term ASR measurements.

Besides, the presence of some cracks through the contact layers is observed, especially for LNC in the first ≈48 μm. The interactions between LNC and interconnect can cause stress, leading an increase of the cracks formation in this conditions. The microstructure of the cathode is similar for both structures, revealing an adequate microstructure.

The principal emission lines of Cr K_α (5.415 KeV) overlap with La L_β (5.041 KeV) emission lines, which hampers the analysis of both elements together. To confirm the presence or absence of Cr, the INCA 350 sofware from Oxford was also used to reconstruct the spectra. Figure 2.39 shows the experimental spectrum for point 1 of each samples and, the reconstructed spectrum considering that Cr is not present. When comparing both spectra, the Cr K_α (5.411 KeV) and Cr K_β (5.946 KeV) energy peaks in the experimental spectrum indicate the presence of Cr. Equivalent analyses for points 4, 6 and 7 were made (Figure 2.39).

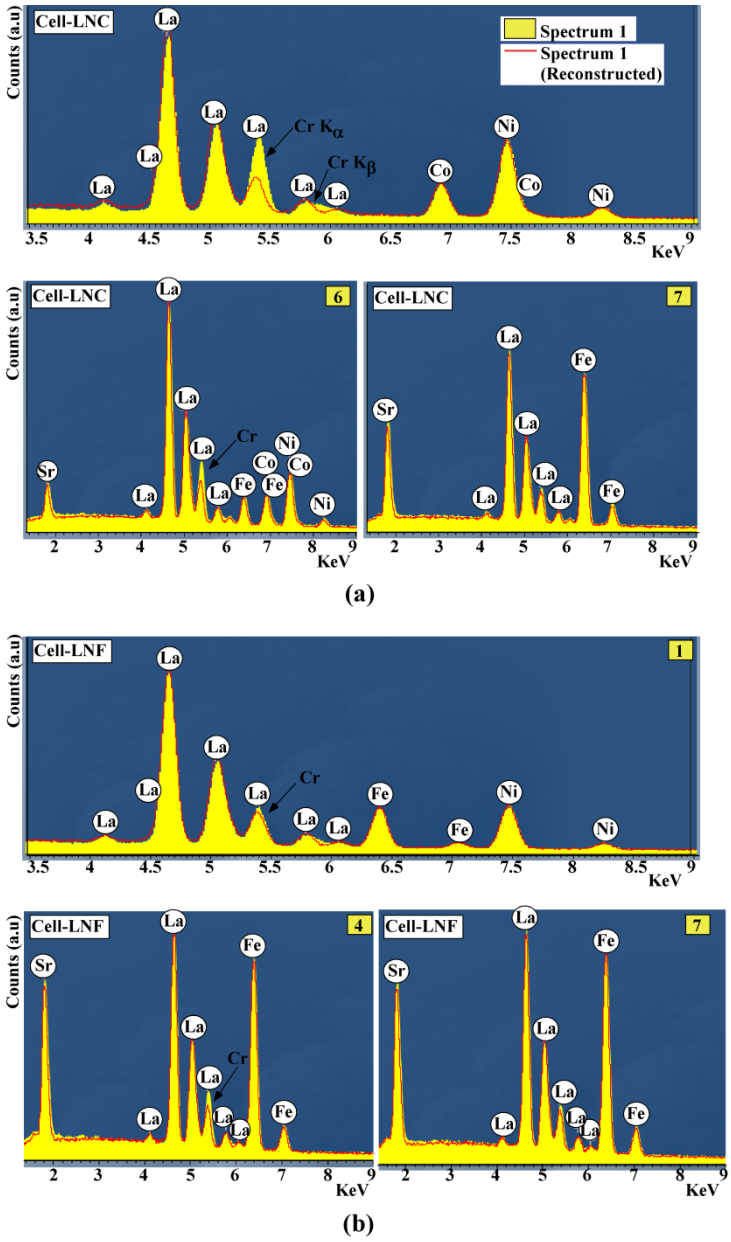

Figure 2.39. Experimental and reconstructed spectra for: (a) Cell-LNC and (b) Cell-LNF, after 1300 h ASR test.

For both samples point 1 revealed the presence of Cr, being the concentration of Cr higher in {Crofer22APU/LNC/LSF} sample, in good agreement with observed "dark" (lower average Z of analyzed elements) area in the first ≈ 48 μm of LNC contact coating; in contrast to {Crofer22APU/LNF/LSF} which present more "brighter" areas. As it has been mentioned before, the adherence between LNC coating and interconnect is worse than for the LNF due to the mismatch between its TECs (Figure 2.38), causing an increase in Cr species. In the points 1, 2, 3, 4 and 5 of LNC coating did not detect the presence of Fe, in good agreement with that the preoxidation treatment, prior to contact coating deposition, reduce outward diffusion of Fe from Crofer22APU due to the formation of a chromia-based thermally grown oxide (TGO) surface layer on the interconnect[94,95]. The diffusion of chromium, in both structures, reached up to ≈ 130 μm. Thus, in the grains (point 9) of both samples no chromium is detected within the cathode, obtaining the presence of La, Sr and Fe, as was expected. For {Crofer22APU/LNC/LSF} structure the small white layer between the contact material and the cathode was detected, which contains La, Sr, Cr, Co, Fe and Ni; so, the contact itself could act as a barrier for element diffusion[86]. Thus, when LNF is used as contact coating, in the first 40 μm of the cathode layer Cr and Sr are observed, probably as $SrCrO_4$ precipitation, which is detected as "white zones" in the images. Thus, the formation of poor conductive strontium chromate phase could increase the ASR value.

When comparing these results with those obtained for similar structures after 1000 h at 800 ºC in air, without using current/voltage source (Figure 2.34), it could be concluded that the use of a current/voltage source is not relevant for the degradation of these systems. Although, according to our previous results[91] the degradation process of the system could be accelerated by a current flow, despite, in this case, the trend in the migration of elements is similar in both cases. Besides, the supplementary data of our previous work[91] shows the degradation of {Crofer22APU/LSFMC/LSF} structure after ASR measurements at 800 ºC up to 100 h in air, which is higher than the one without current load, observed in Figure 2.34 after 1000 h.

2.3.4. Conclusions

The long-term durability of {Crofer22APU interconnect/contact coating/LSF cathode} structure using LNC, LNF and LSFMC as contact materials has been analysed. This study demonstrates that when a perovskite contact coating is applied between Crofer22APU/LSF structure a decrease in ASR of the system is obtained. A low reactivity is observed between contact materials and LSF cathode; in contrast with the interactions observed with Crofer22APU interconnect, especially when no coating was used in these systems. In spite of that, the {Crofer22APU/LNC or LNF/LSF} structures showed a low and stable ASR value after heat treated at 800 ºC for 1300 h in air.

Taking into account the obtained results, the $LaNi_{0.6}B_{0.4}O_{3-\delta}$ (B=Co or Fe) would offer promising opportunities as high conductive cathode contact materials. Moreover, an improvement in the deposition of these materials on metallic interconnect through mechanical compaction of the coatings could be a suitable form to achieve the required conductive/protective interface for SOFC interconnect.

2.3.5. Supplementary material

Section A. Characterization of contact materials

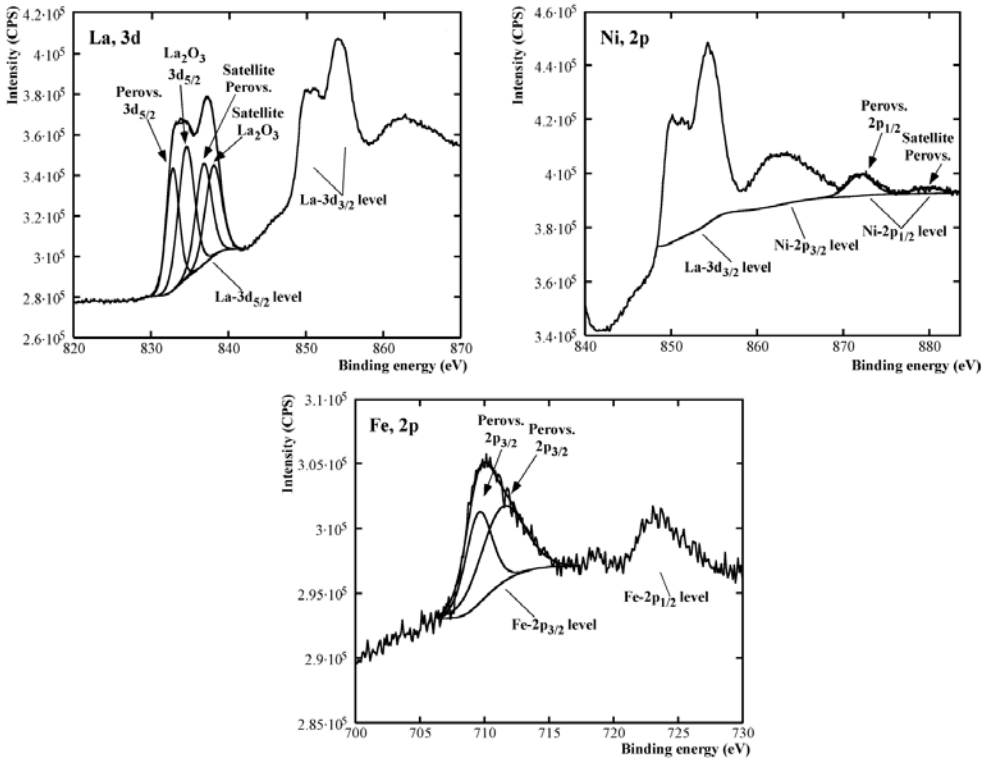

Figure S1. High resolution XPS spectras of the analyzed zones on the surface of the initial LNF powder.

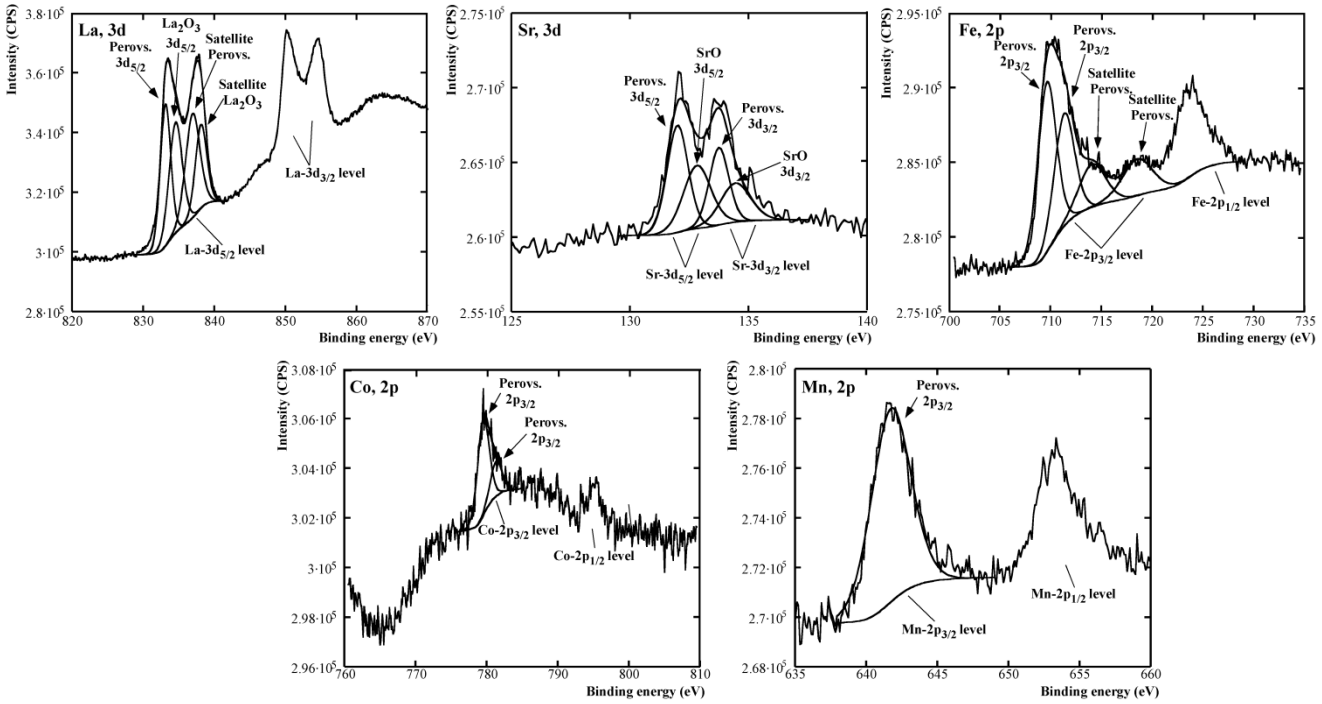

Figure S2. High resolution XPS spectras of the analyzed zones on the surface of the initial LSFMC powder.

Section B. Compatibility between $La_{0.6}Sr_{0.4}FeO_3$ and contact materials after 1000 h at 800 ºC

Policrystalline mixtures of contact coating-LSF (50:50 wt. %) were sintered between 950 and 1350 ºC in air. XRD analyses revealed (Fig. S3) chemical interaction between contact material and cathode forming a compositional $(\text{contact coating})_x(\text{LSF})_{1-x}$ gradient. Due to the similarity of cell parameters of the solid solution compounds it is not possible to determine the number of phases present in each sample. However, at higher temperature (1350 ºC) and longer sintering time (5h) only one intermediate $(\text{contact coating})_{0.5}(\text{LSF})_{0.5}$ single phase was formed (Fig. S4, Table S1).

Table S1. Rietveld refinement results of three contact materials-cathode (1:1) mixtures after heat treated at 1350 ºC for 5 h, in air.

Sample	$(CC)_{0.5}(LSF)_{0.5}$ R-*3c*	NiO F*m-3m*	Fe_2O_3 R-*3c*	Fe_3O_4 F*d-3m*	χ^2
LNC-LSF	98.4(5)	1.6(1)	-	-	3.00
LNF-LSF	96.5(6)	1.8(1)	1.7(4)	-	3.57
LSFMC-LSF	97.3(6)	-	-	2.7(2)	2.98

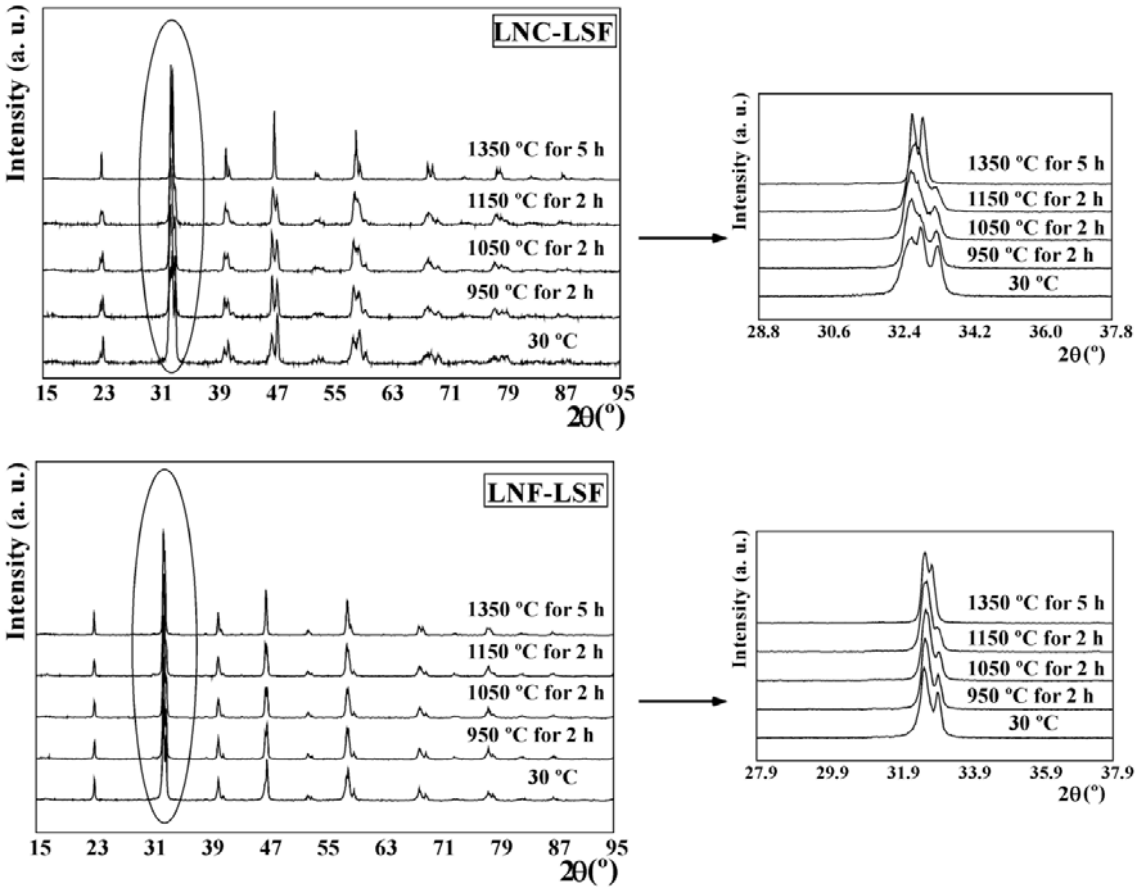

Figure S3. Room temperature X-ray powder diffraction patterns of three contact materials (LNC, LNF, LSFMC) and cathode (LSF) mixtures prepared at different temperatures (25, 950, 1050, 1150 and 1350 ºC).

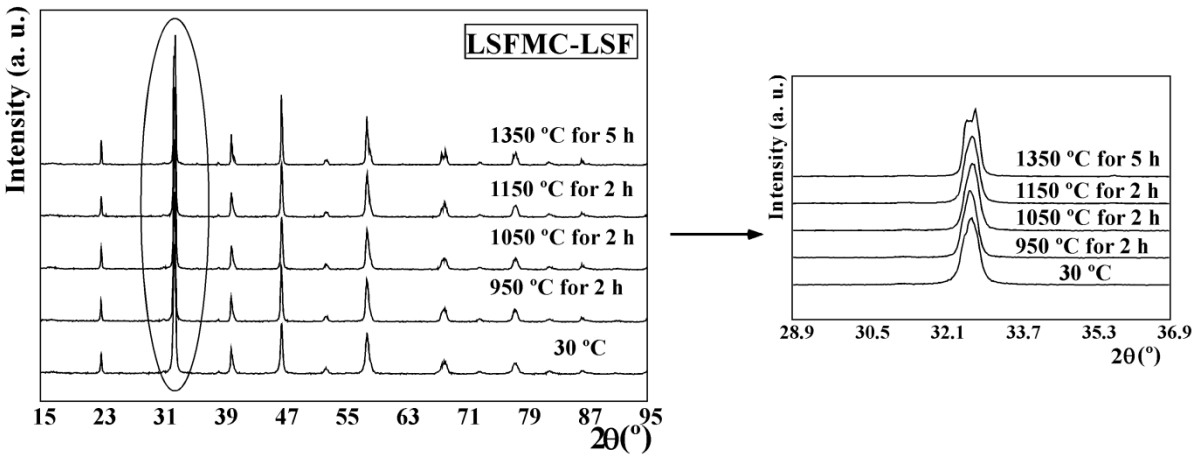

Figure S3. cont. Room temperature X-ray powder diffraction patterns of three contact materials (LNC, LNF, LSFMC) and cathode (LSF) mixtures prepared at different temperatures (25, 950, 1050, 1150 and 1350 ºC).

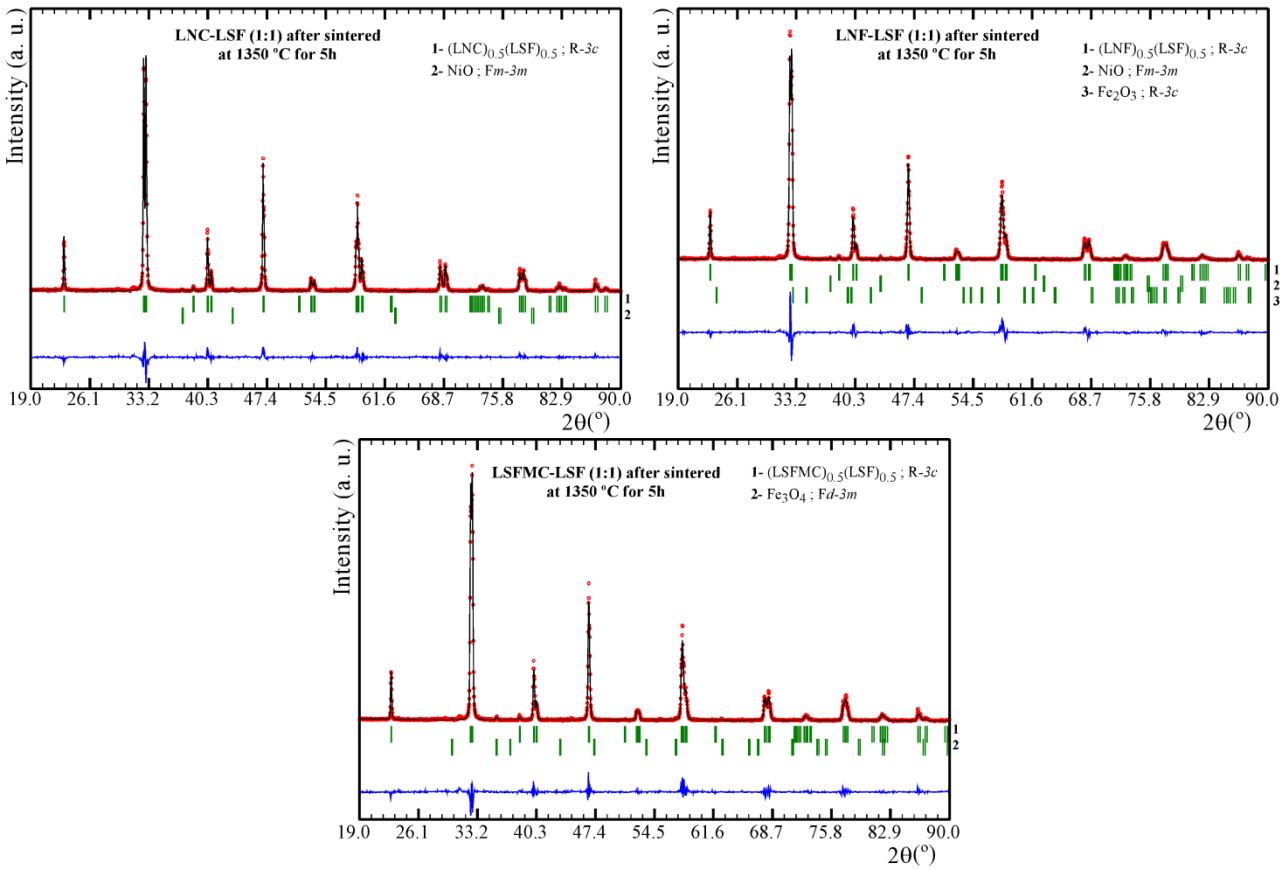

Figure S4. Observed, calculated and difference X-ray powder diffraction patterns for contact coatings mixed with cathode material sintered at 1350 ºC for 5 h, in air.

Section C. Study of {cathode/contact layer/interconnect} systems and effectiveness of contact coatings after 1000 h at 800 ºC

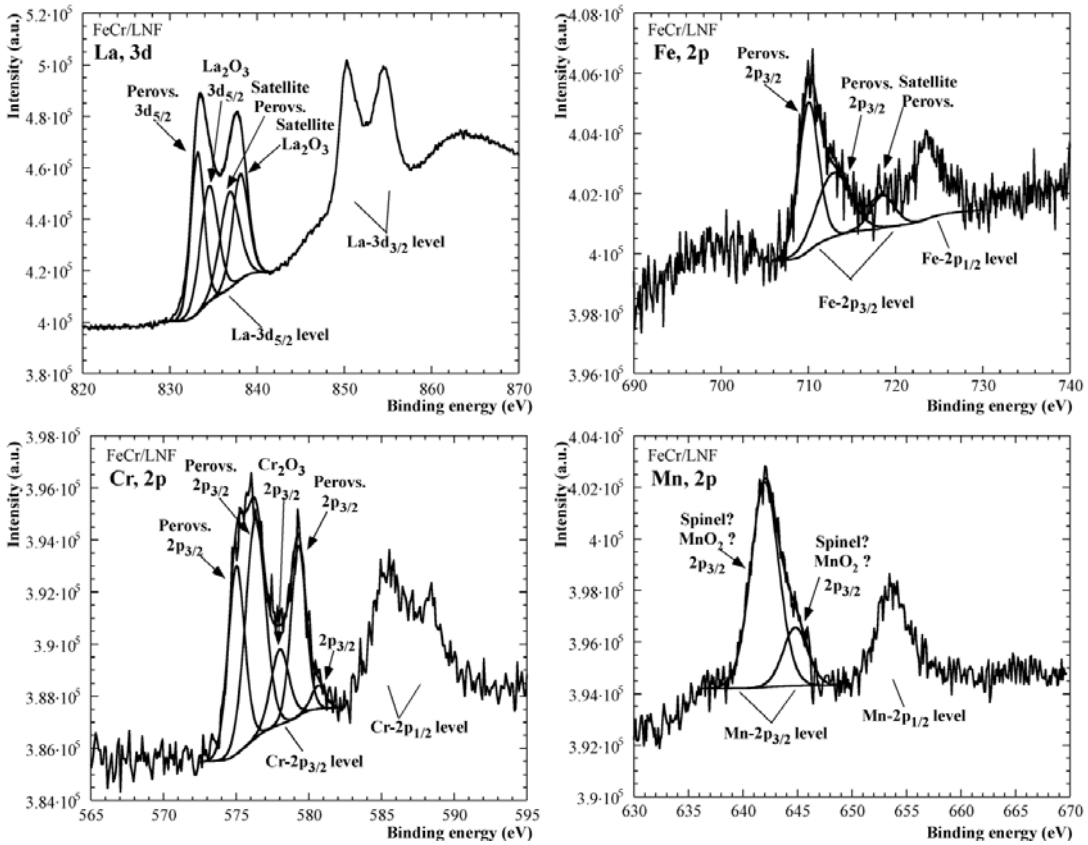

Figure S5. La 3d, Co 2p, Fe 2p Cr 2p and Mn 2p spectral regions of the surface of LNF coating in contact with Crofer22APU interconnect after 1000 h at 800 ºC in air.

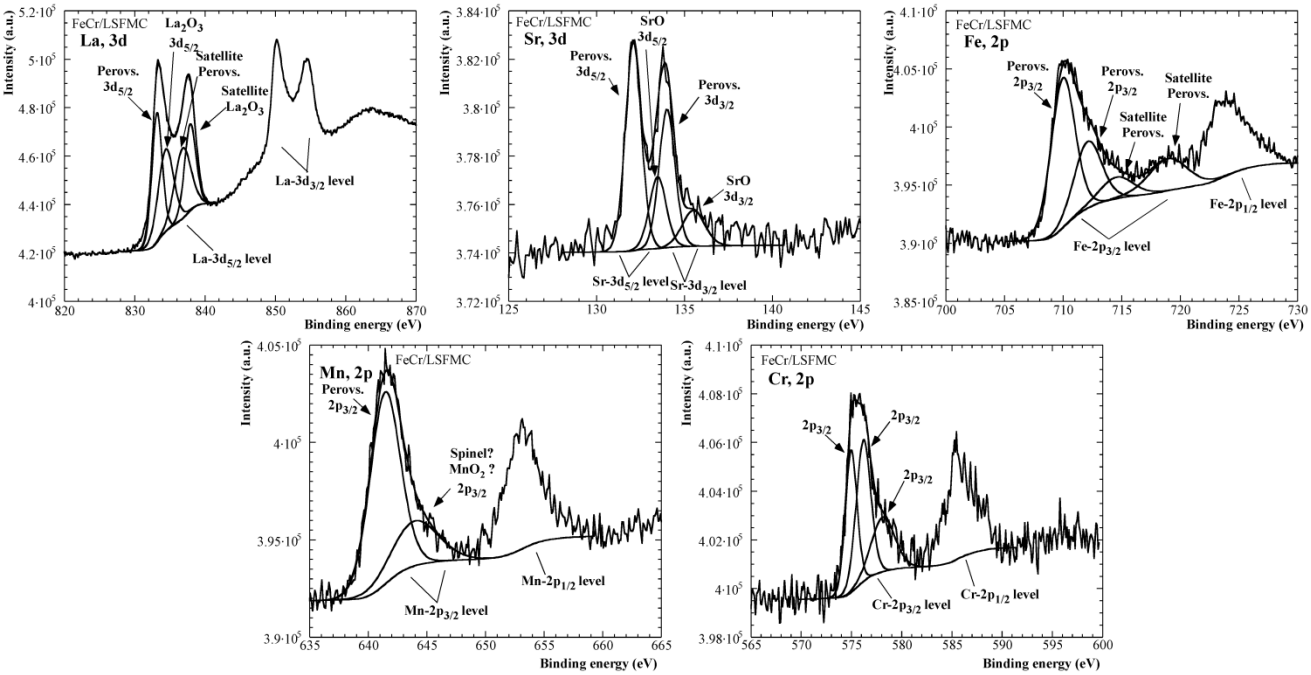

Figure S6. La 3d, Co 2p, Fe 2p Cr 2p and Mn 2p spectral regions of the surface of LSFMC coating in contact with Crofer22APU interconnect after 1000 h at 800 ºC in air.

3. FORMATION AND CHARACTERIZATION OF A NEW COMPOSITE CONTACT MATERIAL. EVALUATION OF THE SYSTEM IN CHANNEL CONFIGURATION.

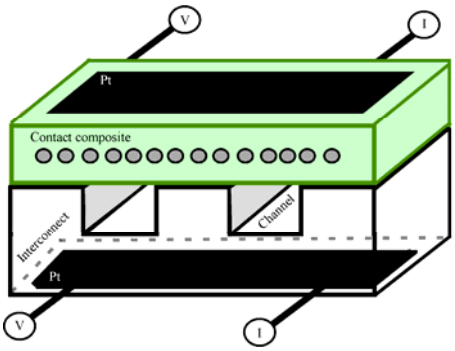

3.1. $LaNi_{0.6}Co_{0.4}O_{3-\delta}$ dip coated on Fe-Cr mesh as a composite cathode contact material on intermediate solid oxide fuel cells. *J. Power Sources* 269 (**2014**) 509-519.

3.2. Evaluation of using protective/conductive coating on Fe-22Cr mesh as a composite cathode contact material for intermediate solid oxide fuel cells. *Int. J. Hydrogen Energ.* 40 (**2015**) 4804-4818.

Resultados más relevantes*

*** Se muestra un resumen de los resultados más relevantes registrados en las publicaciones contenidas en la presente sección.**

La presencia de canales en el interconector ha requerido la fabricación de un nuevo material de contacto que aporte la integridad estructural necesaria para evitar el colapso de las vías de acceso de los gases a las partes activas de las celdas. Este composite está formado por una malla metálica Fe-22Cr, la cual ha sido embebida por inmersión (dip coating) en la suspensión o pasta cerámica formulada a partir de los materiales de contacto seleccionados previamente, y caracterizada mediante medidas de reología. Ambos composites, malla-LNF y –LNC, después de ser tratados a 800 ºC durante 1000 h, han mostrado una adecuada adherencia entre sus componentes, observándose una ligera contaminación por cromo que se extiende a las primeras 35 μm del material cerámico, en el caso de malla-LNC. Los valores iniciales ASR, a 800 ºC, para los sistemas interconector-malla/LNC e interconector-malla/LNF han sido de 0.0046(1) y 0.0425(2) $\Omega \cdot cm^2$, respectivamente. En ambos casos, la alta estabilidad en la señal ASR y su bajo valor están en buen acuerdo con la adherencia observada entre el interconector y composite, a través de la sección transversal de cada una de las celdas, después de las medidas electroquímicas.

Para ambas celdas, los ensayos de larga duración a 800 ºC, han permitido evaluar la naturaleza protectora del composite, a través de la formación de la fase Fe_3O_4 en el canal del interconector expuesto directamente al aire. Asimismo, se han observado dos zonas en la superficie del composite: (i) área en contacto directo con el interconector, y (ii) área bajo el canal del interconector. En ambas superficies se ha detectado la formación de la fase de perovskita de cromo (P*bnm*) y la presencia de manganeso. Este contenido de manganeso se atribuye a la formación de una barrera de espinela de manganeso en la superficie del composite expuesta al interconector, reduciendo así la migración de cromo.

Finalmente, con objeto de mejorar las propiedades del composite desarrollado, se ha empleado una malla en la que previamente se ha depositado la capa protectora $MnCo_{1.9}Fe_{0.1}O_4$ (MCF). Los primeros ensayos muestran que la alta densidad y la homogeneidad de la capa depositada son factores clave para que ésta tenga efecto como barrera para el cromo.

Los resultados satisfactorios obtenidos para las celdas, interconector-malla/LNC e interconector-malla/LNF, han permitido continuar el estudio a partir de estas estructuras.

Relevant results*

*** A brief summary of the research papers results, which are included in the present section, is shown.**

The use of a channeled interconnect has led to the fabrication of a new contact material, which requires adequate mechanical integrity to provide the continuity of the coating on the interconnect, thus enhancing rapid oxidant transfer through interconnect-electrode interface. Hence, previously selected contact materials were applied onto Fe-22Cr mesh squares by dipping them into the ceramic slurries, thus, obtaining a new metallic/ceramic contact composite. Prior to forming the composite, adequate formulation of the paste was obtained and characterized by rheological measurements. Both materials, mesh-LNF and –LNC, showed good adherence between ceramic and metallic parts after heated at 800 ºC for 1000 h, showing a continuous and homogeneous layer. However, a chromium deposit ring along the edge of the LNF and LNC ceramic coatings, whose width was ~35 μm for mesh-LNC, was also observed. The initial ASR values, measured at 800 ºC, of interconnect-mesh/LNC and interconnect-mesh/LNF cells were 0.0046(1) y 0.0425(2) $\Omega \cdot cm^2$, respectively. For both systems, results from ASR tests showed a low and stable initial signal, and thus a good adherence between the interconnect and composite, in good agreement with each SEM cross-section of the post-test composite-coated interconnect cell.

Evaluation of the long-term chemical compatibility of the studied systems revealed that the direct exposure to air increased the oxidation of interconnect, leading to the growth of a Cr_2O_3 layer and formation of Fe_3O_4 oxide on the channel of the alloy substrate. Thus, both composite materials are acting as a protective layer. Moreover, two different areas were identified at the composite contact surface: the area of the composite (i) under the rib and, (ii) under channel of the interconnect. The formation of chromium perovskite (Pbnm) and the presence of manganese were detected on both surfaces. The presence of manganese is attributed to the formation of a low thickness Mn-spinel barrier layer, thereby reducing the migration of chromium.

In order to improve the properties of the developed composites, the effectiveness of using $MnCo_{1.9}Fe_{0.1}O_4$ (MCF) spinel to protect mesh, prior to coat with LNF or LNC conductive perovskite was also discussed. Starting results demonstrated that if the deposition of the protective coating was not enough to form a dense and continuous layer across the width of the mesh, then the use of MCF spinel layer is not enough to prevent chromium migration up to LNF and LNC ceramic coatings.

The achieved satisfactory results in both samples, interconnect-mesh/LNC and interconnect-mesh/LNF, have made possible to continue the study starting from these structures.

3.1. $LaNi_{0.6}Co_{0.4}O_{3-\delta}$ dip coated on Fe-Cr mesh as a composite cathode contact material on intermediate solid oxide fuel cells

Journal of Power Sources 269 **(2014)** 509-519.

Abstract

The feasibility of using Crofer22APU mesh dip coated with $LaNi_{0.6}Co_{0.4}O_{3-\delta}$ (LNC) ceramic paste as a uniform contact layer on a Crofer22APU channelled interconnect was studied. The control of LNC dip coating thickness on Fe-Cr mesh was carried out by rheological measurements of the suspension. SEM cross-section of formed composite contact material showed good adherence between ceramic and metallic components. The measured area specific resistance (ASR) value at 800 ºC was 0.46±0.01 $m\Omega \cdot cm^2$, indicating low contact resistance itself. The long term stability of metallic/ceramic composite was also studied. The contact resistance, when composite contact material was adhered to channelled Crofer22APU interconnect, was 5.40±0.01 $m\Omega \cdot cm^2$, which is a suitable value for the performance of IT-SOFC stack. The stability of the system after treating at 800 ºC for 1000 h was characterized using X-ray Micro-Diffraction (XRMD), Scanning Electron Microscope equipped with an Energy Dispersive X-ray analyzer (SEM-EDX) and X-ray Photoelectron Spectroscopy (XPS) techniques. The oxidation rate of the alloy and Fe_3O_4 phase formation were enhanced on the channels of the interconnect. Thus, the formation of CrO_3 (g) and $CrO_2(OH)_2$ (g) species was accelerated on the composite surface under the channel. Through XRMD and XPS analysis the coexistence of two perovskite phases (initial LNC and Cr-perovskite) was observed.

Keywords: IT-SOFC; Composite contact material; Channeled interconnect; Ohmic resistance losses; Electrical contact; $LaNi_{0.6}Co_{0.4}O_{3-\delta}$.

Highlights

- After 1000 h at 800 ºC LNC/Fe-Cr mesh still present adequate mechanical integrity.
- ASR value for LNC/Fe-Cr mesh with interconnect was 5.40±0.01 $m\Omega \cdot cm^2$ at 800 ºC.
- Cr deposition under the channel is higher than under the rib of the interconnect.

3.1.1. Introduction

Global warming and its detrimental climatological, ecological and sociological effects have led to an increasing interest in more efficient and clean power systems[1]. High temperature solid oxide fuel cells (HT-SOFCs, operating in the range of 800-1000 ºC) have a good potential for being used as stationary stand-alone power generation systems[2]. For these applications, chemical to electrical efficiency of HT-SOFC is in the range of 45-65 % [3]. For smaller scale applications, such as micro combined heat and power (micro-CHP), small auxiliary power units (APUs) and small electrical generators[4], there is a need to lower operation temperatures, into the intermediate temperatures (IT) range of 500-800 ºC. Lower temperature operation affords more rapid start-up and shut-down.

A single SOFC cell produces ~0.6-0.7 V under normal working conditions[3]. Therefore, in order to obtain the desired electric power output, single cells are connected and fabricated together to form a stack using interconnect and sealing materials[5]. In HT-SOFCs, the bond between the cell and the $LaCrO_3$ interconnect is typically realized by sintering at 1300 ºC. A solid bond with good electrical contact is obtained and no other contact material is then required. However, for IT-SOFC chromium-containing ferritic stainless steels are generally used as interconnect[6,7] and, contact materials are needed to provide a homogeneous bonding between interconnect and electrode to avoid power losses[8]. Previous studies[9,10], based on the effect of contact between electrode and current collector on the performance of SOFCs, concluded that when the contact area of the current collector increased from 4.6 % to 27.2 %, the cell resistance decreased from 1.43 to 0.19 $\Omega \cdot cm^2$ at 800 ºC.

The oxide scale formed on the surface of Fe-Cr alloys, after long exposure in the SOFC environment, results in volatile chromium (Cr) species such as CrO_3 and $Cr_2(OH)_2$ (in presence of vapor)[3]. These species can cause rapid performance deterioration in SOFCs due to the deposition of Cr at the bulk electrode and at the electrolyte/electrode interface regions[11]. The cathode contact

---

1 Klugman J., "Human Development Report 201. Sustainability and Equity: A Better Future for All", United Nations Development Programme, New York, USA, **2011**.

2 Spivey B.J., Edgar T.F. Dynamic modeling, simulation, and MIMO predictive control of a tubular solid oxide fuel cell. *J. Process Contr*. 22 (**2012**) 1502-1520.

3 Jiang S.P., Chen X. Chromium deposition and poisoning of cathodes of solid oxide fuel cells – A review. *Int. J. Hydrogen Energ*. 39(1) (**2014**) 505-531.

4 Huang K., Singhal S.C. Cathode-supported tubular solid oxide fuel cell technology: A critical review. *J. Power Sources* 237 (**2013**) 84-97.

5 Singhal S.C. Advances in solid oxide fuel cell technology. *Solid State Ionics* 135 (**2000**) 305-313.

6 Wu J., Liu X. Recent development of SOFC metallic interconnect. *J. Mater. Sci. Technol*. 26(4) (**2010**) 293-305.

7 Sun C., Hui R., Roller J. Cathode materials for solid oxide fuel cells: a review. *J. Solid State Electrochem*. 14 (**2010**) 1125-1144.

8 Mat A., Timurkutluk B., Timurkutluk C., Kaplan Y. Effects of ceramic based pastes on electrochemical performance of solid oxide fuel cell. *Ceram. Int*. 40 (**2014**) 8575-8583.

9 Guan W.B., Zhai H.J., Jin L., Li T.S., Wang W.G. Effect of contact between electrode and interconnect on performance of SOFC stacks. *Fuel Cells* 11(3) (**2011**) 445-450.

10 Wu W., Wang G.L., Guan W.B., Zhen Y.F., Wang W.G., *Fuel Cells* 5 (**2013**) 743. Wu W., Wang G.L., Guan W.B., Zhen Y.F., Wang W.G. Effect of contact method between interconnects and electrodes on area specific resistance in planar solid oxide fuel cells. *Fuel Cells* 5 (**2013**) 743-750.

11 Guan W., Jin L., Wu W., Zheng Y., Wang G.,Wang W.G. Effect and mechanism of Cr deposition in cathode current collecting layer on cell performance inside stack for planar oxide fuel cells. *J. Power Sources* 245 (**2014**) 119-128.

materials can act as a barrier to the migration of chromium from the metallic to the cathode and further minimize the area specific resistance (ASR) between both materials[12-14].

The cathode contact materials compositions should fulfill the following requirements[15,16]: i) high electrical conductivity and appropriate sintering activity to minimize the resistance of the contact layer itself and to protect the steel substrate from excessive oxidation, ii) chemically compatible and appropriate thermal expansion behavior with adjacent materials and, iii) high thermochemical and structural stability in the oxidizing cathode environment. The materials used as contact layers include: i) noble metals (Ag) or noble metal-perovskite composites (Ag-$(La_{0.6}Sr_{0.4})(Co_{0.8}Fe_{0.2})O_3$, Ag-$La_{0.8}Sr_{0.2}MnO_3$), ii) conventional perovskite cathode materials (such as, $La_{0.6}Sr_{0.4}Co_{0.2}Fe_{0.8}O_3$, $La_{0.8}Sr_{0.2}FeO_3$), iii) oxides with a spinel structure, M_3O_4 (M=Ni, Mn, Co, Cu, Fe), or iv) recently developed oxides like $Ni_{0.33}Co_{0.67}O$. Despite the interactions of these kind of materials which formed oxide scale on metal surface, due to their susceptibility to form phases like Ag_2CrO_4, $AgCrO_2$, $SrCrO_4$, Cr-spinels or Cr-perovskites, the use of those materials, in most cases, are quite effective for improving the electrical contact between the cathodes and metallic interconnects[17-25]. In addition, these materials can reduce the oxidation rate of the steel and minimize the formation of new phases arising from the oxidation of metal itself such as, Fe_2O_3 and Fe_3O_4 [26]. In this study, $LaNi_{0.6}Co_{0.4}O_{3-\delta}$ (LNC) ceramic composition was selected, due to the adequate sintering activity, electrical conductivity and thermal expansion coefficient (TEC)[17], coupled with ferritic stainless steel Crofer22APU mesh to form a ceramic/metallic composite contact material. Crofer22APU was

---

[12] Montero X., Tietz F., Stöver D., Cassir M., Villarreal I. Comparative study of perovskites as cathode contact materials between a $La_{0.8}S_{r0.2}FeO_3$ cathode and a Crofer22APU interconnect in solid oxide fuel cells. *J. Power Sources* 188 (**2009**) 148-155.

[13] Jin L., Guan W., Niu J., Ma X., Wang W.G. Effect of contact area and depth between cell cathode and interconnect on stack performance for planar solid oxide fuel cells. *J. Power Sources* 240 (**2013**) 796-805.

[14] Zhang W., Wang F., Wang K., Pu J., Chi B., Jian L. Chemical compatibility and electrical contact between Ni–Cr–Mo alloy and $LaCo_{0.6}Ni_{0.4}O_{3-\delta}$ in intermediate temperature solid oxide fuel cells. *Int. J. Hydrogen Energ*. 37 (**2012**) 17253-17257.

[15] Wang F., Yan D., Zhang W., Chi B., Pu J., Jian L. $LaCo_{0.6}Ni_{0.4}O_{3-\delta}$ as cathode contact material for intermediate temperature solid oxide fuel cells. *Int. J. Hydrogen Energ*. 38 (**2013**) 646-651.

[16] Yang Z., Xia G., Singh P., Stevenson J.W. Electrical contacts between cathodes and metallic interconnects in solid oxide fuel cells. *J. Power Sources* 155 (**2006**) 246-252.

[17] Morán-Ruiz A., Vidal K., Laguna-Bercero M.A., Larrañaga A., Arriortua M.I. Effects of using $(La_{0.8}Sr_{0.2})_{0.95}Fe_{0.6}Mn_{0.3}Co_{0.1}O_3$ (LSFMC), $LaNi_{0.6}Fe_{0.4}O_{3-\delta}$ (LNF) and $LaNi_{0.6}Co_{0.4}O_{3-\delta}$ (LNC) as contact material on solid oxide fuel cells. *J. Power Sources* 248 (**2014**) 1067-1076.

[18] Tucker M.C., Cheng L., DeJonghe L.C. Selection of cathode contact materials for solid oxide fuel cells. *J. Power Sources* 196 (**2011**) 8313-8322.

[19] Tucker M.C., Cheng L., DeJonghe L.C. Glass-containing composite cathode contact materials for solid oxide fuel cells. *J. Power Sources* 196 (**2011**) 8435-8443.

[20] Tucker M.C., Cheng L., De Jonghe L.C. Inorganic binder-containing composite cathode contact materials for solid oxide fuel cells. *J. Power Sources* 224 (**2013**) 174-179.

[21] Lu Z., Xia G., Templeton J.D., Li X., Nie Z., Yang Z., Stevenson J.W. Development of $Ni_{1-x}Co_xO$ as the cathode/interconnect contact for solid oxide fuel cells. *Electrochem. Commun*. 13 (**2011**) 642-645.

[22] Fu Q.X., Sebold D., Tietz F., Buchkremer H.P. Electrodeposited cobalt coating on Crofer22APU steels for interconnect applications in solid oxide fuel cells. *Solid State Ionics* 192 (**2011**) 376-382.

[23] Shaigan N., Ivey D.G., Chen W. Co/$LaCrO_3$ composite coatings for AISI 430 stainless steel solid oxide fuel cell interconnects. *J. Power Sources* 185 (**2008**) 331-337.

[24] Wilkinson L.T., Zhu J.H. Ag-Perovskite composite materials for SOFC cathode-interconnect contact. *J. Electrochem. Soc.* 156(8) (**2009**) B905-B912.

[25] Montero X., Jordán N., Pirón-Abellán J., Tietz F., Stöver D., Cassir M., Villarreal I. Spinel and perovskite protection layers between Crofer22APU and $La_{0.8}Sr_{0.2}FeO_3$ cathode materials for SOFC interconnects. *J. Electrochem. Soc*. 156(1) (**2009**) B188-B196.

[26] Miguel-Pérez V., Martínez-Amesti A., Nó M.L., Larrañaga A., Arriortua M.I. Oxide scale formation on different metallic interconnects for solid oxide fuel cells. *Corros. Sci*. 60 (**2012**) 38-49.

developed to increase the electrical conductivity of the scale and to reduce the chromium vaporization. This is achieved by adding 0.5% Mn in its composition which facilities the $(Cr,Mn)_3O_4$ spinel formation[3]. The use of a high conductivity perovskite type material in conjunction with stainless steel mesh is expected to improve current collection. At the same time, it achieves a continuous contact on the ribs without sacrificing the flow of the air through the channels. Taking into account our previous studies[17,27] the use of this composite material between Crofer22APU interconnect and $La_{0.6}Sr_{0.4}FeO_3$ cathode in flow channel configuration, can offer an adequate mechanical integrity and low reactivity between the applied layers without compromising the contact resistance of the system.

The goal of this work is to develop a metallic/ceramic composite contact material achieving a good bonding between this contact material and the channeled metallic interconnect. An adequate formulation of the LNC ceramic slurry was set and then dip coated[28,29] on Crofer22APU mesh. The electrical resistance, chemical compatibility and adherence between ceramic and metallic parts of the composite material, under long term IT-SOFC operating conditions, were determined. Results of electrical performance of the contact material/interconnect system are presented. In addition, long-term contact stability of the metallic/ceramic composite material under the rib (direct contact) and channel (indirect contact) of the interconnect was analyzed.

In order to understand the interactions between the Crofer22APU alloy and the LNC ceramic material the following issues were considered[3,30]: i) the preoxidized alloys form protective and semi-conductive chromia oxide and a dense and stable $(Cr,Mn)_3O_4$ spinel on the surface of the alloy, which is effective to reduce the generation of volatile Cr species ii) the reason for the Cr volatility is the thermodynamic instability of chromia scales formed on the alloy, forming gaseous species (CrO_x (x=1,2,3)); and iii) the deposition process of Cr species at the ceramic coating, under SOFC operation conditions, can be described by the nucleation deposition theory.

3.1.2. Experimental

The formulation of ceramic powder used in this study was $LaNi_{0.6}Co_{0.4}O_{3-\delta}$ (LNC) (NexTech, Fuel Cell Materials). To obtain metallic/ceramic contact composite, Crofer22APU stainless steel mesh (Fiaxell SOFC Technologies), with mesh opening of about 175 μm and a thickness of 250 μm, was cut into 10 x 10 mm squares, cleaned with acetone in an ultrasonic bath and dried. The squared-meshes squares were preoxidized at 600 ºC for 10 h and then dip coated with a LNC ceramic paste (dip coating rate = 4.5 mm/s). The chemical composition of the steel, as given by the supplier, is listed in Table 3.1.

---

[27] Morán-Ruiz A., Vidal K., Larrañaga A., Arriortua M.I. Chemical compatibility and electrical contact of $LaNi_{0.6}Co_{0.4}O_{3-\delta}$ (LNC) between Crofer22APU interconnect and $La_{0.6}Sr_{0.4}FeO_3$ (LSF) cathode for IT-SOFC. *Fuel Cells* 13(3) (**2013**) 398-403.

[28] Torabi A., Etsell T.H., Sarkar P. Dip coating fabrication process for micro-tubular SOFCs. *Solid State Ionics* 192 (**2011**) 372-375.

[29] Conceição L., Dessemond L., Djurado E., Souza M.M.V.M. Thin films of $La_{0.7}Sr_{0.3}MnO_{3+\delta}$ dip-coated on Fe-Cr alloys for SOFC metallic interconnect. *Int. J. Hydrogen Energ*. 38 (**2013**) 15335-15347.

[30] Hilpert K., Das D., Miller M., Peck D.H., Wei R. Chromium vapor species over solid oxide fuel cell interconnect materials and their potential for degradation processes. *J. Electrochem. Soc*. 143 (**1996**) 3642-3647.

Table 3.1. Composition of the Crofer22APU steel in wt%.

	Cr	Fe	Mn	Ti	Si	Al	La	Others
Crofer22APU	22	Bal.*	0.5	0.1	0.25	0.25	0.15	0.28

* Balance

The ceramic slurry was composed of ceramic powder (LNC), dispersant (Dolapix, Zschimmer & Schwarz, Chemische Fabriken), binder (PVB, polyvinyl butyral, Solutia Solutions) and solvent (ethanol, Panreac). The paste composition was based on the formulation shown in Table 3.2. Particle size distribution of the ceramic powder was carried out using a Mastersizer particle size analyzer (Malvern Instruments). Rheology of the suspensions was analyzed using a rheometer (HAAKE MARS II) at shear rates from 0.1 s^{-1} to 1000 s^{-1}, and at room temperature. Ceramic/metallic material was sintered at 1050 ºC for 2 h [9] and then treated at 800 ºC for 1000 h, in open air.

Table 3.2. Ceramic slurry composition prepared for dip-coating.

Ceramic slurry composition	Volume %
Ceramic powder, LNC	12.5
EtOH	87.5
Dispersant, Dolapix	1% regarding to the ceramic powder
Binder, PVB	5% regarding to the ceramic powder

The composite contact material was bonded to a Crofer22APU channeled interconnect (ThyssenKrupp VDM). The channels of substrate are 2 mm width, 0.5 mm depth, 10 mm length and the distance between neighboring is 2 mm (Fig. 3.1). The substrate was cut into 10 x 10 mm and 1 mm thick pieces, polished using #800 grit SiC paper and then, cleaned with acetone in an ultrasonic bath and dried. Subsequently, they were preoxidized at 800 ºC for 100 h. An additional layer of LNC was coated on the ribs of the interconnect substrate by colloidal spray technique[31]. The composite contact material was directly adhered to the interconnect, sintered at 1050 ºC for 2h and then treated at 800 ºC for 1000 h. The reactivity between the contact material and the rib and channel of the Fe-Cr interconnect, after long term heated at 800 ºC in open air, was characterized according to the scheme shown in Fig. 3.1. All the experiments were performed in open air so the moisture level in the incoming air stream can be establish considering that the water vapor (H_2O) in air is around 0.001-5 % by volume. However, these values depend on the temperature so it was difficult to determine a moisture numerical value in the performed experiments. Nevertheless, in order to analyze Cr species formation over the chromium scale it has been considered a wet atmosphere.

[31] Miguel Pérez V., "Interconectores metálicos y capas protectoras para su aplicación en pilas SOFC", Ph.D. thesis work, UPV/EHU, (**2013**).

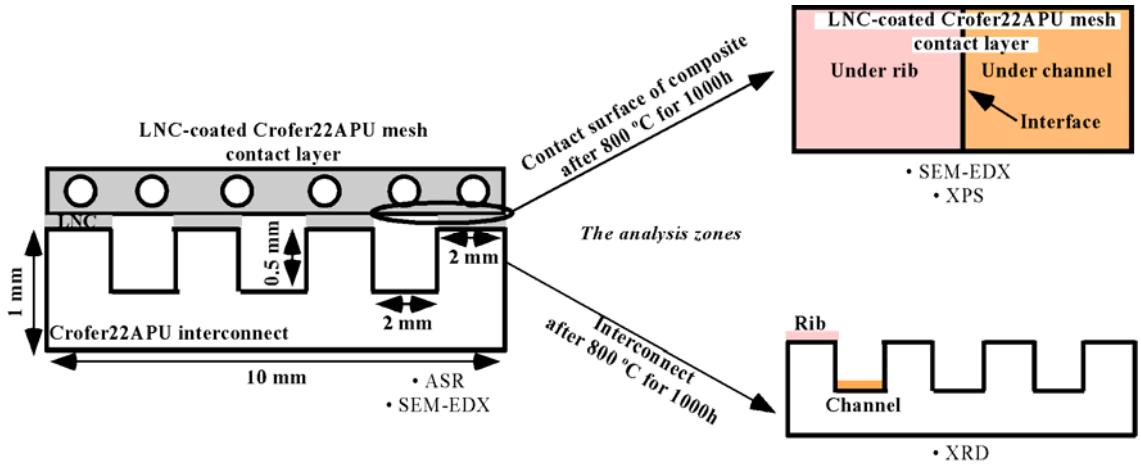

Figure 3.1. Schematic representation of the characterization of {LNC dip-coated on Crofer22APU mesh composite contact material/ Crofer22APU channeled interconnect} system.

X-ray micro-diffraction (XRMD) data were collected using a Bruker D8 Discover diffractometer equipped with a Cu Twist tube, Ni filter (λ = 1.5418 Å), PolyCap^{TM} (1μ single crystal cylinders) system for parallel been generation (divergence of 0.25°), and a 1-D LynxEye PSD detector (active length in 2θ 2.7º). The sample was mounted on an Eulerian Cradle with automatic controlled X-Y-Z stage. The sample illumination was adjusted with 1mm PinHole collimator in the incident beam, the position control was tested by using the interference of two lasers. Data were collected from 10 to 100° 2θ (step size = 0.04 and time per step = 10 s total time 6.5h) at RT.

Surface and cross-section of the samples were analyzed by a scanning electron microscope (SEM, JEOL LSM-6400) equipped with an Oxford Pentafet energy dispersive X-ray analyzer (EDX). Secondary electron images (SE) were taken at 20 kV and $1.1 \cdot 10^{-11}$ A using a working distance of 7 mm. Composition analysis was performed using back-scattered electrons (BSE) at 20 kV accelerating voltage, $1 \cdot 10^{-9}$ A current density and 15 mm working distance. For the cross-section analysis, samples were embedded in epoxy resin, polished using standard metallographic techniques, and coated with a coal graphite layer (10 nm) that was deposited by evaporation (BLA-TEC SCD 004 Sputter Coater) to provide electrical conductivity. INCA 350 software (Oxford Instrument) was used to reconstruct the spectra, and Fe, Cr, Mn and a LNC pellet were used as standards.

X-ray photoelectron spectroscopy (XPS) measurements were carried out in a SPECS (Berlin, Germany) system equipped with a Phoibos 150 1D-DLD analyzer and monochromatic Al K_α radiation (1486.6 eV). The analysis of the present elements were made at wide scan mode (step energy 1 eV, dwell time 0.1 s, pass energy 80 eV) and after that, high-resolution spectra of the found elements were acquired (step energy 0.1 eV, dwell time 0.1 s, pass energy 20 eV) with an electron take-off angle of 90 º. The binding energies were calibrated using C1s peak (BE = 284.6 eV) as an internal standard.

Area Specific Resistance (ASR) measurements were performed using the DC four-probe method (the resistance value was estimated from the voltage value (Thurlby Thandar Instruments 1604 Digital Multimeter) measured on applying a current of 1A (Thurlby Thandar Instruments PL300

current source)[32], on both LNC dip-coated Crofer22APU mesh composite (Fig. 3.2(a)) and on a system, which was prepared according to the geometries shown in Fig. 3.2(b), in open air.

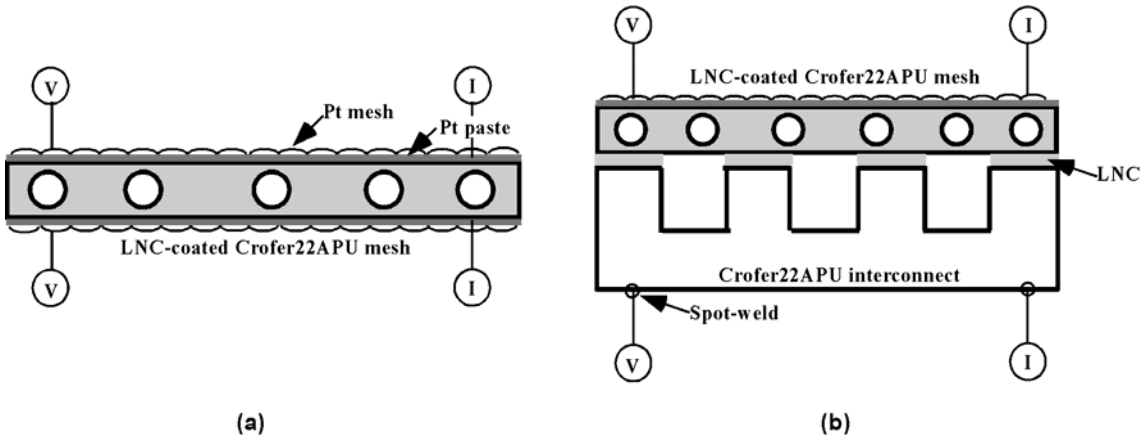

Figure 3.2. Schematic view of the system configuration for ASR measurements for: a) composite contact material and b) composite contact material on channeled interconnect.

Electrical contacts between samples and external measuring circuit were made using two Pt wires directly welded onto the sides of the interconnect, and using Pt paste and Pt mesh onto the surface of the composite contact material.

3.1.3. Results and discussion

3.1.3.1. Control of LNC dip coating thickness on Fe-Cr mesh

Prior to the rheological characterization, particle size distribution measurements were performed on LNC powders, since this parameter influences the rheological properties. Fig. 3.3 shows a monomodal size distribution of LNC powder (d_{50}: 2.37 μm). The characterization of LNC slurries by rheological measurements is important to control coated thicknesses during the dip coating process.

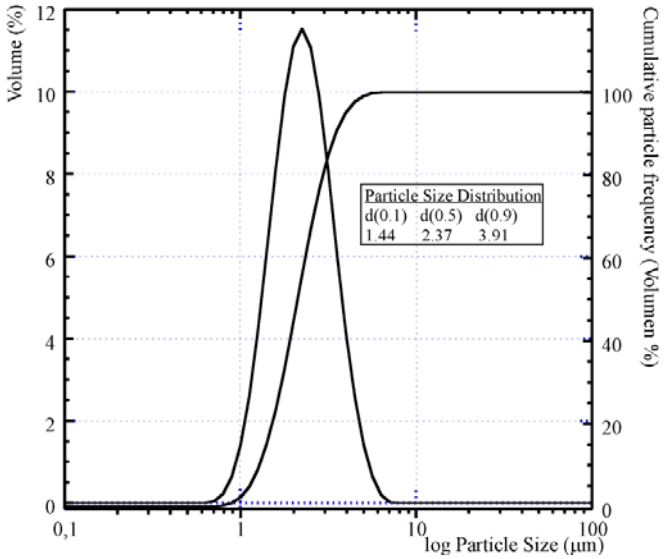

Figure 3.3. Particle size distribution of LNC powder.

[32] Schroder D.K. Semiconductor material and device characterization, 3rd Edition, John Wiley & Sons, New York, Cap. 3, p. 149-156, **1998**.

A summary of the composition of the slurry is shown in table 3.2. Rheological characterization of the suspensions showed a newtonian fluid behavior, which means that the viscosity values are independent of the shear rate. Typical viscosity values are in the range of 0.054 Pa·s, leading to a LNC thickness of the layers after dip-coating and sintering of ~500 µm.

3.1.3.2. Characterization of composite contact material

LNC ceramic slurries were dip coated on preoxidized Crofer22APU stainless steel mesh and sintered at 1050 ºC for 2h in order to form the composite contact material. Fig. 3.4 shows surface morphology SEM micrographs of Fe-Cr mesh before and after sintering the LNC layers. The area specific resistance (ASR) value of the metallic/ceramic composite material was 0.46±0.01 mΩ·cm^2 at 800 ºC. This minimal ASR value confirms that the use of this composite material as a contact layer is adequate.

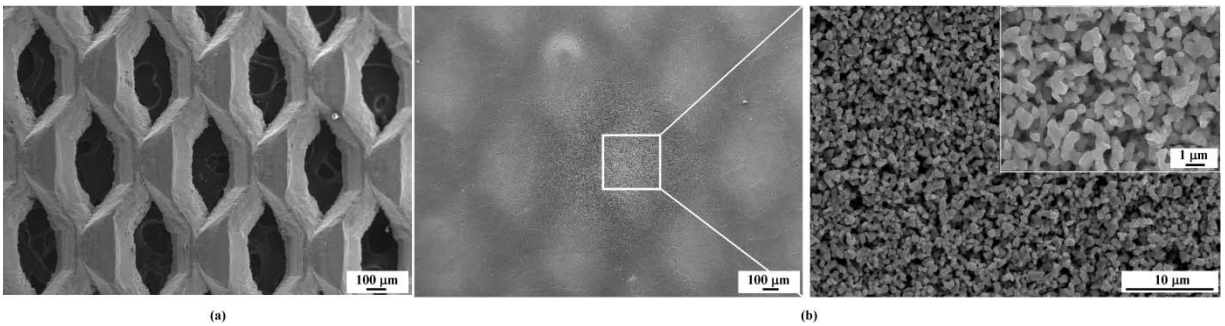

Figure 3.4. Surface SEM micrographs of Fe-Cr mesh: a) before and b) after sintered LNC.

SEM cross-section (Fig. 3.5) of the obtained ceramic-metallic composite contact material, after ASR measurements, showed good adherence between LNC ceramic material and Crofer22APU mesh, due to similar TEC values between Crofer22APU and LNC materials[17].

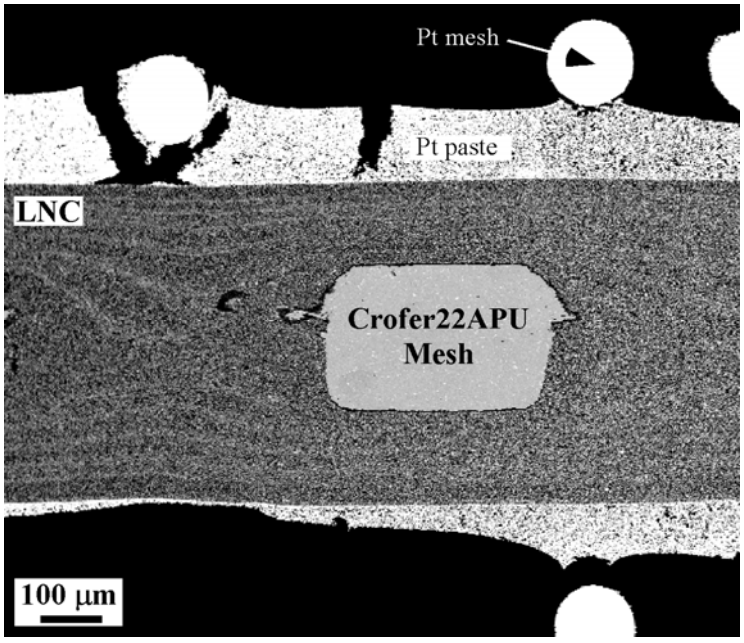

Figure 3.5. SEM cross-section of the ceramic/metallic composite contact material after ASR measurements.

As observed from figure 3.5, the ceramic coating is continuous and homogenous along the sample.

3.1.3.2.1. Long term stability of composite contact material

In order to study the chemical compatibility and also to establish the adherence between the ceramic and metallic parts, the sintered at 1050 ºC composite contact material was heated at 800 ºC for 1000 h, in open air. EDX mapping (Fig. 3.6 and 3.7) were performed of a cross-section of the composite material after long-term operation was performed, and compared with another sample just sintering at 1050 ºC for 2 h used to establish initial reactivity. According to figure 3.6, the initial material showed a Cr_2O_3 and $(Mn,Cr)_3O_4$ spinel protection layer to minimize Cr migration through ceramic coated, as expected. Nevertheless, the formed passive chromia layer is not enough to prevent the migration of Cr since the evaporation of protective chromia layer takes place. Early investigations[33] revealed that $(Mn,Cr)_3O_4$ spinel offers lower volatility of Cr than chromia. However, this reduction is less than an order of magnitude. Thus, a Cr deposit ring along the edge of the LNC ceramic coated, whose width was ~35 μm, was also observed. The redeposition of chromium at the contact material, usually as poor conductive phases, could decrease the cell performance[34].

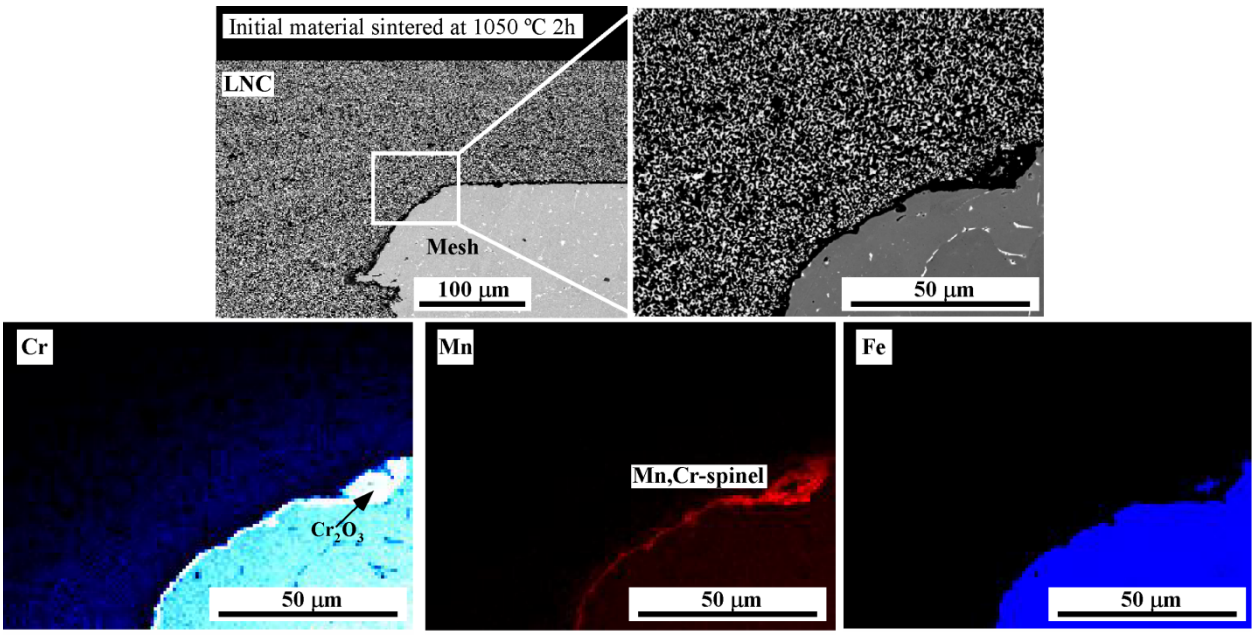

Figure 3.6. Cross-section of composite contact material after sintering at 1050 ºC for 2 h in air and EDX mapping of the selected zone (in white continuous line).

The direct contact between the ceramic contact material and the alloy makes possible solid phase diffusion of Cr[35]. However, the microstructure of the ceramic material revealed open porosity in the initial material and composite after heating at 800 ºC for 1000 h in open air, allowing vapor phase

[33] Choi J.P., Weil K.S., Chou Y.M., Stevenson J.W., Yang Z.G. Development of MnCoO coating with new aluminizing process for planar SOFC stacks. *Int. J. Hydrogen Energ.* 36 (**2011**) 4549-4556.

[34] Miguel-Pérez V., Martínez-Amesti A., Nó M.L., Larrañaga A., Arriortua M.I. The effect of doping $(Mn,B)_3O_4$ materials as protective layers in different metallic interconnects for solid oxide fuel cells. *J. Power Sources* 243 (**2013**) 419-430.

[35] Lau G.Y., Tucker M.C., Jacobson C.P., Visco S.J., Gleixner S.H., DeJonghe L.C. Chromium transport by solid state diffusion on solid oxide fuel cell cathode. *J. Power Sources* 195 (**2010**) 7540-7547.

transport of volatile Cr-species (CrO_3 (g), $CrO_2(OH)_2$ (g)) throughout the LNC coating. It has been found that[36] the most dominant chromium species are CrO_3 in dry air and $CrO_2(OH)_2$ in humidified air. However, the partial pressure of $CrO_2(OH)_2$ and CrO_3 varies significantly with the temperature. At the temperature decreases, $CrO_2(OH)_2$ species become increasingly dominant. The partial pressure of CrO_3 decreases rapidly with the decrease of temperature while the change in the partial pressure of $CrO_2(OH)_2$ with the temperature is relatively small. So, when the samples are sintered at 1050 ºC, considering a wet atmosphere, the main chromium vapor specie is $CrO_2(OH)_2$. Besides, it could be found CrO_3 because its partial pressure is still high. However, when the samples are treated at 800 ºC, the partial pressure of CrO_3 is low being the dominant specie chromium oxyhydroxide. The deposition process of these Cr species at the contact material can be described by the nucleation reaction between the high valence Cr phases and the nucleation agents (Ni^{2+}, Co^{2+}), forming Cr-Ni^{2+},Co^{2+}-O nucleus. The reaction between these nucleus, gaseous Cr compounds and nucleation agents leads to the deposition and formation[3] of Cr_2O_3, $(Cr,Mn)_3O_4$, $CoCr_2O_4$, etc. One should consider that[37] the magnitude of the Cr deposition is smaller with reducing the test temperature, using the same time exposure in each experiment. Thus, in first sintering step at 1050 ºC the Cr deposition is accelerated by temperature and, in the long heat treatment at 800 ºC by the exposure time. Thus, different ceramic material densifications were observed between the initial material and composite after the long term treatment, showing that the latter was denser. The formation of dense new phases like spinels might change the pore distribution of the ceramic material. Therefore, the microstructure of the ceramic coating depends on the reactions undergone by the material.

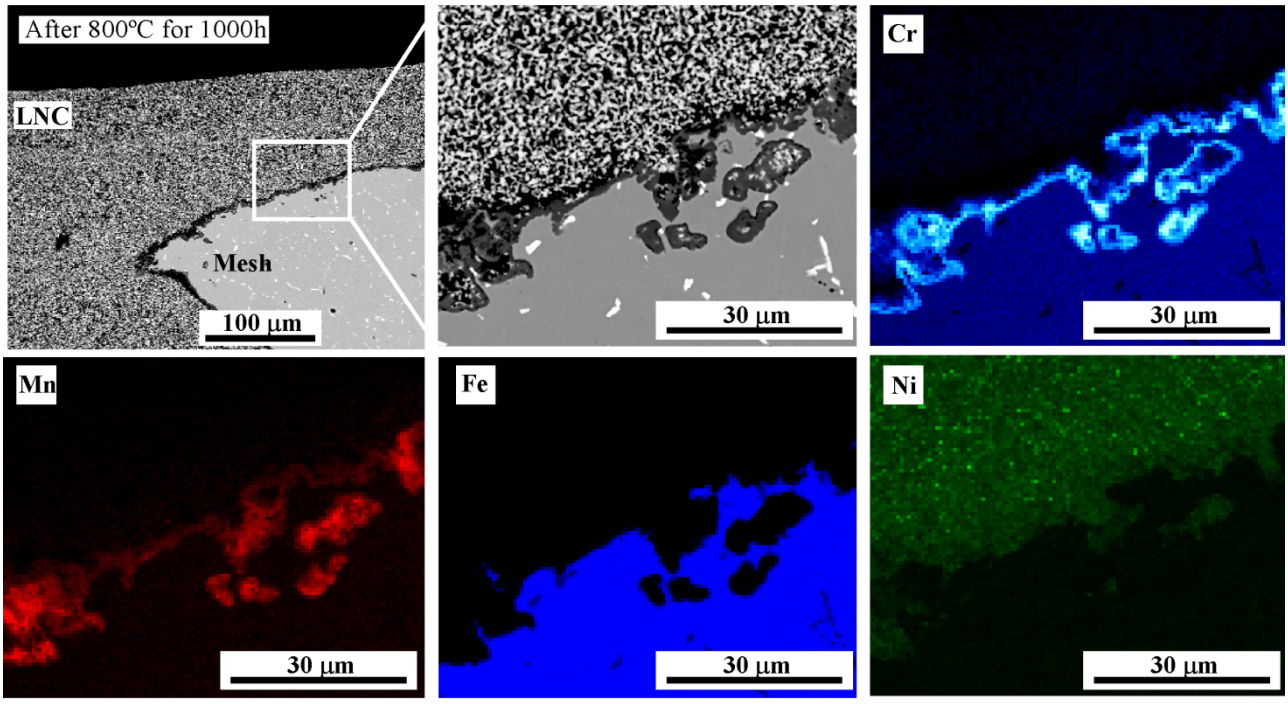

Figure 3.7. Cross-section of composite contact material after heating at 800 ºC for 1000 h in air and EDX mapping of the selected zone (in white continuous line).

[36] Chen X., Zhen Y., Li J., Jiang S.P. Chromium deposition and poisoning in dry and humidified air at $(La_{0.8}Sr_{0.2})_{0.9}MnO_{3+\delta}$ cathodes of solid oxide fuel cells. *Int. J. Hydrogen Energ.* 35 (**2010**) 2477-2485.

[37] Jiang S.P., Zhang S., Zhen Y.D. Early interaction between Fe-Cr alloy metallic interconnect and Sr-doped $LaMnO_3$ cathodes of solid oxide fuel cells. *J. Mater. Res.* 20(3) (**2005**) 747-758.

High magnification cross-sectional BSE micrographs and the corresponding EDX elemental line scans of the initial (Fig. 3.8a) and treated (Fig. 3.8b) material are shown in Fig. 3.8. According to other studies[38,39], the oxide scale growth rate is strongly affected by the temperature. With increasing temperature the growth rate constant increases exponentially. Besides, it was found[40] the chromium oxide scale rates at longer exposure time, on the cathode side, can be interpreted as being parabolic. Thus, the oxide scale formed on the mesh after 1000 h was slightly more noticeable. According to Ref.[41] and taking into account the Fe-Cr phase diagram[42], the oxide scale formed on mesh steel surface, after the sintering process of the composite at 1050 ºC, is formed by FCC-Fe/Cr_2O_3 in contact with the stainless steel and, by Fe_2O_3 as the oxide surface. Between these two layers, several oxides may form, such as, Fe_3O_4, FeO, $(Cr,B)_3O_4$ spinel (B= Co, Fe, Mn, Ni)[43-45]. The similar ionic radii of Co, Fe, Mn and/or Ni, make it difficult to determine the exact chemistry of the grown spinel. At 800 ºC the composition of the oxide scale has a similar trend to that at 1050 ºC. However, in the oxide/metal interface Cr_2O_3 may form instead of FCC-Fe/Cr_2O_3 as in the 1050 ºC case. These results are in good agreement with performed EDX line scans (Fig. 3.8a and 3.8b).

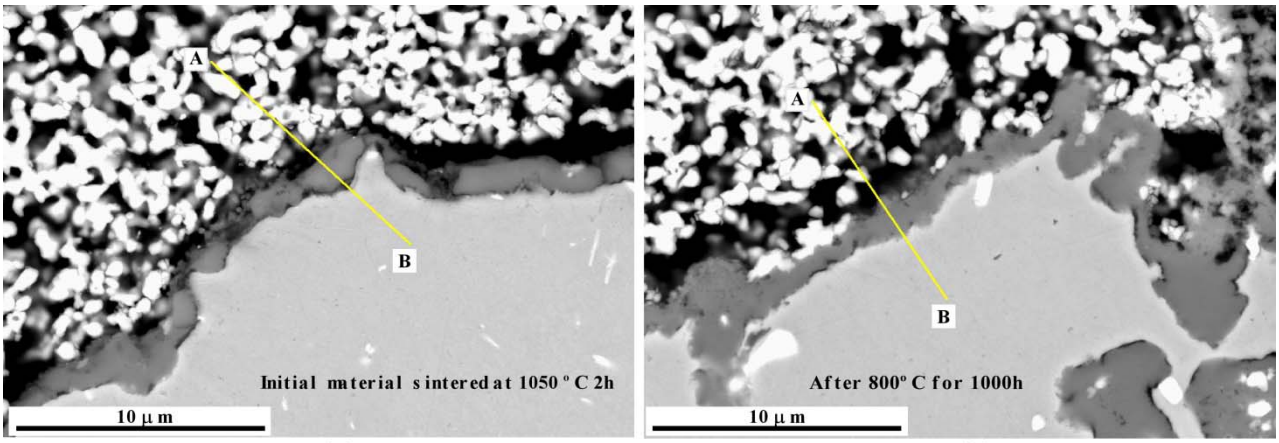

(a) **(b)**

Figure 3.8. Cross-sectional BSE images and the corresponding EDX elemental line scans of a) initial material and b) composite after the long heat treatment.

[38] Kofstad P., High Temperature Corrosion, Elsevier Applied Science, London, **1988**.

[39] Palcut M., Mikkelsen L., Neufeld K., Chen M., Knibbe R., Hendriksen P.V. Corrosion stability of ferritic stainless steels for solid oxide electrolyser cell interconnects. *Corros. Sci*. 52 (**2010**) 3309-3320.

[40] Linder M., Hocker T., Holzer L., Friedrich K.A., Iwanschitz B., Mai A., Schuler J.A. Cr_2O_3 scale growth rates on metallic interconnectors derived from 40.000 h solid oxide fuel cell stack operation. *J. Power Sources* 243 (**2013**) 508-518.

[41] Dheeradhada V.S., Cao H., Alinger M.J. Oxidation of ferritic stainless steel interconnects: thermodynamic and kinetic assessment. *J. Power Sources* 196 (**2011**) 1975-1982.

[42] Andersson J.O., Sundman B. Thermodynamic properties of the Cr-Fe system. *Calphad* 11 (**1987**) 83-92.

[43] Wang K., Liu Y., Fergus J.W. Interaction between SOFC interconnect coating materials and chromia. *J. Am. Ceram. Soc.* 94(12) (**2011**) 4490-4495.

[44] Shong W.J., Liu C.K., Chen C.Y., Peng C.C., Tu H.J., Fey G.T.K., Lee R.Y., Kao H.M., Effects of lanthanum-based perovskite coatings on the formation of oxide scale for ferritic SOFC interconnect. *Mater. Chem. Phys*. 127 (**2011**) 45-50.

[45] Przybylski K., Brylewski T., Durda E., Gawel R., Kruk A. Oxidation properties of the Crofer 22 APU steel coated with $La_{0.6}Sr_{0.4}Co_{0.2}Fe_{0.8}O_3$ for IT-SOFC interconnect applications. *J. Therm. Anal. Calorim*. 116 (**2014**) 825-834.

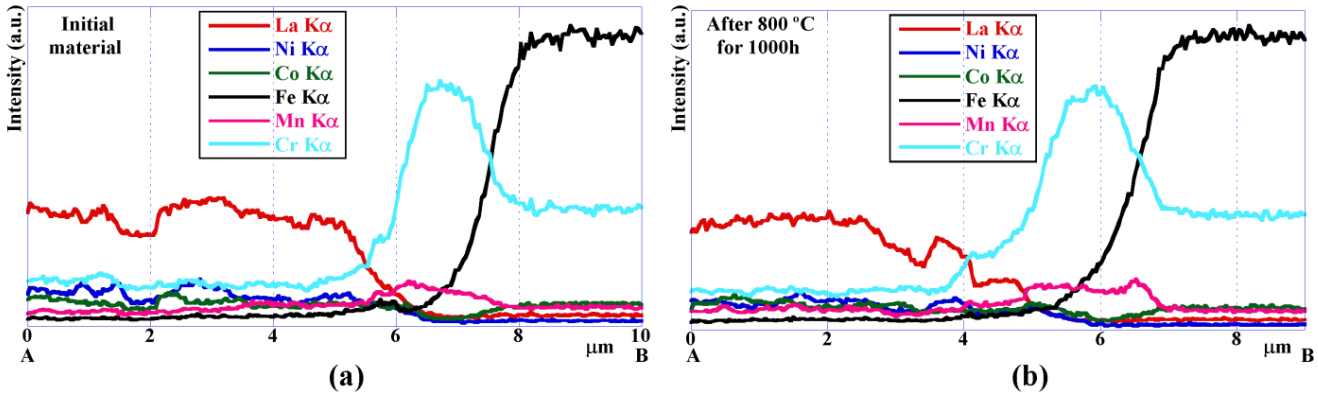

Figure 3.8.cont. Cross-sectional BSE images and the corresponding EDX elemental line scans of a) initial material and b) composite after the long heat treatment.

The formation of iron oxides in oxide scale makes alloy be more susceptible to breakaway oxidation[46]. The white zones observed on alloys (Fig. 3.8) were identified as LNC contamination due to the polishing process. Besides, locally internal precipitates of Cr_2O_3 followed by $(Mn,Cr)_3O_4$ spinel were also found (Fig. 3.7). These internal precipitates could be related to the external oxide scale or it could be that the diffusion rate of oxygen in the alloy was stronger than that of Cr, forming internal Cr_2O_3 precipitates[47].

3.1.3.3. Characterization of composite contact material with channeled Crofer22APU interconnect

As starting point, the metallic substrates were oxidized at 800 ºC for 100 h. This preoxidation of the steel may reduce Cr and Fe transport into the contact coating after long oxidation times[48]. A composite contact material without sintering was directly adhered to preoxidized channeled Crofer22APU interconnect. In order to achieve good adhesion between both materials, the ribs of the interconnect substrate were coated with LNC ceramic material by colloidal spray. Then, the system composed of {composite contact material/channeled interconnect} was sintered at 1050 ºC for 2h in open air. In order to check the reproducibility of the process, different systems were prepared. Fig. 3.9 and Table 3.3 show ASR values of two systems, indicating good stability and similar signal during the contact resistance measurements, and thus a good adherence between the composite contact material and the interconnect.

[46] Essuman E., Meier G.H., Zurek J., Hänsel M., Norby T., Singheiser L., Quadakkers W.J. Protective and non-protective scale formation of NiCr alloys in water vapour containing high- and low-pO_2 gases. *Corros. Sci*. 50(6) (**2008**) 1753-1760.

[47] Ali-Löytty H. Microalloying mediated segregation and interfacial oxidation of FeCr alloys for solid-oxide fuel cell applications, Ph.D. thesis work, Tampere University of Technology, **2013**.

[48] Hoyt K.O., Gannon P.E., White P., Tortop R., Ellingwood B.J., Khoshuei H. Oxidation behavior of $(Co,Mn)_3O_4$ coatings on preoxidized stainless steel for solid oxide fuel cell interconnects. *Int. J. Hydrogen Energ.* 37 (**2012**) 518-529.

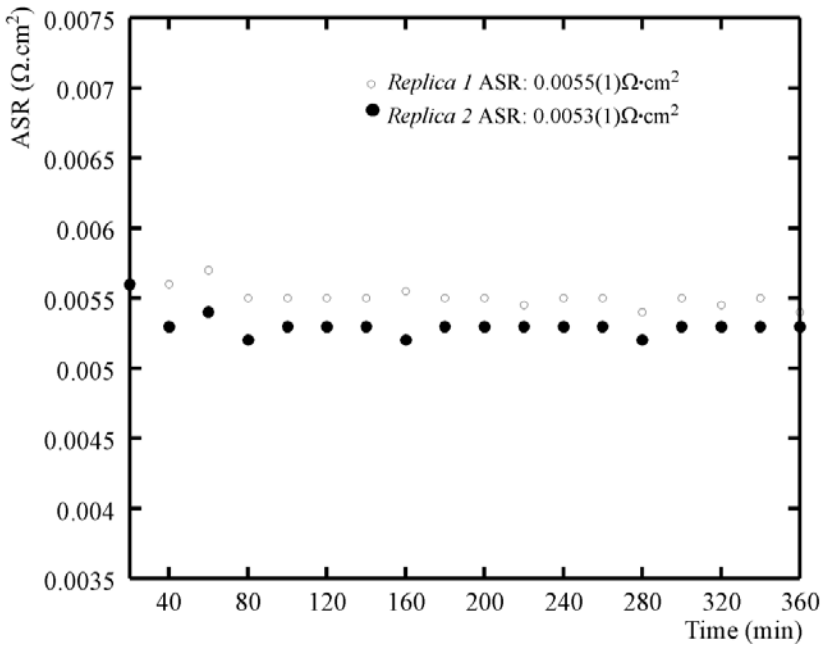

Figure 3.9. ASR for {composite contact material/channeled interconnect} interface as a function of time.

The ASR values are in good agreement with those obtained in {Crofer22APU interconnect without channels/ LNC contact layer/ $La_{0.6}Sr_{0.4}FeO_3$ cathode} system[17]. The contact composite/interconnect ASR value was 5.40±0.01 mΩ·cm^2, which is a suitable value for the performance of IT-SOFC stack. In addition, the obtained ASR value is lower than the systems without applying a contact layer[12,16,17].

Table 3.3. Area specific resistance values for composite contact material, with and without interconnect, measured at 800 ºC in air.

Sample	≈ ASR (mΩ·cm^2)
Composite contact material	0.46±0.01
Replica 1	5.50±0.01
Replica 2	5.30±0.01

According to SEM cross-section of the system after ASR measurements with EDX mapping to estimate element diffusion (Fig. 3.10), the formed oxide scale acts as protective layer: Cr_2O_3 followed by $(Cr,Mn)_3O_4$ spinel top layer.

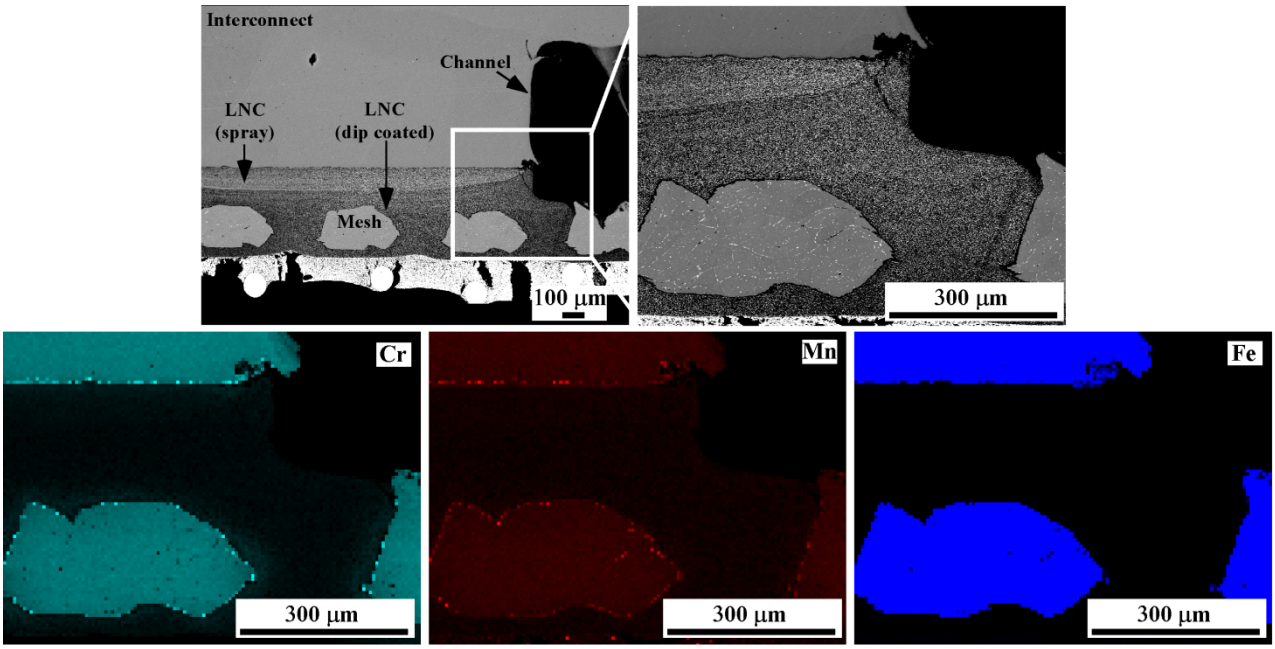

Figure 3.10. Cross-section of {composite contact material/channeled interconnect} sintered system after ASR test and EDX mapping of the selected zone (in white continuous line).

The composite direct contacted (the rib) and indirect contacted (channel) with the interconnect present similar Cr, Mn and Fe distributions. Along the ceramic bulk, Cr^{3+} and Mn^{2+} deposition was observed, indicating that Mn dopant promotes Cr deposition on the ceramic material.

3.1.3.3.1. Long term stability of composite contact material with channeled Crofer22APU interconnect

The {LNC dip-coated on Crofer22APU mesh composite contact material/ Crofer22APU channelled interconnect} sintered system at 1050 ºC, was treated at 800 ºC for 1000 h in open air to study the long term compatibility between the metallic substrate and the composite. Fig. 3.11 shows X-ray micro-diffraction pattern refinements performed on the rib (right) and the channel (left) of the interconnect in contact with the composite material, after the long term treatment.

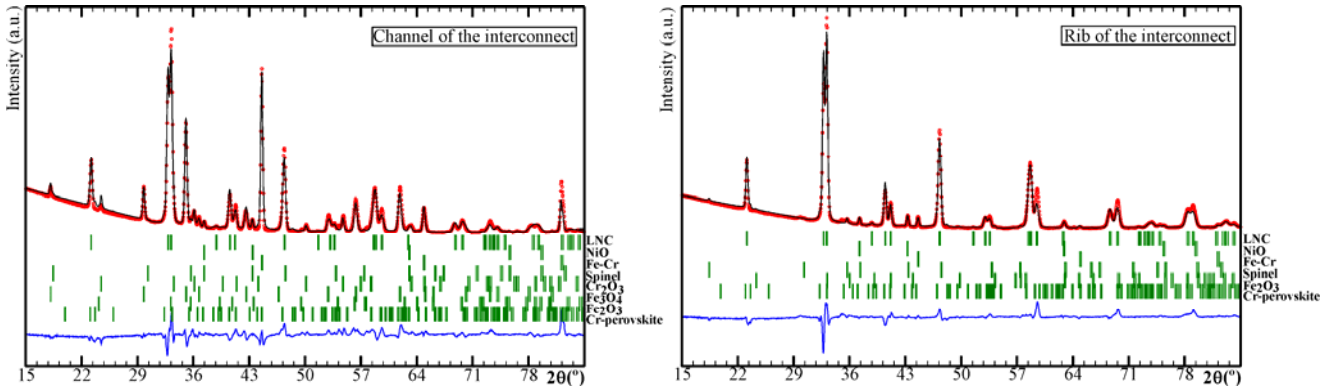

Figure 3.11. X-ray micro-diffraction pattern refinements performed on the rib and on channel of the interconnect in contact with composite material, after long-term heat treatment.

The preliminary analysis of the studied points was carried out using the X´Pert HighScore software 2003. After the identification, the observed phases, in both areas, were quantified; full-profile refinements were performed using the FULLPROF program[49]. The formed phases and their semiquantitative analysis (% in weight) are presented in Table 3.4.

Table 3.4. Semiquantitative % in weight of the formed phases on the rib and channel of the interconnect in contact with composite material after heating at 800 ºC for 1000 h.

Phases	Space Group	Nº PDF	Channel	Rib
$LaNi_{0.6}Co_{0.4}O_3$	R-*3c*	32-0296	~ 46	~ 82
$LaCrO_3$	P*bnm*	24-1016	~ 6	~ 7
Fe-Cr	I*m3m*	34-0396	< 2	< 2
Fe_2O_3	R-*3c*	73-2234	< 2	~ 2
NiO	F*m-3m*	73-1519	~ 2	~ 5
$MnCr_2O_4$	F*d-3m*	31-630	< 2	< 2
Cr_2O_3	R-*3c*	85-0730	~ 4	-
Fe_3O_4	F*d-3m*	19-629	~ 36	-

* Estimated error: ± 1-2 %.

These analyses reveal that in the rib zone the main phases were $LaNi_{0.6}Co_{0.4}O_{3-\delta}$, La(Cr, B)$O_3$ (B= Ni, Co) and NiO. In addition, secondary phases were also detected: Fe-Cr, $(Cr,B)_3O_4$ spinel (B= Co, Fe, Mn, Ni) and Fe_2O_3. In contrast, the channel zone present as main phases $LaNi_{0.6}Co_{0.4}O_{3-\delta}$, Fe_3O_4, La(Cr, B)O_3 (B= Ni, Co), Cr_2O_3 and as secondary phases: Fe-Cr, (Cr, B)$_3O_4$ (B= Co, Fe, Mn, Ni) spinel and Fe_2O_3. The original Fe-Cr substrate was identified indicating that the X-ray penetration was enough to observe the signal of all the formed layers. The quality factors of the refinements are given in Tables 3.5 and 3.6.

Table 3.5. The quality of refinement performed on the rib of the interconnect in contact with composite material, after long term heat treatment.

Rib Phases	$LaNi_{0.6}Co_{0.4}O_3$	$LaCrO_3$	Fe-Cr	Fe_2O_3	NiO	$MnCr_2O_4$
R_{Bragg}	13	29	31	30	16	40
R_f	8	23	16	24	9	18
χ^2			5			

Table 3.6. The quality of refinement performed on the channel of the interconnect in contact with composite material, after heated at 800 ºC for 1000 h.

Channel Phases	$LaNi_{0.6}Co_{0.4}O_3$	$LaCrO_3$	Fe-Cr	Fe_2O_3	NiO	$MnCr_2O_4$	Cr_2O_3	Fe_3O_4
R_{Bragg}	13	32	21	43	13	32	31	18
R_f	10	25	11	29	11	21	18	11
χ^2				18				

The presence of the LNC perovskite phase in the channel zone is probably due to the contamination during the spray deposition on the ribs. The presence of NiO might entail that Ni is partially extracted from the LNC perovskite lattice, whereas Cr is incorporated, most likely to form

[49] Rodríguez-Carvajal J., Fullprof Rietveld Pattern Matching Analysis of Power Patterns, Grenoble, **1994**.

La(Ni, Co, Cr)O_3 [27,50]. It is known that applying a protective layer to the metallic interconnect alloy can reduce the oxidation rate[34]. Fig. 3.12 shows cross-section EDX elemental line scans performed on the channel (Fig. 3.12a) and on the rib (Fig. 3.12b) of the interconnect, which was in contact with the composite material after treated at 800 ºC for 1000h in open air.

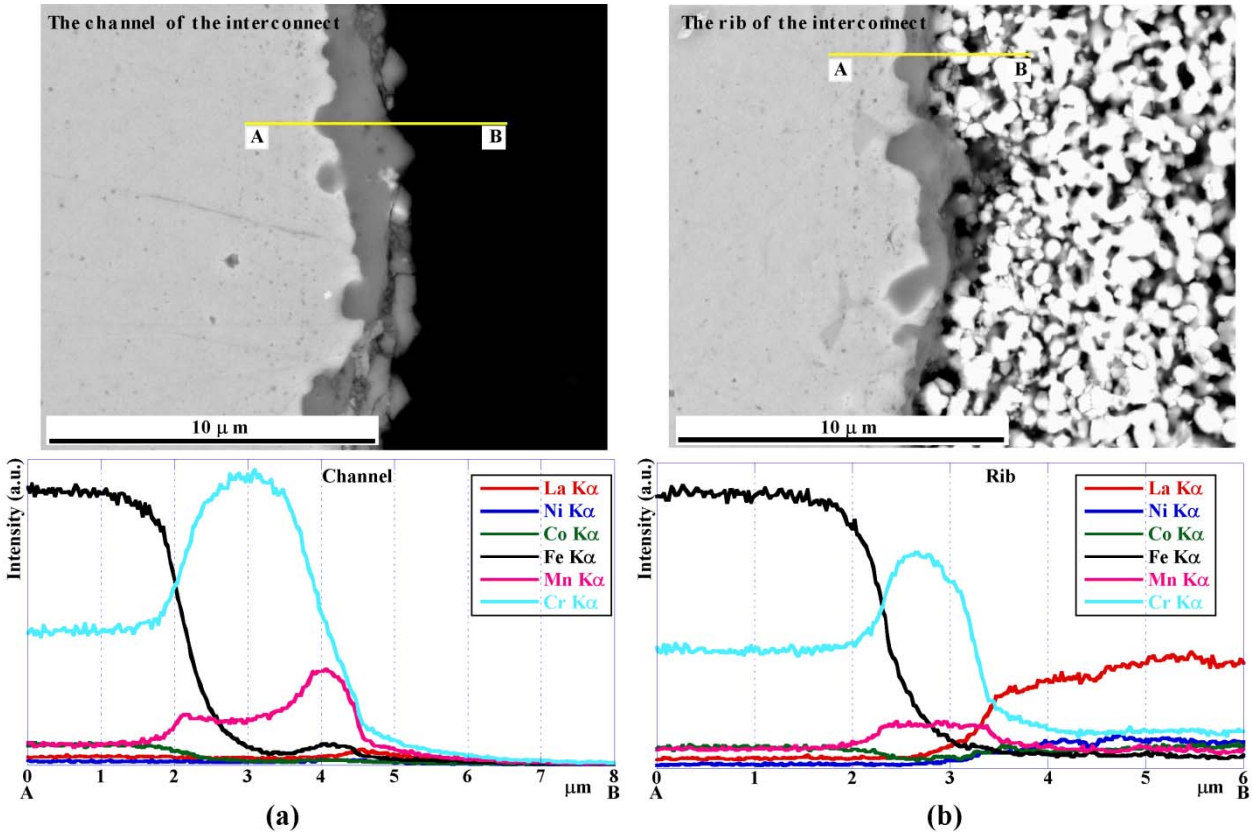

Figure 3.12. Cross-sectional BSE images and the corresponding EDX elemental line scans performed on a) the channel and b) the rib of the interconnect which was in contact with the composite contact material after treated at 800 ºC for 1000 h in open air.

The surface oxide layers, both on the channel and on the rib, of the interconnect range from approximately 0.5 to 2 μm. Before ASR test, the metallic substrate was preoxidized at 800 ºC for 100 h, making difficult to observe differences between both zones. However, the Fe and Cr detected in the channel is bigger than in the rib, probably due to the formation of a passive layer on the metal surface, more severe in the case of an uncoated area. According to this, ceramic coating might act as a protective layer. Hence, Cr_2O_3 is observed on the channels. Furthermore, the absence of Cr_2O_3 on the rib of the interconnect, can also imply that it has completely reacted to form La(Cr, B)O_3 (B= Ni, Co) and (Cr, B)$_3O_4$ (B= Mn, Fe, Ni, Co) phases. The formed oxides at analyzed channel zones contain: Fe_2O_3 (<2 % in weight) and Fe_3O_4 (~36 % in weight) whereas for those on the rib zone, Fe_2O_3 (~2 % in weight) was semi-quantified. The presence of iron oxides is in good agreement with the previous studies performed on composite contact material. According to XRMD results, an interconnect without ceramic coating at long exposure rate to air, can promote the Fe_3O_4 formation

[50] Stodolny M.K., Boukamp B.A., Blank D.H.A., Van Berkel F.P.F. La(Ni,Fe)O_3 stability in the presence of chromia-A solid-state reactivity study. *J. Electrochem. Soc.* 158(2) (**2011**) B112-B116.

rather than the formation of a chromia/spinel protective scale, concluding in the formation of non-protective or Fe-rich scale.

Fig. 3.13 shows the surface of the composite material which was in contact with the interconnect, after long term IT-SOFC conditions. EDX mapping analysis is also shown. Three different areas were identified at the composite contact surface: the area of the composite i) under the rib and, ii) under channel of the interconnect and, iii) the interface between both zones. Formation of Cr and Mn deposit along the interface of both areas is observed, probably in the form of $(Cr,Mn)_3O_4$ protective spinel. Besides, EDX analysis showed that the zone under the channel presents Cr, Mn and La enrichment, possibly associated with Cr-Mn-spinel and Cr-perovskite crystalline phases.

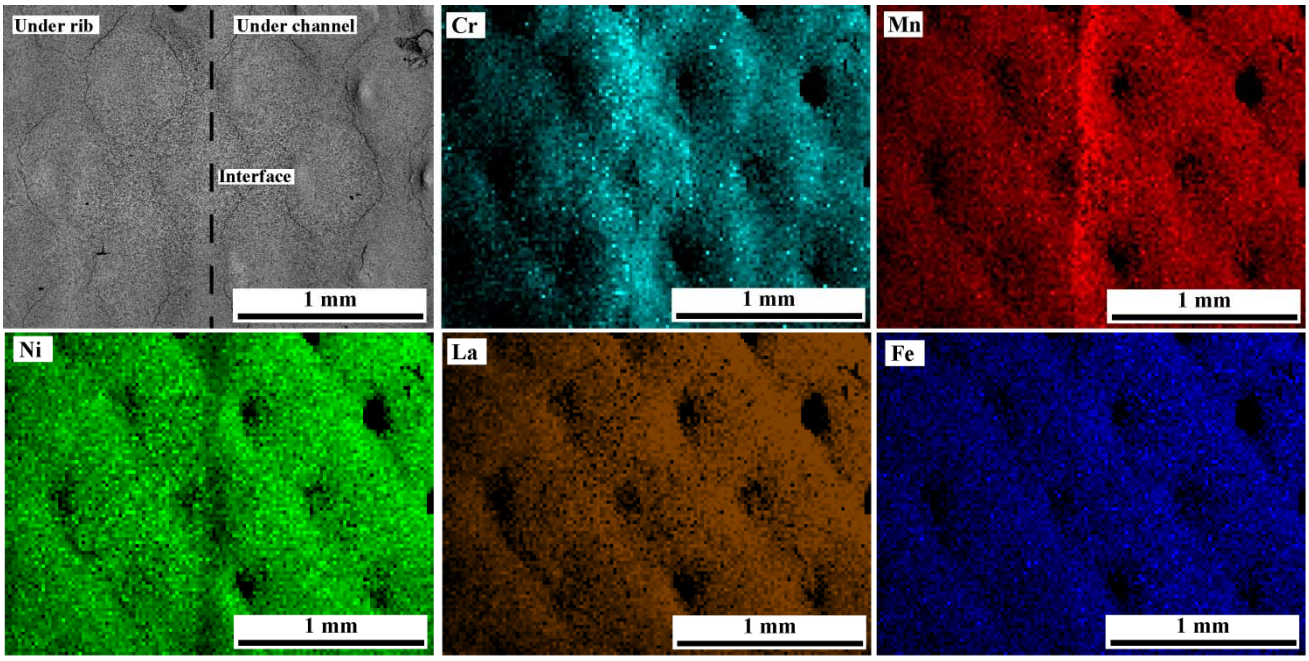

Figure 3.13. EDX mapping of the surface of the composite material which was in contact with interconnect, after long term IT-SOFC conditions.

The significant difference in the amount of Cr deposition on the composite material surface under the rib and under the channel of the interconnect can indicate that the direct exposure to air accelerates the formation of CrO_3 (g) and $CrO_2(OH)_2$ (g) species. Thus, vapor phase transport of Cr specie molecules would be much faster and more significant than the solid phase diffusion of atoms, in LNC and chromia scale, through defects in these solids. Increasing volatile Cr species enhances Cr-depletion from the alloy, thereby enabling the formation of iron oxides[46].

XPS measurements were performed on the observed channel and rib contact areas of the surface of the metallic/ceramic composite material. Fig. 3.14 shows high resolution spectra of the different zones including La $3d_{5/2}$, Cr 2p and Mn $2p_{3/2}$ spectral regions.

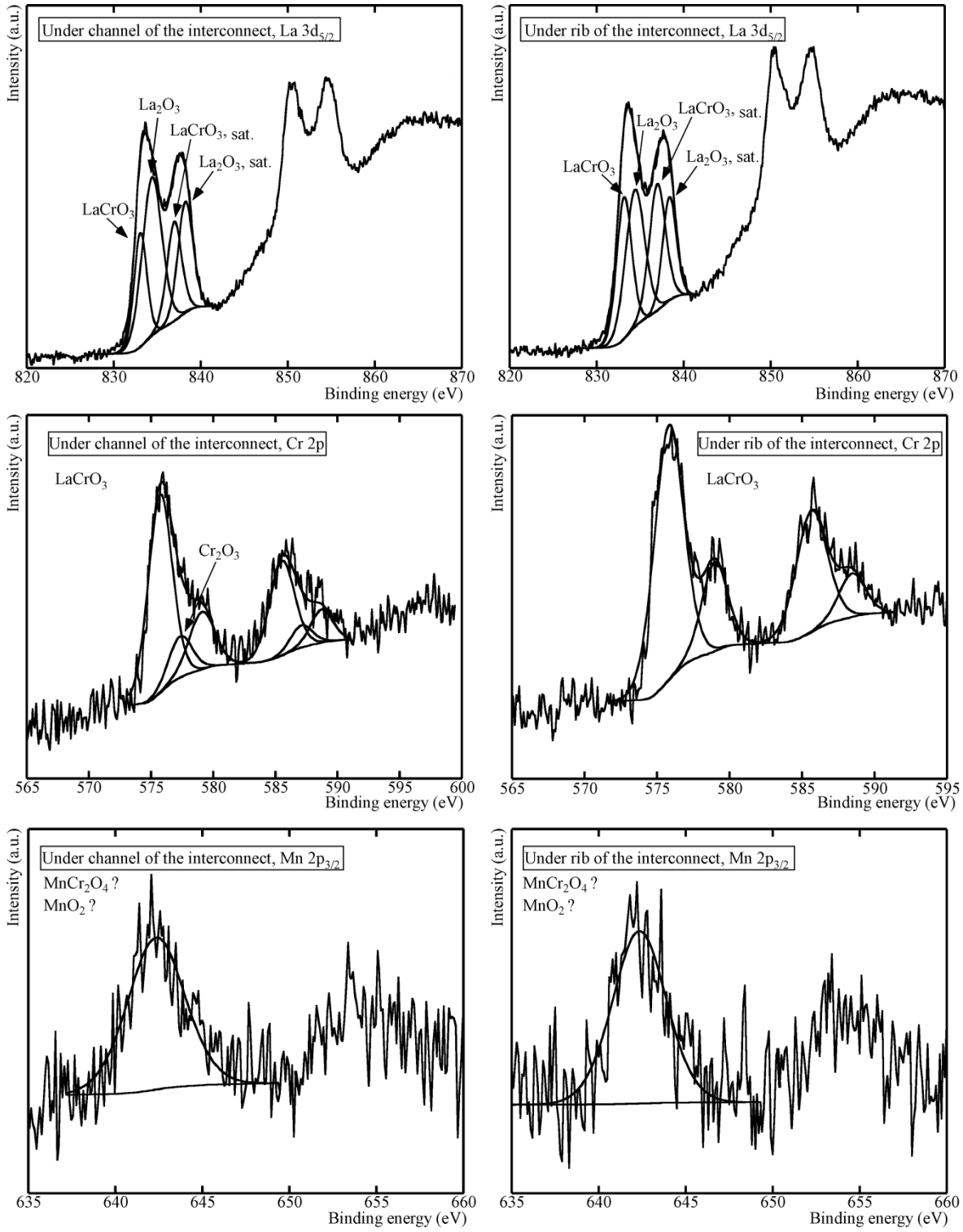

Figure 3.14. La $3d_{5/2}$, Cr 2p and Mn $2p_{3/2}$ spectral regions of the surface of composite contact material under the rib and channel after long term heated at 800 ºC in air.

The binding energies and relative atomic percentage concentration of the detected elements are listed in Tables 3.7 and 3.8, respectively. In both studied areas, for La, there are two peaks, one at

833 eV which corresponds to La^{3+} in perovskite phase[51] and, another at 834 eV which is assigned to La^{3+} in La_2O_3 [52]. In addition, the peaks appearing at 575 eV and 579 eV could be assigned to Cr^{3+} in perovskite[53,54]. The atomic concentration of Cr assigned to the perovskite remains a ratio of 1:1, and La component is assigned to the binding energy of 833 eV, in good agreement with ABO_3 structure (Tables 3.7 and 3.8).

Table 3.7. XPS analysis results of the detected elements for the contact surface of the composite in contact with the rib of the interconnect, after heating at 800 ºC for 1000 h in air.

Peak	Binging energy (eV)	% At. Conc.
La $3d_{5/2}$ in ABO_3	833.14	9.5
La $3d_{5/2}$ in La_2O_3	834.4	9.1
Cr 2p in ABO_3	575.82; 578.98	9.1
Mn $2p_{3/2}$	642.35	3.2
O 1s	528.93; 530.74	69.1

Table 3.8. XPS analysis results of the detected elements for the contact surface of the composite under channel of the interconnect, after heating at 800 ºC for 1000 h in air.

Peak	Binging energy (eV)	% At. Conc.
La $3d_{5/2}$ in ABO_3	833.07	7.1
La $3d_{5/2}$ in La_2O_3	834.41	11.8
Cr 2p in ABO_3	575.73; 579.1	7.2
Cr 2p in Cr_2O_3	577.35	1.1
Mn $2p_{3/2}$	642.34	3.2
O 1s	528.98; 530.99	69.6

In the contact channel zone, the peak at 577 eV might be ascribed to Cr^{3+} species, possibly forming Cr_2O_3 [55] in good agreement with XRD results. The binding energy of 642 eV, which corresponds to $Mn2p_{3/2}$, is in good agreement with Mn^{4+} in MnO_2 superficial oxide[56]. However, the content of Mn is too low to be assigned to Mn^{2+} or Mn^{4+} species.

---

51 Bin F., Song C., Lu G., Song J., Gong C., Huang Q. $La_{1-x}K_xCoO_3$ and $LaCo_{1-y}Fe_yO_3$ perovskite oxides: preparation, characterization, and catalytic performance in the simultaneous removal of NO_x and diesel soot. *Ind. Eng. Chem. Res*. 50 (**2011**) 6660-6667.

52 Wagner C.D., Riggs W.M., Davis L.E., Moulder J.F., Mullenberg G.E., *Handbook of X-ray Photoelectron Spectroscopy*, Perkin-Elemer Corporation, Physical Electronics Division, Eden Prairie, MN 55344, **1979**.

53 Howng W.Y., Thorn R.J. Investigation of the electronic structure of $La_{1-x}(M^{2+})_xCrO_3$, Cr_2O_3 and La_2O_3 by X-ray photoelectron spectroscopy. *J. Chem. Phys. Solids* 41 (**1980**) 75-81.

54 Stojanovic M., Haverkamp R.G., Mims C.A., Moudallal H., Jacobson A.J. Synthesis and characterization of $LaCr_{1-x}Ni_xO_3$ perovskite oxide catalysts. *J. Catal*. 165 (**1997**) 315-323.

55 Battistoni C., Dormann J.L., Fiorani D., Paparazzo E., Viticali S. An XPS and Mössbauer study of the electronic properties of $ZnCrxGa_{2-x}O_4$ spinel solid solutions. *Solid State Commun*. 39(4) (**1981**) 581-585.

56 Aoki A. X-ray photoelectron spectroscopic studies on ZnS: MnF_2 phosphors. *Jpn. J. Appl. Phys*. 15 (**1976**) 305-311.

3.1.4. Conclusions

The application of composite LNC/Crofer22APU mesh coatings as a contact material for Fe-Cr channelled interconnect was studied as a solution to limit electrical losses between both materials and also to reduce chromium migration from the interconnect. Prior to forming the composite material, adequate formulation of the LNC paste was obtained and characterizated by rheological measurements. This slurry was dip coated on Fe-Cr mesh to obtain metallic-ceramic composite contact material. The results showed good adherence between ceramic and metallic material, showing a continuous and homogeneous coated LNC layer. The system presented an ASR value of 0.46±0.01 $m\Omega \cdot cm^2$ at 800 ºC. After treatment under long term IT-SOFC conditions, the composite material still present noticeable oxide scale and adequate mechanical integrity of the LNC/Fe-Cr mesh interface.

When the composite contact material was directly adhered to the interconnect, the obtained ASR values were reproducible and stable indicating good adherence between the composite material and interconnect. After 1000h at 800 ºC in open air, X-ray micro-diffraction, performed at the rib and channel of the interconnect, revealed interactions between the oxide scale and the LNC material to form Cr-perovskite which was related with NiO presence. In both zones semi-quantified Fe_2O_3 was also present, arising from the oxidation of the metal itself. According to XRMD results, the interconnect without ceramic coating on the metal surface, and the direct exposure to air increased the oxidation rate and Fe_3O_4 formation as non-protective layer. The direct exposure to air accelerates the formation of CrO_3 (g) and $CrO_2(OH)_2$ (g) species on channel surface.

Taking into account the obtained contact resistance, mechanical integrity and chemical compatibility of the studied system, LNC dip-coated on Fe-Cr mesh would offer promising opportunities as a high conductivity composite contact material. Future work will include the integration of the $La_{0.6}Sr_{0.4}FeO_3$ cathode to form {interconnect/composite contact material/cathode} system, in flow channel configuration, to study its long-term stability in terms of contact resistance and chemical compatibility.

3.2. Evaluation of using protective/conductive coating on Fe-22Cr mesh as a composite cathode contact material for intermediate solid oxide fuel cells

Int. J. Hydrogen Energ. 40 **(2015)** 4804-4818.

An uncoated and $MnCo_{1.9}Fe_{0.1}O_4$ (MCF) coated Fe-22Cr meshes were dipped into $LaNi_{0.6}Fe_{0.4}O_{3-\delta}$ (LNF) slurry to form a continuous protective/conductive layer for Crofer22APU interconnect. After aged these samples at 800 ºC for 1000 h, energy dispersive X-ray (EDX) results concluded that: if the deposition of the protective coating was not enough to form a dense and continuous layer across the width of the mesh, then the use of MCF spinel layer is not enough to prevent chromium migration. For mesh-LNF/interconnect structure the area specific resistance (ASR) value of 0.0425(2) $\Omega \cdot cm^2$ was stable for 400 min at 800 ºC, indicating initial good adherence between both materials. After aged this structure at 800 ºC for 1000 h, without applying a current source, X-ray micro-diffraction (XRMD) results, performed at the rib and channel of the interconnect, revealed that the LNF material is acting as a protective layer. Moreover, X-ray photoelectron spectroscopy (XPS) analysis indicated that manganese is concentrated on the mesh/LNF contact surface.

Keywords: SOFC; Composite contact coating; channeled interconnect; chromium poisoning; contact resistance.

Highlights

- Long-term stability of protective/conductive coating on Fe-Cr mesh was studied.
- ASR value of Fe-Cr mesh coated with LNF/interconnect interface was 0.0425(2) $\Omega \cdot cm^2$.
- Mn is concentrated on the composite surface in contact with channeled interconnect.

3.2.1. Introduction

Alternative technologies need to be developed for long-term sustainable energy supply due to socio-political, economic and environmental problems associated with the burning of fossil fuels. Solid oxide fuel cells (SOFCs) have the potential to be efficient and cost-effective system for the direct conversion of a wide variety of fuels to clean electricity. These benefits will only be achieved by society if SOFC technology can become commercially available[57,58].

Despite SOFC advantages, they still have problems related to: i) poor contact between cell component and ii) microstructure degradation of the porous electrodes due to chromium poisoning[59,60]. Growth of a poorly conductive oxide layer between the metallic interconnect ribs and the electrode results in a lack of contact between both materials. Moreover, the use of ferritic steel substrates is associated with another issue called "cathode Cr poisoning"[61]. Thus, the application of conductive/protective coatings acting as an adhesive to connect cathode with substrate, and as chromium diffusion barrier and oxide scale inhibitor is the subject of many research[62-64]. It is important to ensure that the materials exhibit high chemical and microstructural stability, high electrical conductivity, compatibility with the interconnect materials, reasonable thermal compatibility match with other cell components, and high sinterability to ensure high mechanical strength and good bonding with the adjacent components[65,66]. Various materials have been used in an effort to inhibit Cr migration from the chromia-rich subscales and to improve oxide scale-to-electrode adhesion, reducing oxide growth kinetics. Basically, SOFC interconnect coatings fall into four main categories[65]: reactive element oxides (REOs), MAlCrYO (M represents a metal, e.g., Co, Mn, Ti or Ni), conductive perovskites and spinels.

---

57 Millar L., Taherparvar H., Filkin N., Slater P., Yeomans J. Interaction of $(La_{1-x}Sr_x)_{1-y}MnO_3$-$Zr_{1-z}Y_zO_{2-\delta}$ cathodes and $LaNi_{0.6}Fe_{0.4}O_3$ current collecting layers for solid oxide fuel cell application. Proceedings of the **2008** Conference for the Engineering Doctorate in Enviromental Technology.

58 Sharaf O.Z., Orhan M.F. An overview of fuel cell technology: Fundamentals and applications. *Renew. Sust. Energ. Rev.* 32 (**2014**) 810-853.

59 Guan W., Jin L., Wu W., Zheng Y., Wang G.,Wang W.G. Effect and mechanism of Cr deposition in cathode current collecting layer on cell performance inside stack for planar oxide fuel cells. *J. Power Sources* 245 (**2014**) 119-128.

60 Guan W.B., Jin L., Ma X., Wang W.G. Investigation of impactors on cell degradation inside planar SOFC stacks. *Fuel Cells* 6 (**2012**) 1085-1094.

61 Schuler J.A., Wuillemin Z., Hessler-Wyser A., Comminges C., Steiner N.Y., Van Herle J.. Cr-poisoning in $(Ls,Sr)(Co,Fe)O_3$ cathodes after 10.000 h SOFC stack testing. *J. Power Sources* 211 (**2012**) 177-183.

62 Tucker M.C., Cheng L., DeJonghe L.C. Selection of cathode contact materials for solid oxide fuel cells. *J. Power Sources* 196 (**2011**) 8313-8322.

63 Guan W.B., Zhai H.J., Jin L., Li T.S., Wang W.G. Effect of contact between electrode and interconnect on performance of SOFC stacks. *Fuel Cells* 3 (**2011**) 445-450.

64 Stodolny M.K., Boukamp B.A., Blank D.H.A., Van Berkel F.P.F. Cr-poisoning of $LaNi_{0.6}Fe_{0.4}O_3$ cathode under current load. *J. Power Sources* 209 (**2012**) 120-129.

65 Shaigan N., Qu W., Douglas G.I., Chen W. A review of recent progress in coatings, fuel cell ferritic stainless Steel interconnects. *J. Power Sources* 195 (**2010**) 1529-1542.

66 Lu Z., Xia G., Templeton J.D., Li X., Nie Z., Yang Z., Stevenson J.W. Development of $Ni_{1-x}Co_xO$ as the cathode/interconnect contact for solid oxide fuel cells. *Electrochem. Commun.* 13 (**2011**) 642-645.

The perovskite structure oxides, $A^{3+}B^{3+}O^{2-}_{3-\delta}$, where A is a rare-earth element and B is a first row transition metal, have been investigated widely for cathode contact applications[67][69]. Compositions with B=Co, Ni have been used becouse of their high conductivity, while the oxides with B=Cr, Fe, Mn are known to be stable at high temperaturas[57,70,71]. Moreover, the introduction of alkali-earth elements, such as Sr, increases the sintering activity and the conductivity[66,72]. Other authors indicated that $(La_{1-x}Sr_x)MnO_3$ coatings change the oxidation behaviour and enhance the long term stability of metallic interconnects[73]. Moreover, more studies reported that[74] $La_{0.8}Sr_{0.2}CrO_3$ and $La_{0.8}Sr_{0.2}FeO_3$ coatings on ferritic alloys are not effective to prevent Cr outward diffusion. In another work, $(La,Sr)CoO_3$, $(La,Sr)(Co,Fe)O_3$ and $La(Ni,Fe)O_3$ coated ferritic alloys (Crofer22APU, E-Brite and 430) were studied[75], concluding that perovskite B-site cations (Ni,Fe,Co) diffuse to form stable spinel with transition metals from the interconnect. In our previous studies[76] $(La_{0.8}Sr_{0.2})_{0.95}Fe_{0.6}Mn_{0.3}Co_{0.1}O_3$, $LaNi_{0.6}Fe_{0.4}O_{3-\delta}$, $LaNi_{0.6}Co_{0.4}O_{3-\delta}$ were evaluated as contact materials between a Crofer22APU interconnect and a $La_{0.6}Sr_{0.4}FeO_3$ cathode. The formation of phases like $SrCrO_4$ and Cr-containing perovskite in short exposure times was observed. However, an adequate integrity and low reactivity is achieved when LNF contact coating is applied without compromising the contact resistance of the system.

Comparing to uncoated samples, perovskite coatings reduced the oxide scale growth so these coatings decrease the interfacial contact resistance; however, high sintering temperature of the perovskites leads to low compaction of these coatings and cell performance may still be degraded due to Cr poisoning. In addition to the perovskites, AB_2O_4 (A and B: divalent, trivalent and quadrivalent cations) spinel oxides can reduce oxidation and inhibit chromium volatility from ferritic stainless steels[65].

---

67 Tietz F., Sebold D. Interface reactions between electrically conductive ceramics and ferritic steel-I. The system Cr-22Fe-0.5Mn/Mn_2O_3/(La,Ca)(Cr,Co,Cu)O_3. *Mater. Sci. Eng. B* 150 (**2008**) 135-140.

68 Sharma V.I., Yildiz B. Degradation mechanism in $La_{0.8}Sr_{0.2}CoO_3$ as contact layer on the solid oxide electrolysis cell anode. *J. Electrochem. Soc.* 157(3) (**2010**) B441-B448.

69 Montero X., Tietz F., Stöver D., Cassir M., Villarreal I. Comparative study of perovskites as cathode contact materials between an $La_{0.8}Sr_{0.2}FeO_3$ cathode and a Crofer22APU interconnect in solid oxide fuel cells. *J. Power Sources* 188 (**2009**) 148-155.

70 Basu R.N., Tietz F., Teller O., Wessel E., Buchkremer H.P., Stöver D. $LaNi_{0.6}Fe_{0.4}O_3$ as a cathode contact material for solid oxide fuel cells, *J. Solid State Electrochem.* 7 (**2003**) 416-420.

71 Konysheva E., Laatsch J., Wessel E., Tietz F., Christiansen N., Singheiser L., Hilpert K. Influence of different perovskite interlayers on the electrical conductivity between $La_{0.65}Sr_{0.3}MnO_3$ and Fe/Cr based steels. *Solid State Ionics* 177 (**2006**) 923-930.

72 Zhou Q., Xu L., Guo Y., Jia D., Li Y., Wei W.C.J. $La_{0.6}Sr_{0.4}Fe_{0.8}Cu_{0.2}O_{3-\delta}$ perovskite oxide as cathode for IT-SOFC. *Int. J. Hydrogen Energ.* 37(16) (**2012**) 11963-11968.

73 Conceiçao L.D., Dessemond L., Djurado E., Souza M.M.V.M. $La_{0.7}Sr_{0.3}MnO_3$-coated SS444 alloy by dip-coating process for metallic interconnect supported solid oxide fuel cells. *J. Power Sources* 241 (**2013**) 159-167.

74 Yang Z., Xia G.G., Maupin G.D., Stevenson J.W. Evaluation of perovskite overlay coatings on ferritic steels for SOFC interconnect applications. *J. Electrochem. Soc.* 153 (**2006**) A1852-A1858.

75 Lacey R., Pramanick A., Lee J.C., Jung J.I., Jiang B., Edwards D.D., Naum R., Misture S.T. Evaluation of Co and perovskite Cr-blocking thin films on SOFC interconnects. *Solid State Ionics* 181 (**2010**) 1294-1302.

76 Morán-Ruiz A., Vidal K., Laguna-Bercero M.A., Larrañaga A., Arriortua M.I. Effects of using $(La_{0.8}Sr_{0.2})_{0.95}Fe_{0.6}Mn_{0.3}Co_{0.1}O_3$ (LSFMC), $LaNi_{0.6}Fe_{0.4}O_{3-\delta}$ (LNF) and $LaNi_{0.6}Co_{0.4}O_{3-\delta}$ (LNC) as contact material on solid oxide fuel cells. *J. Power Sources* 248 (**2014**) 1067-1076.

$Mn_{1-\delta}Co_{2-\delta}O_4$ spinels have been the most extensively studied[77-82]. However, ASR test of MCO coated Crofer22 showed that the adhesion of these coatings may be an issue for long-term applications[77,83]. For this reason Ce was added to the coating as reactive element in order to increase oxide scale and coating adherence to the metal substrate. A composition of $Ce_{0.05}Mn_{1.475}Co_{1.475}O_4$ was used and results have looked promising[84,85]. Moreover, other research groups have also studied Mn-Co spinels doped with Fe, Ti or Cu which exhibits higher electrical conductivity and a better densification than $MnCo_2O_4$ due to a partial substitution of Co by Fe, Ti and/or Cu[86-90]. Our previous work also concluded that[91] $MnCo_{1.9}Fe_{0.1}O_4$ was a more effective barrier than $MnCo_2O_4$, resulting in better electrochemical results and a similar microstructure; the presence of a low Fe content in $MnCo_{1.9}Fe_{0.1}O_4$ improved the stability of coating. In addition, due to the low cost of Ni, $NiMn_2O_4$ [92] and $NiFe_2O_4$ [93] spinels were also studied as protective coatings, providing effective conducting path to metallic substrate.

---

77 Magdefrau N.J. Evaluation of solid oxide fuel cell interconnect coatings: reaction layer microstructure, chemistry and formation mechanisms. Doctoral dissertations. University of Connecticut **2013**.

78 Fang Y., Wu C., Duan X., Wang S., Chen Y. High-temperature oxidation process analysis of $MnCo_2O_4$ coatings on Fe-21Cr alloy. *Int. J. Hydrogen Energ.* 36(9) (**2011**) 5611-5616.

79 Abdoli H., Alizadeh P. Electrophoretic deposition of $(Mn,Co)_3O_4$ spinel nano powder on SOFC metallic interconnects. *Mater. Lett.* 80 (**2012**) 53-55.

80 Uehara T., Yasuda N., Okamoto M., Baba Y. Effect of Mn-Co spinel coating for Fe-Cr ferritic alloys ZMG232L and 232J3 for solid oxide fuel cell interconnects on oxidation behavior and Cr-evaporation. *J. Power Sources* 196(17) (**2011**) 7251-7256.

81 Zhang H.H., Zeng C.L. Preparation and performances of Co-Mn spinel coating on a ferritic stainless steel interconnect material for solid oxide fuel cell application. *J. Power Sources* 252 (**2014**) 122-129.

82 Zhang H., Wu J., Liu X., Baker A. Studies on elements diffusion of Mn/Co coated ferritic stainless Steel for solid oxide fuel cell interconnects application. *Int. J. Hydrogen Energ.* 38 (**2013**) 5075-5083.

83 Akanda S.R., Walter M.E., Kidner N.J., Seabaugh M.M. Lifetime prediction for manganese cobalt spinel oxide coatings on metallic interconnects. *Thin Solid Films* 565 (**2014**) 237-248.

84 Yang Z., Xia G., Nie Z., Templeton J.D., Stevenson J.W. Ce-modified $(Mn,Co)_3O_4$ spinel coatings on ferritic stainless steels for SOFC interconnect applications. *Electrochem. Solid St.* 11(8) (**2008**) B140-B143.

85 Chou Y.S., Stevenson J.W., Choi J.P. Long-term evaluation of solid oxide fuel cell candidate materials in a 3-cell generic stack test fixture, part III: stability and microstructure of Ce-(Mn,Co)-spinel coating, AISI441 interconnect, alumina coating, cathode and anode. *J. Power Sources* 257 (**2014**) 444-453.

86 Montero X., Jordán N., Pirón-Abellán J., Tietz F., Stöver D., Cassir M., Villarreal I. Spinel and perovskite protection layers between Crofer22APU and $La_{0.8}Sr_{0.2}FeO_3$ cathode materials for SOFC interconnects. *J. Electrochem. Soc.* 156(1) (**2009**) B188-B196.

87 Chou P.Y., Ciou C.J., Lee Y.C., Hung I.M. Effect of $La_{0.1}Sr_{0.9}Co_{0.5}Mn_{0.5}O_{3-\delta}$ protective coating layer on the performance of $La_{0.6}Sr_{0.4}Co_{0.8}Fe_{0.2}O_{3-\delta}$ solid oxide fuel cell cathode. *J. Power Sources* 197 (**2012**) 12-19.

88 Hosseini N., Abbasi M.H., Karimzadeh F., Choi G.M. Development of $Cu_{1.3}Mn_{1.7}O_4$ spinel coating on ferritic stainless steel for solid oxide fuel cell interconnects. *J. Power Sources* 273 (**2015**) 1073-1083.

89 Puranen J., Pihlatie M., Lagerbom J., Bolelli G., Laakso J., Hyvärinen L., Kylmälahti M., Himanen O., Kiviaho J., Lusvarghi L., Vuoristo P. Post-mortem evaluation of oxidized atmospheric plasma sprayed Mn-Co-Fe oxide spinel coatings on SOFC interconnects. *Int. J. Hydrogen Energ.* 39(30) (**2014**) 17284-17294.

90 Montero X., Tietz F., Sebold D., Buchkremer H.P., Ringuede A., Cassir M., Laresgoiti A., Villarreal I. $MnCo_{1.9}Fe_{0.1}O_4$ spinel protection layer on commercial ferritic steels for interconnect applications in solid oxide fuel cells. *J. Power Sources* 184 (**2008**) 172-179.

91 Miguel-Pérez V., Martínez-Amesti A., Nó M.L., Larrañaga A., Arriortua M.I. The effect of doping $(Mn,B)_3O_4$ materials as protective layers in different metallic interconnects for solid oxide fuel cells. *J. Power Sources* 243 (**2013**) 419-430.

92 Zhang W., Pu J., Chi B., Jian L. $NiMn_2O_4$ spinel as an alternative coating material for metallic interconnects of intermediate temperatura solid oxide fuel cells. *J. Power Sources* 196 (**2011**) 5591-5594.

93 Liu Y., Chen D.Y. Protective coatings for Cr_2O_3-forming interconnects of solid oxide fuel cells. *Int. J. Hydrogen Energ.* 34 (**2009**) 9220-9226.

Despite the usefulness of conductive/protective coatings, the stack degradation rates are still higher than the required values for SOFC commercialization. It was found that $Ni_{80}Cr_{20}/(La_{0.75}Sr_{0.25})_{0.95}MnO_3$ dual-layer coating can improve the thermal stability and electrical performance of metallic interconnect[94]. In this context, according to other studies[95], the incorporation of conduction wires in the electrodes could increase cell performance via improved transport of electrons. In our previous work[96] a Fe-Cr mesh coated with $LaNi_{0.6}Co_{0.4}O_{3-\delta}$ high conductive perovskite was developed as an alternative to conventional contact materials. Taking into account that the generally accepted upper limit of ASR for SOFC interconnect is 0.1 $\Omega \cdot cm^2$ [65,97,98], low and reproducible area specific resistance value (ASR) was achieved, being 0.0054(1) $\Omega \cdot cm^2$, when this metallic/ceramic material was used to coat a channeled Crofer22APU interconnect.

In this study, LNF paste is developed to dip coated on Fe-22Cr mesh, forming a metallic/ceramic continuous layer in which ferritic mesh is fully covered with slurry. Because of Cr diffusion from steel was expected[96], the effectiveness of using MCF to protect mesh, prior to coat with LNF conductive perovskite, was discussed based on the long term behaviour of these samples at 800 ºC. LNF/MCF conductive/protective coatings were selected due to our previous experience and good results with these materials[76,91,99].

The obtained mixed material is expected to increase the conductivity and adhesive ability of the formed interface with interconnect ribs. Therefore, in order to evaluate this adherence, the resistance between these both materials was determined by relatively short-time ASR testing. Finally, this system was aged for 1000 h at 800 ºC in order to establish the degradation trends under the rib (direct contact) and channel (no-contact) of the interconnect.

3.2.2. Experimental

The powder of $LaNi_{0.6}Fe_{0.4}O_{3-\delta}$ (LNF) was from Fuel Cell Materials and, uncoated and $MnCo_{1.9}Fe_{0.1}O_4$ (MCF)-coated Fe-22Cr mesh (both with mesh opening of 175 μm and thickness of 250 μm) from Fiaxell SOFC Technologies (Crofer22H M-grid™ micro mesh). According to technical specifications the MCF coated mesh was sintered at 850 ºC for 6 h, in air. LNF coating was applied onto uncoated and coated mesh squares (10 x 10 mm) by dipping them into the prepared ceramic slurry, thus obtaining a metallic/ceramic material. The LNF slurry was composed

---

94 Wu W., Guan W., Wang G., Liu W., Zhang Q., Chen T., Wang W.G. Evaluation of $Ni_{80}Cr_{20}/(La_{0.75}Sr_{0.25})_{0.95}MnO_3$ dual layer coating on SUS 430 stainless steel used as metallic interconnect for solid oxide fuel cells. *Int. J. Hydrogen Energ.* 39 (**2014**) 996-1004.

95 Yoon C. Computational design, fabrication, and characterization of microarchitectured solid oxide fuel cells with improved energy efficiency, Ph.D. thesis work, Georgia Institute of Technology, **2010**.

96 Morán-Ruiz A., Vidal K., Larrañaga A., Laguna-Bercero M.A., Porras-Vázquez J.M., Slater P.R., Arriortua M.I. $LaNi_{0.6}Co_{0.4}O_{3-\delta}$ dip-coated on Fe-Cr mesh as a composite cathode contact material on intermediate solid oxide fuel cells. *J. Power Sources* 269 (**2014**) 509-519.

97 Zhu W.Z., Deevi S.C. Development of interconnect materials for solid oxide fuel cells. *Mat. Sci. Eng. A-Struct.* 348 (**2003**) 227-243.

98 Piccardo P., Gannon P., Chevalier S., Viviani M., Burbucci A., Caboche G., Amendola R., Fontana S. ASR evaluation of different kinds of coatings on a ferritic stainless steel as SOFC interconnect. *Surf. Coat. Tech.* 202 (**2007**) 1221-1225.

99 Vidal K., Morán-Ruiz A., Larrañaga A., Porras-Vázquez J.M., Slater P.R., Arriortua M.I. Characterization of $LaNi_{0.6}Fe_{0.4}O_3$ perovskite synthesized by glycine-nitrate combustion method. *Solid State Ionics* 269 (**2015**) 24-29.

of ceramic powder (LNF, 12.5% in volume), dispersant (Dolapix, 1% relative to the ceramic powder, Zschimmer & Schwarz, Chemische Fabriken), binder (PVB, polyvinyl butyral, 5% relative to the ceramic powder, Solutia Solutions) and solvent (ethanol, 87.5% in volume, Panreac). The process performed to form a contact composite was described in Ref. [96]. The rheology of the suspensions was analyzed using a rheometer (HAAKE MARS II) at shear rates from 0.1 s^{-1} to 1000 s^{-1}, at room temperature. Composite materials were sintered at 1050 ºC for 2 h and then treated at 800 ºC for 1000 h, in air.

The composite contact material was directly bonded to a Crofer22APU channeled interconnect (ThyssenKrupp VDM). Nominal steel composition given by the supplier is summarized in Ref. [100]. The interconnect squares (10 x 10 x 1 mm) were preoxidized at 800 ºC for 100 h, reducing Cr and Fe transport into the contact coating after long oxidation times[101]. The channel dimensions of the interconnect as well as the procedure to obtain {composite contact material/interconnect} system was detailed in previous work[96]. The obtained structure was sintered at 1050 ºC for 2 h and then treated at 800 ºC for 1000 h, in air.

X-ray diffraction (XRD) patterns of the samples were measured with an Philips X´Pert PRO diffractometer, powered at 40 kV and 40 mA using Cu K_α radiation (λ=1.5418 Å) in air at room temperature. The patterns were recorded in 2θ steps of 0.026º in the 20-90º range, counting for 181 seconds for step. X-ray micro-diffraction (XRMD) data were collected using a Bruker D8 Discover diffractometer equipped with a Cr Twist tube, V filter (λ=2.2898 Å), PolyCap^{TM} (1μ single crystal cylinders) system for parallel been generation (divergence of 0.25°), and a 1-D LynxEye PSD detector (active length in 2θ 2.7º). The sample was mounted on an Eulerian Cradle with automatically controlled X-Y-Z stage. The sample illumination was adjusted with 1mm PinHole collimator in the incident been, the position control was tested by using the interference of two lasers. Data were collected from 10 to 100° 2θ (step size = 0.04 and time per step = 10 s total time 6.5 h) at RT. Phases were identified from the measured XRD and XRMD patterns using X´Pert HighScore software based on the powder diffraction file (PDF) database. The fitting of a measured and calculated pattern was done by Rietveld method using the FULLPROF program[102].

X-ray photoelectron spectroscopy (XPS) measurements were performed using a XPS spectrometer (SPECS). All XPS spectra were acquired using a monochromatic X-ray source producing Al Kα radiation (h·ν=1486.6 eV) and recorded using a SPECS PHOIBOS 150 analyser. An initial analysis of the elements present in the sample was carried out (wide scan: step energy 1 eV, dwell time 0.1 s, pass energy 80 eV) and individual high resolution spectra were obtained (detail scan: step energy 0.1 eV, dwell time 0.1 s, pass energy 20 eV). The take-off angle of the photoelectrons was 90º with respect to the sample. The binding energies (BEs) were calibrated against the surface carbon contamination at 284.6 eV. The spectra were fitted by CasaXPS 2.3.16 software, modeling properly weighted sum of Gaussian and Lorentzian component curves, after background subtraction according to Shirley.

---

[100] Miguel-Pérez V., Martínez-Amesti A., Nó M.L., Larrañaga A., Arriortua M.I. Oxide scale formation on different metallic interconnects for solid oxide fuel cells. *Corros. Sci.* 60 (**2012**) 38-49.

[101] Hoyt K.O., Gannon P.E., White P., Tortop R., Ellingwood B.J., Khoshuei H. Oxidation behavior of $(Co,Mn)_3O_4$ coatings on preoxidized stainless steel for solid oxide fuel cell interconnects. *Int. J. Hydrogen Energ.* 37 (**2012**) 518-529.

[102] Rodríguez-Carvajal J. FULLPROF Rietveld pattern matching analysis of powder patterns, Grenoble, **2011**.

For microstructure and composition analysis, sample cross-sections were mounted in resin, polished and sputtered with coal graphite. A JEOL LSM-6400 instrument equipped with a tungsten filament gun and an Oxford Inca Pentafet X3 energy dispersive X-ray analyzer (EDX) was used to examine the samples. The operating voltage used was 20 kV and a current density of $1 \cdot 10^{-9}$ A. The EDX analysis was carried out through point analysis (the live time was set to 100 s).

Area Specific Resistance (ASR) measurements were performed using a DC four-probe method (the resistance value was estimated from the voltage value (Thurlby Thandar Instruments 1604 Digital Multimeter) measured on applying a current of 1A (Thurlby Thandar Instruments PL300 current source)), on both a composite and on a system, which were prepared according to the geometries shown in Figure 3.15. Electrical contacts between samples and external measuring circuit were obtained by two Pt wires welded directly onto the sides of the interconnect and by Pt paste onto the surface of the composite contact material in combination with a Pt mesh.

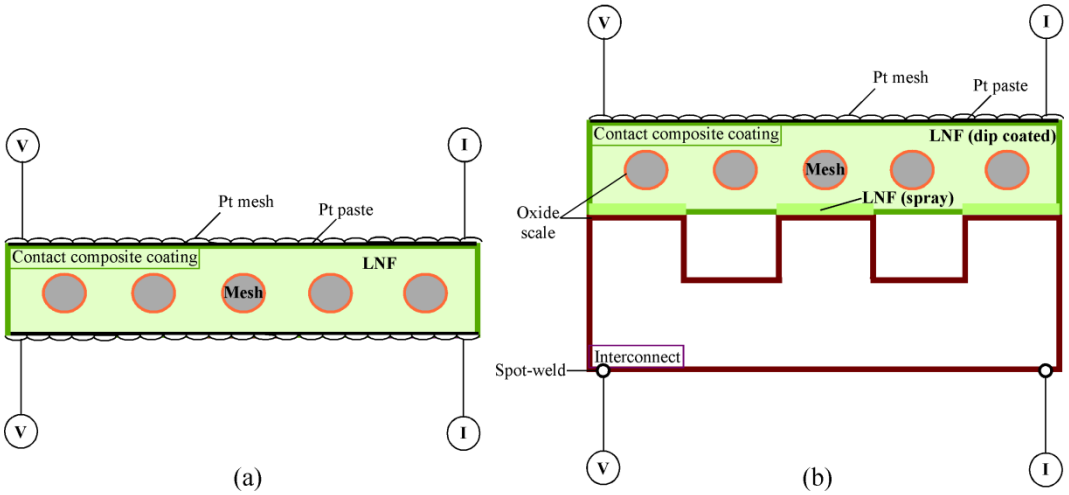

Figure 3.15. Schematic views of the used system configurations for ASR measurements: (a) composite contact material and (b) composite contact material on channeled interconnect.

3.2.3. Results and discussion

In order to investigate the crystal structure of uncoated and coated FeCr mesh squares, the samples were analysed using X-ray diffraction (XRD) measurements (Figure 3.16).

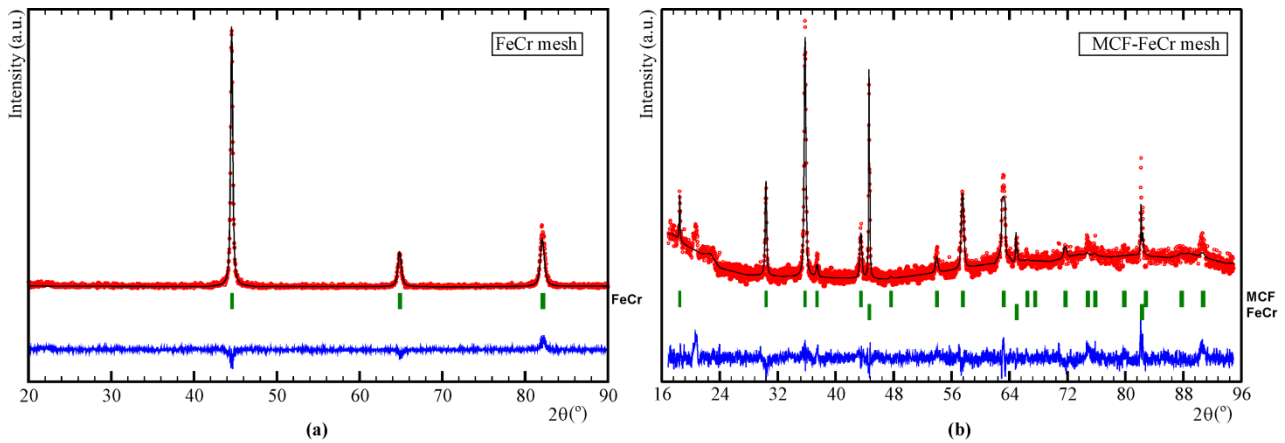

Figure 3.16. Rietveld X-ray diffraction patters for: (a) commercial uncoated and (b) $MnCo_{1.9}Fe_{0.1}O_4$ spinel coated Fe-22Cr mesh.

The refined cell parameters, unit cell volumes and the quality of the refinements are summarized in Table 3.9. For the coated mesh, MCF (3.1(1) % in weight) was quantified (Figure 3.16(b)).

Table 3.9. Structural parameters for Fe-22Cr mesh and $MnCo_{1.9}Fe_{0.1}O_4$-coated Fe-22Cr mesh from the Rietveld refinement by using X-ray power diffraction data at room temperature.

Sample	Phase	Space group	Lattice parameters a (Å)	V (Å^3)	% in weight	χ^2
FeCr mesh	FeCr	I*m-3m*	2.876(1)	23.78(1)	100	5.42
MCF-FeCr mesh	MCF	F*d-3m*	8.324(1)	576.78(1)	3.1(1)	1.70
	FeCr	I*m-3m*	2.871(1)	23.67(1)	96.9(8)	

The phase structures of studied commercial $LaNi_{0.6}Fe_{0.4}O_{3-\delta}$ and Crofer22APU were analysed in detail in our group[76]. The chemical composition of the surface of the alloys used as interconnect and, as mesh to form composite material were quantitatively analysed using SEM-EDX. The measured values of the elements were checked on different points to obtain the average composition grade (Table 3.10). In order to ensure the determined chemical formulation of the samples, nominal compositions for each steel given by the technical specifications are also listed in Table 3.10.

As an example, Figure 3.17 shows EDX spectra from one point results. The quantitative EDX analysis revealed that Fe-Cr mesh contains tungsten (W) and niobium (Nb), in contrast to interconnect which did not present these elements.

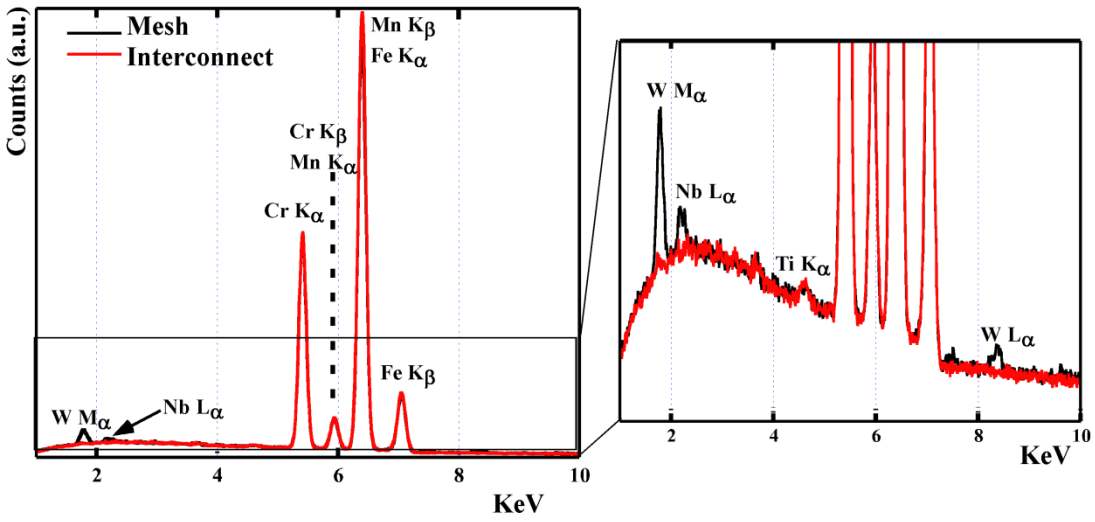

Figure 3.17. EDX spectra analyses for Fe-22Cr interconnect and mesh samples.

The strength of a steel is related to the combination of solid solution and precipitation strengthening given by Nb and W addition[103]. Lanthanum, titanium and niobium additives are concentrated in specific regions of the alloy (identified as A point of each sample in Figure 3.18) differently from tungsten, which is dissolved in the ferritic matrix. Thus, the average chemical composition of steels showed undetectable levels of La and low concentrations for Ti and Nb for EDX technique.

[103] Froitzheim J., Meier G.H., Niewolak L., Ennis P.J., Hattendorf H., Singheiser L., Quadakkers W.J. Development of high strength ferritic steel for interconnect application in SOFCs. *J. Power Sources* 178 (**2008**) 163-173.

Table 3.10. Chemical composition in wt (%) of Fe-22Cr alloy used as interconnect and as mesh, given by the technical specifications and obtained by EDX microanalysis.

Sample		Fe(%wt.)	Cr(%wt.)	Mn(%wt.)	Ti(%wt.)	Nb(%wt.)
Crofer22H	min.	Bal.*	20.0	0.3	0.02	0.2
	max.		24.0	0.8	0.20	1.0
Mesh	EDX	73.1(3)	23.5(2)	0.6(1)	< 0.1	0.4(1)
Crofer22APU	min.	Bal.*	20.0	0.3	0.03	-
	max.		24.0	0.8	0.20	-
Interconnect	EDX	76.3(2)	23.0(2)	0.6(1)	< 0.1	-

* Balance.

Sample		W(% wt.)	Si(%wt.)	Al(%wt.)	Cu(%wt.)	La(%wt.)
Crofer22H	min.	1.0	0.1			0.04
	max.	3.0	0.6	0.1	0.5	0.20
Mesh	EDX	2.3(2)	-	-	-	-
Crofer22APU	min.	-				0.04
	max.	-	0.50	0.50	0.50	0.20
Interconnect	EDX	-	-	-	-	-

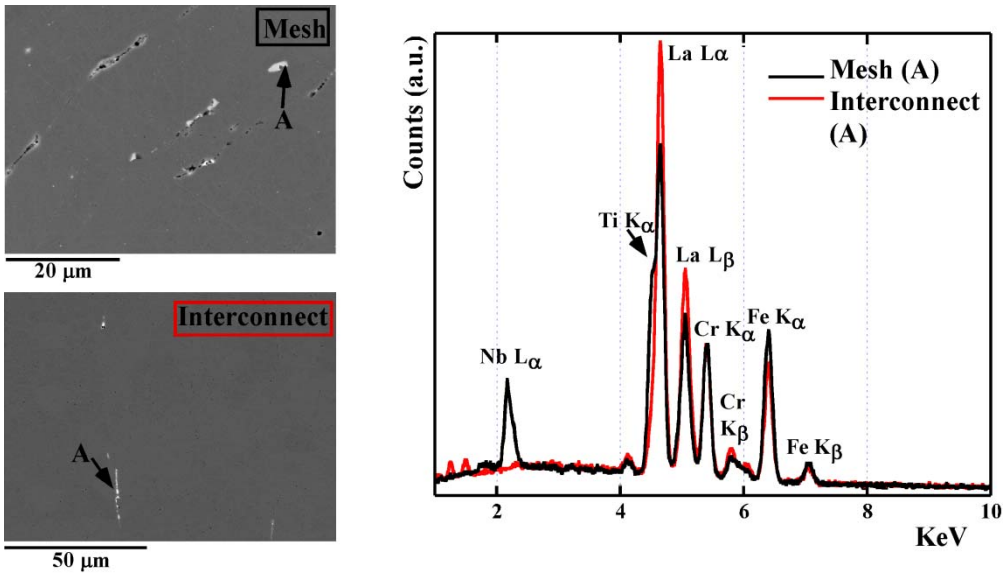

Figure 3.18. EDX point analysis performed on specific regions of the alloys.

The characterization of LNF slurry rheology is important for coated thickness control during the dip coating process. The effort against the shear rate of LNF paste is represented graphically in Figure 3.19. As shown, the slurry behaves like a Newtonian fluid, and so the viscosity values are independent of the shear rate.

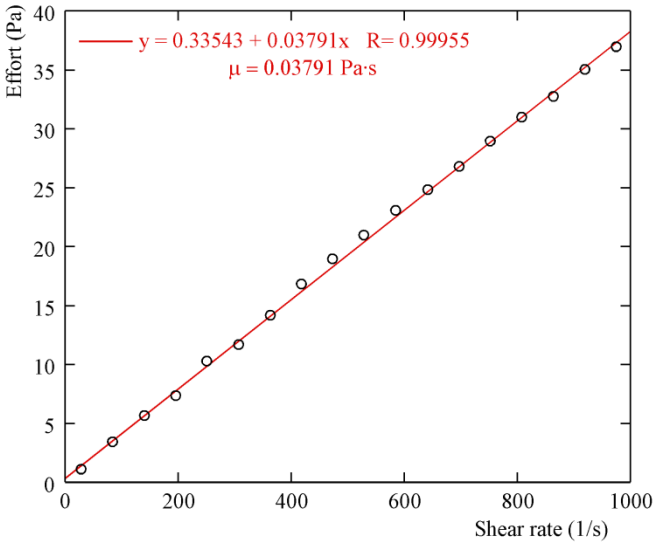

Figure 3.19. Plot of the effort against shear rate of $LaNi_{0.6}Fe_{0.4}O_{3-\delta}$ paste.

The viscosity value can be extracted from the slope of the represented line, being 0.038 Pa·s, in good agreement with obtained results in our previous studies[96].

3.2.3.1. Effectiveness of using a protective coating on Fe-Cr mesh

The formed Fe-Cr mesh/LNF and Fe-Cr mesh/MCF/LNF composites, after sintering at 1050 ºC for 2 h in air, are shown in Figure 3.20. As observed from Figure 3.20(a), the ceramic coating is continuous and homogeneous along the samples. However, the MCF protective coating was not a continuous layer along the width of the Fe-Cr mesh (Figure 3.20(b)). Laves phase precipitates were observed along the steel grain boundaries[104], in good agreement with Figure 3.20.

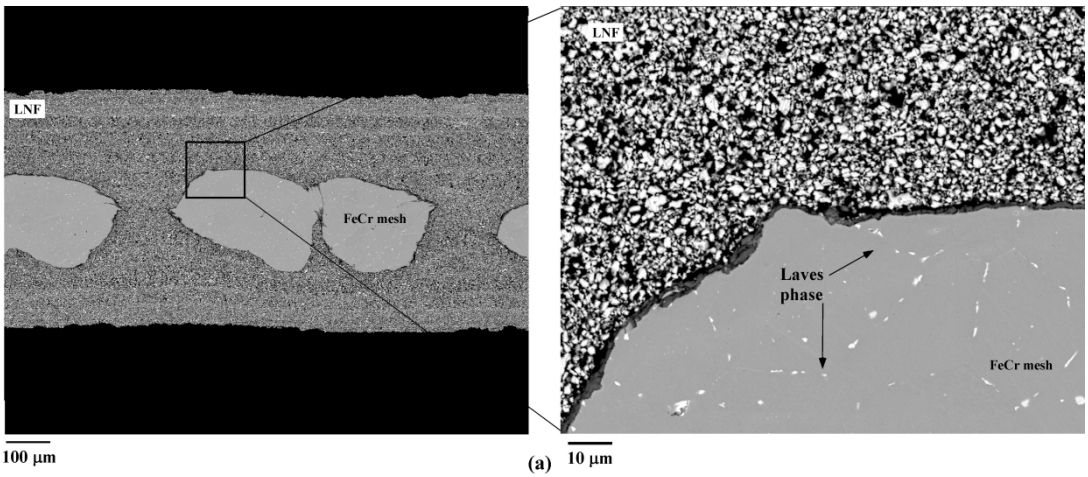

Figure 3.20. SEM cross-section of (a) Fe-22Cr mesh and (b) MCF coated Fe-22Cr mesh after dipping into LNF slurry and the following sintering at 1050 ºC for 2 h, in air.

[104] Chiu Y.T., Lin C.K. Effects of Nb and W additions on high-temperature creep properties of ferritic stainless steels for solid oxide fuel cell interconnect. *J. Power Sources* 198 (**2012**) 149-157.

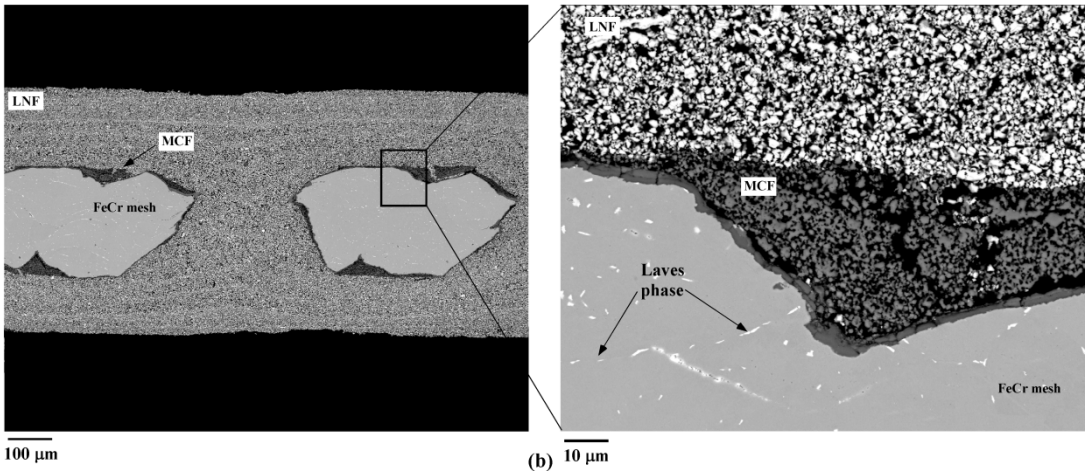

Figure 3.20. cont. SEM cross-section of (a) Fe-22Cr mesh and (b) MCF coated Fe-22Cr mesh after dipping into LNF slurry and the following sintering at 1050 ºC for 2 h, in air.

The area specific resistance (ASR) values of sintered Fe-Cr/LNF and Fe-Cr/MCF/LNF composite materials were 0.00453(1) and 0.00341(1) $\Omega \cdot cm^2$, respectively. Despite the observed porous coarse microstructure in both LNC and MCF coatings (Figure 3.20), the determined low ohmic resistance confirms that the use of these composite materials as a contact layer is adequate.

EDX point analysis was performed on a cross-section of just sintering at 1050 ºC for 2 h mesh/LNF material (Figure 3.21), and compared with another sample after heat treated at 800 ºC for 1000 h in air (Figure 3.22).

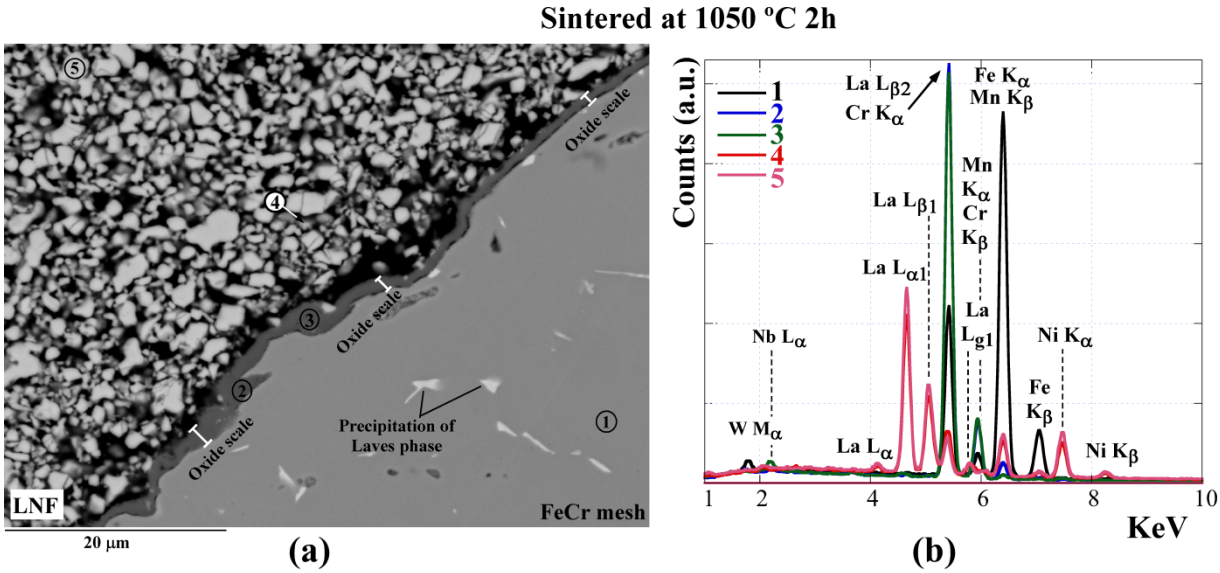

Figure 3.21. (a) Cross-section microstructure image obtained by backscattered electrons signal (BSE) and (b) EDX analysis on different points of LNF/mesh sintered at 1050 ºC for 2 h, in air.

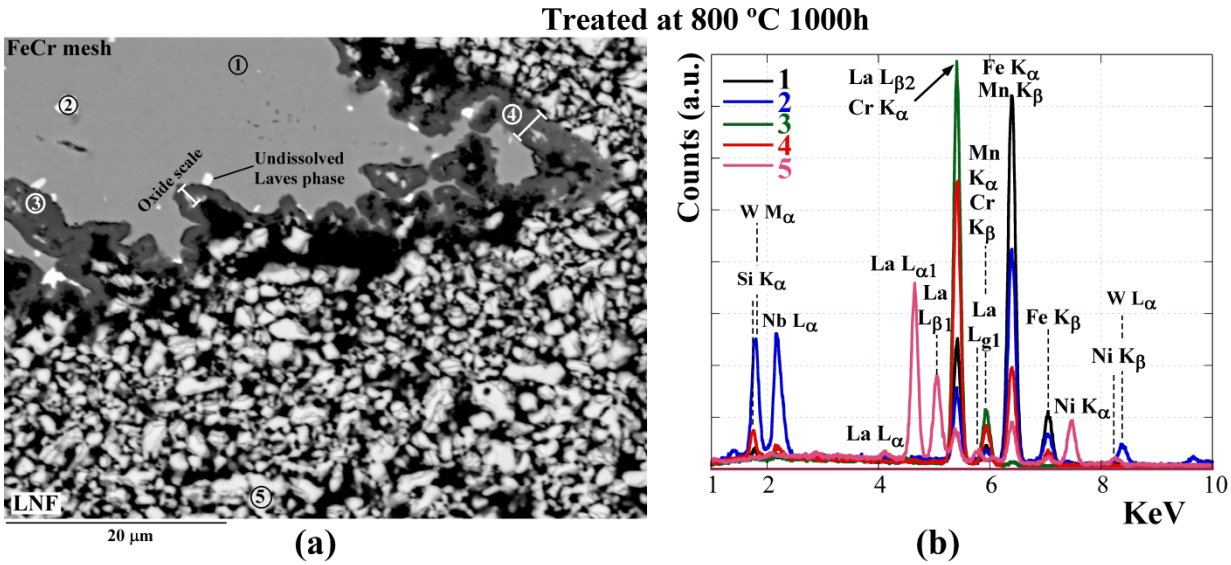

Figure 3.22. (a) Cross-section microstructure (BSE) and (b) EDX analysis on different points of LNF/mesh sintered at 1050 ºC and then treated at 800 ºC for 1000 h, in air.

The obtained k ratios for identified elements, in these both samples, were listed in Tables 3.11 (corresponding to Figure 3.21) and 3.12 (corresponding to Figure 3.22).

Table 3.11. Elemental k ratios measured by EDX point analysis performed on mesh/LNF just sintering at 1050 ºC for 2 h, in air (corresponding to Figure 3.21).

Spectrum	*Cr (k ratio)*	*Fe (k ratio)*	*Mn (k ratio)*	*La (k ratio)*	*Ni (k ratio)*	*Nb (k ratio)*	*W (k ratio)*
1	0.24	0.65	-	-	-	-	0.01
2	0.58	0.03	-	-	-	-	-
3	0.57	0.01	0.01	0.01	0.01	0.01	-
4	0.03	0.06	-	0.43	0.1	-	-
5	-	0.08	-	0.50	0.13	-	-

Table 3.12. K ratios for identified elements on mesh/LNF sample after sintered and aged at 800 ºC for 1000 h, in air (corresponding to Figure 3.22).

Spectrum	*Cr (k ratio)*	*Fe (k ratio)*	*Mn (k ratio)*	*La (k ratio)*	*Ni (k ratio)*	*Nb (k ratio)*	*W (k ratio)*	*Si (k ratio)*
1	0.19	0.74	-	-	-	-	0.01	-
2	0.09	0.41	-	-	-	0.12	0.18	-
3	0.61	0.01	0.01	-	-	0.01	-	-
4	0.45	0.19	-	0.01	-	0.01	-	0.01
5	-	0.08	-	0.52	0.13	-	-	-

Moreover, Figure 3.23 and Table 3.13 show a cross-section microstructure image of $MnCo_{1.9}Fe_{0.1}O_4$ coated mesh after dipping into $LaNi_{0.6}Fe_{0.4}O_{3-\delta}$ slurry with EDX point analysis, and the obtained elemental k ratios, respectively. The INCA 350 software from Oxford was used to reconstruct the spectra, separating the overlapping peaks.

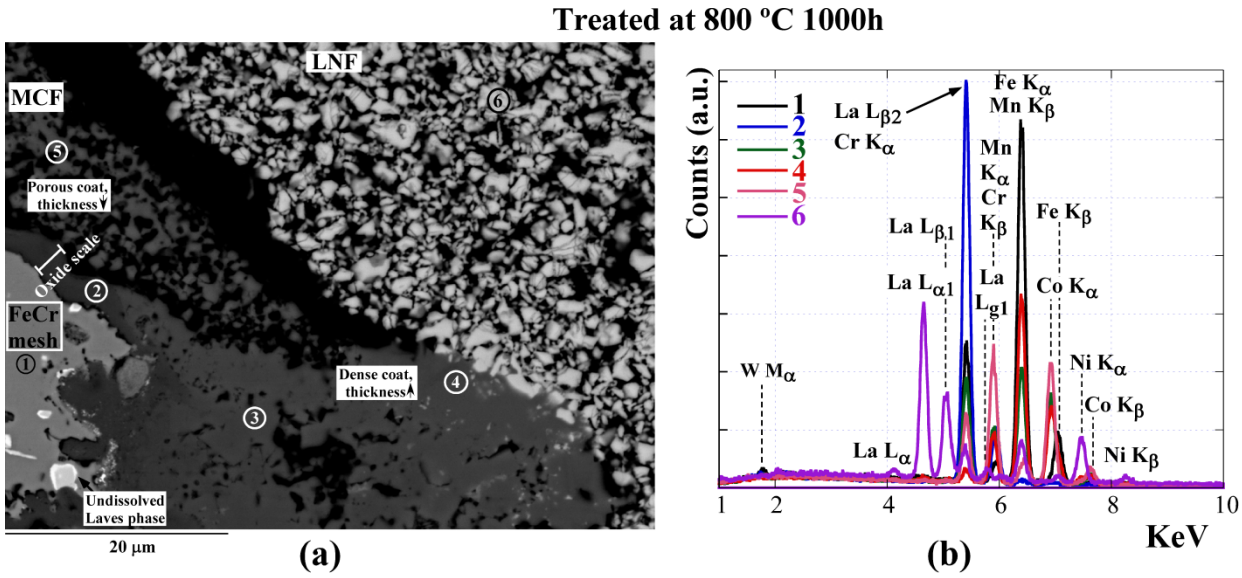

Figure 3.23. (a) Cross-section BSE image and (b) EDX point analysis of MCF coated mesh after dipping into LNF paste and the following sintering and aging processes.

Table 3.13. The corresponding k ratios for identified elements on mesh/MCF/LNF sample after sintered and heat treated at 800 ºC for 1000 h, in air (corresponding to Figure 3.23).

Spectrum	*Cr (k ratio)*	*Fe (k ratio)*	*Mn (k ratio)*	*La (k ratio)*	*Ni (k ratio)*	*Co (k ratio)*	*W (k ratio)*
1	0.19	0.65	0.01	-	-	-	0.01
2	0.56	0.01	0.01	-	-	-	-
3	0.15	0.2	0.07	-	-	0.19	-
4	0.02	0.33	0.07	0.01	0.02	0.17	-
5	0.09	0.02	0.19	-	0.01	0.28	-
6	-	0.07	-	0.47	0.13	-	-

The ceramic/metallic interface was relatively smooth in the initial composite (Figure 3.21), while the interface was more irregular in the LNF dip coated mesh after 1000 h at 800 ºC (Figure 3.22), as was expected[105]. Moreover, locally internal precipitates, which could be related to the external not uniform oxide scale[106], were also found. According to microstructure, LNF showed relatively inhomogeneity between sintered particles, which could decrease their adherence to the alloy[107,108]. Thus, these particle contact points are irregular through the mesh surface that might also be associated to the observed irregular oxide scale, being noticeable after 1000 h at 800 ºC. Therefore, for both Fe-Cr mesh/LNF materials ceramic layer contains pores whereas some of them are formed at the scale interface. Thus, especially the long-term heat treated sample shows areas without contact. As observed from Figure 3.23, for spinel coated mesh loss of adherence was observed

[105] Linder M., Hocker T., Holzer L., Friedrich K.A., Iwanschitz B., Mai A., Schuler J.A. Cr_2O_3 scale growth rates on metallic interconnectors derived from 40.000 h solid oxide fuel cell stack operation. *J. Power Sources* 243 (**2013**) 508-518.

[106] Ali-Löytty H. Microalloying mediated segregation and interfacial oxidation of FeCr alloys for solid oxide fuel cell applications, Ph.D. thesis work, Tampere University of Technology, **2013**.

[107] Mohammadi M., Javadpoura S., Kobayashi A., Shirvani K., Jenabali J.A., Khakpour I. Cyclic oxidation behavior of CoNiCrAlY coatings produced by LVPS and HVOF processes. *Transactions of JWRI* 40 (**2011**) 53-58.

[108] Fayette S., Smith D.S., Smith A., Martin C. Influence of grain size on the termal conductivity of tin oxide ceramics. *J. Eur. Ceram. Soc.* 20(3) (**2000**) 297-302.

between the $MnCo_{1.9}Fe_{0.1}O_4$ protective and LNF contact layers. According to Ref. [86] the formation of these cracks could be as a result of cooling down to room temperature. However, MCF spinel layer showed different microstructures between points 3-4 and 5 (Figure 3.23), which could be related to the protective layer thickness, being in the zone where point 3-4 were analysed higher than in the point 5 analysed area. In this way, the highest thickness allowed high enough density to improve adherence between metallic substrate and protective coating. The EDX point analysis, which were made on alloy, revealed in most of the cases α-Fe(Cr,W) phase. The analysed Laves phase precipitates (Figure 3.22, point 2) were composed of $(Fe,Cr)_2(Nb,W)$, in good agreement with Ref. [104], in which Laves phase precipitates of Fe_2Nb type were formed on small additions of Nb. The combined additions of Nb and Si, which came from the alloy, allowed the formation of Fe-Cr-Nb-Si system[109], as can observed in Figure 3.22, point 4. However, the results showed that the Nb was also incorporated in the external oxide scale. In some areas of Figures 3.22 and 3.23, there is undissolved Laves phase in contact with the scale, indicating the thermodynamic stability of this compound.

According to EDX analysis, for sample without MCF protective layer, a passive chromia layer (Cr_2O_3/$(Mn,Cr)_3O_4$ [91]) about 1.3 μm thick (measured directly from Figure 3.22) was grown between the metal substrate and the LNF coating. For the spinel coated mesh specimen, an oxide scale was also formed beneath the MCF coating, in good agreement with EDX analysis. According to our previous studies[100], the presence of Fe in oxide scale indicated the formation of small amount of hematite phase (α-Fe_2O_3) and/or Fe_3O_4 phases. Moreover, the appearance, in the oxide scale, of Cr, Mn and Fe simultaneously allows the formation of $(Mn,Fe,Cr)_3O_4$ spinel. In addition, EDX point analyses, performed on the interface close to the contact coating, indicated the migration of lanthanum and nickel from the LNF layer into the passive oxide scale or MCF protective layer. However, due to the porosity of the sample, and because the resolution of the energy dispersive X-rays source from the sample is approximately 1 μm, it is noted that the point analysis results should be interpreted with caution.

With EDX, evidence of Cr penetration through the protective spinel coating, as well as into the LNF coating, was found. Darker grey-coloured Cr-rich grains were observed in the LNF coating for uncoated and coated FeCr mesh samples, which decrease as the distance from the mesh is increased (Figures 3.22 and 3.23). In terms of the microstructure, the open porosity observed in LNF and MCF coatings might reduce the adherence to the alloy and enhance the transport of Cr to gas phase.

Since the deposition of the commercial protective coating was not homogeneous across the width of the Fe-22Cr mesh, the use of an MCF spinel protective layer is not enough to prevent chromium migration up to the contact coating. Thus, the uncoated sample was selected to evaluate the electrical performances of the composite contact material/interconnect system, including long-term contact stability of the metallic/ceramic composite material under the rib (direct contact) and channel (no- contact) of the interconnect.

---

[109] Vilasi M., Francois M., Brequel H., Podor R., Venturini G., Steinmetz J. Phase equilibria in the Nb-Fe-Cr-Si system. *J. Alloy Compd.* 269 (**1998**) 187-192.

3.2.3.2. Characterization of the composite contact material with channelled Crofer22APU interconnect

Ceramic/metallic material was directly adhered to the channeled substrate and sintered at 1050 ºC for 2 h. Results from ASR test (Figure 3.24) showed initial good stability of the signal during the contact resistance measurements, and thus a good adherence between both materials, exhibiting ASR value of 0.0425(2) $\Omega \cdot cm^2$ for 400 min, in air.

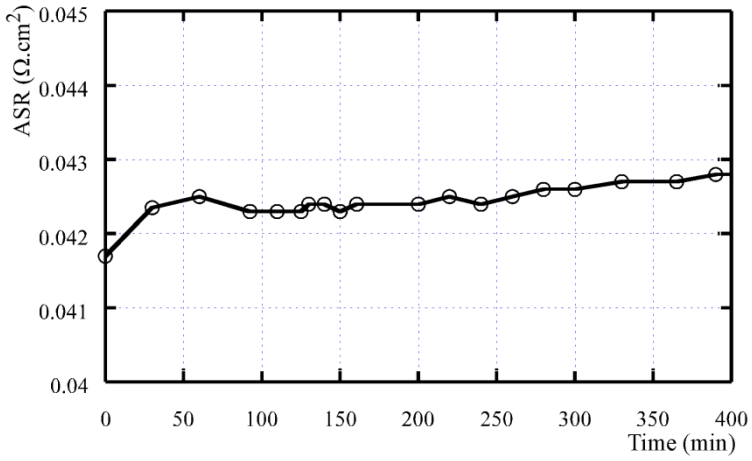

Figure 3.24. ASR for {composite contact material/channeled interconnect} interface as a function of time.

Figure 3.25 shows a representative SEM cross-section of the post-test composite-coated Crofer22APU interconnect on which EDX point analyses were performed. When comparing different EDX spectra, similar compositions were observed. All of the analyzed particles are composed mainly of La, Ni, Fe, and amounts of Cr. However, Figure 3.25(b) shows the lowest chromium content distribution in point 1.

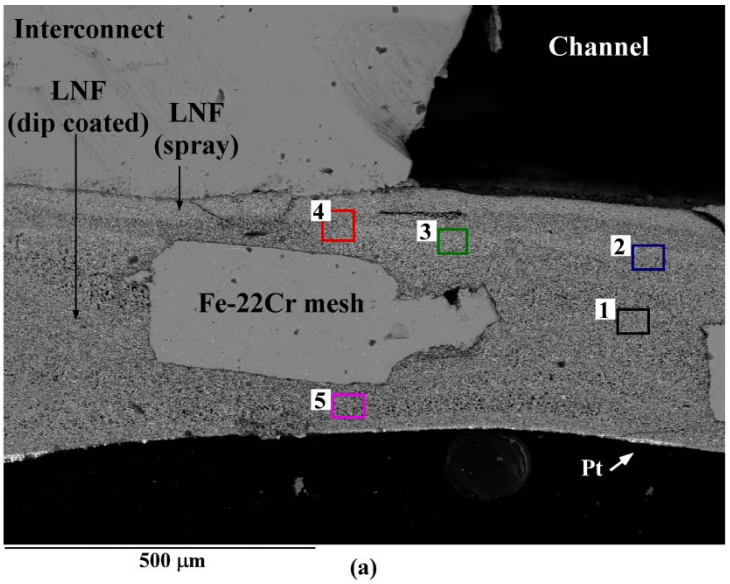

Figure 3.25. (a) SEM cross-section of studied system after ASR test with corresponding (b) EDX point analysis.

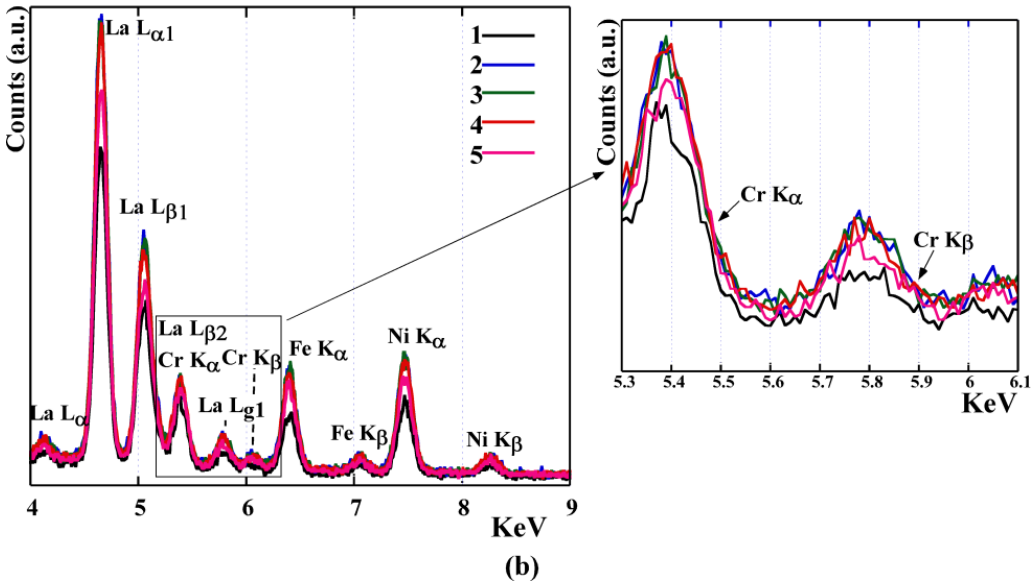

Figure 3.25. cont. (a) SEM cross-section of studied system after ASR test with corresponding (b) EDX point analysis.

The results of the initial characterization indicate that the developed coated interconnect system shows a low area specific resistance value since the generally accepted upper limit of ASR for SOFC substrate is 0.1 $\Omega \cdot cm^2$ [65,97,98]. Its contact resistance is also smaller than those reported in other studies[69,110,111], in which the electrical performance of perovskite coated metallic interconnect was studied. Thus, the mesh/LNF layer could be a suitable alternative for the SOFC interconnect coatings development.

3.2.3.2.1. Long-term stability of the system

The sintered system composed of {LNF-steel mesh contact composite/Crofer22APU channeled interconnect} was treated at 800 ºC for 1000 h, in air. Figure 3.26 shows X-ray micro-diffraction pattern refinements performed on the rib (Figure 3.26(a)) and the channel (Figure 3.26(b)) of the interconnect in contact with the composite material, after the long term treatment.

[110] Ming-Jui T., Chun-Lin C., Shyong L. $La_{0.6}Sr_{0.4}Co_{0.2}Fe_{0.8}O_3$ protective coatings for solid oxide fuel cell interconnect deposited by screen printing. *J. Alloy Compd.* 489 (**2010**) 576-581.

[111] Tucker M.C., Cheng L., DeJonghe L.C. Inorganic binder-containing composite cathode contact materials for solid oxide fuel cells. *J. Power Sources* 224 (**2013**) 174-179.

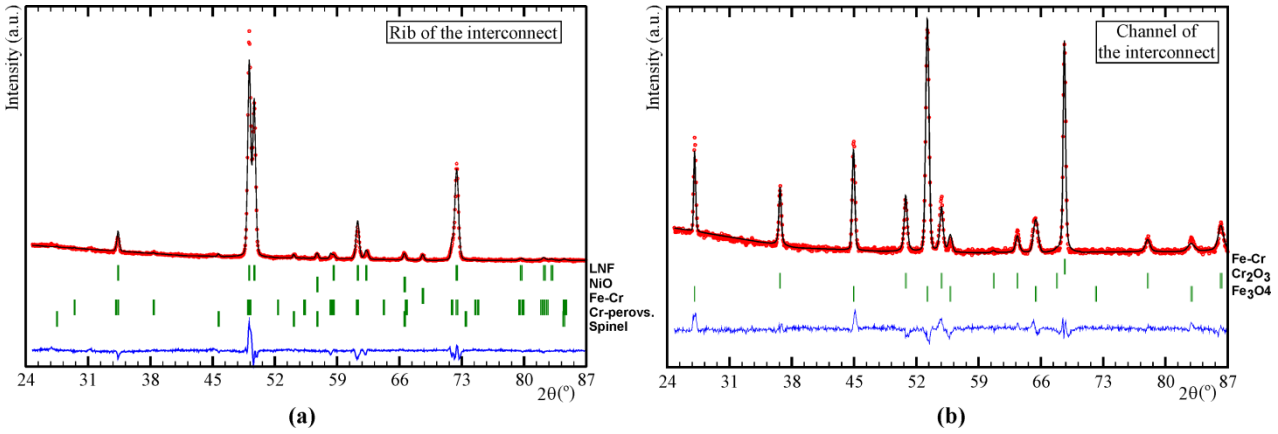

Figure 3.26. X-ray micro-diffraction pattern refinements performed (a) on the rib and (b) on channel of the interconnect in contact with composite material, after long term heat treatment.

The formed phases and their quantitative analysis (% in weight) are presented in Table 3.14. These analyses reveal that in the rib zone the main and secondary phases were $LaNi_{0.6}Fe_{0.4}O_3$ (83.4(8)% in weight) and $La(Ni,Fe,Cr)O_3$ (13.3(4)% in weight) as well as, NiO, Fe-Cr, and $(Cr,B)_3O_4$ spinel (B= Fe, Mn, Ni), respectively. In contrast, the channel zone results show as the main phase Fe_3O_4 (69.9(8)% in weight) and as secondary phases: Fe-Cr, and Cr_2O_3.

Table 3.14. X-ray micro-diffraction quantitative (%wt.) analysis of the formed phases on the rib and channel of the interconnect in contact with composite material after long-term heating in air.

Phase	Space group	Nº PDF	Rib (%wt.)	Channel (%wt.)
$LaNi_{0.6}Fe_{0.4}O_3$	R-*3c*	88-0637	83.2(8)	-
$La(Ni,Fe,Cr)O_3$	P*bnm*	24-1016	13.3(4)	
Fe-Cr	I*m3m*	34-0396	1.1(1)	16.2(2)
NiO	F*m-3m*	73-1519	2.2(2)	-
$MnCr_2O_4$	F*d-3m*	31-0630	< 0.2	-
Cr_2O_3	R-*3c*	85-0730	-	13.9(3)
Fe_3O_4	F*d-3m*	19-0629	-	69.9(8)

The original Fe-Cr substrate was identified indicating that the X-ray penetration was enough to observe the signal of all the formed layers. The presence of NiO might entail that Ni is partially extracted from the LNF perovskite lattice, allowing the formation of $La(Ni,Fe,Cr)O_3$, in good agreement with Ref. [112].

The LNF ceramic coating might act as a protective coating. Hence, Cr_2O_3 and Fe_3O_4 phases are observed on the channels. Furthermore, the absence of Cr_2O_3 on the rib of the interconnect, can also imply that chromium has completely reacted to form Cr-perovskite and/or $(Cr,B)_3O_4$ (B= Mn, Fe, Ni) spinel phase[113]. An interconnect without ceramic coating at long exposure to air, can promote Fe_3O_4 formation rather than the formation of a chromia/spinel protective scale, concluding in the

[112] Stodolny M.K., Boukamp B.A., Blank D.H.A., Van Berkel F.P.F. $La(Ni,Fe)O_3$ stability in the presence of chromia-A solid-state reactivity study. *J. Electrochem. Soc.* 158(2) (**2011**) B112-B116.

[113] Wang K., Liu Y., Fergus J.W. Interaction between SOFC interconnect coating materials and chromia. *J. Am. Ceram. Soc.* 94(12) (**2011**) 4490-4495.

formation of a non-protective or Fe-rich scale[114-116]. Figure 3.27 shows the surface of the composite material which was in contact with the interconnect, after long term IT-SOFC conditions, EDX point analysis is also shown. The corresponding k ratios for identified elements in each point were listed in Table 3.15.

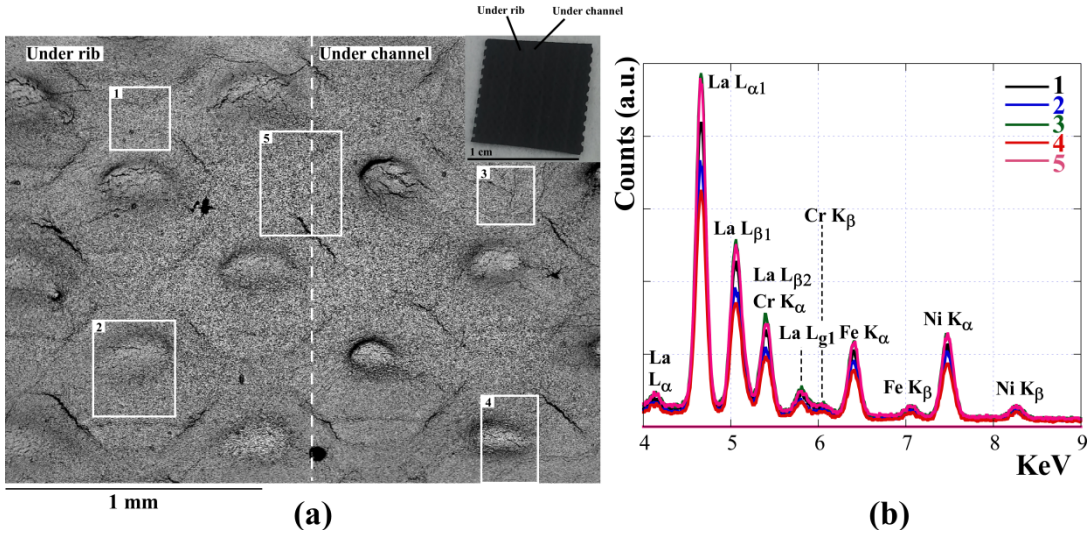

Figure 3.27. (a) SEM image and (b) EDX point analysis of the surface of the composite material which was in contact with the interconnect, after heated at 800 ºC for 1000 h, in air.

Table 3.15. Elemental k ratios measured by EDX point analysis performed on mesh/LNF material which was in contact with the interconnect after 1000 h at 800 ºC, in air (corresponding to Figure 3.27).

Spectrum	*La (k ratio)*	*Ni (k ratio)*	*Fe (k ratio)*	*Cr (k ratio)*
1	0.4	0.11	0.06	0.02
2	0.34	0.1	0.05	0.02
3	0.46	0.12	0.07	0.03
4	0.31	0.08	0.04	0.02
5	0.45	0.12	0.07	0.03

Two different areas were identified at the composite contact surface: the area of the composite (i) under the rib, and (ii) under channel of the interconnect. In both zones, the qualitative EDX analyses indicate that the analyzed grains contain La, Ni, Fe and Cr elements. Thus, the composite direct contacted (the rib) and no-contacted (channel) with the interconnect present similar elements distribution. These results indicate that the dominant cause for system degradation depends on both Cr vaporization from the interconnect steel and solid phase diffusion of Cr from the mesh alloy[117].

[114] Shong W.J., Liu C.K., Chen C.Y., Peng C.C., Tu H.J., Fey G.T.K., Lee R.Y., Kao H.M. Effects of lanthanum-based perovskite coatings on the formation of oxide scale for ferritic SOFC interconnect. *Mater. Chem. Phys.* 127 (**2011**) 45-50.

[115] Stojanovic M., Haverkamp R.G., Mims C.A., Moudallal H., Jacobson A.J. Synthesis and characterization of $LaCr_{1-x}Ni_xO_3$ perovskite oxide catalysts. *J. Catal.* 165 (**1997**) 315-323.

[116] Essuman E., Meier G.H., Zurek J., Hänsel M., Norby T., Singheiser L., Quadakkers W.J. Protective and non-protective scale formation of NiCr alloys in water vapour containing high- and low-pO_2 gases. *Corros. Sci.* 50(6) (**2008**) 1753-1760.

[117] Jiang S.P., Chen X. Chromium deposition and poisoning of cathodes of solid oxide fuel cells-A review. *Int. J. Hydrogen Energ.* 39(1) (**2014**) 505-531.

The composite contact surface was also characterized using XPS. Five relatively strong peaks were detected in the observed channel and rib contact areas of the surface of the metallic/ceramic composite material, after long-term heat treatment, using wide scan to 1385 eV, attributable to O 1s, Cr 2p, Mn 2p, Fe 2p and La 3d photoelectrons in Figure 3.28.

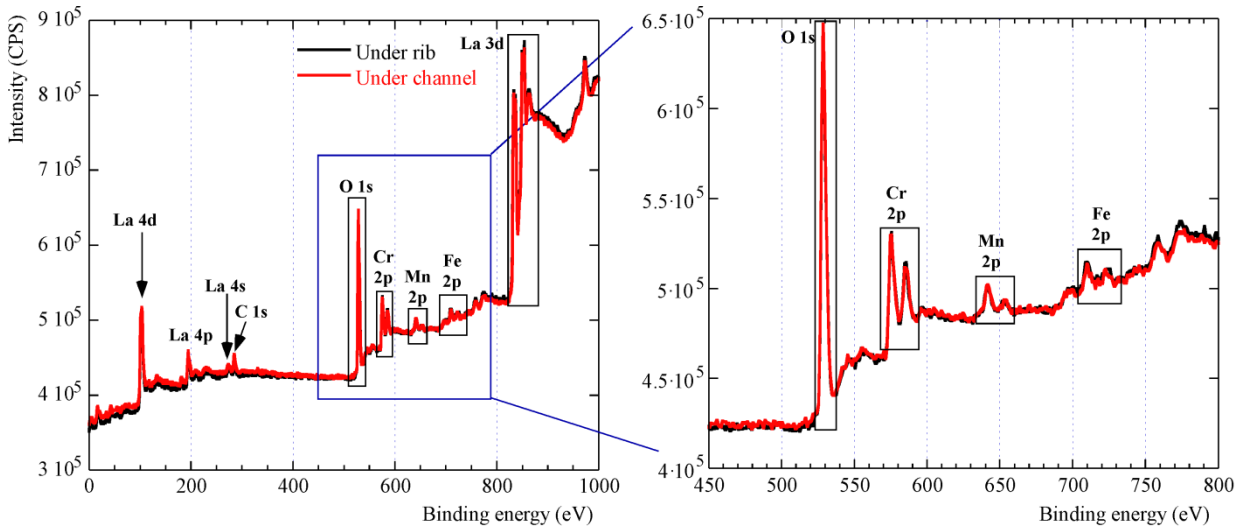

Figure 3.28. Wide scan XPS spectra of composite contact material under the rib and channel after long-term heated at 800 ºC in air.

The deconvolution of these peaks for both studied zones is shown in Figures 3.29 (surface of the composite under channel) and 3.30 (surface of the composite under the rib).

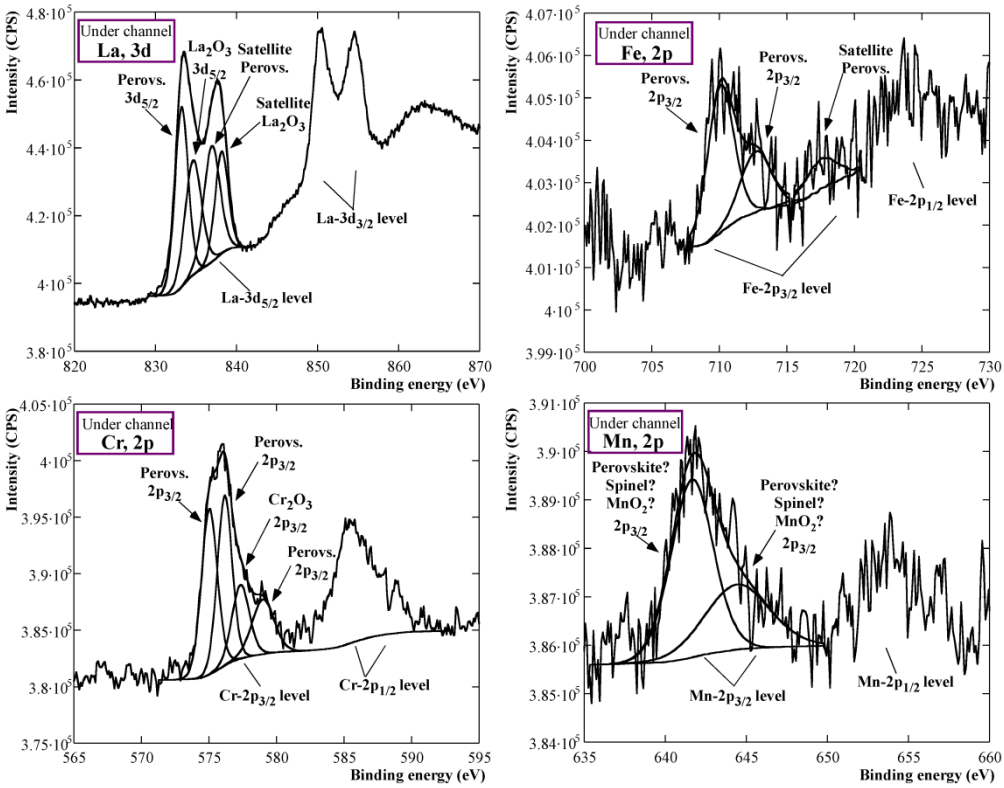

Figure 3.29. Detailed XPS spectra of La $3d_{5/2}$, Cr $2p_{3/2}$, Mn $2p_{3/2}$ and Fe $2p_{3/2}$ of the surface of LNF/Fe-22Cr composite contact material under the channel of the interconnect, after long-term heated at 800 ºC in air.

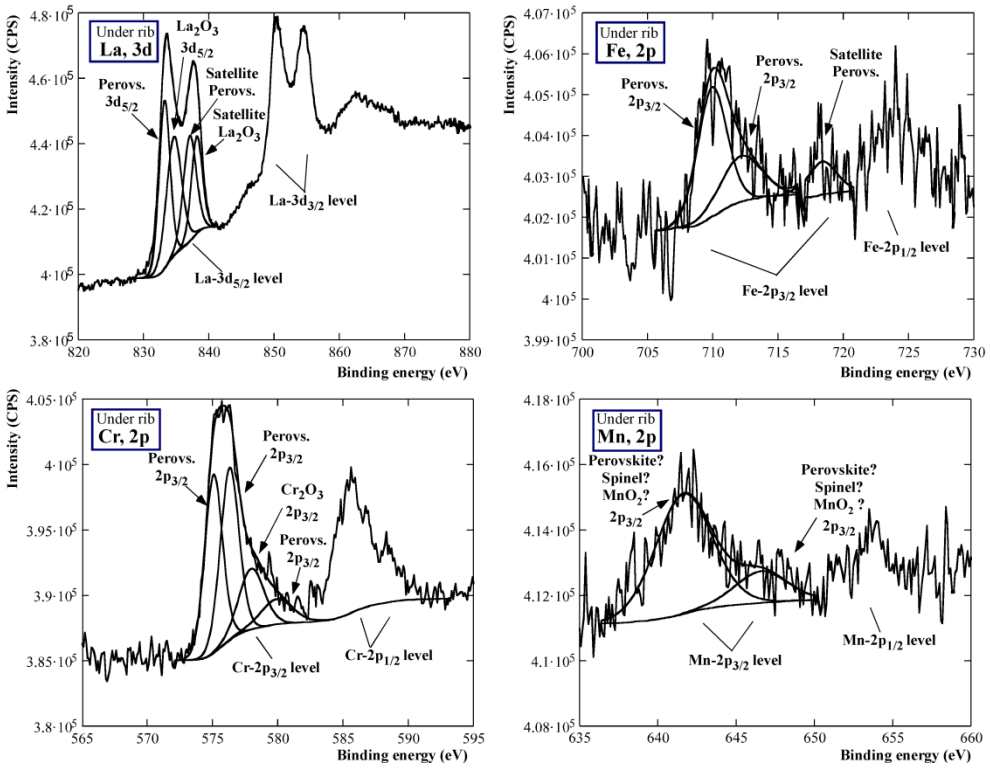

Figure 3.30. Deconvolution of La $3d_{5/2}$, Cr $2p_{3/2}$, Mn $2p_{3/2}$ and Fe $2p_{3/2}$ XPS peaks identified on the surface of LNF/Fe-22Cr composite contact material under the rib of the interconnect, after long-term heated at 800 ºC in air.

Detailed analysis of the main deconvolution peaks, including binding energies (BEs) and relative atomic percentage concentration of detected elements are listed in Table 3.16.

Table 3.16. XPS analysis results of detected elements for the contact surface of the composite in contact with the rib and under channel of the interconnect, after heating at 800 ºC for 1000 h in air.

Peak	**Surface under channel**		**Surface in contact with the rib**	
	BE (eV)	% at. Conc.	BE (eV)	% at. Conc.
La $3d_{5/2}$ in ABO_3	833.22; 836.95(sat.)	9.2	833.23; 837.09(sat.)	8.8
La $3d_{5/2}$ in La_2O_3	834.65; 838.16(sat.)	7.0	834.66; 838.17(sat.)	7.9
Cr $2p_{3/2}$ in ABO_3	575.04;576.17; 579	8.3	575.1;576.32; 579.94	8.4
Cr $2p_{3/2}$ in Cr_2O_3	577.35	1.7	577.99	1.8
Fe $2p_{3/2}$ in ABO_3	710.1;712.69; 717.53(sat.)	1.7	709.96;712.17; 718.38(sat.)	1.8
Mn $2p_{3/2}$	641.65;644.42	2.6	641.65;646.59	2.8
O 1s	528.85;530.46; 531.72;532.9	69.5	528.89;530.57; 531.76;533.26	68.5

The data measured in the present study were compared with the XPS spectra for perovskite-type oxide structures[118,119]. This comparison indicated, in both areas, for La, there are two peaks, one at ~833 eV corresponding to La^{3+} in perovskite phase and, another at ~835 eV which is assigned to La^{3+} in La_2O_3, in good agreement with our previous studies[76]. In addition, the binding energies of ~710 eV and ~712 eV could allow the presence of iron in perovskite[120]. Thus, the peaks appearing at ~575 eV, ~576 eV and ~579 eV indicated the appearance of chromium in perovskite with ABO_3 structure[96,121] (Table 3.16), in good agreement with the obtained XRMD results in which Cr-perovskite was quantified (Table 3.14). Besides, in Ref. [112], the $LaNi_{0.6}Fe_{0.4}O_3$ stability in the presence of chromia was investigated, concluding Cr-cations moves into the perovskite structure, replacing first Ni- and then Fe-cations. The presence of nickel was not detected by XPS, which could indicate the exchange of Ni with Cr in the initial perovskite structure. In addition, for both analyzed zones, the presence of Mn is observed from the peaks at ≈642 eV, ≈644 eV and ≈647 eV (Mn $2p_{3/2}$), in good agreement with other authors[122-124].

Analyses from both EDX and XPS showed similar results for the analyzed composite material areas which were in contact with interconnect. According to other authors[125], the XPS technique is more sensitive for surface composition analysis and detects a depth of ~5 nm while EDX is able to measure ~1μm depth. Thus, the difference means that Mn is more concentrated on the composite surface (surface in contact with the rib and under channel of the interconnect), not through the bulk, providing the formation of a low thickness Mn-spinel barrier layer[126]. This might also partly explain why the detected (% in weight) $MnCr_2O_4$, by XRMD, is low.

Evaluation of the long-term chemical compatibility of the studied system revealed that the direct exposure to air increased the oxidation of interconnect, leading to the growth of a Cr_2O_3 layer and formation of Fe_3O_4 oxide on the channel of the alloy substrate. Since chromium appears to have a tendency to incorporate into the LNF structure, this material could be considered a suitable candidate for reducing the degradation of the cell.

---

[118] Crumlin E.J., Mutoro E., Liu Z., Grass M.E., Biegalski M.D., Lee Y.L., Morgan D., Christen H.M., Bluhm H., Shao-Horn Y. Surface strontium enrichment on highly active perovskites for oxygen electrocatalysis in solid oxide fuel cells. *Energ. Environ. Sci.* 5 (**2012**) 6081-6088.

[119] Konysheva E.Y., Francis S.M. Identification of surface composition and chemical states in composites comprised of phases with fluorite and perovskite structures by X-ray photoelectron spectroscopy. *Appl. Surf. Sci.* 268 (**2013**) 278-287.

[120] Ghaffari M., Shannon M., Hui H., Tan O.K., Irannejad A. Preparation, surface state and band structure studies of $SrTi_{(1-x)}Fe_{(x)}O_{(3-\delta)}$ (x=0-1) perovskite-type nano structure by X-ray and ultraviolet photoelectron spectroscopy. *Surf. Sci.* 606 (**2012**) 670-677.

[121] Jiang Y., Gao J., Liu M., Wang Y., Meng G. Synthesis of $LaCrO_3$ films using spray pyrolysis technique. *Mater. Lett.* 61 (**2007**) 1908-1911.

[122] Nesbitt H.W., Banerjee D. Interpretation of XPS Mn(2p) spectra of Mn oxyhydroxides and constraints on the mechanism of MnO_2 precipitation. *Am. Mineral.* 83 (**1998**) 305-315.

[123] Ramana C.V., Massot M., Julien C.M. XPS and Raman spectroscopic characterization of $LiMn_2O_4$ spinels. *Surf. Interface Anal.* 37 (**2005**) 412-416.

[124] Wei Z.X., Xiao C.M., Zeng W.W., Liu J.P. Magnetic properties and photocatalytic activity of $La_{0.8}Ba_{0.2}Fe_{0.9}Mn_{0.1}O_{3-\delta}$ and $LaFe_{0.9}Mn_{0.1}O_{3-\delta}$. *J. Mol. Catal. A-Chem.* 370 (**2013**) 35-43.

[125] Li W., Lu K., Xia Z. Interaction of $(La_{1-x}Sr_x)_nCo_{1-y}Fe_yO_{3-\delta}$ cathodes and AISI 441 interconnect for solid oxide fuel cells. *J. Power Sources* 237 (**2013**) 119-127.

[126] Sabioni A.C.S., Huntz A.M., Borges L.C., Jomard F. First study of manganese diffusion in Cr_2O_3, polycrystals and thin films, by SIMS. *Phil. Mag. Lett.* 87(12) (**2007**) 1921-1937.

3.2.4. Conclusions

An uncoated and $MnCo_{1.9}Fe_{0.1}O_4$ (MCF) coated Fe-22Cr meshes were dipped into $LaNi_{0.6}Fe_{0.4}O_{3-\delta}$ (LNF) slurry to form a continuous conductive/protective layer for Crofer22APU interconnect. It has been demonstrated that if the deposition of the protective coating was not enough to form a dense and continuous layer across the width of the Fe-22Cr mesh, then the use of MCF spinel layer is not enough to prevent chromium migration up to the LNF coating. However, when mesh/LNF material was directly adhered to the interconnect, the obtained ASR value of 0.0425(2) $\Omega \cdot cm^2$ was stable for 400 min, indicating initial good adherence between both materials. The evaluation of long-term chemical compatibility of this system, without applying a current source, revealed that the presence of a composite coating on the rib of interconnect limited the growth of the chromia-based layer and formation of iron oxides on alloy substrate, reducing the contact resistance of the system. Future work will include electrochemical measurements of mesh-LNF/interconnect structure for extended periods.

4. REAL SYSTEM EVALUATION: CHANNELED INTERCONNECT-LASER MICROMACHINED COMPOSITE CONTACT LAYER-CATHODE STRUCTURE

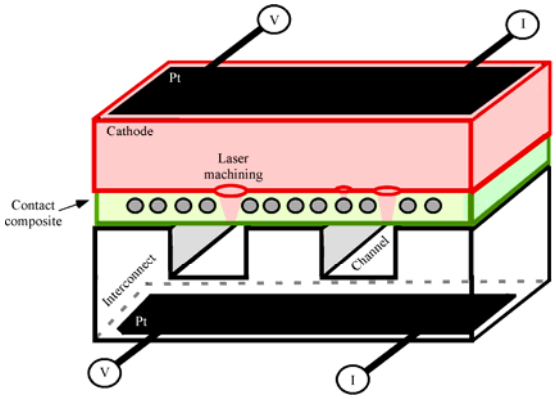

4.1. Femtosecond laser micromachining of metallic/ceramic composite material for solid oxide fuel cell devices. *J. Power Sources*, under review (D-15-02057), **2015**.

4.2. Laser machining of $LaNi_{0.6}M_{0.4}O_{3-\delta}$ (M: Fe,Co) dip coated on a Fe-22Cr mesh material to obtain a new contact coating for SOFC: interaction between Crofer22APU interconnect and $La_{0.6}Sr_{0.4}FeO_3$ cathode. *Int. J. Hydrogen Energ.*, in press (doi: 10.1016/j.ijhydene.2015.04.134), **2015**.

Resultados más relevantes *

*** Se muestra un resumen de los resultados más relevantes registrados en las publicaciones contenidas en la presente sección.**

Con objeto de garantizar el flujo de gas oxidante a través del composite metálico-cerámico, mostrado en la sección anterior, se han realizado microperforaciones sobre el mismo, utilizando un laser de femtosegundos. Se han optimizado los parámetros del laser con objeto de conseguir la perforación completa del material con el mínimo daño en la zona adyacente al cráter. Los resultados muestran que la eficiencia del micromecanizado es independiente de la composición del material cerámico empleado, siendo necesarios 4000 pulsos de 20 μJ y 40 fs de ancho, cada uno. Se observan dos zonas diferenciadas en la muestra: (i) área próxima, y (ii) área lejana a la malla metálica. En la zona expuesta al material metálico se identifican depósitos de óxidos de hierro y cromo superficiales, debidos a la volatilización y oxidación de la malla y su posterior resolidificación, consecuencia de la interacción laser-metal. Sin embargo, los análisis EDX de diferentes puntos de la sección transversal del composite micromecanizado, han indicado que se mantiene la composición del material cerámico inicial en las zonas próximas a la microperforación, y que la oxidación causada en la malla es de corto alcance, manteniendo su carácter metálico en las zonas analizadas a ~65 μm del cráter.

Después de los resultados satisfactorios obtenidos en el micromecanizado del composite, se ha seguido el mismo patrón de micromecanizado en los sistemas interconector-composite y, a continuación se ha depositado el cátodo LSF sobre el material de contacto irradiado. La reproducibilidad del proceso se ha estudiado mediante la repetición de, al menos, cuatro réplicas para cada sistema y su posterior caracterización electroquímica. El buen acuerdo entre las señales de ASR justifica la reproducibilidad del proceso, obteniéndose un valor promedio de 0.02(1) y 0.06(1) $\Omega \cdot cm^2$ para las celdas interconector-malla/LNC "micro" -LSF e interconector-malla/LNF "micro" -LSF, respectivamente. Los ensayos de durabilidad a 800 ºC, han mostrado que la efectividad del composite de contacto, con el tiempo, depende de la adherencia de la parte cerámica con el interconector. Se ha observado una pérdida de adherencia para el sistema interconector-malla/LNC micromecanizada-LSF, debida al desajuste entre los correspondientes coeficientes de expansión térmicos (TECs); este efecto ha favorecido el transporte de las especies volátiles de cromo (CrO_3 (g), $CrO_2(OH)_2$ (g)), aumentado así la reactividad en esta celda. Los análisis cuantitativos de EDX han mostrado que una disminución en el contenido de hierro y cromo, tanto de la malla como del interconector, conlleva el aumento o la presencia de estos elementos en el material cerámico adyacente, siendo este efecto más notable cuando se emplea LNC. Asimismo, se ha observado un aumento de cromo en el cátodo que se ha introducido en la microperforaciones.

Los resultados obtenidos muestran una mayor estabilidad estructural y química para la celda interconector-malla/LNF micromecanizada-LSF, siendo ésta la más prometedora para su empleo en sistemas de pilas de combustible de óxido sólido (SOFC).

Relevant results *

*** A brief summary of the research papers results, which are included in the present section, is shown.**

Femtosecond laser machined holes are produced on the previously prepared composites. The laser parameters have been optimized to obtain a complete pore, in a reasonable amount of time and with the minimal damage in the adjacent material. Femtosecond laser ablation on these developed composites has been successfully performed using 4000 laser pulses of 20 μJ and 40 fs width each one. It has been demonstrated that the efficiency of laser micromachining in the studied specimens is independent of the ceramic composition. Two different areas are identified: the area of the ceramic coated (i) under the mesh opening and (ii) under the mesh wires. Around the craters close to metallic mesh, an accumulation of chromium, iron and oxygen deposits is identified due to the oxidation of metallic iron and chromium from the steel, allowing the formation of iron and/or chromium oxides. However, the EDX data of the border crater residues and of the more distant areas showed similar ceramic elemental composition. Moreover, the laser effect on the initial mesh elemental composition is very located, maintaining mesh metallic character from the crater up to 65 μm away.

Matrixes of holes are machined on interconnect-composite systems since femtosecond laser ablation on the formed contact materials has been successfully performed. Then, the LSF cathode was spray deposited onto the micromachined composite. In order to check the reproducibility of the process, at least four specimens were tested for each ceramic contact paste. The results support the reproducibility for all the measured structures, indicating similar signal during the contact resistance tests; ASR mean values for interconnect-ablated mesh/LNC-LSF and interconnect-ablated mesh/LNF-LSF are 0.02 (1) and 0.06 (1) $\Omega \cdot cm^2$, respectively. The effectiveness of the contact composite over time depends on the adherence of the ceramic coating on the alloy material. A loss of adherence has been reported between LNC paste coating and interconnect due to an insufficient match of the corresponding thermal expansion coefficients (TECs), which favours the transport or vaporization rate of Cr species (CrO_3 (g), $CrO_2(OH)_2$ (g)). From EDX quantitative analysis, a chromium content reduction in the interconnect as well as in the mesh followed by a Cr enrichment in the contact coating is observed, particularly when LNC is used. Moreover, the Cr is mainly concentrated in the LSF cathode, which was inside the holes.

Considering the obtained results, the application of laser micromachined mesh/LNF as a contact composite coating between Crofer22APU interconnect and $La_{0.6}Sr_{0.4}FeO_3$ cathode, in flow channel configuration, could provide adequate mechanical integrity and rapid oxidant gas transfer through interconnect/electrode interface, without compromising the contact resistance of the system.

4.1. Femtosecond laser micromachining of metallic/ceramic composite material for solid oxide fuel cell devices

J. Power Sources, under review (D-15-02057), **2015**.

Abstract

The possible commercialization of solid oxide fuel cell (SOFC) devices depends on its long-term durability, being the contact resistance between interconnect/cathode a key factor. A Fe-22Cr mesh is dipped into a ceramic slurry to form a high electron conduction metallic/ceramic layer as contact material for SOFC, using three different ceramic compositions: $LaNi_{0.6}Co_{0.4}O_{3-\delta}$ (LNC), $LaNi_{0.6}Fe_{0.4}O_{3-\delta}$ (LNF) and $(La_{0.8}Sr_{0.2})_{0.95}Fe_{0.6}Mn_{0.3}Co_{0.1}O_3$ (LSFMC). The viability of drilling holes with minimal damage in these composites to enhance the transport of the gas has been evaluated. The diagnosis of laser damage has been determined using a scanning electron microscopy (SEM) equipped with an energy dispersive X-ray spectroscopy (EDX) system. Femtosecond laser ablation on the samples has been successfully performed; the results indicated that the effect of drilling on the initial elemental composition is very located, considering little to produce a significant alteration of the system performance.

Keywords: Femtosecond laser; micromachining; metallic/ceramic composite; microstructure; solid oxide fuel cells.

Highlights

- Femtosecond laser ablation on metallic/ceramic composite has been performed.
- The efficiency of laser is independent of the ceramic composition.
- The effect on the initial elemental composition is very located.

4.1.1. Introduction

High electrical conductivity with an appropriate microstructure and gas permeability of electro-ceramic materials are critical issues in many electrochemical devices[1]. In particular, in the oxidizing side of solid oxide fuel cells (SOFCs) the cathode contact materials are required to reduce cell power losses, improving electrical contact between the interconnect ribs and the electrode[2] . Another critical issue, which limits the commercialization of SOFCs, is the evaporation of volatile Cr-rich species from chromia-forming ferritic stainless steel interconnect materials, i. e. CrO_3 (g) or $CrO_2(OH)_2$ (g), leading to rapid cathode degradation known as Cr-poisoning. Upon combination with oxygen ions, the volatile Cr-rich species are reduced back to Cr_2O_3 and decrease the cathode active area[3]. A cathode contact material has to be formulated to fulfill the requirements of a high electrical conductivity, low chromium cation and oxygen anion diffusivity, chemical compatibility with the chromia-forming interconnects and the perovskite cathodes, and an adequate gas permeability, maintaining the mechanical integrity of the formed layer[4]. The perovskite structured oxides, $A^{3+}B^{3+}O^{2-}{}_3$, where A is a rare-earth element and B is a first row transition metal, have been used by several authors as highly protective/conductive "Cr getter" interconnect coatings[5-7]. An improvement in electrons mobility through the interconnect/contact material interface could be achieved using a dense and continuous contact oxide layer on the metallic interconnect. According to previous studies[8], the incorporation of conducting wires and the design of porous channels in SOFC electrodes could increase cell performance via enhancing the transport of electrons as well as of the gases. In this context, we have recently demonstrated the viability of a new system configuration[9,10] consisting in the combination of a dense electron conduction ceramic material with Fe-22Cr composed mesh, that could give to a contact layer the required good mechanical properties to provide the continuity of the coating on the channeled interconnect. The obtained area specific resistance (ASR) values were reproducible and stable indicating good adherence between the composite material and interconnect. However, one of the main drawbacks of the mentioned alternative configuration is the lack of O_2 permeability. In order to overcome this problem, here we propose the dense microstructure adaptation at the requirement of the contact materials by means of

---

1 Sharaf O.Z., Orhan M. F. An overview of fuel cell technology: Fundamentals and applications. *Renew. Sust. Energ. Rev.* 32 (**2014**) 810-853.

2 Guoliang W., Guan W., Miao F., Wang W.G. Factors of cathode current-collecting layer affecting cell performance inside solid oxide fuel cell stacks. *Int. J. Hydrogen Energ.* 39 (**2014**) 17836-17844.

3 Hosseini N., Abbasi M.H., Karimzadeh F., Choi G.M. Development of $Cu_{1.3}Mn_{1.7}O_4$ spinel coating on ferritic stainless steel for solid oxide fuel cell interconnects. *J. Power Sources* 273 (**2015**) 1073-1083.

4 Tucker M.C., Cheng L., DeJonghe L.C. Selection of cathode contact materials for solid oxide fuel cells. *J. Power Sources* 196 (**2011**) 8313-8322.

5 Tietz F., Sebold D. Interface reactions between electrically conductive ceramics and ferritic steel-I. The system Cr-22Fe-0.5Mn/Mn_2O_3/(La,Ca)(Cr,Co,Cu)O_3. *Mater. Sci. Eng. B* 150 (**2008**) 135-140.

6 Sharma V.I., Yildiz B.. Degradation mechanism in $La_{0.8}Sr_{0.2}CoO_3$ as contact layer on the solid oxide electrolysis cell anode. *J. Electrochem. Soc.* 157(3) (**2010**) B441-B448.

7 Montero X., Tietz F., Stöver D., Cassir M., Villarreal I. Comparative study of perovskites as cathode contact materials between an $La_{0.8}Sr_{0.2}FeO_3$ cathode and a Crofer22APU interconnect in solid oxide fuel cells. *J. Power Sources* 188 (**2009**) 148-155.

8 Yoon C. Computational design, fabrication, and characterization of microarchitectured solid oxide fuel cells with improved energy efficiency. Ph.D. thesis work, Georgia Institute of Technology, **2010**.

9 Morán-Ruiz A., Vidal K., Larrañaga A., Laguna-Bercero M.A., Porras-Vázquez J.M., Slater P.R., Arriortua M.I. $LaNi_{0.6}Co_{0.4}O_{3-\delta}$ dip-coated on Fe-Cr mesh as a composite cathode contact material on intermediate solid oxide fuel cells. *J. Power Sources* 269 (**2014**) 509-519.

10 Morán-Ruiz A., Vidal K., Larrañaga A., Porras-Vázquez J.M., Slater P.R., Arriortua M.I. Evaluation of using protective/conductive coating on Fe-22Cr mesh as a composite cathode contact material for intermediate solid oxide fuel cells. *Int. J. Hydrogen Energ.* 40 (**2015**) 4804-4818.

high aspect ratio laser drilled micropores (Figure 4.1).

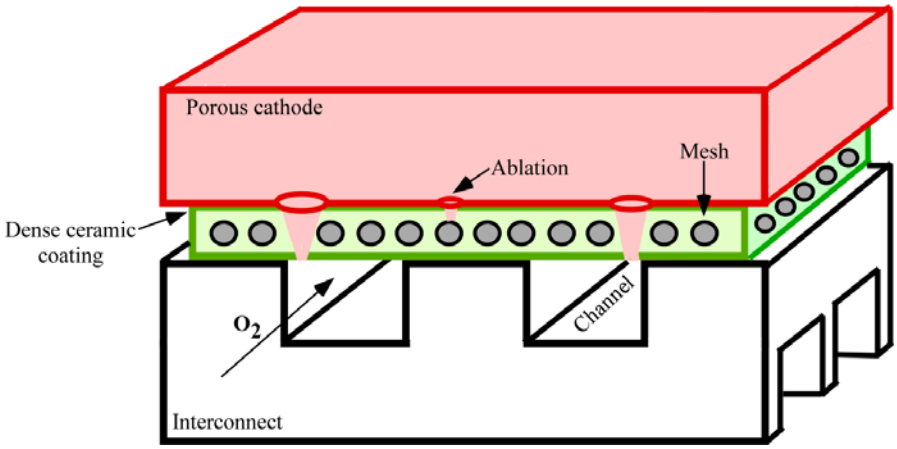

Figure 4.1. Schematic representation of oxidizing side of a single solid oxide fuel cell.

In this work we take advantage of the capability of ultrashort pulses to efficiently drill holes, without sample degradation caused by thermal decomposition[11-20], in a Fe-22Cr mesh/ceramic contact composite with different ceramic compositions: $LaNi_{0.6}Co_{0.4}O_{3-\delta}$ (LNC), $LaNi_{0.6}Fe_{0.4}O_{3-\delta}$ (LNF) and $(La_{0.8}Sr_{0.2})_{0.95}Fe_{0.6}Mn_{0.3}Co_{0.1}O_3$ (LSFMC). The optimal conditions to induce micro-pores with minimal damage in the composite materials have been determined. The morphology and chemical composition changes due to the laser processing have been analyzed by a scanning electron microscopy (SEM) equipped with an energy dispersive X-ray spectroscopy (EDX) system.

4.1.2. Experimental equipment and materials

4.1.2.1. Laser system

The laser set-up is described elsewhere (Figure 4.2)[19]. Femtosecond laser pulses were generated by a Ti: Saphire oscillator-regenerative amplifier system (1 kHz, 4.0 mJ, 40 fs pulses at 800 nm).

---

[11] Zhang N., Zhao Y., Zhu X. Light propulsion of microbeads with femtosecond laser pulses. *Opt. Express* 12 (**2004**) 3590-3598.

[12] Yang J.L., Yu J.L., Cui Y.Y., Huang Y. New laser machining technology of Al_2O_3 ceramic with complex shape. *Ceram. Int.* 38 (**2012**) 3643-3648.

[13] Hung C.H., Chang F.Y., Chang T.L., Chang Y.T., Huang K.W., Liang P.C. Micromachining NiTi tubes for use in medical devices by using a femtosecond laser. *Opt. Lasers Eng.* 66 (**2015**) 34-40.

[14] Leitz K.H., Redlingshöfer B., Reg Y., Otto A., Schmidt M. Metal ablation with short and ultrashort laser pulses. *Physics Procedia* 12 (**2011**) 230-238.

[15] Kim S.H., Sohn I.–B., Jeong S. Ablation characteristics of aluminum oxide and nitride ceramics during femtosecond laser micromachining. *Appl. Surf. Sci.* 255(24) (**2009**) 9717-9720.

[16] Türkoglu A.K., Ersoy T., Canbaz F., Akturk S. Effects of waveguide behavior during femtosecond-laser drilling of metals. *Appl. Phys. A* 108 (**2012**) 935-941.

[17] Kamlage G., Bauer T., Ostendorf A., Chichkov B.N. Deep drilling of metals by femtosecond laser pulses. *Appl. Phys. A* 77 (**2003**) 307-310.

[18] Döring S., Richter S., Nolte S., Tünnermann A. In situ imaging of hole shape evolution in ultrashort pulse laser drilling. *Opt. Express* 18(19) (**2010**) 20395-20400.

[19] Di Maio Y., Colombier J.P., Cazottes P., Audouard E. Ultrafast laser ablation characteristics of PZT ceramic: Analysis methods and comparison with metals. *Opt. Laser Eng.* 50 (**2012**) 1582-1591.

[20] Tong T., Li J., Longtin J.P. Real-time control of ultrafast laser micromachining by laser-induced breakdown spectroscopy. *Appl. Opt.* 43 (**2004**) 1971-1980.

The pulse energy is controlled by means of a variable neutral density filter in the 1-40μj range. The light is focused onto the sample, which is mounted in a 3D translation stage (1 μm precision) at atmospheric pressure, using a fused silica lens (f=100mm).

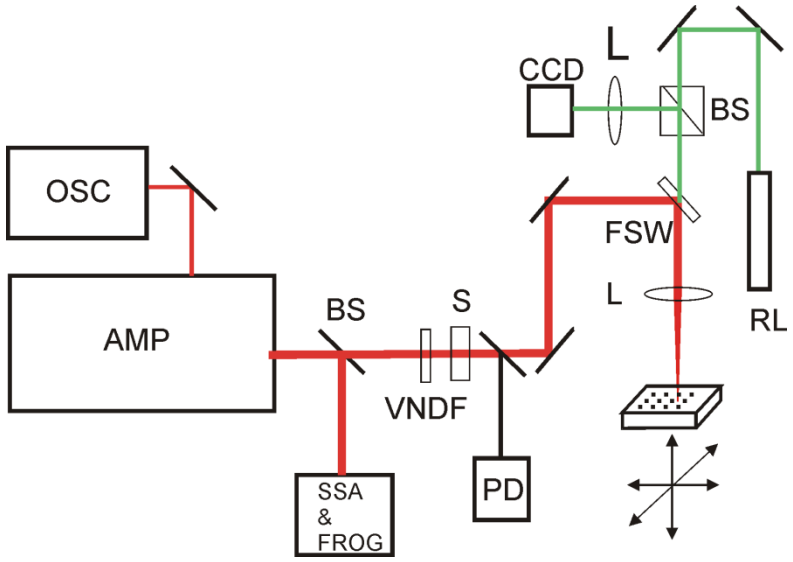

Figure 4.2. Schematic diagram of the experimental set-up: OSC: Ti: Shapphire oscillator. AMP: Ti: Shapphire regenerative amplifier. BS: Beam splitter. SSA & FROG: Single shot autocorrelator and FROG. VNDF: Variable neutral density filter. S: Shutter. L: f=100mm lens. RL: reference laser. CCD: camera.

Figure 4.3 shows an image of the beam obtained by placing a CMOS camera at the focal plane. The diameter of the spot ($FW1/e^2M$) is 40 μm. Polarization is linear and parallel to the sample surface.

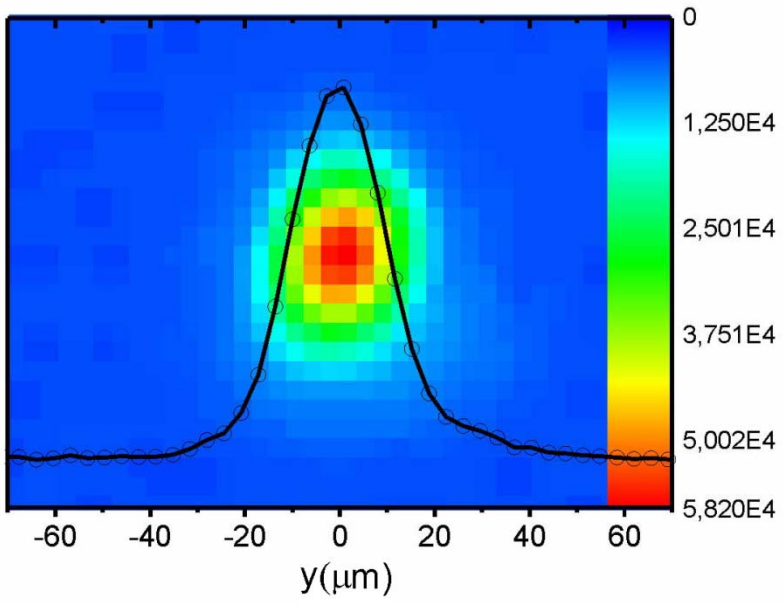

Figure 4.3. Image of the beam obtained by placing a CMOS camera at the focal plane.

In some of the experiments a Si photodiode is placed under the "sample" with the aim of

determine the number of pulses needed to through it.

4.1.2.2. Materials

The compositions of ceramic powders used in this study were $LaNi_{0.6}Co_{0.4}O_{3-\delta}$ (LNC), $LaNi_{0.6}Fe_{0.4}O_{3-\delta}$ (LNF) and $(La_{0.8}Sr_{0.2})_{0.95}Fe_{0.6}Mn_{0.3}Co_{0.1}O_3$ (LSFMC), all of them from NexTech, Fuel Cell Materials. In order to obtain metallic/ceramic composite, a Fe-22Cr stainless steel mesh (Fiaxell SOFC Technologies), with mesh opening of about 175 μm and a thickness of ~250 μm, was cut into 10 x 10 mm squares, cleaned with acetone in an ultrasonic bath and dried. The quantitative EDX analysis revealed that Fe-22Cr mesh contains as additives: tungsten (W) (2.3(2) % wt.), niobium (Nb) (0.4(1) % wt.), manganese (Mn) (0.6(1) % wt.) and titanium (Ti) (<0.1 % wt.). The squared-meshes were preoxidized at 600 ºC for 10 h and then dip coated[21] with corresponding ceramic paste (dip coating rate = 4.5 $mm \cdot s^{-1}$). The ceramic slurry was composed of ceramic powder (12.5 % in volume), dispersant (Dolapix, 1 % relative to ceramic powder, Zschimmer & Schwarz, Chemische Fabriken) to avoid the accumulation of ceramic particles and a binder (PVB, polyvinyl butyral, 5 % relative to the ceramic powder, Solutia Solutions) to increase the viscosity of the mixture and solvent (ethanol, 87.5 % in volume, Panreac). Finally, the formed metallic/ceramic composite was sintered at 1050 º C for 2 h to allow a dense ceramic contact material with a thickness of ~200 μm.

4.1.2.3. Characterization of microstructures

The morphology and chemical compositions of irradiated samples were characterized by a scanning electronic microscopy (SEM, JEOL JSM LSM-6400) equipped with an Oxford instrument INCA E-350 energy dispersive X-ray spectroscopy (EDX) system. Surface morphology was observed using secondary electrons (SE) at an accelerating voltage of 20 kV, a current of $1.1 \cdot 10^{-11}$ A, and working distances of 7 and 15 mm. Composition analysis was performed using back-scattered electrons (BSE) at 20 kV accelerating voltage and $5 \cdot 10^{-9}$ A current density. For EDX mapping the live time was set to 2457.60 s, using 1024 x 768 pixels. For the cross-section analysis, samples were embedded in epoxy resin to cut along its cross-section using a 127 x 0.4 mm diamond disk (speed: 3000 rpm, 0.010 mm/s) mounted in a conventional cutting-machine (Secotom-10, Struers), under a water flow. The obtained mould was polished using standard metallographic techniques, and coated with a coal graphite layer (10 nm) that was deposited by evaporation (Quorum Technologies Q150T ES sputter coater) to provide electrical conductivity. For the EDX point analysis the live time was set to 100 s. EDX system calibration was performed measuring the beam current on pure element standards. The intensity of X-rays produced at a given energy provides a measure of the amount of the element present in the sample by comparison with measured standards. The data processing was carried out using Oxford INCA software. The characteristic emission lines used for the analysis were L_α for La and Nb, K_α for Co, Cr, Fe, Ni and O, and M_α for W.

[21] Gurauskis J. Deposition via dip coating technique of dense yttrium stabilized zirconia layers. *Int. J. Appl. Ceram. Technol.* 10(1) (**2013**) 79-86.

4.1.3. Results and discussion

This section is organized as follows: first we will present some of the results that allow us to define laser parameters such as pulse energy and number of pulses for an adequate processing, it is, to obtain a complete pore, in a reasonable amount of time and with the minimal damage in the adjacent material. After that we will show EDX analysis of the surface and cross sections that will allow us to determine the magnitude and extension of the laser induced damage.

Figure 4.4 shows the effect of 4000 laser shots with 1, 2 and 5 μJ on the LNC/Fe-22Cr mesh composite. It can be observed that no morphologic changes are produced with 1 μJ pulses. When the laser intensity is increased to 2 μJ, a small mark is engraved into sample. It must be notice that its diameter (~6 μm) is clearly smaller than the FWHM of the laser spot at the focus. As expected, further increase of the intensity produces wider and deeper holes. Without other analysis of this results, a threshold for multipulse laser ablation close to 2 μm can be estimated.

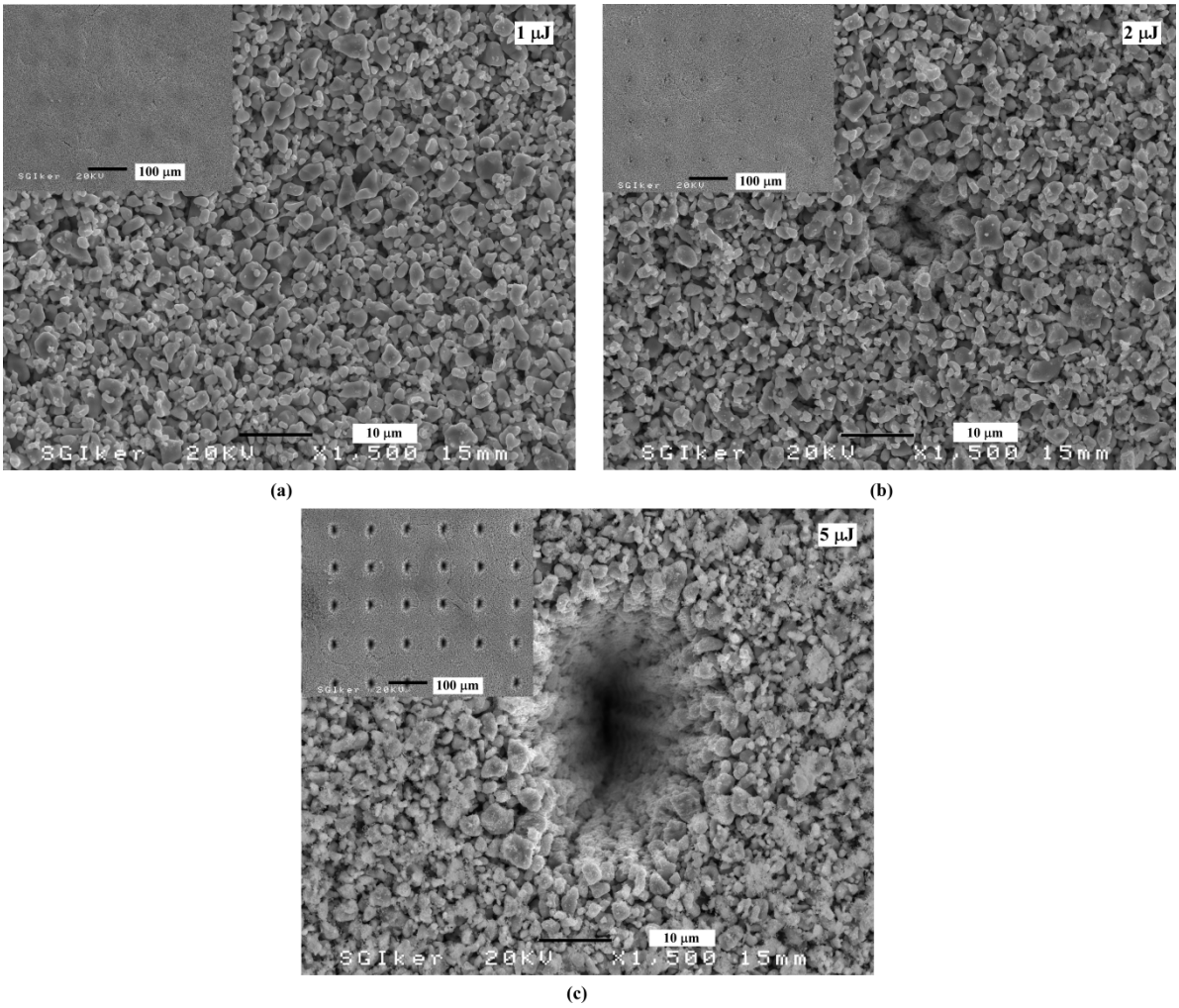

Figure 4.4. SEM images of the effect of 4000 laser shots with (a) 1 μJ, (b) 2 μJ and (c) 5 μJ on LNC/mesh composite.

A more rigorous determination of this parameter can be carried out by the extrapolation of the ablated diameter as a function of pulse energy according to this expression[15,19] (and references therein):

$$D^2=2\ w_0^2\ \ln(E_0/E_{th}) \qquad (4.1)$$

Being D the crater diameter, w_0 the laser beam waist ($FW1/e^2M$), E_0 the pulse energy (or fluence) and E_{th} the threshold energy (or fluence). Figure 4.5 includes the experimental crater diameter measured as a function of the laser intensity together with the fitting to eq. 4.1, yielding a threshold energy of 1.9 μJ (0.12 J/cm^2).

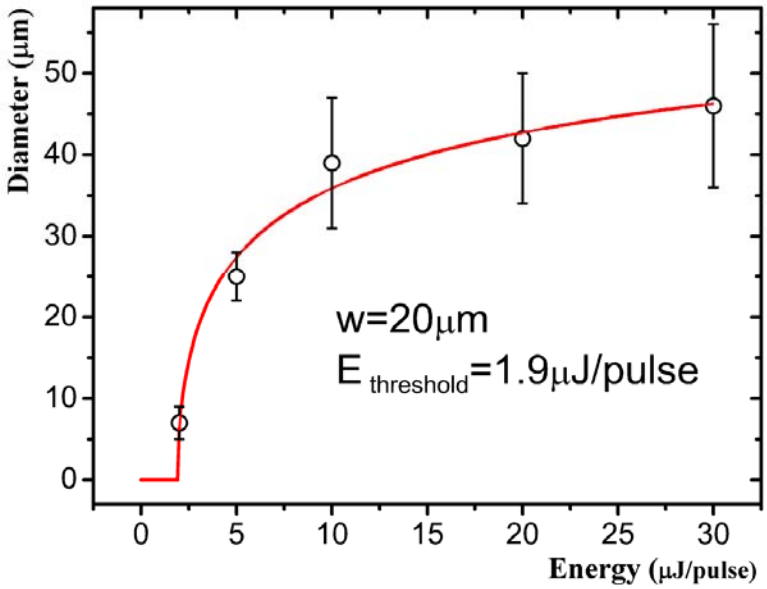

Figure 4.5. Experimental values of entrance hole diameter for different pulse energies (circles) together with the fitting to Eq. 4.1.

In order to measure the number of laser shots needed to go through the material, a Si photodiode was placed under the sample, and the magnitude of its signal recorded with a digital oscilloscope as a function of the pulse number in a fixed position is recorded, as it is shown in Figure 4.6. The recorded curves correspond to different pulse energies 10, 20 and 30 μJ. It must be mentioned that each of them correspond to the average of 20 runs acquired in different positions on the sample separated 100 μm, and transmitted light was only observed when the laser does not hit the mesh wires at any intensity, because of the higher ablation rate of Fe-22Cr. This observation corroborated by the SEM images presented later, in which the exit hole is only observed in wire free zones, as it said before. The data presented in Figure 4.6 show that while the pore is completed during the first 350 pulses for pulse energies greater that 20 μJ, no light is detected in the 10 s observation window what reduces the intensity operating range. This dramatic change from 10 to 20 μJ could be induced by non linear propagation and air ionization inside the hole[16,17]. While no important dependence of the entrance hole has been observed with the number of pulses, the increase of photodiode signal with the number of pulses points to growth of the inner and exit hole. This fact, previously reported in other materials[17,18], indicates that there is some degree of control of pore size by adjusting the number of shots used to go through the sample, an interesting aspect for future fuel flow control.

Another aspect that can be pointed out in the light of these measurements is that while the slope in the 20μJ case is more uniform along the experiment, a more clear change is appreciated at 2-3 seconds at higher intensities. This presumably indicates that the pore is about to reach an asymptotic size (<20μm). Although the comparison between the two curves must be taken cautiously due to the mesh wire interference, it indicates that more light is transmitted through the 30μJ hole indicating a greater pore diameter, specially during the first 4000 shots. Ablation rate can be also estimated on the basis of the data presented in Figure 4.6. If we consider the 200 μm thickness of the sample and that, using 20 μJ pulses, light is detected after the 350 first shots, and approximate value for the ablation rate of 570 nm/pulse can be provided for multipulse operation.

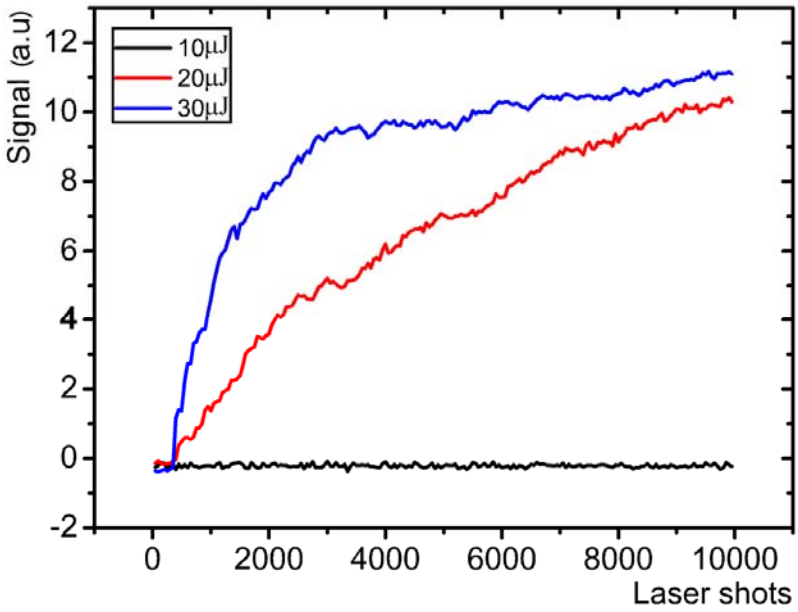

Figure 4.6. Laser intensity registered at the backside of the sample by means of a Si photodiode as a function of the number of laser pulses applied.

Similar studies have been carried out in three different composites, LNC/Fe-22Cr mesh, LNF/Fe-22Cr mesh and LSFMC/Fe-22Cr mesh obtaining identical results. To illustrate this fact, Figure 4.7 shows the results of machining these samples using 4000 laser pulses of 20 μJ. To avoid reiteration, in the following, only results corresponding to LNC/Fe-22Cr mesh will be presented. Prior studies of our group[9] have been evaluated the feasibility of using a Fe-Cr mesh dipped into LNC slurry as a uniform cathode contact layer for solid oxide fuel cells, obtaining promising results.

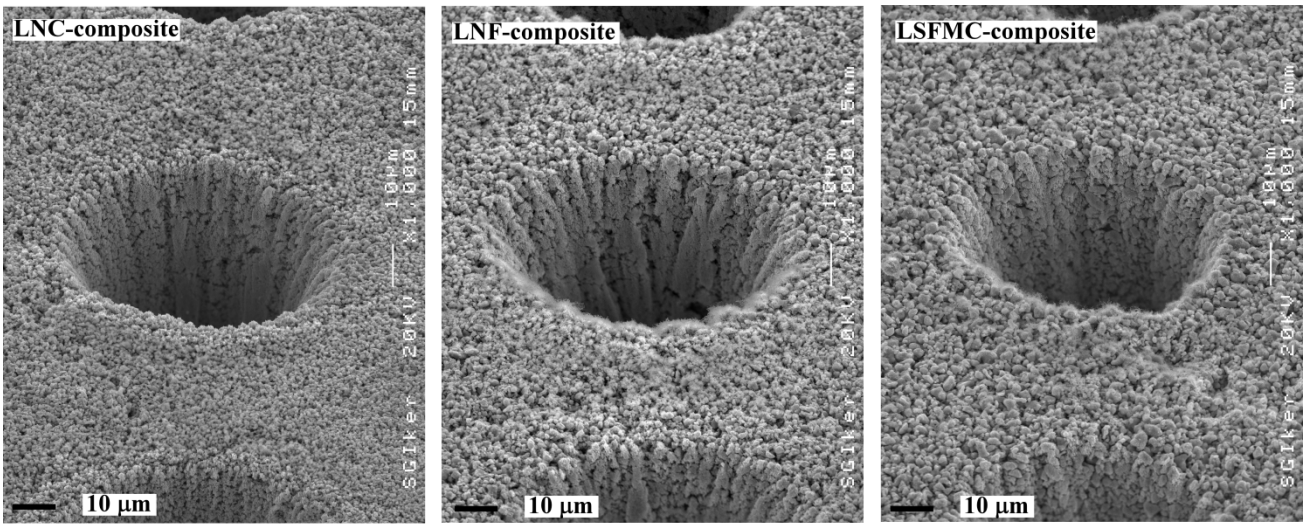

Figure 4.7. Secondary electrons (SE) micrographs of craters performed in: (a) $LaNi_{0.6}Co_{0.4}O_{3-\delta}$ /Fe-22Cr mesh, (b) $LaNi_{0.6}Fe_{0.4}O_{3-\delta}$ /Fe-22Cr mesh and (c) $(La_{0.8}Sr_{0.2})_{0.95}Fe_{0.6}Mn_{0.3}Co_{0.1}O_3$/Fe-22Cr mesh composites. Laser parameters: wavelength 800 nm; pulse energy 20 μJ; pulse duration 40 fs; pulse repetition rate 1 kHz; number of pulses per hole 4000.

In order to study laser-induced damage by varying pulse laser energy, matrixes of holes are machined with separation between drillings equal to 100 μm in both horizontal (x) and vertical (y) directions to complete an area of 2 x 2 mm^2. Three different matrixes are performed using 10 μJ, 20 μJ and 30 μJ pulse energy of each one (Figure 4.8). The first aspect that should be mentioned in the light of the SEM images presented in Figures 4.7, 4.8 and 4.10 is that hole surroundings are relatively free of molten and resolidified material at any laser condition. However, the surface appears darkened, specially at pulse energies greater than 10 μJ. The distribution of these dark zones resembles the mesh pattern (Figure 4.9), corresponding to areas in contact with the mesh (Figures 4.8 and 4.10). They are associated with the oxidation of evaporated metallic substrate, which makes the formation of an oxide layer on the surface of the wires. This effect is especially clear when 20 and 30 μJ pulse energy is used, in good agreement with Figures 4.8 and 4.10. The surface morphology of the exit holes is very irregular, with important damages when 30 μJ irradiation is used, as can be observed from Figure 4.11. Thus, 20 μJ laser energy condition is selected to EDX mapping analysis of the ablated composite surface (Figure 4.12).

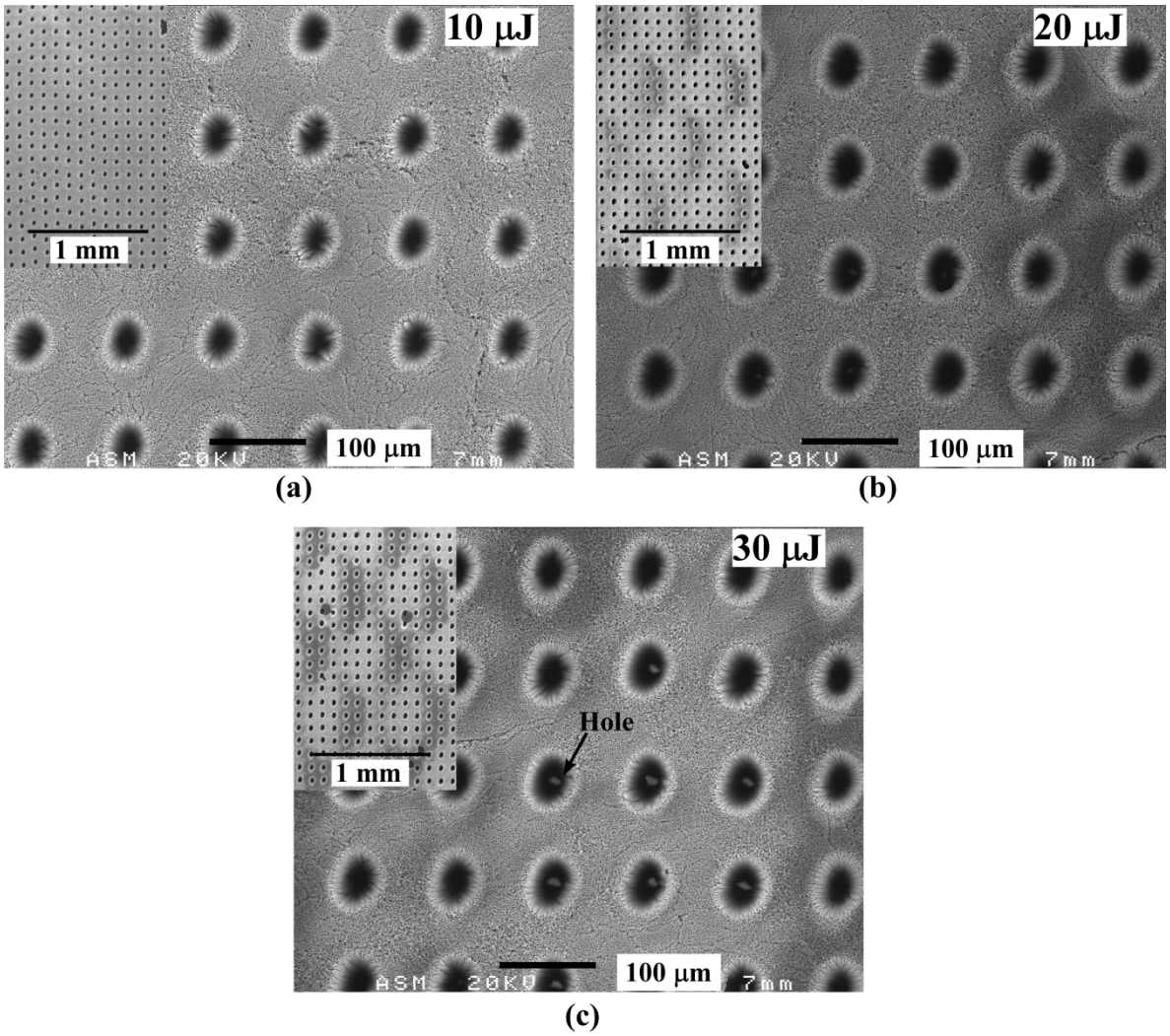

Figure 4.8. Back-scattered electrons (BSE) images of matrixes of holes performed in $LaNi_{0.6}Co_{0.4}O_{3-\delta}$/Fe-22Cr mesh composite with 4000 pulses of (a) 10 μJ, (b) 20 μJ and (c) 30 μJ, using 1kHz repetition rate and 40 fs pulse width.

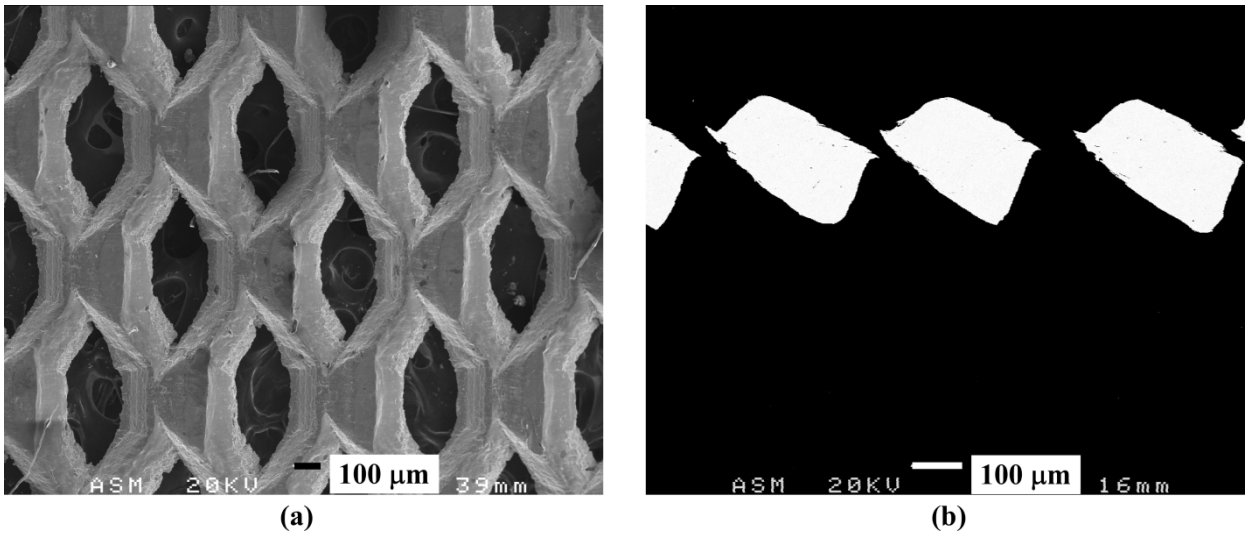

Figure 4.9. (a) Surface and (b) cross-section SEM micrographs of Fe-22Cr mesh.

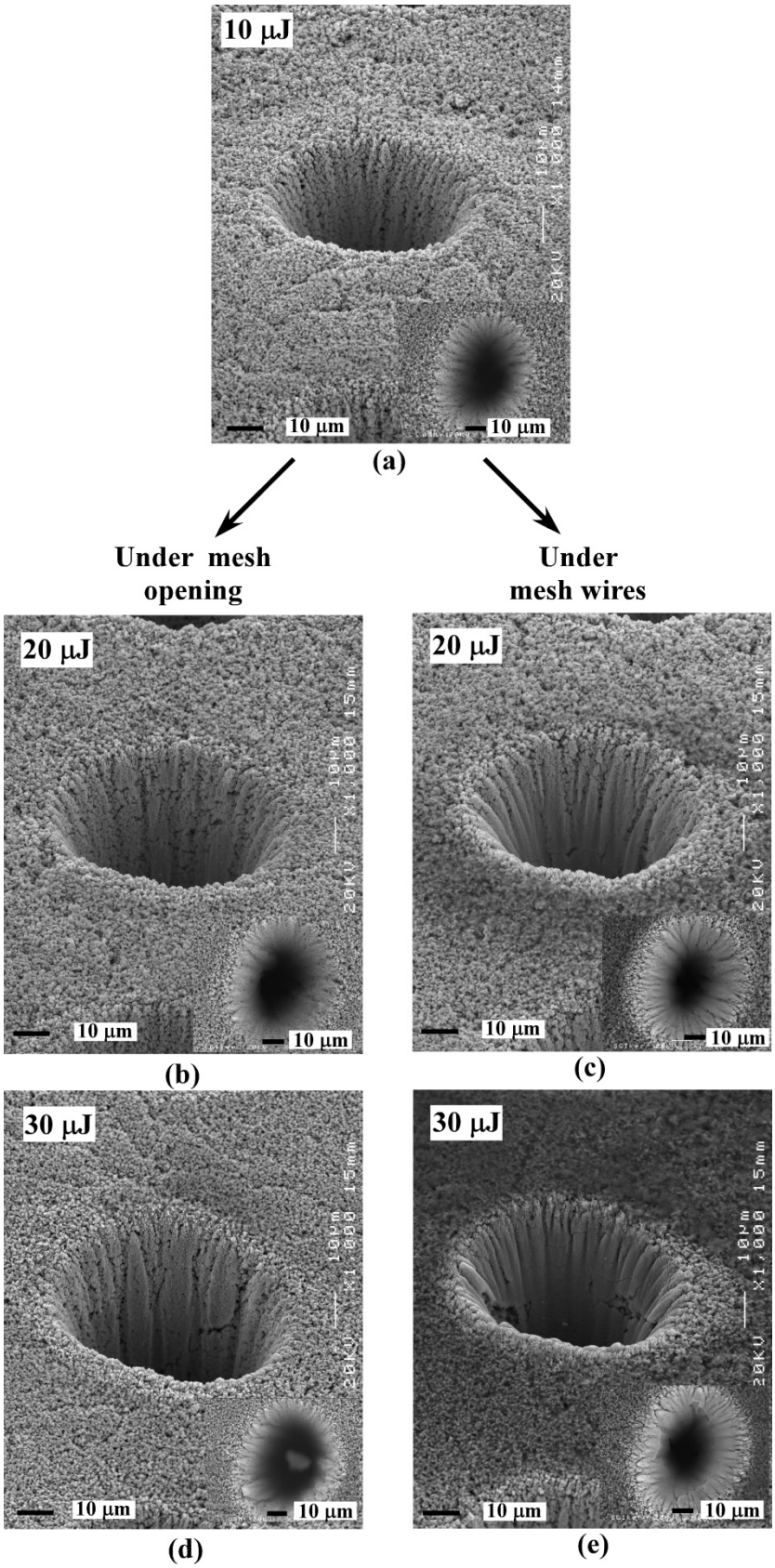

Figure 4.10. SEM micrographs of craters ablated in $LaNi_{0.6}Co_{0.4}O_{3-\delta}$/Fe-22Cr mesh sample. Effect of pulse laser energy: (a) 10 μJ, 20 μJ (b) under mesh opening (c) under mesh wires and 30 μJ (d) under mesh opening (e) under mesh wires. Laser parameters: wavelength 800 nm; pulse duration: 40 fs; pulse repetition rate 1 kHz; number of pulses per hole 4000.

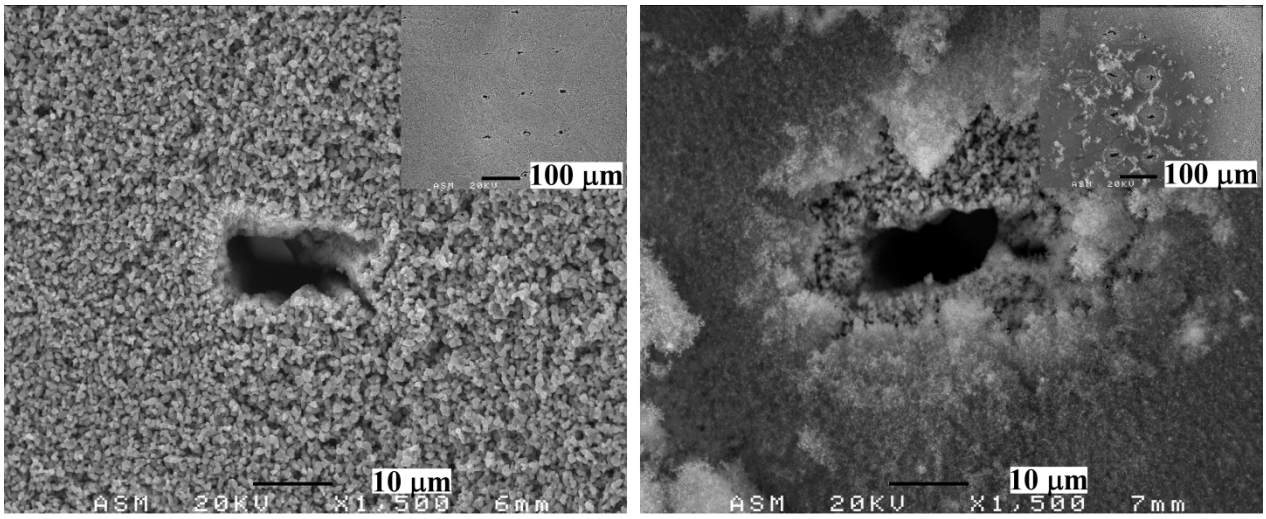

(a) **(b)**

Figure 4.11. SEM images of the back face of the $LaNi_{0.6}Co_{0.4}O_{3-\delta}$/Fe-22Cr mesh ablated sample using: (a) 20 μJ and (b) 30 μJ pulse energy.

In good agreement with examined microstructure from Figure 4.8, two different areas are also identified: the area of the ceramic coated (i) under the mesh opening and (ii) under the mesh wires. The initial reactivity of the sample without ablation is established from our previous study[9], in which is concluded that a Cr deposit ring along the edge of the LNC ceramic coating is detected when composite has just been sintered at 1050 ºC for 2 h. Moreover, other authors[22-25] have also shown that chromium deposition increases with the increase the temperature, being 1050 ºC enough to observe Cr migration.

From EDX analysis, around the crater close to metallic mesh, an accumulation of chromium, iron and oxygen deposits is identified due to the oxidation of metallic Fe and Cr from the steel, allowing the formation of Cr_2O_3 and/or Fe_2O_3. The presence of these oxides could accelerate the Cr-poisoning effect in a single solid oxide fuel cell. Different attempts were done to avoid chromium deposition by the introduction of a nitrogen flow during the laser processing but no satisfactory results were obtained. In this context, the integration of a laser induced breakdown spectroscopy (LIBS) system to stop the lasing when the Fe and Cr spectral features are detected, is planned to limit chromium deposits[20].

---

22 Chen X., Jiang S.P. Highly active and stable $(La_{0.24}Sr_{0.16}Ba_{0.6})(Co_{0.5}Fe_{0.44}Nb_{0.06})O_{3-\delta}$ (LSBCFN) cathodes for solid oxide fuel cells prepared by a novel mixing synthesis method. *J. Mater. Chem. A* 1 (**2013**) 4871-4878.

23 Wang C.C., Becker T., Chen K., Zhao L., Wei B., Jiang S.P. Effect of temperature on the chromium deposition and poisoning of $La_{0.6}Sr_{0.4}Co_{0.2}Fe_{0.8}O_{3-\delta}$ cathodes of solid oxide fuel cells. *Electrochim. Acta* 139 (**2014**) 173-179.

24 Jiang S.P., Zhang S., Zhen Y.D. Deposition of Cr species at $(La,Sr)(Co,Fe)O_3$ cathodes of solid oxide fuel cells. *J. Electrochem. Soc.* 153(1) (**2006**) A127-A134.

25 Jiang S.P., Chen X. Chromium deposition and poisoning of cathodes of solid oxide fuel cells – A review. *Int. J. Hydrogen Energ.* 39(1) (**2014**) 505-531.

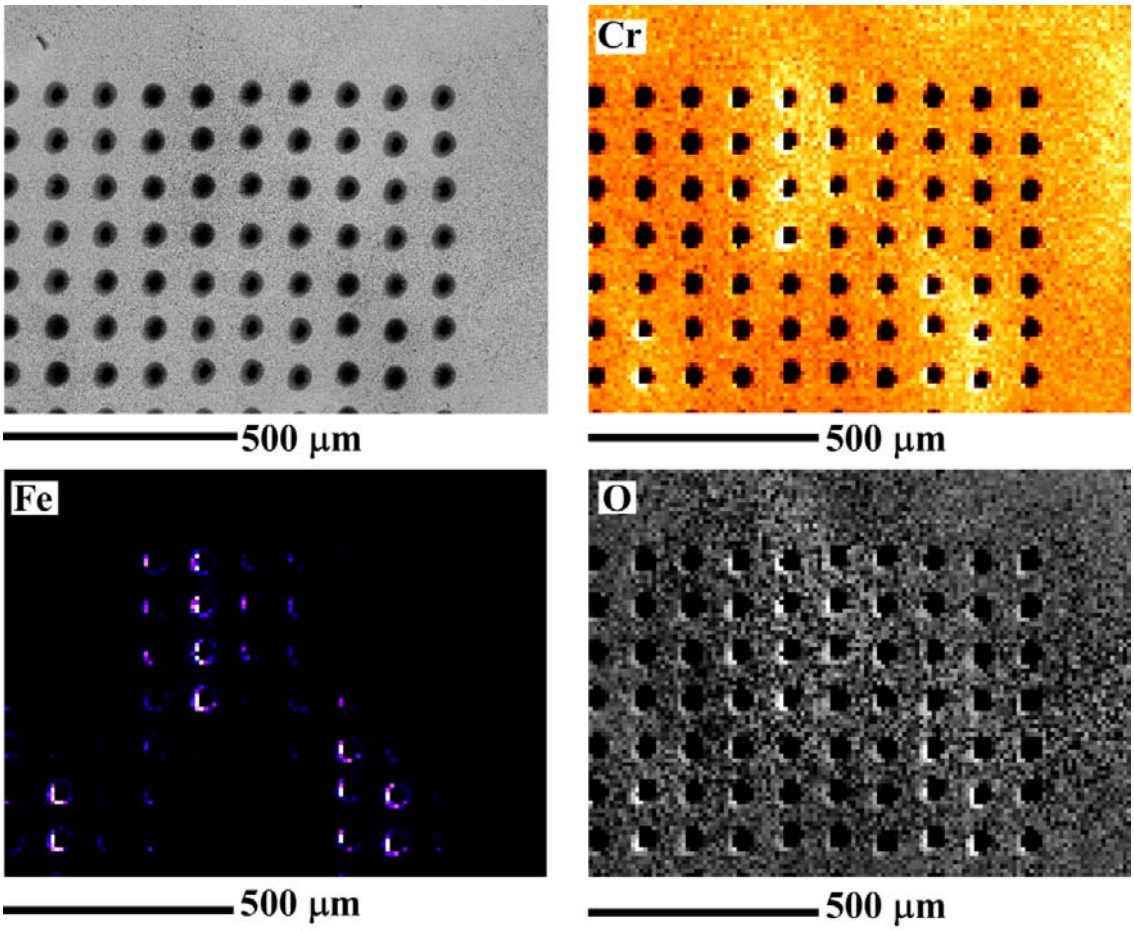

Figure 4.12. EDX mapping of the ablated surface of $LaNi_{0.6}Co_{0.4}O_{3-\delta}$/Fe-22Cr sample.

SEM/EDX analysis is also performed on the cross-section of mesh/LNC sample, using 10, 20, 25 and 30 μJ pulse laser energies to complete the study of laser induced damage (Figures 4.13 and 4.14). Although the topology of the hole cross sections depends on the cutting angle of the sample, they show a funnel shaped entrance followed by a long channel with a diameter in the order of 15 μm. The internal walls of the holes present multiple inhomogeneities caused by internal reflections and interaction with plasma producing changes in the propagation direction and giving rise to irregular exit holes (see Figures 4.13 and 4.14) and even the branching of the beam. This effect could be enhanced by inhomogeneities in the material density.

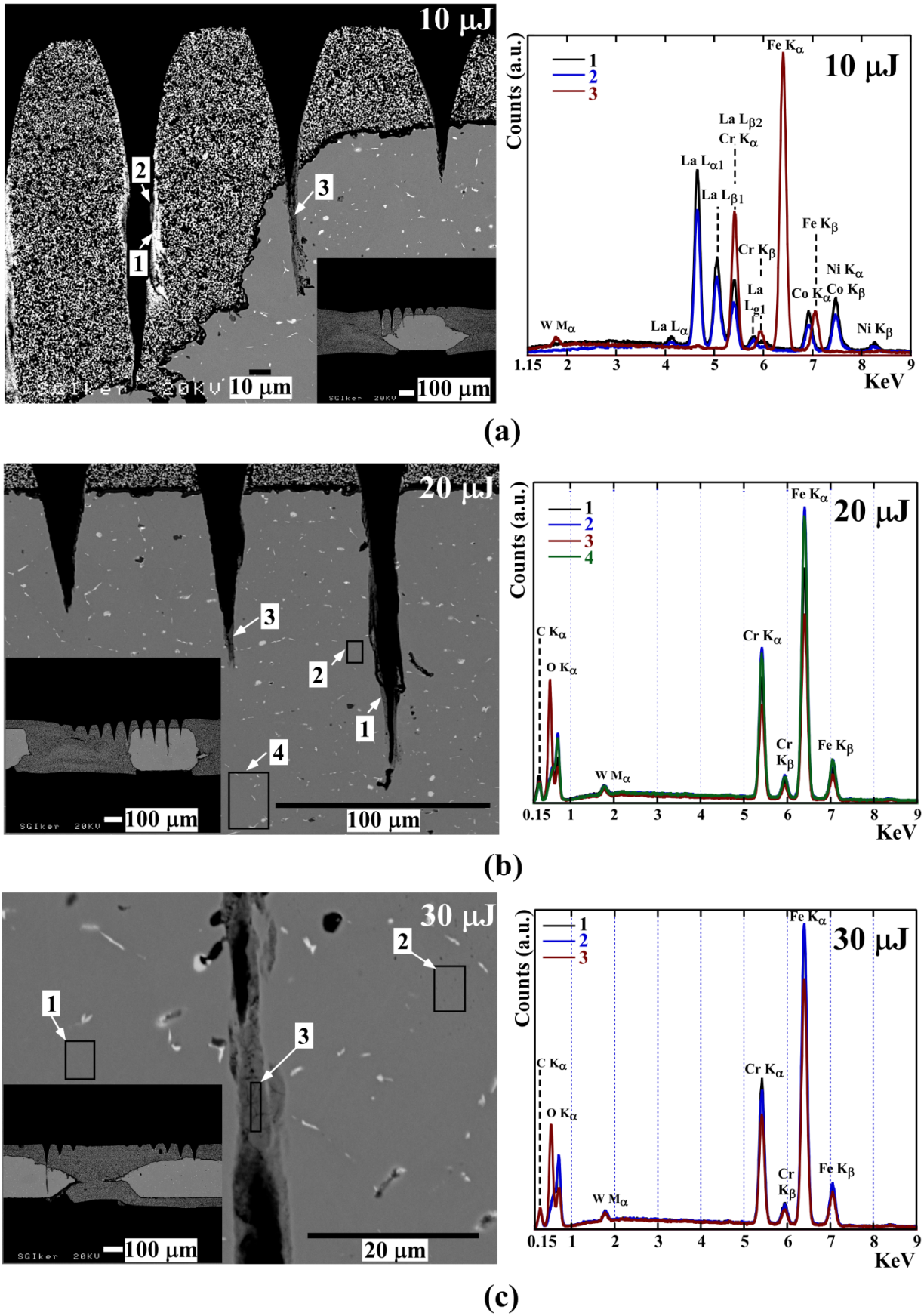

Figure 4.13. SEM micrographs of the cross-section of $LaNi_{0.6}Co_{0.4}O_{3-\delta}$/Fe-22Cr mesh composite at different pulse energies: (a) 10 µJ, (b) 20 µJ and (c) 30 µJ. EDX point analyses spectra of the regions indicated in the micrographs were also performed.

The microstructure comparison between sample cross section and surface shows similar results. Thus, on the border of the ceramic crater, a white layer of a few micrometers width is distinguished which could attribute to molten residues obtained during the laser-LNC interaction. For these residues, the observed morphologies seem consistent with a rapid expulsion of liquid and vapor droplets which then cooled quickly and resolidified. Moreover, on the edge of the mesh crater a resolidified layer of evaporated-oxidized metallic substrate is noticed.

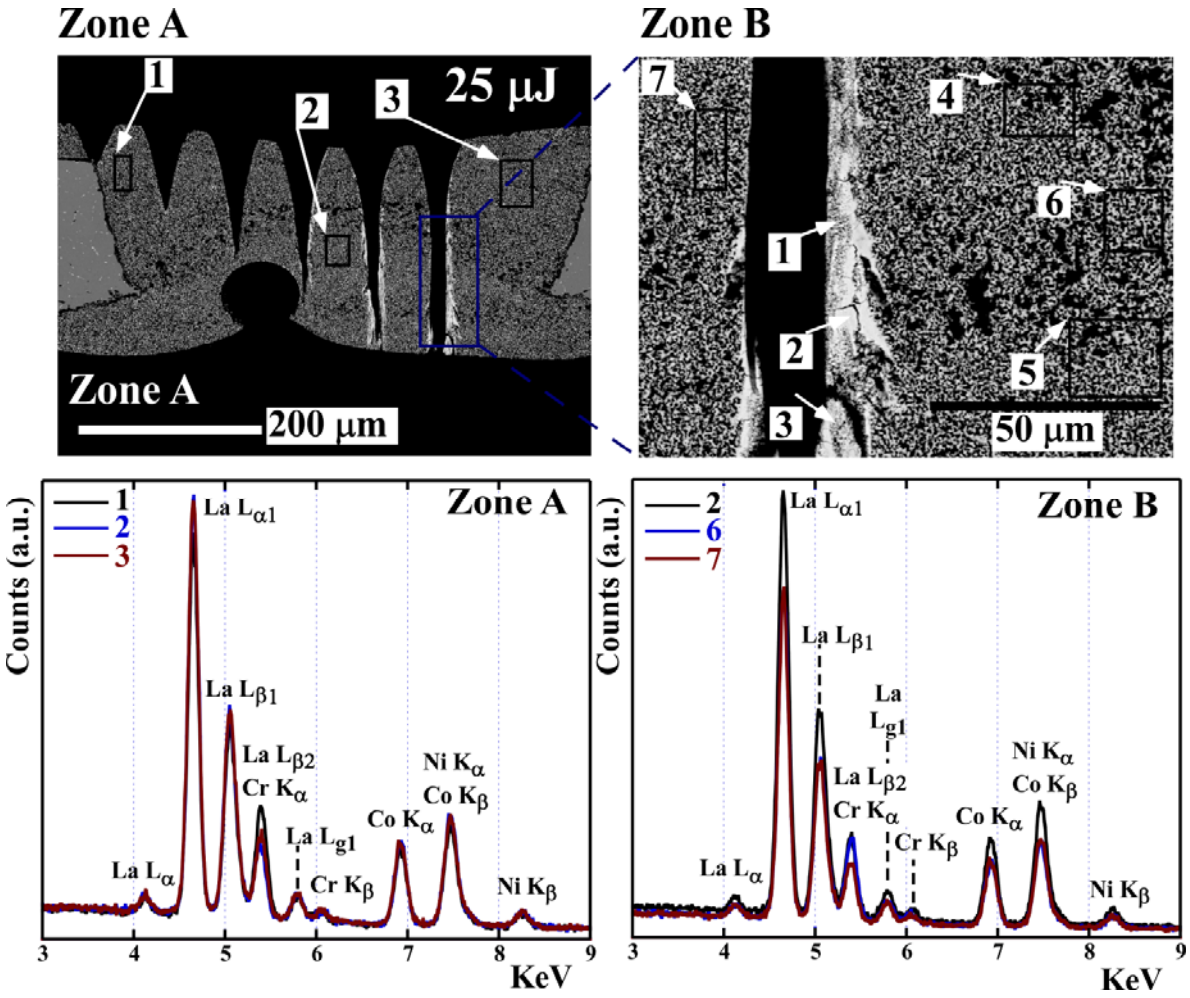

Figure 4.14. Cross-section microstructure (BSE) and EDX analysis on different points of $LaNi_{0.6}Co_{0.4}O_{3-\delta}$/mesh using 25 µJ pulse energy.

As observed from Figures 4.13 and 4.14, different analyses are performed on areas close to the ceramic/mesh craters as well as on the formed border residues, and farther from the ablation region, obtaining similar results for all the studied pulse laser energy conditions. It seems that the EDX data of the border crater residues and also of the more distant areas exhibit similar results. For ceramic crater, initial LNC composition (La, Ni, Co, O) including rest of chromium, which comes from the mesh in the initial sintering process[9], is observed. However, if the ablation was performed through the mesh, Cr-Fe oxides and metallic Cr-Fe were identified in border crater residues and in the mesh surface, respectively. The obtained data confirm that the elements vaporized synchronously

conserving the initial stoichiometry of ablated phases[26]; thus, the damage of femtosecond laser micromachining on the sample is very little and located.

4.1.4. Conclusions

A Fe-22Cr mesh has been dipped into LNC, LNF and LSFMC slurries to form high electron conduction metallic/ceramic layers, as contact materials for SOFC. Femtosecond laser ablation on these developed composites has been successfully performed using 4000 laser pulses of 20 μJ and 40 fs width each one. After analysed samples, it has been demonstrated that the efficiency of laser micromachining in the studied specimens is independent of the ceramic composition. According to EDX chemical analysis, the formation of iron and chromium oxides is given due to the evaporation and oxidation of the mesh. However, the laser effect on the initial elemental composition is very located, and is not significant to influence on the system performance. Future work will include the integration of laser induced breakdown spectroscopy (LIBS) to reduce the chromium contamination, obtaining interesting results for SOFC cathode contact materials.

[26] Jia W., Peng Z., Wang Z., Ni X., Wang C.-Y. The effect of femtosecond laser micromachining on the surface characteristics and subsurface microstructure of amorphous FeCuNbSiB alloy. *Appl. Surf. Sci.* 253 (**2006**) 1299–1303.

4.2. Laser machining of $LaNi_{0.6}M_{0.4}O_{3-\delta}$ (M: Fe, Co) dip coated on a Fe-22Cr mesh material to obtain a new contact coating for SOFC: interaction between Crofer22APU interconnect and $La_{0.6}Sr_{0.4}FeO_3$ cathode

Int. J. Hydrogen Energ., in press (doi: 10.1016/j.ijhydene.2015.04.134), **2015**.

Abstract

A Fe-22Cr mesh was dipped into a ceramic ($LaNi_{0.6}M_{0.4}O_{3-\delta}$; M: Co, Fe) slurry to form a metallic/ceramic material as contact coating for solid oxide fuel cells (SOFCs). This composite was directly adhered to a Crofer22APU channeled interconnect and micro-holes were performed on coating using a femtosecond laser. Then, $La_{0.6}Sr_{0.4}FeO_3$ (LSF) cathode was spray deposited on top of this ablated system to analyze the formed structures in terms of the electrical performance, processing reproducibility and long-term behaviour at 800 ºC. The adequate reproducibility of the process was confirmed through area specific resistance (ASR) testing on four replicas for each system. After long-term treatment, the chromium diffusion within both the interconnect and mesh of the composite was quantitatively analysed using energy dispersive X-ray spectroscopy (EDX). The laser irradiated composite showed short-range damage, which was limited to the formation of iron and chromium oxides due to the evaporation and oxidation of the mesh.

Keywords: SOFC; composite contact material; femtosecond laser; contact resistance; degradation.

Highlights

- Laser machined holes are produced on a metallic mesh coated with a ceramic paste.
- The laser irradiated composite showed short-range damage.
- Reproducible ASR values were obtained for interconnect/contact layer/cathode setup.
- A Cr reduction in interconnect or mesh means a Cr enrichment in the contact paste.

4.2.1 Introduction

Despite the fact that the world is trying to reduce carbon emissions through the expansion of clean and renewable energy resources, the use of fossil fuels continues to dominate the global energy sector. An alternative to conventional methods of energy production could be the direct conversion of chemical energy into electrical energy via electrochemical reactions between fuel and oxidant without involving combustion, which is the main characteristic of Solid Oxide Fuel Cells (SOFCs)[27,28]. High temperature operating conditions of SOFCs (1000-800 ºC) lead to a variety of degradation mechanisms which represent a significant challenge in meeting lifetime requirements[29]. For stationary applications, the commercial lifetime requirement is generally more than 40000 h. In comparison, up to a 20000 h lifetime with more frequent thermal cycles is required for auxiliary power units in transportation applications[30]. However, these extensive lifetime requirements have not been met yet. The key degradation issues of these cells could be related with the chemical and thermomechanical instability at the interfaces[31]. Moreover, it has been extensively studied[32-34] that the oxidation of the interconnect at a high temperature allows the vaporization of chromium, which poisons the cell cathode, thus contributing to the cell degradation during stack operation. In order to prevent the cell degradation caused by the use of metal interconnects, dense protective layers are used to coat the metallic substrate. Spinel oxide protective materials are usually applied to the metallic interconnect to achieve this protection[35-37]. However, despite the usefulness of protective coatings, the stack degradation rates are still higher than the required value for SOFC commercialization.

According to other authors and to our previous studies[38,39], the interconnect-cathode interface plays an important role in the electrical resistance of the cell. Thus, the use of a

---

[27] Hosseini N., Abbasi M.H., Karimzadeh F., Choi G.M. Development of $Cu_{1.3}Mn_{1.7}O_4$ spinel coating on ferritic stainless steel for solid oxide fuel cell interconnects. *J. Power Sources* 273 (**2015**) 1073-1083.

[28] Shishkin M., Ziegler T. Direct modeling of the electrochemistry in the three-phase boundary of solid oxide fuel cell anodes by density functional theory: a critical overview. *Phys. Chem. Chem. Phys.* 16 (**2014**) 1798-1808.

[29] Badwal S.P.S. Stability of solid oxide fuel cell components. *Solid State Ionics* 143 (**2001**) 39-46.

[30] Yokokawa H., Tu H., Iwanschitz B., Mai A. Fundamental mechanisms limiting solid oxide fuel cell durability. *J. Power Sources* 182 (**2008**) 400-412.

[31] Barelli L., Barluzzi E., Bidini G. Diagnosis methodology and technique for solid oxide fuel cells: A review. *Int. J. Hydrogen Energy* 38 (**2013**) 5060-5074.

[32] Guan W.B., Jin L., Ma X., Wang W.G. Investigation of impactors on cell degradation inside planar SOFC stacks. *Fuel Cells* 12(6) (**2012**) 1085-1094.

[33] Jiang S.P., Chen X. Chromium deposition and poisoning of cathodes of solid oxide fuel cells – A review. *Int. J. Hydrogen Energy* 39(1) (**2014**) 505-531.

[34] Ardigò M.R., Perron A., Combemale L., Heintz O., Caboche G., Chevalier S. Interface reactivity study between $La_{0.6}Sr_{0.4}Co_{0.2}Fe_{0.8}O_{3-\delta}$ (LSCF) cathode material and metallic interconnect for fuel cell. *J. Power Sources* 196 (**2011**) 2037-2045.

[35] Kruk A., Stygar M., Brylewski T. Mn–Co spinel protective–conductive coating on AL453 ferritic stainless steel for IT-SOFC interconnect applications. *J. Solid State Electrochem.* 17 (**2013**) 993-1003.

[36] Liu Y., Chen D.Y. Protective coatings for Cr_2O_3-forming interconnects of solid oxide fuel cells. *Int. J. Hydrogen Energy* 34 (**2009**) 9220-9226.

[37] Sung-Il L., Jongsup H., Hyoungchul K., Ji-Won S., Jong-Ho L., Byung-Kook K., Hae-Weon L., Kyung-Joong Y. Highly dense Mn-Co spinel coating for protection of metallic interconnect of solid oxide fuel cells. *J. Electrochem. Soc.* 161(14) (**2014**) F1389-F1394.

[38] Guan W.B., Zhai H.J., Jin L., Li T.S., Wang W.G. Effect of contact between electrode and interconnect on performance of SOFC stacks. *Fuel Cells* 11(3) (**2011**) 445–450.

protective/conductive layer between interconnect and cathode could reduce electron transmission resistance as well as the interaction between both materials, thus acting as a diffusion barrier for chromium species (CrO_3 (g), $CrO_2(OH)_2$ (g)). The types of contact materials are diverse, but basically they must possess both adequate porosity and electronic conductivity to perform their functions in the cell[40]. The most commonly used contact coatings are highly conductive perovskites[41,42], i. e. $La_{0.8}Sr_{0.2}Co_{0.75}Fe_{0.25}O_3$, $LaNi_{0.6}Fe_{0.4}O_{3-\delta}$, $LaNi_{0.6}Co_{0.4}O_{3-\delta}$. An important drawback of these oxides is that their sintering temperature is limited since the high temperature favours the oxidation of iron-chromium alloys. Thus, these ceramic contact materials sintered at lower temperatures have lower density and, therefore, reduced electronic conductivity. The development of metallic-ceramic coatings, such as $Ni_{80}Cr_{20}/(La_{0.75}Sr_{0.25})_{0.95}MnO_3$ dual-layer[43], could bridge the gap between interconnect and electrode, increasing the conductivity and adhesive ability of the interface between both materials, when using low temperature sintering process. In this context, according to previous studies[44], the incorporation of conducting wires and designed porous channels in the electrodes could increase cell performance via improved transport of electrons as well as gases. However, to our knowledge, few studies have investigated the incorporation of pore channels in the electrodes.

In this work, femtosecond laser machined holes are produced in a contact coating based on a Fe-22Cr mesh dipped into a ceramic ($LaNi_{0.6}M_{0.4}O_{3-\delta}$; M: Co, Fe) slurry. This composite, which could provide electronic conduction as well as rapid oxidant gases transfer through interconnect/electrode interface, is directly adhered to Crofer22APU interconnect and then $La_{0.6}Sr_{0.4}FeO_3$ (LSF) cathode is spray deposited to form an {interconnect/contact layer/cathode} configuration. The electrical performance, processing reproducibility and long-term behaviour at 800 ºC of the formed structures are discussed. Moreover, the electrical resistance of interconnect/cathode interface is also studied.

4.2.2. Experimental

The structure of interconnect-cathode interface used in the experiments consists of {interconnect/contact material/cathode}: Crofer22APU (ThyssenKrupp VDM)/$LaNi_{0.6}Co_{0.4}O_{3-\delta}$ (LNC) or $LaNi_{0.6}Fe_{0.4}O_{3-\delta}$ (LNF) (NexTech, Fuel Cell Materials) dip coated on Fe-22Cr mesh (Fiaxell SOFC Technologies)/$La_{0.6}Sr_{0.4}FeO_3$ (LSF) (NexTech, Fuel Cell Materials). The chemical composition of the steels was determined using a scanning electron microscopy (SEM, JEOL LSM-6400) equipped with an Oxford instrument INCA E-350 energy dispersive X-ray spectroscopy (EDX) (Table 4.1).

---

[39] Morán-Ruiz A., Vidal K., Laguna-Bercero M.A., Larrañaga A., Arriortua M.I. Effects of using $(La_{0.8}Sr_{0.2})_{0.95}Fe_{0.6}Mn_{0.3}Co_{0.1}O_3$ (LSFMC), $LaNi_{0.6}Fe_{0.4}O_{3-\delta}$ (LNF) and $LaNi_{0.6}Co_{0.4}O_{3-\delta}$ (LNC) as contact materials on solid oxide fuel cells. *J. Power Sources* 248 (**2014**) 1067-1076.

[40] Yang Z., Xia G., Singh P., Stevenson J.W. Electrical contacts between cathodes and metallic interconnects in solid oxide fuel cells. *J. Power Sources* 155 (**2006**) 246-252.

[41] Tucker M.C., Cheng L., DeJonghe L.C. Selection of cathode contact materials for solid oxide fuel cells. *J. Power Sources* 196 (**2011**) 8313-8322.

[42] Vidal K., Morán-Ruiz A., Larrañaga A., Porras-Vázquez J.M., Slater P.R., Arriortua M.I. Characterization of $LaNi_{0.6}Fe_{0.4}O_3$ perovskite synthesized by glycine-nitrate combustion method. *Solid State Ionics* 269 (**2015**) 24-29.

[43] Wu W., Guan W., Wang G., Liu W., Zhang Q., Chen T., Wang W.G. Evaluation of $Ni_{80}Cr_{20}/(La_{0.75}Sr_{0.25})_{0.95}MnO_3$ dual layer coating on SUS 430 stainless steel used as metallic interconnect for solid oxide fuel cells. *Int. J. Hydrogen Energy* 39 (**2014**) 996-1004.

[44] Yoon C. Computational design, fabrication, and characterization of microarchitectured solid oxide fuel cells with improved energy efficiency. Ph.D. thesis work, Georgia Institute of Technology, **2010**.

Table 4.1. Chemical composition average in wt (%) of Fe-22Cr alloy used as interconnect and as mesh, obtained by EDX microanalysis.

Sample	Fe (%wt.)	Cr (%wt.)	Mn (%wt.)	Ti (%wt.)	Nb (%wt.)	W (%wt.)
Mesh	73.1(3)	23.5(2)	0.6(1)	< 0.1	0.4(1)	2.3(2)
Interconnect	76.3(2)	23.0(2)	0.6(1)	< 0.1	-	-

In order to obtain metallic/ceramic contact composite, stainless steel mesh, with mesh opening of about 175 μm and a thickness of 250 μm, was cut into 10 mm x 10 mm squares, cleaned with acetone in an ultrasonic bath and dried. Flat squared-meshes were preoxidized at 600 ºC for 10 h, in air. LNC and LNF commercial powders were fabricated into pastes. The slurries were prepared by mixing each of the $LaNi_{0.6}Co_{0.4}O_{3-\delta}$ and $LaNi_{0.6}Fe_{0.4}O_{3-\delta}$ powders (12.5 vol. %) in 87.5 vol. % ethanol (Panreac) with 1 vol. % Dolapix (Zschimmer & Schwarz, Chemische Fabriken). The mixtures, containing 5 vol. % of PVB (polyvinyl butyral, Solutia Solutions) organic binder, were homogenized for 5 h using a magnetic stirrer. The ceramic slurry composition employed were chosen in order to obtain dense contact layer. The obtained paste was then deposited on the preoxidized squared-meshes via controlled dipping at 4.5 $mm \cdot s^{-1}$ speed. This step was repeated several times in order to achieve the required thickness. The interconnect was cut into square substrates measuring 10 mm x 10 mm with a thickness of 1 mm. The machined channels of substrate are 2 mm width, 0.5 mm depth, 10 mm length and the distance between neighboring is 2 mm. The obtained squared-steels were hand polished with 800 grit abrasive paper, cleaned with acetone in an ultrasonic bath and dried. All substrates were preoxidized at 800 ºC for 100 h in air, to inhibit Fe and Cr transport from the alloys to the ceramic coating and to avoid the growth of the chromium based layer, which is known to increase the interfacial stress[45,46]. An additional layer of LNC or LNF was coated on the ribs of the interconnect substrate using wet colloidal spraying. The suspensions were made by mixing the powders, ethanol and ZrO_2 cylinders, as grinding media, in a ball mill for 1 h. The formed composite contact material was directly adhered to the interconnect and sintered at 1050 ºC for 2 h, in air, to favour a dense ceramic coating. In order to achieve a better mechanical contact between the coated ribs of interconnect/composite interface, a weight load was placed on the top of the structure.

The laser set-up is described elsewhere[47]. Femtosecond laser pulses were generated by a Ti:Sapphire oscillator-regenerative amplifier system (1 kHz, 4.0 mJ, 40 fs pulses at 800 nm). The pulse energy was controlled by means of a variable neutral density filter, using 20 μJ. The light was focused onto the sample, which was mounted in a 3D translation stage (1μm precision) at atmospheric pressure, using a fused silica lens (f=100mm). Matrixes of holes were machined with separation between drillings equal to 77 μm in both horizontal (x) and vertical (y) directions to complete the area of a channel of the interconnect, approximately 2 mm x 6 mm. Then, $La_{0.6}Sr_{0.4}FeO_3$ (LSF) cathode was spray deposited on the micromachined composite material, which

[45] Hoyt K.O., Gannon P.E., White P., Tortop R., Ellingwood B.J., Khoshuei H. Oxidation behavior of $(Co,Mn)_3O_4$ coatings on preoxidized stainless steel for solid oxide fuel cell interconnects. *Int. J. Hydrogen Energy* 37 (**2012**) 518-529.

[46] Ou D.R., Cheng M. Effect of pre-oxidation on the oxidation resistance of spinel-coated Fe–Cr ferritic alloy for solid oxide fuel cell applications. *J. Power Sources* 247 (**2014**) 84-89.

[47] Di-Maio Y., Colombier J.P., Cazottes P., Audouard E. Ultrafast laser ablation characteristics of PZT ceramic: Analysis methods and comparison with metals. *Opt. Laser Eng.* 50 (**2012**) 1582-1591.

was already connected with the channeled substrate, and heated at 950 ºC for 2 h, in air, allowing a porous cathode morphology. These systems were then treated at 800 ºC for 1000 h, in air.

Area Specific Resistance (ASR) measurements were performed using a DC four-probe method (the resistance value was estimated from the voltage value (Thurlby Thandar Instruments 1604 Digital Multimeter) measured on applying a current of 1A (Thurlby Thandar Instruments PL300 current source)), on systems, which were prepared according to the geometries shown in Figure 4.15. In order to check the reproducibility of the procedures described above, duplicate samples were prepared. Moreover, the electrical resistance of interconnect-cathode interface setup was also determined. Electrical contacts between samples and the external measuring circuit were made by pressing two Pt foils (99.95%, 0.0125-mm thick, Advent Research Materials Ltd. England/Oxford) against the sides of the interconnect as well as the surface of the composite contact material, in combination with a Pt paste.

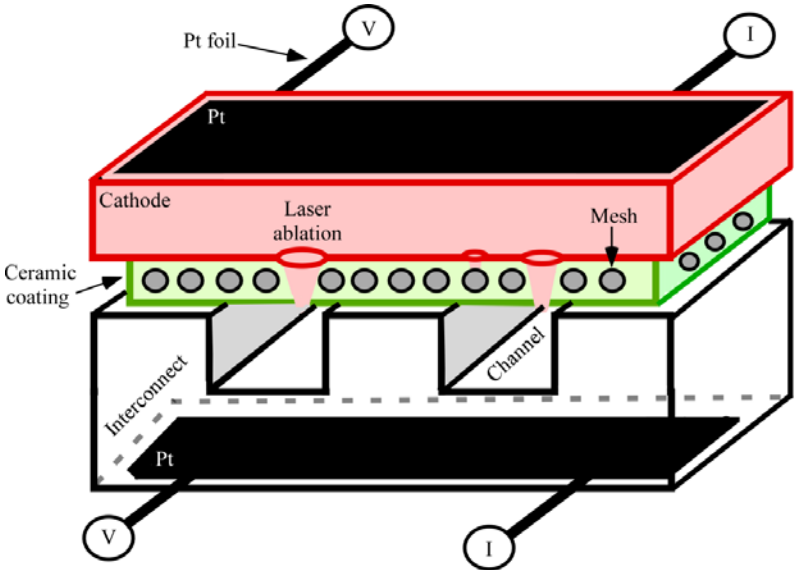

Figure 4.15. Scheme of the setup for the ASR measurements.

Once the ASR tests were completed, the samples were epoxy-mounted, sectioned, and polished. Cross sections of the samples were analyzed using SEM/EDX system. Composition analysis was performed using back-scattered electrons (BSE) at 20 kV accelerating voltage and $5 \cdot 10^{-9}$ A current. For EDX point analysis the live time was set to 100 s. EDX system calibration was performed measuring the beam current on pure element standards, allowing quantitative elemental analyses. Moreover, EDX mapping was carried out using 13762.56 s (70 ms/pixel) as live time. The data processing was performed using Oxford INCA software. The characteristic emission lines used for the analysis were L_α for La and Nb, K_α for Co, Cr, Fe and Ni, and M_α for W.

4.2.3. Results and discussion

4.2.3.1. ASR measurements

Figure 4.16 depicts the ASR values, as a function of time at 800 ºC, for {interconnect/contact coating/cathode} structure composed of: channelled Crofer22APU interconnect adhered to the laser machined composite contact material, which is formed by LNC or LNF paste dip coated on a Fe-22Cr mesh, with a LSF top cathode coating. For comparison, the obtained ASR data, under similar conditions, for the {interconnect/ablated cathode-mesh layer/cathode} (interconnect/cathode) setup is also presented in Figure 4.16.

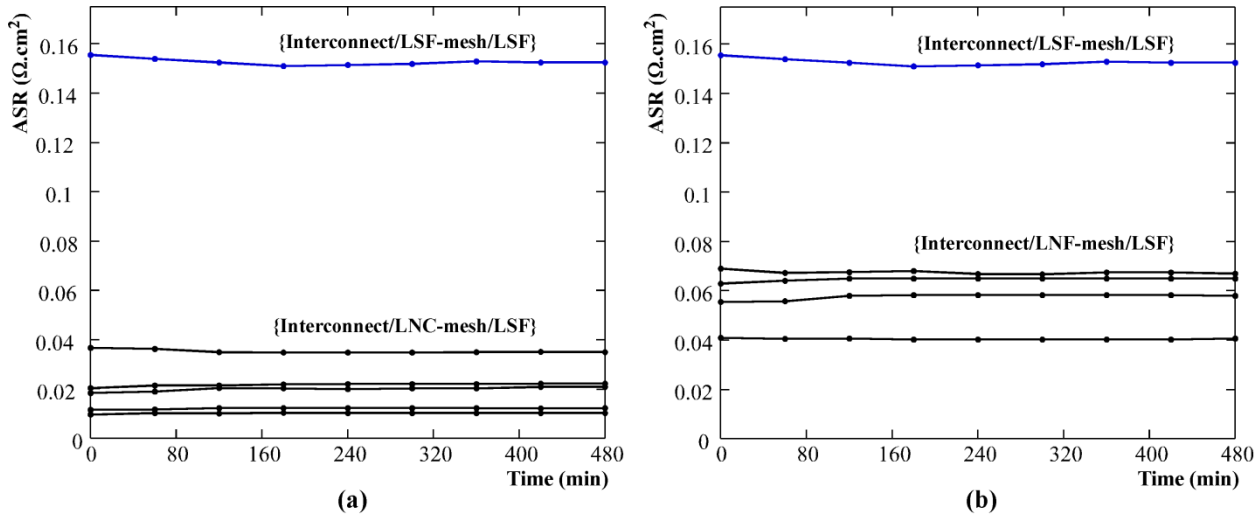

Figure 4.16. Area specific resistance values, at 800 ºC in air, for different interfaces tested in the {interconnect/ablated LSF-mesh/cathode} structure as well as (a) {interconnect/ablated LNC-mesh/cathode} and (b) {interconnect/ablated LNF-mesh/cathode} systems, as a function of time.

In order to check the reproducibility of the process, at least four specimens were tested for each ceramic contact paste, and, Table 4.2 shows the average ASR value of the measured replicas. The results support the reproducibility for all the measured structures, indicating similar signal during the contact resistance tests.

Table 4.2. Area specific resistance values for different tested systems measured at 800 ºC in air. ASR mean value for each system is included.

Replica	1	2	3	4	5	Mean
Cell-LNC ASR(Ω·cm^2)	0.0201(9)	0.0122(3)	0.0219(5)	0.0353(7)	0.0103(2)	0.02(1)
Cell-LNF ASR(Ω·cm^2)	0.0675(7)	0.0576(9)	0.0405(2)	0.0647(7)	-	0.06(1)

However, the ASR of the {interconnect/cathode} system is higher than that of the {interconnect/contact material/cathode} structures, being 0.153 (1) Ω·cm^2. The initial resistance value for {interconnect/contact material/cathode} structure depends on the electrical conductivity of the selected contact ceramic paste; ASR mean values for LNC and LNF are 0.02 (1) and 0.06 (1) Ω·cm^2, respectively. These values are good enough for the performance of SOFC

stack[48-51]. Taking into account the obtained results, the application of LNC and LNF perovskite as contact pastes results in a significant decrease in the contact resistance between the LSF cathode and the Crofer22APU interconnect. These results are in good agreement with the representative SEM images of the cross-section observed for each sample after ASR test (Figure 4.17).

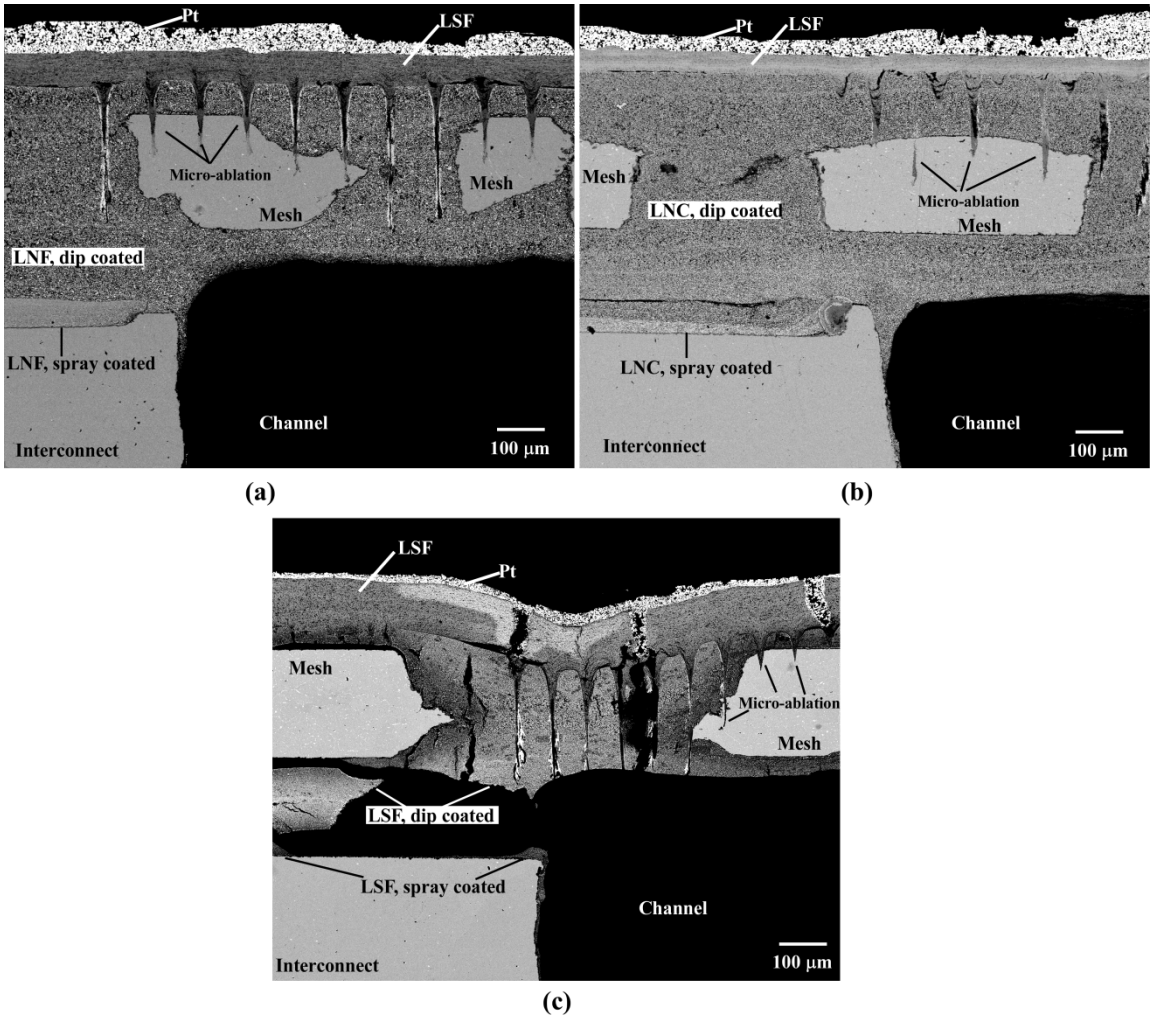

Figure 4.17. Cross-section microstructure images obtained by backscattered electrons signal (BSE) of (a) {interconnect/ablated LNF-mesh/cathode}, (b) {interconnect/ablated LNC-mesh/cathode} and (c) {interconnect/ablated LSF-mesh/cathode} structures after ASR measurements.

A good adherence between the composite contact material and the interconnect corroborates the adequate reproducibility of the process. In this context, a more efficient contact material

[48] Zhu W.Z., Deevi S.C. Development of interconnect materials for solid oxide fuel cells. *Mat. Sci. Eng A-Struct.* 348 (**2003**) 227-243.

[49] Piccardo P., Gannon P., Chevalier S., Viviani M., Burbucci A., Caboche G., Amendola R., Fontana S. ASR evaluation of different kinds of coatings on a ferritic stainless steel as SOFC interconnects. *Surf. Coat. Tech.* 202 (**2007**) 1221-1225.

[50] Shaigan N., Qu W., Douglas G.I., Chen W. A review of recent progress in coatings, surface modifications and alloy developments for solid oxide fuel cell ferritic stainless steel interconnects. *J. Power Sources* 195 (**2010**) 1529-1542.

[51] Da-Conceiçao L., Dessemond L., Djurado E., Souza M.M.V.M. $La_{0.7}Sr_{0.3}MnO_3$-coated SS444 alloy by dip-coating process for metallic interconnect supported solid oxide fuel cells. *J. Power Sources* 241 (**2013**) 159-167.

microstructure is achieved for LNC and LNF contact pastes, improving the adherence of the system. According to other authors and our previous studies[52-54] cathode compositions tend to react with Cr (VI, III) from the interconnect to form phases like $SrCrO_4$, while LNC and LNF materials often incorporate chromium forming Cr-containing perovskites. However, it is believed that the remarkable crack at the interface interconnect/cathode composite coating could have resulted from the infiltration of the sample with epoxy resin.

The initial ASR values reported in previous studies based on {Crofer22APU interconnect sheet /$LaNi_{0.6}Fe_{0.4}O_3$ contact coating/$La_{0.8}Sr_{0.2}FeO_3$ cathode} and {Crofer22APU interconnect sheet /$MnCo_{1.9}Fe_{0.1}O_4$ protective layer/ $La_{0.8}Sr_{0.2}Co_{0.75}Fe_{0.25}O_3$ contact coating/ $La_{0.8}Sr_{0.2}FeO_3$ cathode} are 0.0864 and 0.0417 $\Omega \cdot cm^2$, respectively, at 800 ºC[55]. Moreover, other authors pointed out that the $Cu_{1.3}Mn_{1.7}O_4$ coated AISI 430 interconnect sheet steel shows an initial ASR value of 0.0151 $\Omega \cdot cm^2$, at 750 ºC[56]. Our previous studies indicated that for {Crofer22APU interconnect sheet/$LaNi_{0.6}Co_{0.4}O_{3-\delta}$ contact coating/$La_{0.8}Sr_{0.2}FeO_3$ cathode} and {Crofer22APU interconnect sheet/$LaNi_{0.6}Fe_{0.4}O_{3-\delta}$ contact coating/ $La_{0.8}Sr_{0.2}FeO_3$ cathode} structures, the ASR values are 0.006 (1) and 0.010 (1) $\Omega \cdot cm^2$, respectively, at 800 ºC after 16 h[38]. All of these values are of the same order of magnitude as those determined in the present study.

In this context, in order to understand the adherence between the metallic/ceramic contact composite and channeled steel interconnect, our previous work[53] has focused on characterizing the long-term stability and electrical performance of: $LaNi_{0.6}Co_{0.4}O_{3-\delta}$–mesh adhered to Crofer22APU, using the same processing conditions that are used in this paper. For this system, the obtained contact resistance value was 0.0054 (1) $\Omega \cdot cm^2$, at 800 ºC, which is lower than that produced by the proposed micromachined system. It is believed that the action of creating a line of craters on the sample might debilitate the adherence between ribs of the interconnect and composite, which could be the main factor influencing the initial contact resistance in this kind of system. The possible effect of using femtosecond irradiation on these systems in terms of long-term structural/chemical compatibility has been included in the following section.

---

52 Menzler N.H., Sebold D., Wessel E. Interaction of $La_{0.58}Sr_{0.40}Co_{0.20}Fe_{0.80}O_{3-\delta}$ cathode with volatile Cr in a stack test – Scanning electron microscopy and transmission electron microscopy investigations. *J. Power Sources* 254 (**2014**) 148-152.

53 Morán-Ruiz A., Vidal K., Larrañaga A., Arriortua M.I. Chemical compatibility and electrical contact of $LaNi_{0.6}Co_{0.4}O_{3-\delta}$ (LNC) between Crofer22APU interconnect and $La_{0.6}Sr_{0.4}FeO_3$ (LSF) cathode for IT-SOFC. *Fuel Cells* 13(3) (**2013**) 398-403.

54 Morán-Ruiz A., Vidal K., Larrañaga A., Laguna-Bercero M.A., Porras-Vázquez J.M., Slater P.R., Arriortua M.I. $LaNi_{0.6}Co_{0.4}O_{3-\delta}$ dip-coated on Fe-Cr mesh as a composite cathode contact material on intermediate solid oxide fuel cells. *J. Power Sources* 269 (**2014**) 509-519.

55 Montero X., Tietz F., Stöver D., Cassir M., Villarreal I. Comparative study of perovskites as cathode contact materials between an $La_{0.8}Sr_{0.2}FeO_3$ cathode and a Crofer22APU interconnect in solid oxide fuel cells. *J. Power Sources* 188 (**2009**) 148-155.

56 Hosseini N., Abbasi M.H., Karimzadeh F., Choi G.M. Development of $Cu_{1.3}Mn_{1.7}O_4$ spinel coating on ferritic stainless steel for solid oxide fuel cell interconnects. *J. Power Sources* 273 (**2015**) 1073-1083.

4.2.3.2. Long-term stability of {Crofer22APU interconnect/ablated composite contact coating/$La_{0.6}Sr_{0.4}FeO_3$ cathode} system at 800 ºC

The long-term stability analysis of {Crofer22APU interconnect/ablated composite contact coating/$La_{0.6}Sr_{0.4}FeO_3$ cathode} structures is focused on the areas with and without craters. Figures 4.18 and 4.19 show the cross-section view of the studied samples, selecting the zone without evidence of laser ablation.

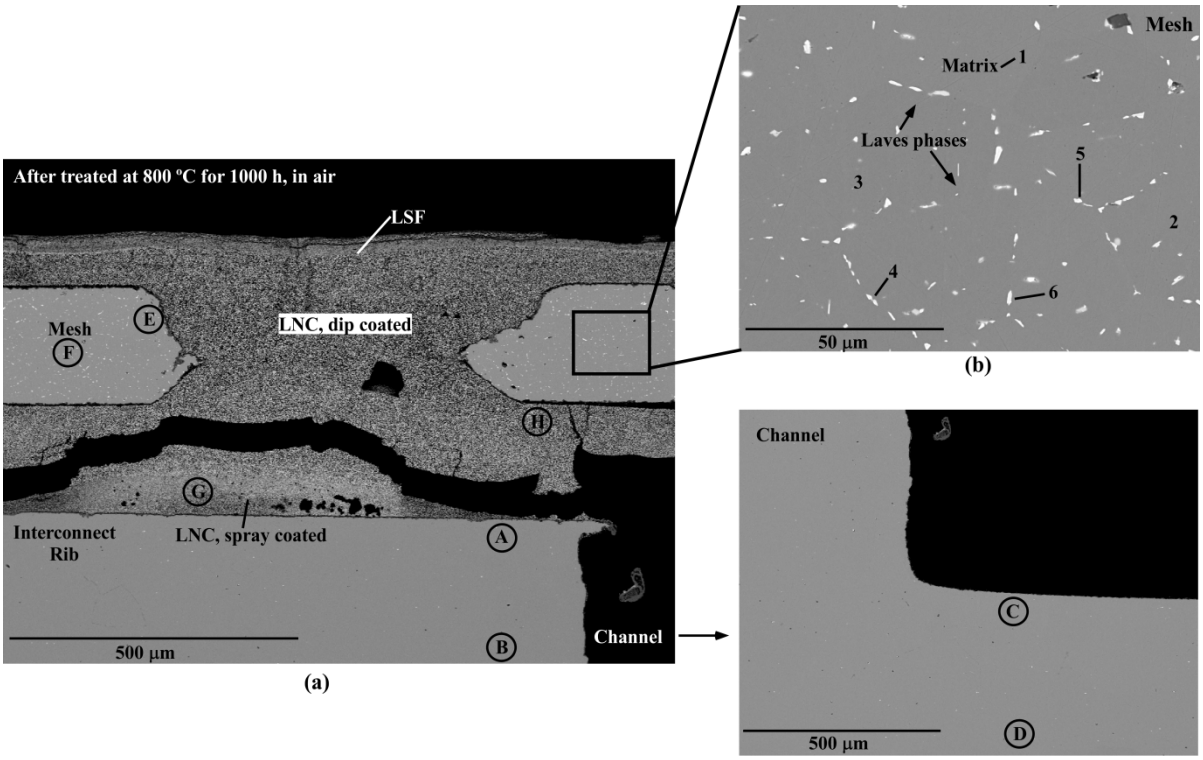

Figure 4.18. Cross-section view of (a) {interconnect/ablated LNC-mesh/cathode} sample, selecting the zone without evidence of laser ablation, after aging at 800 ºC for 1000 h, in air. Capital letters indicate analysis areas shown in Table 4.3, (b) detail of Laves phase formation on the contact mesh during the long-term testing at 800 ºC. Numbers indicate analysis areas shown in Table 4.5.

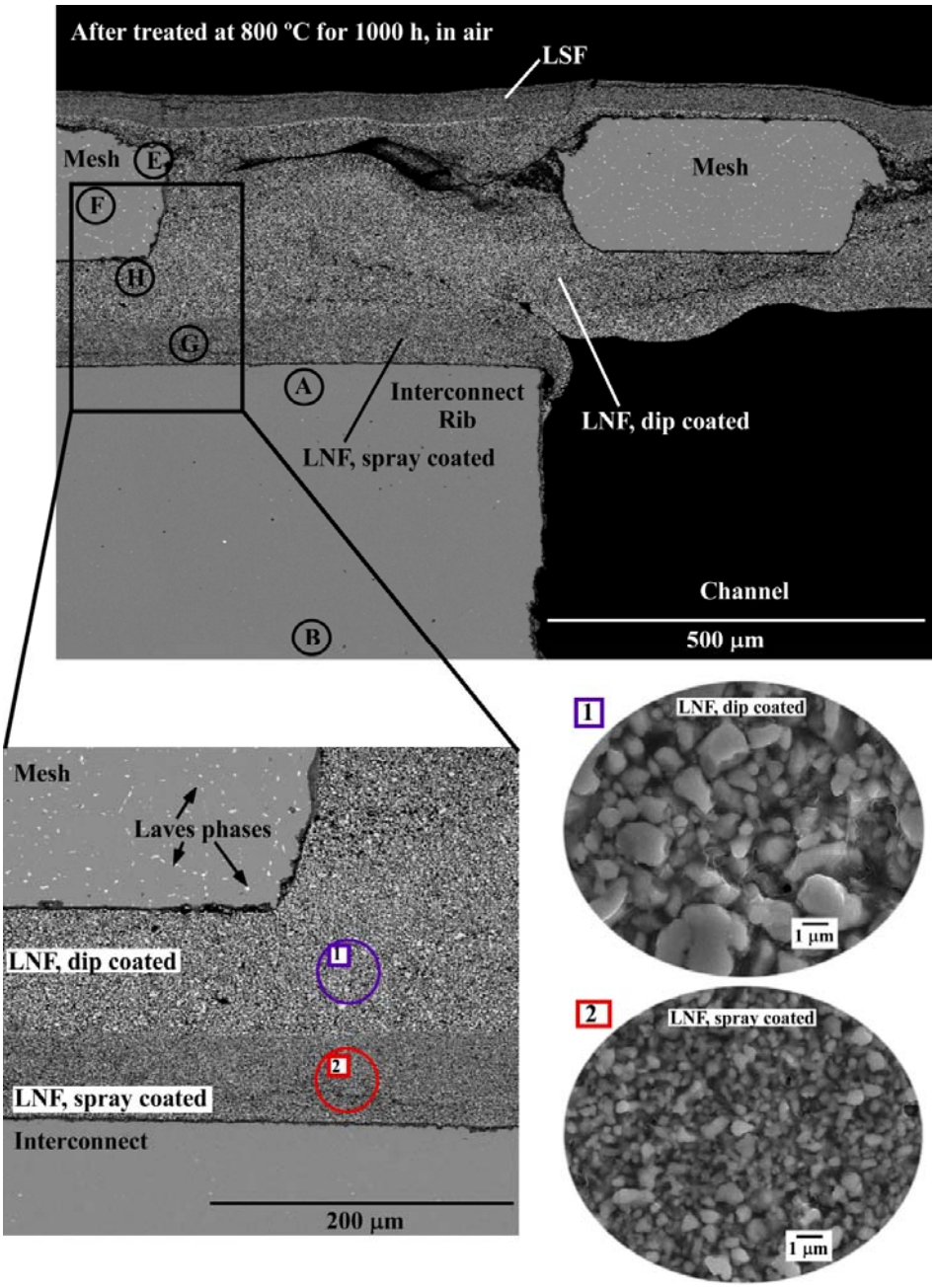

Figure 4.19. Cross-section image of {interconnect/ablated LNF-mesh/cathode} sample, selecting the zone without evidence of laser ablation, after aging at 800 ºC for 1000 h, in air. Capital letters indicate analysis areas shown in Table 4.4. The microstructure of the LNF coatings formed by spraying and dipping are included.

A loss of adherence has been reported between LNC paste coating and substrate due to an insufficient match of the corresponding thermal expansion coefficients (TECs). Moreover, the formation of the crack at the interface interconnect/LNC-mesh coating (Figure 4.18) could also be due to the infiltration of the sample with epoxy resin. For both systems the EDX analyses (see Supplementary material; section A: Figures S1 and S2, section B: Figures S5 and S6) listed in Tables 4.3 and 4.4 and shown in Figures 4.18 and 4.19, respectively, revealed a Cr content reduction on the outside area of the rib (zone A), channel (zone C) and contact mesh (zone E). In both systems, the ceramic material was also quantitatively analysed, focusing on both the area close

to the rib (zone G) and to the mesh (zone H) (see Supplementary material; section A: Figure S3, section B: Figure S7). Moreover, Cr enrichment was observed, in both LNC and LNF materials in addition to each contact paste elements (Tables 4.3 and 4.4), as was expected.

According to these results, the migration of chromium out of the steel to deposit into ceramic contact paste is demonstrated. Furthermore, this transportation or vaporization rate of Cr species (CrO_3 (g), $CrO_2(OH)_2$ (g)) is enhanced in the LNC composite material, which shows a more obvious Cr deposit ring along the edge of the mesh (Figure 4.20).

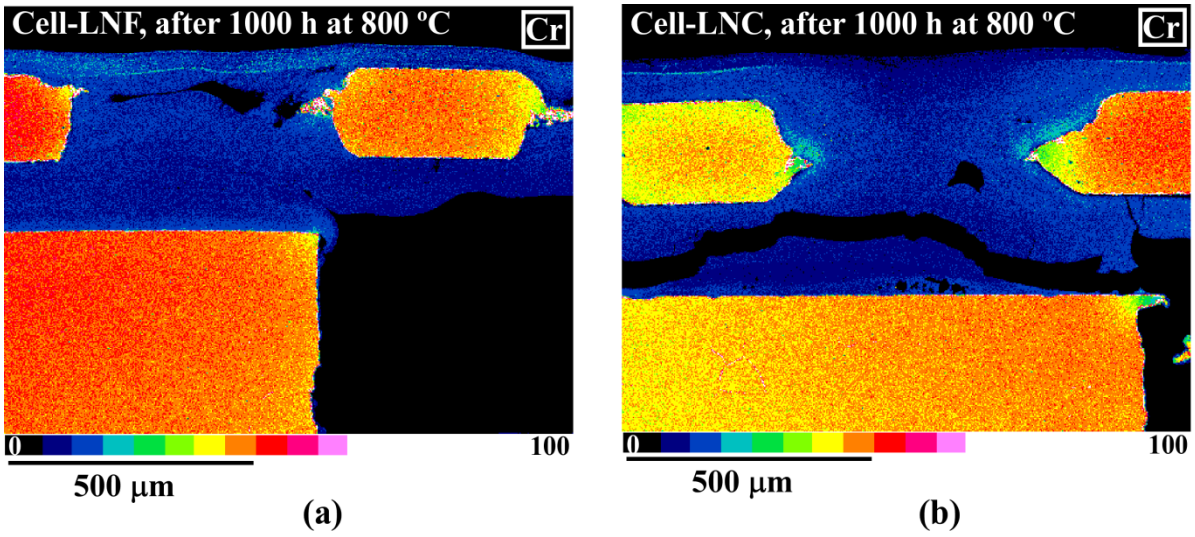

Figure 4.20. Cr-EDX mapping of the cross-section of (a) {interconnect/ablated LNF-mesh/cathode} and (b) {interconnect/ablated LNC-mesh/cathode} systems after heating at 800 ºC for 1000 h, in air.

As stated previously, the TEC mismatch between LNC and Fe-22Cr reduces their adherence, causing an increase in Cr (VI) species from steel. However, as observed in Figure 4.20, for both systems, chromium enrichment is detected in areas close to the interconnect and mesh steels, as was expected[32,57,58]. In addition, a Cr rich interlayer is formed between the cathode and both contact pastes, probably due to the formation of $SrCrO_4$ [59].

[57] Chun-Lin C., Jian-Yih W., Shyong L. Effects of $La_{0.67}Sr_{0.33}MnO_3$ protective coating on SOFC interconnect by plasma-sputtering. *Int. J. Hydrogen Energy* 33(10) (**2008**) 2536-2546.

[58] Stodolny M.K. Cr-tolerance of the IT-SOFC $La(Ni,Fe)O_3$ material. Ph.D. thesis work, University of Twente, **2012**.

[59] Yokokawa H., Horita T., Sakai N., Yamaji K., Brito M.E., Xiong Y.P., Kishimoto H. Thermodynamic considerations on Cr poisoning in SOFC cathodes. *Solid State Ionics* 117(35-36) (**2006**) 3193-3198.

Table 4.3. Chemical composition in % wt. of points indicated in Figure 4.18(a).

LNC	Zone	Cr	Fe	W	La	Ni	Co	O
Inter. Fe-Cr rib	(A) outside	22.4(1)	77.6(1)	-	-	-	-	-
	(B) inside	23.3(2)	76.7(2)	-	-	-	-	-
Inter. Fe-Cr channel	(C) outside	22.7(1)	77.3(1)	-	-	-	-	-
	(D) inside	23.5(1)	76.5(1)	-	-	-	-	-
Mesh Fe-Cr	(E) outside	19.3(4)	78.7(4)	2.0(1)	-	-	-	-
	(F) inside	22.6(2)	75.4(3)	2.0(1)	-	-	-	-
Ceramic material	(G) close to the rib	1.5(4)	-	-	55.0(3)	14.2(1)	9.4(3)	19.8(1)
	(H) close to the mesh	3.8(2)	-	-	53.3(2)	13.8(2)	8.9(1)	20.2(1)

Table 4.4. Chemical composition in % wt. of points indicated in Figure 4.19.

LNF	Zone	Cr	Fe	W	La	Ni	O
Inter. Fe-Cr rib	(A) outside	22.2(3)	77.8(3)	-	-	-	-
	(B) inside	23.3(1)	76.7(1)	-	-	-	-
Inter. Fe-Cr channel	(C) outside	22.4(1)	77.6(1)	-	-	-	-
	(D) inside	23.2(1)	76.8(1)	-	-	-	-
Mesh Fe-Cr	(E) outside	20.8(10)	77.2(9)	2.1(2)	-	-	-
	(F) inside	23.3(1)	74.7(1)	2.0(1)	-	-	-
Ceramic material	(G) close to the rib	1.9(1)	9.0(3)	-	54.8(3)	14.3(4)	20.0(1)
	(H) close to the mesh	1.2(2)	9.1(3)	-	55.6(2)	14.2(2)	19.9(1)

Other authors have reported[60] that a ferritic type mesh steel possesses a higher creep strength than the Crofer22APU interconnect. Its higher strength is related to minor additions of Nb and W which result in a combination of solid-solution and precipitation strengthening by Laves phase formation, which have been analysed after the steel was treated at 800 ºC for 1000 h (Figure 4.18). As was expected[61], stable precipitation composed of mixed (Fe,Cr)(Nb,W) elements is quantified (Table 4.5).

Table 4.5. The average composition in % wt. of matrix and Laves phase indicated in Figure 4.18(b).

Spectrum	Cr	Fe	Ni	Nb	W
Matrix: 1,2,3	22.8(4)	74.8(3)	0.4(1)	0.1(1)	1.9(1)
Laves phase: 4,5,6	10.7(2)	43.1(11)	0.4(1)	21.2(16)	24.6(28)

Figure 4.21 shows the cross-section of {Crofer22APU/LNC- and LNF-mesh/LSF} systems of laser ablated areas after long term heating at 800 ºC, including EDX analysis zones (see Supplementary material; section A: Figure S4, section B: Figure S8).

[60] Kuhn B., Asensio-Jimenez C., Niewolak L., Hüttel T., Beck T., Hattendorf H., Singheiser L., Quadakkers W.J. Effect of Laves phase strengthening on the mechanical properties of high Cr ferritic steels for solid oxide fuel cell interconnect application. *Mat. Sci. Eng. A* 528 (**2011**) 5888-5899.

[61] Chiu Y.T., Lin C.K. Effects of Nb and W additions on high-temperature creep properties of ferritic stainless steels for solid oxide fuel cell interconnect. *J. Power Sources* 198 (**2012**) 149-157.

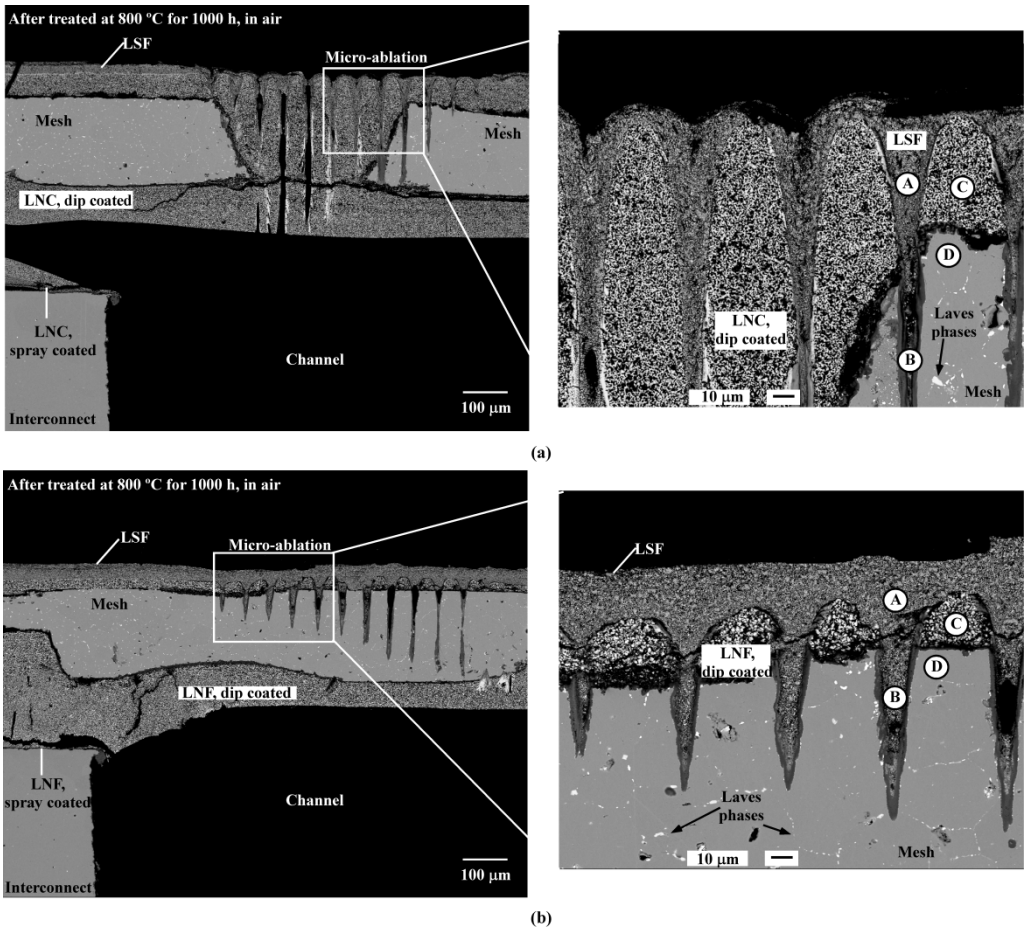

Figure 4.21. Cross-section views of (a) {interconnect/ablated LNC-mesh/cathode} and (b) {interconnect/ablated LNF-mesh/cathode} samples after long-term aging at 800 ºC, selecting the ablation craters. Capital letters indicate analysis areas shown in Tables 4.6 and 4.7.

In order to complement the quantitative results obtained, EDX mapping of both structures (Figures 4.22 and 4.23) were also performed.

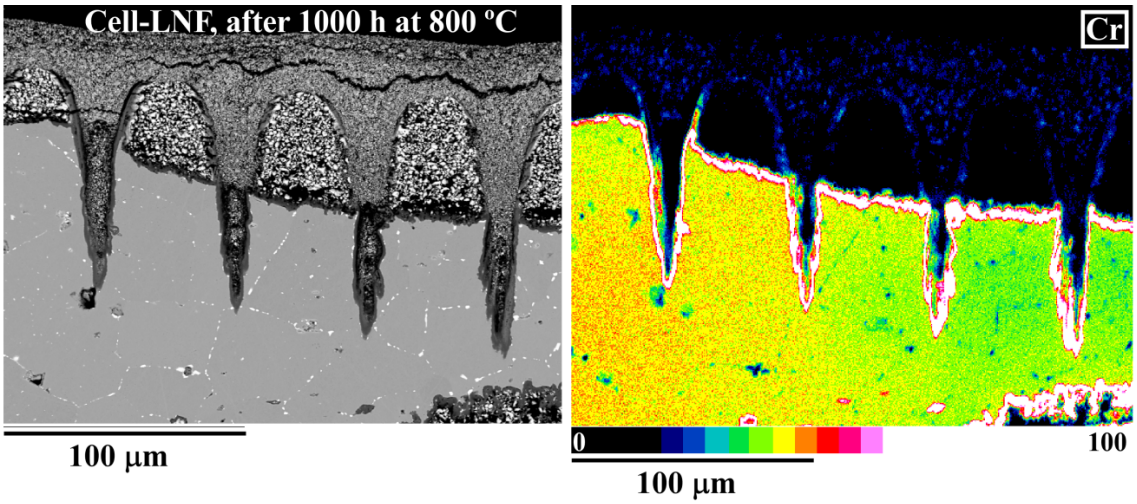

Figure 4.22. EDX mapping of the ablation cross-section of {interconnect/ablated LNF-mesh/cathode} sample after heating at 800 ºC for 1000 h in air.

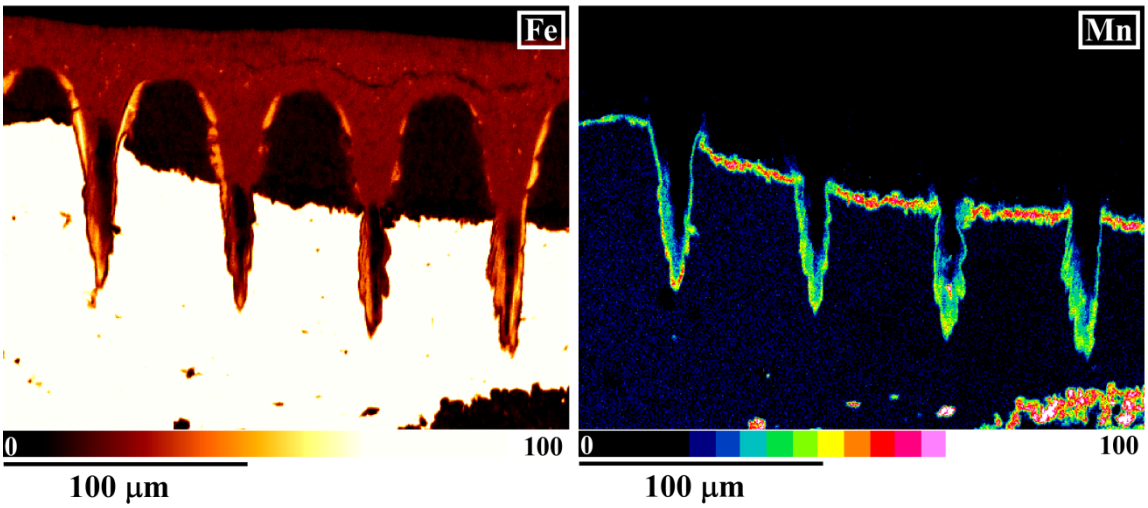

Figure 4.22. cont. EDX mapping of the ablation cross-section of {interconnect/ablated LNF-mesh/cathode} sample after heating at 800 ºC for 1000 h in air.

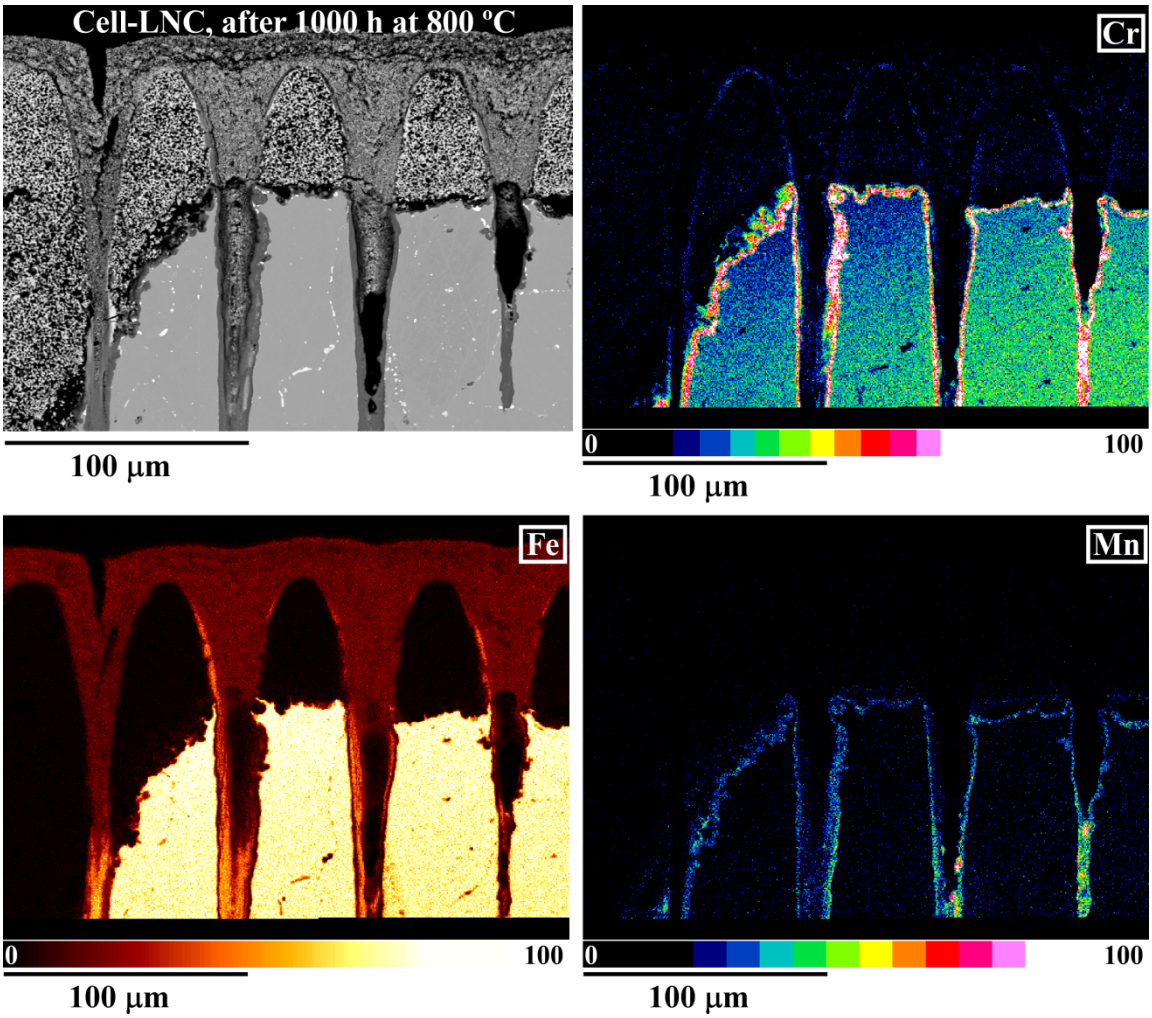

Figure 4.23. EDX mapping of the ablation cross-section of {interconnect/ablated LNC-mesh/cathode} sample after heating at 800 ºC for 1000 h in air.

According to both analyses, when LNC paste is used the detected Cr content reduction in the contact mesh is higher than that observed in the mesh in contact with LNF (Tables 4.6 and 4.7). At the same time, Fe content reduction is also observed into LNC coated mesh, which could indicate that the formation of Fe-oxides in the border of the crater is favoured.

Table 4.6. Chemical compositions in % wt. of points indicated in Figure 4.21(a).

LNC	Cr	Fe	W	Mn	La	Sr	Ni	Co	O
(A) cathode LSF	6.2(2)	23.0(4)	-	-	34.6(1)	14.9(2)	-	-	21.4(1)
(B cathode LSF	26.0(1)	23.4(1)	-	4.6(1)	17.7(1)	1.1(1)	-	-	27.3(1)
(C) contact LNC	5.2(4)	-	-	-	52.6(6)	-	13.1(3)	8.7(2)	20.4(1)
(D) mesh Fe-Cr	14.7(25)	82.6(25)	2.7(1)	-	-	-	-	-	-

Table 4.7. Chemical compositions in % wt. of points indicated in Figure 4.21(b).

LNF	Cr	Fe	W	Mn	La	Sr	Ni	O
(A) cathode LSF	4.7(1)	23.6(1)	-	-	34.3(1)	14.2(1)	-	23.2(1)
(B) cathode LSF	24.3(1)	31.6(1)	-	5.2(1)	30.3(1)	1.2(1)	-	7.5(1)
(C) contact LNF	1.9(2)	9.8(4)	-	-	56.8(9)	-	12.6(7)	18.9(8)
(D) mesh Fe-Cr	18.7(2)	78.8(2)	2.5(1)	-	-	-	-	-

In good agreement with these results, the observed Mn content through the mesh is lower when LNC is applied. Thus, the detected high concentration of Cr in LNC coating indicated that the chromium concentration in the mesh is not enough to form a $(Mn,Cr)_3O_4$ spinel protective layer, which was observed using LNF, allowing an increase in Fe oxides formation[62,63]. Moreover, the Cr is mainly concentrated in the LSF cathode layer; this indicates that Sr dopant promotes the Cr deposition on the contact material surface, in good agreement with both other authors and our previous studies[38,51,58,64,65] and, consistent with the results obtained in ASR test (see section 4.2.3.1).

It seems that the obtained data confirm that laser-metal interactions accelerate the oxidation of metallic chromium and iron, arising from the Fe-22Cr mesh, to deposit at the border of the craters as Fe-Cr oxides. However, EDX analyses performed on the crater environment confirm that the initial elemental composition, of each ceramic paste and metallic mesh, remains constant

---

62 Wang K., Liu Y., Fergus J.W. Interactions between SOFC interconnect coating materials and chromia. *J. Am. Ceram. Soc.* 94(12) (**2011**) 4490-4495.

63 Essuman E., Meier G.H., Zurek J., Hänsel M., Norby T., Singheiser L., Quadakkers W.J. Protective and non-protective scale formation of NiCr alloys in water vapour containing high- and low-pO_2 gases. *Corros. Sci.* 50(6) (**2008**) 1753-1760.

64 Shong W.J., Liu C.K., Chen C.Y., Peng C.C., Tu H.J., Fey G.T.K., Lee R.Y., Kao H.M., Effects of lanthanum-based perovskite coatings on the formation of oxide scale for ferritic SOFC interconnect. *Mater. Chem. Phys.* 127 (**2011**) 45-50.

65 Miguel-Pérez V. Interconnectores metálicos y capas protectoras para su aplicación en pilas SOFC. Ph.D. thesis work, UPV/EHU, **2013**.

(Figure 4.21, Tables 4.6 and 4.7). As a result, only very limited damage is observed in metal heat-affected zones.

4.2.4. Conclusions

Femtosecond laser machined micro-holes have been successfully achieved on LNC and LNF dip-coated on Fe-22Cr mesh material, obtaining a new contact composite. The initial ASR value of formed {interconnect/ablated contact layer/cathode} setup depends on the electrical conductivity of the ceramic contact coating. Multiple (four replicas) ASR testing for each system confirms the adequate reproducibility of the process.

However, the effectiveness of the contact composite over time depends on the adherence of the ceramic coating on the alloy material. A loss of adherence has been reported between LNC paste coating and interconnect due to an insufficient match of the corresponding thermal expansion coefficients (TECs), which favours the transport or vaporization rate of Cr species (CrO_3 (g), $CrO_2(OH)_2$ (g)). Furthermore, after 1000 h at 800 ºC, the laser irradiated composite showed short-range damage, which was limited to the formation of iron and chromium oxides due to the evaporation and oxidation of the mesh. Considering these results, ablated LNF-mesh material could be a good candidate to use as a contact coating between Crofer22APU channeled interconnect and LSF cathode.

4.2.5. Supplementary material

Section A. Details of EDX analyses performed on {Crofer22APU interconnect/laser ablated Fe-22Cr mesh-LNC contact composite/LSF cathode} sample after 1000 h at 800 ºC in air

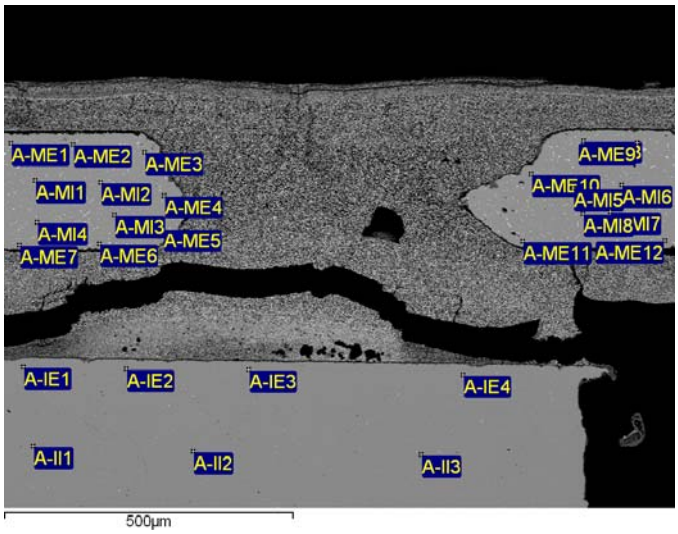

Figure S1. The EDX point analyses performed on Fe-22Cr steels of {rib/mesh-LNC/cathode} structure after aged at 800 ºC for 1000 h, in air.

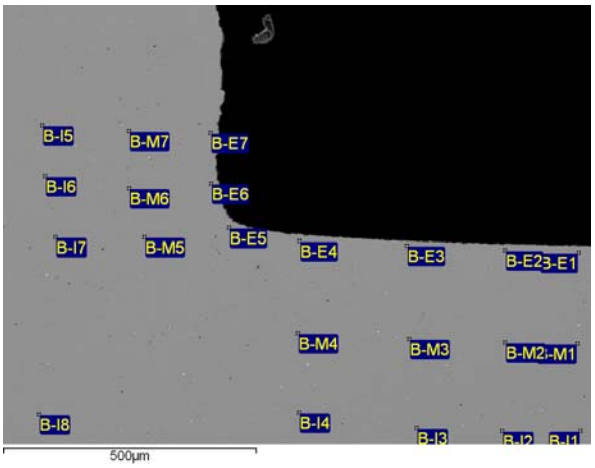

Figure S2. The EDX point analyses performed on channel of {channel/mesh-LNC/cathode} structure after aged at 800 ºC for 1000 h, in air.

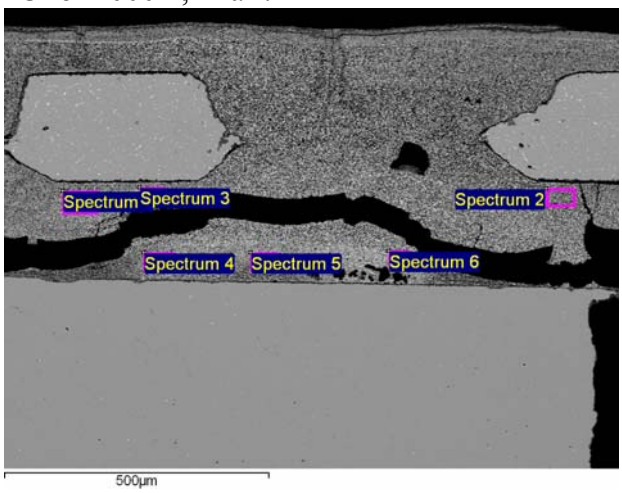

Figure S3. The EDX point analyses performed on ceramic coatings of {rib/mesh-LNC/cathode} structure after aged at 800 ºC for 1000 h, in air.

A.1. Details of micro-ablation zone

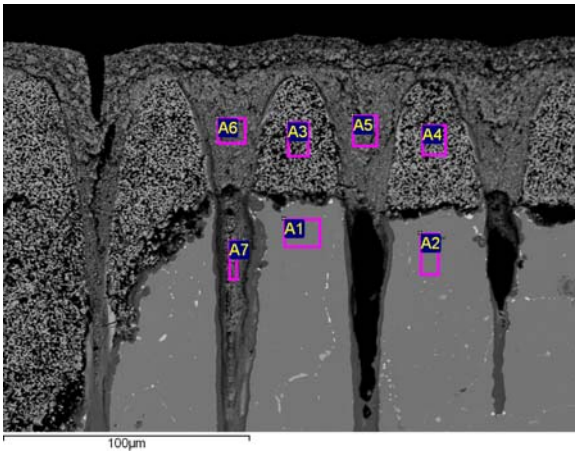

Figure S4. The EDX point analyses performed on ablated area of {rib/mesh-LNC/cathode} structure after aged at 800 ºC for 1000 h, in air.

Section B. Details of EDX analyses performed on {Crofer22APU interconnect/laser ablated Fe-22Cr mesh-LNF contact composite/LSF cathode} sample after 1000 h at 800 ºC in air

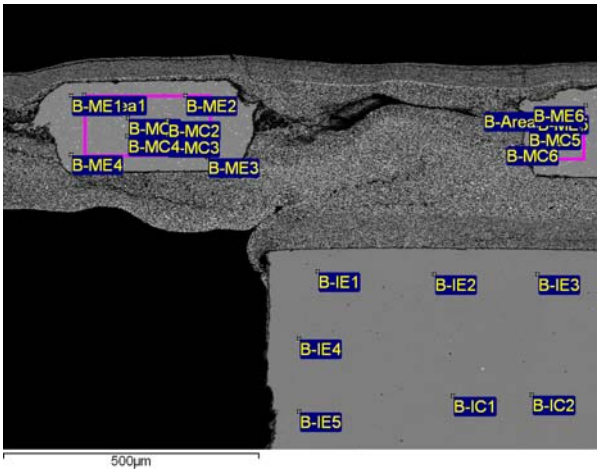

Figure S5. The EDX point analyses performed on Fe-22Cr steels of {rib/mesh-LNF/cathode} structure after aged at 800 ºC for 1000 h, in air.

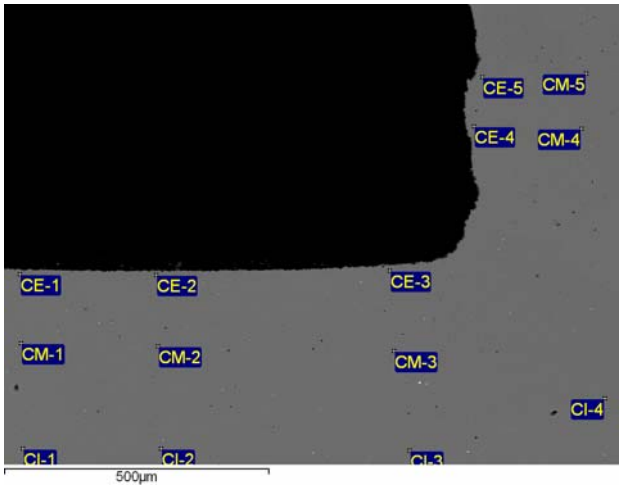

Figure S6. The EDX point analyses performed on channel of {channel/mesh-LNF/cathode} structure after aged at 800 ºC for 1000 h, in air.

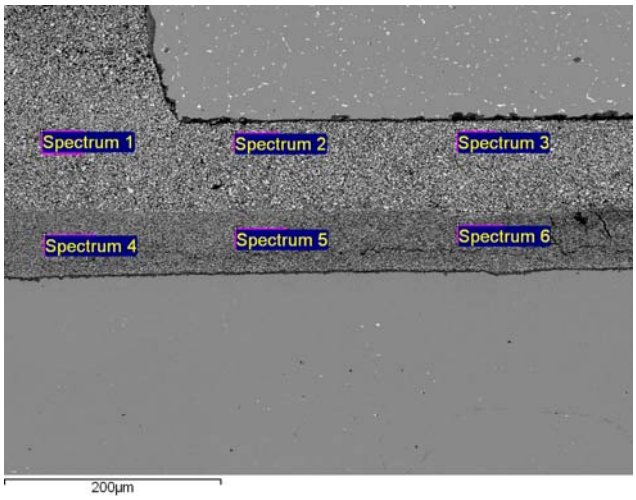

Figure S7. The EDX point analyses performed on ceramic coatings of {rib/mesh-LNF/cathode} structure after aged at 800 ºC for 1000 h, in air.

B.1. Details of micro-ablation zone

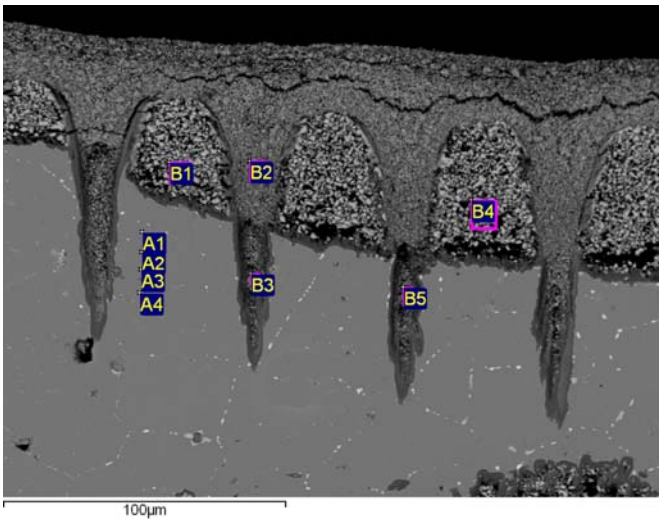

Figure S8. The EDX point analyses performed on ablated area of {rib/mesh-LNF/cathode} structure after aged at 800 ºC for 1000 h, in air.

5. CONCLUSIONES / CONCLUSIONS

Las conclusiones más importantes a las que ha conducido el desarrollo y posterior estudio de las estructuras interconector-capa de contacto-cátodo se detallan a continuación:

1. La introducción de una capa de contacto entre el interconector Crofer22APU y el cátodo $La_{0.6}Sr_{0.4}FeO_3$ (LSF), ha inducido un aumento en el flujo de corriente entre ambos materiales. Asimismo, la misma ha actuado como barrera para la migración de cromo, reduciendo la formación de fases secundarias en el cátodo.

2. La resistencia eléctrica de la celda Crofer22APU-capa de contacto-LSF, ha dependido de la conductividad del material de contacto, aumentando en el siguiente orden: LSFMC, LNF y LNC. Asimismo, para los sistemas en los que se han empleado los óxidos mixtos de contacto LNF y LNC, la señal ASR (Resistencia Superficial Específica) obtenida se ha mantenido constante durante 1300 h a 800 ºC, en aire.

3. La interacción entre el cátodo LSF y las capas de contacto, LNF, LNC o LSFMC, ha favorecido la formación de la solución solida $(LSF)_x(LNF, LNC \text{ o } LSFMC)_{1-x}$. Por otra parte, la formación de una interfase interconector-capa de contacto, compuesta por una capa interna Cr_2O_3 y otra externa M_3O_4 (M=Fe, Cr, Mn), ha favorecido la formación de fases secundarias como los óxidos $SrCrO_4$, perovskitas de Cr, y Cr_2O_3, debido a la difusión de cromo. No obstante, la presencia de manganeso, cobalto y hierro, en las perovskitas de contacto, ha hecho posible la formación de espinelas de diferente composición, las cuales han podido contribuir a una menor resistencia en la celda, especialmente las espinelas de cobalto debido a su elevada conductividad.

4. Los composites de contacto, metálicos/cerámicos, compuestos de una malla Fe-22Cr recubierta de LNF o LNC, y desarrollados a partir de la técnica de dip coating, han aportado a la estructura interconector-material de contacto, la integridad mecánica necesaria para hacer uso de interconectores acanalados en las celdas, sin reducir la adherencia del sistema. El empleo de la capa protectora MCF sobre la malla, como barrera para el cromo, sólo es efectiva si ésta presenta una alta densidad y homogeneidad.

5. La utilización de un láser de femtosegundos ha permitido micromecanizar el composite de contacto, facilitando así el flujo del gas oxidante a través del mismo, limitándose el área afectada por la interacción láser a las zonas próximas a la malla, debido a la evaporación y oxidación de la misma.

6. El proceso de formación de celdas interconector con canales-composite micromecanizado-cátodo es reproducible. La estructura compuesta por Crofer22APU-malla/LNC microperforado-LSF ha presentado la menor resistencia al paso de electrones. Sin embargo, a largos tiempos de operación la misma ha sufrido una pérdida de adherencia aumentando la reactividad en el sistema. Se concluye que el sistema más prometedor para su empleo en la tecnología SOFC es el formado por la estructura interconector acanalado Crofer22APU-malla recubierta por LNF y micromecanizada-cátodo LSF.

From the development and subsequent study of interconnect-contact coating-cathode structures, the following conclusions can be drawn:

1. Electrical current through the Crofer22APU interconnect-$La_{0.6}Sr_{0.4}FeO_3$ (LSF) structure has increased using a contact coating between both materials. In addition, cathode contact material has also worked as a barrier to the migration of chromium, minimizing the formation of secondary phases in the cathode.

2. The initial area specific resistance (ASR) of Crofer22APU-contact coating-LSF has depended on the electrical conductivity of the contact material, which increases in the following order: LSFMC, LNF and LNC. Moreover, the Crofer22APU-LNC or LNF-LSF structures have shown a stable ASR value after heat treated at 800 ºC for 1300 h, in air.

3. The interaction between LSF cathode and contact perovskites, LNF, LNC or LSFMC, has favoured the formation of a solid solution $(LSF)_x$(LNF, LNC or $LSFMC)_{1-x}$. On the other hand, the formation of a chromia (Cr_2O_3) layer under a M_3O_4 (M=Fe, Cr, Mn) spinel layer as a interconnect-contact material interface, has encouraged the formation of secondary phases, such as $SrCrO_4$, Cr-perovskites and Cr_2O_3, due to the diffusion of chromium. However, contact perovskites with Mn, Co and Fe transition metal elements on the B-site have enabled the formation of spinel phases with different compositions, which might have contributed to reduce the resistance of the cell, particularly Co-spinels due to their high electrical conductivity.

4. LNF or LNC dip-coated on Fe-22Cr mesh as a contact metallic/ceramic composite have provided to interconnect-contact material structure the required mechanical integrity, allowing the use of channeled interconnect in the cell without reducing the adherence of the system. The spinel protective layer used to coat the surface of the mesh must be dense and continuous across the width of the metal to prevent chromium migration up to the contact coating.

5. Femtosecond laser ablation on the contact composites has been successfully performed, thus, allowing oxidant gas flows therethrough. The area damaged by the laser interaction is located close to the mesh due to the evaporation and oxidation of metallic elements from the steel.

6. The formation process of channeled interconnect-micromachined contact composite-cathode cells has been reproducible. The structure of Crofer22APU-micromachined Fe-22Cr mesh/LNC-LSF has shown the lowest electrical resistance, however, a loss of adherence has undergone, increasing the overall reactivity of the system. Therefore, Crofer22APU channeled interconnect-micromachined composite consist of LNF dip coated on Fe-22Cr mesh-LSF cathode has been the most promising system for use in SOFC technology.

6. BIBLIOGRAFÍA / BIBLIOGRAPHY

Abas N., Kalair A., Khan N. Review of fossil fuels and future energy technologies. *Futures* (**2015**), doi:10.1016/j.futures.**2015**.03.003.

Abdoli H., Alizadeh P. Electrophoretic deposition of $(Mn,Co)_3O_4$ spinel nano powder on SOFC metallic interconnects. *Mater. Lett.* 80 (**2012**) 53-55.

Akanda S.R., Walter M.E., Kidner N.J., Seabaugh M.M. Lifetime prediction for manganese cobalt spinel oxide coatings on metallic interconnects. *Thin Solid Films* 565 (**2014**) 237-248.

Akhmat G., Zaman K., Shukui T., Sajjad F. Does energy consumption contribute to climate change? Evidence from major regions of the world. *Renew. Sust. Energ. Rev.* 36 (**2014**) 123-134.

Ali-Löytty H. Microalloying mediated segregation and interfacial oxidation of FeCr alloys for solid oxide fuel cell applications. Ph. D. thesis work, Tampere University of Technology, **2013**.

Allmann R., Hinek R., Bergerhoff G., Brown I.D. ICSD – Inorganic Crystal Structure database, FIZ Karlsruhe, National Institute of Standards and Technology (NIST), **2009**.

Al-Qattan A., Elsherbini A., Al-Ajmi K. Solid oxide fuel cell application in district cooling. *J. Power Sources* 257 (**2014**) 21-26.

Alvarado-Flores J. Avances en el desarrollo de interconectores metálicos de celdas SOFC. *Bol. Soc. Esp. Ceram. Vidr.* 52 (**2013**) 194-206.

Amorós. J. L. El Cristal. Morfología, Estructura y Propiedades Físicas. Ed. Atlas, p. 1-33, 201-217, **1990**.

Andersson J.O., Sundman B. Thermodynamic properties of the Cr-Fe system. *Calphad* 11 (**1987)** 83-92.

Aoki A. X-ray photoelectron spectroscopic studies on ZnS: MnF_2 phosphors. *Jpn. J. Appl. Phys.* 15 (**1976)** 305-311.

Ardigò M.R., Perron A., Combemale L., Heintz O., Caboche G., Chevalier S. Interface reactivity study between $La_{0.6}Sr_{0.4}Co_{0.2}Fe_{0.8}O_{3-\delta}$ (LSCF) cathode material and metallic interconnect for fuel cell. *J. Power Sources* 196 (**2011**) 2037-2045.

Azhar-Khan M., Zahir-Khan M., Zaman K., Naz L. Global estimates of energy consumption and greenhouse gas emissions. *Renew. Sust. Energ. Rev.* 29 (**2014**) 336–344.

Badwal S.P.S. Stability of solid oxide fuel cell components. *Solid State Ionics* 143 (**2001**) 39-46.

Badwal S.P.S., Deller R., Foger K., Ramprakash Y., Zhang J.P. Interaction between chromia forming alloy interconnects and air electrode of solid oxide fuel cells. *Solid State Ionics* 99 (**1997)** 297-310.

Badwal S.P.S., Foger K. Materials for solid oxide fuel cells. *Mater. Forum* 21 (**1997**) 187-224.

Bahteeva J.A., Leonidov I.A., Patrakeev M.V., Mitberg E.B., Kozhevnokov V.L., Poeppelmeier K.R. High-temperature ion transport in $La_{1-x}Sr_xFeO_{3-\delta}$. *J. Solid State Electr.* 8 (**2004**) 578-584.

Bannikov D.O., Cherepanov V.A. Thermodynamic properties of complex oxides in the LaNiO system. *J. Solid State Chem.* 179 (**2006**) 2721-2727.

Barelli L., Barluzzi E., Bidini G. Diagnosis methodology and technique for solid oxide fuel cells: A review. *Int. J. Hydrogen Energ.* 38 (**2013**) 5060-5074.

Barnes H.A., Hutton J.F., Walters F.R.S.K. An introduction to rheology, Ed. Elsevier, p. 1-35, **1989**.

Basu R.N., Tietz F., Teller O., Wessel E., Buchkremer H.P., Stöver D. $LaNi_{0.6}Fe_{0.4}O_3$ as a cathode contact material for solid oxide fuel cells, *J. Solid State Electrochem.* 7 (**2003**) 416-420.

Battistoni C., Dormann J.L., Fiorani D., Paparazzo E., Viticali S. An XPS and Mössbauer study of the electronic properties of $ZnCr_xGa_{2-x}O_4$ spinel solid solutions. *Solid State Commun.* 39(4) (**1981**) 581-585.

Bevilacqua M., Montini T., Tavagnacco C., Vicario G., Fornasiero P., Graziani M. Influence of synthesis route on morphology and electrical properties of $LaNi_{0.6}Fe_{0.4}O_3$. *Solid State Ionics* 177 (**2006)** 2957-2965.

Bin F., Song C., Lu G., Song J., Gong C., Huang Q. $La_{1-x}K_xCoO_3$ and $LaCo_{1-y}Fe_yO_3$ perovskite oxides: preparation, characterization, and catalytic performance in the simultaneous removal of NO_x and diesel soot. *Ind. Eng. Chem. Res.* 50 (**2011**) 6660-6667.

Brandon N.P., Brett D.J. Engineering porous materials for fuel cell applications. *Phil. Trans. R. Soc. A* 364 (**2006**) 147-159.

Brett D.J.L., Atkirson A., Brandon N.P., Skinner S.J. Intermediate temperature solid oxide fuel cells. *Chem. Soc. Rev.* 37 (**2008**) 1568-1578.

Carter S., Seluck A., Charter R.J., Kajda J., Kilner J.A., Steele B.C.H. Oxygen transport in selected nonstoichiometric perovskite-structure oxides. *Solid State Ionics* 53-56 (**1992**) 597-605.

Chapman I. The end of peak oil? Why this topic is still relevant despite recent denials. *Energ. Policy* 64 (**2014**) 93-101.

Charpentier P., Fragnaud P., Schleich D.M., Gehain E. Preparation of thin film SOFCs working at reduced temperature. *Solid State Ionics* 135 (**2000**) 373-380.

Chen X., Jiang S.P. Highly active and stable $(La_{0.24}Sr_{0.16}Ba_{0.6})(Co_{0.5}Fe_{0.44}Nb_{0.06})O_{3-\delta}$ (LSBCFN) cathodes for solid oxide fuel cells prepared by a novel mixing synthesis method. *J. Mater. Chem. A* 1 (**2013**) 4871-4878.

Chen X., Zhang L., Liu E., Jiang S.P. A fundamental study of chromium deposition and poisoning at $(La_{0.8}Sr_{0.2})_{0.95}(Mn_{1-x}Co_x)O_{3\pm\delta}$ ($0.0\leq x \leq 1.0$) cathodes of solid oxide fuel cells. *Int. J. Hydrogen Energ.* 36 (**2011**) 805-821.

Chen X., Zhen Y., Li J., Jiang S.P. Chromium deposition and poisoning in dry and humidified air at $(La_{0.8}Sr_{0.2})_{0.9}MnO_{3+\delta}$ cathodes of solid oxide fuel cells. *Int. J. Hydrogen Energ.* 35 (**2010)** 2477-2485.

Chiu Y.T., Lin C.K. Effects of Nb and W additions on high-temperature creep properties of ferritic stainless steels for solid oxide fuel cell interconnect. *J. Power Sources* 198 (**2012**) 149-157.

Choi J.P., Weil K.S., Chou Y.M., Stevenson J.W., Yang Z.G. Development of MnCoO coating with new aluminizing process for planar SOFC stacks. *Int. J. Hydrogen Energ.* 36 (**2011)** 4549-4556.

Chou P.Y., Ciou C.J., Lee Y.C., Hung I.M. Effect of $La_{0.1}Sr_{0.9}Co_{0.5}Mn_{0.5}O_{3-\delta}$ protective coating layer on the performance of $La_{0.6}Sr_{0.4}Co_{0.8}Fe_{0.2}O_{3-\delta}$ solid oxide fuel cell cathode. *J. Power Sources* 197 (**2012**) 12-19.

Chou Y.S., Stevenson J.W., Choi J.P. Long-term evaluation of solid oxide fuel cell candidate materials in a 3-cell generic stack test fixture, part III: stability and microstructure of Ce-(Mn,Co)-spinel coating, AISI441 interconnect, alumina coating, cathode and anode. *J. Power Sources* 257 (**2014**) 444-453.

Chun-Lin C., Jian-Yih W., Shyong L. Effects of $La_{0.67}Sr_{0.33}MnO_3$ protective coating on SOFC interconnect by plasma-sputtering. *Int. J. Hydrogen Energy* 33(10) (**2008**) 2536-2546.

Conceição L.D, Dessemond L., Djurado E., Souza M.M.V.M. $La_{0.7}Sr_{0.3}MnO_3$-coated SS444 alloy by dip-coating process for metallic interconnect supported solid oxide fuel cells. *J. Power Sources* 241 (**2013**) 159-167.

Conceição L.D, Dessemond L., Djurado E., Souza M.M.V.M. Thin films of $La_{0.7}Sr_{0.3}MnO_{3+\delta}$ dip-coated on Fe-Cr alloys for SOFC metallic interconnect. *Int. J. Hydrogen Energ.* 38 (**2013)** 15335-15347.

Conceição L.D., Dessemond L., Djurado E., Muccillo E.N.S. $La_{0.7}Sr_{0.3}MnO_{3-\delta}$ barrier for Cr_2O_3-forming SOFC interconnect alloy coated by electrostatic spray deposition. *Surf. Coat. Tech.* 254 (**2014**) 157-166.

Conti J.J., Holtberg P.D. The *Annual Energy Outlook 2014* (AEO2014), U.S. Energy Information Administration (EIA), **2014**.

Cox P.A. The Electronic Structure and Chemistry of Solids, Oxford Science Publications, Oxford, UK, **1987**.

Crumlin E.J., Mutoro E., Liu Z., Grass M.E., Biegalski M.D., Lee Y.L., Morgan D., Christen H.M., Bluhm H., Shao-Horn Y. Surface strontium enrichment on highly active perovskites for oxygen electrocatalysis in solid oxide fuel cells. *Energ. Environ. Sci.* 5 (**2012**) 6081-6088.

Dasgupta N., Krishnamoorthy R., Jacob K.T. Crystal structure and thermal and electrical properties of the perovskite solid solution $Nd_{1-x}Sr_xFeO_{3-\delta}$ ($0 \leq x \leq 0.4$). *Solid State Ionics* 149 (**2002**) 227-236.

De Nalda R., Bañares L. El láser en ciencias de la vida, **2007**. http://www.rsef.org.

Dheeradhada V.S., Cao H., Alinger M.J. Oxidation of ferritic stainless steel interconnects: thermodynamic and kinetic assessment. *J. Power Sources* 196 (**2011)** 1975-1982.

Di-Maio Y., Colombier J.P., Cazottes P., Audouard E. Ultrafast laser ablation characteristics of PZT ceramic: Analysis methods and comparison with metals. *Opt. Laser Eng.* 50 (**2012**) 1582-1591.

Döring S., Richter S., Nolte S., Tünnermann A. In situ imaging of hole shape evolution in ultrashort pulse laser drilling. *Opt. Express* 18(19) (**2010**) 20395-20400.

Dunlap M., Adaskaveg J.E. Introduction to the scanning electron microscope, Cambridge, p. 3-33, **1997**.

Dutta A., Mukhopadhyay J., Basu R.N. Combustion synthesis and characterization of LSCF-based materials as cathode of intermediate temperature solid oxide fuel cells. *J. Eur. Ceram. Soc.* 29 (**2009)** 2003-2011.

Echevarria-Huaman R.N., Xiu-Jun T. Energy related CO_2 emissions and the progress on CCS projects: A review. *Renew. Sust. Energ. Rev.* 31 (**2014**) 368-385.

Ecija-Verdejo A. Óxidos mixtos tipo perovskita $Ln_{0.5}M_{0.5}FeO_{3-\delta}$ (Ln=La, Sm, Nd, Gd; M=Ba, Sr) para su aplicación como cátodos en pilas SOFC. Ph.D. thesis work, UPV/EHU, **2012**.

EG&G Technical Services, Fuel Cell Handbook, 7th ed., Morgantown, U.S. Deparment of Energy, **2004**.

Elmer T., Worall M., Wu S., Riffat S.B. Fuel cell technology for domestic built environment applications. State of-the-art review. *Renew. Sust. Energ. Rev.* 42 (**2015**) 913-931.

Essuman E., Meier G.H., Zurek J., Hänsel M., Norby T., Singheiser L., Quadakkers W.J. Protective and non-protective scale formation of NiCr alloys in water vapour containing high- and low-pO_2 gases. *Corros. Sci.* 50(6) (**2008**) 1753-1760.

Fang Y., Wu C., Duan X., Wang S., Chen Y. High-temperature oxidation process analysis of $MnCo_2O_4$ coatings on Fe-21Cr alloy. *Int. J. Hydrogen Energ.* 36(9) (**2011**) 5611-5616.

Fayette S., Smith D.S., Smith A., Martin C. Influence of grain size on the termal conductivity of tin oxide ceramics. *J. Eur. Ceram. Soc.* 20(3) (**2000**) 297-302.

Fontana S., Amendola R., Chevalier S., Piccardo P., Caboche G., Viviani M., Molins R., Sennour M. Metallic interconnects for SOFC: Characterisation of corrosion resistance and conductivity evaluation at operating temperature of differently coated alloys. *J. Power Sources* 171 (**2007**) 652–662.

Fontana S., Chevalier S., Caboche G. Metallic interconnects for solid oxide fuel cell: performance of reactive element oxide coating during 10, 20 and 30 months exposure. *Oxid. Met.* 78 (**2012**) 307-328.

Froitzheim J., Meier G.H., Niewolak L., Ennis P.J., Hattendorf H., Singheiser L., Quadakkers W.J. Development of high strength ferritic steel for interconnect application in SOFCs. *J. Power Sources* 178 (**2008**) 163-173.

Fu Q.X., Sebold D., Tietz F., Buchkremer H.P. Electrodeposited cobalt coating on Crofer22APU steels for interconnect applications in solid oxide fuel cells. *Solid State Ionics* 192 (**2011)** 376-382.

Fujita K., Hashimoto T., Ogasawara K., Kameda H., Matsuzaki Y., Sakurai T. Relationship between electrochemical properties of SOFC cathode and composition of oxide layer formed on metallic interconnects. *J. Power Sources* 131 (**2004**) 270-277.

Gao Z., Mao Z., Wang C., Liu Z. Preparation and characterization of $La_{1-x}Sr_xNi_yFe_{1-y}O_{3-\delta}$ cathodes for low-temperature solid oxide fuel cells. *Int. J. Hydrogen Energ*. 35 (**2010)** 12905-12910.

Gazzarri J.I., Kesler O. Short-stack modeling of degradation in solid oxide fuel cells Part I. Contact degradation. *J. Power Sources* 176 (**2008**) 138-154.

Gerwen R.J.F. Systems and Applications, in High temperature solid oxide fuel cells fundamentals, design and applications (eds. Singhal S.C., Kendall K.), Elsevier, Oxford, UK, p. 363-392, **2003**.

Ghaffari M., Shannon M., Hui H., Tan O.K., Irannejad A. Preparation, surface state and band structure studies of $SrTi_{(1-x)}Fe_{(x)}O_{(3-\delta)}$ (x=0-1) perovskite-type nano structure by X-ray and ultraviolet photoelectron spectroscopy. *Surf. Sci.* 606 (**2012**) 670-677.

Girod B., Van-Vuuren D.P., Hertwich E.G. Climate policy through changing consumption choices: Options and obstacles for reducing greenhouse gas emissions. *Global Environ. Chang.* 25 (**2014**) 5–15.

Grolig J.G., Froitzheim J., Svensson J.E. Coated stainless steel 441 as interconnect material for solid oxide fuel cells: oxidation performance and chromium evaporation. *J. Power Sources* 248 (**2014**) 1007-1013.

Guan W., Jin L., Wu W., Zheng Y., Wang G.,Wang W.G. Effect and mechanism of Cr deposition in cathode current collecting layer on cell performance inside stack for planar oxide fuel cells. *J. Power Sources* 245 (**2014**) 119-128.

Guan W.B., Jin L., Ma X., Wang W.G. Investigation of impactors on cell degradation inside planar SOFC stacks. *Fuel Cells* 12(6) (**2012**) 1085-1094.

Guan W.B., Zhai H.J., Jin L., Li T.S., Wang W.G. Effect of contact between electrode and interconnect on performance of SOFC stacks. *Fuel Cells* 11(3) (**2011**) 445-450.

Guoliang W., Guan W., Miao F., Wang W.G. Factors of cathode current-collecting layer affecting cell performance inside solid oxide fuel cell stacks. *Int. J. Hydrogen Energ.* 39 (**2014**) 17836-17844.

Gurauskis J. Deposition via dip coating technique of dense yttrium stabilized zirconia layers. *Int. J. Appl. Ceram. Technol.* 10(1) (**2013**) 79-86.

Hahn Th., "International tables for crystallography, Volume A: Space-group symmetry", D. Reidel Publishing Company, Boston, USA, **1983**.

Hamnett A. The components of an electrochemical cell, in Handbook of Fuel Cells- Fundamentals, Technology and Applications (eds. Vielstich W., Lamm A, Gasteiger H.A.), John Wiley & Sons, New Jersey, USA, p. 3-12, **2003**.

Hilpert K., Das D., Miller M., Peck D.H., Wei R. Chromium vapor species over solid oxide fuel cell interconnect materials and their potential for degradation processes. *J. Electrochem. Soc.* 143 (**1996)** 3642-3647.

Hilpert K., Quadakkers J., Singheiser L. Interconnects, in Handbook of Fuel Cells- Fundamentals, Technology and Applications (eds. Vielstich W., Lamm A., Gasteiger H.A.), Ed. John Wiley & Sons, New Jersey, USA, p. 1037-1051, **2003**.

Hjalmarsson P. Strontium and nickel substituted lanthanum cobaltite as cathode in solid oxide fuel cells. Ph. D. thesis work, Technical University of Denmark, **2008**.

Hjalmarsson P., Sogaard M., Hagen A., Mogensen M. Structural properties and electrochemical performance of strontium- and nickel-substituted lanthanum cobaltite. *Solid State Ionics* 179 (**2008**) 636-646.

Hong S., Bradshaw C.J.A., Brook B.W. Global zero-carbon energy pathways using viable mixes of nuclear and renewables. *Appl. Energ.* 143 (**2015**) 451–459.

Hosseini N., Abbasi M.H., Karimzadeh F., Choi G.M. Development of $Cu_{1.3}Mn_{1.7}O_4$ spinel coating on ferritic stainless Steel for solid oxide fuel cell interconnects. *J. Power Sources* 273 (**2015**) 1073-1083.

Howng W.Y., Thorn R.J. Investigation of the electronic structure of $La_{1-x}(M^{2+})_xCrO_3$, Cr_2O_3 and La_2O_3 by X-ray photoelectron spectroscopy. *J. Chem. Phys. Solids* 41 (**1980)** 75-81.

Hoyt K.O., Gannon P.E., White P., Tortop R., Ellingwood B.J., Khoshuei H. Oxidation behavior of $(Co,Mn)_3O_4$ coatings on preoxidized stainless steel for solid oxide fuel cell interconnects. *Int. J. Hydrogen Energ.* 37 (**2012**) 518-529.

Hrovat M., Katsarakis N., Reichmann K., Bernik S., Kuscer D., Holc J. Characterization of $LaNi_{1-x}Co_xO_3$ as a possible SOFC cathode material. *Solid State Ionics* 83 (**1996**) 99-105.

Hsiao Y.C., Selman J.R. The degradation of SOFC electrodes. *Solid State Ionics* 98 (**1997**) 33-38.

http://ec.europa.eu/europe2020/index_es.htm.

http://ec.europa.eu/programmes/horizon2020/.

http://queaprendemoshoy.com/algo-mas-sobre-la-interaccion-luz-materia-la-ampliacion-optica-principio-base-para-el-efecto-laser/.

http://www.bp.com/statisticalreview. BP Statistical review of world energy. June 2014.

http://www.eshorizonte2020.es/.

http://www.iea.org/publications/freepublications/publication/co2-emissions-from-fuel-combustion-highlights-2014.html. CO_2 Emissions from fuel combustion, IEA, **2014**.

http://www.interempresas.net/Deformacion-y-chapa/Articulos/99796-El-laser-de-pulsos-ultracortos.html.

http://www.springer.com/978-1-84996-027-4 (Chapter 2: Thermodynamics of Fuel Cells), **2011**.

http://www.xtal.iqfr.csic.es/Cristalografia/parte_02.html.

http://www6.uniovi.es/usr/fblanco/Tema6.MaterialesCERAMICOS.SinterizacionEstadoSolido.pdf.

Huang A., Yao K., Wang J. Conducting perovskite $LaNi_{0.6}Co_{0.4}O_3$ ceramics with glass additions. *J. Electroceram.* 16 (**2006)** 313-319.

Huang K., Lee H.Y., Goodenough J.B. Sr- and Ni-doped $LaCoO_3$ and $LaFeO_3$ perovskites-new cathode materials for solid oxide fuel cells. *J. Electrochem. Soc.* 145(9) (**1998**) 3220-3227.

Huang K., Singhal S.C. Cathode-supported tubular solid oxide fuel cell technology: A critical review. *J. Power Sources* 237 (**2013**) 84-97.

Huczkowski P., Quadakkers W.J., Effect of geometry and composition of Cr steels on oxide scale properties relevant for interconnector applications in solid oxide fuel cells (SOFCs), Forschungszentrum Jülich, **2007**.

Hung C.H., Chang F.Y., Chang T.L., Chang Y.T., Huang K.W., Liang P.C. Micromachining NiTi tubes for use in medical devices by using a femtosecond laser. *Opt. Lasers Eng.* 66 (**2015**) 34-40.

ICDD, "Powder Diffraction File-Inorganic and Organic", Pennsylvania, USA, **1995**.

Introduction to energy dispersive X-ray spectroscopy (EDS), http://micron.ucr.edu/public/manuals/EDX-intro.pdf

Ivers-Tiffée E., Weber A., Herbstritt D. Materials and technologies for SOFC-components. *J. Eur. Ceram. Soc.* 21 (**2001**) 1805–1811.

Ivers-Tiffée E., Weber A., Schichlein H., chapter 40, in W. Vielstich, H.A. Gasteiger and A. Lamm (eds.), *"Handbook of Fuel cells"*. vol. 2, John Wiley & Sons, Chichester, **2003**.

Jia W., Peng Z., Wang Z., Ni X., Wang C.-Y. The effect of femtosecond laser micromachining on the surface characteristics and subsurface microstructure of amorphous FeCuNbSiB alloy. *Appl. Surf. Sci.* 253 (**2006**) 1299–1303.

Jiang S.P. Resistance measurement in solid oxide fuel cells. *J. Electrochem. Soc.* 148(8) (**2001)** A887-A897.

Jiang S.P., Chen X. Chromium deposition and poisoning of cathodes of solid oxide fuel cells – A review. *Int. J. Hydrogen Energ.* 39(1) (**2014**) 505-531.

Jiang S.P., Love J.G., Apateanu L. Effect of contact between electrode and current collector on the performance of solid oxide fuel cells. *Solid State Ionics* 160 (**2003)** 15-26.

Jiang S.P., Zhang J.P., Apateanu L., Foger K. Deposition of chromium species at Sr-doped $LaMnO_3$ electrodes in solid oxide fuel cells I. Mechanism and kinetics. *J. Electrochem. Soc.* 147 (**2000**) 4013-4022.

Jiang S.P., Zhang S., Zhen Y.D. Deposition of Cr species at $(La,Sr)(Co,Fe)O_3$ cathodes of solid oxide fuel cells. *J. Electrochem. Soc.* 153(1) (**2006**) A127-A134.

Jiang S.P., Zhang S., Zhen Y.D. Early interaction between Fe-Cr alloy metallic interconnect and Sr-doped $LaMnO_3$ cathodes of solid oxide fuel cells. *J. Mater. Res.* 20(3) (**2005**) 747-758.

Jiang S.P., Zhen Y. Mechanism of Cr deposition and its application in the development of Cr-tolerant cathodes of solid oxide fuel cells. *Solid State Ionics* 179 (**2008**) 1459-1464.

Jiang Y., Gao J., Liu M., Wang Y., Meng G. Synthesis of $LaCrO_3$ films using spray pyrolysis technique. *Mater. Lett.* 61 (**2007**) 1908-1911.

Jin L., Guan W., Niu J., Ma X., Wang W.G. Effect of contact area and depth between cell cathode and interconnect on stack performance for planar solid oxide fuel cells. *J. Power Sources* 240 (**2013**) 796-805.

Kamlage G., Bauer T., Ostendorf A., Chichkov B.N. Deep drilling of metals by femtosecond laser pulses. *Appl. Phys. A* 77 (**2003**) 307-310.

Kawada T. Perovskite oxide for cathode of SOFCs, in perovskite oxide for solid oxide fuel cells (eds. Ishihara T.), p. 147-166, **2009**.

Kharton V.V., Figueiredo F.M., Kovalevsky A.V., Viskup A.P., Naumovich E.N., Yaremchenko A.A., Bashmakov I.A., Marques F.M.B. Processing, microstructure and properties of $LaCoO_{3+\delta}$ ceramics. *J. Eur. Ceram. Soc.* 21 (**2001**) 2301-2309.

Kim J.H. X-ray photoelectron spectroscopy analysis of $(Ln_{1-x}Sr_x)CoO_{3-\delta}$ (Ln: Pr, Nd and Sm). *Appl. Surf. Sci.* 258 (**2011**) 350-355.

Kim S.H., Sohn I.–B., Jeong S. Ablation characteristics of aluminum oxide and nitride ceramics during femtosecond laser micromachining. *Appl. Surf. Sci.* 255(24) (**2009**) 9717-9720.

Kiselev E.A., Cherepanov V.A. p (O_2)-stability of $LaFe_{1-x}Ni_xO_{3-\delta}$ solid solutions at 1100 ºC. *J. Solid State Chem.* 183 (**2010**) 1992-1997.

Klein C., Hurlbut J.C.S., *"Manual de Mineralogía"*, Ed. Reverté S.A., Barcelona, **1996**.

Klugman J., "Human Development Report 201. Sustainability and Equity: A Better Future for All", United Nations Development Programme, New York, USA, **2011**.

Kofstad P. High temperature corrosion, Elsevier Applied Science, London, **1988**.

Kofstad P. Oxidation of alloys, in High-temperature oxidation of metals. John Wiley & Sons, INC, New York, p. 264-299, **1966**.

Konysheva E., Francis S.M. Identification of surface composition and chemical states in composites comprised of phases with fluorite and perovskite structures by X-ray photoelectron spectroscopy. *Appl. Surf. Sci.* 268 (**2013**) 278-287.

Konysheva E., Irvine J.T.S. Evolution of conductivity, structure and thermochemical stability of lanthanum manganese iron nickelate perovskites. *J. Mater. Chem.* 18 (**2008**) 5147-5154.

Konysheva E., Laatsch J., Wessel E., Tietz F., Christiansen N., Singheiser L., Hilpert K. Influence of different perovskite interlayers on the electrical conductivity between $La_{0.65}Sr_{0.3}MnO_3$ and Fe/Cr based steels. *Solid State Ionics* 177 (**2006**) 923-930.

Kostogloudis G.-Ch., Ftikos Ch. Properties of A-site deficient $La_{0.6}Sr_{0.4}Co_{0.2}Fe_{0.8}O_{3-\delta}$ based perovskite oxides. *Solid State Ionics* 126 (**1999**) 143-151.

Kruk A., Stygar M., Brylewski T. Mn–Co spinel protective–conductive coating on AL453 ferritic stainless steel for IT-SOFC interconnect applications. *J. Solid State Electrochem.* 17 (**2013**) 993-1003.

Kuhn B., Asensio-Jimenez C., Niewolak L., Hüttel T., Beck T., Hattendorf H., Singheiser L., Quadakkers W.J. Effect of Laves phase strengthening on the mechanical properties of high Cr ferritic steels for solid oxide fuel cell interconnect applications. *Mat. Sci. Eng. A* 528 (**2011**) 5888-5899.

Kumar R., Yi E., Hang Y., Myung C. Thermal, micro-structural, and electrical properties of a $La_{1-x}Sr_xMn_{0.85}Fe_{0.05}Co_{0.05}Ni_{0.05}O_{3+\delta}$ (x=0-0.4 mole) cathode system. *Met. Mater. Int.* 15 (**2009)** 1055-1060.

Lacey R., Pramanick A., Lee J.C., Jung J.I., Jiang B., Edwards D.D., Naum R., Misture S.T. Evaluation of Co and perovskite Cr-blocking thin films on SOFC interconnects. *Solid State Ionics* 181 (**2010**) 1294-1302.

Lal B., Raghunandan M.K., Gupta M., Singh R.N. Electrocatalytic properties of perovskite-type obtained by a novel stearic acid sol-gel method for electrocatalysis of O_2 evolution in KOH solutions. *Int. J. Hydrogen Energ.* 30 (**2005**) 723-729.

Larminie J.C., Dicks A., Fuel Cell System Explained, John Wiley & Sons Ltd., New York, p. 1-66, **2003**.

Lau G.Y., Tucker M.C., Jacobson C.P., Visco S.J., Gleixner S.H., DeJonghe L.C. Chromium transport by solid state diffusion on solid oxide fuel cell cathode. *J. Power Sources* 195 (**2010)** 7540-7547.

Lee K.T., Manthiram A. Synthesis and characterization of $Nd_{0.6}Sr_{0.4}Co_{1-y}Mn_yO_{3-\delta}$ ($0\leq y\leq 1.0$) cathodes for intermediate temperature solid oxide fuel cells. *J. Power Sources* 158 (**2006)** 1202-1208.

Lee Y.D., Ahn K.Y., Morosuk T., Tsatsaronis G. Environmental impact assessment of a solid-oxide fuel-cell-based combined-heat-and-power-generation system. *Energy* 79 (**2015**) 455-466.

Leitz K.H., Redlingshöfer B., Reg Y., Otto A., Schmidt M. Metal ablation with short and ultrashort laser pulses. *Physics Procedia* 12 (**2011**) 230-238.

Li K., Bian H., Liu C., Zhang D., Yang Y. Comparison of geothermal with solar and wind power generation systems. *Renew. Sust. Energ. Rev.* 42 (**2015**) 1464–1474.

Li S., Lü Z., Huang X., Su W. Thermal, electrical, and electrochemical properties of Nd-doped $Ba_{0.5}Sr_{0.5}Co_{0.8}Fe_{0.2}O_{3-\delta}$ as a cathode material for SOFC. *Solid State Ionics* 178 (**2008)** 1853-1858.

Li W., Lu K., Xia Z. Interaction of $(La_{1-x}Sr_x)_nCo_{1-y}Fe_yO_{3-\delta}$ cathodes and AISI 441 interconnect for solid oxide fuel cells. *J. Power Sources* 237 (**2013**) 119-127.

Li Z., Wei B., Lü Z., Huang X., Su W. Structure, electrical and thermal properties of $(Ba_{0.5}Sr_{0.5})_{1-x}Gd_xCo_{0.8}Fe_{0.2}O_{3-\delta}$ perovskite as a solid-oxide fuel cell cathode. *Solid State Ionics* 207 (**2012)** 38-43.

Lima S.M.D., Peña M.A., Fierro J.L.G., Assaf J.M. $La_{1-x}Ca_xNiO_3$ perovskite oxides: characterization and catalytic reactivity in dry reforming of methane. *Catal. Lett.* 124 (**2008**) 195-203.

Linder M., Hocker T., Holzer L., Friedrich K.A., Iwanschitz B., Mai A., Schuler J.A. Cr_2O_3 scale growth rates on metallic interconnectors derived from 40.000 h solid oxide fuel cell stack operation. *J. Power Sources* 243 (**2013**) 508-518.

Liu B., Zhang Y., Tang L. X-ray photoelectron spectroscopic studies of $Ba_{0.5}Sr_{0.5}Co_{0.8}Fe_{0.2}O_{3-\delta}$ cathode for solid oxide fuel cells. *Int. J. Hydrogen Energ.* 34 (**2009**) 435-439.

Liu Y., Chen D.Y. Protective coatings for Cr_2O_3-forming interconnects of solid oxide fuel cells. *Int. J. Hydrogen Energ.* 34 (**2009**) 9220-9226.

Lu Z., Xia G., Templeton J.D., Li X., Nie Z., Yang Z., Stevenson J.W. Development of $Ni_{1-x}Co_xO$ as the cathode/interconnect contact for solid oxide fuel cells. *Electrochem. Commun.* 13 (**2011**) 642-645.

Lv H., Zhao B-Y., Wu Y-J., Sun G., Chen G., Hu K-A. Effect of B-site doping on $Sm_{0.5}Sr_{0.5}B_xCo_{1-x}O_{3-\delta}$ properties for IT-SOFC cathode material (M=Fe, Mn). *Int. Mater. Res. Bull*. 42(12) (**2007)** 1999-2012.

Magdefrau N.J. Evaluation of solid oxide fuel cell interconnect coatings: reaction layer microstructure, chemistry and formation mechanisms. Ph.D. thesis work, University of Connecticut, **2013**.

Mahato N., Banerjee A., Gupta A., Omar S. Balani K. Progress in material selection for solid oxide fuel cell technology: A Review. *Prog. Mater. Sci.*, (**2015**), doi:10.1016/j.pmatsci.2015.01.001.

Mandrino Dj., Donik C. Chemical-state information obtained by AES and XPS from thin oxide layers on duplex stainless steel surfaces. *Vacuum* 86 (**2011**) 18-22.

Martínez-Amesti A. Celdas de combustible de óxido de sólido. Estudios de reactividad y optimización de la intercapa cátodo-electrolito. Ph.D. thesis work, UPV/EHU, **2009**.

Martínez-Amesti A., Larrañaga A., Rodríguez-Martínez L.M., Aguayo A.T., Pizarro J.L., Nó M.L., Laresgoiti A., Arriortua M.I. Reactivity between $La(Sr)FeO_3$ cathode, doped CeO_2 interlayer and yttria-stabilized zirconia electrolyte for solid oxide fuel cell applications. *J. Power Sources* 185 (**2008**) 401-410.

Martínez-Amesti A., Larrañaga A., Rodríguez-Martínez L.M., Nó M.L., Pizarro J.L., Laresgoiti A., Arriortua M.I. Chemical compatibility between YSZ and SDC sintered at different atmospheres for SOFC applications. *J. Power Sources* 192(1) (**2009**) 151-157.

Mat A., Timurkutluk B., Timurkutluk C., Kaplan Y. Effects of ceramic based pastes on electrochemical performance of solid oxide fuel cell. *Ceram. Int.* 40 (**2014)** 8575-8583**.**

McCarthy B.P., Pederson L.R., Chou Y.S., Zhou X.D., Surdoval W.A., Wilson L.C. Low-temperature sintering of lanthanum strontium manganite-based contact pastes for SOFCs. *J. Power Sources* 180 (**2008)** 294-300.

Menzler N.H., Sebold D., Wessel E. Interaction of $La_{0.58}Sr_{0.40}Co_{0.20}Fe_{0.80}O_{3-\delta}$ cathode with volatile Cr in a stack test – Scanning electron microscopy and transmission electron microscopy investigations. *J. Power Sources* 254 (**2014**) 148-152.

Miguel-Pérez V. Interconnectores metálicos y capas protectoras para su aplicación en pilas SOFC. Ph.D. thesis work, UPV/EHU, **2013**.

Miguel-Pérez V., Martínez-Amesti A., Nó M.L., Larrañaga A., Arriortua M.I. Oxide scale formation on different metallic interconnects for solid oxide fuel cells. *Corros. Sci.* 60 (**2012**) 38-49.

Miguel-Pérez V., Martínez-Amesti A., Nó M.L., Larrañaga A., Arriortua M.I. The effect of doping $(Mn,B)_3O_4$ materials as protective layers in different metallic interconnects for solid oxide fuel cells. *J. Power Sources* 243 (**2013**) 419-430.

Millar L., Taherparvar H., Filkin N., Slater P., Yeomans J. Interaction of $(La_{1-x}Sr_x)_{1-y}MnO_3$-$Zr_{1-z}Y_zO_{2-\delta}$ cathodes and $LaNi_{0.6}Fe_{0.4}O_3$ current collecting layers for solid oxide fuel cell application. Proceedings of the Conference for the Engineering Doctorate in Environmental Technology, University of Surrey, **2008**.

Ming-Jui T., Chun-Lin C., Shyong L. $La_{0.6}Sr_{0.4}Co_{0.2}Fe_{0.8}O_3$ protective coatings for solid oxide fuel cell interconnect deposited by screen printing. *J. Alloy Compd.* 489 (**2010**) 576-581.

Minh N.Q. Ceramic fuel cells. *J. Am. Ceram. Soc.* 76(3) (**1993**) 563-588.

Minh N.Q. Solid oxide fuel cell technology-features and applications. *Solid State Ionics* 174 (**2004**) 271-277.

Mizusaki J., Tabuchi J., Matsuura T., Yamauchi S., Fueki K. Electrical conductivity and Seebeck Coefficient of nonstoichiometric $La_{1-x}Sr_xCoO_{3-\delta}$. *J. Electrochem. Soc.* 136 (**1989**) 2082-2088.

Mohammadi M., Javadpoura S., Kobayashi A., Shirvani K., Jenabali J.A., Khakpour I. Cyclic oxidation behavior of CoNiCrAlY coatings produced by LVPS and HVOF processes. *Transactions of JWRI* 40 (**2011**) 53-58.

Montero X., Jordán N., Pirón-Abellán J., Tietz F., Stöver D., Cassir M., Villarreal I. Spinel and perovskite protection layers between Crofer22APU and $La_{0.8}Sr_{0.2}FeO_3$ cathode materials for SOFC interconnects. *J. Electrochem. Soc.* 156(1) (**2009**) B188-B196.

Montero X., Tietz F., Sebold D., Buchkremer H.P., Ringuede A., Cassir M., Laresgoiti A., Villarreal I. $MnCo_{1.9}Fe_{0.1}O_4$ spinel protection layer on commercial ferritic steels for interconnect applications in solid oxide fuel cells. *J. Power Sources* 184 (**2008**) 172-179.

Montero X., Tietz F., Stöver D., Cassir M., Villarreal I. Comparative study of perovskites as cathode contact materials between a $La_{0.8}Sr_{0.2}FeO_3$ cathode and a Crofer22APU interconnect in solid oxide fuel cells. *J. Power Sources* 188 (**2009**) 148-155.

Montero X., Tietz F., Stöver D., Cassir M., Villarreal I. Evaluation of commercial alloys as cathode current collector for metal-supported tubular solid oxide fuel cells. *Corros. Sci.* 51(1) (**2009**) 110-118.

Morán-Ruiz A., Vidal K., Laguna-Bercero M.A., Larrañaga A., Arriortua M.I. Effects of using $(La_{0.8}Sr_{0.2})_{0.95}Fe_{0.6}Mn_{0.3}Co_{0.1}O_3$ (LSFMC), $LaNi_{0.6}Fe_{0.4}O_{3-\delta}$ (LNF) and $LaNi_{0.6}Co_{0.4}O_{3-\delta}$ (LNC) as contact material on solid oxide fuel cells. *J. Power Sources* 248 (**2014**) 1067-1076.

Morán-Ruiz A., Vidal K., Larrañaga A., Arriortua M.I. Chemical compatibility and electrical contact of $LaNi_{0.6}Co_{0.4}O_{3-\delta}$ (LNC) between Crofer22APU interconnect and $La_{0.6}Sr_{0.4}FeO_3$ (LSF) cathode for IT-SOFC. *Fuel Cells* 13(3) (**2013**) 398-403.

Morán-Ruiz A., Vidal K., Larrañaga A., Laguna-Bercero M.A., Porras-Vázquez J.M., Slater P.R., Arriortua M.I. $LaNi_{0.6}Co_{0.4}O_{3-\delta}$ dip-coated on Fe-Cr mesh as a composite cathode contact material on intermediate solid oxide fuel cells. *J. Power Sources* 269 (**2014**) 509-519.

Morán-Ruiz A., Vidal K., Larrañaga A., Porras-Vázquez J.M., Slater P.R., Arriortua M.I. Evaluation of using protective/conductive coating on Fe-22Cr mesh as a composite cathode contact material for intermediate solid oxide fuel cells. *Int. J. Hydrogen Energ.* 40 (**2015**) 4804-4818.

Moruzzi V.L., Shafer M.W. Phase equilibria in the system La_2O_3-iron oxide in air. *J. Am. Ceram. Soc.* 43 (**1960**) 367-372.

Nagde K.R., Bhoga S.S. Effect of Sr content on structure and electrical properties of $La_{1-x}Sr_xMnO_3$ from ITSOFC cathode view point. *Ionics* 15 (**2009**) 571-578.

Nakamura T., Petzow G., Gauckler L.J. Stability of the perovskite phase $LaBO_3$ (B=V, Cr, Mn, Fe, Co, Ni) in reducing atmosphere I. Experimental results. *Mater. Res. Bull.* 14 (**1979**) 649-659.

National institute of standards and technology gaithersburg: Inorganic crystal structure database ICSD realease **2001**/1. Fachinformationszentrum Karlsruhe.

Nejat P., Jomehzadeh F., Taheri M.M., Gohari M., Majid M.Z. Abd. A global review of energy consumption, CO_2 emissions and policy in the residential sector (with an overview of the top ten CO_2 emitting countries). *Renew. Sust. Energ. Rev.* 43 (**2015**) 843-862.

Nesbitt H.W., Banerjee D. Interpretation of XPS Mn(2p) spectra of Mn oxyhydroxides and constraints on the mechanism of MnO_2 precipitation. *Am. Mineral* 83 (**1998**) 305-315.

Orera A., Slater P.R. New chemical systems for solid oxide fuel cells. *Chem. Mater.* 22 (**2010**) 675-690.

Otaegui-Ameztegui L. Desarrollo de celdas de combustible de tipo SOFC tubulares de soporte metálico. Ph.D. thesis work, Universidad de Navarra, **2013**.

Ou D.R., Cheng M. Effect of pre-oxidation on the oxidation resistance of spinel-coated Fe–Cr ferritic alloy for solid oxide fuel cell applications. *J. Power Sources* 247 (**2014**) 84-89.

Palcut M., Mikkelsen L., Neufeld K., Chen M., Knibbe R., Hendriksen P.V. Corrosion stability of ferritic stainless steels for solid oxide electrolyser cell interconnects. *Corros. Sci.* 52 (**2010)** 3309-3320.

PANalytical, Almelo B.V., Versión 1.0e, The Netherlands, **2003**.

Park E., Taniguchi S., Daio T., Chou J.-T., Sasaki K. Influence of cathode polarization on the chromium deposition near the cathode/electrolyte interface of SOFC. *Int. J. Hydrogen Energ.* 39 (**2014**) 1463-1475.

Perry M.L., Fuller T.F. A Historical perspective of fuel cell technology in the 20th Century. *J. Electrochem. Soc.* 149(7) (**2002**) S59-S67.

Petrov A.N, Cherepanov V.A., Zuev A.Y. Thermodynamics, defect structure, and charge transfer in doped lanthanum cobaltites: an overview. *J. Solid State Electrochem.* 10 (**2006**) 517-537.

Piccardo P., Gannon P., Chevalier S., Viviani M., Burbucci A., Caboche G., Amendola R., Fontana S. ASR evaluation of different kinds of coatings on a ferritic stainless steel as SOFC interconnect. *Surf. Coat. Tech.* 202 (**2007**) 1221-1225.

Przybylski K., Brylewski T., Durda E., Gawel R., Kruk A. Oxidation properties of the Crofer 22 APU steel coated with $La_{0.6}Sr_{0.4}Co_{0.2}Fe_{0.8}O_3$ for IT-SOFC interconnect applications. *J. Therm. Anal. Calorim.* 116 (**2014**) 825-834.

Puranen J., Pihlatie M., Lagerbom J., Bolelli G., Laakso J., Hyvärinen L., Kylmälahti M., Himanen O., Kiviaho J., Lusvarghi L., Vuoristo P. Post-mortem evaluation of oxidized atmospheric plasma sprayed Mn-Co-Fe oxide spinel coatings on SOFC interconnects. *Int. J. Hydrogen Energ.* 39(30) (**2014**) 17284-17294.

Pyo S.S., Lee S.B., Lim T.H., Song R.H., Shin D.R., Hyun S.H., Yoo Y.S. Characteristic of $(La_{0.8}Sr_{0.2})_{0.98}MnO_3$ coating on Crofer22APU used as metallic interconnects for solid oxide fuel cells. *Int. J. Hydrogen Energ.* 36 (**2011**) 1868-1881.

Qiu L., Hirano A., Imanishi N., Takeda Y. $Ln_{1-x}Sr_xCo_{1-y}Fe_yO_{3-\delta}$ (Ln=Pr, Nd, Gd; x=0.2, 0.3) for the electrodes of solid oxide fuel cells. *Solid State Ionics* 158 (**2003**) 55-65.

Ralph J.M., Kilner J.A., Steele B.C.H. Improving Gd-doped ceria electrolytes for low temperature solid oxide fuel cells. *Mater. Res. Soc. Symp. Proc*. 575 (**2001)** 309-314.

Ramana C.V., Massot M., Julien C.M. XPS and Raman spectroscopic characterization of $LiMn_2O_4$ spinels. *Surf. Interface Anal.* 37 (**2005**) 412-416.

Ramos V., Carballo R., Álvarez M., Sánchez M., Iglesias G. A port towards energy self-sufficiency using tidal stream power. *Energy* 71 (**2014**) 432–444.

Rietveld H.M. A profile refinement method for nuclear and magnetic structures. *J. Appl. Cryst.* 2 (**1969**) 65-71.

Rietveld H.M. Line profiles of neutron powder-diffraction peaks for structure refinement. *Acta Cryst.* 22 (**1967**) 151-152.

Robards A.W., Wilson A.J. Procedures in electron microscopy, John Wiley & Sons, Chichester, UK, **1993**.

Rodríguez-Carvajal J. Fullprof program: Rietveld pattern matching analysis of powder patterns, Grenoble, **2011**.

Rodríguez-Carvajal J. Recent advances in magnetic structure determination by neutron powder diffraction. *Physica B* 192 (**1993)** 55-69.

Ruiz-Morales J.C., Canales-Vázquez J., Marrero-López D., Peña-Martínez J., Pérez-Coll D., Núñez P., Savaniu C., Rodríguez-Placeres C., Dorta-Martín V.I., Ballesteros B. Pilas de combustible de óxido sólido (SOFC). Centro de la cultura popular canaria, (**2008**) 127-141.

Sabioni A.C.S., Huntz A.M., Borges L.C., Jomard F. First study of manganese diffusion in Cr_2O_3, polycrystals and thin films, by SIMS. *Phil. Mag. Lett.* 87(12) (**2007**) 1921-1937.

Schroder D.K. Semiconductor material and device characterization, John Wiley & Sons, New York, p. 149-156, **1998**.

Schuler J.A., Wuillemin Z., Hessler-Wyser A., Comminges C., Steiner N.Y., Van Herle J.. Cr-poisoning in (Ls,Sr)(Co,Fe)O_3 cathodes after 10.000 h SOFC stack testing. *J. Power Sources* 211 (**2012**) 177-183.

Seabaugh M.M., Day M., Beachy M., McCormick B.E., Ibanez S. Materials development for SOFC applications. *ECS Trans.* 25(2) (**2009**) 619-628.

Shaigan N., Ivey D.G., Chen W. Co/$LaCrO_3$ composite coatings for AISI 430 stainless steel solid oxide fuel cell interconnects. *J. Power Sources* 185 (**2008)** 331-337.

Shaigan N., Qu W., Douglas G.I., Chen W. A review of recent progress in coatings, surface modifications and alloy developments for solid oxide fuel cell ferritic stainless steel interconnects. *J. Power Sources* 195 (**2010**) 1529-1542.

Sharaf O.Z., Orhan M.F. An overview of fuel cell technology: Fundamentals and applications. *Renew. Sust. Energ. Rev.* 32 (**2014**) 810-853.

Sharma V.I., Yildiz B. Degradation mechanism in $La_{0.8}Sr_{0.2}CoO_3$ as contact layer on the solid oxide electrolysis cell anode. *J. Electrochem. Soc.* 157(3) (**2010**) B441-B448.

Shishkin M., Ziegler T. Direct modeling of the electrochemistry in the three-phase boundary of solid oxide fuel cell anodes by density functional theory: a critical overview. *Phys. Chem. Chem. Phys.* 16 (**2014**) 1798-1808.

Shong W.J., Liu C.K., Chen C.Y., Peng C.C., Tu H.J., Fey G.T.K., Lee R.Y., Kao H.M., Effects of lanthanum-based perovskite coatings on the formation of oxide scale for ferritic SOFC interconnect. *Mater. Chem. Phys.* 127 (**2011**) 45-50.

Singh P., Minh N.Q. Solid oxide fuel cells: technology status. *Int. J. Appl. Ceram. Technol.* 1(1) (**2004**) 5-15.

Singh R.N. Sealing technology for solid oxide fuel cells (SOFC). *Int. J. Appl. Ceram. Technol.* 4(2) (**2007**) 134-144.

Singh S., Kennedy C. Estimating future energy use and CO_2 emissions of the world´s cities. *Environ. Pollut*. (**2015**), http://dx.doi.org/10.1016/j.envpol.2015.03.039.

Singhal S.C. Advances in solid oxide fuel cell technology. *Solid State Ionics* 135 (**2000**) 305-313.

Singhal S.C., Kendall K. Introduction to SOFCs, in High temperature solid oxide fuel cells fundamentals, design and applications (eds. Singhal S.C., Kendall K.), Elsevier, Oxford, UK, p. 1-19, **2003**.

Skinner S.J. Recent advances in perovskite-type materials for solid oxide fuel cell cathodes. *Int. J. Inorg. Mater.* 3 (**2001**) 113-121.

Skinner S.J., Laguna-Bercero M.A. Advanced Inorganic Materials for Solid Oxide Fuel Cells, in Energy Materials (eds. D. W. Bruce, D. O'Hare and R. I. Walton), John Wiley & Sons, Ltd, Chichester, UK. doi:10.1002/9780470977798.ch2. **2011**.

Sogaard M., Hendriksen P.V., Mogensen M. Oxygen nonstoichiometry and transport properties of strontium substituted lanthanum ferrite. *J. Solid State Chem.* 180 (**2007**) 1489-1503.

Soimakallio S., Saikku L. CO_2 emissions attributed to annual average electricity consumption in OECD (the Organisation for Economic Co-operation and Development) countries. *Energy* 38(1) (**2012)** 13-20.

Specchia S. Fuel processing activities at European level: A panoramic overview. *Int. J. Hydrogen Energ.* 39 (**2014**) 17953-17968.

Spivey B.J., Edgar T.F. Dynamic modeling, simulation, and MIMO predictive control of a tubular solid oxide fuel cell. *J. Process Contr.* 22 (**2012**) 1502-1520.

Srirangan K., Akawi L., Moo-Young M., Chou C.P. Towards sustainable production of clean energy carriers from biomass resources. *Appl. Energ.* 100 (**2012**) 172–186.

Stambouli A.B. Fuel cells: The expectations for an environmental-friendly and sustainable source of energy. *Renew. Sust. Energ. Rev.* 15(9) (**2011**) 4507–4520.

Stodolny M.K. Cr-tolerance of the IT-SOFC La(Ni,Fe)O_3 material. Ph. D. thesis work, University of Twente, **2012**.

Stodolny M.K., Boukamp B.A., Blank D.H.A., Berkel F.P.F.V. Cr-poisoning of $LaNi_{0.6}Fe_{0.4}O_3$ cathode under current load. *J. Power Sources* 209 (**2012**) 120-129.

Stodolny M.K., Boukamp B.A., Blank D.H.A., Berkel F.P.F.V. Impact of Cr-poisoning on the conductivity of $LaNi_{0.6}Fe_{0.4}O_3$. *J. Power Sources* 196 (**2011**) 9290-9298.

Stodolny M.K., Boukamp B.A., Blank D.H.A., Berkel F.P.F.V. La(Ni,Fe)O_3 stability in the presence of chromia-A solid-state reactivity study. *J. Electrochem. Soc.* 158(2) (**2011**) B112-B116.

Stojanovic M., Haverkamp R.G., Mims C.A., Moudallal H., Jacobson A.J. Synthesis and characterization of $LaCr_{1-x}Ni_xO_3$ perovskite oxide catalysts. *J. Catal.* 165 (**1997**) 315-323.

Stöver D., Buchkremer H.P., Huijsmans J.P.P. MEA/cell preparation methods: Europe/USA, in Handbook of Fuel Cells- Fundamentals, Technology and Applications (eds. Vielstich W., Lamm A., Gasteiger H. A.), Ed. John Wiley & Sons, New Jersey, USA, p. 1015-1032, **2003**.

Sukpirom N., Iamsaard S., Charojrochkul S., Yeyongchaiwat J. Synthesis and properties of $LaNi_{1-x}Fe_xO_{3-\delta}$ as cathode materials in SOFC. *J. Mater. Sci.* 46 (**2011)** 6500-6507.

Sun C., Hui R., Roller J. Cathode materials for solid oxide fuel cells: a review. *J. Solid State Electrochem.* 14 (**2010**) 1125-1144.

Sung-Il L., Jongsup H., Hyoungchul K., Ji-Won S., Jong-Ho L., Byung-Kook K., Hae-Weon L., Kyung-Joong Y. Highly dense Mn-Co spinel coating for protection of metallic interconnect of solid oxide fuel cells. *J. Electrochem. Soc.* 161(14) (**2014**) F1389-F1394.

Szabo P., Ansar A., Franco T., Gindrat M., Kiefer T. Stack tests of metal-supported plasma-sprayed SOFC, 10th European SOFC Forum, Lucerne, *European Fuel Cell Forum Proceedings*, **2012**.

Tabata K., Matsumoto I., Kohiki S. Surface characterization and catalytic properties of $La_{1-x}Sr_xCoO_3$. *J. Mater. Sci.* 22 (**1987**) 1882-1886.

Taguchi H., Komatsu T., Chiba R., Nozawa K., Orui H., Arai H. Characterization of $LaNi_xCo_yFe_{1-x-y}O_3$ as a cathode material for solid oxide fuel cells. *Solid State Ionics* 182 (**2011)** 127-132.

Tao Y. Nishino H., Ashidate S., Kokubo H., Watanabe M., Uchida H. Polarization properties of $La_{0.6}Sr_{0.4}Co_{0.2}Fe_{0.8}O_3$-based double layer-type oxygen electrodes for reversible SOFCs. *Electrochim. Acta* 54 (**2009**) 3309-3315.

Tavner P. Wind power as a clean-energy contributor. *Energ. Policy* 36(12) (**2008**) 4397–4400.

Tietz F., Raj I-A., Zahid M., Stöver D. Electrical conductivity and thermal expansion of $La_{0.8}Sr_{0.2}(Mn,Fe,Co)O_{3-\delta}$ perovskites. *Solid State Ionics* 177 (**2006)** 1753-1756.

Tietz F., Sebold D. Interface reactions between electrically conductive ceramics and ferritic steel-I. The system Cr-22Fe-0.5Mn/Mn_2O_3/(La,Ca)(Cr,Co,Cu)O_3. *Mater. Sci. Eng. B* 150 (**2008**) 135-140.

Tong T., Li J., Longtin J.P. Real-time control of ultrafast laser micromachining by laser-induced breakdown spectroscopy. *Appl. Opt.* 43 (**2004**) 1971-1980.

Torabi A., Etsell T.H., Sarkar P. Dip coating fabrication process for micro-tubular SOFCs. *Solid State Ionics* 192 (**2011)** 372-375.

Tsalikis G., Martinopoulos G. Solar energy systems potential for nearly net zero energy residential buildings. *Sol. Energy* 115 (**2015**) 743–756.

Tucker M.C., Cheng L., DeJonghe L.C. Glass-containing composite cathode contact materials for solid oxide fuel cells. *J. Power Sources* 196 (**2011)** 8435-8443.

Tucker M.C., Cheng L., DeJonghe L.C. Inorganic binder-containing composite cathode contact materials for solid oxide fuel cells. *J. Power Sources* 224 (**2013**) 174-179.

Tucker M.C., Cheng L., DeJonghe L.C. Selection of cathode contact materials for solid oxide fuel cells. *J. Power Sources* 196 (**2011**) 8313-8322.

Türkoglu A.K., Ersoy T., Canbaz F., Akturk S. Effects of waveguide behavior during femtosecond-laser drilling of metals. *Appl. Phys. A* 108 (**2012**) 935-941.

Uehara T., Yasuda N., Okamoto M., Baba Y. Effect of Mn-Co spinel coating for Fe-Cr ferritic alloys ZMG232L and 232J3 for solid oxide fuel cell interconnects on oxidation behavior and Cr-evaporation. *J. Power Sources* 196(17) (**2011**) 7251-7256.

Ullmann H., Trofimenko N. Composition, structure and transport properties of perovskite-type oxides. *Solid State Ionics* 119 (**1999**) 1-8.

Ullmann H., Trofimenko N., Tietz F., Stöver D., Ahmad-khanlou A. Correlation between thermal expansion and oxide ion transport in mixed conducting perovskite-type oxides for SOFC cathodes. *Solid State Ionics* 138 (**2000)** 79-90.

Vidal K. Perovskitas $AFeO_3$ para cátodos SOFC. Efecto de los parámetros que controlan la posición A en sus propiedades. Ph. D. thesis work, UPV/EHU, **2008**.

Vidal K., Morán-Ruiz A., Larrañaga A., Porras-Vázquez J.M., Slater P.R., Arriortua M.I. Characterization of $LaNi_{0.6}Fe_{0.4}O_3$ perovskite synthesized by glycine-nitrate combustion method. *Solid State Ionics* 269 (**2015**) 24-29.

Vidal K., Rodríguez-Martínez L.M., Ortega-San Martín L., Martínez-Amesti A., Nó M. L., Rojo T., Laresgoiti A., Arriortua M.I. The effect of doping in the electrochemical performance of $(Ln_{1-x}M_x)FeO_{3-\delta}$ SOFC cathodes. *J. Power Sources* 192 (**2009**) 175-179.

Vidal K., Rodríguez-Martínez L.M., Ortega-San-Martín L., Nó M.L., Rojo T., Arriortua M.I. Effect of the A cation size disorder on the properties of an iron perovskite series for their use as cathode for SOFCs. *Fuel Cells* 11 (**2011)** 51-58.

Vilasi M., Francois M., Brequel H., Podor R., Venturini G., Steinmetz J. Phase equilibria in the Nb-Fe-Cr-Si system. *J. Alloy Compd.* 269 (**1998**) 187-192.

Vogt U.F., Holtappels P., Sfeir J., Richter J., Duval S., Wiedenmann D., Züttel A. Influence of A-site variation and B-site substitution on the physical properties of (La, Sr)FeO_3 based perovskites. *Fuel Cells* 6 (**2009**) 899-906.

Wagner C. Theoretical Analysis of the Diffusion Processes Determining the Oxidation Rate of Alloys. *J. Electrochem. Soc.* 99 (**1952**) 369-380.

Wagner C.D., Riggs W.M., Davis L.E., Moulder J.F., Mullenberg G.E., Handbook of X-ray Photoelectron Spectroscopy, Perkin-Elemer Corporation, Physical Electronics Division, Eden Prairie, MN 55344, **1979**.

Wang C.C., Becker T., Chen K., Zhao L., Wei B., Jiang S.P. Effect of temperature on the chromium deposition and poisoning of $La_{0.6}Sr_{0.4}Co_{0.2}Fe_{0.8}O_{3-\delta}$ cathodes of solid oxide fuel cells. *Electrochim. Acta* 139 (**2014**) 173-179.

Wang F., Yan D., Zhang W., Chi B., Pu J., Jian L. $LaCo_{0.6}Ni_{0.4}O_{3-\delta}$ as cathode contact material for intermediate temperature solid oxide fuel cells. *Int. J. Hydrogen Energ.* 38 (**2013**) 646-651.

Wang G., Guan W., Miao F., Wang W.G. Factors of cathode current-collecting layer affecting cell performance inside solid oxide fuel cells stacks. *Int. J. Hydrogen Energ.* 39 (**2014**) 17836-17844.

Wang K., Liu Y., Fergus J.W. Interaction between SOFC interconnect coating materials and chromia. *J. Am. Ceram. Soc.* 94(12) (**2011**) 4490-4495.

Wei W., Chen W., Ivey D.G. Oxidation resistance and electrical properties of anodically electrodeposited Mn-Co oxide coatings for solid oxide fuel cell interconnect applications. *J. Power Sources* 186 (**2009**) 428-434.

Wei Z.X., Xiao C.M., Zeng W.W., Liu J.P. Magnetic properties and photocatalytic activity of $La_{0.8}Ba_{0.2}Fe_{0.9}Mn_{0.1}O_{3-\delta}$ and $LaFe_{0.9}Mn_{0.1}O_{3-\delta}$. *J. Mol. Catal. A-Chem.* 370 (**2013**) 35-43.

Wilkinson L.T., Zhu J.H. Ag-Perovskite composite materials for SOFC cathode-interconnect contact. *J. Electrochem. Soc.* 156(8) (**2009)** B905-B912.

Wincewicz K.C., Cooper J.S. Taxonomies of SOFC materials and manufacturing alternatives. *J. Power Sources* 140 (**2005**) 280-296.

Wu J., Liu X. Recent development of SOFC metallic interconnect. *J. Mater. Sci. Technol.* 26(4) (**2010)** 293-305.

Wu W., Guan W., Wang G., Liu W., Zhang Q., Chen T., Wang W.G. Evaluation of $Ni_{80}Cr_{20}/(La_{0.75}Sr_{0.25})_{0.95}MnO_3$ dual layer coating on SUS 430 stainless steel used as metallic interconnect for solid oxide fuel cells. *Int. J. Hydrogen Energ.* 39 (**2014**) 996-1004.

Wu W., Wang G.L., Guan W.B., Zhen Y.F., Wang W.G. Effect of contact method between interconnects and electrodes on area specific resistance in planar solid oxide fuel cells. *Fuel Cells* 5 (**2013**) 743-750.

Yamamoto O. Low temperature electrolytes and catalysts, in Handbook of Fuel Cells-Fundamentals, Technology and Applications (eds. Vielstich W., Lamm A, Gasteiger H.A.), John Wiley & Sons, New Jersey, USA, p. 1002-1014, **2003**.

Yang J.L., Yu J.L., Cui Y.Y., Huang Y. New laser machining technology of Al_2O_3 ceramic with complex shape. *Ceram. Int.* 38 (**2012**) 3643-3648.

Yang P., Liu C.K., Wu J.Y., Shong W.J., Lee R.Y., Sung C.C. Effects of pre-oxidation on the microstructural and electrical properties of $La_{0.67}Sr_{0.33}MnO_{3-\delta}$ coated ferritic stainless steels. *J. Power Sources* 213 (**2012**) 63-68.

Yang Z., Guan-Guang X., Maupin G.D., Stevenson J.W. Conductive protection layers on oxidation resistant alloys for SOFC interconnect applications. *Surf. Coat. Tech.* 201(7) (**2006**) 4476–4483.

Yang Z., Xia G., Nie Z., Templeton J.D., Stevenson J.W. Ce-modified $(Mn,Co)_3O_4$ spinel coatings on ferritic stainless steels for SOFC interconnect applications. *Electrochem. Solid St.* 11(8) (**2008**) B140-B143.

Yang Z., Xia G., Singh P., Stevenson J.W. Electrical contacts between cathodes and metallic interconnects in solid oxide fuel cells. *J. Power Sources* 155 (**2006**) 246-252.

Yang Z., Xia G.G., Maupin G.D., Stevenson J.W. Evaluation of perovskite overlay coatings on ferritic steels for SOFC interconnect applications. *J. Electrochem. Soc.* 153 (**2006**) A1852-A1858.

Yokokawa H., Horita T., Sakai N., Yamaji K., Brito M.E., Xiong Y.P., Kishimoto H. Thermodynamic considerations on Cr poisoning in SOFC cathodes. *Solid State Ionics* 117(35-36) (**2006**) 3193-3198.

Yokokawa H., Sakai N., Horita T., Yamaji K. Recent developments in solid oxide fuel cell materials. *Fuel Cells* 1(2) (**2001**) 117-131.

Yokokawa H., Tu H., Iwanschitz B., Mai A. Fundamental mechanisms limiting solid oxide fuel cell durability. *J. Power Sources* 182 (**2008**) 400-412.

Yoon C. Computational design, fabrication, and characterization of microarchitectured solid oxide fuel cells with improved energy efficiency. Ph. D. thesis work, Georgia Institute of Technology, **2010**.

Young R.A., *"The Rietveld method"*. International Union of Crystallography-Oxford Science Publications: Oxford (**1995**).

Yousfi-Steiner N., Hissel D., Moçotéguy P., Candusso D., Marra D., Pianese C. Sorrentino M. Application of fault tree analysis to fuel cell diagnosis. *Fuel Cells* 12(2) (**2012**) 302-309.

Zhang H., Wu J., Liu X., Baker A. Studies on elements diffusion of Mn/Co coated ferritic stainless steel for solid oxide fuel cell interconnects application. *Int. J. Hydrogen Energ.* 38 (**2013**) 5075-5083.

Zhang H.H., Zeng C.L. Preparation and performances of Co-Mn spinel coating on a ferritic stainless steel interconnect material for solid oxide fuel cell application. *J. Power Sources* 252 (**2014**) 122-129.

Zhang N., Zhao Y., Zhu X. Light propulsion of microbeads with femtosecond laser pulses. *Opt. Express* 12 (**2004**) 3590-3598.

Zhang W., Pu J., Chi B., Jian L. $NiMn_2O_4$ spinel as an alternative coating material for metallic interconnects of intermediate temperature solid oxide fuel cells. *J. Power Sources* 196 (**2011**) 5591-5594.

Zhang W., Wang F., Wang K., Pu J., Chi B., Jian L. Chemical compatibility and electrical contact between Ni–Cr–Mo alloy and $LaCo_{0.6}Ni_{0.4}O_{3-\delta}$ in intermediate temperature solid oxide fuel cells. *Int. J. Hydrogen Energ.* 37 (**2012**) 17253-17257.

Zhao Y. Oxidation behavior of ferritic alloys as interconnect of solid oxide fuel cell (SOFC). Ph. D. thesis work, Auburn University, **2012**.

Zhen Y.D., Tok A.I.Y., Boey F.Y.C., Jiang S.P. Development of Cr-tolerant cathodes of solid oxide fuel cells. *Electrochem. Solid-State Lett.* 11 (**2008**) B42-B46.

Zhen Y.D., Tok A.I.Y., Jiang S.P., Boey F.Y.C. La(Ni, Fe)O_3 as a cathode material with high tolerance to chromium poisoning for solid oxide fuel cells. *J. Power Sources* 170 (**2007**) 61-66.

Zhou Q., Xu L., Guo Y., Jia D., Li Y., Wei W.C.J. $La_{0.6}Sr_{0.4}Fe_{0.8}Cu_{0.2}O_{3-\delta}$ perovskite oxide as cathode for IT-SOFC. *Int. J. Hydrogen Energ.* 37(16) (**2012**) 11963-11968.

Zhu W.Z., Deevi S.C. Development of interconnect materials for solid oxide fuel cells. *Mat. Sci. Eng. A-Struct.* 348 (**2003**) 227-243.

7. ANEXO. TÉCNICAS EXPERIMENTALES

- **Técnicas de procesado**
- **Técnicas instrumentales**

7.1. Técnicas de procesado

7.1.1. Dip coating

La deposición de las capas de contacto sobre la malla metálica se ha realizado mediante la técnica de dip coating o inmersión (Figura 7.1), obteniéndose el recubrimiento completo del substrato. Este proceso se ha realizado en los laboratorios del Instituto de Ciencia de Materiales de Aragón (ICMA) de la Universidad de Zaragoza. El substrato sobre el que se desea depositar la capa, se ha sumergido a velocidad controlada en una suspensión que la contiene. El substrato se ha mantenido sumergido durante un determinado tiempo y, a continuación, se ha extraído a velocidad también controlada. Debido a la tensión superficial que han presentado los fluidos newtonianos, al introducirse el substrato en la suspensión cerámica, cuando éste se ha desalojado de la misma, ha arrastrado una parte del líquido. Este fenómeno se debe a que las moléculas de la superficie tienen un mayor nivel de energía que las interiores por lo que el fluido tratará de disminuir su superficie externa para reducir así sus niveles de energía. El espesor de la capa arrastrada va a depender de la velocidad de desalojo y de la viscosidad de la suspensión. Así, se han obtenido espesores más gruesos para tiempos de inmersión y velocidades de extracción más altos. Por otra parte, la obtención de espesores más elevados puede realizarse, también, aumentando la carga de sólidos de la suspensión.

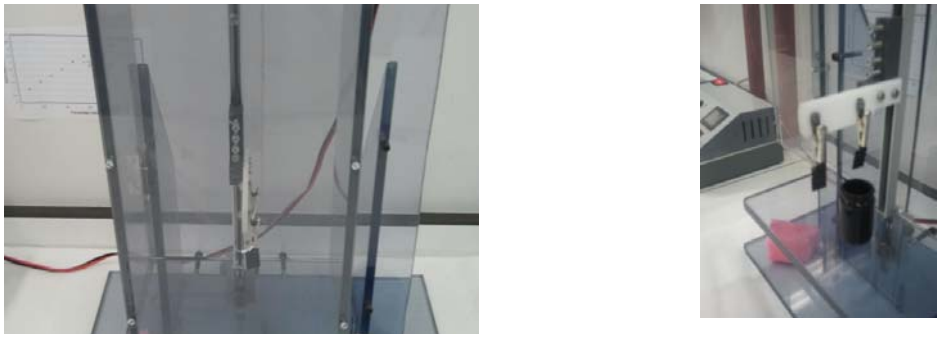

Figura 7.1. Imágenes tomadas durante el proceso de dip coating.

En esta investigación, la suspensión está compuesta por polvo cerámico (LNC, LNF, LSFMC), un agente dispersante (Beycostat, BY) que evita que las partículas del polvo cerámico se acumulen, un agente aglomerante (Polivinil butiral, PVB), cuya función es otorgar una mayor viscosidad a la mezcla, y un compuesto disolvente (Etanol, EtOH). En la Tabla 7.1 se resume el procedimiento de preparación de la pasta o suspensión.

Tabla 7.1. Procedimiento de preparación de la pasta.

Paso	*Proceso*
1	Se mezcla el dispersante (BY) con el elemento disolvente (EtOH) y se ágita con el fin de que la mezcla se homogenice.
2	Se añade el polvo cerámico a la disolución (disolvente + dispersante) y se deja el conjunto en agitación durante 30 min.
3	Se aplica ultrasonidos a la mezcla durante un minuto. Se utiliza un cristalizador con hielo para evitar el sobrecalentamiento de la muestra.
4	Se añade el agente aglomerante (PVB), y se finaliza la preparación después de quince minutos de agitación.

7.1.1.1. Suspensión para dip coating: cálculos

La suspensión para dip coating está compuesta por un 12.5 % de sólidos y un 87.5 % de disolvente en volumen.

$$V_{suspensión} = 15\ ml \begin{cases} V_{sólido} = 1.875\ ml \\ V_{disolvente} = 13.125\ ml \end{cases}$$

$$m_{sólido} = \rho_{sólido} \cdot 1.875\ ml$$
$$m_{disolvente} = \rho_{EtOH} \cdot 13.125\ ml$$

El dispersante (BY) y el agente aglomerante (PVB) se añaden con respecto a la cantidad de sólido introducido, siendo un 1 % y 5 %, respectivamente.

$$m_{BY} = 0.01 \cdot m_{sólido}$$
$$m_{PVB} = 0.05 \cdot m_{sólido}$$

Teniendo en cuenta que el aglomerante se encuentra disuelto en el disolvente a una concentración de $[PVB]_{dis.}$, la masa que hay que añadir de esta disolución es:

$$m_{PVB\ disolución} = m_{PVB} / [PVB]_{dis.}$$

Por lo tanto, la cantidad real de disolvente que hay que añadir es:

$$m_{\ EtOH} = (\rho_{EtOH} \cdot 13.125\ ml) - (m_{\ PVB\ dis.} - m_{PVB})$$

7.1.2. Spray manual coloidal

El cátodo (LSF) y las capas de contacto (LNF, LNC, LSFMC) se han depositado sobre un substrato plano mediante spray manual coloidal, utilizando como pistola de pulverización un aerógrafo (Figura 7.2). La deposición de capas mediante esprayado de líquidos es una técnica versátil que permite el recubrimiento de superficies tubulares y planas. La calidad del espesor de la capa depositada dependerá de la reología de la suspensión, de la adherencia de ésta al componente a recubrir, y de la combinación de los siguientes factores: (i) presión del aire del aerógrafo, (ii) distancia de pulverización, (iii) fijación del substrato, y (iv) ángulo de pulverización.

Figura 7.2. Imagen tomada durante el proceso de spray coating.

La mezcla de los componentes utilizados en la preparación de las suspensiones para su deposición por spray manual coloidal se ha realizado mediante un molino de bolas Labmill-8000 (Figura 7.3). El ball-milling es un método preparativo a través del cual se obtiene la dispersión y la mezcla de materiales mediante la acción de un medio de molienda que, habitualmente, son esferas o cilindros de alúmina o zirconia. En este trabajo, para la preparación de la suspensión se ha mezclado el material cerámico en polvo (LNF, LNC, LSFMC, LSF) con etanol como disolvente, y se ha añadido dolapix ET 85 como dispersante. Una adecuada homogeneización se ha logrado mediante el molino de bolas, utilizando como medio de dispersión cilindros de ZrO_2 de 95 mm de diámetro, sometiéndose el conjunto a una velocidad de 125 r.p.m. durante 1 h.

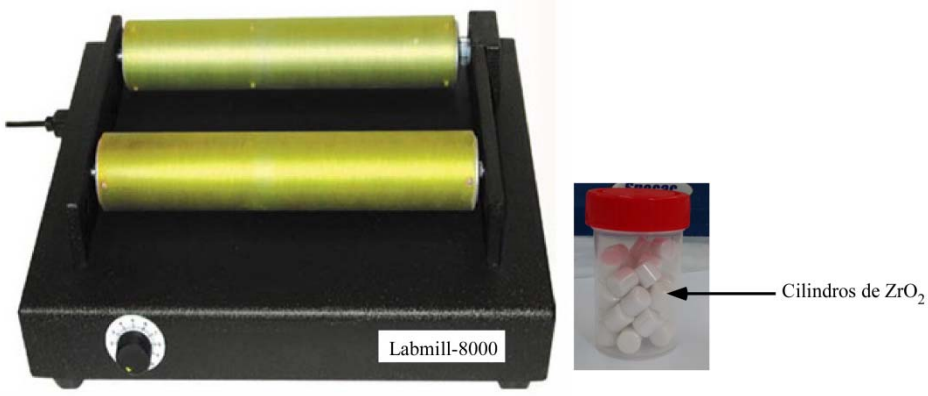

Figura 7.3. Imagen del molino de bolas Labmill-8000.

7.1.3. Sinterizado

Es habitual que los materiales cerámicos sean sinterizados para producir una microestructura con las propiedades requeridas[1]. La sinterización es un proceso de transporte de materia, activado por la temperatura, en una masa de polvos o en un compuesto poroso, en el que disminuye la superficie especifica por el crecimiento de contacto entre partículas, contrayéndose el volumen de porosidad, y cambiando la geometría de los poros. Este contacto entre partículas puede reforzarse mediante la aplicación de presión durante el proceso. También se define como el tratamiento térmico de un polvo o compacto a temperatura inferior a la de fusión del principal constituyente, con el propósito de aumentar su resistencia a través de la unión de las partículas. Se distinguen tres etapas durante el proceso de sinterizado y éstas se resumen en la Tabla 7.2.

Tabla 7.2. Resumen de las principales etapas en el proceso de sinterizado.

Etapa	*Proceso*	*Pérdida de área superficial*	*Densificación*
Inicial	Crecimiento de cuellos de enlace.	Significativa, hasta 50 %.	Poco al inicio.
Intermedia	Densificación y crecimiento de grano. Redondeo de poros.	Próxima a la pérdida total de la porosidad abierta.	Significativa.
Final	Fase final con espacio de poros cerrado.	Insignificante.	Lenta.

A nivel microscópico, la sinterización ocurre mediante la formación de cuellos entre partículas adyacentes, para lo cual son necesarios procesos de transferencia de masa que sustituyan las superficies de contacto sólido/vapor por nuevas superficies de contacto sólido/sólido. La reducción de la entalpía libre del sistema proporciona la fuerza motriz del proceso de sinterización y se debe a: (i) la disminución del área específica debido a la iniciación y/o crecimiento de los contactos, (ii) la reducción del volumen de poros y de su superficie, y (iii) la eliminación de los estados de no equilibrio de la red.

Sin embargo, para lograr el proceso dentro de un tiempo razonable, también se debe considerar la cinética del transporte de materia. Así, la movilidad de las partículas aumenta a altas temperaturas debido al incremento de átomos activos y vacantes disponibles. Los mecanismos de sinterizado describen la trayectoria del flujo de materia. Para la mayoría de los polvos inorgánicos, el mecanismo dominante es la difusión; difusión a través de la superficie, a través de los bordes de grano o a través de la red cristalina.

Los hornos que se han utilizado en los tratamientos de sinterizado de las muestras, están ubicados en el laboratorio de Mineralogía y Petrología de la Facultad de Ciencia y Tecnología de la UPV/EHU (Figura 7.4).

[1] http://www6.uniovi.es/usr/fblanco/Tema6.MaterialesCERAMICOS.SinterizacionEstadoSolido.pdf.

Figura 7.4. Horno de sinterizado Carbolite RWF 1200 utilizado en los tratamientos de sinterizado de las muestras.

7.2. Técnicas instrumentales

7.2.1. Análisis granulométrico

El conocimiento del tamaño de las partículas que constituyen un material tiene relación directa con sus propiedades. Los analizadores de distribución de tamaño de partícula están basados en el fenómeno de la dispersión láser. El principio físico de un analizador de difracción láser se basa en que las partículas dispersan la luz en todas las direcciones, con un patrón de intensidad que es dependiente del tamaño de la partícula. Al hacer pasar un haz láser monocromático a través de una muestra en suspensión, la luz se dispersa y se produce una figura de dispersión de simetría radial en el plano focal de la lente.

La intensidad luminosa de los anillos dispersados es directamente proporcional al número de partículas, y los radios de los anillos son inversamente proporcionales al diámetro de las partículas. Si todas las partículas iluminadas son de tamaño único, el haz láser formará una figura de dispersión, cuya energía de distribución sigue la Ley de Airy. Cuando las partículas tienen tamaños diferentes, la figura de dispersión obtenida se basa en la superposición de imágenes Airy, cada una de las cuales corresponde a un diámetro diferente de partícula. A partir de estas figuras de dispersión se obtienen las correspondientes distribuciones de tamaño de las partículas.

Los análisis de tamaño de las partículas de los diferentes materiales a emplear como capas de contacto (LNF, LNC, LSFMC) se han realizado en un analizador de tamaño de partículas *"Malvern MasterSizerX 2000E"* (Figura 7.5), ubicado en los Servicios Generales de Investigación (SGIker), de la UPV/EHU.

Figura 7.5. Analizador de distribución de partícula "Malvern MasterSizerX".

El equipo dispone de un software de adquisición y tratamiento de datos *"Mastersizer 2000"*. Todas las medidas se han realizado empleando como medio de dispersión etanol, utilizando ultrasonidos para deshacer los aglomerados que se forman en los materiales.

7.2.2. Conductividad eléctrica total y medida de resistencia superficial específica (ASR)

Las medidas de conductividad en *bulk* (barras rectangulares) se han realizado mediante el método de cuatro puntos (Figura 7.6) haciendo uso de la ecuación de Ohm.

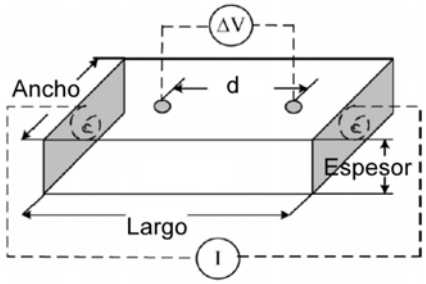

Figura 7.6. Sistema de cuatro puntos utilizado para las medidas de conductividad eléctrica para los compuestos en bulk.

Por lo tanto, la conductividad (σ) se ha determinado a partir de los valores V-I, según la siguiente ecuación 7.1:

$$\sigma = \frac{1}{\rho} = \frac{d}{A \cdot R} \qquad (7.1)$$

donde σ es la conductividad eléctrica ($S \cdot cm^{-1}$) (inversa de la resistividad, ρ), d es la distancia entre las conexiones (cm), A es el área de la sección transversal (cm^2) y R es la resistencia ($\Omega \cdot cm^{-2}$).

La conductividad total media consta de dos componentes: la conductividad electrónica debida a un movimiento de electrones entre los portadores de carga y la conductividad iónica que resulta del movimiento de iones oxígeno. Sin embargo, la conductividad iónica observada para los compuestos medidos es de aproximadamente dos órdenes de magnitud inferior a la electrónica[2-4]. Como consecuencia de ello, suele considerarse que los valores de conductividad que se obtienen siguiendo este método se atribuyen casi exclusivamente a la conductividad electrónica.

El mecanismo de conducción, de alguno de los materiales analizados, se produce a través del modelo conocido como "small polaron hopping". Este mecanismo se activa térmicamente, existiendo una dependencia de la movilidad de los portadores de carga y, por consiguiente, de la conductividad con la temperatura, que viene dada por la ecuación de Arrhenius:

$$\sigma = \left(\frac{C}{T}\right) exp\left(-\frac{Ea}{K \cdot T}\right) \qquad (7.2)$$

donde T es la temperatura absoluta, Ea es la energía de activación, K es la constante de Boltzmann y C es un factor pre-exponencial relacionado con la movilidad de las cargas. Para cada composición, el valor de Ea se ha calculado a partir de la pendiente de la recta correspondiente (ecuación 7.3) entre las temperaturas en las que se cumple el modelo de Arrhenius.

$$Ln(\sigma \cdot T) = lnC - \frac{Ea}{K \cdot T} \qquad (7.3)$$

---

2 Ivers-Tiffée E., Weber A., Schichlein H., in Handbook of Fuel cells. vol. 2 (eds. Vielstich W., Gasteiger H.A., Lamm A.), John Wiley & Sons, Chichester, **2003**.

3 Carter S., Seluck A., Charter R.J., Kajda J., Kilner J.A., Steele B.C.H. Oxygen transport in selected nonstoichiometric perovskite-structure oxides. *Solid State Ionics* 53-56 (**1992**) 597-605.

4 Bahteeva J.A., Leonidov I.A., Patrakeev M.V., Mitberg E.B., Kozhevnokov V.L., Poeppelmeier K.R. High-temperature ion transport in $La_{1-x}Sr_xFeO_{3-\delta}$. *J. Solid State Electr.* 8 (**2004**) 578-584.

Asimismo las medidas en celda también se han llevado a cabo mediante el método de cuatro puntos desarrollado por Van der Pauw. A partir del conjunto de datos V-I recogidos, se ha calculado el valor de resistencia superficial específica (ASR) ($\Omega \cdot cm^{-2}$) de las muestras mediante la ley de Ohm (Ecuación 7.4). Los valores ASR, corresponden a la suma de estas dos resistencias, resistencia de polarización (R_p) y la resistencia óhmica (R_Ω), y se refieren a la resistencia transversal al paso de corriente.

$$ASR = \frac{V}{I \cdot A} \qquad (7.4)$$

donde V es la diferencia de potencial, medida en voltios, I es la corriente eléctrica, medida en amperios, y A es el área medida.

Estos estudios se han llevado a cabo empleando tres equipos:

- Se ha utilizado una fuente de corriente continua (DC), controlada por un ordenador PC mediante el sistema Lab Windows/CVI, perteneciente al Centro Tecnológico "Ikerlan Energía", situado en el Parque Tecnológico de Álava en Miñano (Figura 7.7a).
- Se ha empleado un potenciostato/galvanostato VSP (Princeton Applied Research, Oak Ridge, EEUU) y una sonda de cuatro puntas (Figura 7.7b), ubicado en el Instituto de Ciencia de Materiales de Aragón (ICMA) de la Universidad de Zaragoza. Este dispositivo suministra a la celda tanto intensidad de corriente como potencial. En este caso, el dispositivo actúa como una carga electrónica, permitiendo registrar la caída de potencial en la celda para cada valor de intensidad extraída.
- Se ha dispuesto un sistema compuesto por los instrumentos *Thurlby Thandar Instruments 1604 Digital Mutimeter*, que mide la diferencia de potencial al aplicar una corriente mediante *Thurlby Thandar Instruments PL300* (Figura 7.7c). Estos equipos se encuentran en la "School of Chemistry", de la Universidad de Birmingham, UK.

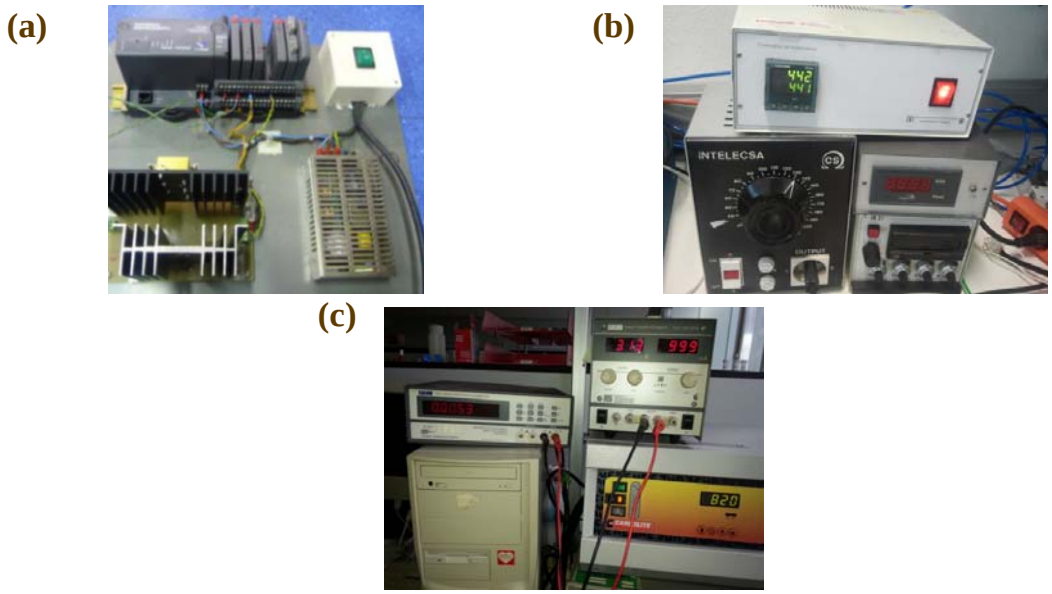

Figura 7.7. Montajes para llevar a cabo la caracterización electroquímica de las muestras presentadas en esta memoria: (a) fuente de corriente continua (DC)[5], (b) potenciostato/galvanostato VSP, y (c) sistema que incluye los instrumentos *Thurlby Thandar Instruments 1604 Digital Mutimeter* y *Thurlby Thandar Instruments PL300*.

[5] Otaegui-Ameztegui L. Desarrollo de celdas de combustible de tipo SOFC tubulares de soporte metálico, Ph.D. thesis work, Universidad de Navarra, **2013**.

7.2.3. Difracción de rayos X sobre muestra policristalina (DRXP)

Hace más de un siglo, en 1895, el físico alemán Wilhelm Conrad Röntgen (1845-1923) descubrió una radiación (entonces desconocida y de ahí su nombre de rayos X) que tenía la propiedad de penetrar los cuerpos opacos. Esta radiación se genera en un tubo de vacío, en el cual se produce una diferencia de potencial (~ 40 kV) entre cátodo (filamento incandescente) y ánodo (placa metálica). Se hace circular una cantidad de corriente por el filamento que se calienta creando una nube de electrones a su alrededor (miliamperios, mA). Los electrones de la nube, que se sienten fuertemente atraídos hacia el lado positivo, salen disparados a gran velocidad e impactan contra un blanco metálico, el ánodo. En este choque se producen los rayos X, característicos del elemento metálico que constituye el ánodo[6].

Los rayos X son una radiación electromagnética con una longitud de onda λ del mismo orden de magnitud que las distancias entre los átomos que forman los cristales. Esto hace que las sustancias cristalinas sean capaces de difractar los rayos X. Cuando esta radiación indice sobre la nube electrónica de los átomos de una red cristalina, éstos se convierten en emisores puntuales de esa misma radiación. La radiación emitida por cada átomo se expande en forma de onda esférica e interfiere con la creada por los átomos del entorno. Esta interferencia puede ser destructiva o constructiva. Las direcciones en las que la interferencia es constructiva son las que cumplen la Ley de Bragg (ecuación 7.5):

$$\lambda = 2\, d_{hkl} \,\text{sen}\, \theta \qquad (7.5)$$

donde θ es el ángulo de incidencia de la radiación y d_{hkl} (Å) es la distancia entre dos planos consecutivos definidos por un vector de componentes hkl[7].

La difracción de rayos X sobre muestra policristalina se ha utilizado para el análisis cualitativo y cuantitativo de las fases presentadas en esta memoria, principalmente formadas como consecuencia de reactividades entre los materiales de contacto y los componentes adyacentes. Estos experimentos han sido útiles tanto para la identificación de las fases como para la determinación de su pureza química, ya que todos los sólidos cristalinos tienen un difractograma característico (huella dactilar)[8].

Un material policristalino está formado por un gran número de cristales diminutos dispuestos al azar unos respecto a otros. Una muestra de estas características, al ser irradiada con un haz de rayos X, siempre presentará un determinado número de cristalitos que satisfagan la ley de Bragg. Los difractómetros permiten determinar con precisión la dirección en la que se produce la difracción. La geometría más habitual de los difractómetros, y la que poseen los difractómetros utilizados en este trabajo, se denomina Bragg-Brentano. En este tipo de geometría, el goniómetro incorpora dos giros coaxiales: uno para la muestra y otro para el detector. Estos giros están acoplados, de tal forma que si la muestra se desplaza un ángulo θ, el detector recorre en el mismo tiempo un ángulo 2θ. La representación de la intensidad de la radiación X que llega al detector con respecto al ángulo de giro 2θ es lo que se denomina difractograma.

---

6 http://www.xtal.iqfr.csic.es/Cristalografia/parte_02.html.

7 Klein C., Hurlbut J.C.S., *"Manual de Mineralogía"*, 4ª Ed., Ed. Reverté S.A., Barcelona, **1996**.

8 Amorós. J.L. "El Cristal. Morfología, Estructura y Propiedades Físicas". Ed. Atlas, p. 1-33, 201-217, **1990**.

Los difractogramas realizados con el fin de caracterizar las muestras presentadas en esta memoria se han registrado en un difractómetro Philips X´Pert PRO, equipado con anticátodo de cobre (λ=1.5418 Å), con una geometría tipo Bragg-Brentano y con un detector ultrarrápido PIXcel (Figura 7.8a). Además, para una mayor resolución del difractograma se ha utilizado el difractómetro Bruker D8 Advance Vario dotado de un monocromador primario (Cu-$K_{\alpha 1}$) y un detector sólido SolX con una ventana de discriminación de energías optimizada para la radicación $K_{\alpha 1}$ del cobre (Figura 7.8b).

Los estudios de la evolución de la cristalinidad en función de la temperatura y el tiempo, se han realizado mediante termodifractometría de rayos X en muestra policristalina. Este método permite conocer los intervalos de estabilidad térmica de las fases estudiadas, identificar las fases originadas por la descomposición térmica y caracterizar los procesos de cambio de fase. Los análisis se han llevado a acabo empleando el difractómetro Bruker D8 Advance, equipado con una cámara de temperatura variable Anton Para HTK2000 (Figura 7.8c).

Las medidas de micro-difracción se han realizado en el difractómetro Bruker D8 Discover utilizando el tubo de rayos X de Cr y filtro de V (λ=2.2898 Å), con una óptica de haz paralelo, PolyCap^{TM}. El equipo dispone de Cuna de Euler, con traslaciones en x-y-z motorizadas, para colocar el porta-muestras (Figura 7.8d).

Todos los difractómetros empleados en esta memoria pertenecen a los Servicios Generales de Investigación (SGIker), de la Universidad del País Vasco/Euskal Herriko Unibertsitatea (UPV/EHU) (Figura 7.8).

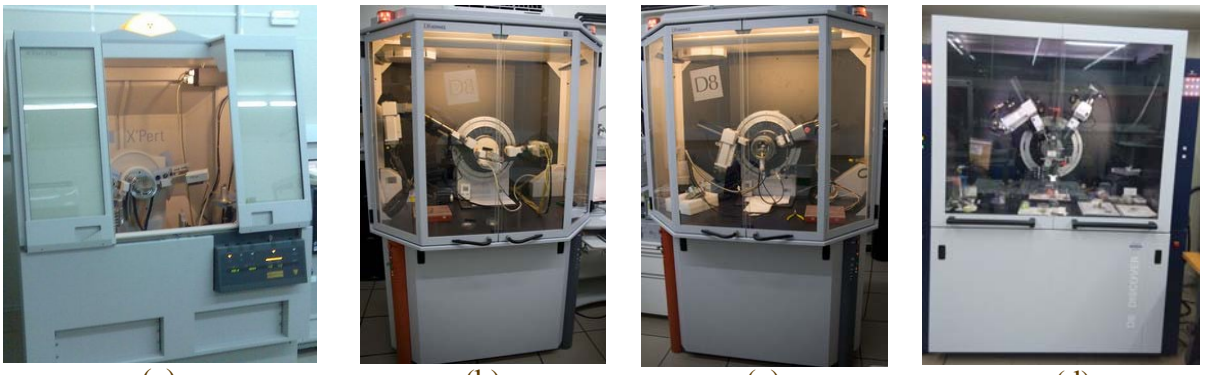

(a) (b) (c) (d)

Figura 7.8. (a) Difractómetro Philips X'Pert PRO, (b) difractómetro Bruker D8 Advance Vario, (c) difractómetro Bruker D8 Advance Vantec con cámara HTK 2000, y (d) difractómetro Bruker D8 Discover con óptica de haz paralelo.

Para obtener información de los difractogramas es preciso hacer un análisis de los mismos, en el que se deben tener en cuenta la posición de los máximos de difracción, su perfil y su intensidad. Las fases presentadas en esta memoria se han identificado utilizando el programa X´Pert HighScore[9] a través de la base de datos Power Diffraction File (PDF)[10] y las tablas cristalográficas[11]. El ajuste de

[9] PANalytical, Almelo B.V., Versión 1.0e, The Netherlands, **2003**.
[10] ICDD, "Powder Diffraction File-Inorganic and Organic", Pennsylvania, USA, **1995**.
[11] Hahn Th., "International tables for crystallography, Volume A: Space-group symmetry", D. Reidel Publishing Company, Boston, USA, **1983**.

los diagramas de difracción se ha realizado mediante el afinamiento de perfil completo sin/ o con modelo estructural, método Rietveld[12] mediante el programa informático Fullprof[13].

7.2.3.1. Método Rietveld

El método de Rietveld fue desarrollado a principio de los años sesenta para el afinamiento de estructuras cristalinas a partir de datos de difracción de neutrones con longitud de onda constante[14]. Con posterioridad, su utilización se ha extendido a la difracción de rayos X[15,16].

El método de Rietveld permite el afinamiento de estructuras cristalinas de moderada complejidad ajustando, mediante mínimos cuadrados, el perfil completo del diagrama de difracción a un perfil calculado para un modelo estructural (que depende de los parámetros a afinar). No existe un paso intermedio para extraer los factores de estructura de las reflexiones individuales a partir de las intensidades medidas para cada posición 2θ del difractograma.

El método de Rietveld se basa en la minimización de la función residuo 7.6:

$$\chi^2 = \sum_{i=1}^{n} w_i \left\{ y_i - y_{i,c} \right\}^2 \qquad (7.6)$$

siendo:

n Número total de posiciones $2\theta_i$.
w_i Factor de pesada (peso estadístico de cada reflexión).
y_i Número de cuentas observadas para cada ángulo $2\theta_i$.
$y_{i,c}$ Número de cuentas calculado para cada ángulo $2\theta_i$ a partir de la expresión:

$$y_{i,c} = S \cdot \sum_{k=0}^{k} L_k \cdot |F_k|^2 \cdot W \cdot (2\theta_i - 2\theta_k) \cdot T_k . P_k \cdot + y_{ib} \qquad (7.7)$$

k Número de reflexiones que contribuyen a y_i en una posición $2\theta_i$.
S Factor de escala.
L_k Factores de Lorentz, polarización y multiplicidad de la reflexión k.
F_k Factor de estructura de la reflexión k.
W Función de perfil de la reflexión k.
T_k Factor de transmisión.
P_k Función de orientación preferente de la muestra.
y_{ib} Intensidad del fondo continuo en la posición $2\theta_i$.

La minimización de la ecuación (7.6) conduce al afinamiento de dos tipos de parámetros: estructurales y de perfil, pudiéndose destacar:

---

[12] Rietveld H.M. A profile refinement method for nuclear and magnetic structure. *J. Appl. Crystallogr.* 2 (**1969**) 65-71.
[13] Rodríguez-Carvajal J., "Fullprof program: Rietveld pattern matching analysis of powder patterns", Grenoble, **1994**.
[14] Rietveld H.M. Line profiles of neutron powder diffraction peaks for structure refinement. *Acta Cryst.* 22 (**1967**) 151-152.
[15] Young R.A. *"The Rietveld method"*. International Union of Crystallography-Oxford Science Publications: Oxford, **1995**.
[16] Rodríguez-Carvajar J. Fullprof program: Rietveld pattern matching analysis of powder patterns, Grenoble, **2011**.

- Parámetros estructurales:
  - Coordenadas reducidas de cada átomo: x_i, y_i, z_i.
  - Factores de ocupación: n_i.
  - Parámetros de agitación térmica (isotrópicos o anisotrópicos).

- Parámetros de perfil:
  - Factor de escala: S.
  - Parámetros U, V, W, que determinan la evolución angular de la anchura a media altura de la reflexión k, según la expresión: $FWHM^2 = U\ tg^2\ \theta_k + V\ tg\ \theta_k + W$.
  - Posición del cero del detector: $2\theta_o$.
  - Parámetros de celda: a, b, c, α, β, γ.
  - Parámetro del fondo continuo: m_i.
  - Parámetro de asimetría: P.
  - Parámetros de orientación preferente: G_1, G_2.

La bondad de los afinamientos se expresa mediante los factores de acuerdo R_P, R_{WP}, R_B, R_E, y χ^2, definidos por las expresiones:

Perfil	$R_P = 100\ \Sigma\ \lvert y_i - y_{ic}\rvert\ /\ \Sigma\ \lvert y_i\rvert$
Perfil ponderado	$R_{WP} = 100\ \Sigma\ [w_i\ \lvert yi - y_{ic}\rvert^{\ 2}\ /\ \Sigma\ w_i\ \lvert y_i\rvert^{\ 2}]^{\ 1/2}$
Bragg	$R_B = 100\ \Sigma\ \lvert A_{,vii} - A_{,viic}\rvert\ /\ \Sigma\ \lvert A_{,vii}\rvert$
Esperado	$R_E = 100\ [\ (N-P+C)\ /\ \Sigma\ w_i y_i^{\ 2}]^{1/2}$
Índice de bondad del ajuste	$\chi^2 = (R_{WP}/R_E)^2$

siendo:

w_i	Factor de pesada (peso estadístico de cada reflexión).
y_i	Número de cuentas observadas para cada ángulo $2\theta_i$.
y_{ic}	Número de cuentas calculado para cada ángulo $2\theta_i$.
A_{vii}	Intensidad integrada para cada ángulo $2\theta_i$.
A_{viic}	Intensidad integrada calculada para cada ángulo $2\theta_i$.
(N-P+C)	Número de grados de libertad.

El factor de acuerdo más representativo es R_{WP}. El índice de bondad del ajuste, χ^2, que debiera ser próximo a la unidad, está sujeto a errores sistemáticos, fundamentalmente derivados de la representación deficiente de la función de perfil. El factor de acuerdo R_B está relacionado con el área de los máximos de difracción y refleja la calidad del modelo estructural.

Unos valores adecuados de los factores de acuerdo no siempre son condición necesaria para considerar un afinamiento como correcto: este criterio debe acompañarse con el examen de la diferencia entre el difractograma observado y el calculado, con el fin de detectar posibles errores sistemáticos. La bondad del afinamiento final dependerá de varios factores, entre los que destacan: la calidad del difractograma experimental (y de la muestra), el tipo de radiación utilizado (neutrones, rayos X, radiación sincrotrón, etc), y la presencia de impurezas y errores sistemáticos durante el proceso de afinamiento.

7.2.4. Dilatometría

Los dilatómetros se utilizan para medir la expansión o contracción de los sólidos a diferentes temperaturas.

La obtención de la expansión térmica lineal de una muestra, viene dada por la siguiente expresión:

$$\frac{\Delta L}{L_0} = \frac{L_T - L_0}{L_0} \qquad (7.8)$$

donde:
L_0 Longitud de la muestra a la temperatura de referencia (normalmente, Tª ambiente).
L_T Longitud de la muestra a una temperatura T.

En realidad, el valor de $\Delta L/L_0$ viene dado por:

$$\frac{\Delta L}{L_0} = \frac{\Delta L_a}{L_0} + \frac{\Delta L_s}{L_0} \qquad (7.9)$$

donde:
$\Delta L_a/L_0$ Es el cambio aparente en la longitud de la muestra.
$\Delta L_s/L_0$ Es el cambio en la longitud del sistema de medición (dilatómetro).

Normalmente, esta corrección se ajusta automáticamente en el software del equipo. El valor resultante de $\Delta L/L_0$ se expresa habitualmente en partes por millón ($\cdot 10^{-6}$) o bien en µm/m.

La expansión lineal de la muestra se puede expresar en porcentaje de expansión, para lo cual se utiliza la siguiente ecuación:

$$\frac{\Delta L}{L_0} \cdot 100 = \text{Coef}\,\% \qquad (7.10)$$

El coeficiente medio de expansión térmica lineal ($\alpha_m \equiv$ TEC) es el coeficiente promedio de la expansión térmica lineal en el intervalo de temperatura, desde $T_{ambiente}$ a T, y viene dado por la expresión:

$$\alpha_m = \frac{1}{L_0} \cdot \frac{\Delta L}{\Delta T} = \frac{1}{L_0} \cdot \frac{L_T - L_0}{T - T_a} \qquad (7.11)$$

El α_m se expresa como parte por millón por grado centígrado:

$$\text{TEC}\alpha_m = \frac{10^{-6}}{{}^{o}C} = \frac{\mu m}{m\,{}^{o}C} \qquad (7.12)$$

Con objeto de registrar cambios de dimensión asociados a procesos de expansión/contracción de los materiales en bulk recogidos en esta memoria, se han llevado a cabo ensayos de dilatometría, utilizando un dilatómetro *Unitherm™ Model 1161* (Figura 7.9, Servicios Generales de Investigación (SGIker) de la UPV/EHU). Así, se ha obtenido una idea del efecto de adición de los componentes de las celdas SOFC.

Figura 7.9. Dilatómetro Unitherm™ Model 1161.

7.2.5. Espectroscopia fotoeléctrica de rayos X (XPS)

El físico alemán Heinrich Rudolf Hertz (1857-1894) descubrió el efecto fotoeléctrico, en 1887, principio en el que se basa la espectroscopia fotoeléctrica: cuando se irradia una muestra con fotones con una energía superior a la de ligadura de los electrones de los átomos, los electrones salen de la muestra con una energía cinética igual al exceso de energía del fotón respecto de la energía de ligadura. En este contexto, el físico alemán Albert Einstein (1879-1955) propuso, en 1905, la física básica del proceso de fotoemisión, basada en la ley de conservación de la energía, mediante la ecuación 7.13:

$$E_K = h\nu - E_B \qquad (7.13)$$

donde E_B es la energía de enlace del electrón en el átomo, hν es la energía de la fuente de rayos X, y K_E es la energía cinética del electrón detectado que es medida por el espectrómetro del XPS (espectroscopia fotoeléctrica de rayos X).

La energía (BE) de los niveles electrónicos internos depende, fundamentalmente, del número atómico. Estas energías de ligadura son conocidas, permitiendo identificar la composición atómica de la superficie de la muestra analizada. No obstante, las líneas espectrales XPS, para un mismo átomo, pueden tener diferentes valores en función de la capa de la cual el electrón fue emitido (1s, 2s, 2p, etc).

Los fotoelectrones son fuertemente atenuados por el paso a través de la muestra; así la información obtenida proviene de la superficie de la misma, con una profundidad de muestreo del orden de 5-10 nm. El entorno del átomo analizado, tiene un efecto sobre la energía de enlace electrón-orbital, y da lugar a un desplazamiento químico en la energía cinética del fotoelectrón. Estos cambios en la energía de ligadura se pueden utilizar para extraer información de la naturaleza química (estado de oxidación, por ejemplo) de la superficie analizada.

Los espectros XPS de los materiales presentados en esta memoria, se obtuvieron mediante un espectrómetro SPECS con un analizador de energía SPECS PHOIBOS 150 (Figura 7.10).

Figura 7.10. Sistema de espectroscopia fotoelectrónica de rayos X (XPS).

El equipo pertenece al Servicio General de Rayos X, SGIker, de la UPV/EHU. Todos los espectros se han calibrado a partir del pico del carbono (~ 284.6 eV). Los espectros se registran utilizando una potencia monocromatizada producida por la radiación del Al K_α ($h\nu$ = 1486.6 eV).

7.2.6. Microscopia electrónica de barrido (MEB)

Las diferentes técnicas de microscopía electrónica se basan en el análisis de los efectos que se producen de la interacción electrones-muestra, en la que se generan diferentes procesos de absorción y emisión (Figura 7.11a). Adecuados sistemas de detección para cada uno de los procesos, permiten obtener información sobre la muestra irradiada.

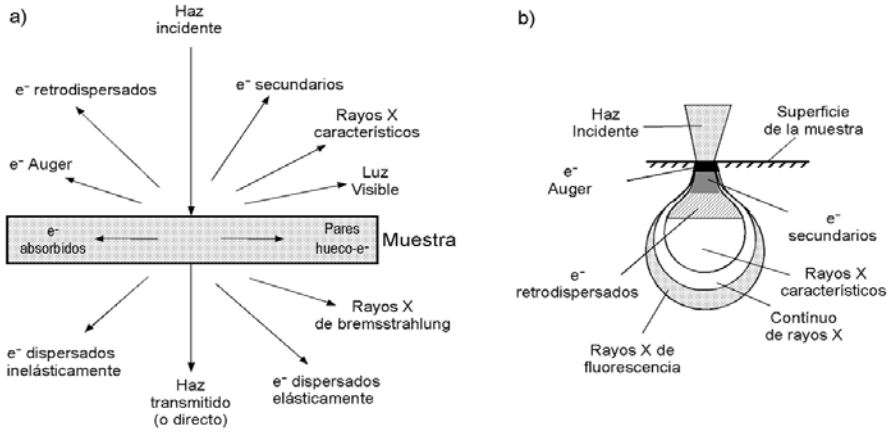

Figura 7.11. (a) Efectos producidos en una muestra cuando ésta es irradiada con un haz de electrones; (b) Origen de los electrons analizados en un microscopio MEB cuando el haz indice sobre una muestra.

El microscopio electrónico funciona con un haz de electrones generados por un cañón electrónico, acelerados por un alto voltaje y focalizados por medio de lentes magnéticas, todo ello en alto vacío. Los electrones interaccionan con la muestra y la amplificación se produce por un

conjunto de lentes magnéticas, que forman una imagen sobre una placa fotográfica o sobre una pantalla sensible al impacto de los electrones que transfiere la imagen formada a la pantalla de un ordenador. Además, estos aparatos suelen combinar la posibilidad de obtener imágenes de gran resolución con el análisis químico de pequeñas áreas del material.

Desde el punto de vista de la Microscopía Electronica de Barrido (MEB) interesa analizar los electrones secundarios y los retrodispersados. El origen de estos electrones se muestra en la Figura 7.11b: los retrodispersados son electrones del haz que han sido dispersados elásticamente al colisionar con núcleos y los electrones de los átomos; estos electrones proporcionan imágenes con información composicional. El número de electrones retrodispersados varía con el número atómico promedio (<Z>) de la muestra, de tal manera que cuanto mayor es Z, mayor es la probabilidad de choque y mayor es la cantidad de electrones retrodispersados. Por lo tanto las imágenes con menor número atómico promedio aparecerán más oscuras que las de mayor (<Z>). Además, estos electrones pueden aportar información topográfica de la muestra, en función del modo de trabajo del detector y son sensibles a la orientación cristalina. Los electrones secundarios son electrones arrancados de las capas más externas de los átomos y proporcionan imágenes de la topografía superficial de la muestra. La cantidad de electrones secundarios dispersados depende de la energía del haz incidente, de la densidad y de la topografía de la superficie de la muestra.

Otra emisión importante que resulta de la interacción del haz de electrones con los átomos de las muestras, son los rayos X, con energía y longitud de onda característicos de los elementos que constituyen la muestra. Esta radiación es recogida por un detector adecuado para obtener el microanálisis del material. El detector utilizado en los microanálisis mostrados en esta memoria es un espectrómetro de dispersión de energía (EDX), que analiza de forma simultánea las energías de los fotones de rayos X, en todo el intervalo desde el boro hasta el uranio. Cuando un haz electrónico suficientemente acelerado, incide en la superficie de un sólido, se produce, entre otros fenómenos, la ionización de los átomos presentes en el mismo; ésto es, la pérdida de electrones internos. Cuando un átomo se encuentra en este estado, otro electrón de la capa más externa salta a la capa deficitaria, y rellena el hueco producido. Este salto implica la liberación de energía, cuyo valor es igual a la diferencia entre las energías que tenía cada electrón en su orbital correspondiente. Dicha energía se manifiesta de dos formas: mediante emisión de una radiación electromagnética (rayos X) o por emisión de otro electrón de un orbital exterior (electrón Auger). La probabilidad de que tenga lugar una u otra emisión queda determinada por el rendimiento de fluorescencia[17,18].

Los análisis morfológicos, microestructurales y composicionales de las muestras se han realizado en un Microscopio Electrónico de Barrido (MEB), JEOL JSM-6400, con filamento de wolframio. La configuración de este microscopio incluye un analizador de energía dispersada de rayos X, Oxford Inca Pentafet X3 (EDX), provisto de un software de adquisición de datos INCA Energy 350. Este equipo está instalado en los Servicios Generales de Investigación (SGIker), de la UPV/EHU (Figura 7.12).

[17] Robards A.W., Wilson A.J. Procedures in electron microscopy, John Wiley & Sons, Chichester, UK, **1993**.
[18] Dunlap M., Adaskaveg J.E. Introduction to the scanning electron microscope, Cambridge, p. 3-33, **1997**.

Figura 7.12. Microscopio Electrónico de Barrido (MEB), JEOL JSM-6400.

7.2.6.1. Preparación de la muestras (sección transversal) para observaciones por MEB

El objetivo principal en la preparación de muestra, para observar su sección transversal por MEB, es preparar una pastilla de resina que contenga las partes de interés que se desean analizar. Esta pastilla debe estar pulida de forma que la parte superior de las muestras se encuentre libre de resina y no se haya alterado la microestructura durante el proceso de pulido.

Procedimiento:
A. *Colocar las muestras en un molde.* Depositar la muestra en un molde y fijar la zona de interés.
B. *Activación de la resina.* Mezcla de la resina epoxi con el catalizador para que se inicie la polimerización.
C. *Infiltración.* Se han utilizado dos procesos: (i) añadir la resina al molde hasta cubrir la muestra, y (ii) se cubre la muestra con resina, y se hace vacío hasta que la resina esté en estado de ebullición; posteriormente se elimina el vacío, facilitando la penetración de la resina en los poros. Este proceso permite que la pastilla no presente burbujas.
D. *Endurecimiento.* Una vez con la resina en el molde se deja en reposo hasta que la reacción de polimerización finalice (24 h).
E. *Corte y Pulido.* El corte por abrasión de las muestras embebidas en resina, se lleva a cabo mediante un disco de diamante con un equipo Secotom 10 de la marca Struers (Figura 7.13a). Una vez cortada la probeta, es necesario llevar a cabo el pulido de la misma con el fin de que la muestra que se quiere observar quede en la superficie de la probeta. Para ello se llevaran a cabo una serie de etapas de pulido con lijas de mayor a menor tamaño de partícula (Figura 7.13b). Si se han llevado a cabo todos los pasos de forma adecuada, tras esta operación, la probeta no debería presentar ninguna imperfección al observarse con un microscopio óptico. El proceso de pulido se realiza utilizando una pulidora automática TegraPol-31 (Struers) (Figura 7.13c). La pulidora consiste en una placa giratoria donde se colocan los discos con el material abrasivo. También dispone de un cabezal automático para la sujeción de la muestra y que permite ejercer una presión controlada sobre los discos con el material abrasivo. Estos equipos pertenecen al Departamento de Mineralogía y Petrología de la Facultad de Ciencia y Tecnología de la UPV/EHU.

Finalmente, se utiliza un equipo Sputter Coater (Quorum Q150T) que permite recubrir la muestra con carbono y así convertirla en conductora de electrones para poder ser observada en el MEB. Este equipo pertenece a los Servicios Generales de Investigación (SGIker), de la UPV/EHU (Figura 7.13d).

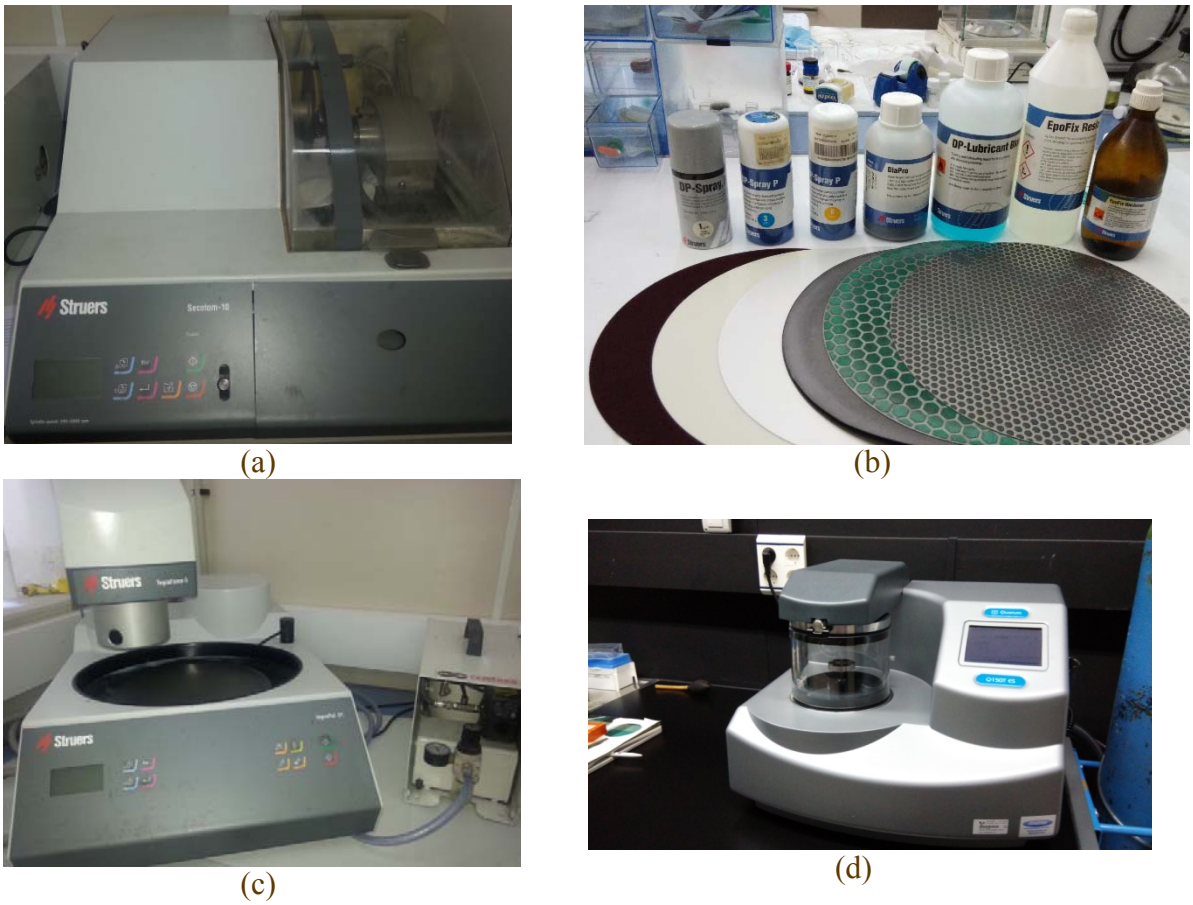

Figura 7.13. (a) Cortadora Secotom 10 de Struers, (b) discos y material abrasivo necesarios para llevar a cabo el pulido, (c) pulidora TegraPol-31 de Struers y (d) equipo Sputter Coater (Quorum Q150T).

7.2.7. Reología

El comportamiento reológico de una sustancia viene dado por la respuesta que ofrece a un esfuerzo externo o a una deformación. En el caso de que la muestra se comporte como un líquido, sus propiedades reológicas se pueden ilustrar representando dos placas paralelas, de superficie A (m^2), cuyo espacio de separación está lleno del líquido al que se le aplica una fuerza tangencial F ($N = kg \cdot m/s^2$). Al aplicar esta fuerza tangencial sobre la placa móvil superior, ésta se desplaza con una velocidad relativa v (m/s). La distancia entre las dos placas que el material adhiere es h (m) (Figura 7.14)[19,20].

[19] Barnes H.A., Hutton J.F., Walters F.R.S.K. An introduction to rheology, Ed. Elsevier, p. 1-35, **1989**.
[20] Otaegui-Ameztegui L. Desarrollo de celdas de combustible de tipo SOFC tubulares de soporte metálico, Ph.D. thesis work, Universidad de Navarra, **2013**.

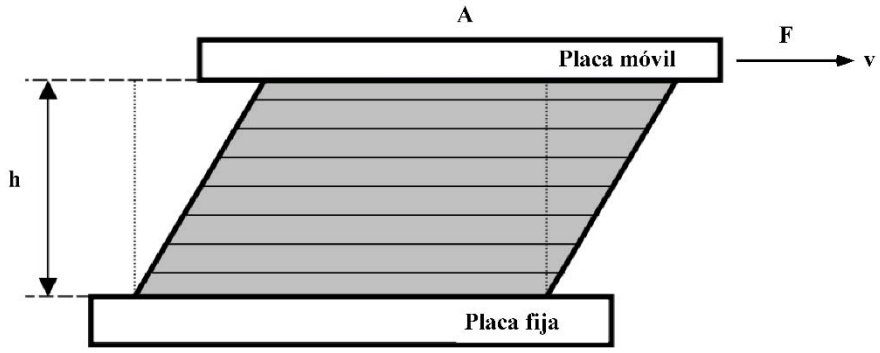

Figura 7.14. Ilustración del modelo de placas paralelas.

La tensión de cizalla (τ) se define como la fuerza F que actúa sobre el área A para provocar un movimiento en el elemento liquido entre las dos placas.

$$\tau = \frac{F}{A} = Pa \tag{7.14}$$

Al aplicar una tensión de cizalla, se genera un flujo laminar entre las dos placas en el que la velocidad de las sucesivas capas de líquido disminuye al aumentar la distancia con el plano cizallado. Por lo tanto, las capas que se encuentran en contacto con la placa móvil se mueven a máxima velocidad mientras que aquellas en contacto con la placa fija se mantienen quietas. Así, el esfuerzo de cizalla aplicado es proporcional al gradiente de velocidad generado (γ):

$$\gamma = \frac{dv}{dh} \tag{7.15}$$

donde dv es el diferencial de velocidad entre capas adyacentes y dh es el diferencial de espesor de las capas. Cuando el flujo es laminar, dv y dh serían constantes por lo que la ecuación 7.15 podría representarse de la siguiente manera:

$$\gamma = \frac{v}{h} = \frac{m/s}{m} = {}^{1}/_{s} \tag{7.16}$$

y obtener así la proporcionalidad entre τ (esfuerzo de cizalla) y γ (gradiente de velocidad):

$$\tau = \eta\gamma \rightarrow \eta = \frac{\tau}{\gamma} = Pa \cdot s \tag{7.17}$$

donde el coeficiente de proporcionalidad η es la viscosidad. En este sentido, la viscosidad describe la resistencia del material a la fluencia.

Los principales parámetros que afectan a la viscosidad de un líquido son los siguientes: (i) la naturaleza del líquido, (ii) la temperatura, (iii) la presión, (iv) la velocidad y tiempo de cizalla, y (v) los campos eléctricos y magnéticos. Así, las medidas de reología mostradas en este trabajo se han llevado a cabo a temperatura constante y representadas mediante curvas de flujo.

En función del tipo de dependencia que la viscosidad presente con la velocidad de cizalla, los materiales se clasifican como newtonianos, plásticos, plásticos de Bingham, pseudoplásticos y dilatantes (Figura 7.15). En un fluido newtoniano, la curva de flujo es una línea recta que comienza en el origen cuya pendiente será el valor de la viscosidad, siendo éste similar e independiente de la velocidad de cizalla.

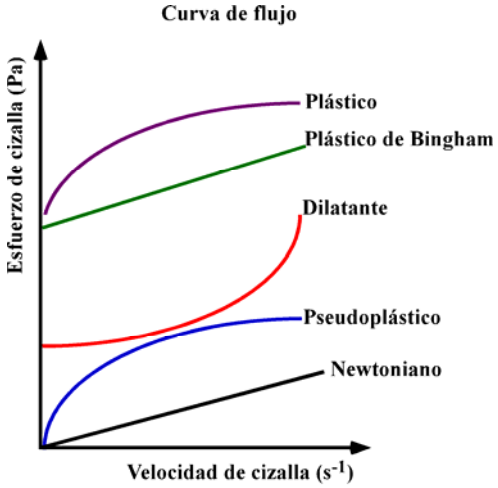

Figura 7.15. Curva de flujo en función del comportamiento del fluido.

El control de calidad de las suspensiones cerámicas para su deposición por dip coating se ha llevado a cabo mediante medidas de viscosidad utilizando un equipo Haake Mars II (Figure 7.16).

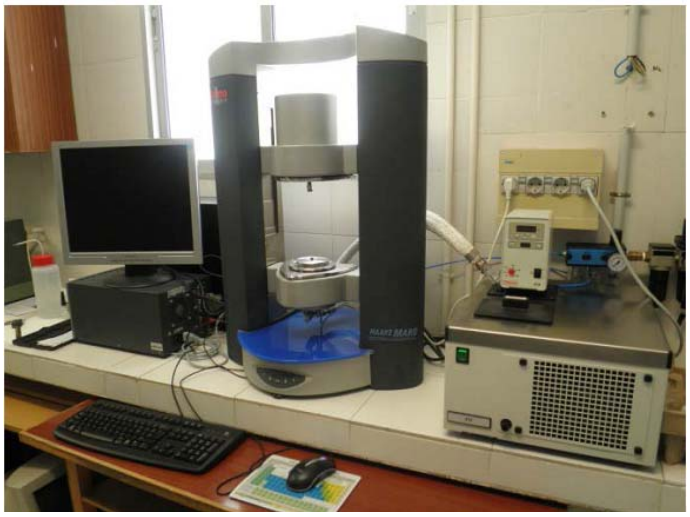

Figura 7.16. Reómetro Haake Mars II.

Este equipo se encuentra ubicado en el Instituto de Ciencia de Materiales de Aragón, Universidad de Zaragoza.

7.2.8. Sistema de láser de pulsos ultracortos

Se entiende por láser la amplificación de luz por emisión estimulada de radiación. El primero en sugerir la emisión estimulada fue el físico alemán Albert Einstein (1879-1955) en 1916. El láser consta de un medio activo capaz de generar luz. Los principales procesos que se producen en la generación del láser son: bombeo, emisión espontánea de radiación, emisión estimulada de radiación y absorción[21].

El bombeo se provoca mediante una fuente de radiación, como puede ser una fuente energética que provoque una emisión, manteniendo así un mecanismo de excitación. La emisión estimulada se produce cuando un átomo en estado excitado recibe un estímulo externo, que lo lleva a emitir fotones, y así retornar a un estado menos excitado. El estímulo en cuestión proviene de la llegada de un fotón con energía similar a la diferencia de energía entre los dos estados energéticos (Figura 7.17). La particularidad de esta emisión es que el fotón emitido tiene tres características que lo hacen "especial": (i) el fotón emitido se propagará en la misma dirección y sentido del fotón causante de la emisión estimulada, (ii) el fotón emitido tiene la misma frecuencia del que estimula, y (iii) el campo eléctrico del fotón emitido estará sincronizado en fase temporal con el fotón estimulante[22]. Así, esta emisión estimulada produce luz coherente y monocromática, y además amplifica la emisión de luz, ya que por cada fotón que incide sobre un átomo excitado se genera otro fotón. Finalmente, la absorción consiste en incorporar un fotón. El sistema atómico se excita a un estado de energía más alto, pasando un electrón al estado metaestable. Este fenómeno compite con el de la emisión estimulada de radiación.

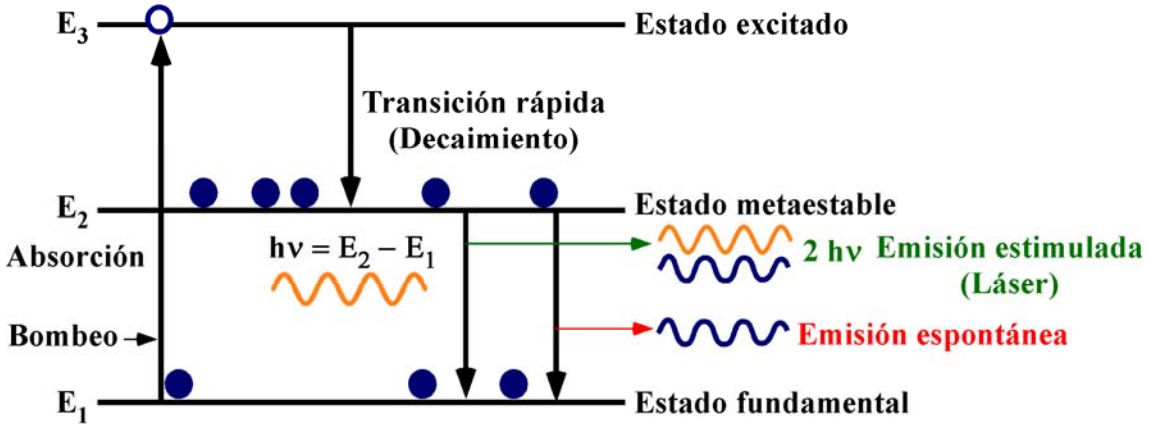

Figura 7.17. Principio de la emisión estimulada, también conocida como emisión coherente, por la cual se explica el fenómeno de amplificación de la luz incidente.

Los principales principios de un láser son la amplificación óptica y la retroalimentación. El ingeniero físico estadounidense Theodore Harold Maiman (1927-2007) obtuvo la primera emisión láser. En este sentido, demostró que una varilla de rubí excitado, colocada en una cavidad, para que hubiera retroalimentación óptica, producía un haz intenso de luz láser. La cavidad es el espacio entre dos espejos. La varilla hace de amplificador óptico y la luz que se genera rebota en los

[21] http://www.interempresas.net/Deformacion-y-chapa/Articulos/99796-El-laser-de-pulsos-ultracortos.html.
[22] http://queaprendemoshoy.com/algo-mas-sobre-la-interaccion-luz-materia-la-ampliacion-optica-principio-base-para-el-efecto-laser/.

espejos, generando así intensidad. Uno de los espejos es parcialmente transmisor, y deja que una porción de luz escape en forma de haz, o de rayo láser.

Esta cavidad sólo tolera luz de ciertas longitudes de onda. Un láser usual de onda continua emite un haz de luz, cuyo color corresponde a la frecuencia de una de esas longitudes de onda. En cambio, los láseres de pulsos ultracortos generan un conjunto de frecuencias, así cuanto mayor sea el ancho de banda espectral, menor será la duración del pulso. El desarrollo de generadores de pulsos láser de femtosegundos ($1fs=10^{-15}s$) ha hecho posible la observación de procesos multifotónicos[23]. La brevísima duración del pulso hace que el pico instantáneo de potencia resulte muy grande, produciendo la ablación en aceros y cerámicas. Así, el láser arranca iones de la superficie sin darles tiempo a transferir su energía al sustrato inferior.

El sistema de láser de pulsos ultracortos (Figura 7.18) se ha utilizado para el micromecanizado del composite metálico-cerámico presentado en esta memoria. Estos experimentos han sido útiles para aportar a la capa de contacto una mejora en su transporte de gas oxidante.

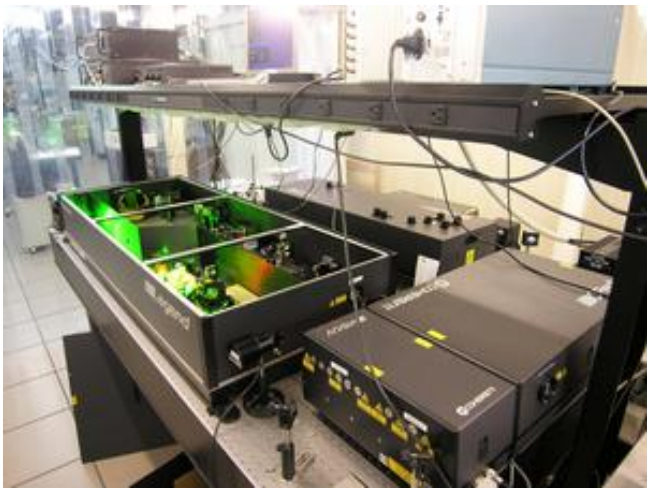

Figura 7.18. Sistema láser de femtosegundos, SGIker, UPV/EHU.

El láser de femtosegundos utilizado consiste en un oscilador y un amplificador regenerativo de Ti:zafiro cuya salida es un tren de pulsos de 40 fs y 2 mJ. El equipo pertenece a la unidad de Facilidad Láser de los Servicio Generales de Investigación, SGIker, de la UPV/EHU (Figura 7.18).

[23] De-Nalda R., Bañares L. El láser en ciencias de la vida. http://www.rsef.org, **2007**.

8. DIFUSIÓN DE RESULTADOS

- **Publicaciones**
- **Contribuciones a congresos**

8.1. Publicaciones

1.- **Aroa Morán-Ruiz**, Karmele Vidal, Aitor Larrañaga, María Isabel Arriortua. Chemical compatibility and electrical contact of $LaNi_{0.6}Co_{0.4}O_{3-\delta}$ (LNC) between Crofer22APU interconnect and $La_{0.6}Sr_{0.4}FeO_3$ (LSF) cathode for IT-SOFC. *Fuel Cells* 3 (**2013**) 398-403.

2.- **Aroa Morán-Ruiz**, Karmele Vidal, Miguel Ángel Laguna-Bercero, Aitor Larrañaga, María Isabel Arriortua. Effects of using $(La_{0.8}Sr_{0.2})_{0.95}Fe_{0.6}Mn_{0.3}Co_{0.1}O_3$ (LSFMC), $LaNi_{0.6}Fe_{0.4}O_{3-\delta}$ (LNF) and $LaNi_{0.6}Co_{0.4}O_{3-\delta}$ (LNC) as contact materials on solid oxide fuel cells. *J. Power Sources* 248 (**2014**) 1067-1076.

3.- **Aroa Morán-Ruiz**, Karmele Vidal, Aitor Larrañaga, Miguel Ángel Laguna-Bercero, Jose Manuel Porras-Vázquez, Peter Raymond Slater, María Isabel Arriortua. $LaNi_{0.6}Co_{0.4}O_{3-\delta}$ dip-coated on Fe-Cr mesh as a composite cathode contact material on intermediate solid oxide fuel cells. *J. Power Sources* 269 (**2014**) 509-519.

4.- Karmele Vidal, **Aroa Morán-Ruiz**, Aitor Larrañaga, Jose Manuel Porras-Vázquez, Peter Raymond Slater, María Isabel Arriortua. Characterization of $LaNi_{0.6}Fe_{0.4}O_3$ perovskite synthesized by glycine-nitrate combustión method. *Solid State Ionics* 269 (**2015**) 24-29.

5.- **Aroa Morán-Ruiz**, Karmele Vidal, Aitor Larrañaga, Jose Manuel Porras-Vázquez, Peter Raymond Slater, María Isabel Arriortua, Evaluation of using protective/conductive coatings on Fe-22Cr mesh as a composite cathode contact material for intermediate solid oxide fuel cells, *Int. J. Hydrogen Energ.* 40 (**2015**) 4804-4818.

6.- **Aroa Morán-Ruiz**, Karmele Vidal, Aitor Larrañaga, Jose Manuel Porras-Vázquez, Peter Raymond Slater, María Isabel Arriortua. Laser machining of $LaNi_{0.6}M_{0.4}O_{3-\delta}$ (M: Fe,Co) dip coated on a Fe-22Cr mesh material to obtain a new contact coating for SOFC: interaction between Crofer22APU interconnect and $La_{0.6}Sr_{0.4}FeO_3$ cathode. *Int. J. Hydrogen Energ.*, in press (doi: 10.1016/j.ijhydene.2015.04.134), **2015**.

7.- **Aroa Morán-Ruiz**, Karmele Vidal, Aitor Larrañaga, Raúl Montero Santos, María Isabel Arriortua. Femtosecond laser micromachining of metallic/ceramic composite material for solid oxide fuel cell devices. *J. Power Sources*, under review (D-15-02057), **2015**.

8.- **Aroa Morán-Ruiz**, Karmele Vidal, Aitor Larrañaga, María Isabel Arriortua, Solid oxide fuel cell improvement using a ceramic contact material between Crofer22APU interconnect and $La_{0.6}Sr_{0.4}FeO_3$ cathode. *Mater. Charact*., sent (MTL-15064), **2015**.

8.2. Contribuciones a congresos

1.- The Energy and Materials Research Conference (EMR2012). Torremolinos, 20-22 de Junio de 2012.
Autores: Aroa Morán-Ruiz, Aitor Larrañaga, Karmele Vidal, María Isabel Arriortua
Título: Metallic-ceramic composite on Crofer22APU channeled interconnect for cathode contact layer application in solid oxide fuel cells.
Presentación: Póster

2.- 10th European Fuel Cell Forum 2012. Lucerna (Suiza), 26-29 de Junio de 2012.
Autores: Aroa Morán-Ruiz, Aitor Larrañaga, Ana Martinez-Amesti, Karmele Vidal, María Isabel Arriortua
Título: Metallic-ceramic composite materials as cathode/interconnect contact layers for solid oxide fuel cells.
Presentación: Poster

3.- 13th European Power Diffraction Conference. Grenoble (Francia), 28-31 de Octubre de 2012.
Autores: Aroa Morán-Ruiz, Aitor Larrañaga, Karmele Vidal, María Isabel Arriortua
Título: Reactivity of $LaNi_{0.6}Co_{0.4}O_{3-\delta}$, $LaNi_{0.6}Fe_{0.4}O_{3-\delta}$ and $(La_{0.8}Sr_{0.2})_{0.95}Fe_{0.6}Mn_{0.3}Co_{0.1}O_3$ with $La_{0.6}Sr_{0.4}FeO_3$ materials for SOFC applications.
Presentación: Póster

4.- 13th International Conference of the European Ceramic Society. Limoges (Francia), 23-27 de Junio de 2013.
Autores: Aroa Morán-Ruiz, Aitor Larrañaga, Karmele Vidal, María Isabel Arriortua
Título: $LaNi_{0.6}Co_{0.4}O_{3-\delta}$ and $(La_{0.8}Sr_{0.2})_{0.95}Fe_{0.6}Mn_{0.3}Co_{0.1}O_3$ compounds as contact materials for intermediate temperature solid oxide fuel cells.
Presentación: Póster

5.- IV Iberian Symposium on Hydrogen, Fuel Cells and Advanced Batteries. Hyceltec 2013. Estoril (Portugal), 26-28 de Junio de 2013.
Autores: Aroa Morán-Ruiz, Aitor Larrañaga, Karmele Vidal, María Isabel Arriortua
Título: $LaNi_{0.6}Fe_{0.4}O_{3-\delta}$ (LNF) as contact material between Crofer22APU interconnect and $La_{0.6}Sr_{0.4}FeO_3$ (LSF) cathode for IT-SOFC.
Presentación: Póster

6.- XXIV SIMPOSIO del GE3C. Cristalografía y Sostenibilidad. Kristalografia eta Jasangarritasuna. Bilbao (España), 23-26 de Junio de 2014.
Autores: Karmele Vidal, María Jauregui-Vicente, Aroa Morán-Ruiz, Aitor Larrañaga, María Isabel Arriortua
Título: Condiciones de preparación y propiedades de las perovskitas $La_{1-x}Nd_xNi_{0.6}Fe_{0.4}O_3$ (x = 0, 0.3 y 0.5) como material capa de contacto entre cátodo e interconector para IT-SOFCs.
Presentación: Oral

7.- XXIV SIMPOSIO del GE3C. Cristalografía y Sostenibilidad. Kristalografia eta Jasangarritasuna. Bilbao (España), 23-26 de Junio de 2014.
Autores: María Jauregui-Vicente, Karmele Vidal, Aroa Morán-Ruiz, Aitor Larrañaga, María Isabel Arriortua
Título: Síntesis y propiedades de las capas de contacto $La_{1-x}Nd_xNi_{0.6}Fe_{0.4}O_3$ (x = 0, 0.3 y 0.5) para su aplicación en celdas SOFCs.
Presentación: Póster

8.- 11th European SOFC and SOE Forum 2014. Lucerna (Suiza), 1-4 de Julio de 2014.
Autores: Aroa Morán-Ruiz, Karmele Vidal, Aitor Larrañaga, Miguel Ángel Laguna-Bercero, Jose Manuel Porras-Vázquez, Peter Raymond Slater, María Isabel Arriortua
Título: Feasibility of using LNF-coated Crofer22APU mesh as cathode contact material for SOFC.
Presentación: Póster

9.- 11th European SOFC and SOE Forum 2014. Lucerna (Suiza), 1-4 de Julio de 2014.
Autores: Karmele Vidal, Aroa Morán-Ruiz, Aitor Larrañaga, Miguel Ángel Laguna-Bercero, Jose Manuel Porras-Vázquez, Peter Raymond Slater, María Isabel Arriortua
Título: Combustion synthesis of $LaNi_{0.6}Fe_{0.4}O_3$ perovskite as cathode contact material for IT-SOFCs.
Presentación: Póster

10.- 1st International Symposium on Energy Challenges & Mechanics. Aberdeen, Escocia, UK, 8-10 de Julio de 2014.
Autores: Aroa Morán-Ruiz, Karmele Vidal, Aitor Larrañaga, María Isabel Arriortua
Título: Development of Solid Oxide Fuel Cell (SOFC) components.
Presentación: Oral

11.- The Energy and Materials Research Conference (EMR2015). Madrid, 25-27 de Febrero de 2015.
Autores: Karmele Vidal, Aitor Larrañaga, Aroa Morán-Ruiz, Miguel Ángel Laguna-Bercero, María Pilar Yeste, José Juan Calvino, María Isabel Arriortua
Título: Effect of the A cation size disorder and synthesis conditions on the properties of an iron perovskite series.
Presentación: Póster

12.- V Iberian Symposium on Hydrogen, Fuel Cells and Advance Batteries (HYCELTEC2015). Tenerife, 5-8 de Julio de 2015.
Autores: Karmele Vidal, Aitor Larrañaga, Aroa Morán-Ruiz, Andrés Tomas Aguayo, Miguel Ángel Laguna-Bercero, María Pilar Yeste, Jose Juan Calvino, María Isabel Arriortua
Título: Characterization of $La_{0.15}Sm_{0.35}Sr_{0.08}Ba_{0.42}FeO_{3-\delta}$ perovskite: effect of synthesis conditions.
Presentación: Póster

13.- XXXV Bienal RSEQ. A Coruña, 19-23 de Julio de 2015.
Autores: Aritza Wain, Aroa Morán-Ruiz, Karmele Vidal, Aitor Larrañaga, María Isabel Arriortua
Título: Materials para su aplicación en celdas SOFCs.
Presentación: Póster

14.- ECS Conference on Electrochemical Energy Conversion & Storage with SOFC-XIV. Glasgow (Escocia), 26-31 de Julio de 2015.
Autores: Aroa Morán-Ruiz, Karmele Vidal, Aitor Larrañaga, Peter Raymond Slater, María Isabel Arriortua.
Título: Metallic/ceramic (Fe-22Cr mesh/$LaNi_{0.6}Fe_{0.4}O_{3-\delta}$) composite as contact material for SOFCs.
Presentación: Póster.

ORIGINAL RESEARCH PAPER

Fuel Cells DOI: 10.1002/fuce.201300016

Chemical Compatibility and Electrical Contact of $LaNi_{0.6}Co_{0.4}O_{3-\delta}$ (LNC) between Crofer22APU Interconnect and $La_{0.6}Sr_{0.4}FeO_3$ (LSF) Cathode for IT-SOFC

A. Morán-Ruiz[1], K. Vidal[1], A. Larrañaga[1]*, M. I. Arriortua[1]*

[1] Facultad de Ciencia y Tecnología, Departamento de Mineralogía y Petrología, Universidad del País Vasco (UPV/EHU), Barrio Sarriena S/N, 48940 Leioa, Vizcaya, Spain

Received January 18, 2013; accepted April 11, 2013; published online April 30, 2013

Abstract

In order to simulate the contact situation of interconnect/contact layer/cathode in SOFC stacks, contact resistance and chemical compatibility of $LaNi_{0.6}Co_{0.4}O_{3-\delta}$ (LNC) as contact layer between Crofer22APU interconnect and $La_{0.6}Sr_{0.4}FeO_3$ (LSF) cathode was investigated at 800 °C in air for more than 1300 h using X-ray diffraction (XRD), scanning electron microscopy (SEM) set-up equipped with an energy dispersive X-ray analyser (EDX) and area specific resistance (ASR) measurements. The XRD analysis reveals that multiple phases were formed during ASR test. The point microanalysis on cross-section of Fe–Cr/LNC/LSF system, after ASR measurements, shows chromium within the porous contact material mainly concentrated close to interconnect, but no Cr, Ni ,or Co was detected in the cathode. It was found between LNC and LSF cathode, a thin and uniform layer which contains Sr, La, Cr, Co, Ni, and Fe. The contact between layers could act as a physical barrier for element migration and thus can suppress degradation of the cathode for these systems. The area specific resistance slope depends on the interactions between the contact material and/or cathode and the interconnect. Co-containing spinels formed during ASR test can be responsible of the resistance decrease of the system, related to the low degradation of the cell.

Keywords: Area specific resistance, Chemical compatibility, Interconnect, LNC contact material, Solid oxide fuel cells

1 Introduction

In recent years, great efforts have been dedicated to develop low or intermediate temperature solid oxide fuel cells (IT-SOFC) operating at 500–800 °C. Lowering the operating temperature will improve cell durability and reduce the system final cost [1]. Thus, it can suppress degradation of components and extend the range of acceptable material selection, such as metallic interconnects like Crofer22APU [2]. However, there always exists a ceramic/metallic interface, which potentially contributes to a high contact resistance and thus to power losses [3–5]. Recent investigations [6] indicate the necessity to distinguish experimentally the resistance associated with the electrode coating/current collector contact from the total cell resistance due to the high value of the contact resistance associated with it.

Connection of the cathode to the interconnect is usually accomplished by compression of the stack using an external load frame, and is helped by use of a contact material layer between the porous ceramic cathode and metallic interconnect. Thus, a suitable cathode contact material minimizes the interfacial electrical resistance and maximizes the power output of SOFC stacks.

The cathode contact material is required to possess high electrical conductivity and appropriate sintering activity to minimize the resistance of the contact layer itself and to protect the steel substrate from excessive oxidation. Besides, it must be chemically compatible with both the protective materials or chromia-forming interconnects and the perovskite cathodes. The contact material, as well as, its reaction products should demonstrate an appropriate thermal expansion behavior and high thermochemical and structural stability in the oxidizing cathode environment [7, 8].

Cathode/interconnect contact materials in SOFC includes many types of compounds: (i) noble metals (Ag) or noble

[*] *Corresponding authors, maribel.arriortua@ehu.es, aitor.larranaga@ehu.es*

metal-perovskite composites (Ag–$(La_{0.6}Sr_{0.4})(Co_{0.8}Fe_{0.2})O_3$, Ag–$La_{0.8}Sr_{0.2}MnO_3$), (ii) conventional perovskite cathode materials (such as, $LaNi_{0.6}Fe_{0.4}O_3$, $La_{0.8}Sr_{0.2}Co_{0.75}Fe_{0.25}O_3$, $La_{0.8}Sr_{0.2}FeO_3$), (iii) oxides with a spinel structure, M_3O_4 (M = Ni, Mn, Co, Cu, Fe), or (iv) recently developed compositions like $Ni_{0.33}Co_{0.67}O$. Despite of interactions of these kind of materials with Cr-containing steel interconnects, due to their susceptibility to form phases like Ag_2CrO_4, $AgCrO_2$, $SrCrO_4$, Cr-spinels, or Cr-perovskites, the use of those materials, in most of the cases, are quite effective for improving the electrical contact between the cathodes and metallic interconnects [9–14].

In the present study LNC contact layer is symmetrically sandwiched between Crofer22APU metallic interconnect and LSF ceramic cathode, following Crofer22APU/LNC/LSF/Pt/LSF/LNC/Crofer22APU configuration, to measure the contact area specific resistance (ASR). Long time chemical compatibility of the system was tested after 1300 h at 800 °C in air. Previously the feasibility of combining LNC as contact material and LSF as cathode was checked.

2 Experimental

The Crofer22APU alloy used in the present study is a Fe–Cr based alloy that was developed for application of metallic interconnects in intermediate temperature SOFCs. It was provided by Thyssenkrupp VDM, and its chemical composition, given by the supplier, is listed in Table 1. The powder materials used were: $LaNi_{0.6}Co_{0.4}O_{3-\delta}$ (LNC; NexTech, Fuel Cell Material) as contact material, and $La_{0.6}Sr_{0.4}FeO_3$ (LSF; NexTech, Fuel Cell Material) as cathode material.

For conductivity measurements, to achieve full density, LNC and LSF were sintered at 1200 and 1150 °C for 5 h, respectively. The electrical conductivity was measured with the standard dc four-point method on rectangular bars of approximate dimensions 1 mm × 3 mm × 7 mm. Two Pt electrodes were utilized for conducting current along the length, and two Pt electrodes were used for measuring voltage across the section at a certain distance (Figure 1). Conductivity measurements were performed from room temperature to 900 °C in air using a heating rate of 2 °C min^{-1} using a power source controlled by PC using Lab Windows/CVI field point system.

Table 1 Composition of the steel in wt.%.

	Cr	Fe	Mn	Ti	Si	Al	Mo	Others
Crofer22APU	76.45	22.78	0.4	0.07	0.02	0.006	–	La 0.086

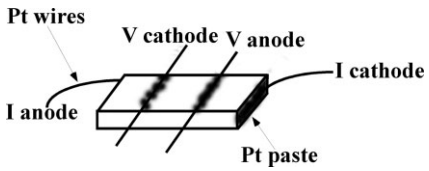

Fig. 1 Schematic representation for conductivity measurements by the four-probe dc method of LNC and LSF.

In order to understand the chemical compatibility between the contact material and cathode, both materials were thoroughly mixed (50:50 wt.%). Ten grams of each sample with 220 g of zirconia balls and 25 ml of acetone were milled during 8 h and then, the solvent was evaporated. The starting materials and the powders mixture, were sintered at 950 °C for 2 h and then treated at 800 °C for 1080 h in air.

The contact and compatibility evaluation of contact layer between a Crofer22APU interconnect and LSF cathode was carried out with the interconnect pre-oxidized at 800 °C for 100 h. Prior to the oxidation, the sheets were cut into 10 × 10 mm squares with 1 mm thicknesses. Metals were polished using #800 grit SiC and cleaned with acetone in an ultrasonic bath and dried. It was necessary to pre-oxidized interconnect to reduce interfacial stress over time between the contact material and the interconnect [15]. The deposition of the contact materials was carried out using wet colloidal spray deposition technique on interconnects and sintered at 1050 °C for 2 h to obtain a rather dense coating. LSF cathode was deposited on contact layer using the same deposition technique and sintered at 950 °C for 2 h to produce a porous layer. The suspensions were made mixing in a ball mill during 1 h the powders, ethanol and ZrO_2 cylinders as grinding media. An assembly of Crofer22APU/LNC/LSF was symmetrically sandwiched following the configuration showed in Figure 2. In order to achieve a better mechanical contact during measurement a 1 kg cm^{-2} weight is placed on top of the layer system. The overall ASR of the Crofer22APU/LNC/LSF setup was measured by four-point method at 800 °C for up to 1316 h. Pt wires were spot-welded on the opposite side to the interconnect and the area was painted by Pt paste. Area specific resistance (ASR) was estimated by the voltage value measured after applying a current of 300 mA.

X-ray diffractometer (XRD, X'Pert PRO) with Cu kα radiation (λ = 1.5418 Å) was used to identify the commercial materials, to study the evolution of the LNC, LSF, and the LNC-LSF mixture after they prolonged heating at 800 °C, and to analyze the possible chemical process after the ASR test. The power generator has been provided at 40 kV and 40 mA. The patterns were recorded in 2θ steps of 0.026° in the 15–95°

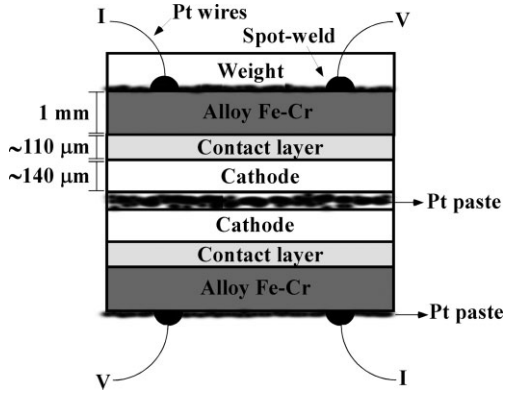

Fig. 2 Sample setup for contact ASR measurement of the Crofer22APU/LNC/LSF symmetrical system.

range, counting for 181 second per step. In addition, scanning electron microscope (SEM, JEOL LSM-6400) equipped with an Oxford Pentafet energy dispersive X-ray analyzer (EDX) was used for cross-sectional microstructure examination and composition analysis. The composition analysis on the sample cross-section was made using back-scattered electrons (BSE) at 20 kV accelerating voltage, 1×10^{-9} A current density and 15 mm working distance. Due to the overlap of the emission lines for the studied elements (Table 2), the INCA 350 software from Oxford was used to reconstruct the spectra and it was compared with measured one and to confirm the presence or absence of these elements.

Table 2 The principal emission lines for analyzed elements.

Element	Kα (keV)	Kβ (keV)	Lα (keV)
La			4.650
Cr	5.411	5.946	
Mn	5.894	6.489	
Fe	6.398	7.057	
Co	6.924	7.648	
Ni	7.471	8.263	

3 Characterization and Results

The crystal structure given by technical specifications of studied materials (LNC, LSF, and Crofer22APU) were checked by XRD. Figure 3 shows the X-ray full-profile refinement of starting materials fitted by the Rietveld method. The quantitative analysis shows that the analyzed materials are pure except LNC in which two very weak peaks corresponding to NiO were found (1.5% in weight).

Figure 4 presents full-profile refinements of contact and cathode materials and the mixture of both (50:50 wt.%) after been sintered at 950 °C for 2 h and been treated at 800 °C for 1080 h in air. The resulting Rietveld analysis demonstrates that LNC remains stable after prolonged heating in air, but the cathode degrades to LSF phase (91.8 wt.%), $LaSrFeO_4$ (6.6 wt.%), and Fe_3O_4 (1.6 wt.%). Nevertheless, for the treated mixture no reactions products were identified; only the starting NiO corresponding to the contact material, so it can be concluded that the use of LNC/LSF might avoid the formation of decomposition phases from the cathode.

The conductivity of LNC and LSF was measured in the temperature range from room tempera-

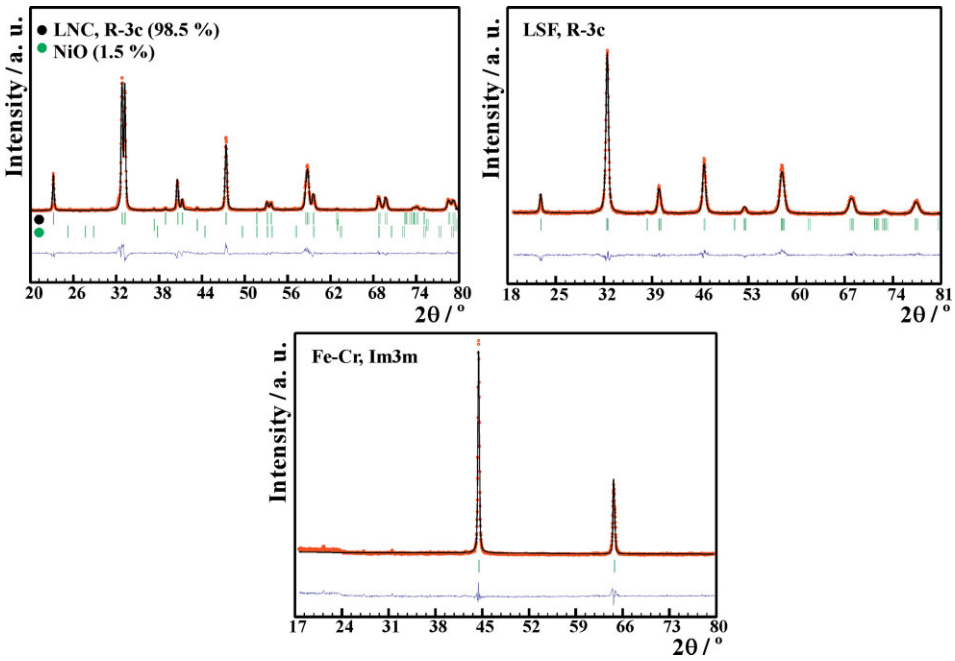

Fig. 3 Rietveld X-ray diffraction patters for commercial LNC, LSF and Crofer22APU materials. Circles denote experimental points; upper solid lines are calculated profiles. Theoretical peak positions (vertical sticks) and difference lines are shown in the bottom of each pattern.

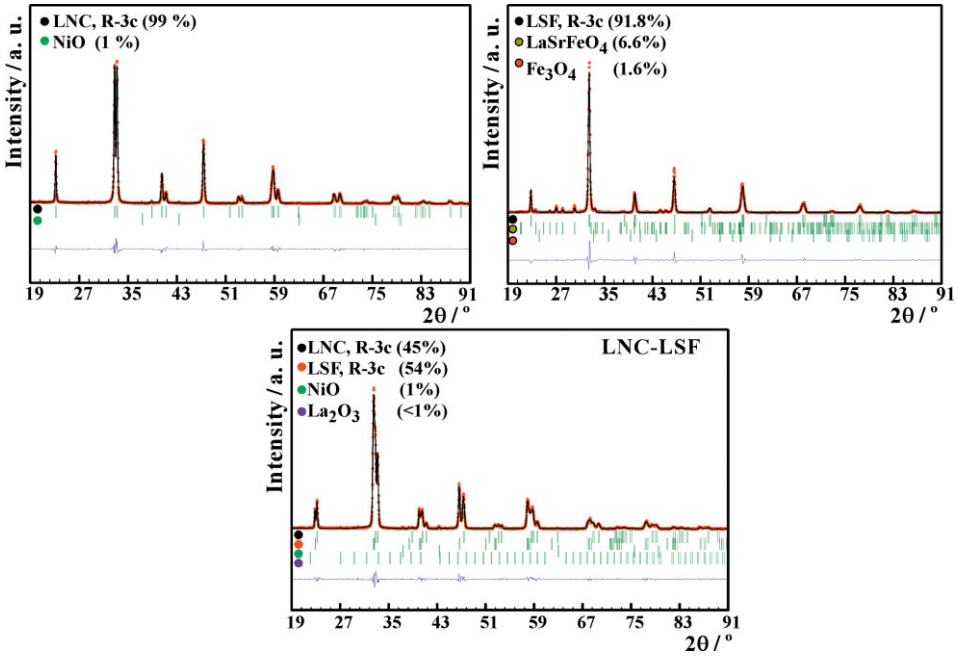

Fig. 4 Rietveld analysis of LNC, LSF and LNC-LSF mixture after heated at 800 °C for 1080 h in air.

ture to 900 °C, as shown in Figure 5. The electronic conductivity of LNC is mainly carried by the narrow itinerant conduction band of the Ni-arrays [16] so this material exhibits metallic like conductivity. For LSF material the electrical conduction occurs by thermally activated of small polarons hopping as was shown in previous researches [17–19].

The conductivity values of LNC and LSF at 800 °C are ≈1200 and ≈200 S cm^{-1}, respectively, in good agreement with the observed in other works for these type of compounds [20,21]. Those values are appropriated to use LNC as contact material in solid oxide fuel cells.

The chemical compatibility of LNC with LSF at 800 °C after 1080 h and their appropriate values of conductivity make possible to use these materials.

3.1 ASR Measurements and Post-Test Analysis

The XRD results of the Crofer22APU/LNC/LSF system after ASR test at 800 °C in air for 1080 h, presented in Figure 6, reveal that the main and secondary phases are (La,Sr)(Ni,Co,Fe)O_3 (rhombohedral, space group: R-3c), (La)(Ni,Co,Cr)O_3 (rhombic, space group: Pbnm) and $SrCrO_4$, NiO, respectively. Apart from those compounds, $SrNiO_3$, Cr_2O_3, and the M_3O_4 (M = Fe, Mn, Ni, Co, or Cr) spinel can be observed in smaller amount. The original Fe–Cr substrate was identified indicating that the X-ray penetration was enough to observe the signal of all the formed layers. Due to the similarity of the ionic radio of Cr, Mn, Ni, Co, and/or Fe, it is difficult to determine the exact chemistry of the M_3O_4 spinel using the XRD technique.

The formation of (La)(Ni, Co, Cr)O_3 can be understood through two possible mechanism, according to the following equations [22].

$$1.5Cr_2O_3(s) + 3(La)(Ni,Co)O_3 = 3(La)(Ni_yCo_xCr_{1-x-y})O_3 + (Cr_{1-x-y}Co_xNi_y)_3O_4 + 0.25O_2 \quad (1)$$

$$3CrO_3(g) + 3(La)(Ni,Co)O_3 = 3(La)(Ni_yCo_xCr_{1-x-y})O_3 + (Cr_{1-x-y}Co_xNi_y)_3O_4 + 2.5O_2 \quad (2)$$

The structure of Cr-containing perovskite is rhombic in contrast to LNC which is rhombohedral. The deconvolution of doublet peak (in the range of 39–42° in 2θ) provides the option to detect the rhomboedral and rhombic phases (Figure 7), this procedure was described in previous studies [23]. For the pure LNC, heated at 800 °C in air for 1080 h, two single peaks can be indexed as (202) and (006) of the rhomboedral phase. In the sample Crofer22APU/LNC/LSF after heated in the same conditions, two single peaks begin evolving into a double peak with additional two reflections of the rhombic phase indicating the presence of both rhombohedral and rhombic perovskite phases.

The cross-section back-scattered electron image of the Crofer22APU/LNC/LSF interface after ASR measurements (Figure 8a) shows poor sinterability between particles and large holes were detected in the contact layer. Their presence could be an accidental effect due to a surface inhomogeneity in the steel. Nevertheless, the contact layer looks adherent to the cathode.

Throughout the contact layer can be observed differences in the emission of the backscattered electrons from different regions. High average atomic number layers were close to the cathode material. In addition a white colored thin and uniform layer was formed between the contact layer and the cathode. The surface of Crofer22APU was covered by a thin and discontinuous oxide scale.

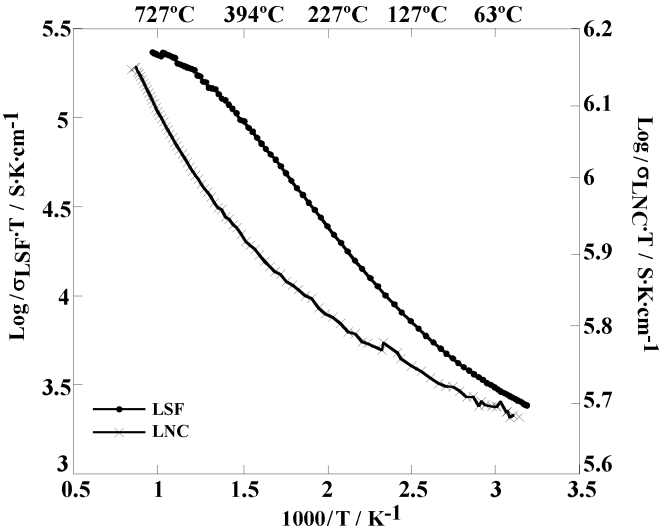

Fig. 5 Arhenius plot of $LaNi_{0.6}Co_{0.4}O_{3-\delta}$ and $La_{0.6}Sr_{0.4}FeO_3$ perovskites as a function of temperature.

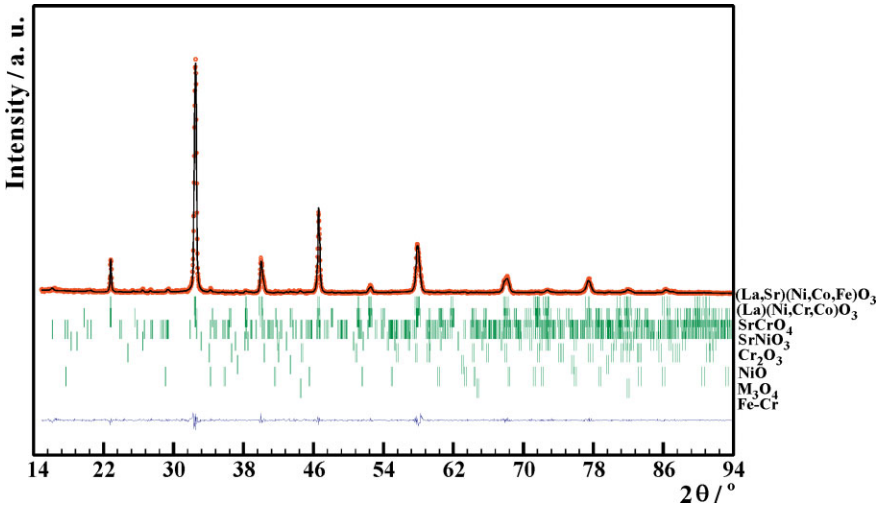

Fig. 6 Pattern matching of Crofer22APU/LNC/LSF system after heated at 800 °C in air for 1080 h.

ORIGINAL RESEARCH PAPER

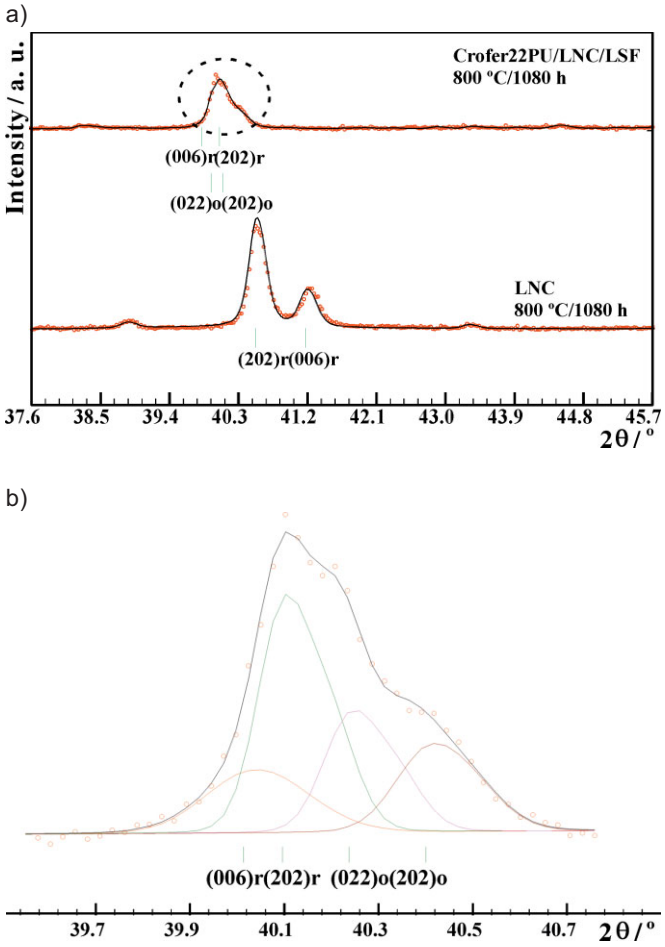

Fig. 7 (a) X-ray diffraction peaks variation of LNC and Crofer22APU/LNC/LSF system after heated at 800 °C in air for 1080 h, in the 2θ range ≈37° to 45°, and (b) deconvolution of formed signal of system.

EDX was used to estimate the extent of element interdiffusion across assembly interfaces. Linescans were produced from a points analysis along the sample, representative results are shown in Figure 8b. Large amounts of Cr were detected all around the contact material, especially in the first 45 µm, but no chromium was detected within the cathode neither Ni nor Co. The small white layer between the contact material and the cathode contains La, Sr, Cr, Co, Ni, and Fe, so the contact itself could act as a barrier for element diffusion.

Figure 9 shows variation of ASR of Crofer22APU/LNC/LSF contact with testing time at 800 °C in air. The obtained signal was relatively stable near 0.04 Ω cm^2 until the end of the test. Different studies, point out the relative initial ASR follows the trend of the conductivity of the contact layer [10]. After 1300 h, the low degradation of ASR is likely due to small element migration between interconnect and contact materials to form Co-containing spinels, which protects the Cr poisoning and improves the scale conductivity of the system.

The aim of this work was to simulate the contact situation of Crofer22APU/LNC/LSF in IT-SOFC conditions. After prolonged heating at 800 °C in air, $SrCrO_4$ might have been formed between contact layer and the cathode. The presence

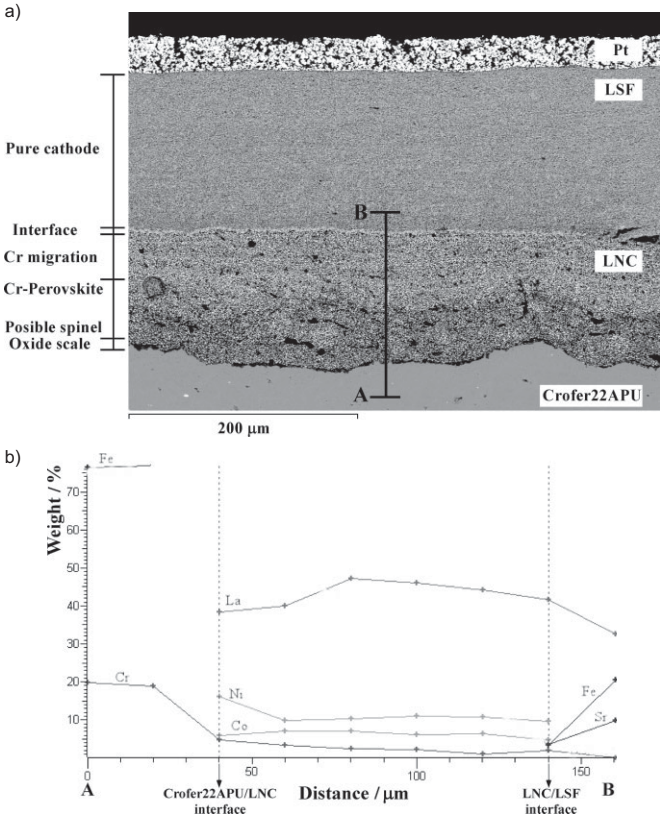

Fig. 8 (a) SEM cross-section (back-scattered electron image) of Crofer22APU/LNC/ LSF system after heated at 800 °C for 1300 h in air with (b) representative results to estimate the extent of interdiffusion at the system interfaces from EDX points analysis.

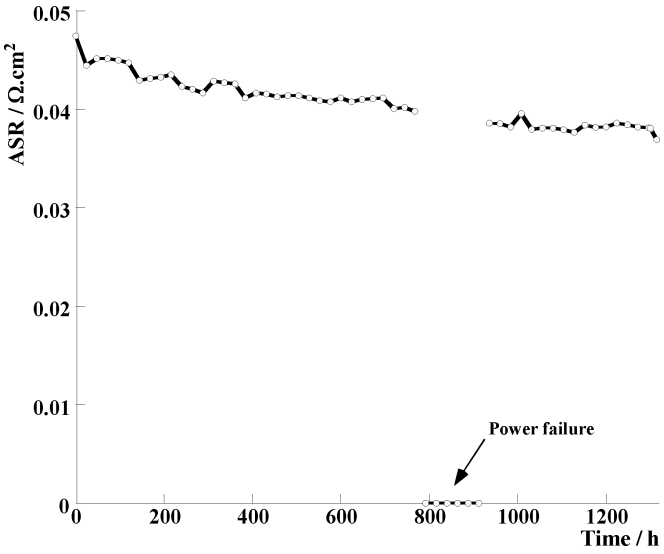

Fig. 9 Area specific resistance (ASR) for Crofer22APU/LNC/LSF system as a function of time.

of NiO and $SrNiO_3$ might mean that Ni was practically extracted from LNC perovskite lattice, whereas Cr was incorporated to form a rhombic $La(Ni,Co,Cr)O_3$ phase, which was mainly concentrated in the first 50 µm of contact layer. The use of LNC as contact layer with thicknesses of 110 µm might

avoid migration of elements toward the cathode. In addition, the low presence of Cr_2O_3 suggests that this element presents diffusion to be incorporated to the spinel phase, or that the growth rate of created metal oxides on the metal surface, under oxidation atmosphere, could be lowered if a conductive layer, such as LNC coated, is applied on the surface of interconnect.

4 Conclusion

After checked the feasibility of LNC as contact material using LSF as cathode, the contact situations of LNC between Crofer22APU interconnect and LSF was studied after prolonged heating at 800 °C in air. From the results obtained, the following conclusions could be extracted.

The combination of LNC contact layer and LSF cathode with Crofer22APU interconnect leads to the formation of, principally, $(La,Sr)(Ni,Co,Fe)O_3$, $La(Ni,Co,Cr)O_3$, $SrCrO_4$, and NiO phases. Therefore, this result demonstrates the intrinsic instability of the LNC and LSF when Cr-containing metallic interconnect is in direct contact with them.

LNC/LSF contact interface acts as physical elements diffusion barrier. Thus prevents the migration of Cr, Ni, Co toward the cathode.

The ASR contributed by the Crofer22APU/LNC/LSF contact, around 0.04 Ω cm^2, is acceptable for the performance of a SOFC stack operated in the intermediate temperature range (600–800 °C). Co-containing spinels formed during the ASR test reduce the resistance of the system.

Taking into account the previous points, LNC material would seem to offer promising opportunities as a Cr-resistant contact coating.

Acknowledgement

This research has been funded by the Consejería de Industria, Innovación, Comercio y Turismo (SAIOTEK 2012 programmes), by the Consejería de Educación, Universidades e Investigación of the Basque Goverment (IT-177-07) and by Ministerio de Ciencia e Innovación (MAT2010-15375). The authors thank Ikerlan's Fuel Cell group and SGIker technical support (UPV/EHU, MEC, GV/EJ, and European Social Fund). A. Morán-Ruiz thanks UPV/EHU for funding her PhD work.

References

[1] D. J. L. Brett, A. Atkinson, N. P. Brandon, S. J. Skinnerd, *Chem. Soc. Rev.* **2008**, *37*, 1568.
[2] V. Miguel-Perez, A. Martínez-Amesti, M. L. Nó, A. Larrañaga, M. I. Arriortua, *Corros. Sci.* **2012**, *60*, 38.
[3] W. B. Guan, H. J. Zhai, L. Jin, T. S. Li, W. G. Wang, *Fuel Cells* **2011**, *3*, 445.
[4] S. P. Jiang, J. G. Love, L. Apateanu, *Solid State Ionics* **2003**, *160*, 15.
[5] M. C. Tucker, L. Cheng, L. C. Dejonghe, *J. Power Sources* **2011**, *196*, 8313.
[6] S. P. Jiang, *J. Electrochem. Soc.* **2001**, *148*, A887.
[7] Z. Yang, G. Xia, P. Singh, J. W. Stevenson, *J. Power Sources* **2006**, *155*, 246.
[8] B. P. McCarthy, L. R. Pederson, Y. S. Chou, X. D. Zhou, W. A. Surdoval, L. C. Wilson, *J. Power Sources* **2008**, *180*, 294.
[9] L. T. Wilkinson, J. H. Zhu, *J. Electrochem. Soc.* **2009**, *156*, B905.
[10] X. Montero, F. Tietz, D. Stöver, M. Cassir, I. Villarreal, *J. Power Sources* **2009**, *188*, 148.
[11] Z. Lu, G. Xia, J. D. Templeton, X. Li, Z. Nie, Z. Yang, J. W. Stevenson, *Electrochem. Commun.* **2011**, *13*, 642.
[12] M. T. Tucker, L. Cheng, L. C. Dejonghe, *J. Power Sources* **2011**, *196*, 8435.
[13] F. Wang, D. Yan, W. Zhang, B. Chi, J. Pu, L. Jian, *Int. J. Hydrogen Energ.* **2013**, *38*, 646.
[14] W. Zhang, F. Wang, K. Wang, J. Pu, B. Chi, L. Jian, *Int. J. Hydrogen Energ.* **2012**, *37*, 17253.
[15] K. O. Hoyt, P. E. Gannon, P. White, R. Tortop, B. J. Ellingwood, H. Khoshuei, *Int. J. Hydrogen Energ.* **2012**, *37*, 518.
[16] A. Huang, K. Yao, J. Wang, *J. Electroceram.* **2006**, *16*, 313.
[17] M. Sogaard, P. V. Hendriksen, M. Mogensen, *J. Solid State Chem.* **2007**, *180*, 1489.
[18] K. Vidal, L. M. Rodríguez-Martínez, L. Ortega-San-Martín, M. L. Nó, T. Rojo, M. I. Arriortua, *Fuel Cells* **2011**, *11*, 51.
[19] Ana Écija Verdejo, Óxidos Mixtos Tipo Perovskita $Ln_{0.5}M_{0.5}FeO_{3-\delta}$ (Ln = La, Sm, Nd, Gd; M = Ba, Sr) para su Aplicación como Cátodos en Pilas SOFC. *Thesis*, University of Basque Country, Bilbao, Spain, **2012**.
[20] C. Sun, R. Hui, J. Roller, *J. Solid State Electrochem.* **2009**, *14*, 1125.
[21] A. Huang, K. Yao, J. Wang, *J. Electroceram.* **2006**, *16*, 313.
[22] S. P. S. Badwal, R. Deller, K. Foger, Y. Ramprakash, J. P. Zhang, *Solid State Ionics* **1997**, *99*, 297.
[23] M. K. Stodolny, B. A. Boukamp, D. H. A. Blank, F. P. F. van Berkela, *J. Electrochem. Soc.* **2011**, *158*, B112.

Journal of Power Sources 248 (2014) 1067–1076

Contents lists available at ScienceDirect

Journal of Power Sources

journal homepage: www.elsevier.com/locate/jpowsour

Effects of using $(La_{0.8}Sr_{0.2})_{0.95}Fe_{0.6}Mn_{0.3}Co_{0.1}O_3$ (LSFMC), $LaNi_{0.6}Fe_{0.4}O_{3-\delta}$ (LNF) and $LaNi_{0.6}Co_{0.4}O_{3-\delta}$ (LNC) as contact materials on solid oxide fuel cells

Aroa Morán-Ruiz [a], Karmele Vidal [a], Miguel Ángel Laguna-Bercero [b], Aitor Larrañaga [a,*], María Isabel Arriortua [a,*]

[a] Universidad del País Vasco (UPV/EHU), Facultad de Ciencia y Tecnología, Departamento de Mineralogía y Petrología, Barrio Sarriena S/N, 48940 Leioa, Vizcaya, Spain
[b] Instituto de Ciencia de Materiales de Aragón, ICMA, CSIC-Universidad de Zaragoza, Pedro Cerbuna 12, 50009 Zaragoza, Spain

HIGHLIGHTS

- Lanthanum-based perovskite ceramic contact materials were studied.
- Contact resistance of $La_{0.6}Sr_{0.4}FeO_3$/contact layer/Crofer22APU is evaluated.
- Contact resistance of contact materials studied depends on their conductivity.

ARTICLE INFO

Article history:
Received 12 July 2013
Received in revised form
23 September 2013
Accepted 2 October 2013
Available online 23 October 2013

Keywords:
SOFC
Interconnect
Contact perovskite
Ohmic resistance losses
Electrical contact

ABSTRACT

Three lanthanum-based perovskite ceramic compounds were studied as contact materials, $(La_{0.8}Sr_{0.2})_{0.95}Fe_{0.6}Mn_{0.3}Co_{0.1}O_3$ (LSFMC), $LaNi_{0.6}Fe_{0.4}O_{3-\delta}$ (LNF) and $LaNi_{0.6}Co_{0.4}O_{3-\delta}$ (LNC), between a Crofer22APU interconnect and a $La_{0.6}Sr_{0.4}FeO_3$ (LSF) cathode. The layers were deposited using in all cases wet colloidal spray technique. Phase structures of materials were checked by X-ray Diffraction (XRD) measurements. Electrical conductivity and thermal expansion coefficient (TEC) for these selected compounds were also determined.

The important properties of the resulting {interconnect/contact layer/cathode} systems; including area specific resistance (ASR), reactivity, and adhesion of contact materials to the interconnect and to the cathode were investigated. Moreover, the electrical resistance and reactivity of the system without a contact layer, {steel/LSF/LSF} system, was measured for comparison. The contact resistance is strongly influenced by the conductivity of selected contact materials, showing the lowest ASR values for {Crofer22APU/LNC/LSF} assembly. The point microanalysis on cross-section of the systems, after ASR measurements, reveals that there is chromium enrichment in the contact and cathode layers which allows the formation of phases like $SrCrO_4$ and Cr-containing perovskite in short exposure times. An adequate integrity and low reactivity is achieved when LNF contact coating is applied between Crofer22APU and LSF cathode without compromising the contact resistance of the system.

1. Introduction

Despite IT-SOFCs advantages, lacks of contact between interconnect ribs and electrode is still unsolved. The interfacial adhesion between the oxide scale and electrode is very important for the durability of the cell [1]. To solve this problem, cathode contact layers are used between interconnect an electrode, and is often accomplished by compression of the stack using and external load frame [2,3]. In practice, however, adhesion between contact material/interconnect needs even to be improved. Cathode contact materials, apart from providing electrical contact between adjacent components, can also serve to improve in-plane conduction over the area of the cathode. In this case, contact material acts as a layer of the electrocatalyst used in the cathode [4,5].

Earlier studies have concluded that the use of cathode contact layers improves electrons transfer through the contact interface from interconnect to activate cathode layer [6]. Therefore, the

* Corresponding authors. Tel.: +34 946012534, +34 946015984.
E-mail addresses: aitor.larranaga@ehu.es (A. Larrañaga), maribel.arriortua@ehu.es (M.I. Arriortua).

0378-7753/$ – see front matter © 2013 Elsevier B.V. All rights reserved.
http://dx.doi.org/10.1016/j.jpowsour.2013.10.031

Table 1
Sintering procedure used for fabrication of rectangular bars for electrical conductivity and the degree of compaction (%) obtained for each material.

Composition	Sintering procedure	Relative density (%)[a]
LNF	1350 °C, 5 h	90
LSFMC	1250 °C, 10 h	98
LNC	1200 °C, 5 h	79
LSF	1150 °C, 5 h	93

[a] Theoretical density was calculated from the results obtained in Rietveld analysis. Experimental density was determinated geometrically from the volume and weight of the samples.

oxygen reduction reaction in the cathode triple-phase boundaries has more electrons from the interconnect, resulting in a substantial increase in cell performance. It was also found that cell degradation inside the stack, is principally dependent on the interfacial contact between the cathode current collecting layer and the interconnect [7].

The cathode contact material composition is required to possess high electrical conductivity and appropriate sintering activity to minimize the resistance of the contact layer itself and to protect the steel substrate from excessive oxidation. Besides, it must be chemically compatible with both the protective materials or chromia-forming interconnects and the perovskite cathodes. The contact material, as well as, its reaction products should demonstrate an appropriate thermal expansion behavior and high thermochemical and structural stability in the oxidizing cathode environment [8,9].

Cathode/interconnect contact materials in SOFCs include many type of compounds: i) noble metals (Ag) or noble metal–perovskite composites (Ag-$(La_{0.6}Sr_{0.4})(Co_{0.8}Fe_{0.2})O_3$, Ag–$La_{0.8}Sr_{0.2}MnO_3$), ii) conventional perovskite cathode materials [10] (such as, $La_{0.8}Sr_{0.2}Co_{0.75}Fe_{0.25}O_3$, $La_{0.8}Sr_{0.2}FeO_3$), iii) oxides with a spinel structure, M_3O_4 (M = Ni, Mn, Co, Cu, Fe), or iv) recently developed oxides like $Ni_{0.33}Co_{0.67}O$. Despite the interactions of these kind of materials with Cr-containing steel interconnects, due to their susceptibility to form phases like Ag_2CrO_4, $AgCrO_2$, $SrCrO_4$, Cr-spinels or Cr-perovskites, the use of those materials, in most of the cases, are quite effective for improving the electrical contact between the cathodes and metallic interconnects [11–15]. In this study, $(La_{0.8}Sr_{0.2})_{0.95}Fe_{0.6}Mn_{0.3}Co_{0.1}O_3$ (LSFMC), $LaNi_{0.6}Fe_{0.4}O_{3-\delta}$ (LNF) and $LaNi_{0.6}Co_{0.4}O_{3-\delta}$ (LNC) were selected for their use as contact layers, for intermediate cell operation temperature (IT-SOFC, 600–800 °C), due to their adequate sintering activity, electrical conductivity and thermal expansion coefficient (TEC). To carry out this study, lanthanum strontium ferrite, $La_{0.6}Sr_{0.4}FeO_3$ (LSF), has been chosen as cathode due to its acceptable electric and ionic conductivity, relative control of the porosity and enough catalytic activity that allows the reduction of the oxidant gas (air or oxygen) at low operating temperatures [16]. As interconnect Crofer22APU was selected due to its good workability, high corrosion resistance and cost-effectiveness [17].

In the present research, three perovskites, LSFMC, LNF and LNC were investigated as contact materials. Phase structure using XRD, electrical conductivity and TEC values of selected materials were determinated. Results of electrical performance and chemical stability of cathode contact materials in combination with Crofer22-APU and $La_{0.6}Sr_{0.4}FeO_3$ as interconnect and cathode, respectively, are presented and discussed. In addition, the system {steel/LSF/LSF} without a contact layer was also studied for comparison. The use of different perovskites as contact materials based on its properties and, on contacting resistance and chemical compatibility of each system will be discussed.

2. Experimental

Powders of $(La_{0.8}Sr_{0.2})_{0.95}Fe_{0.6}Mn_{0.3}Co_{0.1}O_3$ (LSFMC), $LaNi_{0.6}Fe_{0.4}O_{3-\delta}$ (LNF), $LaNi_{0.6}Co_{0.4}O_{3-\delta}$ (LNC) and $La_{0.6}Sr_{0.4}FeO_3$ (LSF) were purchased from NexTech, Fuel Cell Materials, and Crofer22APU was obtained from ThyssenKrupp VDM. X-ray Diffraction (XRD) at room temperature, using a Philips X'Pert PRO diffractometer equipped with Cu K_α radiation (λ = 1.5418 Å), was used to check phase structures of the commercial materials. The power generator has been provided at 40 kV and 40 mA. The patterns were recorded in 2θ steps of 0.026° in the 18–90° range. The diffraction data of the samples were fitted in all the cases by Rietveld method using the FULLPROF program [18–20].

For bulk conductivity and TEC measurements, pellets of powders were sintered at the temperatures shown in Table 1 to achieve full density. Then, sintered pellets were cut in ~1 × 3 × 7 mm bars; the conductivity measurements were carried out with the standard dc four-point method on the rectangular sintered bars, from room temperature to 1000 °C in air with a heating rate of 2 °C min^{-1}, using a power source controlled by PC using Lab Windows/CVI field point system. The measured conductivity values were corrected taking into account the porosity of the samples [21]. Thermal expansion measurements (TEC) for the contact layers, cathode and interconnect were carried out from room temperature to 1000 °C in air with a heating rate of 5 °C min^{-1} by using a Unitherm Model 1161 dilatometer.

The contact evaluation of the studied material layers between Crofer22APU interconnect and LSF cathode was carried out with the interconnect preoxidized at 800 °C for 100 h in air in a Carbolite furnace. Prior to the oxidation, the sheets were cut into 10 × 10 mm

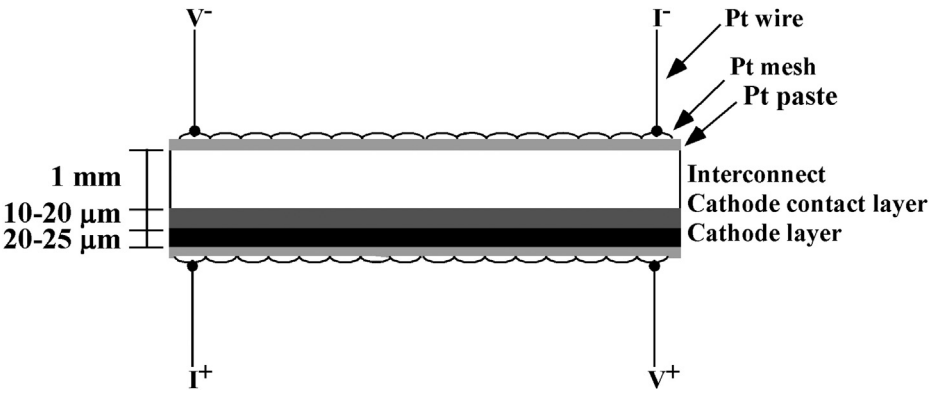

Fig. 1. Sample setup for contact ASR measurement of {Crofer22APU/contact layer/LSF} system.

Table 2
Main emission lines for the analyzed elements.

Element	K_α (keV)	K_β (keV)	L_α (keV)	L_β (keV)
La			4.650	5.041
Cr	5.411	5.946		
Mn	5.894	6.489		
Fe	6.398	7.057		
Co	6.924	7.648		
Ni	7.471	8.263		

squares with 1 mm thickness, and also were polished using #800 grit SiC, cleaned with acetone in an ultrasonic bath and dried. As observed in other studies, preoxidation of interconnect may reduce Cr and Fe transport into the contact coating, after long oxidation times. In addition, preoxidized samples developed thin coating which may decrease interfacial stress over time between the contact layer and interconnect [22]. The deposition of the contact materials was carried out using wet colloidal spray deposition technique, as was described in Refs. [23], and sintered at 1050 °C for 2 h to obtain a rather dense coating. LSF cathode was deposited on contact layers using the same deposition technique and sintered at 950 °C for 2 h to produce a porous layer. The suspensions were made mixing in a ball mill during 1 h the powders, ethanol and ZrO_2 cylinders as grinding media. For the area specific resistance (ASR) measurements a dc four-point method was used and, samples were prepared according to the geometries shown in Fig. 1. Electrical contact between the sandwich structure and external measuring circuit were obtained with two Pt wires welded to the Pt mesh at interconnect and cathode side, in combination with Pt paste onto the surface of interconnect and cathode. The overall ASR of {Crofer22APU/contact material/cathode} setup was measured at 800 °C for up to 16 h to evaluate the starting point stability of the obtained contact resistance values, and it was estimated by the voltage value measured by chronoamperometry applying a current of 300 mA, using a VSP Potentiostat/Galvanostat (Princeton Applied Research, Oak Ridge, US). Cross-section of the sandwich structures, after contact resistance measurements, were then metallographically prepared and investigated with scanning electron microscope (SEM, JEOL LSM-6400) equipped with an Oxford Pentafet energy dispersive X-ray analyzer (EDX) to study the microstructure of the systems and, to determinate extend of interdiffusion between materials. The composition analysis on the samples cross-section was made using back-scattered electrons (BSE) at 20 kV accelerating voltage, $1{\cdot}10^{-9}$ A current density and 15 mm working distance. Due to the overlap of the emission lines for the studied

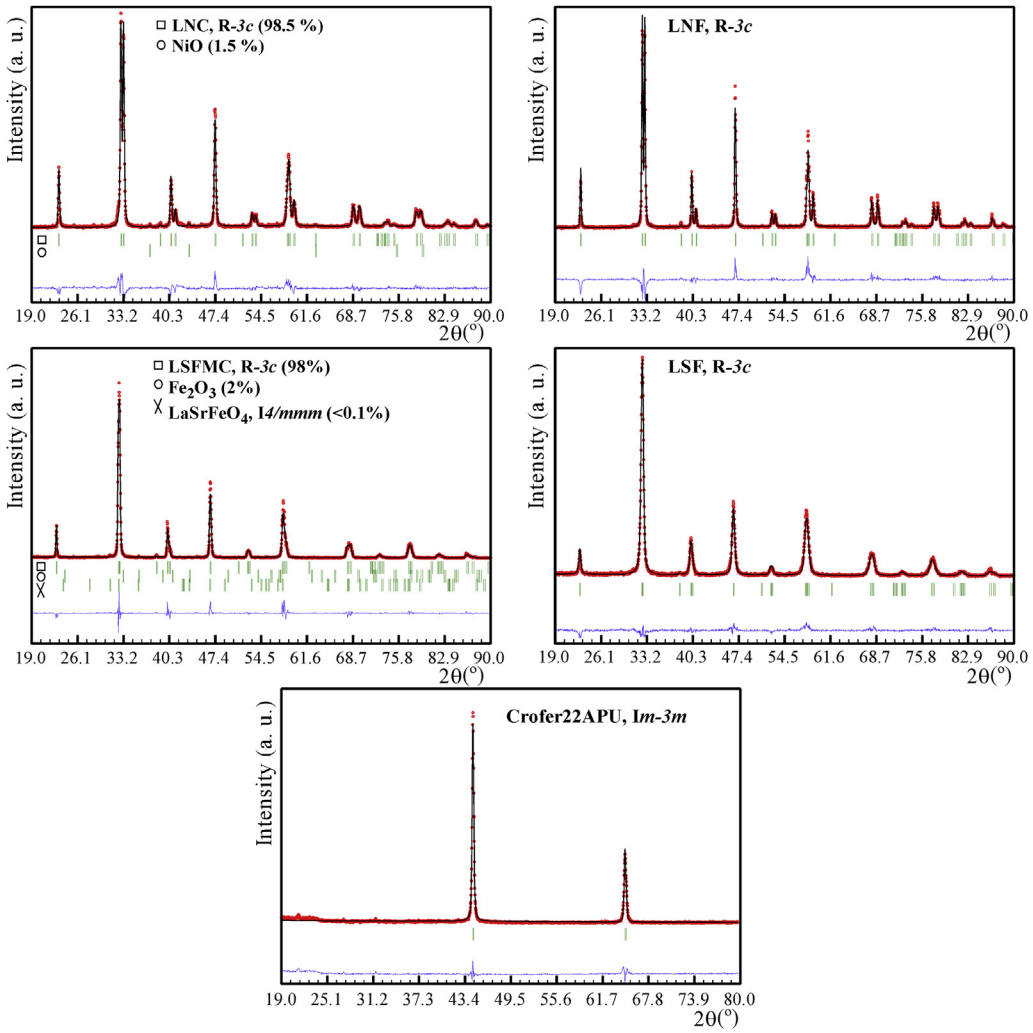

Fig. 2. Rietveld X-ray diffraction pattern refinements for commercial LSF, LSFMC, LNF, LNC and Crofer22APU materials. Circles denote experimental points; upper solid line the calculated profile. Theoretical peak positions (vertical sticks) and difference lines are shown in the bottom of each pattern.

Table 3
General structural parameters obtained from the Rietveld analysis.

Material	Space group	Lattice parameters a (Å)/c (Å)	V (Å^3)	χ^2
LNC	R-3*c*	5.459(1)/13.137(1)	339.04(1)	3.29
LNF	R-3*c*	5.513(1)/13.272(1)	349.33(1)	3.77
LSFMC	R-3*c*	5.522(1)/13.412(1)	354.22(1)	3.33
LSF	R-3*c*	5.528(1)/13.451(2)	355.93(1)	2.03
Crofer22APU	I*m*-3*m*	2.881(1)	23.91(1)	7.31

elements (Table 2), the INCA 350 software from Oxford was used to reconstruct the spectra and it was compared with the measured one to confirm the presence or absence of these elements.

3. Results and discussion

3.1. Phase characterization

The phase structures of studied commercial materials (LNC, LNF, LSFMC, LSF and Crofer22APU) were refined by the Rietveld method, as shown in Fig. 2. All the perovskite phases showed a rhombohedral structure with R-3*c* space group; however, steel has a cubic arrangement and it crystallizes in space group I*m*-3*m*, as expected. The refined cell parameters and unit cell volumes are summarized in Table 3. The quantitative analysis demonstrates that the studied materials were pure except LSFMC and LNC. For LNC two very weak peaks corresponding to NiO were found (1.5% in weight) and for LSFMC, Fe_2O_3 phase (2% in weight) and traces of $LaSrFeO_4$ (<0.1% in weight) were quantified.

The dependence of conductivity of each perovskite on temperature and the Arrhenius plot for the electrical conductivity in air is shown in Figs. 3 and 4, respectively. The conductivity increases with increasing temperature up to a maximum and then decreases due to the lattice oxygen loss, for the LSFMC, LSF and LNF perovskites, implying a small semiconductor behavior [21]. For the LNC material, however, the conductivity decreases continuously with increasing temperature, implying a metallic behavior [24].

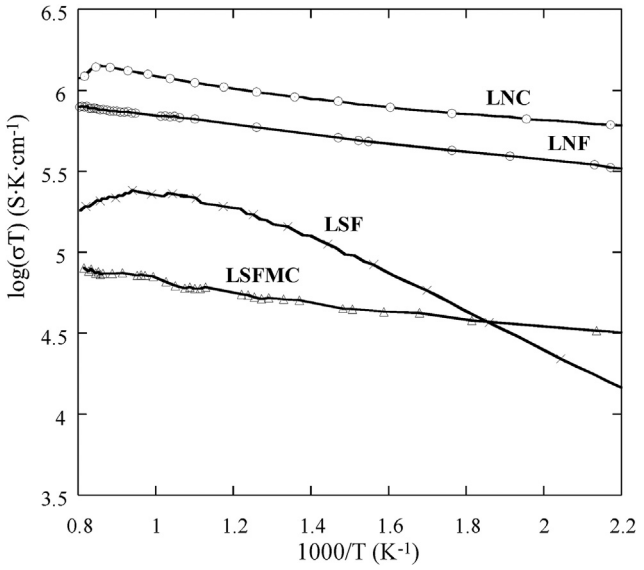

Fig. 4. Arrhenius plot of selected perovskites as a function of temperature.

For the compositions with semiconducting behavior, the temperature dependence of the conductivity can be described by the small polaron hopping mechanism [25] as it shown in Equation (1):

$$\sigma = \frac{A}{T}\exp\left(\frac{-Ea}{KT}\right) \quad (1)$$

where A is the pre-exponential factor, T is the temperature, k is the Boltzmann constant, and Ea is the activation energy for the hopping

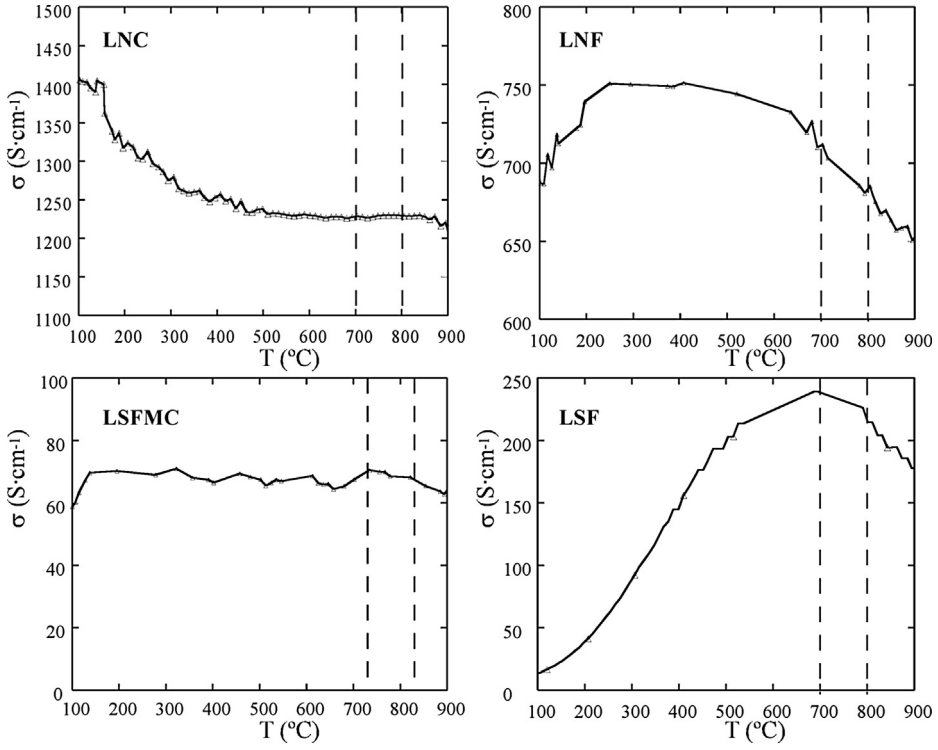

Fig. 3. Electrical conductivity of $(La_{0.8}Sr_{0.2})_{0.95}Fe_{0.6}Mn_{0.3}Co_{0.1}O_3$, $LaNi_{0.6}Fe_{0.4}O_{3-\delta}$, $LaNi_{0.6}Co_{0.4}O_{3-\delta}$ and $La_{0.6}Sr_{0.4}FeO_3$ perovskites as a function of temperature.

Table 4
Maxima in conductivity, conductivity values at 800 °C and activation energy obtained from the Arrhenius plots for all the compounds.

Composition	σ_{Max} (S cm^{-1}), T_{Max} (°C)	$\sigma_{800\,°C}$ (S cm^{-1})	E_a ($RT - T_{Max}$) (eV)
$LaNi_{0.6}Co_{0.4}O_{3-\delta}$ (LNC)[a]	1405.9	1229	–
$LaNi_{0.6}Fe_{0.4}O_{3-\delta}$ (LNF)	751.4	685	0.02
$(La_{0.8}Sr_{0.2})_{0.95}Fe_{0.6}Mn_{0.3}Co_{0.1}O_3$ (LSFMC)	71.3	65	0.08
$La_{0.6}Sr_{0.4}FeO_3$ (LSF)	239.7	214	0.11

[a] For LNC sample the activation energy was not calculated due to it exhibit metallic electrical conduction in every range of temperature.

of the small polarons. The activation energy obtained from the Arrhenius plots (for LSFMC, LSF and LNF samples) and the maximum in conductivity and at 800 °C for all compounds are given in Table 4.

The obtained conductivity values of the samples are in good agreement with other studies for these types of compounds [14,26–29]. As observed, at 800 °C the LNC and LNF show higher conductivity than LSFMC, whose conductivity value is smaller than the one obtained for the cathode material (LSF). It is known that conductivity of contact materials is one of the most important properties for ensuring acceptable ASR. However, the selection of contact material also depends on mechanical integrity of the Crofer22APU/contact layer/LSF interfaces and on its stability. Thus, in terms of conductivity LNF and LNC are appropriate to use as contact layer and, LSFMC is a suitable choice according to its mechanical integrity [3] and also because its TEC value is closely matched with that of the interconnect, as shown below.

Fig. 5 shows the thermal expansion curves of the five materials obtained upon heating from 200 to 1000 °C. The TEC results present close to linear dependence in the temperature range of 30–1000 °C for the Crofer22APU and LNC samples. For the other materials, however, the curves become steeper above the temperature at which each compound shows the maximum in conductivity, corresponding probably to a lattice oxygen loss giving rice to the lattice expansion. As it has been discussed in other works [29–31], this lattice expansion, associated with the formation of oxygen vacancies, can be attributed to: a) the repulsion force arised between those mutually exposed cations when oxygen ions are extracted from the lattice; and/or b) the increase in cation size due to the

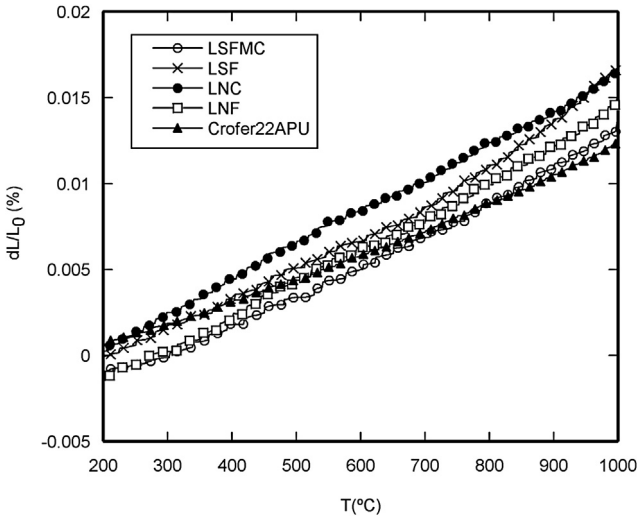

Fig. 5. Thermal expansion curves of the materials that compose the studied systems, obtained upon heating from 200 to 1000 °C in air.

Table 5
Thermal expansion coefficients for the studied materials.

Component	Material	$\alpha_{30-800\,°C}$ (K^{-1})	$\alpha_{30-1000\,°C}$ (K^{-1})
Interconnect	Crofer22APU	$11.8\cdot10^{-6}$	$12.8\cdot10^{-6}$
Contact layer	LNC	$17.9\cdot10^{-6}$	$17.5\cdot10^{-6}$
Contact layer	LNF	$16.1\cdot10^{-6}$	$16.0\cdot10^{-6}$
Contact layer	LSFMC	$14.5\cdot10^{-6}$	$14.6\cdot10^{-6}$
Cathode	LSF	$16.1\cdot10^{-6}$	$17.5\cdot10^{-6}$

reduction of Co and Fe ions from higher to lower valences, which must occur concurrently with the formation of oxygen vacancies in order to maintain the electrical neutrality.

The average TECs at different temperatures for all the components studied are listed in Table 5. As expected, Co based perovskite shows higher TEC values than obtained for Co-free perovskites, such as manganites, nickelites and ferrites [32–35]. As can be observed, for LNF and LNC, the $\alpha_{30-800\,°C}$ and $\alpha_{30-1000\,°C}$ values are comparables to those obtained for the cathode, respectively. For LSFMC, however, these TEC values are smaller showing intermediate values between LSF cathode and Crofer22APU interconnect. The measured average TECs are higher than the ones reported in other works [16,36–38] for this type of compositions. Those small differences can be attributed to the influence of the sample preparation method and different sintering temperatures [39].

The TEC values obtained for the interconnect material is smaller than for the other components of the cell, especially for the LNC and LNF compositions. Although the TEC values are not exactly the same, they present an obvious concern for integrity of the contact layers and interfaces during thermal cycling. It is necessary to remark that for the cell preparation, the contact layer will be relatively thin with a certain porosity to ensure the flow of oxygen, properties that are expected to reduce thermal stress. In the preparation of the cells, all of these materials have been successfully employed as contact layer between cathode and interconnect, despite having larger TEC than Crofer22APU material.

From these results, it can be concluded that: a) LNC and LNF compounds present the highest conductivity values and their TECs values are comparables to those obtained for the cathode and, b) despite the fact that LSFMC showed the lowest conductivity, the TEC results obtained for this perovskite presents the best fit with the TEC values obtained for the interconnect.

3.2. ASR measurements and post-test analysis

Fig. 6 shows that ASR values (Table 6) of the different contact perovskites tested are stable during the contact resistance

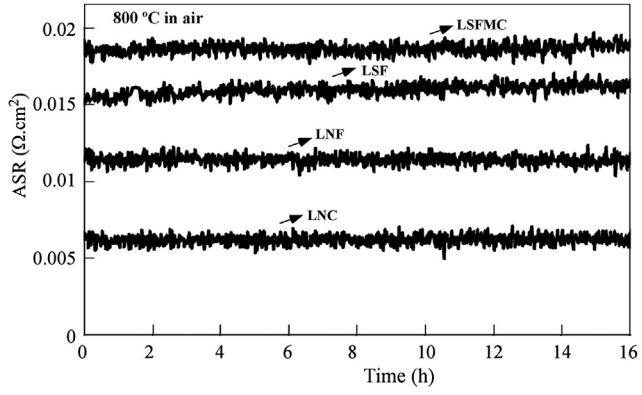

Fig. 6. ASR for {Crofer22APU/contact layer/LSF} interfaces as a function of time with different contact materials and for the {Crofer22APU/LSF/LSF} system.

Table 6
Area specific resistance values for the different tested contact perovskites measured at 800 °C in air.

System: Crofer22APU/contact layer/LSF	≈ ASR (Ω cm^2)
LNC	0.006(1)
LNF	0.010(1)
LSF	0.015(1)
LSFMC	0.018(1)

measurements. The contact made by LNC, which has the lowest electrical resistance among the three selected perovskites, gives the lowest ASR, while the contact made by LSFMC, which present a lower electrical conductivity, leads to a higher contact resistance. The value of the electrical resistance for the system with only LSF amounts to 0.015 Ω cm^2, and it was relatively constant during the experiment. The ASR values for the systems with the LNC and LNF contact layers are 0.006 and 0.010 Ω cm^2, respectively. These values are lower than that for the system with LSF only, as was expected for LSFMC this value is higher and amounts to 0.018 Ω cm^2. The achieved contact resistance values are considerably lower than that of previously reported results for this kind of materials [3]. However, it has been published for {interconnect: AISI441/contact layer: $Ni_{0.33}Co_{0.67}O$/cathode: $La_{0.8}Sr_{0.2}MnO_3$} combination and for {interconnect: 441SS/protective coating: $Mn_{1.5}Co_{1.5}O_4$/contact layer: $La_{0.7}Sr_{0.3}CoO_3$/cathode: $La_{0.6}Sr_{0.4}Co_{0.8}Fe_{0.2}O_3$} assemblies the same order of ASR values [2,12]. The significantly low ASR was probably due to the microstructure and thickness of the different layers, and/or due to the good bonding of the interfaces between contact layer and cathode, and contact layer and interconnect. It is known [40] for this kind of systems that the initial area specific resistance mainly depends on electrical conductivity of the measured perovskites while the time evolution of the ASR depends on the interactions between the contact materials and adjacent components. For this reason it is difficult to assert that the reaction products between ferritic steel and contact or cathode layers exhibit sufficiently high electronic conductivity not to increasing the contact resistance.

The polished cross-sections of different systems after ASR measurements at 800 °C are shown in Fig. 7. Five layers can be distinguished in all the samples, including: the interconnect, the oxide scale, the contact layer, the cathode and the Pt paste. The thicknesses of the contact materials can be estimated to be between 10 and 20 μm, respectively. In addition, in all cases, the thickness of the cathode is about 20–25 μm. The total thickness of the oxide scale for the combination with LSFMC is similar to the system with LNF, which is about 1.5 μm. The oxide layers formed at the LNC/and LSF/Crofer22APU interfaces are not completely homogeneous in thickness. It is likely that the protective chromia scale growth rate, depends on the contact material composition. This effect can be also related to the amount and distribution of minor alloying additions in Crofer22APU, such as reduction of Si and Al additives, leading to an increase of oxidation rates during the preoxidation of the interconnect [41].

The microstructure of the cathode layer in all the samples is similar, revealing open porosity with a pore size of approximately 0.5–2 μm. The pore size distribution of the contact pastes depends on the reactivity undergone by each system after ASR measurements. The pores over the contact layer cross-sections for LNF, LNC and LSFMC have a diameter of about 1 μm, whereas for LSF is about 0.5–1 μm. Compared to other three contact materials, LSF has fewer pores and it shows a quite uniform distribution of the pores. In all the samples the contact layers were well bonded to the metallic substrate. However, during the preoxidation process of

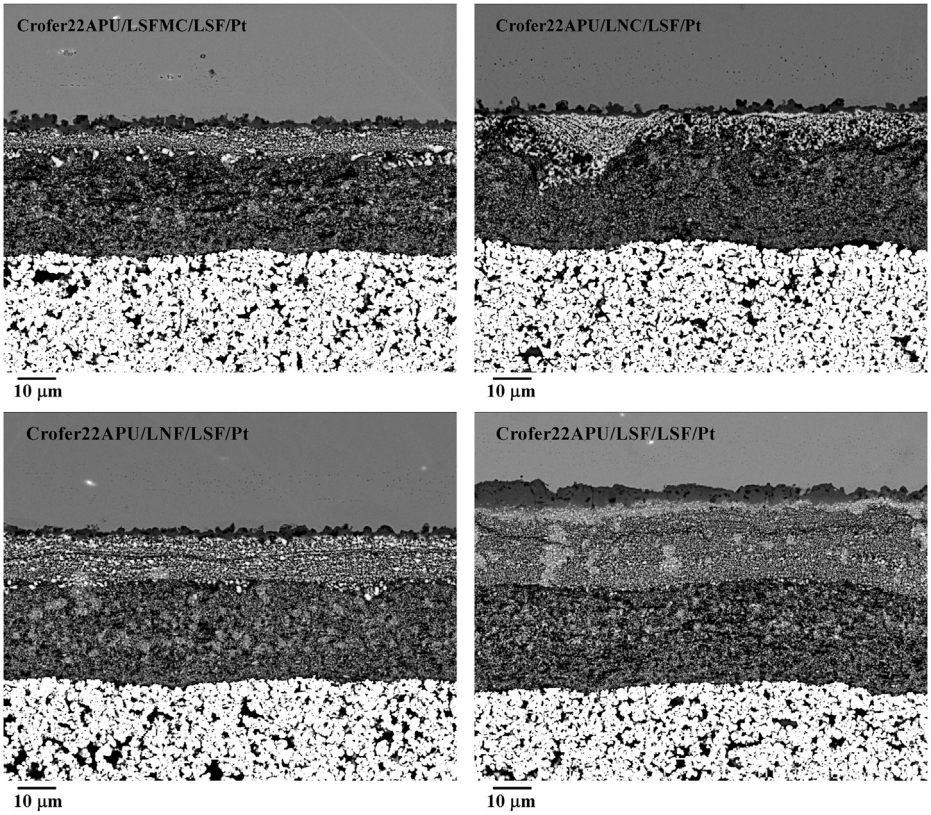

Fig. 7. Metallographic cross-sections (back-scattered electron image) of the different {Crofer22APU/contact layer/LSF} systems after ASR measurements at 800 °C in air.

the interconnect, the formation of voids at the interface between the oxide scale and the steel can be detected. According to other studies [41] insufficient La in the steel melt can lead to void formation. The cathode and contact layer are well attached especially when LSF was used as contact material and also for LNF combination. For LNC and LSFMC systems the cathode is not so properly attached to the contact layer, probably due to the mismatch between TECs values.

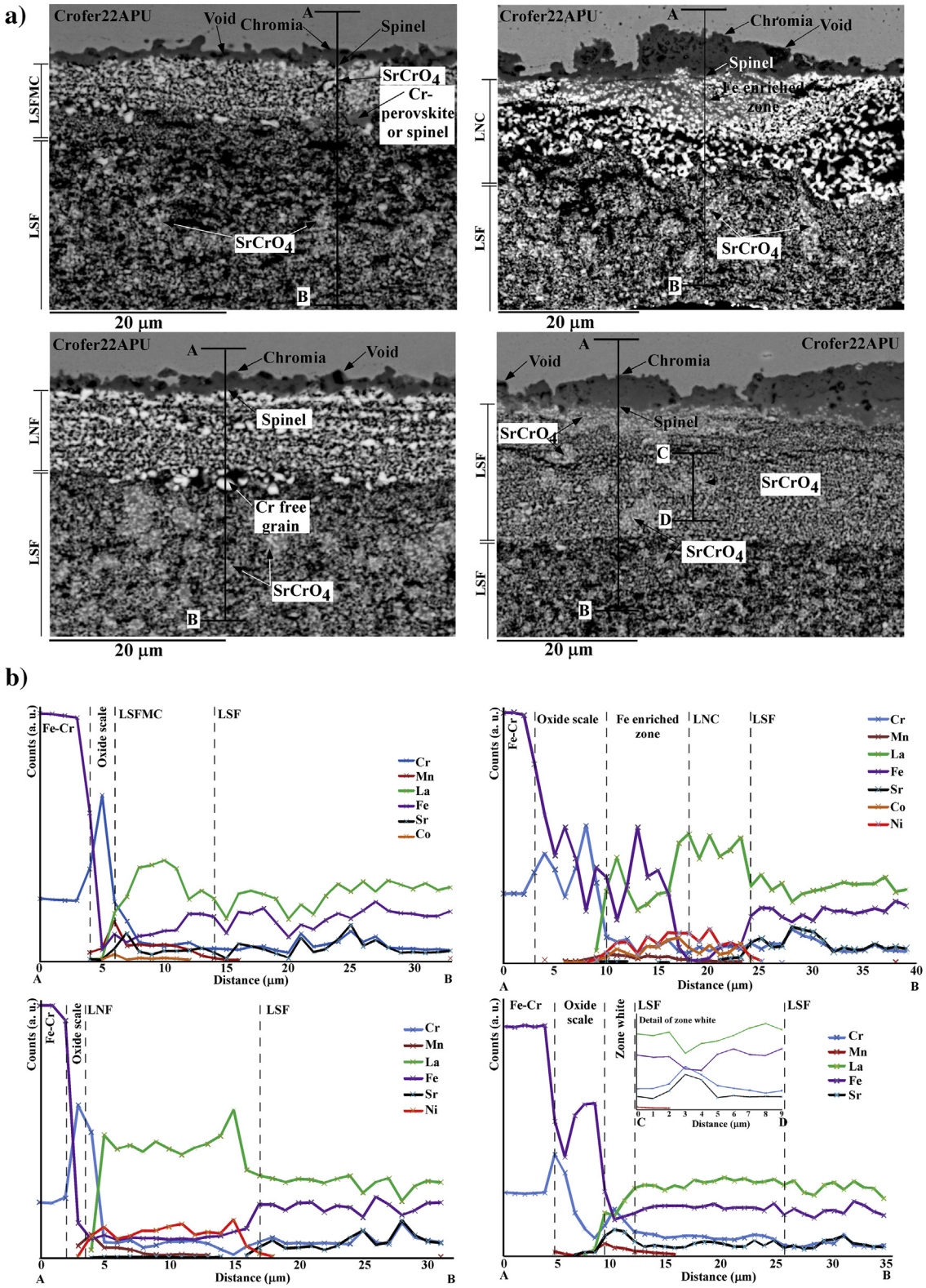

Fig. 8. a) Details of SEM cross-sections of studied systems after contact resistance measurements, b) representative results to estimate the extent of interdiffusion at the different systems interfaces from EDX point analysis.

To estimate the extent of interfacial interdiffusion, in the starting hours, for the contact material and the interconnect, or the contact material and the cathode, linescans were performed using EDX analysis along the samples as shown in Fig. 8. For all the cases, oxide scale is composed of two layers: Cr_2O_3 bonded to the metal substrate followed by $(B)_3O_4$ spinel layer (B = Cr, Co, Fe, Ni, Mn) in good agreement with the literature [42]. The growth of chromia is governed by an outward and inward diffusion of Cr and O, respectively [43].

The addition of manganese as additive in the alloy enhances the formation of the spinel formed under the Cr_2O_3 layer and, it improves the scale conductivity which prevents chromium migration and formation of Cr(VI) oxide and oxy-hydroxide species. Thus, the reduction in the rate of cathode degradation by Cr poisoning is

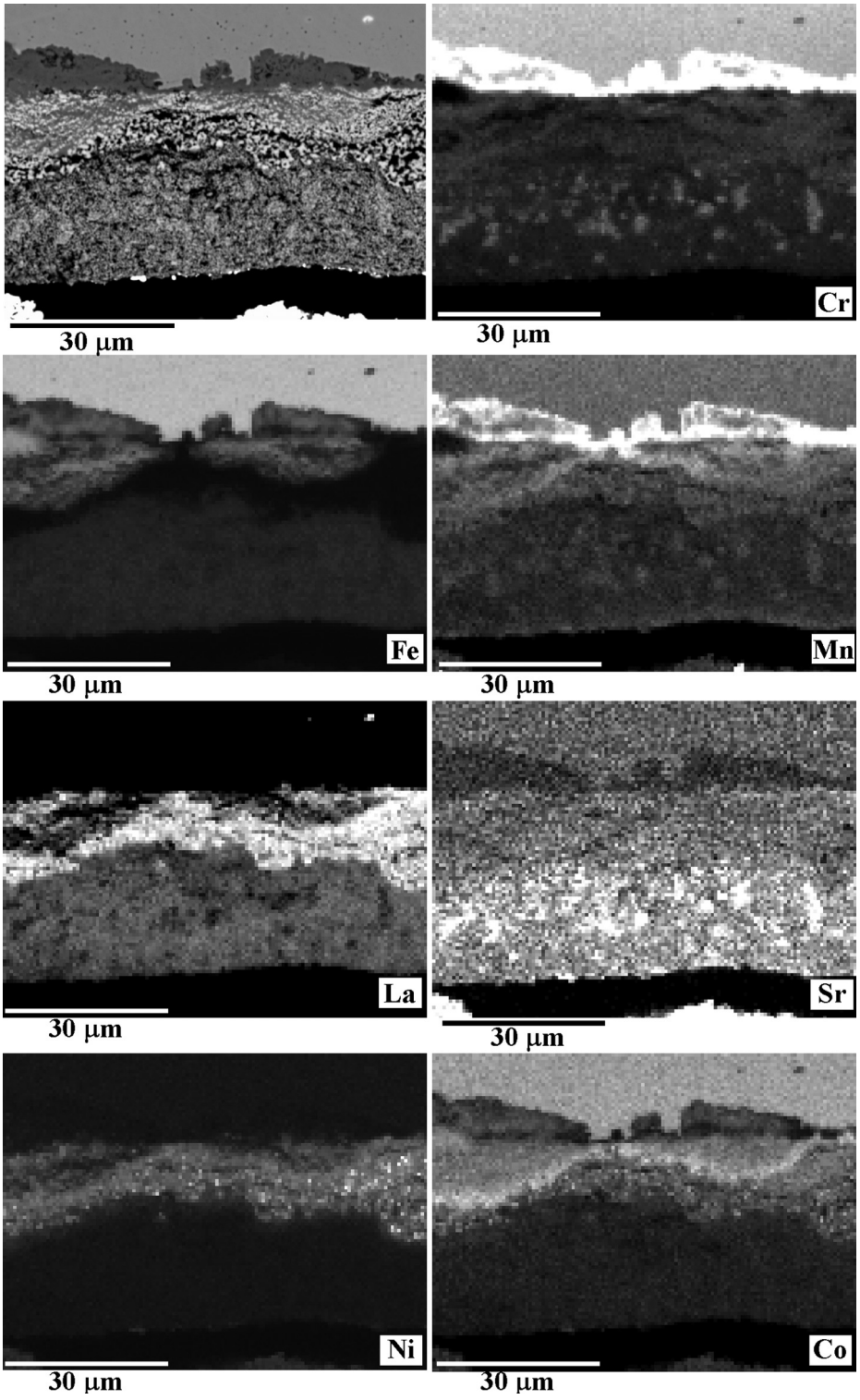

Fig. 9. EDX mapping of the cross-section of {Crofer22APU/LNC/LSF} combination after ASR measurements in air at 800 °C.

given. Therefore, Mn-containing perovskites like LSFMC can also facilitate the formation of Cr–Mn spinels. For Co- and Fe-containing perovskites, such as LNC and LNF, the cobalt and iron released from the perovskite lattice can react with the Cr and Mn from the oxide scale to form $(Cr, Mn, Co, Fe)_3O_4$ spinels. The existence of Fe or Co ions in the spinel grains might improve considerably the electrical conductivity of the coated sample.

For all the systems, the element interdiffusion between cell components is mainly concentrated on Fe, Cr and Mn which released from the interconnect. In the cross-section imagenes gray colored zones can be detected within the contact and cathode material probably associated to the formation of Cr-containing perovskites [44–46]. The presence of some cracks through the ceramic layers, specially observed for LNC, and the chromium enrichment zones observed for all the systems, can contribute to a higher densification of coating causing in some of the systems cracks. In addition, the cracks can be explained by interactions between contact material and oxide scale, leading to expanded volume of the layer.

Due to the mobility of Sr in cathode environment, large regions enriched with Cr and Sr are observed within the LSF and LSFMC layers owing to $SrCrO_4$ precipitation [47], which is detected [3] as "white zones" in the images.

When LNC contact material is used, a Fe enriched zone with many different compositions was formed between chromia scale and LNC coating (Fig. 9). Considering that denser contact layer retains better Cr, it can be deduced that a decrease in the degree of compaction of the layer makes increasing in chromia evaporation, thereby leading to the low concentration of Cr_2O_3 in Crofer22APU/LNC interface. Thus, the increase in the concentration of Fe oxides like Fe_2O_3 is given. This oxide is less dense than Cr_2O_3 and may facilitate cation diffusion of Cr^{3+}, Mn^{3+} and Fe^{3+} to the surface, resulting in a reaction with the contact coating [48]. Despite the open porosity of the contact layer, LNC gives the lower ASR due to its higher conductivity.

4. Conclusions

Direct contact between interconnect and cathode in IT-SOFC stack generally leads to electrical losses. They can be diminished by appropriate contact layers. Three lanthanum-based perovskite ceramic compounds, $(La_{0.8}Sr_{0.2})_{0.95}Fe_{0.6}Mn_{0.3}Co_{0.1}O_3$ (LSFMC), $LaNi_{0.6}Fe_{0.4}O_{3-\delta}$ (LNF) and $LaNi_{0.6}Co_{0.4}O_{3-\delta}$ (LNC) were selected as contact materials for this study. The observed high conductivity values for LNF and LNC and, the good fit between TECs values of LSFMC and the interconnect make the use of these materials as contact layers interesting.

The thickness of oxide scale observed for the combination with LSFMC and LNF is reasonable homogeneous in contrast with systems with LNC and LSF in which this oxide scale is not uniform. This effect can be related to the distribution of minor additives within interconnect which produces differences in scale growth or, it can be also associated to the contact material compositions. For all cases, oxide scale is composed of two layers: Cr_2O_3 bonded to the metal substrate followed by spinel layer. The Mn-, Co- and Fe-containing perovskites used in this study lead to the formation of spinels with different compositions which can improve electrical conductivity of coated samples. In the four systems the chromium enrichment observed in contact and cathode layers allowed the formation of phases like $SrCrO_4$ and Cr-containing perovskite in short exposure times. When LNC contact material is used, a Fe enriched zone with many different compositions is formed between chromia scale and contact coating probably due to the open porosity of the contact layer which prevents the formation of protective coating of chromia. The obtained contact resistance values are strongly influenced by the conductivity of the selected contact material. The ASR contribution of all the systems is fairly acceptable for the performance of a SOFC stack operating in the intermediate temperature range.

The selection of the best contact layer is based on a compromise between mechanical integrity of the Crofer22APU/contact layer/LSF interfaces and, contact resistance and chemical compatibility of the system. In the present case, LNF coating can be a suitable choice as contact coating due to the adequate integrity and low reactivity between the applied layers without compromising the contact resistance of the system. Future work will include long-term stability of {Crofer22APU/LNF/LSF} system in terms of contact resistance and chemical compatibility.

Acknowledgment

This research has been funded by the Consejería de Industria, Innovación, Comercio y Turismo (SAIOTEK 2012 programmes), by Dpto. Educación, Política Lingüística y Cultura of the Basque Goverment (IT-630-13) and by Ministerio de Ciencia e Innovación (MAT2010-15375 and MAT2012-30763). The authors thank Ikerlan's Fuel Cell group and SGIker technical support (UPV/EHU, MEC, GV/EJ and European Social Fund). A. Morán-Ruiz thanks UPV/EHU for funding her PhD work.

Appendix A. Supplementary data

Supplementary data related to this article can be found at http://dx.doi.org/10.1016/j.jpowsour.2013.10.031.

References

[1] S.P. Jiang, J. Electrochem. Soc. 148 (8) (2001) A887.
[2] M.C. Tucker, L. Cheng, L.C. Dejonghe, J. Power Sources 196 (2011) 8313.
[3] X. Montero, F. Tietz, D. Stöver, M. Cassir, I. Villarreal, J. Power Sources 188 (2009) 148.
[4] M.C. Tucker, L. Cheng, L.C. DeJonghe, J. Power Sources 224 (2013) 174.
[5] Y. Tao, H. Nishino, S. Ashidate, H. Kokubo, M. Watanabe, H. Uchida, Electrochim. Acta 54 (2009) 3309.
[6] W.B. Guan, H.J. Zhai, L. Jin, T.S. Li, W.G. Wang, Fuel Cells 3 (2011) 445.
[7] W.B. Guan, L. Jin, X. Ma, W.G. Wang, Fuel Cells 6 (2012) 1085.
[8] Z. Yang, G. Xia, P. Singh, J.W. Stevenson, J. Power Sources 155 (2006) 246.
[9] B.P. McCarthy, L.R. Pederson, Y.S. Chou, X.D. Zhou, W.A. Surdoval, L.C. Wilson, J. Power Sources 180 (2008) 294.
[10] S.J. Skinner, M.A. Laguna-Bercero, in: D.W. Bruce, D. O'Hare, R.I. Walton (Eds.), Energy Materials, John Wiley & Sons, Ltd, Chichester, UK, 2011, http://dx.doi.org/10.1002/9780470977798.ch2.
[11] L.T. Wilkinson, J.H. Zhu, J. Electrochem. Soc. 156 (8) (2009) B905.
[12] Z. Lu, G. Xia, J.D. Templeton, X. Li, Z. Nie, Z. Yang, J.W. Stevenson, Electrochem. Commun. 13 (2011) 642.
[13] M.T. Tucker, L. Cheng, L.C. Dejonghe, J. Power Sources 196 (2011) 8435.
[14] F. Wang, D. Yan, W. Zhang, B. Chi, J. Pu, L. Jian, Int. J. Hydrogen Energy 38 (2013) 646.
[15] W. Zhang, F. Wang, K. Wang, J. Pu, B. Chi, L. Jian, Int. J. Hydrogen Energy 37 (2012) 17253.
[16] U.F. Vogt, P. Holtappels, J. Sfeir, J. Richter, S. Duval, D. Wiedenmann, A. Züttel, Fuel Cells 6 (2009) 899.
[17] V. Miguel-Perez, A. Martínez-Amesti, M.L. Nó, A. Larrañaga, M.I. Arriortua, Corros. Sci. 60 (2012) 38.
[18] H.M. Rietveld, J. Appl. Crystallogr. 2 (1969) 65.
[19] J. Rodríguez-Carvajal, Phys. B 192 (1993) 55.
[20] J. Rodríguez-Carvajal, FULLPROF Rietveld Pattern Matching Analysis of Powder Patterns, 1994. Grenoble.
[21] K. Vidal, L.M. Rodríguez-Martínez, L. Ortega-San-Martín, M.L. Nó, T. Rojo, M.I. Arriortua, Fuel Cells 11 (2011) 51.
[22] K.O. Hoyt, P.E. Gannon, P. White, R. Tortop, B.J. Ellingwood, H. Khoshuei, Int. J. Hydrogen Energy 37 (2012) 518.
[23] A. Martínez-Amesti, Celdas de Combustible de Óxido Sólido. Estudios de Reactividad y Optimización de la Intercapa Cátodo-Electrolito (Ph. D. thesis), UPV/EHU, 2009.
[24] A. Huang, K. Yao, J. Wang, J. Electroceram. 16 (2006) 313.
[25] P.A. Cox, The Electronic Structure and Chemistry of Solids, Oxford Science Publications, Oxford, UK, 1987.
[26] K. Huang, H.Y. Lee, J.B. Goodenough, J. Electrochem. Soc. 145 (9) (1998) 3220.

[27] M. Bevilacqua, T. Montini, C. Tavagnacco, G. Vicario, P. Fornasiero, M. Graziani, Solid State Ionics 177 (2006) 2957.
[28] H. Ullmann, N. Trofimenko, F. Tietz, D. Stöver, A. Ahmad-khanlou, Solid State Ionics 138 (2008) 79.
[29] J.M. Ralph, J.A. Kilner, B.C.H. Steele, Mater. Res. Soc. Symp. Proc. 575 (2001) 309.
[30] S. Li, Z. Lü, X. Huang, W. Su, Solid State Ionics 178 (2008) 1853.
[31] Z. Li, B. Wei, Z. Lü, X. Huang, W. Su, Solid State Ionics 207 (2012) 38.
[32] Z. Gao, Z. Mao, C. Wang, Z. Liu, Int. J. Hydrogen Energy 35 (2010) 12905.
[33] H. Lv, B.-Y. Zhao, Y.-J. Wu, G. Sun, G. Chen, K.-A. Hu, Int. Mater. Res. Bull. 42 (12) (2007) 1999.
[34] K.T. Lee, A. Manthiram, J. Power Sources 158 (2006) 1202.
[35] H. Taguchi, T. Komatsu, R. Chiba, K. Nozawa, H. Orui, H. Arai, Solid State Ionics 182 (2011) 127.
[36] N. Sukpirom, S. Iamsaard, S. Charojrochkul, J. Yeyongchaiwat, J. Mater. Sci. 46 (2011) 6500.
[37] R. Kumar, E. Yi, Y. Hang, C. Myung, Met. Mater. Int. 15 (2009) 1055.
[38] F. Tietz, I.-A. Raj, M. Zahid, D. Stöver, Solid State Ionics 177 (2006) 1753.
[39] A. Dutta, J. Mukhopadhyay, R.N. Basu, J. Eur. Ceram. Soc. 29 (2009) 2003.
[40] W.J. Shong, C.K. Liu, C.Y. Chen, C.C. Peng, H.J. Tu, G.T.K. Fey, R.Y. Lee, H.M. Kao, Mater. Chem. Phys. 127 (2011) 45.
[41] P. Huczkowski, W.J. Quadakkers, Effect of Geometry and Composition of Cr Steels on Oxide Scale Properties Relevant for Interconnector Applications in Solid Oxide Fuel Cells (SOFCs), Forschungszentrum Jülich, 2007.
[42] S. Fontana, S. Chevalier, G. Caboche, Oxid. Met. 78 (2012) 307.
[43] Y. Zhao, Oxidation Behavior of Ferritic Alloys as Interconnect of Solid Oxide Fuel Cell (SOFC) (Ph. D. thesis), Auburn University, 2012.
[44] M.K. Stodolny, B.A. Boukamp, D.H.A. Blank, F.P.F. van Berkela, J. Electrochem. Soc. 158 (2) (2011) B112.
[45] A. Morán-Ruiz, K. Vidal, A. Larrañaga, M.I. Arriortua, Fuel Cells 3 (2013) 398.
[46] S.P.S. Badwal, R. Deller, K. Foger, Y. Ramprakash, J.P. Zhang, Solid State Ionics 99 (1997) 297.
[47] M.R. Ardigò, A. Perron, L. Combemale, O. Heintz, G. Caboche, S. Chevalier, J. Power Sources 196 (2011) 2037.
[48] V. Miguel-Pérez, A. Martínez-Amesti, M.L. Nó, A. Larrañaga, M.I. Arriortua, J. Power Sources 243 (2013) 419.

Journal of Power Sources 269 (2014) 509–519

Contents lists available at ScienceDirect

Journal of Power Sources

journal homepage: www.elsevier.com/locate/jpowsour

$LaNi_{0.6}Co_{0.4}O_{3-\delta}$ dip-coated on Fe–Cr mesh as a composite cathode contact material on intermediate solid oxide fuel cells

Aroa Morán-Ruiz [a], Karmele Vidal [a], Aitor Larrañaga [a, *], Miguel Angel Laguna-Bercero [b], Jose Manuel Porras-Vázquez [c], Peter Raymond Slater [c], María Isabel Arriortua [a, *]

[a] Universidad del País Vasco (UPV/EHU), Facultad de Ciencia y Tecnología, Departamento de Mineralogía y Petrología, Barrio Sarriena S/N, 48940 Leioa, Vizcaya, Spain
[b] CSIC-Universidad de Zaragoza, Instituto de Ciencia de Materiales de Aragón (ICMA), Pedro Cerbuna 12, 50009 Zaragoza, Spain
[c] University of Birmingham, School of Chemistry, Birmingham B15 2TT, UK

HIGHLIGHTS

- After 1000 h at 800 °C LNC/Fe–Cr mesh still present adequate mechanical integrity.
- ASR value for LNC/Fe–Cr mesh with interconnect was 5.40 ± 0.01 mΩ cm^2 at 800 °C.
- Cr deposition under the channel is higher than under the rib of the interconnect.

ARTICLE INFO

Article history:
Received 24 March 2014
Received in revised form
13 June 2014
Accepted 7 July 2014
Available online 15 July 2014

Keywords:
IT-SOFC
Composite contact material
Channeled interconnect
Ohmic resistance losses
Electrical contact
$LaNi_{0.6}Co_{0.4}O_{3-\delta}$

ABSTRACT

The feasibility of using Crofer22APU mesh dip coated with $LaNi_{0.6}Co_{0.4}O_{3-\delta}$ (LNC) ceramic paste as a uniform contact layer on a Crofer22APU channeled interconnect was studied. The control of LNC dip coating thickness on Fe–Cr mesh was carried out by rheological measurements of the suspension. SEM cross-section of formed composite contact material showed good adherence between ceramic and metallic components. The measured area specific resistance (ASR) value at 800 °C was 0.46 ± 0.01 mΩ cm^2, indicating low contact resistance itself. The long term stability of metallic/ceramic composite was also studied. The contact resistance, when composite contact material was adhered to channeled Crofer22APU interconnect, was 5.40 ± 0.01 mΩ cm^2, which is a suitable value for the performance of IT-SOFC stack. The stability of the system after treating at 800 °C for 1000 h was characterized using X-ray Micro-Diffraction (XRMD), Scanning Electron Microscope equipped with an Energy Dispersive X-ray analyzer (SEM-EDX) and X-ray Photoelectron Spectroscopy (XPS) techniques. The oxidation rate of the alloy and Fe_3O_4 phase formation were enhanced on the channels of the interconnect. Thus, the formation of CrO_3 (g) and $CrO_2(OH)_2$ (g) species was accelerated on the composite surface under the channel. Through XRMD and XPS analysis the coexistence of two perovskite phases (initial LNC and Cr-perovskite) was observed.

1. Introduction

Global warming and its detrimental climatological, ecological and sociological effects have led to an increasing interest in more efficient and clean power systems [1]. High temperature solid oxide fuel cells (HT-SOFCs, operating in the range of 800–1000 °C) have a good potential for being used as stationary stand-alone power generation systems [2]. For these applications, chemical to electrical efficiency of HT-SOFC is in the range of 45–65% [3]. For smaller scale applications, such as micro combined heat and power (micro-CHP), small auxiliary power units (APUs) and small electrical generators [4], there is a need to lower operation temperatures, into the intermediate temperatures (IT) range of 500–800 °C. Lower temperature operation affords more rapid start-up and shutdown.

A single SOFC cell produces ~0.6–0.7 V under normal working conditions [3]. Therefore, in order to obtain the desired electric power output, single cells are connected and fabricated together to form a stack using interconnect and sealing materials [5]. In HT-

* Corresponding authors. Tel.: +34 946015984; fax: +34 946013500.
E-mail addresses: aitor.larranaga@ehu.es (A. Larrañaga), maribel.arriortua@ehu.es (M.I. Arriortua).

http://dx.doi.org/10.1016/j.jpowsour.2014.07.040
0378-7753/

SOFCs, the bond between the cell and the $LaCrO_3$ interconnect is typically realized by sintering at 1300 °C. A solid bond with good electrical contact is obtained and no other contact material is then required. However, for IT-SOFC chromium-containing ferritic stainless steels are generally used as interconnect [6,7] and, contact materials are needed to provide a homogeneous bonding between interconnect and electrode to avoid power losses [8]. Previous studies [9,10], based on the effect of contact between electrode and current collector on the performance of SOFCs, concluded that when the contact area of the current collector increased from 4.6% to 27.2%, the cell resistance decreased from 1.43 to 0.19 Ω cm^2 at 800 °C.

The oxide scale formed on the surface of Fe–Cr alloys, after long exposure in the SOFC environment, results in volatile chromium (Cr) species such as CrO_3 and $Cr_2(OH)_2$ (in presence of vapor) [3]. These species can cause rapid performance deterioration in SOFCs due to the deposition of Cr at the bulk electrode and at the electrolyte/electrode interface regions [11]. The cathode contact materials can act as a barrier to the migration of chromium from the metallic to the cathode and further minimize the area specific resistance (ASR) between both materials [12–14].

The cathode contact materials compositions should fulfill the following requirements [15,16]: i) high electrical conductivity and appropriate sintering activity to minimize the resistance of the contact layer itself and to protect the steel substrate from excessive oxidation, ii) chemically compatible and appropriate thermal expansion behavior with adjacent materials and, iii) high thermochemical and structural stability in the oxidizing cathode environment. The materials used as contact layers include: i) noble metals (Ag) or noble metal-perovskite composites (Ag-$(La_{0.6}Sr_{0.4})(Co_{0.8}Fe_{0.2})O_3$, Ag–$La_{0.8}Sr_{0.2}MnO_3$), ii) conventional perovskite cathode materials (such as, $La_{0.6}Sr_{0.4}Co_{0.2}Fe_{0.8}O_3$, $La_{0.8}Sr_{0.2}FeO_3$), iii) oxides with a spinel structure, M_3O_4 (M = Ni, Mn, Co, Cu, Fe), or iv) recently developed oxides like $Ni_{0.33}Co_{0.67}O$. Despite the interactions of these kind of materials which formed oxide scale on metal surface, due to their susceptibility to form phases like Ag_2CrO_4, $AgCrO_2$, $SrCrO_4$, Cr-spinels or Cr-perovskites, the use of those materials, in most cases, are quite effective for improving the electrical contact between the cathodes and metallic interconnects [17–25]. In addition, these materials can reduce the oxidation rate of the steel and minimize the formation of new phases arising from the oxidation of metal itself such as, Fe_2O_3 and Fe_3O_4 [26]. In this study, $LaNi_{0.6}Co_{0.4}O_{3-\delta}$ (LNC) ceramic composition was selected, due to the adequate sintering activity, electrical conductivity and thermal expansion coefficient (TEC) [17], coupled with ferritic stainless steel Crofer22APU mesh to form a ceramic/metallic composite contact material. Crofer22APU was developed to increase the electrical conductivity of the scale and to reduce the chromium vaporization. This is achieved by adding 0.5% Mn in its composition which facilities the $(Cr,Mn)_3O_4$ spinel formation [3]. The use of a high conductivity perovskite type material in conjunction with stainless steel mesh is expected to improve current collection. At the same time, it achieves a continuous contact on the ribs without sacrificing the flow of the air through the channels. Taking into account our previous studies [17,27] the use of this composite material between Crofer22APU interconnect and $La_{0.6}Sr_{0.4}FeO_3$ cathode in flow channel configuration, can offer an adequate mechanical integrity and low reactivity between the applied layers without compromising the contact resistance of the system.

The goal of this work is to develop a metallic/ceramic composite contact material achieving a good bonding between this contact material and the channeled metallic interconnect. An adequate formulation of the LNC ceramic slurry was set and then dip coated [28,29] on Crofer22APU mesh. The electrical resistance, chemical compatibility and adherence between ceramic and metallic parts of the composite material, under long term IT-SOFC operating conditions, were determined. Results of electrical performance of the contact material/interconnect system are presented. In addition, long term contact stability of the metallic/ceramic composite material under the rib (direct contact) and channel (indirect contact) of the interconnect was analyzed.

In order to understand the interactions between the Crofer22-APU alloy and the LNC ceramic material the following issues were considered [3,30]: i) the preoxidized alloys form protective and semi-conductive chromia oxide and a dense and stable $(Cr,Mn)_3O_4$ spinel on the surface of the alloy, which is effective to reduce the generation of volatile Cr species ii) the reason for the Cr volatility is the thermodynamic instability of chromia scales formed on the alloy, forming gaseous species (CrO_x (x = 1,2,3)); and iii) the deposition process of Cr species at the ceramic coating, under SOFC operation conditions, can be described by the nucleation deposition theory.

2. Experimental

The formulation of ceramic powder used in this study was $LaNi_{0.6}Co_{0.4}O_{3-\delta}$ (LNC) (NexTech, Fuel Cell Materials). To obtain metallic/ceramic contact composite, Crofer22APU stainless steel mesh (Fiaxell SOFC Technologies), with mesh opening of about 175 μm and a thickness of 250 μm, was cut into 10 × 10 mm squares, cleaned with acetone in an ultrasonic bath and dried. The squared-meshes squares were preoxidized at 600 °C for 10 h and then dip coated with an LNC ceramic paste (dip coating rate = 4.5 mm s^{-1}). The chemical composition of the steel, as given by the supplier, is listed in Table 1. The ceramic slurry was composed of ceramic powder (LNC), dispersant (Dolapix, Zschimmer & Schwarz, Chemische Fabriken), binder (PVB, polyvinyl butyral, Solutia Solutions) and solvent (ethanol, Panreac). The paste composition was based on the formulation shown in Table 2. Particle size distribution of the ceramic powder was carried out using a Mastersizer particle size analyzer (Malvern Instruments). Rheology of the suspensions was analyzed using a rheometer (HAAKE MARS II) at shear rates from 0.1 s^{-1} to 1000 s^{-1}, and at room temperature. Ceramic/metallic material was sintered at 1050 °C for 2 h [9] and then treated at 800 °C for 1000 h, in open air.

The composite contact material was bonded to a Crofer22APU channeled interconnect (ThyssenKrupp VDM). The channels of substrate are 2 mm width, 0.5 mm depth, 10 mm length and the distance between neighboring is 2 mm (Fig. 1). The substrate was cut into 10 × 10 mm and 1 mm thick pieces, polished using #800 grit SiC paper and then, cleaned with acetone in an ultrasonic bath and dried. Subsequently, they were preoxidized at 800 °C for 100 h. An additional layer of LNC was coated on the ribs of the interconnect substrate by colloidal spray technique [31]. The composite contact material was directly adhered to the interconnect, sintered at 1050 °C for 2 h and then treated at 800 °C for 1000 h. The reactivity between the contact material and the rib and channel of the Fe–Cr interconnect, after long term heated at 800 °C in open air, was characterized according to the scheme shown in Fig. 1. All the experiments were performed in open air so the moisture level in the incoming air stream can be establish considering that the water vapor (H_2O) in air is around 0.001–5% by volume. However, these

Table 1
Composition of the Crofer22APU steel in wt%.

	Cr	Fe	Mn	Ti	Si	Al	La	Others
Crofer22APU	22	Bal.[a]	0.5	0.1	0.25	0.25	0.15	0.28

[a] Balance.

Table 2
Ceramic slurry composition prepared for dip-coating.

Ceramic slurry composition	Volume %
Ceramic powder, LNC	12.5
EtOH	87.5
Dispersant, Dolapix	1% regarding to the ceramic powder
Binder, PVB	5% regarding to the ceramic powder

values depend on the temperature so it was difficult to determine a moisture numerical value in the performed experiments. Nevertheless, in order to analyze Cr species formation over the chromium scale it has been considered a wet atmosphere.

X-ray Micro-Diffraction (XRMD) data were collected using a Bruker D8 Discover diffractometer equipped with a Cu Twist tube, Ni filter (λ = 1.5418 Å), PolyCap™ (1μ single crystal cylinders) system for parallel been generation (divergence of 0.25°), and a 1-D LynxEye PSD detector (active length in 2θ 2.7°). The sample was mounted on an Eulerian Cradle with automatic controlled X–Y–Z stage. The sample illumination was adjusted with 1 mm PinHole collimator in the incident beam, the position control was tested by using the interference of two lasers. Data were collected from 10 to 100° 2θ (step size = 0.04 and time per step = 10 s total time 6.5 h) at RT.

Surface and cross-section of the samples were analyzed by a scanning electron microscope (SEM, JEOL LSM-6400) equipped with an Oxford Pentafet energy dispersive X-ray analyzer (EDX). Secondary electron images (SE) were taken at 20 kV and $1.1 \cdot 10^{-11}$ A using a working distance of 7 mm. Composition analysis was performed using back-scattered electrons (BSE) at 20 kV accelerating voltage, $1 \cdot 10^{-9}$ A current density and 15 mm working distance. For the cross-section analysis, samples were embedded in epoxy resin, polished using standard metallographic techniques, and coated with a coal graphite layer (10 nm) that was deposited by evaporation (BLA-TEC SCD 004 Sputter Coater) to provide electrical conductivity. INCA 350 software (Oxford Instrument) was used to reconstruct the spectra, and Fe, Cr, Mn and an LNC pellet were used as standards.

X-ray photoelectron spectroscopy (XPS) measurements were carried out in an SPECS (Berlin, Germany) system equipped with a Phoibos 150 1D-DLD analyzer and monochromatic Al K_α radiation (1486.6 eV). The analysis of the present elements were made at wide scan mode (step energy 1 eV, dwell time 0.1 s, pass energy 80 eV) and after that, high-resolution spectra of the found elements were acquired (step energy 0.1 eV, dwell time 0.1 s, pass energy 20 eV) with an electron take-off angle of 90°. The binding energies were calibrated using C1s peak (BE = 284.6 eV) as an internal standard.

Area Specific Resistance (ASR) measurements were performed using the DC four-probe method (the resistance value was estimated from the voltage value (c 1604 Digital Multimeter) measured on applying a current of 1A (Thurlby Thandar Instruments PL300 current source) [32], on both LNC dip-coated Crofer22APU mesh composite (Fig. 2a) and on a system, which was prepared according to the geometries shown in Fig. 2b, in open air. Electrical contacts between samples and external measuring circuit were made using two Pt wires directly welded onto the sides of the interconnect, and using Pt paste and Pt mesh onto the surface of the composite contact material.

3. Results and discussion

3.1. Control of LNC dip coating thickness on Fe–Cr mesh

Prior to the rheological characterization, particle size distribution measurements were performed on LNC powders, since this parameter influences the rheological properties. Fig. 3 shows a monomodal size distribution of LNC powder (d_{50}: 2.37 μm). The characterization of LNC slurries by rheological measurements is important to control coated thicknesses during the dip coating process. A summary of the composition of the slurry is shown in Table 2. Rheological characterization of the suspensions showed a newtonian fluid behavior, which means that the viscosity values are independent of the shear rate. Typical viscosity values are in the range of 0.054 Pa s, leading to a LNC thickness of the layers after dip-coating and sintering of ~500 μm.

3.2. Characterization of composite contact material

LNC ceramic slurries were dip coated on preoxidized Crofer22-APU stainless steel mesh and sintered at 1050 °C for 2 h in order to form the composite contact material. Fig. 4 shows surface morphology SEM micrographs of Fe–Cr mesh before and after sintering the LNC layers. The area specific resistance (ASR) value of the metallic/ceramic composite material was 0.46 ± 0.01 mΩ cm^2 at 800 °C. This minimal ASR value confirms that the use of this composite material as a contact layer is adequate. SEM cross-section (Fig. 5) of the obtained ceramic-metallic composite contact material, after ASR measurements, showed good adherence between LNC ceramic material and Crofer22APU mesh, due to similar TEC values between Crofer22APU and LNC materials [17]. As observed from Fig. 5, the ceramic coating is continuous and homogenous along the sample.

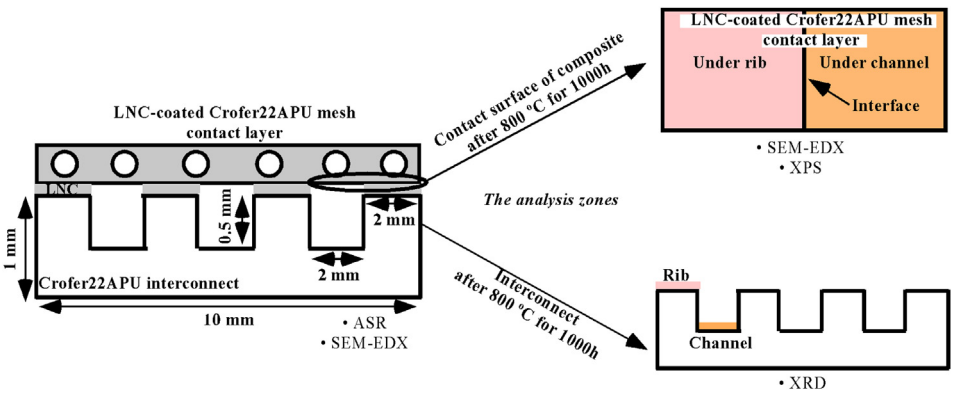

Fig. 1. Schematic representation of the characterization of {LNC dip-coated on Crofer22APU mesh composite contact material/Crofer22APU channeled interconnect} system.

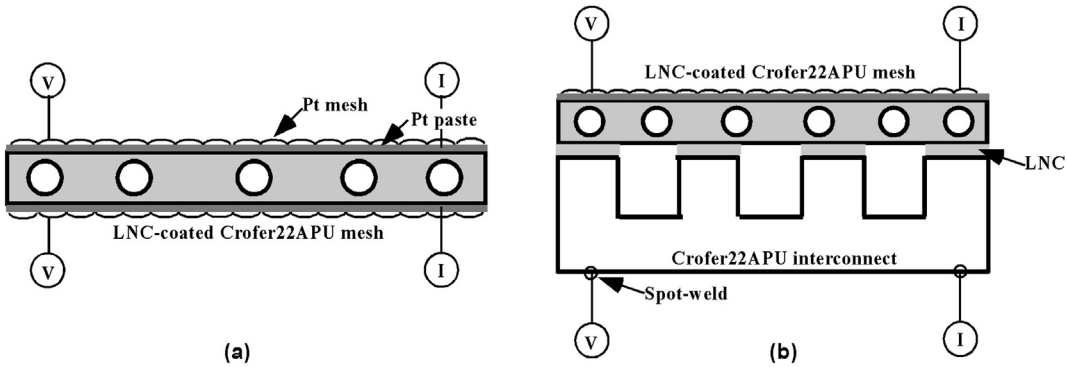

Fig. 2. Schematic view of the system configuration for ASR measurements for: a) composite contact material and b) composite contact material on channeled interconnect.

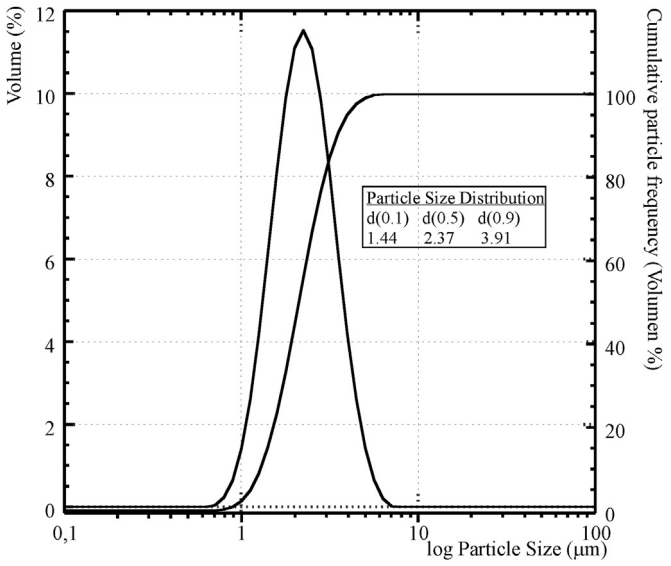

Fig. 3. Particle size distribution of LNC powder.

3.2.1. Long term stability of composite contact material

In order to study the chemical compatibility and also to establish the adherence between the ceramic and metallic parts, the sintered at 1050 °C composite contact material was heated at 800 °C for 1000 h, in open air. EDX mapping (Figs. 6 and 7) were performed of a cross-section of the composite material after long-term operation was performed, and compared with another sample just sintering at 1050 °C for 2 h used to establish initial reactivity. According to Fig. 6, the initial material showed a Cr_2O_3 and $(Mn,Cr)_3O_4$ spinel protection layer to minimize Cr migration through ceramic coated, as expected. Nevertheless, the formed passive chromia layer is not enough to prevent the migration of Cr since the evaporation of protective chromia layer takes place. Early investigations [33] revealed that $(Mn,Cr)_3O_4$ spinel offers lower volatility of Cr than chromia. However, this reduction is less than an order of magnitude. Thus, a Cr deposit ring along the edge of the LNC ceramic coated, whose width was ~35 μm, was also observed. The redeposition of chromium at the contact material, usually as poor conductive phases, could decrease the cell performance [34].

The direct contact between the ceramic contact material and the alloy makes possible solid phase diffusion of Cr [35]. However, the microstructure of the ceramic material revealed open porosity in the initial material and composite after heating at 800 °C for 1000 h in open air, allowing vapor phase transport of volatile Cr-species (CrO_3 (g), $CrO_2(OH)_2$ (g)) throughout the LNC coating. It has been found that [36] the most dominant chromium species are CrO_3 in dry air and $CrO_2(OH)_2$ in humidified air. However, the partial pressure of $CrO_2(OH)_2$ and CrO_3 varies significantly with the temperature. At the temperature decreases, $CrO_2(OH)_2$ species become increasingly dominant. The partial pressure of CrO_3 decreases rapidly with the decrease of temperature while the change in the partial pressure of $CrO_2(OH)_2$ with the temperature is relatively small. So, when the samples are sintered at 1050 °C, considering a wet atmosphere, the main chromium vapor specie is $CrO_2(OH)_2$. Besides, it could be found CrO_3 because its partial pressure is still high. However, when the samples are treated at 800 °C, the partial pressure of CrO_3 is low being the dominant specie chromium oxyhydroxide. The deposition process of these Cr species at the contact material can be described by the nucleation reaction between the high valence Cr phases and the nucleation agents (Ni^{2+},

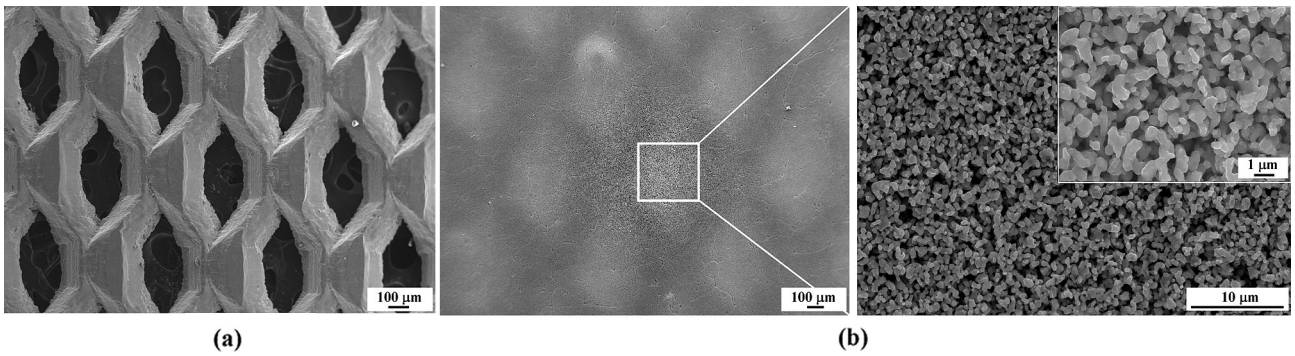

Fig. 4. Surface SEM micrographs of Fe–Cr mesh: a) before and b) after sintered LNC.

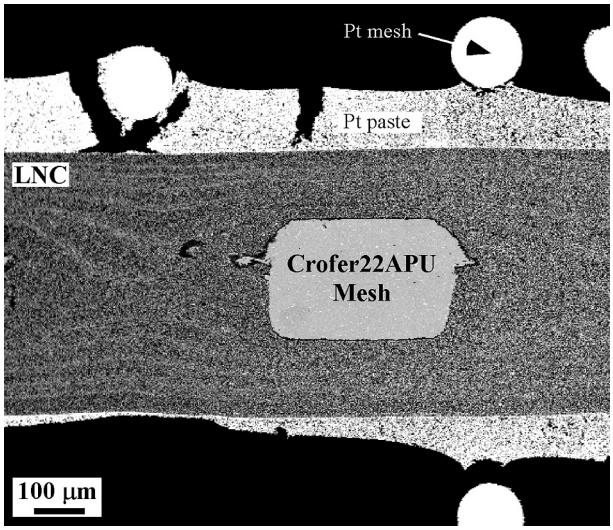

Fig. 5. SEM cross-section of the ceramic/metallic composite contact material after ASR measurements.

Co^{2+}), forming Cr–Ni^{2+}, Co^{2+}-O nucleus. The reaction between these nucleus, gaseous Cr compounds and nucleation agents leads to the deposition and formation of Cr_2O_3, $(Cr,Mn)_3O_4$, $CoCr_2O_4$, etc [3]. One should consider that [37] the magnitude of the Cr deposition is smaller with reducing the test temperature, using the same time exposure in each experiment. Thus, in first sintering step at 1050 °C the Cr deposition is accelerated by temperature and, in the long heat treatment at 800 °C by the exposure time. Thus, different ceramic material densifications were observed between the initial material and composite after the long term treatment, showing that the latter was denser. The formation of dense new phases like spinels might change the pore distribution of the ceramic material. Therefore, the microstructure of the ceramic coating depends on the reactions undergone by the material.

High magnification cross-sectional BSE micrographs and the corresponding EDX elemental line scans of the initial (Fig. 8a) and treated (Fig. 8b) material are shown in Fig. 8. According to other studies [38,39], the oxide scale growth rate is strongly affected by the temperature. With increasing temperature the growth rate constant increases exponentially. Besides, it was found [40] the chromium oxide scale rates at longer exposure time, on the cathode side, can be interpreted as being parabolic. Thus, the oxide scale formed on the mesh after 1000 h was slightly more noticeable. According to Ref. [41] and taking into account the Fe–Cr phase diagram [42], the oxide scale formed on mesh steel surface, after the sintering process of the composite at 1050 °C, is formed by FCC-Fe/Cr_2O_3 in contact with the stainless steel and, by Fe_2O_3 as the oxide surface. Between these two layers, several oxides may form, such as, Fe_3O_4, FeO, $(Cr,B)_3O_4$ spinel (B = Co, Fe, Mn, Ni) [43–45]. The similar ionic radii of Co, Fe, Mn and/or Ni, make it difficult to determine the exact chemistry of the grown spinel. At 800 °C the composition of the oxide scale has a similar trend to that at 1050 °C. However, in the oxide/metal interface Cr_2O_3 may form instead of FCC-Fe/Cr_2O_3 as in the 1050 °C case. These results are in good agreement with performed EDX line scans (Fig. 8a and b). The formation of iron oxides in oxide scale makes alloy be more susceptible to breakaway oxidation [46]. The white zones observed on alloys (Fig. 8) were identified as LNC contamination due to the polishing process. Besides, locally internal precipitates of Cr_2O_3 followed by $(Mn,Cr)_3O_4$ spinel were also found (Fig. 7). These internal precipitates could be related to the external oxide scale or it could be that the diffusion rate of oxygen in the alloy was stronger than that of Cr, forming internal Cr_2O_3 precipitates [47].

3.3. Characterization of composite contact material with channeled Crofer22APU interconnect

As starting point, the metallic substrates were oxidized at 800 °C for 100 h. This preoxidation of the steel may reduce Cr and Fe transport into the contact coating after long oxidation times [48]. A composite contact material without sintering was directly adhered

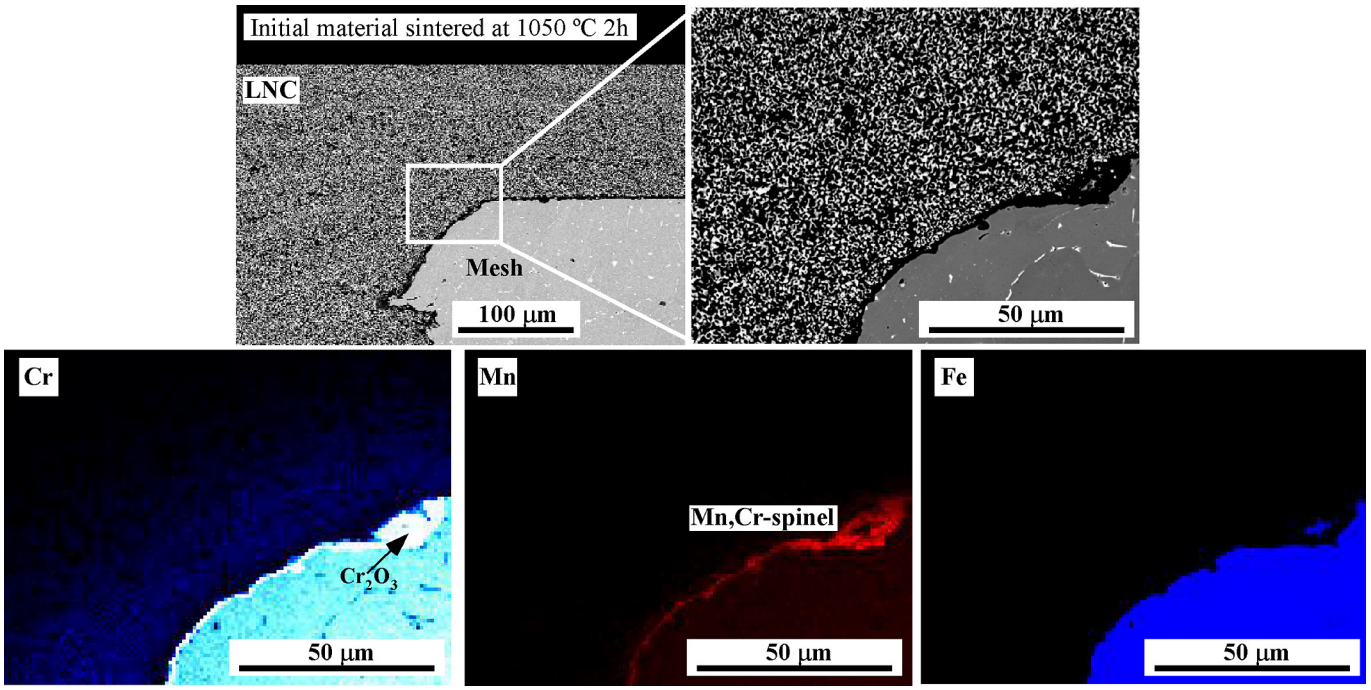

Fig. 6. Cross-section of composite contact material after sintering at 1050 °C for 2 h in air and EDX mapping of the selected zone (in white continuous line).

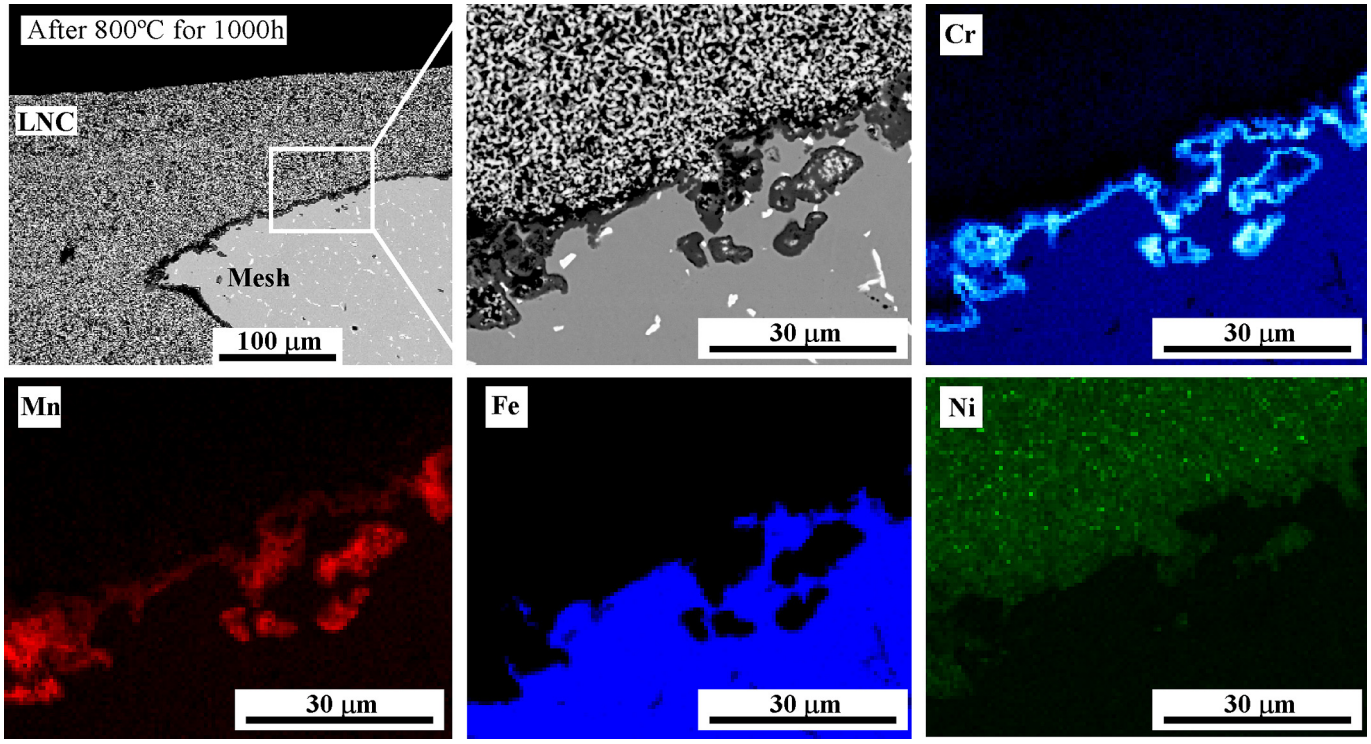

Fig. 7. Cross-section of composite contact material after heating at 800 °C for 1000 h in air and EDX mapping of the selected zone (in white continuous line).

to preoxidized channeled Crofer22APU interconnect. In order to achieve good adhesion between both materials, the ribs of the interconnect substrate were coated with LNC ceramic material by colloidal spray. Then, the system composed of {composite contact material/channeled interconnect} was sintered at 1050 °C for 2 h in open air. In order to check the reproducibility of the process, different systems were prepared. Fig. 9 and Table 3 show ASR values of two systems, indicating good stability and similar signal during the contact resistance measurements, and thus a good adherence between the composite contact material and the

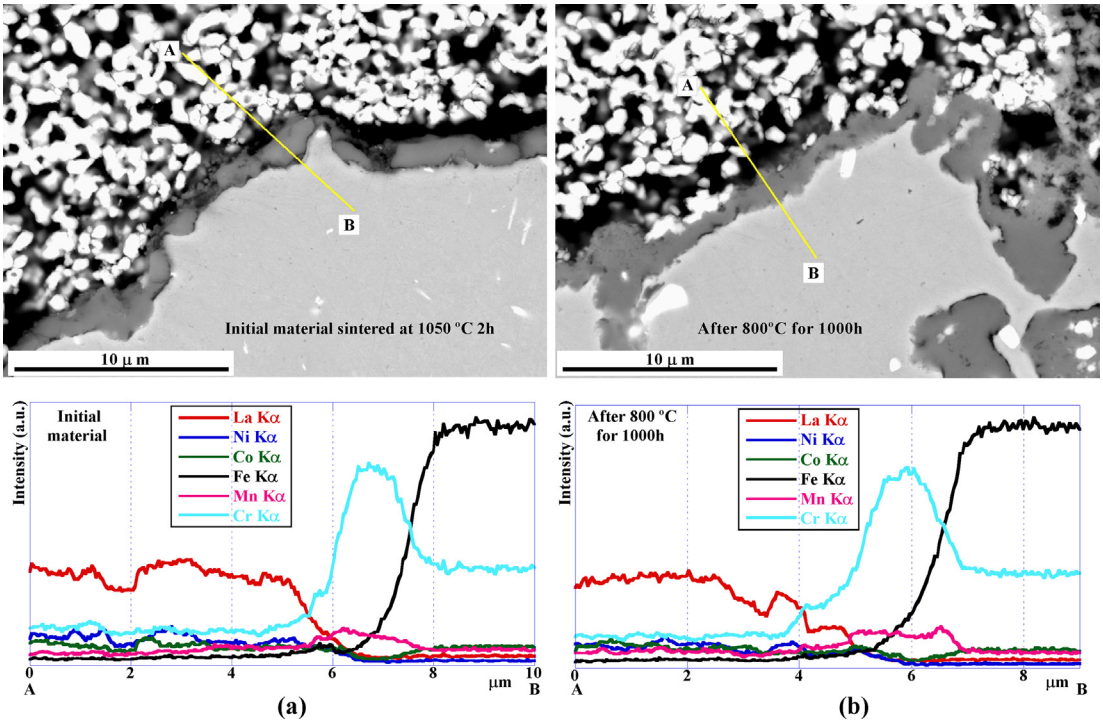

Fig. 8. Cross-sectional BSE images and the corresponding EDX elemental line scans of a) initial material and b) composite after the long heat treatment.

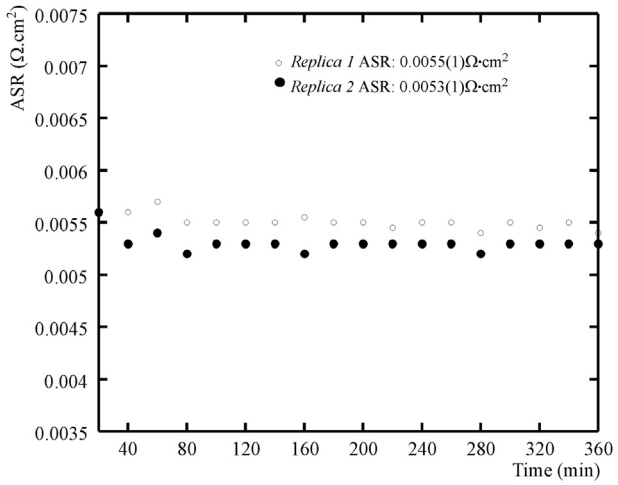

Fig. 9. ASR for {composite contact material/channeled interconnect} interface as a function of time.

Table 3
Area specific resistance values for composite contact material, with and without interconnect, measured at 800 °C in air.

Sample	≈ASR (mΩ cm^2)
Composite contact material	0.46 ± 0.01
Replica 1	5.50 ± 0.01
Replica 2	5.30 ± 0.01

interconnect. The ASR values are in good agreement with those obtained in {Crofer22APU interconnect without channels/LNC contact layer/$La_{0.6}Sr_{0.4}FeO_3$ cathode} system [17]. The contact composite/interconnect ASR value was 5.40 ± 0.01 mΩ cm^2, which is a suitable value for the performance of IT-SOFC stack. In addition, the obtained ASR value is lower than the systems without applying a contact layer [12,16,17]. According to SEM cross-section of the system after ASR measurements with EDX mapping to estimate element diffusion (Fig. 10), the formed oxide scale acts as protective layer: Cr_2O_3 followed by $(Cr,Mn)_3O_4$ spinel top layer. The composite direct contacted (the rib) and indirect contacted (channel) with the interconnect present similar Cr, Mn and Fe distributions. Along the ceramic bulk, Cr^{3+} and Mn^{2+} deposition was observed, indicating that Mn dopant promotes Cr deposition on the ceramic material.

3.3.1. *Long term stability of composite contact material with channeled Crofer22APU interconnect*

The {LNC dip-coated on Crofer22APU mesh composite contact material/Crofer22APU channeled interconnect} sintered system at 1050 °C, was treated at 800 °C for 1000 h in open air to study the long term compatibility between the metallic substrate and the composite. Fig. 11 shows X-ray Micro-Diffraction pattern refinements performed on the rib (right) and the channel (left) of the interconnect in contact with the composite material, after the long term treatment. The preliminary analysis of the studied points was carried out using the X'Pert HighScore software 2003. After the identification, the observed phases, in both areas, were quantified; full-profile refinements were performed using the FULLPROF program [49]. The formed phases and their semiquantitative analysis (% in weight) are presented in Table 4. These analyses reveal that in the rib zone the main phases were $LaNi_{0.6}Co_{0.4}O_{3-\delta}$, La(Cr, B)$O_3$ (B = Ni, Co) and NiO. In addition, secondary phases were also detected: Fe–Cr, $(Cr,B)_3O_4$ spinel (B = Co, Fe, Mn, Ni) and Fe_2O_3. In contrast, the channel zone present as main phases $LaNi_{0.6}Co_{0.4}O_{3-\delta}$, Fe_3O_4, La(Cr, B)O_3 (B = Ni, Co), Cr_2O_3 and as secondary phases: Fe–Cr, $(Cr, B)_3O_4$ (B = Co, Fe, Mn, Ni) spinel and Fe_2O_3. The original Fe–Cr substrate was identified indicating that the X-ray penetration was enough to observe the signal of all the formed layers. The quality factors of the refinements are given in Tables 5 and 6. The presence of the LNC perovskite phase in the channel zone is probably due to the contamination during the spray deposition on the ribs. The presence of NiO might entail that Ni is partially

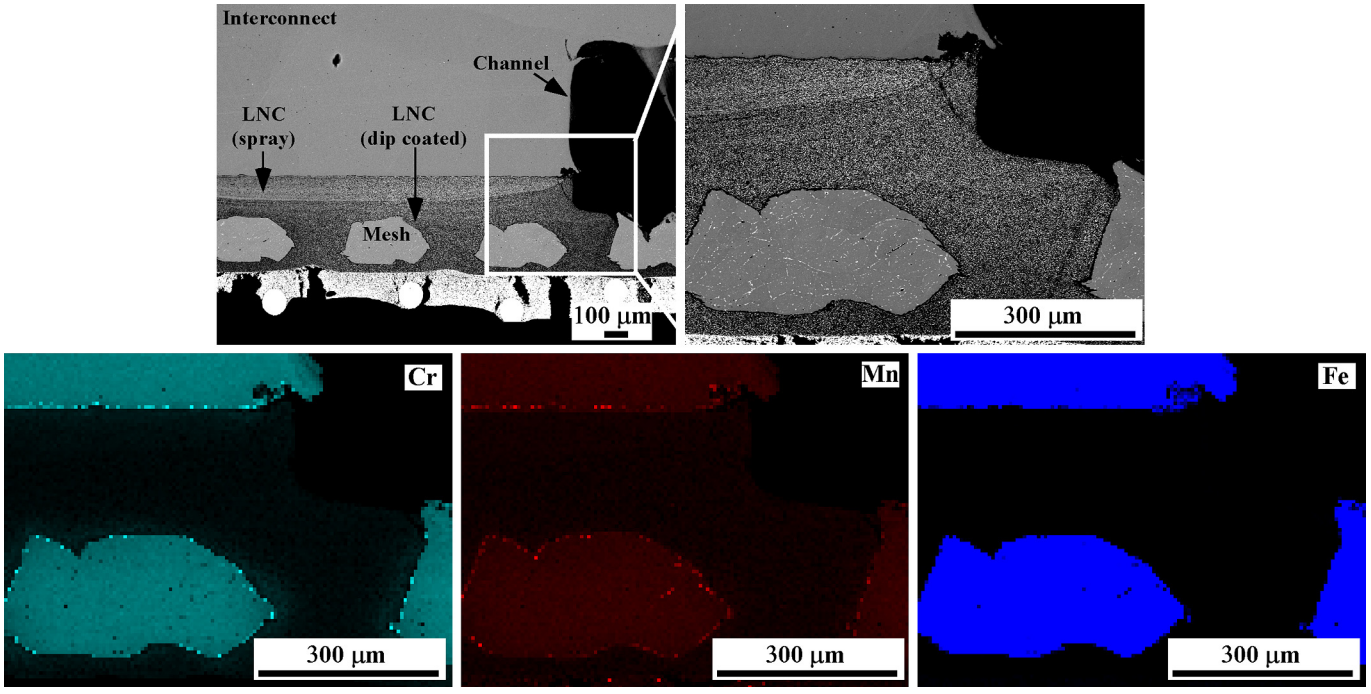

Fig. 10. Cross-section of {composite contact material/channeled interconnect} sintered system after ASR test and EDX mapping of the selected zone (in white continuous line).

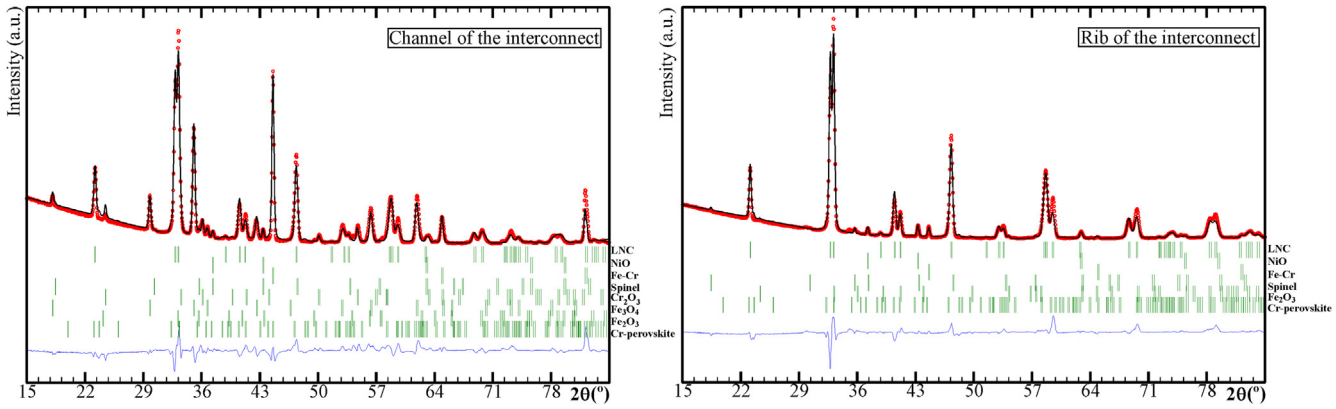

Fig. 11. X-ray Micro-Diffraction pattern refinements performed on the rib and on channel of the interconnect in contact with composite material, after long term heat treatment.

extracted from the LNC perovskite lattice, whereas Cr is incorporated, most likely to form La(Ni, Co, Cr)O_3 [27,50]. It is known that applying a protective layer to the metallic interconnect alloy can reduce the oxidation rate [34]. Fig. 12 shows cross-section EDX elemental line scans performed on the channel (Fig. 12a) and on the rib (Fig. 12b) of the interconnect, which was in contact with the composite material after treated at 800 °C for 1000 h in open air. The surface oxide layers, both on the channel and on the rib, of the interconnect range from approximately 0.5 to 2 μm. Before ASR test, the metallic substrate was preoxidized at 800 °C for 100 h, making difficult to observe differences between both zones. However, the Fe and Cr detected in the channel is bigger than in the rib, probably due to the formation of a passive layer on the metal surface, more severe in the case of an uncoated area. According to this, ceramic coating might act as a protective layer. Hence, Cr_2O_3 is observed on the channels. Furthermore, the absence of Cr_2O_3 on the rib of the interconnect, can also imply that it has completely reacted to form La(Cr, B)O_3 (B = Ni, Co) and (Cr, B)$_3O_4$ (B = Mn, Fe, Ni, Co) phases. The formed oxides at analyzed channel zones contain: Fe_2O_3 (<2% in weight) and Fe_3O_4 (~36% in weight) whereas for those on the rib zone, Fe_2O_3 (~2% in weight) was semi-quantified. The presence of iron oxides is in good agreement with the previous studies performed on composite contact material (Section 3.2.1.). According to XRMD results, an interconnect without ceramic coating at long exposure rate to air, can promote the Fe_3O_4 formation rather than the formation of a chromia/spinel protective scale, concluding in the formation of non-protective or Fe-rich scale.

Fig. 13 shows the surface of the composite material which was in contact with the interconnect, after long term IT-SOFC conditions. EDX mapping analysis is also shown. Three different areas were identified at the composite contact surface: the area of the composite i) under the rib and, ii) under channel of the interconnect and, iii) the interface between both zones. Formation of Cr and Mn deposit along the interface of both areas is observed, probably in the form of (Cr,Mn)$_3O_4$ protective spinel. Besides, EDX analysis showed that the zone under the channel presents Cr, Mn and La enrichment, possibly associated with Cr–Mn-spinel and Cr-perovskite crystalline phases. The significant difference in the amount of Cr deposition on the composite material surface under the rib and under the channel of the interconnect can indicate that the direct exposure to air accelerates the formation of CrO_3 (g) and $CrO_2(OH)_2$ (g) species. Thus, vapor phase transport of Cr specie molecules would be much faster and more significant than the solid phase diffusion of atoms, in LNC and chromia scale, through defects in these solids. Increasing volatile Cr species enhances Cr-depletion from the alloy, thereby enabling the formation of iron oxides [46].

XPS measurements were performed on the observed channel and rib contact areas of the surface of the metallic/ceramic composite material. Fig. 14 shows high resolution spectra of the different zones including La $3d_{5/2}$, Cr 2p and Mn $2p_{3/2}$ spectral regions. The binding energies and relative atomic percentage concentration of the detected elements are listed in Tables 7 and 8, respectively. In both studied areas, for La, there are two peaks, one at 833 eV which corresponds to La^{3+} in perovskite phase [51] and, another at 834 eV which is assigned to La^{3+} in La_2O_3 [52]. In addition, the peaks appearing at 575 eV and 579 eV could be assigned to Cr^{3+} in perovskite [53,54]. The atomic concentration of Cr assigned to the perovskite remains a ratio of 1:1, and La component is assigned to the binding energy of 833 eV, in good agreement with ABO_3 structure (Tables 6 and 7). In the contact channel zone, the peak at 577 eV might be ascribed to Cr^{3+} species,

Table 4
Semiquantitative % in weight of the formed phases on the rib and channel of the interconnect in contact with composite material after heating at 800 °C for 1000 h.

Phases (space group)	N° PDF	Channel	Rib
$LaNi_{0.6}Co_{0.4}O_3$ (R-3c)	32-0296	~46	~82
$LaCrO_3$ (Pbnm)	24-1016	~6	~7
Fe–Cr (Im3m)	34-0396	<2	<2
Fe_2O_3 (R-3c)	73-2234	<2	~2
NiO (Fm-3m)	73-1519	~2	~5
$MnCr_2O_4$ (Fd-3m)	31-630	<2	<2
Cr_2O_3 (R-3c)	85-0730	~4	–
Fe_3O_4 (Fd-3m)	19-629	~36	–

*Estimated error: ± 1–2%.

Table 5
The quality of refinement performed on the rib of the interconnect in contact with composite material, after long term heat treatment.

Rib phases	$LaNi_{0.6}Co_{0.4}O_3$	$LaCrO_3$	Fe–Cr	Fe_2O_3	NiO	$MnCr_2O_4$
R_{Bragg}	13	29	31	30	16	40
R_f	8	23	16	24	9	18
χ^2	5					

Table 6
The quality of refinement performed on the channel of the interconnect in contact with composite material, after heated at 800 °C for 1000 h.

Channel phases	$LaNi_{0.6}Co_{0.4}O_3$	$LaCrO_3$	Fe–Cr	Fe_2O_3	NiO	$MnCr_2O_4$	Cr_2O_3	Fe_3O_4
R_{Bragg}	13	32	21	43	13	32	31	18
R_f	10	25	11	29	11	21	18	11
χ^2	18							

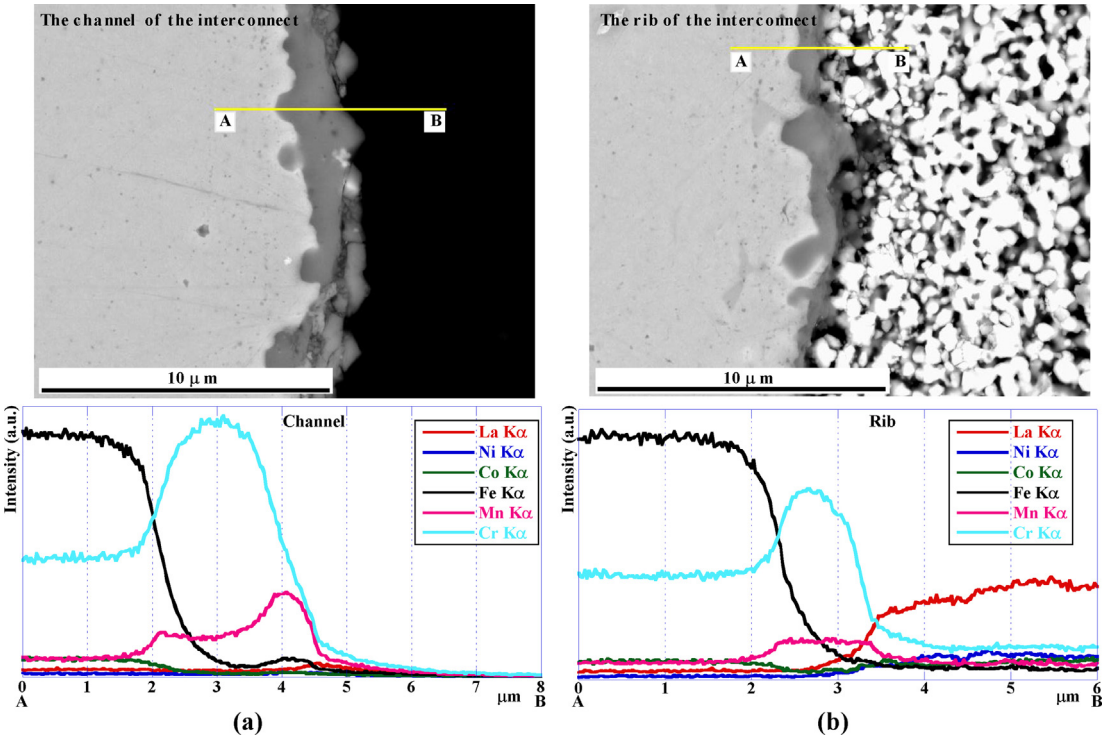

Fig. 12. Cross-sectional BSE images and the corresponding EDX elemental line scans performed on a) the channel and b) the rib of the interconnect which was in contact with the composite contact material after treated at 800 °C for 1000 h in open air.

possibly forming Cr_2O_3 [55] in good agreement with XRD results. The binding energy of 642 eV, which corresponds to Mn $2p_{3/2}$, is in good agreement with Mn^{4+} in MnO_2 superficial oxide [56]. However, the content of Mn is too low to be assigned to Mn^{2+} or Mn^{4+} species.

4. Conclusions

The application of composite LNC/Crofer22APU mesh coatings as a contact material for Fe–Cr channeled interconnect was studied as a solution to limit electrical losses between both materials and

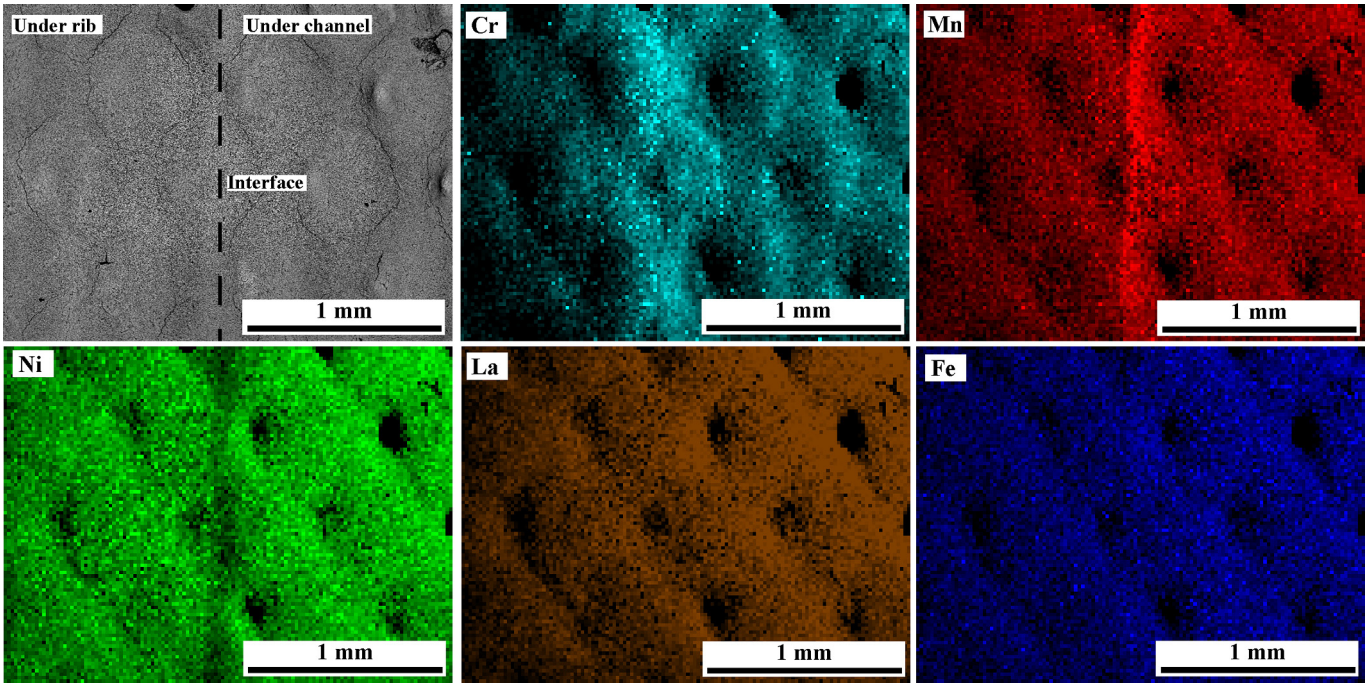

Fig. 13. EDX mapping of the surface of the composite material which was in contact with interconnect, after long term IT-SOFC conditions.

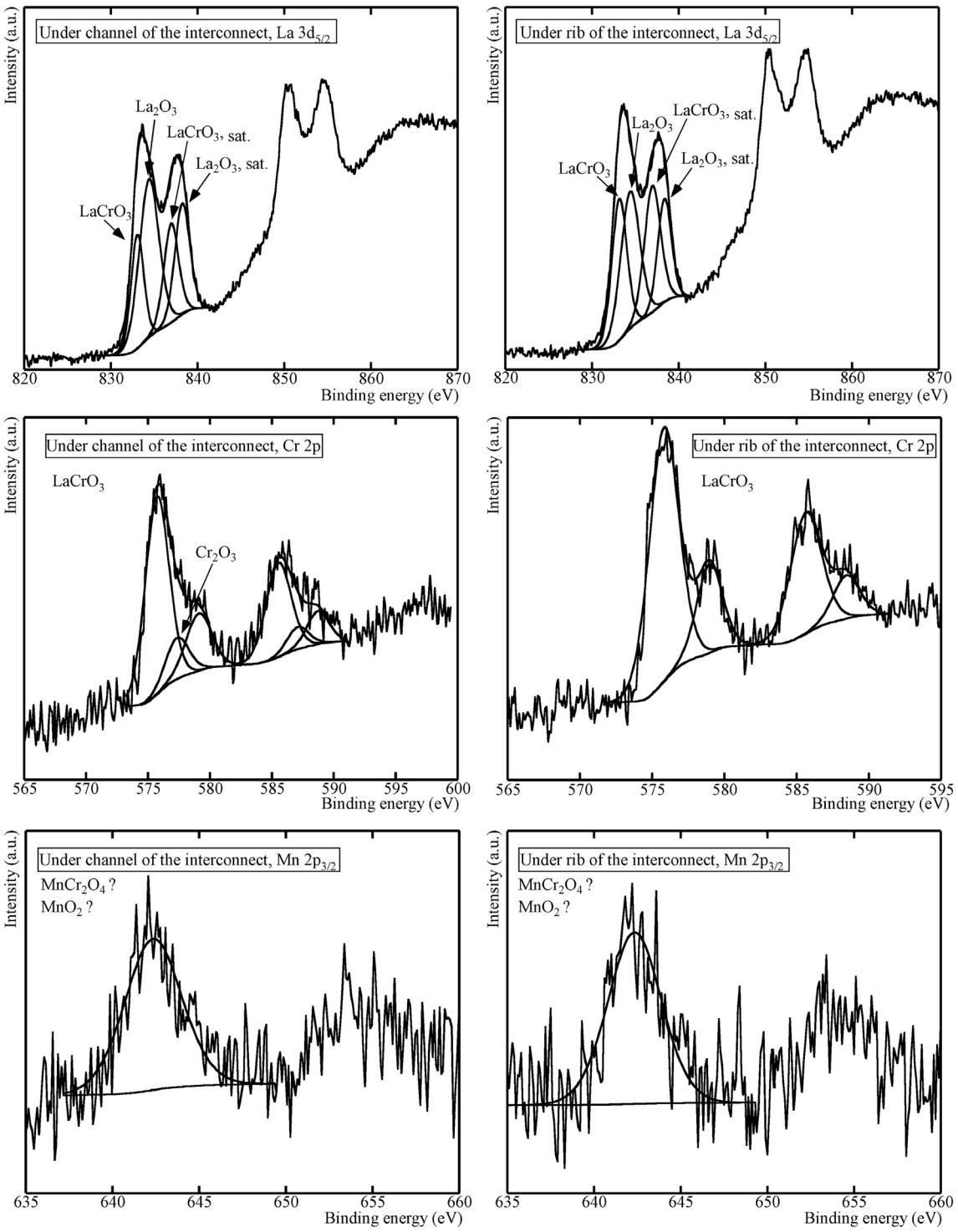

Fig. 14. La $3d_{5/2}$, Cr 2p and Mn $2p_{3/2}$ spectral regions of the surface of composite contact material under the rib and channel after long term heated at 800 °C in air.

also to reduce chromium migration from the interconnect. Prior to forming the composite material, adequate formulation of the LNC paste was obtained and characterizated by rheological measurements. This slurry was dip coated on Fe–Cr mesh to obtain metallic-ceramic composite contact material. The results showed good adherence between ceramic and metallic material, showing a continuous and homogeneous coated LNC layer. The system presented an ASR value of 0.46 ± 0.01 mΩ cm^2 at 800 °C. After treatment under long term IT-SOFC conditions, the composite material still present noticeable oxide scale and adequate mechanical integrity of the LNC/Fe–Cr mesh interface.

When the composite contact material was directly adhered to the interconnect, the obtained ASR values were reproducible and stable indicating good adherence between the composite material and interconnect. After 1000 h at 800 °C in open air, X-ray Micro-Diffraction, performed at the rib and channel of the interconnect,

Table 7
XPS analysis results of the detected elements for the contact surface of the composite in contact with the rib of the interconnect, after heating at 800 °C for 1000 h in air.

Peak	Binging energy (eV)	% at. Conc.
La $3d_{5/2}$ in ABO_3	833.14	9.5
La $3d_{5/2}$ in La_2O_3	834.4	9.1
Cr 2p in ABO_3	575.82; 578.98	9.1
Mn $2p_{3/2}$	642.35	3.2
O 1s	528.93; 530.74	69.1

Table 8
XPS analysis results of the detected elements for the contact surface of the composite under channel of the interconnect, after heating at 800 °C for 1000 h in air.

Peak	Binging energy (eV)	% at. Conc.
La $3d_{5/2}$ in ABO_3	833.07	7.1
La $3d_{5/2}$ in La_2O_3	834.41	11.8
Cr 2p in ABO_3	575.73; 579.1	7.2
Cr 2p in Cr_2O_3	577.35	1.1
Mn $2p_{3/2}$	642.34	3.2
O 1s	528.98; 530.99	69.6

revealed interactions between the oxide scale and the LNC material to form Cr-perovskite which was related with NiO presence. In both zones semi-quantified Fe_2O_3 was also present, arising from the oxidation of the metal itself. According to XRMD results, the interconnect without ceramic coating on the metal surface, and the direct exposure to air increased the oxidation rate and Fe_3O_4 formation as non-protective layer. The direct exposure to air accelerates the formation of CrO_3 (g) and $CrO_2(OH)_2$ (g) species on channel surface.

Taking into account the obtained contact resistance, mechanical integrity and chemical compatibility of the studied system, LNC dip-coated on Fe–Cr mesh would offer promising opportunities as a high conductivity composite contact material. Future work will include the integration of the $La_{0.6}Sr_{0.4}FeO_3$ cathode to form {interconnect/composite contact material/cathode} system, in flow channel configuration, to study its long-term stability in terms of contact resistance and chemical compatibility.

Acknowledgment

This research has been funded by the Dpto. Educación, Política Lingüística y Cultura of the Basque Goverment (IT-630-13), Ministerio de Ciencia e Innovación (MAT2010-15375 and MAT2012-30763) and Engineering and Physical Sciences Research Council (EP/I003932). The authors thank SGIker technical support and Dr. Mª Belén Sánchez Martínez de Ilárduya for XPS measurements. A. Morán-Ruiz thanks UPV/EHU for funding her PhD work.

References

[1] J. Klugman, Human Development Report 201. Sustainability and Equity: a Better Future for All, United Nations Development Programme, New York, USA, 2011.
[2] B.J. Spivey, T.F. Edgar, J. Process Contr. 22 (2012) 1502.
[3] S.P. Jiang, X. Chen, Int. J. Hydrogen Energy 39 (2014) 505.
[4] K. Huang, S.C. Singhal, J. Power Sources 237 (2013) 84.
[5] S.C. Singhal, Solid State Ionics 135 (2000) 305.
[6] J. Wu, X. Liu, J. Mater. Sci. Technol. 26 (4) (2010) 293.
[7] C. Sun, R. Hui, J. Roller, J. Solid State Electrochem. 14 (2010) 1125.
[8] A. Mat, B. Timurkutluk, C. Timurkutluk, Y. Kaplan, Ceram. Int. (2014), http://dx.doi.org/10.1016/j.ceramint.2014.01.073.
[9] W.B. Guan, H.J. Zhai, L. Jin, T.S. Li, W.G. Wang, Fuel Cells 3 (2011) 445.
[10] W. Wu, G.L. Wang, W.B. Guan, Y.F. Zhen, W.G. Wang, Fuel Cells 5 (2013) 743.
[11] W. Guan, L. Jin, W. Wu, Y. Zheng, G. Wang, W.G. Wang, J. Power Sources 245 (2014) 119.
[12] X. Montero, F. Tietz, D. Stöver, M. Cassir, I. Villarreal, J. Power Sources 188 (2009) 148.
[13] L. Jin, W. Guan, J. Niu, X. Ma, W.G. Wang, J. Power Sources 240 (2013) 796.
[14] W. Zhang, F. Wang, K. Wang, J. Pu, B. Chi, L. Jian, Int. J. Hydrogen Energy 37 (2012) 17253.
[15] F. Wang, D. Yan, W. Zhang, B. Chi, J. Pu, L. Jian, Int. J. Hydrogen Energy 38 (2013) 646.
[16] Z. Yang, G. Xia, P. Singh, J.W. Stevenson, J. Power Sources 155 (2006) 246.
[17] A. Morán-Ruiz, K. Vidal, M.A. Laguna-Bercero, A. Larrañaga, M.I. Arriortua, J. Power Sources 248 (2014) 1067.
[18] M.C. Tucker, L. Cheng, L.C. DeJonghe, J. Power Sources 196 (2011) 8313.
[19] M.C. Tucker, L. Cheng, L.C. DeJonghe, J. Power Sources 196 (2011) 8435.
[20] M.C. Tucker, L. Cheng, L.C. DeJonghe, J. Power Sources 224 (2013) 174.
[21] Z. Lu, G. Xia, J.D. Templeton, X. Li, Z. Nie, Z. Yang, J.W. Stevenson, Electrochem. Commun. 13 (2011) 642.
[22] Q.X. Fu, D. Sebold, F. Tietz, H.P. Buchkremer, Solid State Ionics 192 (2011) 376.
[23] N. Shaigan, D.G. Ivey, W. Chen, J. Power Sources 185 (2008) 331.
[24] L.T. Wilkinson, J.H. Zhu, J. Electrochem. Soc. 156 (8) (2009) B905.
[25] X. Montero, N. Jordán, J. Pirón-Abellán, F. Tietz, D. Stöver, M. Cassir, I. Villarreal, J. Electrochem. Soc. 156 (1) (2009) B188.
[26] V. Miguel-Perez, A. Martínez-Amesti, M.L. Nó, A. Larrañaga, M.I. Arriortua, Corros. Sci. 60 (2012) 38.
[27] A. Morán-Ruiz, K. Vidal, A. Larrañaga, M.I. Arriortua, Fuel Cells 3 (2013) 398.
[28] A. Torabi, T.H. Etsell, P. Sarkar, Solid State Ionics 192 (2011) 372.
[29] L. Conceicao, L. Dessemond, E. Djurado, M.M.V.M. Souza, Int. J. Hydrogen Energy 38 (2013) 15335.
[30] K. Hilpert, D. Das, M. Miller, D.H. Peck, R. Wei, J. Electrochem. Soc. 143 (1996) 3642.
[31] V. Miguel Pérez, Interconectores Metálicos y Capas Protectoras para su Aplicación en pilas SOFC, UPV/EHU, 2013. Ph. D. thesis.
[32] D.K. Schroder, Semiconductor Material and Device Characterization, third ed., John Wiley & Sons, New York, 1998, pp. 149–156. Cap. 3.
[33] J.P. Choi, K.S. Weil, Y.M. Chou, J.W. Stevenson, Z.G. Yang, Int. J. Hydrogen Energy 36 (2011) 4549.
[34] V. Miguel-Pérez, A. Martínez-Amesti, M.L. Nó, A. Larrañaga, M.I. Arriortua, J. Power Sources 243 (2013) 419.
[35] G.Y. Lau, M.C. Tucker, C.P. Jacobson, S.J. Visco, S.H. Gleixner, L.C. DeJonghe, J. Power Sources 195 (2010) 7540.
[36] X. Chen, Y. Zhen, J. Li, S.P. Jiang, Int. J. Hydrogen Energy 35 (2010) 2477.
[37] S.P. Jiang, S. Zhang, Y.D. Zhen, J. Mater. Res. 20 (3) (2005) 747.
[38] P. Kofstad, High Temperature Corrosion, Springer, 1988.
[39] M. Palcut, L. Mikkelsen, K. Neufeld, M. Chen, R. Knibbe, P.V. Hendriksen, Corros. Sci. 52 (2010) 3309.
[40] M. Linder, T. Hocker, L. Holzer, K.A. Friedrich, B. Iwanschitz, A. Mai, J.A. Schuler, J. Power Sources 243 (2013) 508.
[41] V.S. Dheeradhada, H. Cao, M.J. Alinger, J. Power Sources 196 (2011) 1975.
[42] J.O. Anderson, B. Sundman, Calphad 11 (1987) 83.
[43] K. Wang, Y. Liu, J.W. Fergus, J. Am. Ceram. Soc. 94 (12) (2011) 4490.
[44] W.J. Shong, C.K. Liu, C.Y. Chen, C.C. Peng, H.J. Tu, G.T.K. Fey, R.Y. Lee, H.M. Kao, Mater. Chem. Phys. 127 (2011) 45.
[45] K. Przybylski, T. Brylewski, E. Durda, R. Gawel, A. Kruk, J. Therm. Anal. Calorim. doi: 10.10007/s10973-013-3594-1.
[46] E. Essuman, G.H. Meier, J. Zurek, M. Hänsel, T. Norby, L. Singheiser, W.J. Quadakkers, Corros. Sci. 50 (2008) 1753.
[47] H. Ali-Löytty, Microalloying Mediated Segregation and Interfacial Oxidation of FeCr Alloys for Solid-oxide Fuel Cell Applications, Tampereen teknillinen yliopisto – Tampere University of Technology, 2013. Ph. D. thesis.
[48] K.O. Hoyt, P.E. Gannon, P. White, R. Tortop, B.J. Ellingwood, H. Khoshuei, Int. J. Hydrogen Energy 37 (2012) 518.
[49] J. Rodríguez-Carvajal, Fullprof Rietveld Pattern Matching Analysis of Power Patterns, 1994. Grenoble.
[50] M.K. Stodolny, B.A. Boukamp, D.H.A. Blank, F.P.F. van Berkela, J. Electrochem. Soc. 158 (2) (2011) B112.
[51] F. Bin, C. Song, G. Lv, J. Song, C. Gong, Q. Huang, Ind. Eng. Chem. Res. 50 (2011) 6660.
[52] C.D. Wagner, W.M. Riggs, L.E. Davis, J.F. Moulder, G.E. Mullenberg, Handbook of X-ray Photoelectron Spectroscopy, Perkin-Elemer Corporation, Physical Electronics Division, Eden Prairie, MN 55344, 1979.
[53] W.Y. Howng, R.J. Thorn, J. Chem. Phys. Solids 41 (1980) 75.
[54] M. Stojanovic, R.G. Haverkamp, C.A. Mims, H. Moudallal, A.J. Jacobson, J. Catal. 165 (1997) 315.
[55] C. Battistoni, J.L. Dormann, D. Fiorani, E. Paparazzo, S. Viticoli, Solid State Commun. 39 (1981) 581.
[56] A. Aoki, Jpn. J. Appl. Phys. 15 (1976) 305.

Solid State Ionics 269 (2015) 24–29

Contents lists available at ScienceDirect

Solid State Ionics

journal homepage: www.elsevier.com/locate/ssi

Characterization of $LaNi_{0.6}Fe_{0.4}O_3$ perovskite synthesized by glycine-nitrate combustion method

K. Vidal [a,*], A. Morán-Ruiz [a], A. Larrañaga [a], J.M. Porras-Vázquez [b], P.R. Slater [b], M.I. Arriortua [a,*]

[a] Universidad del País Vasco/Euskal Herriko Unibertsitatea (UPV/EHU), Dpto. Mineralogía y Petrología, Apdo. 644, E-48080 Bilbao, Spain
[b] University of Birmingham, School of Chemistry, Birmingham B15 2TT, UK

ARTICLE INFO

Article history:
Received 8 May 2014
Received in revised form 27 October 2014
Accepted 3 November 2014
Available online xxxx

Keywords:
Chemical synthesis
Electrical conductivity
Contact material
Perovskite phases
SOFC

ABSTRACT

The perovskite $LaNi_{0.6}Fe_{0.4}O_3$ has been prepared by the glycine–nitrate route using different amounts of glycine/fuel ratio (G/N = 0.5, 1.0 and 1.5), in order to study the sample preparation influence on the properties in the context of their application as a cathode contact material for solid oxide fuel cells (SOFCs). The obtained materials have been characterized by X-ray diffraction, scanning electron microscopy, dilatometry and electrical conductivity measurements. All the compounds have rhombohedral symmetry and a porous microstructure with fine grain sizes. The sample obtained at the G/N of 1.0 has more suitable conductivity values for application as SOFC contact material.

1. Introduction

The need for a clean and efficient energy conversion is a critical technological and economic challenge. Solid oxide fuel cells (SOFCs) have a substantial potential in the application of a clean and efficient electrical power generation. However, the widespread utilization of SOFCs has not been realized because the cost associated with cell fabrication, materials and maintenance is still too high [1].

The development of new materials, as well as advanced SOFC component fabrication techniques, is critical in reducing operation temperature and subsequently in lessening the cost of these systems. Traditionally, most of these ceramic materials have been prepared from the mixture of their constituent oxides in the so called solid state reaction, "shake and bake" or ceramic method, a preparative route which presents as a fundamental handicap the necessity of heating the precursors at high temperature for large periods of reaction time to reach the formation of a desired phase. Therefore, the use of such drastic experimental conditions drives the formation of materials that show particles with a relatively large size [2]. Alternative routes to the solid state reaction method are wet chemical synthetic methods such as co-precipitation (with oxalates, carbonates, cyanides or any other salt precursors), combustion (including all variants from low to high temperature), sol–gel (and all of its modifications with different chelating ligands), spray-pyrolysis, and metathesis reactions. In all cases the idea is to accelerate the pure phase formation, a goal that is achieved due to the liquid media which permit the mixing of the elements at the atomic level, thus resulting in lower firing temperatures [3,4]. Other advantages of these methods are the possibility of having a controlled particle size, morphology and improvement in surface area. Particularly, combustion methods have been proposed as one of the most promising methods to prepare perovskite oxide powders to be used as electrode materials in solid oxide fuel cell technology [5].

Combustion reaction is one of the most accessible, fast and low energy soft methods for the synthesis of a variety of advanced ceramics, catalysts and nanomaterials [6,5]. Combustion synthesis (CS) methods can be classified into three categories, on the basis of the physical nature of reaction mixture itself: (i) flame synthesis or gas phase combustion, (ii) heterogeneous condensed phase combustion synthesis and (iii) solution combustion synthesis (SCS) [6,7]. Focusing our attention on the SCS route, it involves a self-sustained exothermic reaction between an oxidizer (e.g. metal nitrate) and a fuel (e.g. urea, glycine, hydrazides, carbohydrazide). Compared with the ceramic method this synthetic route has much faster reaction times and lower calcination temperatures leading to powders with large compositional homogeneity and nanometric particle sizes, which are desired characteristics for this type of applications. The characteristics (including the purity, structure and size) of the combustion synthesis oxide powders are typically determined by several synthetic parameters, such as the species of fuel and oxidizer reactants, the fuel/oxidizer ratio, and the subsequent sintering treatment after combustion process [8]. The fuel to oxidizer ratio is considered to be the most important one in varying the final properties [9]. This parameter may influence the phase formation

* Corresponding authors. Tel.: +34 946015984; fax: +34 946013500.
E-mail addresses: karmele.vidal@ehu.es (K. Vidal), maribel.arriortua@ehu.es (M.I. Arriortua).

http://dx.doi.org/10.1016/j.ssi.2014.11.002
0167-2738/

process [10], the phase structure of the products [11], the morphology of the as-prepared powders [12], and then, the physical and chemical properties of the materials [13].

Earlier studies have concluded that the use of cathode contact layers improves electron transfer through the contact interface from the interconnect to the cathode layer [14,15]. The cathode contact material composition is required to possess high electrical conductivity and appropriate sintering activity to minimize the resistance of the contact layer itself and to protect the steel substrate from excessive oxidation. Besides, it should demonstrate an appropriate thermal expansion behavior and high thermochemical and structural stability in the oxidizing cathode environment [16,17].

In this study $LaNi_{0.6}Fe_{0.4}O_3$ is selected for its use as contact layers, due to the adequate sintering activity, electrical conductivity, thermal expansion coefficient (TEC), integrity and low reactivity between the interconnect and cathode without compromising the contact resistance of the system [14,18].

Continuing our research on $La(Ni,Fe)O_3$ based systems, in the present work we investigate the effect of the variation of the fuel/oxidizer ratio of glycine/nitrate (G/N = 0.5, 1.0 and 1.5) on the structural, morphological and electrical properties of the $LaNi_{0.6}Fe_{0.4}O_3$ perovskite oxide.

2. Experimental

2.1. Powder preparation

The compound $LaNi_{0.6}Fe_{0.4}O_3$ was prepared by the glycine-nitrate method starting from the reagents $La(NO_3)_3 \cdot 6H_2O$ (>99%), $Ni(NO_3)_2 \cdot 6H_2O$ (98.5%) and $Fe(NO_3)_2 \cdot 9H_2O$ (98.5%), all from Aldrich. These metal nitrates were dissolved in distilled water. The solutions were mixed in a 1 l glass beaker, which was put on a hot plate, under constant stirring, to evaporate excess water. For examining the effect of combustion fuel condition on the properties of the final powder, different combustion fuel conditions were designed by adding different amounts of fuel. Then, the glycine was added to obtain a glycine/nitrate molar ratio of 0.5, 1.0 and 1.5, respectively. The resulting viscous liquid autoignited after putting the glass beaker directly in a preheated plate (at 450 °C). The resulting powders were pelletized and calcined in air at 850 °C for 6 h to obtain the pure sample.

2.2. Characterization techniques

Room temperature X-ray powder diffraction (XRD) data were collected in the $18 < 2\theta < 110°$ range with an integration time of 10 s/0.02° step using a Philips X'Pert-PRO X-ray diffractometer with secondary beam graphite monochromated Cu–Kα radiation. All samples were single phase without detectable impurities. The crystal structure was refined by the Rietveld method [19] using the GSAS software package [20].

Compositional analysis was performed on all prepared samples to confirm that the expected elemental composition was achieved. All metal contents were determined by inductively coupled plasma atomic emission spectroscopy (ICP-AES) on a Horiba Yobin Yvon Activa spectrophotometer.

The morphologies of the powder samples and of the sintered pellets were observed using a scanning electron microscope (JEOL JSM-7000F). Secondary electron images were taken at 20 kV and $1.1.10^{-11}$ A using a working distance of 8 mm.

For bulk conductivity and thermal expansion (TEC) measurements, pellets of powders were sintered at 1050 °C, and then, cut in $1 \times 3 \times 7$ mm bars. The bulk density of each sample was calculated by measuring the mass and the dimensions of the bars. The samples had a density of around 75% of the theoretical (X-ray) density. DC conductivity measurements were performed in air by the four-point DC method (Thurlby Thandar Instruments 1604 digital multimeter and Thurlby Thandar Instruments PL300 current source). Electrical contacts were made using Pt wires and Pt paste placed over whole end faces ensuring a homogeneous current flow. Voltage contacts were made as small as possible to avoid any disturbance of the contacts on the current flow. Measurements were performed from 300 °C to 850 °C. The conductivity (σ) was determined from a set of V–I values by taking $\sigma = 1 / \rho = L / A \times dI / dV$, where L is the distance between voltage contacts and A is the sample cross section. Finally, TEC measurements were carried out from room temperature to 1000 °C in air with a heating rate of 5 °C/min by using a Unitherm Model dilatometer.

3. Results and discussion

3.1. Structural study

Fig. 1 shows the remarkable dependence of phase constitution on fuel condition for the combustion products depending on the glycine/nitrate molar ratio. In the case of the $LaNi_{0.6}Fe_{0.4}O_3$ sample with stoichiometric G/N, the combustion synthesis produced a clearer and brighter flame, and a higher reaction temperature, in comparison with both the samples obtained under an oxidizer and fuel rich conditions, respectively. According to this, as can be observed in the figure, for the sample prepared using a glycine/nitrate molar ratio of 1.0, the product obtained from combustion (as synthesized powders without applying caltination temperature of 850 °C), is nearly a single phase and is better crystallized compared with the other two compounds.

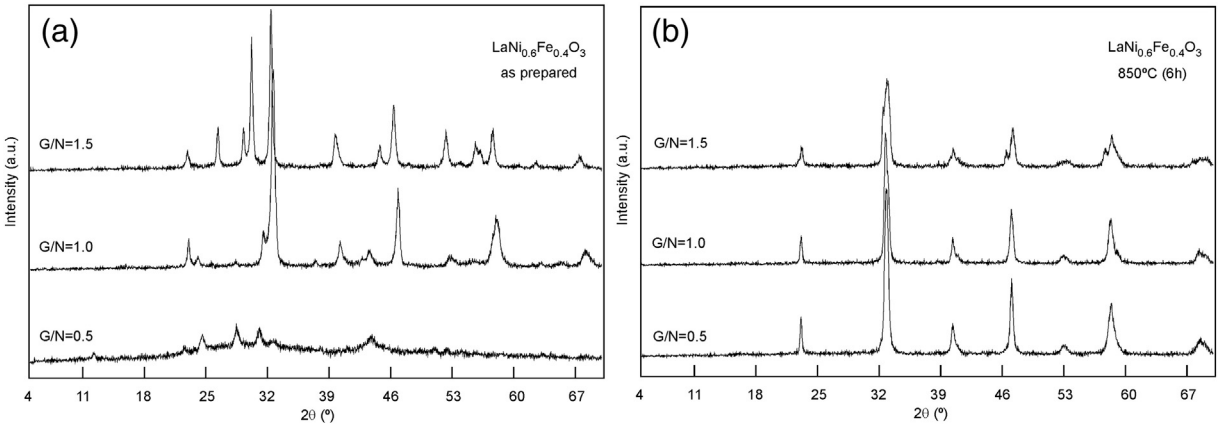

Fig. 1. X-ray diffraction patterns measured (a) before and (b) after calcination at 850 °C for $LaNi_{0.6}Fe_{0.4}O_3$ perovskites obtained by the glycine-nitrate route using different amounts of fuel/oxidizer ratio (G / N = 0.5, 1.0 and 1.5), respectively.

Table 1
Summary of the ICP analyses.

G/N	Nominal composition	Experimental composition
0.5	$LaNi_{0.6}Fe_{0.4}O_3$	$La_{0.96(2)}Ni_{0.61(1)}Fe_{0.40(1)}O_3$
1.0	$LaNi_{0.6}Fe_{0.4}O_3$	$La_{1.00(2)}Ni_{0.63(2)}Fe_{0.40(1)}O_3$
1.5	$LaNi_{0.6}Fe_{0.4}O_3$	$La_{0.98(2)}Ni_{0.63(1)}Fe_{0.41(1)}O_3$

Nevertheless, as shown by the X-ray diffraction patterns, the three $LaNi_{0.6}Fe_{0.4}O_3$ samples were obtained without impurities by applying a calcination temperature of 850 °C in air during 6 h after combustion synthesis.

Results from chemical analyses are presented in Table 1, showing a good agreement between the analyzed chemical compositions of the prepared powders and the nominal compositions.

Fig. 2 shows the Rietveld refinement of the XRD data for the $LaNi_{0.6}Fe_{0.4}O_3$ samples obtained after applying a calcination temperature of 850 °C. The analysis of the X-ray diffraction (XRD) data indicated that the samples with G/N = 0.5 and 1.0 crystallized as a single phase in the rhombohedral space group $R\bar{3}c$. For the compound with G/N 1.5, however, the appearance of extra shoulders in the experimental profile indicates a possible phase segregation to give two perovskite phases of different Ni/Fe ratio. The introduction of two $R\bar{3}c$ phases improves satisfactorily the profile fitting of this sample.

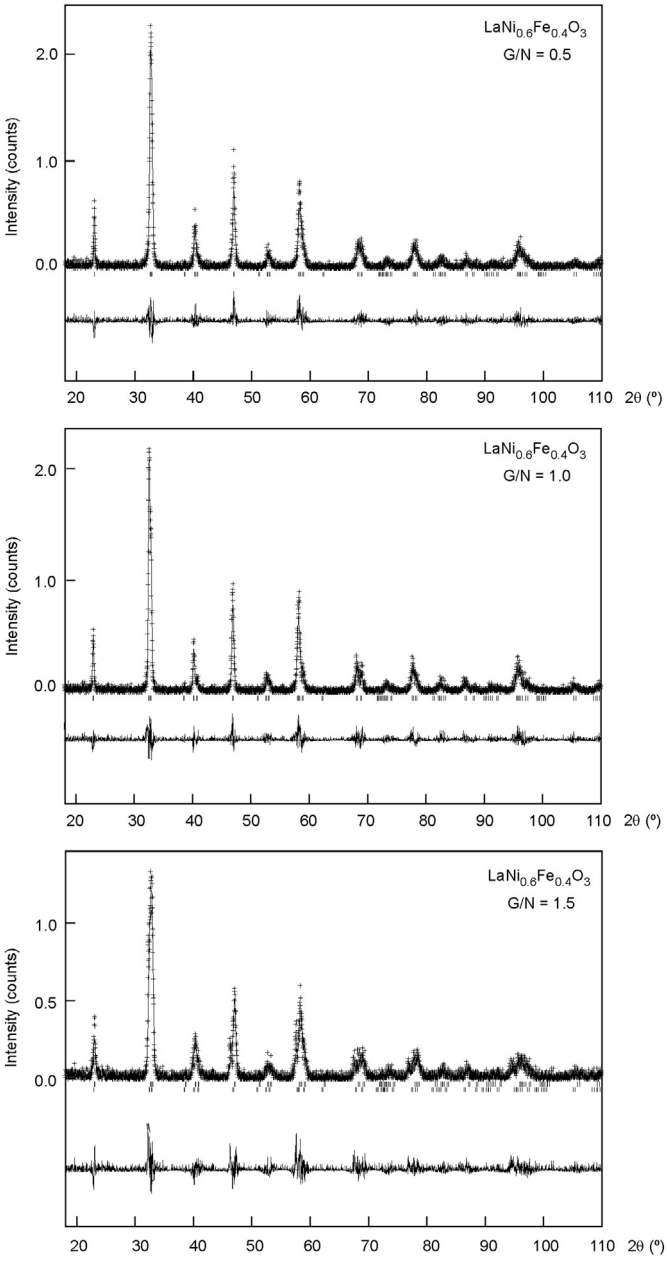

Fig. 2. Rietveld fits of the XRD data for the samples using rhombohedral $R\bar{3}c$ space group.

Final refined values of the structural parameters are summarized in Table 2. A slight decrease in lattice parameters and cell volume is observed with increasing G/N molar ratio. These obtained values are in good agreement with reported parameters [14,21–23].

As can be seen, the average La–O, (Ni,Fe)–O and La–(Ni,Fe) bond distances vary slowly with a small reduction of the (Ni,Fe)–O–(Ni,Fe) angles with the increase of the G/N molar ratio. According to other works [5], by increasing the fuel/oxidant ratio, the perovskite structure changes to a less symmetric structure. In this case, the variation observed seems to be due to a small change in mean ionic radius of the B site ions (Fe^{3+} and Ni^{3+}) as G/N ratio increases, due to varying degrees of oxygen vacancies and hence mean transition metal oxidation state.

3.2. Morphological study

Bevilacqua et al. [24], showed, for this composition, that the synthetic route has a strong influence on the sinterability of the final bars, indicating a different behavior of the materials during the sintering process at high temperatures. In addition, for a particular synthesis method, the experimental conditions used also play an important role in the properties of the final product. In this sense, it is well known that the fuel/oxidizer ratio may have some effects on the power sinterability, and then, on the overall electrical properties of the electrolyte and electrode materials [5,8].

Fig. 3 shows the well-necked morphology of the $LaNi_{0.6}Fe_{0.4}O_3$ powders synthesized by the combustion method and calcined at 850 °C, which are composed of nanosized particles and agglomerations of grains. These agglomerates formed during combustion reaction are usually soft and easy to break due to the higher volume of escaping gases for these samples [8,10].

The SEM micrographs taken on the surface of the three samples sintered (1050 °C during 5 h) bars are shown in Fig. 4.

The samples sintered at 1050 °C show particles of grain sizes of about 0.3–0.4 μm. The material with stoichiometric G/N value seems to sinter more easily with respect to the other two materials. Usually, a smaller particle size is beneficial to sintering and results in higher density when the sintering process is complete.

As previously mentioned, for the sample with G/N = 1.0, the observed flame was clear and bright, with a high ignition temperature (lower adiabatic flame temperature), which gives rise to the formation of less agglomerates, and then, to an increase in sinterability. However, regardless of the synthesis conditions, the porosity will decrease with increasing sintering temperature. Consequently, in this work, the low sintering temperature used may be a reason why the density values obtained for the rectangular bars are low [25].

3.3. Electrical conductivity study

Fig. 5 shows the relation between log(σT) versus the inverse absolute temperature. The electronic conductivity of $LaNi_xFe_{1-x}O_3$ series with $x \leq 0.6$, can be described by the thermally activated small polaron mechanism [24,26] which is generally expressed as:

$$\sigma = \frac{A}{T} \cdot \exp\left(-\frac{E_a}{kT}\right) \quad (1)$$

in which E_a is the activation energy for small polaron hopping conduction, k is the Boltzmann constant, T is the absolute temperature and A is a pre-exponential factor. Before making comparisons between the

Table 2
Structural parameters obtained by Rietveld refinement.

G/N	0.5	1.0	1.5 Rhombohedral	
Symmetry	Rhombohedral	Rhombohedral		
Space group	$R\bar{3}c$	$R\bar{3}c$	$R\bar{3}c$ (wt. frac. = 0.59)	$R\bar{3}c$ (wt. frac. = 0.41)
a (Å)	5.508 (1)	5.507 (1)	5.529 (2)	5.491 (2)
c (Å)	13.335 (2)	13.298 (2)	13.280 (3)	13.265 (2)
V / Z (Å^3)	350.3 (1)	349.2 (1)	351.6 (3)	346.4 (2)
ρ_{the}·(g/cm^3)[a]	6.952	6.974	6.927	7.032
$Uiso_{(La)}$	1.12 (2)	1.52 (1)	1.60 (4)	2.70 (4)
$Uiso_{(Ni,Fe)}$	1.62 (2)	0.58 (1)	2.12 (4)	2.75 (4)
O x	0.467 (4)	0.453 (3)	0.451 (4)	0.447 (4)
$Uiso_{(O)}$	2.12 (2)	1.95 (2)	2.44 (4)	2.54 (4)
La–(Ni,Fe) (x2) (Å)	3.334 (1)	3.325 (1)	3.320 (1)	3.316 (1)
La–(Ni,Fe) (x6) (Å)	3.368 (1)	3.367 (1)	3.379 (1)	3.357 (1)
<La–(Ni,Fe)> (Å)	3.360 (1)	3.356 (1)	3.364 (1)	3.347 (1)
La–O (x3) (Å)	2.936 (2)	3.012 (2)	3.040 (3)	3.040 (3)
La–O (x3) (Å)	2.572 (2)	2.495 (2)	2.490 (3)	2.450 (3)
La–O (x6) (Å)	2.739 (1)	2.740 (1)	2.742 (3)	2.736 (3)
<La–O>	2.746 (1)	2.747 (1)	2.753 (3)	2.740 (3)
(Ni,Fe)–O (x6) (Å)	1.948 (1)	1.955 (1)	1.961 (3)	1.954 (3)
(Ni,Fe)–O–(Ni,Fe) (°)	169.3 (1)	164.8 (1)	164.0 (2)	162.8 (2)
χ^2	1.09	1.08	1.12	

[a] Assuming stoichiometric oxygen content.

electrical conductivity values obtained from the four-probe DC measurements, the porosity of the samples (24, 23 and 28% for the bars with G/N = 0.5, 1.0 and 1.5, respectively) and its effect on the electrical conductivity must be mentioned. The incorporation of pores significantly degrades the electrical characteristics of the material [27]. As has been observed by other authors [26,28], as the porosity in the specimen increases the contact points between the two neighboring grains or interconnectivity between the grains decrease and this results in a decrease in the conductivity of the specimen.

As can be observed, at the same calcination temperature, the material obtained with G/N = 1.0 shows the higher specific conductivity. Therefore the preparation route has an important influence on the electrical properties of the obtained materials. This result consisted of the morphological analysis previously reported which indicates that this material ($LaNi_{0.6}Fe_{0.4}O_3$; G/N = 1.0) seems to be better sintered. Table 3 lists the electrical conductivity obtained for the sintered samples at 600, 700 and 800 °C and the geometrical and relative density calculated for the pellets.

The conductivity values obtained for the present compounds are not directly comparable with the literature conductivity data for $LaNi_{0.6}Fe_{0.4}O_3$ materials [14,24,25,29] because these results are obtained on samples prepared using different chemical routes and/or calcined at different temperatures from ours. Overall, the conductivity values obtained in this work are adequate for the contact layer

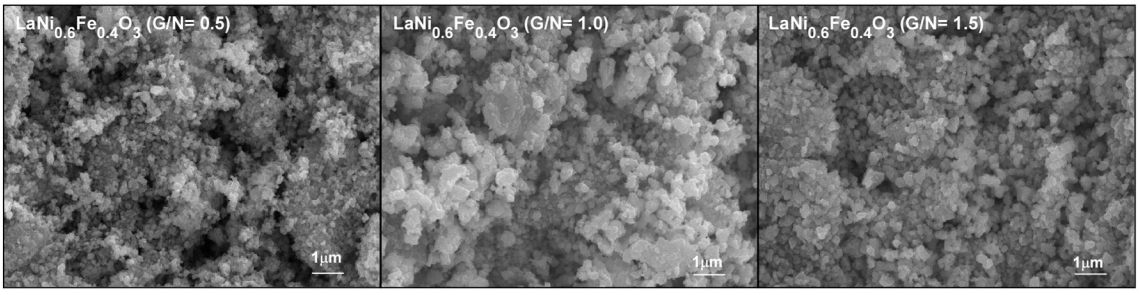

Fig. 3. SEM images for the combustion-synthesized LNF after a sintering treatment at 850 °C, as obtained at different fuel conditions.

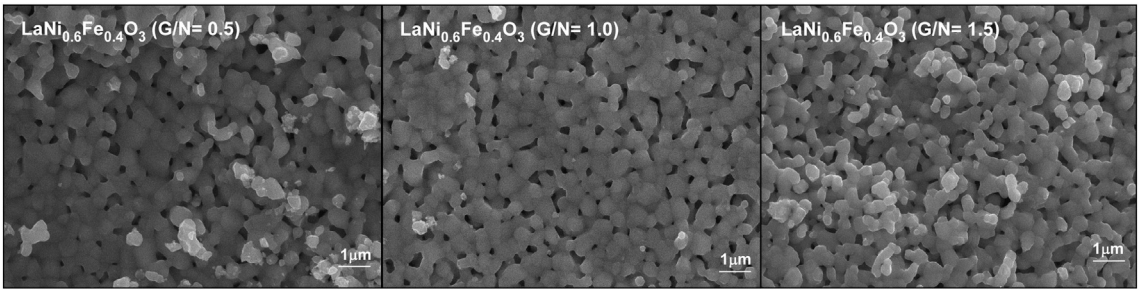

Fig. 4. SEM micrographs taken on the surface of the $LaNi_{0.6}Fe_{0.4}O_3$ pellets sintered at 1050 °C during 5 h.

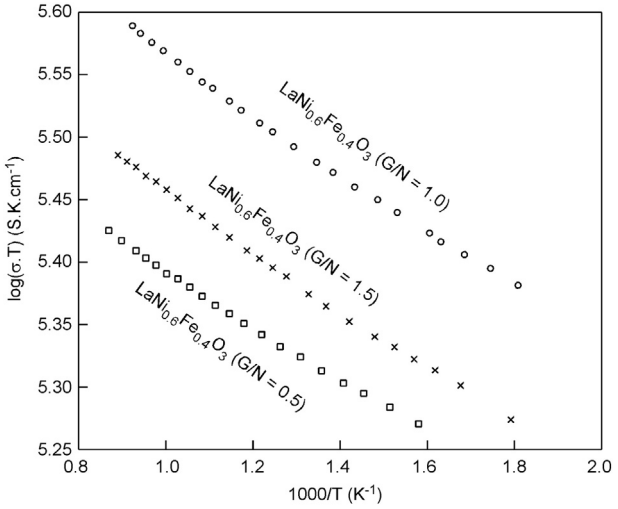

Fig. 5. Arrhenius plot of $LaNi_{0.6}Fe_{0.4}O_3$ perovskites as a function of temperature.

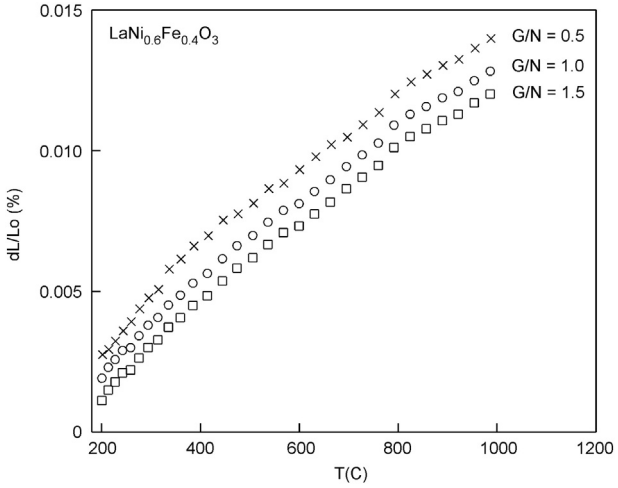

Fig. 6. Thermal expansion behavior of $LaNi_{0.6}Fe_{0.4}O_3$ perovskites obtained by the glycine-nitrate route using different amounts of fuel/oxidizer ratio (G / N = 0.5, 1.0 and 1.5).

application in IT-SOFCs, despite having low values of density (see Table 3).

The activation energy obtained from the Arrhenius plots for all compounds is 0.02 eV, in good agreement with the previously reported value [14].

3.4. Thermal expansion study

In order to determine the mechanical compatibility of the three cathode contact materials with the other cell components, thermal expansion measurements on rectangular bars were carried out in air atmosphere. Fig. 6 shows the thermal expansion curves of the samples obtained upon heating from 200 to 1000 °C.

The thermal expansion curves were fitted by two straight lines. The change in slope observed in high temperature range in the thermal expansion behavior is considered to be due to loss of lattice oxygen and the formation of oxygen vacancies [30,31].

The value of the average linear thermal expansion coefficient of the samples is given in Table 3 for the different temperature ranges.

As can be observed, the TEC values increase slightly with an increase in the G/N molar ratio in the temperature range studied, with the most significant change for the G/N = 1.5 sample, which appeared to contain two closely related perovskite phases. Further studies of the variation of density on the properties of the material [25,32], indicate that the obtained density after sintering only has a negligible influence on TEC of the samples. Consequently, it is possible to say that the TEC values obtained match with those of the cathode and interconnect materials [33,34].

Table 3
Electrical conductivity values at different temperatures, activation energy, geometrical and relative density of the pellets, and average TEC values in different temperature ranges for $LaNi_{0.6}Fe_{0.4}O_3$ perovskites prepared using glycine/nitrate molar ratios of 0.5, 1.0 and 1.5.

G/N	0.5	1.0	1.5
$\sigma_{(600\ °C)}$ (S/cm)	362	387	301
$\sigma_{(700\ °C)}$ (S/cm)	250	373	291
$\sigma_{(800\ °C)}$ (S/cm)	239	360	279
Ea (eV)	0.02	0.02	0.02
ρ_{exp} ($g \cdot cm^{-3}$)	5.30	5.34	5.03
ρ_{exp}/ρ_{the}	0.76	0.77	0.72
Average $TEC_{(200-600\ °C)}$ ($1.10^{-6}\ °C^{-1}$)	15.26	15.81	17.22
Average $TEC_{(600-1000\ °C)}$ ($1.10^{-6}\ °C^{-1}$)	11.93	12.43	12.52

4. Conclusions

Three $LaNi_{0.6}Fe_{0.4}O_3$ compounds have been obtained by glycine-nitrate method varying the fuel/oxidizer ratio (G/N = 0.5, 1.0 and 1.5) in order to study the effect on the structure, morphological and electrical properties. At room temperature, all compounds have rhombohedral symmetry (S.G.: $R\bar{3}c$). A slight structure change to a less symmetric structure of the perovskite by increasing the fuel/oxidant ratio has been observed. The compound obtained with stoichiometric G/N value presents the most suitable characteristics as a cathode contact material: better sinterability, higher values of electrical conductivity and suitable value of TEC. Therefore, it can be concluded that the glycine-nitrate process, with an optimal G/N ratio of 1.0, is a more appropriate technique for preparing a promising $LaNi_{0.6}Fe_{0.4}O_3$ candidate cathode contact material for IT-SOFC applications.

Acknowledgments

This research has been funded by the Dpto. Educación, Política Lingüística y Cultura of the Basque Goverment (IT-630-13), Ministerio de Economía y Competitividad (MAT2013-42092-R) and the Engineering and Physical Sciences Research Council (EP/I003932). The authors thank SGIker Universidad del País Vasco/ Euskal Herriko Unibertsitatea (UPV/EHU) technical support. K. Vidal thanks UPV/EHU for funding.

References

[1] D. Medvedev, A. Murashkina, E. Pikalova, A. Demin, A. Podias, P. Tsiakaras, Prog. Mater. Sci. 60 (2014) 72–129.
[2] K. Vidal, L.M. Rodríguez-Martínez, L. Ortega-San-Martín, M.L. Nó, T. Rojo, M.I. Arriortua, Fuel Cells 11 (1) (2011) 51–58.
[3] A. Ecija, K. Vidal, A. Larrañaga, L. Ortega-San-Martín, M.I. Arriortua, in: Yitzhak Mastai (Ed.), 2012 [ISBN: 978-953-51-0581-7. Available from: http://www.intechopen.com/books/advances-in-crystallization-processes/synthetic-methods-for-perovskite-materials-structure-and-morphology].
[4] C.R. Milian, T. Mariño, E. Pérez, O.L. Alves, P. Aranda, M. Aguilar, Y. Mosqueda, Ceram. Int. 40 (2014) 249–256.
[5] F. Deganello, G. Marcí, G. Deganello, J. Eur. Ceram. Soc. 29 (2009) 439–450.
[6] A. Kumar, A.S. Mukasyan, E.E. Wolf, Appl. Catal. A Gen. 401 (2011) 20–28.
[7] M.Th. Makhlouf, B.M. Abu-Zied, T.H. Mansoure, Adv. Powder Technol. 25 (2014) 560–566.
[8] C. Zhu, A. Nobuta, I. Nakatsugawa, T. Akiyama, Int. J. Hydrogen. Energ. 38 (2013) 12238–13248.
[9] H. Najjar, J.F. Lamonier, O. Mentré, J.M. Giraudon, H. Batis, Appl. Catal. B Environ. 106 (2011) 149–159.
[10] R.S. Guo, Q.T. Wei, H.L. Li, F.H. Wang, Mater. Lett. 60 (2006) 261–265.
[11] J. Ma, C. Jiang, X. Zhou, G. Meng, X. Liu, J. Power Sources 162 (2) (2006) 1082–1087.
[12] L.D. Jadhav, M.G. Chourashiya, K.M. Subhedar, A.K. Tyagi, J.Y. Patil, J. Alloys Compd. 470 (1–2) (2009) 383–386.
[13] Z. Shao, W. Zhou, Z. Zhu, Prog. Mater. Sci. 57 (2012) 804–874.

[14] A. Morán-Ruiz, K. Vidal, M.A. Laguna-Bercero, A. Larrañaga, M.I. Arriortua, J. Power, Sources 248 (2014) 1067–1076.
[15] F. Wang, D. Yan, W. Zhang, B. Chi, J. Pu, L. Jian, J. Pu, L. Jian, Int. J. Hydrogen. Energ. 38 (2013) 646–651.
[16] Z. Yang, G. Xia, P. Singh, J.W. Stevenson, J. Power, Sources 155 (2006) 246–252.
[17] B.P. McCarthy, L.R. Pederson, Y.S. Chou, X.D. Zhou, W.A. Surdova, L.C. Wilson, J. Power, Sources 180 (2008) 294–300.
[18] A. Morán-Ruiz, K. Vidal, A. Larrañaga, M.I. Arriortua, Fuel Cells 13 (2013) 398–403.
[19] M. Rietveld, J. Appl. Crystallogr. 2 (1969) 65–71.
[20] A.C. Larson, R.B. Von Dreele, GSAS: General Structure Analysis System, LAUR, 1994. 86–748.
[21] J.Y. Chen, J. Rebello, V. Vashook, D.M. Trots, S.R. Wan, T.L. Wen, J. Zosel, U. Guth, Solid State Ionics 192 (2011) 424–430.
[22] R.N. Basu, F. Tietz, O. Teller, E. Wessel, H.P. Buchkremer, D. Stöver, J. Solid State Electrochem. 7 (2003) 416–420.
[23] N. Sukpirom, S. Iamsaard, S. Charojrochkul, J. Yenyongchaiwat, J. Mater. Sci. 46 (2011) 6500–6507.
[24] M. Bevilacqua, T. Montini, C. Tavagnacco, G. Vicario, P. Fornasiero, M. Graziani, Solid State Ionics 177 (2006) 2957–2965.
[25] E. Niwa, C. Uematsu, T. Hashimoto, Mater. Res. Bull. 48 (2013) 1–6.
[26] R. Chiba, F. Yoshimura, Y. Sakurai, Solid State Ionics 124 (1999) 281–288.
[27] K.Y. Yiang, W.J. Yoo, A. Krishnamoorthy, IEEE Trans. Electr. Devices 52 (2005) 490–494.
[28] M.B. Kakade, S. Ramanathan, D. Das, Cera. Int. 37 (2011) 195–200.
[29] R.N. Basu, F. Tietz, E. Wessel, H.P. Buchkremer, D. Stöver, Mater. Res. Bull. 39 (2004) 1335–1345.
[30] C. Nityanand, W.B. Nalin, B.S. Rajkumar, C.M. Chandra, Solid State Ionics 13 (2011) 1022–1030.
[31] X. Ding, X. Kong, J. Jiang, C. Cui, X. Guo, Mater. Res. Bull. 45 (2010) 1271–1277.
[32] S. Wang, B. Lin, K. Xie, Y. Dong, X. Liu, G. Meng, J. Alloy. Compd. 468 (2009) 499–504.
[33] J. Piron Abellan, V. Shemet, F. Tietz, L. Singheiser, W.J. Quadakkers, in: H. Yokokawa, S.C. Singhal (Eds.), Proceedings of the 7th International Symposium on Solid Oxide Fuel Cells (SOFC VII), The Electrochemical Society Proceedings, Pennington, NJ, 2001, p. 811 [PV. 2001–16].
[34] C. Sun, R. Hui, J. Roller, J. Solid State Electrochem. 14 (2010) 1125–1144.

Available online at www.sciencedirect.com

ScienceDirect

journal homepage: www.elsevier.com/locate/he

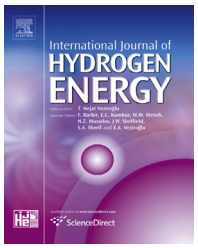

Evaluation of using protective/conductive coating on Fe-22Cr mesh as a composite cathode contact material for intermediate solid oxide fuel cells

Aroa Morán-Ruiz [a], *Karmele Vidal* [a], *Aitor Larrañaga* [a], *Jose Manuel Porras-Vázquez* [c], *Peter Raymond Slater* [c], *María Isabel Arriortua* [a,b,*]

[a] *Universidad del País Vasco (UPV/EHU), Facultad de Ciencia y Tecnología, Departamento de Mineralogía y Petrología, Barrio Sarriena S/N, 48940, Leioa, Vizcaya, Spain*

[b] *BCMaterials (Basque Centre for Materials, Applications & Nanostructures), Technological Park of Zamudio, Camino de Ibaizabal, Bndg. 500-1st, 48160, Derio, Spain*

[c] *University of Birmingham, School of Chemistry, Birmingham, B15 2TT, UK*

ARTICLE INFO

Article history:
Received 3 November 2014
Received in revised form
12 January 2015
Accepted 2 February 2015
Available online 7 March 2015

Keywords:
SOFC
Composite contact coating
Channeled interconnect
Chromium poisoning
Contact resistance

ABSTRACT

An uncoated and $MnCo_{1.9}Fe_{0.1}O_4$ (MCF) coated Fe-22Cr meshes were dipped into $LaNi_{0.6}Fe_{0.4}O_{3-\delta}$ (LNF) slurry to form a continuous protective/conductive layer for Crofer22APU interconnect. After aged these samples at 800 °C for 1000 h, energy dispersive X-ray (EDX) results concluded that: if the deposition of the protective coating was not enough to form a dense and continuous layer across the width of the mesh, then the use of MCF spinel layer is not enough to prevent chromium migration. For mesh-LNF/interconnect structure the area specific resistance (ASR) value of 0.0425(2) Ω cm^2 was stable for 400 min at 800 °C, indicating initial good adherence between both materials. After aged this structure at 800 °C for 1000 h, without applying a current source, X-ray micro-diffraction (XRMD) results, performed at the rib and channel of the interconnect, revealed that the LNF material is acting as a protective layer. Moreover, X-ray photoelectron spectroscopy (XPS) analysis indicated that manganese is concentrated on the mesh/LNF contact surface.

Introduction

Alternative technologies need to be developed for long-term sustainable energy supply due to socio-political, economic and environmental problems associated with the burning of fossil fuels. Solid oxide fuel cells (SOFCs) have the potential to be efficient and cost-effective system for the direct conversion of a wide variety of fuels to clean electricity. These benefits will only be achieved by society if SOFC technology can become commercially available [1,2].

Despite SOFC advantages, they still have problems related to: i) poor contact between cell component and ii)

* *Corresponding author*. Universidad del País Vasco (UPV/EHU), Facultad de Ciencia y Tecnología, Departamento de Mineralogía y Petrología, Barrio Sarriena S/N, 48940 Leioa, Vizcaya, Spain. Tel.: +34 946012534; fax: +34 946013500.
E-mail address: maribel.arriortua@ehu.es (M.I. Arriortua).
http://dx.doi.org/10.1016/j.ijhydene.2015.02.052

microstructure degradation of the porous electrodes due to chromium poisoning [3,4]. Growth of a poorly conductive oxide layer between the metallic interconnect ribs and the electrode results in a lack of contact between both materials. Moreover, the use of ferritic steel substrates is associated with another issue called "cathode Cr poisoning" [5]. Thus, the application of conductive/protective coatings acting as an adhesive to connect cathode with substrate, and as chromium diffusion barrier and oxide scale inhibitor is the subject of many research [6–8]. It is important to ensure that the materials exhibit high chemical and microstructural stability, high electrical conductivity, compatibility with the interconnect materials, reasonable thermal compatibility match with other cell components, and high sinterability to ensure high mechanical strength and good bonding with the adjacent components [9,10]. Various materials have been used in an effort to inhibit Cr migration from the chromia-rich subscales and to improve oxide scale-to-electrode adhesion, reducing oxide growth kinetics. Basically, SOFC interconnect coatings fall into four main categories [9]: reactive element oxides (REOs), MAlCrYO (M represents a metal, e.g., Co, Mn, Ti or Ni), conductive perovskites and spinels.

The perovskite structure oxides, $A^{3+}B^{3+}O^{2-}_{3-\delta}$, where A is a rare-earth element and B is a first row transition metal, have been investigated widely for cathode contact applications [11–13]. Compositions with B=Co, Ni have been used becouse of their high conductivity, while the oxides with B=Cr, Fe, Mn are known to be stable at high temperatures [1,14,15]. Moreover, the introduction of alkali-earth elements, such as Sr, increases the sintering activity and the conductivity [10,16]. Other authors indicated that $(La_{1-x}Sr_x)MnO_3$ coatings change the oxidation behavior and enhance the long term stability of metallic interconnects [17]. Moreover, more studies reported that [18] $La_{0.8}Sr_{0.2}CrO_3$ and $La_{0.8}Sr_{0.2}FeO_3$ coatings on ferritic alloys are not effective to prevent Cr outward diffusion. In another work, $(La,Sr)CoO_3$, $(La,Sr)(Co,Fe)O_3$ and $La(Ni,Fe)O_3$ coated ferritic alloys (Crofer22APU, E-Brite and 430) were studied [19], concluding that perovskite B-site cations (Ni,Fe,Co) diffuse to form stable spinel with transition metals from the interconnect. In our previous studies [20] $(La_{0.8}Sr_{0.2})_{0.95}Fe_{0.6}Mn_{0.3}Co_{0.1}O_3$, $LaNi_{0.6}Fe_{0.4}O_{3-\delta}$, $LaNi_{0.6}Co_{0.4}O_{3-\delta}$ were evaluated as contact materials between a Crofer22APU interconnect and a $La_{0.6}Sr_{0.4}FeO_3$ cathode. The formation of phases like $SrCrO_4$ and Cr-containing perovskite in short exposure times was observed. However, an adequate integrity and low reactivity is achieved when LNF contact coating is applied without compromising the contact resistance of the system.

Comparing to uncoated samples, perovskite coatings reduced the oxide scale growth so these coatings decrease the interfacial contact resistance; however, high sintering temperature of the perovskites leads to low compaction of these coatings and cell performance may still be degraded due to Cr poisoning. In addition to the perovskites, AB_2O_4 (A and B: divalent, trivalent and quadrivalent cations) spinel oxides can reduce oxidation and inhibit chromium volatility from ferritic stainless steels [9]. $Mn_{1-\delta}Co_{2-\delta}O_4$ spinels have been the most extensively studied [21–26]. However, ASR test of MCO coated Crofer22 showed that the adhesion of these coatings may be an issue for long-term applications [21,27]. For this reason Ce was added to the coating as reactive element in order to increase oxide scale and coating adherence to the metal substrate. A composition of $Ce_{0.05}Mn_{1.475}Co_{1.475}O_4$ was used and results have looked promising [28,29]. Moreover, other research groups have also studied Mn–Co spinels doped with Fe, Ti or Cu which exhibits higher electrical conductivity and a better densification than $MnCo_2O_4$ due to a partial substitution of Co by Fe, Ti and/or Cu [30–34]. Our previous work also concluded that [35] $MnCo_{1.9}Fe_{0.1}O_4$ was a more effective barrier than $MnCo_2O_4$, resulting in better electrochemical results and a similar microstructure; the presence of a low Fe content in $MnCo_{1.9}Fe_{0.1}O_4$ improved the stability of coating. In addition, due to the low cost of Ni, $NiMn_2O_4$ [36] and $NiFe_2O_4$ [37] spinels were also studied as protective coatings, providing effective conducting path to metallic substrate.

Despite the usefulness of conductive/protective coatings, the stack degradation rates are still higher than the required values for SOFC commercialization. It was found that $Ni_{80}Cr_{20}$/$(La_{0.75}Sr_{0.25})_{0.95}MnO_3$ dual-layer coating can improve the thermal stability and electrical performance of metallic interconnect [38]. In this context, according to other studies [39], the incorporation of conduction wires in the electrodes could increase cell performance via improved transport of electrons. In our previous work [40] a Fe–Cr mesh coated with $LaNi_{0.6}Co_{0.4}O_{3-\delta}$ high conductive perovskite was developed as an alternative to conventional contact materials. Taking into account that the generally accepted upper limit of ASR for SOFC interconnect is 0.1 Ω cm^2 [9,41,42], low and reproducible area specific resistance value (ASR) was achieved, being 0.0054(1) Ω cm^2, when this metallic/ceramic material was used to coat a channeled Crofer22APU interconnect.

In this study, LNF paste is developed to dip coated on Fe-22Cr mesh, forming a metallic/ceramic continuous layer in which ferritic mesh is fully covered with slurry. Because of Cr diffusion from steel was expected [40], the effectiveness of using MCF to protect mesh, prior to coat with LNF conductive perovskite, was discussed based on the long term behavior of these samples at 800 °C. LNF/MCF conductive/protective coatings were selected due to our previous experience and good results with these materials [20,35,43].

The obtained mixed material is expected to increase the conductivity and adhesive ability of the formed interface with interconnect ribs. Therefore, in order to evaluate this adherence, the resistance between these both materials was determined by relatively short-time ASR testing. Finally, this system was aged for 1000 h at 800 °C in order to establish the degradation trends under the rib (direct contact) and channel (no-contact) of the interconnect.

Experimental

The powder of $LaNi_{0.6}Fe_{0.4}O_{3-\delta}$ (LNF) was from fuel cell materials and, uncoated and $MnCo_{1.9}Fe_{0.1}O_4$ (MCF)-coated Fe-22Cr mesh (both with mesh opening of 175 μm and thickness of 250 μm) from Fiaxell SOFC Technologies (Crofer22H M_grid™ micro mesh). According to technical specifications the MCF coated mesh was sintered at 850 °C for 6 h, in air. LNF coating was applied onto uncoated and coated mesh squares (10 × 10 mm) by dipping them into the prepared ceramic

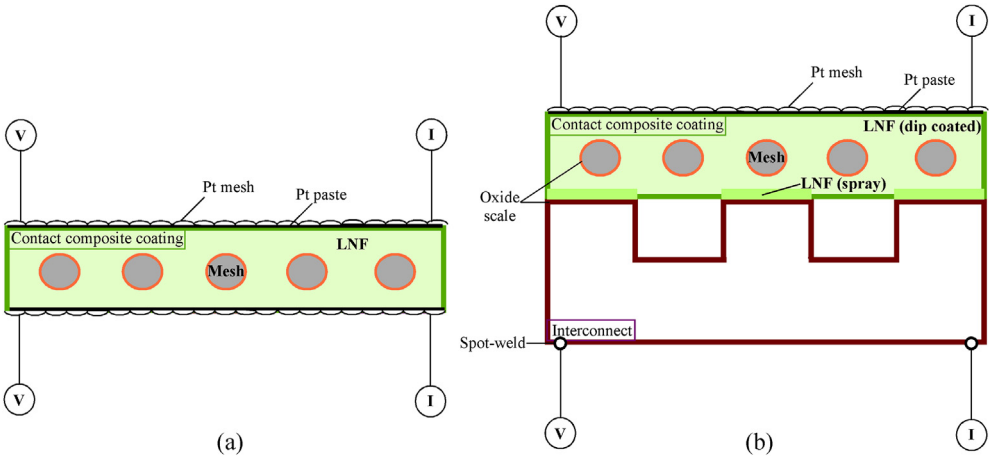

Fig. 1 – Schematic views of the used system configurations for ASR measurements: (a) composite contact material and (b) composite contact material on channeled interconnect.

slurry, thus obtaining a metallic/ceramic material. The LNF slurry was composed of ceramic powder (LNF, 12.5% in volume), dispersant (Dolapix, 1% relative to the ceramic powder, Zschimmer & Schwarz, Chemische Fabriken), binder (PVB, polyvinyl butyral, 5% relative to the ceramic powder, Solutia Solutions) and solvent (ethanol, 87.5% in volume, Panreac). The process performed to form a contact composite was described in Ref. [20]. The rheology of the suspensions was analyzed using a rheometer (HAAKE MARS II) at shear rates from 0.1 s^{-1} to 1000 s^{-1}, at room temperature. Composite materials were sintered at 1050 °C for 2 h and then treated at 800 °C for 1000 h, in air.

The composite contact material was directly bonded to a Crofer22APU channeled interconnect (ThyssenKrupp VDM). Nominal steel composition given by the supplier is summarized in Ref. [44]. The interconnect squares (10 × 10 × 1 mm) were preoxidized at 800 °C for 100 h, reducing Cr and Fe transport into the contact coating after long oxidation times [45]. The channel dimensions of the interconnect as well as the procedure to obtain {composite contact material/interconnect} system was detailed in previous work [40]. The obtained structure was sintered at 1050 °C for 2 h and then treated at 800 °C for 1000 h, in air.

X-ray diffraction (XRD) patterns of the samples were measured with an Philips X'Pert PRO diffractometer, powered at 40 kV and 40 mA using Cu K_α radiation (λ = 1.5418 Å) in air at room temperature. The patterns were recorded in 2θ steps of 0.026° in the 20–90° range, counting for 181 s for step. X-ray micro-diffraction (XRMD) data were collected using a Bruker D8 Discover diffractometer equipped with a Cr Twist tube, V filter (λ = 2.2898 Å), PolyCap™ (1μ single crystal cylinders) system for parallel been generation (divergence of 0.25°), and a 1-D LynxEye PSD detector (active length in 2θ 2.7°). The sample was mounted on an Eulerian Cradle with automatically controlled X-Y-Z stage. The sample illumination was adjusted with 1 mm PinHole collimator in the incident been, the position control was tested by using the interference of two lasers. Data were collected from 10 to 100° 2θ (step size = 0.04 and time per step = 10 s total time 6.5 h) at RT. Phases were identified from the measured XRD and XRMD patterns using X'Pert HighScore software based on the powder diffraction file (PDF) database. The fitting of a measured and calculated pattern was done by Rietveld method using the FULLPROF program [46].

X-ray photoelectron spectroscopy (XPS) measurements were performed using a XPS spectrometer (SPECS). All XPS

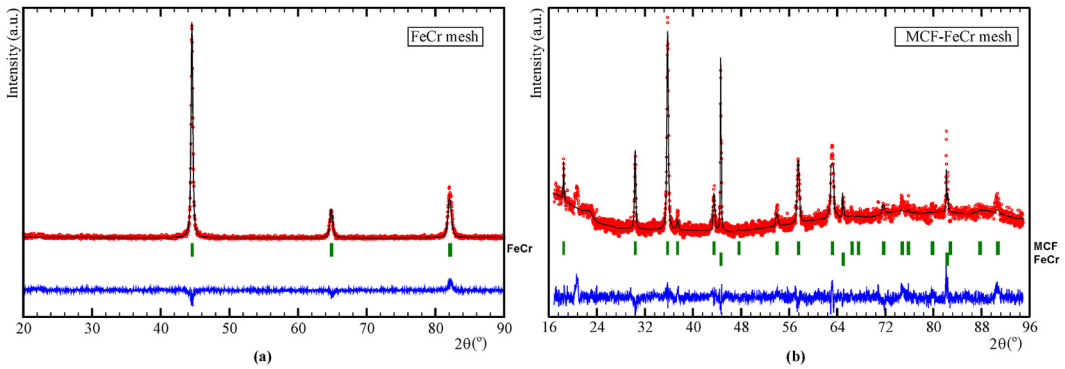

Fig. 2 – Rietveld X-ray diffraction patters for (a) commercial uncoated and (b) $MnCo_{1.9}Fe_{0.1}O_4$ spinel coated Fe-22Cr mesh.

Table 1 – Structural parameters for Fe-22Cr mesh and $MnCo_{1.9}Fe_{0.1}O_4$-coated Fe-22Cr mesh from the Rietveld refinement by using X-ray power diffraction data at room temperature.

Sample	Phase	Space group	Lattice parameters a (Å)	V (Å^3)	% in weight	χ^2
FeCr mesh	FeCr	*Im-3m*	2.876(1)	23.78(1)	100	5.42
MCF-FeCr mesh	MCF	*Fd-3m*	8.324(1)	576.78(1)	3.1(1)	1.70
	FeCr	*Im-3m*	2.871(1)	23.67(1)	96.9(8)	

spectra were acquired using a monochromatic X-ray source producing Al Kα radiation ($h \cdot \nu = 1486.6$ eV) and recorded using a SPECS PHOIBOS 150 analyzer. An initial analysis of the elements present in the sample was carried out (wide scan: step energy 1 eV, dwell time 0.1 s, pass energy 80 eV) and individual high resolution spectra were obtained (detail scan: step energy 0.1 eV, dwell time 0.1 s, pass energy 20 eV). The take-off angle of the photoelectrons was 90° with respect to the sample. The binding energies (BEs) were calibrated against the surface carbon contamination at 284.6 eV. The spectra were fitted by CasaXPS 2.3.16 software, modeling properly weighted sum of Gaussian and Lorentzian component curves, after background subtraction according to Shirley.

For microstructure and composition analysis, sample cross-sections were mounted in resin, polished and sputtered with coal graphite. A JEOL LSM-6400 instrument equipped with a tungsten filament gun and an Oxford Inca Pentafet X3 energy dispersive X-ray analyzer (EDX) was used to examine the samples. The operating voltage used was 20 kV and a current density of $1 \cdot 10^{-9}$ A. The EDX analysis was carried out through point analysis (the live time was set to 100 s).

Area Specific Resistance (ASR) measurements were performed using a DC four-probe method (the resistance value was estimated from the voltage value (Thurlby Thandar Instruments 1604 Digital Multimeter) measured on applying a current of 1A (Thurlby Thandar Instruments PL300 current source)), on both a composite and on a system, which were prepared according to the geometries shown in Fig. 1. Electrical contacts between samples and external measuring circuit were obtained by two Pt wires welded directly onto the sides of the interconnect and by Pt paste onto the surface of the composite contact material in combination with a Pt mesh.

Results and discussion

In order to investigate the crystal structure of uncoated and coated FeCr mesh squares, the samples were analyzed using X-ray diffraction (XRD) measurements (Fig. 2).

The refined cell parameters, unit cell volumes and the quality of the refinements are summarized in Table 1. For the coated mesh, MCF (3.1(1) % in weight) was quantified (Fig. 2b).

The phase structures of studied commercial $LaNi_{0.6}Fe_{0.4}O_{3-\delta}$ and Crofer22APU were analyzed in detail in our group [20]. The chemical composition of the surface of the alloys used as interconnect and, as mesh to form composite material were quantitatively analyzed using SEM-EDX. The measured values of the elements were checked on different points to obtain the average composition grade (Table 2). In order to ensure the determined chemical formulation of the samples, nominal compositions for each steel given by the technical specifications are also listed in Table 2.

As an example, Fig. 3 shows EDX spectra from one point results. The quantitative EDX analysis revealed that Fe–Cr mesh contains tungsten (W) and niobium (Nb), in contrast to interconnect which did not present these elements.

The strength of a steel is related to the combination of solid solution and precipitation strengthening given by Nb and W addition [47]. Lanthanum, titanium and niobium additives are concentrated in specific regions of the alloy (identified as A point of each sample in Fig. 4) differently from tungsten, which is dissolved in the ferritic matrix. Thus, the average chemical composition of steels showed undetectable levels of La and low concentrations for Ti and Nb for EDX technique.

The characterization of LNF slurry rheology is important for coated thickness control during the dip coating process. The effort against the shear rate of LNF paste is represented graphically in Fig. 5. As shown, the slurry behaves like a Newtonian fluid, and so the viscosity values are independent of the shear rate.

The viscosity value can be extracted from the slope of the represented line, being 0.038 Pa s, in good agreement with obtained results in our previous studies [40].

Effectiveness of using a protective coating on Fe–Cr mesh

The formed Fe–Cr mesh/LNF and Fe–Cr mesh/MCF/LNF composites, after sintering at 1050 °C for 2 h in air, are shown

Table 2 – Chemical composition in wt (%) of Fe-22Cr alloy used as interconnect and as mesh, given by the technical specifications and obtained by EDX microanalysis.

Sample		Fe (%wt.)	Cr (%wt.)	Mn (%wt.)	Ti (%wt.)	Nb (%wt.)	W (% wt.)	Si (%wt.)	Al (%wt.)	Cu (%wt.)	La (%wt.)
Crofer22H	Min.	Bal.[a]	20.0	0.3	0.02	0.2	1.0	0.1			0.04
	Max.		24.0	0.8	0.20	1.0	3.0	0.6	0.1	0.5	0.20
Mesh	EDX	73.1(3)	23.5(2)	0.6(1)	<0.1	0.4(1)	2.3(2)	–	–	–	–
Crofer22APU	Min.	Bal.[a]	20.0	0.3	0.03	–	–				0.04
	Max.		24.0	0.8	0.20	–	–	0.50	0.50	0.50	0.20
Interconnect	EDX	76.3(2)	23.0(2)	0.6(1)	<0.1	–	–	–	–	–	–

[a] Balance.

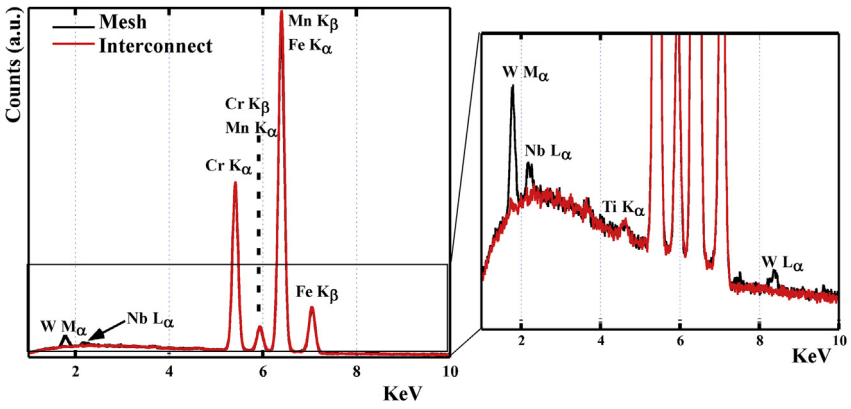

Fig. 3 – EDX spectra analyses for Fe-22Cr interconnect and mesh samples.

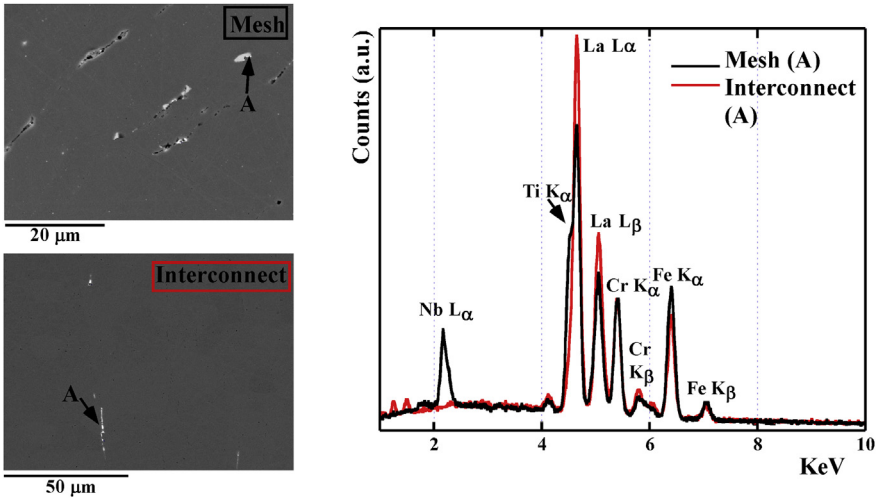

Fig. 4 – EDX point analysis performed on specific regions of the alloys.

in Fig. 6. As observed from Fig. 6a, the ceramic coating is continuous and homogeneous along the samples. However, the MCF protective coating was not a continuous layer along the width of the Fe–Cr mesh (Fig. 6b). Laves phase precipitates were observed along the steel grain boundaries [48], in good agreement with Fig. 6.

The area specific resistance (ASR) values of sintered Fe–Cr/LNF and Fe–Cr/MCF/LNF composite materials were 0.00453(1) and 0.00341(1) Ω cm^2, respectively. Despite the observed porous coarse microstructure in both LNC and MCF coatings (Fig. 6), the determined low ohmic resistance confirms that the use of these composite materials as a contact layer is adequate.

EDX point analysis was performed on a cross-section of just sintering at 1050 °C for 2 h mesh/LNF material (Fig. 7), and compared with another sample after heat treated at 800 °C for 1000 h in air (Fig. 8).

The obtained k ratios for identified elements, in these both samples, were listed in Table 3 (corresponding to Fig. 7) and Table 4 (corresponding to Fig. 8).

Moreover, Fig. 9 and Table 5 show a cross-section microstructure image of $MnCo_{1.9}Fe_{0.1}O_4$ coated mesh after dipping

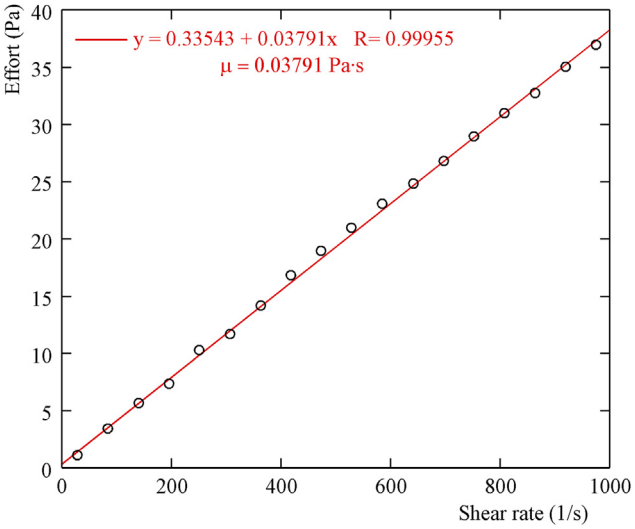

Fig. 5 – Plot of the effort against shear rate of $LaNi_{0.6}Fe_{0.4}O_{3-\delta}$ paste.

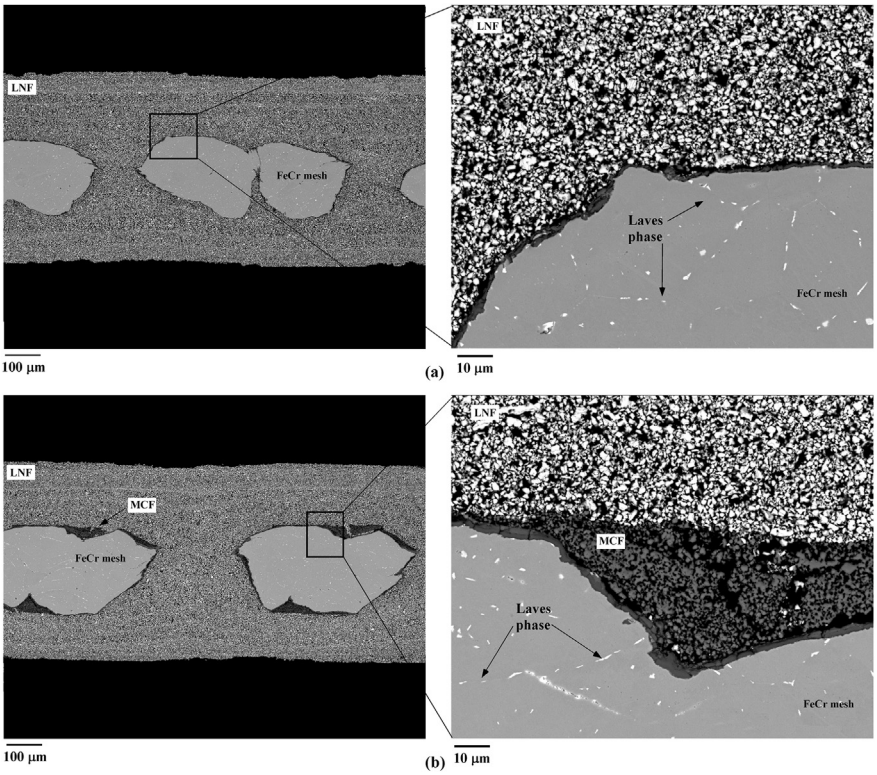

Fig. 6 – SEM cross-section of (a) Fe-22Cr mesh and (b) MCF coated Fe-22Cr mesh after dipping into LNF slurry and the following sintering at 1050 °C for 2 h, in air.

into $LaNi_{0.6}Fe_{0.4}O_{3-\delta}$ slurry with EDX point analysis, and the obtained elemental k ratios, respectively. The INCA 350 software from Oxford was used to reconstruct the spectra, separating the overlapping peaks.

The ceramic/metallic interface was relatively smooth in the initial composite (Fig. 7), while the interface was more irregular in the LNF dip coated mesh after 1000 h at 800 °C (Fig. 8), as was expected [49]. Moreover, locally internal precipitates, which could be related to the external not uniform oxide scale [50], were also found. According to microstructure, LNF showed relatively inhomogeneity between sintered particles, which could decrease their adherence to the alloy [51,52]. Thus, these particle contact points are irregular through the mesh surface that might also be associated to the observed irregular oxide scale, being noticeable after 1000 h at 800 °C. Therefore, for both Fe–Cr mesh/LNF materials ceramic layer contains pores whereas some of them are formed at the scale interface. Thus, especially the long-term heat treated sample shows areas without contact. As observed from Fig. 9, for spinel coated mesh loss of adherence was observed between the $MnCo_{1.9}Fe_{0.1}O_4$ protective and LNF contact layers. According to Ref. [30] the formation of these cracks could be as

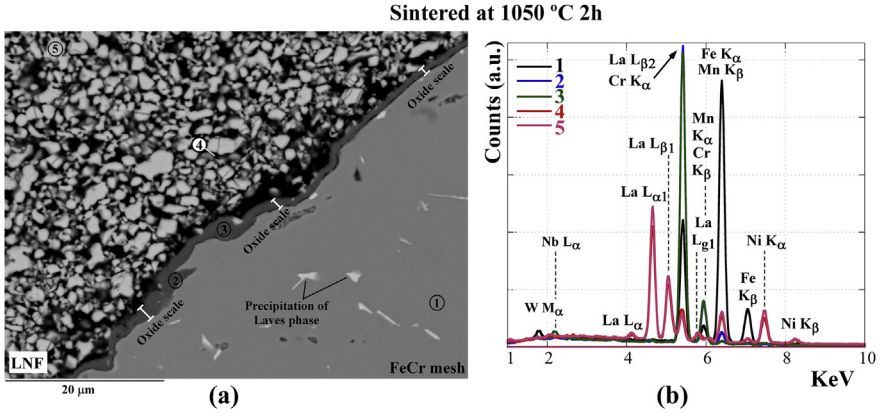

Fig. 7 – (a) Cross-section microstructure image obtained by backscattered electrons signal (BSE) and (b) EDX analysis on different points of LNF/mesh sintered at 1050 °C for 2 h, in air.

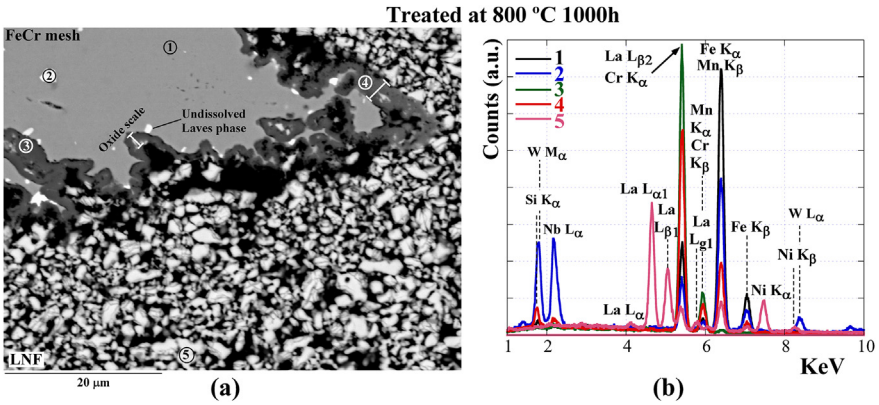

Fig. 8 – (a) Cross-section microstructure (BSE) and (b) EDX analysis on different points of LNF/mesh sintered at 1050 °C and then treated at 800 °C for 1000 h, in air.

Table 3 – Elemental k ratios measured by EDX point analysis performed on mesh/LNF just sintering at 1050 °C for 2 h, in air (corresponding to Fig. 7).

Spectrum	Cr (k ratio)	Fe (k ratio)	Mn (k ratio)	La (k ratio)	Ni (k ratio)	Nb (k ratio)	W (k ratio)
1	0.24	0.65	–	–	–	–	0.01
2	0.58	0.03	–	–	–	–	–
3	0.57	0.01	0.01	0.01	0.01	0.01	–
4	0.03	0.06	–	0.43	0.1	–	–
5	–	0.08	–	0.50	0.13	–	–

Table 4 – K ratios for identified elements on mesh/LNF sample after sintered and aged at 800 °C for 1000 h, in air (corresponding to Fig. 8).

Spectrum	Cr (k ratio)	Fe (k ratio)	Mn (k ratio)	La (k ratio)	Ni (k ratio)	Nb (k ratio)	W (k ratio)	Si (k ratio)
1	0.19	0.74	–	–	–	–	0.01	–
2	0.09	0.41	–	–	–	0.12	0.18	–
3	0.61	0.01	0.01	–	–	0.01	–	–
4	0.45	0.19	–	0.01	–	0.01	–	0.01
5	–	0.08	–	0.52	0.13	–	–	–

a result of cooling down to room temperature. However, MCF spinel layer showed different microstructures between points 3, 4 and 5 (Fig. 9), which could be related to the protective layer thickness, being in the zone where point 3, 4 were analyzed higher than in the point 5 analyzed area. In this way, the highest thickness allowed high enough density to improve adherence between metallic substrate and protective coating. The EDX point analysis, which were made on alloy, revealed in

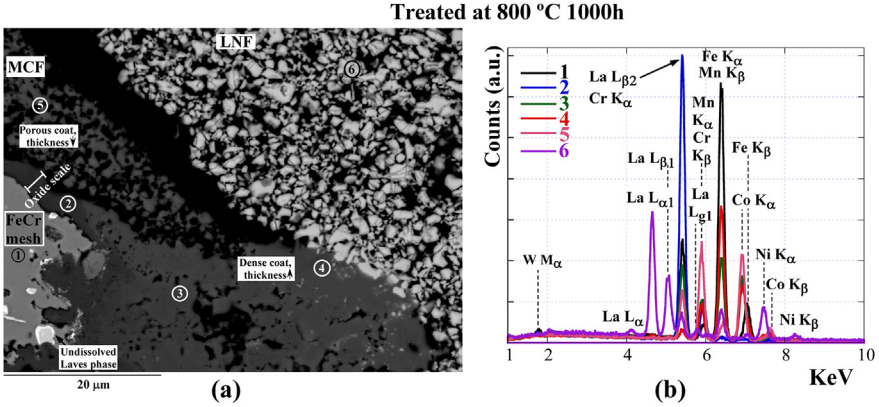

Fig. 9 – (a) Cross-section BSE image and (b) EDX point analysis of MCF coated mesh after dipping into LNF paste and the following sintering and aging processes.

Table 5 – The corresponding k ratios for identified elements on mesh/MCF/LNF sample after sintered and heat treated at 800 °C for 1000 h, in air (corresponding to Fig. 9).

Spectrum	Cr (k ratio)	Fe (k ratio)	Mn (k ratio)	La (k ratio)	Ni (k ratio)	Co (k ratio)	W (k ratio)
1	0.19	0.65	0.01	–	–	–	0.01
2	0.56	0.01	0.01	–	–	–	–
3	0.15	0.2	0.07	–	–	0.19	–
4	0.02	0.33	0.07	0.01	0.02	0.17	–
5	0.09	0.02	0.19	–	0.01	0.28	–
6	–	0.07	–	0.47	0.13	–	–

most of the cases α-Fe(Cr,W) phase. The analysed Laves phase precipitates (Fig. 8, point 2) were composed of $(Fe,Cr)_2(Nb,W)$, in good agreement with Ref. [48], in which Laves phase precipitates of Fe_2Nb type were formed on small additions of Nb. The combined additions of Nb and Si, which came from the alloy, allowed the formation of Fe–Cr–Nb–Si system [53], as can observed in Fig. 8, point 4. However, the results showed that the Nb was also incorporated in the external oxide scale. In some areas of Figs. 8 and 9, there is undissolved Laves phase in contact with the scale, indicating the thermodynamic stability of this compound.

According to EDX analysis, for sample without MCF protective layer, a passive chromia layer (Cr_2O_3/$(Mn,Cr)_3O_4$ [35]) about 1.3 μm thick (measured directly from Fig. 8) was grown between the metal substrate and the LNF coating. For the spinel coated mesh specimen, an oxide scale was also formed beneath the MCF coating, in good agreement with EDX analysis. According to our previous studies [44], the presence of Fe in oxide scale indicated the formation of small amount of hematite phase (α-Fe_2O_3) and/or Fe_3O_4 phases. Moreover, the appearance, in the oxide scale, of Cr, Mn and Fe simultaneously allows the formation of $(Mn,Fe,Cr)_3O_4$ spinel. In addition, EDX point analyses, performed on the interface close to the contact coating, indicated the migration of lanthanum and nickel from the LNF layer into the passive oxide scale or MCF protective layer. However, due to the porosity of the sample, and because the resolution of the energy dispersive X-rays source from the sample is approximately 1 μm, it is noted that the point analysis results should be interpreted with caution.

With EDX, evidence of Cr penetration through the protective spinel coating, as well as into the LNF coating, was found. Darker grey-colored Cr-rich grains were observed in the LNF coating for uncoated and coated FeCr mesh samples, which decrease as the distance from the mesh is increased (Figs. 8 and 9). In terms of the microstructure, the open porosity observed in LNF and MCF coatings might reduce the adherence to the alloy and enhance the transport of Cr to gas phase.

Since the deposition of the commercial protective coating was not homogeneous across the width of the Fe-22Cr mesh, the use of an MCF spinel protective layer is not enough to prevent chromium migration up to the contact coating. Thus, the uncoated sample was selected to evaluate the electrical performances of the composite contact material/interconnect system, including long-term contact stability of the metallic/ceramic composite material under the rib (direct contact) and channel (no-contact) of the interconnect.

Characterization of the composite contact material with channeled Crofer22APU interconnect

Ceramic/metallic material was directly adhered to the channeled substrate and sintered at 1050 °C for 2 h. Results from ASR test (Fig. 10) showed initial good stability of the signal during the contact resistance measurements, and thus a good adherence between both materials, exhibiting ASR value of 0.0425(2) Ω cm^2 for 400 min, in air.

Fig. 11 shows a representative SEM cross-section of the post-test composite-coated Crofer22APU interconnect on which EDX point analyses were performed. When comparing different EDX spectra, similar compositions were observed. All of the analyzed particles are composed mainly of La, Ni, Fe, and amounts of Cr. However, Fig. 10b shows the lowest chromium content distribution in point 1.

The results of the initial characterization indicate that the developed coated interconnect system shows a low area specific resistance value since the generally accepted upper limit of ASR for SOFC substrate is 0.1 Ω cm^2 [9,41,42]. Its contact resistance is also smaller than those reported in other studies [13,54,55], in which the electrical performance of perovskite coated metallic interconnect was studied. Thus, the mesh/LNF layer could be a suitable alternative for the SOFC interconnect coatings development.

Long-term stability of the system

The sintered system composed of {LNF-steel mesh contact composite/Crofer22APU channeled interconnect} was treated at 800 °C for 1000 h, in air. Fig. 12 shows X-ray micro-

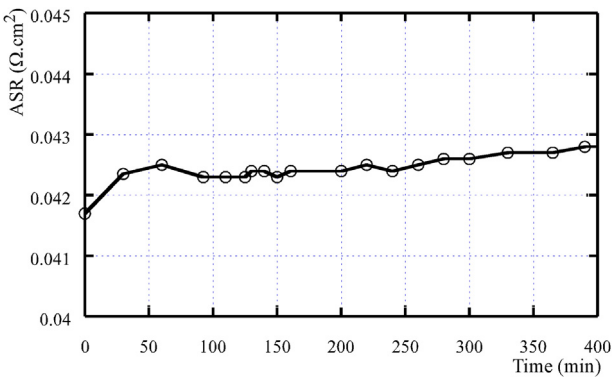

Fig. 10 – ASR for {composite contact material/channeled interconnect} interface as a function of time.

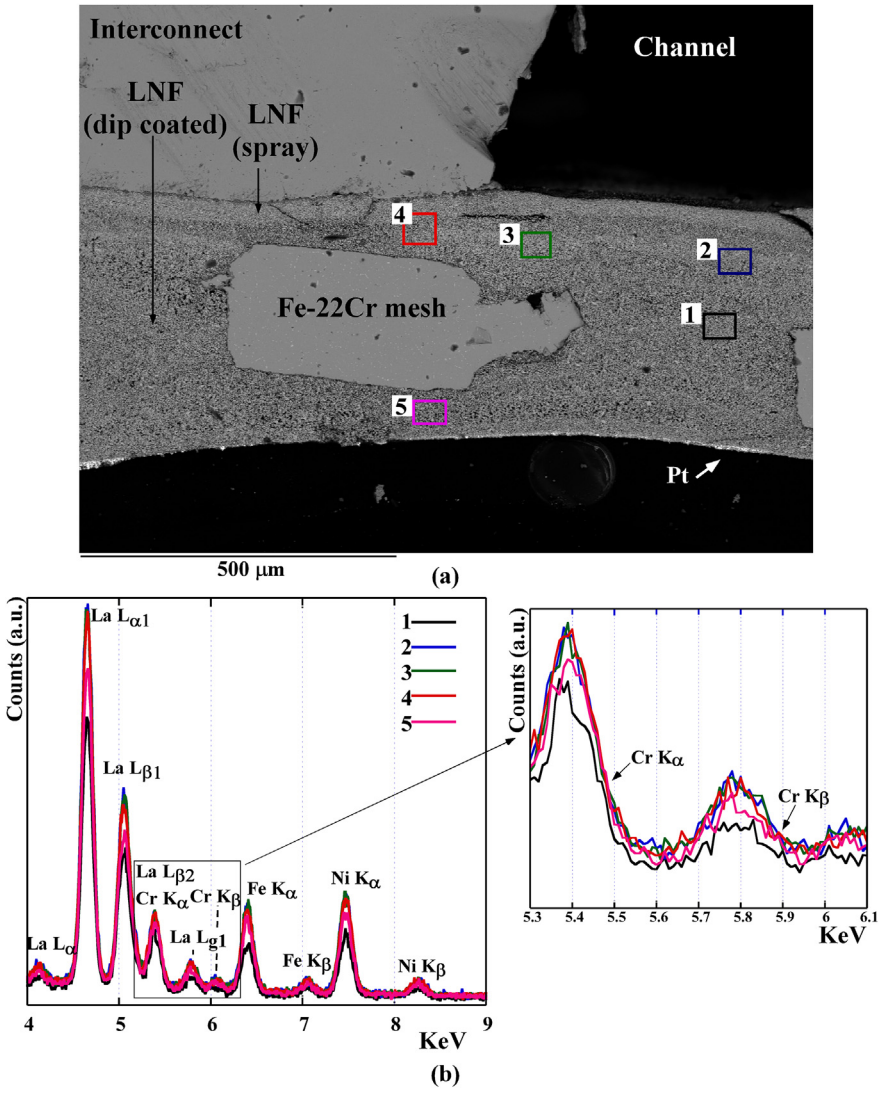

Fig. 11 – (a) SEM cross-section of studied system after ASR test with corresponding (b) EDX point analysis.

diffraction pattern refinements performed on the rib (Fig. 12a) and the channel (Fig. 12b) of the interconnect in contact with the composite material, after the long term treatment.

The formed phases and their quantitative analysis (% in weight) are presented in Table 6. These analyses reveal that in the rib zone the main and secondary phases were $LaNi_{0.6}Fe_{0.4}O_3$ (83.4(8)% in weight) and $La(Ni,Fe,Cr)O_3$ (13.3(4)% in

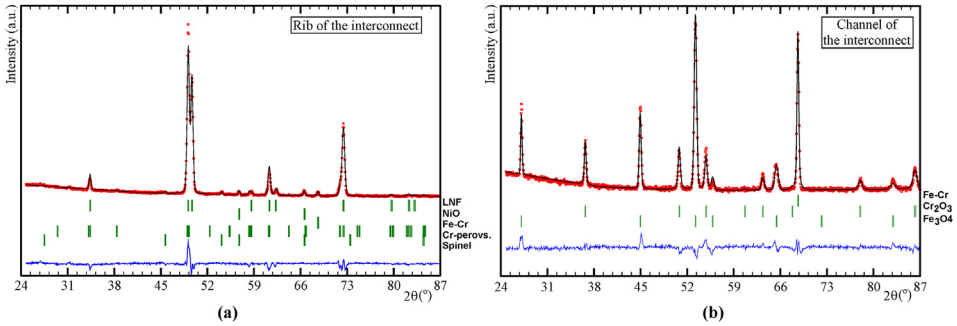

Fig. 12 – X-ray micro-diffraction pattern refinements performed (a) on the rib and (b) on channel of the interconnect in contact with composite material, after long term heat treatment.

Table 6 – X-ray micro-diffraction quantitative (%wt.) analysis of the formed phases on the rib and channel of the interconnect in contact with composite material after long-term heating in air.

Phase	Space group	N° PDF	Rib (%wt.)	Channel (%wt.)
$LaNi_{0.6}Fe_{0.4}O_3$	R-3c	88-0637	83.2(8)	–
$La(Ni,Fe,Cr)O_3$	Pbnm	24-1016	13.3(4)	
Fe–Cr	Im3m	34-0396	1.1(1)	16.2(2)
NiO	Fm-3m	73-1519	2.2(2)	–
$MnCr_2O_4$	Fd-3m	31-0630	<0.2	–
Cr_2O_3	R-3c	85-0730	–	13.9(3)
Fe_3O_4	Fd-3m	19-0629	–	69.9(8)

weight) as well as, NiO, Fe–Cr, and $(Cr,B)_3O_4$ spinel (B = Fe, Mn, Ni), respectively. In contrast, the channel zone results show as the main phase Fe_3O_4 (69.9(8)% in weight) and as secondary phases: Fe–Cr, and Cr_2O_3.

The original Fe–Cr substrate was identified indicating that the X-ray penetration was enough to observe the signal of all the formed layers. The presence of NiO might entail that Ni is partially extracted from the LNF perovskite lattice, allowing the formation of $La(Ni,Fe,Cr)O_3$, in good agreement with Ref. [56].

The LNF ceramic coating might act as a protective coating. Hence, Cr_2O_3 and Fe_3O_4 phases are observed on the channels. Furthermore, the absence of Cr_2O_3 on the rib of the interconnect, can also imply that chromium has completely reacted to form Cr-perovskite and/or $(Cr,B)_3O_4$ (B= Mn, Fe, Ni) spinel phase. An interconnect without ceramic coating at long exposure to air, can promote Fe_3O_4 formation rather than the formation of a chromia/spinel protective scale, concluding in the formation of a non-protective or Fe-rich scale [57–60].

Fig. 13 shows the surface of the composite material which was in contact with the interconnect, after long term IT-SOFC conditions, EDX point analysis is also shown. The corresponding k ratios for identified elements in each point were listed in Table 7.

Two different areas were identified at the composite contact surface: the area of the composite i) under the rib and ii) under channel of the interconnect. In both zones, the qualitative EDX analyses indicate that the analyzed grains contain La, Ni, Fe and Cr elements. Thus, the composite direct contacted (the rib) and no-contacted (channel) with the interconnect present similar elements distribution. These results indicate that the dominant cause for system degradation depends on both Cr vaporization from the interconnect steel and solid phase diffusion of Cr from the mesh alloy [61].

Table 7 – Elemental k ratios measured by EDX point analysis performed on mesh/LNF material which was in contact with the interconnect after 1000 h at 800 °C, in air (corresponding to Fig. 13).

Spectrum	La (k ratio)	Ni (k ratio)	Fe (k ratio)	Cr (k ratio)
1	0.4	0.11	0.06	0.02
2	0.34	0.1	0.05	0.02
3	0.46	0.12	0.07	0.03
4	0.31	0.08	0.04	0.02
5	0.45	0.12	0.07	0.03

The composite contact surface was also characterized using XPS. Five relatively strong peaks were detected in the observed channel and rib contact areas of the surface of the metallic/ceramic composite material, after long-term heat treatment, using wide scan to 1385 eV, attributable to O 1s, Cr 2p, Mn 2p, Fe 2p and La 3d photoelectrons in Fig. 14.

The deconvolution of these peaks for both studied zones is shown in Fig. 15 (surface of the composite under channel) and Fig. 16 (surface of the composite under the rib).

Detailed analysis of the main deconvolution peaks, including binding energies (BEs) and relative atomic percentage concentration of detected elements are listed in Table 8.

The data measured in the present study were compared with the XPS spectra for perovskite-type oxide structures [62,63]. This comparison indicated, in both areas, for La, there are two peaks, one at ~833 eV corresponding to La^{3+} in perovskite phase and, another at ~835 eV which is assigned to La^{3+} in La_2O_3, in good agreement with our previous studies [20]. In addition, the binding energies of ~710 eV and ~712 eV could allow the presence of iron in perovskite [64]. Thus, the

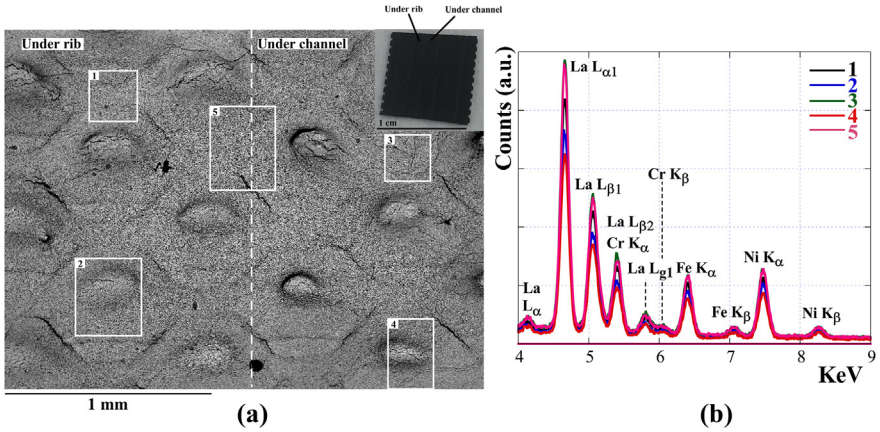

Fig. 13 – (a) SEM image and (b) EDX point analysis of the surface of the composite material which was in contact with the interconnect, after heated at 800 °C for 1000 h, in air.

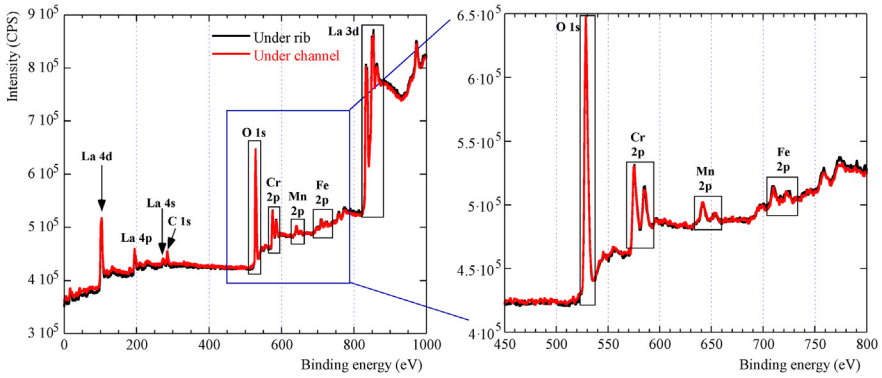

Fig. 14 – Wide scan XPS spectra of composite contact material under the rib and channel after long-term heated at 800 °C in air.

peaks appearing at ~575 eV, ~576 eV and ~579 eV indicated the appearance of chromium in perovskite with ABO_3 structure [40,65] (Table 8), in good agreement with the obtained XRMD results in which Cr-perovskite was quantified (Table 6). Besides, in Ref. [56], the $LaNi_{0.6}Fe_{0.4}O_3$ stability in the presence of chromia was investigated, concluding Cr-cations moves into the perovskite structure, replacing first Ni- and then Fe-cations. The presence of nickel was not detected by XPS, which could indicate the exchange of Ni with Cr in the initial perovskite structure. In addition, for both analyzed zones, the presence of Mn is observed from the peaks at ≈642 eV, ≈644 eV and ≈647 eV (Mn $2p_{3/2}$), in good agreement with other authors [66–68].

Analyses from both EDX and XPS showed similar results for the analyzed composite material areas which were in contact with interconnect. According to other authors [69], the XPS technique is more sensitive for surface composition analysis and detects a depth of ~5 nm while EDX is able to measure ~1 μm depth. Thus, the difference means that Mn is more concentrated on the composite surface (surface in contact with the rib and under channel of the interconnect), not through the bulk, providing the formation of a low thickness

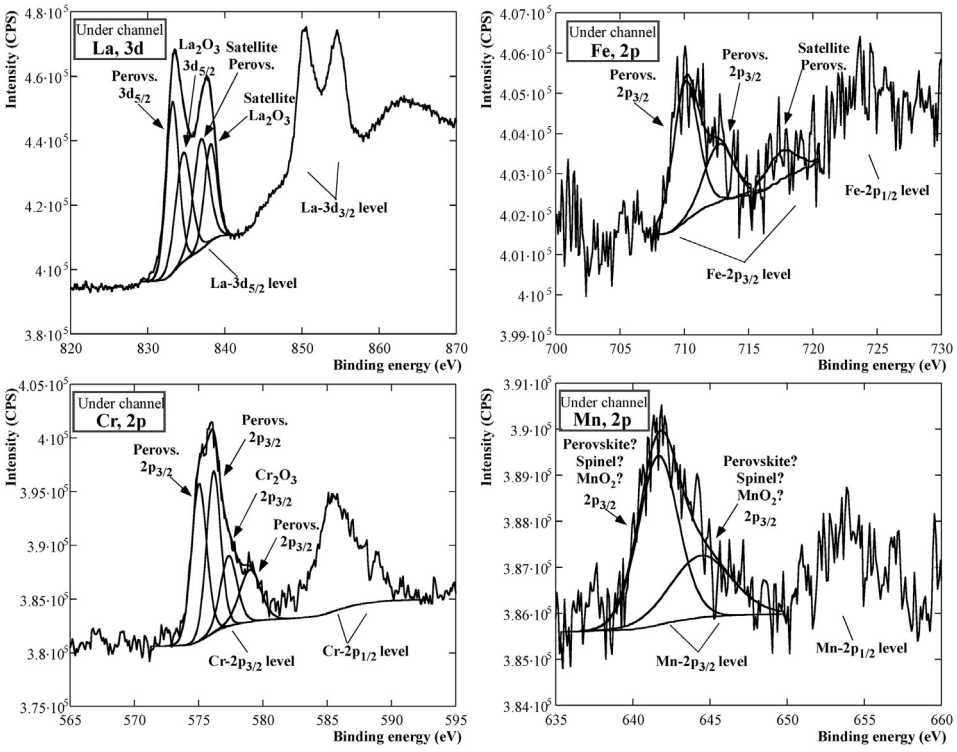

Fig. 15 – Detailed XPS spectra of La $3d_{5/2}$, Cr $2p_{3/2}$, Mn $2p_{3/2}$ and Fe $2p_{3/2}$ of the surface of LNF/Fe-22Cr composite contact material under the channel of the interconnect, after long-term heated at 800 °C in air.

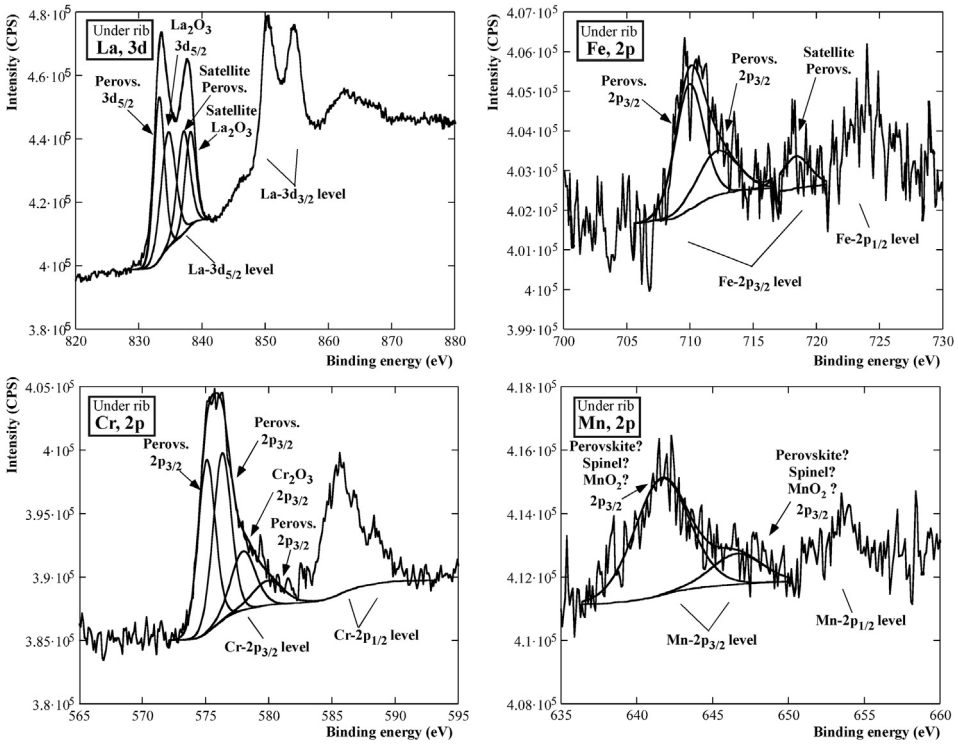

Fig. 16 – Deconvolution of La $3d_{5/2}$, Cr $2p_{3/2}$, Mn $2p_{3/2}$ and Fe $2p_{3/2}$ XPS peaks identified on the surface of LNF/Fe-22Cr composite contact material under the rib of the interconnect, after long-term heated at 800 °C in air.

Mn-spinel barrier layer [70]. This might also partly explain why the detected (% in weight) $MnCr_2O_4$, by XRMD, is low.

Evaluation of the long-term chemical compatibility of the studied system revealed that the direct exposure to air increased the oxidation of interconnect, leading to the growth of a Cr_2O_3 layer and formation of Fe_3O_4 oxide on the channel of the alloy substrate. Since chromium appears to have a tendency to incorporate into the LNF structure, this material could be considered a suitable candidate for reducing the degradation of the cell.

Conclusions

An uncoated and $MnCo_{1.9}Fe_{0.1}O_4$ (MCF) coated Fe-22Cr meshes were dipped into $LaNi_{0.6}Fe_{0.4}O_{3-\delta}$ (LNF) slurry to form a continuous conductive/protective layer for Crofer22APU interconnect. It has been demonstrated that if the deposition of the protective coating was not enough to form a dense and continuous layer across the width of the Fe-22Cr mesh, then the use of MCF spinel layer is not enough to prevent chromium migration up to the LNF coating. However, when mesh/LNF material was directly adhered to the interconnect, the obtained ASR value of 0.0425(2) Ω cm^2 was stable for 400 min, indicating initial good adherence between both materials. The evaluation of long-term chemical compatibility of this system, without applying a current source, revealed that the presence of a composite coating on the rib of interconnect limited the growth of the chromia-based layer and formation of iron oxides on alloy substrate, reducing the contact resistance of the system. Future work will include electrochemical measurements of mesh-LNF/interconnect structure for extended periods.

Table 8 – XPS analysis results of detected elements for the contact surface of the composite in contact with the rib and under channel of the interconnect, after heating at 800 °C for 1000 h in air.

Peak	Surface under channel		Surface in contact with the rib	
	BE (eV)	% at. conc.	BE (eV)	% at. conc.
La $3d_{5/2}$ in ABO_3	833.22; 836.95 (sat.)	9.2	833.23; 837.09 (sat.)	8.8
La $3d_{5/2}$ in La_2O_3	834.65; 838.16 (sat.)	7.0	834.66; 838.17 (sat.)	7.9
Cr $2p_{3/2}$ in ABO_3	575.04; 576.17; 579	8.3	575.1; 576.32; 579.94	8.4
Cr $2p_{3/2}$ in Cr_2O_3	577.35	1.7	577.99	1.8
Fe $2p_{3/2}$ in ABO_3	710.1; 712.69; 717.53 (sat.)	1.7	709.96; 712.17; 718.38 (sat.)	1.8
Mn $2p_{3/2}$	641.65; 644.42	2.6	641.65; 646.59	2.8
O 1s	528.85; 530.46; 531.72; 532.9	69.5	528.89; 530.57; 531.76; 533.26	68.5

Acknowledgements

This research has been funded by the Dpto. Educación, Política Lingüística y Cultura of the Basque Goverment (Research Group of the Basque University System IT-630-13), Ministerio de Economía y Competitividad (MAT2013-42092-R) and Engineering and Physical Sciences Research Council (EP/I003932). The authors wish to thank SGIker-UPV/EHU technical and human support. Dr. Mª Belén Sánchez Martínez de Ilárduya is acknowledged for useful scientific help in discussion of XPS measurements. The authors would also like to express their gratitude to Dr. Sergio Fernandez Armas for helping with EDX measurements. A. Morán-Ruiz thanks UPV/EHU for funding her PhD work.

REFERENCES

[1] Millar L, Taherparvar H, Filkin N, Slater P, Yeomans J. Interaction of $(La_{1-x}Sr_x)_{1-y}MnO_3$-$Zr_{1-z}Y_zO_{2-\delta}$ cathodes and $LaNi_{0.6}Fe_{0.4}O_3$ current collecting layers for solid oxide fuel cell application. In: Proceedings of the 2008 conference for the engineering doctorate in environmental technology.

[2] Sharaf OZ, Orhan MF. An overview of fuel cell technology: fundamentals and applications. Renew Sust Energy Rev 2014;32:810–53.

[3] Guan W, Jin L, Wu W, Zheng Y, Wang G,Wang WG. Effect and mechanism of Cr deposition in cathode current collecting layer on cell performance inside stack for planar oxide fuel cells. J Power Sources 2014;245:119–28.

[4] Guan WB, Jin L, Ma X, Wang WG. Investigation of impactors on cell degradation inside planar SOFC stacks. Fuel Cells 2012;6:1085–94.

[5] Schuler JA, Wuillemin Z, Hessler-Wyser A, Comminges C, Steiner NY, Van Herle J. Cr-poisoning in $(Ls,Sr)(Co,Fe)O_3$ cathodes after 10.000 h SOFC stack testing. J Power Sources 2012;211:177–83.

[6] Tucker MC, Cheng L, DeJonghe LC. Selection of cathode contact materials for solid oxide fuel cells. J Power Sources 2011;196:8313–22.

[7] Guan WB, Zhai HJ, Jin L, Li TS, Wang WG. Effect of contact between electrode and interconnect on performance of SOFC stacks. Fuel Cells 2011;3:445–50.

[8] Stodolny MK, Boukamp BA, Blank DHA, Van Berkel FPF. Cr-poisoning of $LaNi_{0.6}Fe_{0.4}O_3$ cathode under current load. J Power Sources 2012;209:120–9.

[9] Shaigan N, Qu W, Douglas GI, Chen W. A review of recent progress in coatings, fuel cell ferritic stainless steel interconnects. J Power Sources 2010;195:1529–42.

[10] Lu Z, Xia G, Templeton JD, Li X, Nie Z, Yang Z, et al. Development of $Ni_{1-x}Co_xO$ as the cathode/interconnect contact for solid oxide fuel cells. Electrochem Commun 2011;13:642–5.

[11] Tietz F, Sebold D. Interface reactions between electrically conductive ceramics and ferritic steel-I. The system Cr-22Fe-0.5Mn/Mn_2O_3/(La,Ca)(Cr,Co,Cu)O_3. Mater Sci Eng B 2008;150:135–40.

[12] Sharma VI, Yildiz B. Degradation mechanism in $La_{0.8}Sr_{0.2}CoO_3$ as contact layer on the solid oxide electrolysis cell anode. J Electrochem Soc 2010;157(3):B441–8.

[13] Montero X, Tietz F, Stöver D, Cassir M, Villarreal I. Comparative study of perovskites as cathode contact materials between an $La_{0.8}Sr_{0.2}FeO_3$ cathode and a Crofer22APU interconnect in solid oxide fuel cells. J Power Sources 2009;188:148–55.

[14] Basu RN, Tietz F, Teller O, Wessel E, Buchkremer HP, Stöver D. $LaNi_{0.6}Fe_{0.4}O_3$ as a cathode contact material for solid oxide fuel cells. J Solid State Electrochem 2003;7:416–20.

[15] Konysheva E, Laatsch J, Wessel E, Tietz F, Christiansen N, Singheiser L, et al. Influence of different perovskite interlayers on the electrical conductivity between $La_{0.65}Sr_{0.3}MnO_3$ and Fe/Cr based steels. Solid State Ionics 2006;177:923–30.

[16] Zhou Q, Xu L, Guo Y, Jia D, Li Y, Wei WCJ. $La_{0.6}Sr_{0.4}Fe_{0.8}Cu_{0.2}O_{3-\delta}$ perovskite oxide as cathode for IT-SOFC. Int J Hydrogen Energy 2012;37(16):11963–8.

[17] Da Conceiçao L, Dessemond L, Djurado E, Souza MMVM. $La_{0.7}Sr_{0.3}MnO_3$-coated SS444 alloy by dip-coating process for metallic interconnect supported solid oxide fuel cells. J Power Sources 2013;241:159–67.

[18] Yang Z, Xia GG, Maupin GD, Stevenson JW. Evaluation of perovskite overlay coatings on ferritic steels for SOFC interconnect applications. J Electrochem Soc 2006;153:A1852–8.

[19] Lacey R, Pramanick A, Lee JC, Jung JI, Jiang B, Edwards DD, et al. Evaluation of Co and perovskite Cr-blocking thin films on SOFC interconnects. Solid State Ionics 2010;181:1294–302.

[20] Morán-Ruiz A, Vidal K, Laguna-Bercero MA, Larrañaga A, Arriortua MI. Effects of using $(La_{0.8}Sr_{0.2})_{0.95}Fe_{0.6}Mn_{0.3}Co_{0.1}O_3$ (LSFMC), $LaNi_{0.6}Fe_{0.4}O_{3-\delta}$ (LNF) and $LaNi_{0.6}Co_{0.4}O_{3-\delta}$ (LNC) as contact material on solid oxide fuel cells. J Power Sources 2014;248:1067–76.

[21] Magdefrau NJ. Evaluation of solid oxide fuel cell interconnect coatings: reaction layer microstructure, chemistry and formation mechanisms [Doctoral dissertations]. University of Connecticut; 2013.

[22] Fang Y, Wu C, Duan X, Wang S, Chen Y. High-temperature oxidation process analysis of $MnCo_2O_4$ coatings on Fe-21Cr alloy. Int J Hydrogen Energy 2011;36(9):5611–6.

[23] Abdoli H, Alizadeh. Electrophoretic deposition of $(Mn,Co)_3O_4$ spinel nano poder on SOFC metallic interconnects. Mater Lett 2012;80:53–5.

[24] Uehara T, Yasuda N, Okamoto M, Baba Y. Effect of Mn-Co spinel coating for Fe-Cr ferritic alloys ZMG232L and 232J3 for solid oxide fuel cell interconnects on oxidation behavior and Cr-evaporation. J Power Sources 2011;196(17):7251–6.

[25] Zhang HH, Zeng CL. Preparation and performances of Co-Mn spinel coating on a ferritic stainless steel interconnect material for solid oxide fuel cell application. J Power Sources 2014;252:122–9.

[26] Zhang H, Wu J, Liu X, Baker A. Studies on elements diffusion of Mn/Co coated ferritic stainless steel for solid oxide fuel cell interconnects application. Int J Hydrogen Energy 2013;38:5075–83.

[27] Akanda SR, Walter ME, Kidner NJ, Seabaugh MM. Lifetime prediction for manganese cobalt spinel oxide coatings on metallic interconnects. Thin Solid Films 2014;565:237–48.

[28] Yang Z, Xia G, Nie Z, Templeton JD, Stevenson JW. Ce-modified $(Mn,Co)_3O_4$ spinel coatings on ferritic stainless steels for SOFC interconnect applications. Electrochem Solid St 2008;11(8):B140–3.

[29] Chou YS, Stevenson JW, Choi JP. Long-term evaluation of solid oxide fuel cell candidate materials in a 3-cell generic stack test fixture, part III: stability and microstructure of Ce-(Mn,Co)-spinel coating, AISI441 interconnect, alumina coating, cathode and anode. J Power Sources 2014;257:444–53.

[30] Montero X, Jordán N, Pirón-Abellán J, Tietz F, Stöver D, Cassir M, et al. Spinel and perovskite protection layers between Crofer22APU and $La_{0.8}Sr_{0.2}FeO_3$ cathode materials

for SOFC interconnects. J Electrochem Soc 2009;156(1):B188–96.
[31] Chou PY, Ciou CJ, Lee YC, Hung IM. Effect of $La_{0.1}Sr_{0.9}Co_{0.5}Mn_{0.5}O_{3-\delta}$ protective coating layer on the performance of $La_{0.6}Sr_{0.4}Co_{0.8}Fe_{0.2}O_{3-\delta}$ solid oxide fuel cell cathode. J Power Sources 2012;197:12–9.
[32] Hosseini N, Abbasi MH, Karimzadeh F, Choi GM. Development of $Cu_{1.3}Mn_{1.7}O_4$ spinel coating on ferritic stainless steel for solid oxide fuel cell interconnects. J Power Sources 2015;273:1073–83.
[33] Puranen J, Pihlatie M, Lagerbom J, Bolelli G, Laakso J, Hyvärinen L, et al. Post-mortem evaluation of oxidized atmospheric plasma sprayed Mn-Co-Fe oxide spinel coatings on SOFC interconnects. Int J Hydrogen Energy 2014;39(30):17284–94.
[34] Montero X, Tietz F, Sebold D, Buchkremer HP, Ringuede A, Cassir M, et al. $MnCo_{1.9}Fe_{0.1}O_4$ spinel protection layer on commercial ferritic steels for interconnect applications in solid oxide fuel cells. J Power Sources 2008;184:172–9.
[35] Miguel-Pérez V, Martínez-Amesti A, Nó ML, Larrañaga A, Arriortua MI. The effect of doping $(Mn,B)_3O_4$ materials as protective layers in different metallic interconnects for solid oxide fuel cells. J Power Sources 2013;243:419–30.
[36] Zhang W, Pu J, Chi B, Jian L. $NiMn_2O_4$ spinel as an alternative coating material for metallic interconnects of intermediate temperature solid oxide fuel cells. J Power Sources 2011;196:5591–4.
[37] Liu Y, Chen DY. Protective coatings for Cr_2O_3-forming interconnects of solid oxide fuel cells. Int J Hydrogen Energy 2009;34:9220–6.
[38] Wu W, Guan W, Wang G, Liu W, Zhang Q, Chen T, et al. Evaluation of $Ni_{80}Cr_{20}/(La_{0.75}Sr_{0.25})_{0.95}MnO_3$ dual layer coating on SUS 430 stainless steel used as metallic interconnect for solid oxide fuel cells. Int J Hydrogen Energy 2014;39:996–1004.
[39] Yoon C. Computational design, fabrication, and characterization of microarchitectured solid oxide fuel cells with improved energy efficiency [Ph D thesis]. Georgia Institute of Technology; 2010.
[40] Morán-Ruiz A, Vidal K, Larrañaga A, Laguna-Bercero MA, Porras-Vázquez JM, Slater PR, et al. $LaNi_{0.6}Co_{0.4}O_{3-\delta}$ dip-coated on Fe-Cr mesh as a composite cathode contact material on intermediate solid oxide fuel cells. J Power Sources 2014;269:509–19.
[41] Zhu WZ, Deevi SC. Development of interconnect materials for solid oxide fuel cells. Mat Sci Eng A-Struct 2003;348:227–43.
[42] Piccardo P, Gannon P, Chevalier S, Viviani M, Burbucci A, Caboche G, et al. ASR evaluation of different kinds of coatings on a ferritic stainless steel as SOFC interconnect. Surf Coat Tech 2007;202:1221–5.
[43] Vidal K, Morán-Ruiz A, Larrañaga A, Porras-Vázquez JM, Slater PR, Arriortua MI. Characterization of $LaNi_{0.6}Fe_{0.4}O_3$ perovskite synthesized by glycine-nitrate combustion method. Solid State Ionics 2015;269:24–9.
[44] Miguel-Pérez V, Martínez-Amesti A, Nó ML, Larrañaga A, Arriortua MI. Oxide scale formation on different metallic interconnects for solid oxide fuel cells. Corros Sci 2012;60:38–49.
[45] Hoyt KO, Gannon PE, White P, Tortop R, Ellingwood BJ, Khoshuei H. Oxidation behavior of $(Co,Mn)_3O_4$ coatings on preoxidized stainless steel for solid oxide fuel cell interconnects. Int J Hydrogen Energy 2012;37:518–29.
[46] Rodríguez-Carvajal J. FULLPROF rietveld pattern matching analysis of powder patterns. 2011 [Grenoble].
[47] Froitzheim J, Meier GH, Niewolak L, Ennis PJ, Hattendorf H, Singheiser L, et al. Development of high strength ferritic steel for interconnect application in SOFCs. J Power Sources 2008;178:163–73.
[48] Chiu YT, Lin CK. Effects of Nb and W additions on high-temperature creep properties of ferritic stainless steels for solid oxide fuel cell interconnect. J Power Sources 2012;198:149–57.
[49] Linder M, Hocker T, Holzer L, Friedrich KA, Iwanschitz B, Mai A, et al. Cr_2O_3 scale growth rates on metallic interconnectors derived from 40.000 h solid oxide fuel cell stack operation. J Power Sources 2013;243:508–18.
[50] Ali-Löytty H. Microalloying mediated segregation and interfacial oxidation of FeCr alloys for solid oxide fuel cell applications [Ph. D. thesis]. Tampere University of Technology; 2013.
[51] Mohammadi M, Javadpoura S, Kobayashi A, Shirvani K, Jenabali JA, Khakpour I. Cyclic oxidation behavior of CoNiCrAlY coatings produced by LVPS and HVOF processes. Trans JWRI 2011;40:53–8.
[52] Fayette S, Smith DS, Smith A, Martin C. Influence of grain size on the thermal conductivity of tin oxide ceramics. J Eur Ceram Soc 2000;20(3):297–302.
[53] Vilasi M, Francois M, Brequel H, Podor R, Venturini G, Steinmetz J. Phase equilibria in the Nb-Fe-Cr-Si system. J Alloy Compd 1998;269:187–92.
[54] Ming-Jui T, Chun-Lin C, Shyong L. $La_{0.6}Sr_{0.4}Co_{0.2}Fe_{0.8}O_3$ protective coatings for solid oxide fuel cell interconnect deposited by screen printing. J Alloy Compd 2010;489:576–81.
[55] Tucker MC, Cheng L, DeJonghe LC. Inorganic binder-containing composite cathode contact materials for solid oxide fuel cells. J Power Sources 2013;224:174–9.
[56] Stodolny MK, Boukamp BA, Blank DHA, Van Berkel FPF. $La(Ni,Fe)O_3$ stability in the presence of chromia-A solid-state reactivity study. J Electrochem Soc 2011;158(2):B112–6.
[57] Wang K, Liu Y, Fergus JW. Interaction between SOFC interconnect coating materials and chromia. J Am Ceram Soc 2011;94(12):4490–5.
[58] Shong WJ, Liu CK, Chen CY, Peng CC, Tu HJ, Fey GTK, et al. Effects of lanthanum-based perovskite coatings on the formation of oxide scale for ferritic SOFC interconnect. Mater Chem Phys 2011;127:45–50.
[59] Stojanovic M, Haverkamp RG, Mims CA, Moudallal H, Jacobson AJ. Synthesis and characterization of $LaCr_{1-x}Ni_xO_3$ perovskite oxide catalysts. J Catal 1997;165:315–23.
[60] Essuman E, Meier GH, Zurek J, Hänsel M, Norby T, Singheiser L, et al. Protective and non-protective scale formation of NiCr alloys in water vapour containing high- and low-pO_2 gases. Corros Sci 2008;50(6):1753–60.
[61] Jiang SP, Chen X. Chromium deposition and poisoning of cathodes of solid oxide fuel cells-A review. Int J Hydrogen Energy 2014;39(1):505–31.
[62] Crumlin EJ, Mutoro E, Liu Z, Grass ME, Biegalski MD, Lee YL, et al. Surface strontium enrichment on highly active perovskites for oxygen electrocatalysis in solid oxide fuel cells. Energy Environ Sci 2012;5:6081–8.
[63] Konysheva EY, Francis SM. Identification of surface composition and chemical states in composites comprised of phases with fluorite and perovskite structures by X-ray photoelectron spectroscopy. Appl Surf Sci 2013;268:278–87.
[64] Ghaffari M, Shannon M, Hui H, Tan OK, Irannejad A. Preparation, surface state and band structure studies of $SrTi_{(1-x)}Fe_{(x)}O_{(3-\delta)}$ (X = 0-1) perovskite-type nano structure by X-ray and ultraviolet photoelectron spectroscopy. Surf Sci 2012;606:670–7.
[65] Jiang Y, Gao J, Liu M, Wang Y, Meng G. Synthesis of $LaCrO_3$ films using spray pyrolysis technique. Mater Lett 2007;61:1908–11.
[66] Nesbitt HW, Banerjee D. Interpretation of XPS Mn(2p) spectra of Mn oxyhydroxides and constraints on the mechanism of MnO_2 precipitation. Am Mineral 1998;83:305–15.

[67] Ramana CV, Massot M, Julien CM. XPS and Raman spectroscopic characterization of $LiMn_2O_4$ spinels. Surf Interface Anal 2005;37:412–6.
[68] Wei ZX, Xiao CM, Zeng WW, Liu JP. Magnetic properties and photocatalytic activity of $La_{0.8}Ba_{0.2}Fe_{0.9}Mn_{0.1}O_{3-\delta}$ and $LaFe_{0.9}Mn_{0.1}O_{3-\delta}$. J Mol Catal A-Chem 2013;370:35–43.
[69] Li W, Lu K, Xia Z. Interaction of $(La_{1-x}Sr_x)_nCo_{1-y}Fe_yO_{3-\delta}$ cathodes and AISI 441 interconnect for solid oxide fuel cells. J Power Sources 2013;237:119–27.
[70] Sabioni ACS, Huntz AM, Borges LC, Jomard F. First study of manganese diffusion in Cr_2O_3, polycrystals and thin films, by SIMS. Phil Mag Lett 2007;87(12):1921–37.

INTERNATIONAL JOURNAL OF HYDROGEN ENERGY XXX (2015) 1–12

Available online at www.sciencedirect.com

ScienceDirect

journal homepage: www.elsevier.com/locate/he

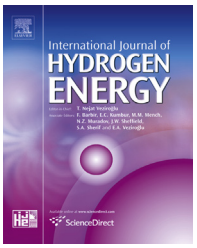

Laser machining of $LaNi_{0.6}M_{0.4}O_{3-\delta}$ (M: Co, Fe) dip-coated on a Fe–22Cr mesh material to obtain a new contact coating for SOFC: Interaction between Crofer22APU interconnect and $La_{0.6}Sr_{0.4}FeO_3$ cathode

Aroa Morán-Ruiz [a], *Karmele Vidal* [a], *Aitor Larrañaga* [a], *Jose Manuel Porras-Vázquez* [b], *Peter Raymond Slater* [b], *María Isabel Arriortua* [a,*]

[a] *Universidad del País Vasco (UPV/EHU), Facultad de Ciencia y Tecnología, Departamento de Mineralogía y Petrología, Barrio Sarriena S/N, 48940 Leioa, Vizcaya, Spain*

[b] *University of Birmingham, School of Chemistry, Birmingham B15 2TT, UK*

ARTICLE INFO

Article history:
Received 5 March 2015
Received in revised form
22 April 2015
Accepted 24 April 2015
Available online xxx

Keywords:
SOFC
Composite contact material
Femtosecond laser
Contact resistance
Degradation

ABSTRACT

A Fe–22Cr mesh was dipped into a ceramic ($LaNi_{0.6}M_{0.4}O_{3-\delta}$; M: Co, Fe) slurry to form a metallic/ceramic material as contact coating for solid oxide fuel cells (SOFCs). This composite was directly adhered to a Crofer22APU channeled interconnect and micro-holes were performed on coating using a femtosecond laser. Then, $La_{0.6}Sr_{0.4}FeO_3$ (LSF) cathode was spray deposited on top of this ablated system to analyze the formed structures in terms of the electrical performance, processing reproducibility and long-term behavior at 800 °C. The adequate reproducibility of the process was confirmed through area specific resistance (ASR) testing on four replicas for each system. After long-term treatment, the chromium diffusion within both the interconnect and mesh of the composite was quantitatively analyzed using energy dispersive X-ray spectroscopy (EDX). The laser irradiated composite showed short-range damage, which was limited to the formation of iron and chromium oxides due to the evaporation and oxidation of the mesh.

Introduction

Despite the fact that the world is trying to reduce carbon emissions through the expansion of clean and renewable energy resources, the use of fossil fuels continues to dominate the global energy sector. An alternative to conventional methods of energy production could be the direct conversion of chemical energy into electrical energy via electrochemical reactions between fuel and oxidant without involving combustion, which is the main characteristic of Solid Oxide Fuel Cells (SOFCs) [1,2]. High temperature

* *Corresponding author*. Tel.: +34 946015984, +34 946013500.
E-mail address: maribel.arriortua@ehu.es (M.I. Arriortua).

http://dx.doi.org/10.1016/j.ijhydene.2015.04.134

Please cite this article in press as: Morán-Ruiz A, et al., Laser machining of $LaNi_{0.6}M_{0.4}O_{3-\delta}$ (M: Co, Fe) dip-coated on a Fe–22Cr mesh material to obtain a new contact coating for SOFC: Interaction between Crofer22APU interconnect and $La_{0.6}Sr_{0.4}FeO_3$ cathode, International Journal of Hydrogen Energy (2015), http://dx.doi.org/10.1016/j.ijhydene.2015.04.134

Table 1 – Chemical composition average in wt (%) of Fe–22Cr alloy used as interconnect and as mesh, obtained by EDX microanalysis.

Sample	Fe (%wt.)	Cr (%wt.)	Mn (%wt.)	Ti (%wt.)	Nb (%wt.)	W (%wt.)
Mesh	73.1(3)	23.5(2)	0.6(1)	<0.1	0.4(1)	2.3(2)
Interconnect	76.3(2)	23.0(2)	0.6(1)	<0.1	–	–

operating conditions of SOFCs (1000–800 °C) lead to a variety of degradation mechanisms which represent a significant challenge in meeting lifetime requirements [3]. For stationary applications, the commercial lifetime requirement is generally more than 40,000 h. In comparison, up to a 20,000 h lifetime with more frequent thermal cycles is required for auxiliary power units in transportation applications [4]. However, these extensive lifetime requirements have not been met yet. The key degradation issues of these cells could be related with the chemical and thermomechanical instability at the interfaces [5]. Moreover, it has been extensively studied [6–8] that the oxidation of the interconnect at a high temperature allows the vaporization of chromium, which poisons the cell cathode, thus contributing to the cell degradation during stack operation. In order to prevent the cell degradation caused by the use of metal interconnects, dense protective layers are used to coat the metallic substrate. Spinel oxide protective materials are usually applied to the metallic interconnect to achieve this protection [9–11]. However, despite the usefulness of protective coatings, the stack degradation rates are still higher than the required value for SOFC commercialization.

According to other authors and to our previous studies [12,13], the interconnect–cathode interface plays an important role in the electrical resistance of the cell. Thus, the use of a protective/conductive layer between interconnect and cathode could reduce electron transmission resistance as well as the interaction between both materials, thus acting as a diffusion barrier for chromium species (CrO_3 (g), $CrO_2(OH)_2$ (g)). The types of contact materials are diverse, but basically they must possess both adequate porosity and electronic conductivity to perform their functions in the cell [14]. The most commonly used contact coatings are highly conductive perovskites [15,16], i. e. $La_{0.8}Sr_{0.2}Co_{0.75}Fe_{0.25}O_3$, $LaNi_{0.6}Fe_{0.4}O_{3-\delta}$, $LaNi_{0.6}Co_{0.4}O_{3-\delta}$. An important drawback of these oxides is that their sintering temperature is limited since the high temperature favours the oxidation of iron–chromium alloys. Thus, these ceramic contact materials sintered at lower temperatures have lower density and, therefore, reduced electronic conductivity. The development of metallic-ceramic coatings, such as $Ni_{80}Cr_{20}/(La_{0.75}Sr_{0.25})_{0.95}MnO_3$ dual-layer [17], could bridge the gap between interconnect and electrode, increasing the conductivity and adhesive ability of the interface between both materials, when using low temperature sintering process. In this context, according to previous studies [18], the incorporation of conducting wires and designed porous channels in the electrodes could increase cell performance via improved transport of electrons as well as gases. However, to our knowledge, few studies have investigated the incorporation of pore channels in the electrodes.

In this work, femtosecond laser machined holes are produced in a contact coating based on a Fe–22Cr mesh dipped into a ceramic ($LaNi_{0.6}M_{0.4}O_{3-\delta}$; M: Co, Fe) slurry. This composite, which could provide electronic conduction as well as rapid oxidant gases transfer through interconnect/electrode interface, is directly adhered to Crofer22APU interconnect and then $La_{0.6}Sr_{0.4}FeO_3$ (LSF) cathode is spray deposited to form an {interconnect/contact layer/cathode} configuration. The electrical performance, processing reproducibility and long-term behavior at 800 °C of the formed structures are discussed. Moreover, the electrical resistance of interconnect/cathode interface is also studied.

Experimental

The structure of interconnect–cathode interface used in the experiments consists of {interconnect/contact material/cathode}: Crofer22APU (ThyssenKrupp VDM)/$LaNi_{0.6}Co_{0.4}O_{3-\delta}$ (LNC) or $LaNi_{0.6}Fe_{0.4}O_{3-\delta}$ (LNF) (NexTech, Fuel Cell Materials) dip coated on Fe–22Cr mesh (Fiaxell SOFC Technologies)/$La_{0.6}Sr_{0.4}FeO_3$ (LSF) (NexTech, Fuel Cell Materials). The chemical composition of the steels was determined using a scanning electron microscopy (SEM, JEOL LSM-6400) equipped with an Oxford instrument INCA E-350 energy dispersive X-ray spectroscopy (EDX) (Table 1).

In order to obtain metallic/ceramic contact composite, stainless steel mesh, with mesh opening of about 175 μm and a thickness of 250 μm, was cut into 10 mm × 10 mm squares, cleaned with acetone in an ultrasonic bath and dried. Flat squared-meshes were preoxidized at 600 °C for 10 h, in air. LNC and LNF commercial powders were fabricated into pastes. The slurries were prepared by mixing each of the $LaNi_{0.6}Co_{0.4}O_{3-\delta}$ and $LaNi_{0.6}Fe_{0.4}O_{3-\delta}$ powders (12.5 vol. %) in 87.5 vol. % ethanol (Panreac) with 1 vol. % Dolapix (Zschimmer & Schwarz, Chemische Fabriken). The mixtures, containing 5 vol. % of PVB (polyvinyl butyral, Solutia Solutions) organic binder, were

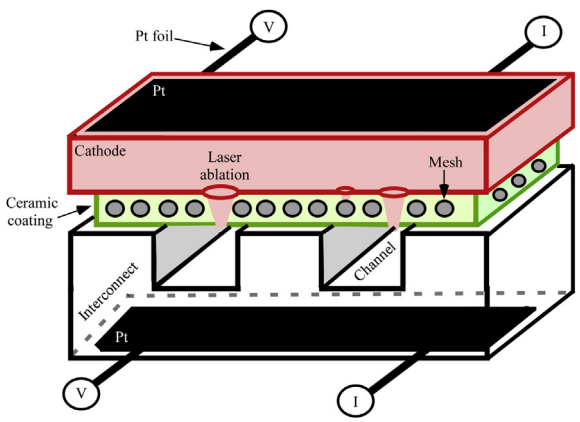

Fig. 1 – Scheme of the setup for the ASR measurements.

Please cite this article in press as: Morán-Ruiz A, et al., Laser machining of $LaNi_{0.6}M_{0.4}O_{3-\delta}$ (M: Co, Fe) dip-coated on a Fe–22Cr mesh material to obtain a new contact coating for SOFC: Interaction between Crofer22APU interconnect and $La_{0.6}Sr_{0.4}FeO_3$ cathode, International Journal of Hydrogen Energy (2015), http://dx.doi.org/10.1016/j.ijhydene.2015.04.134

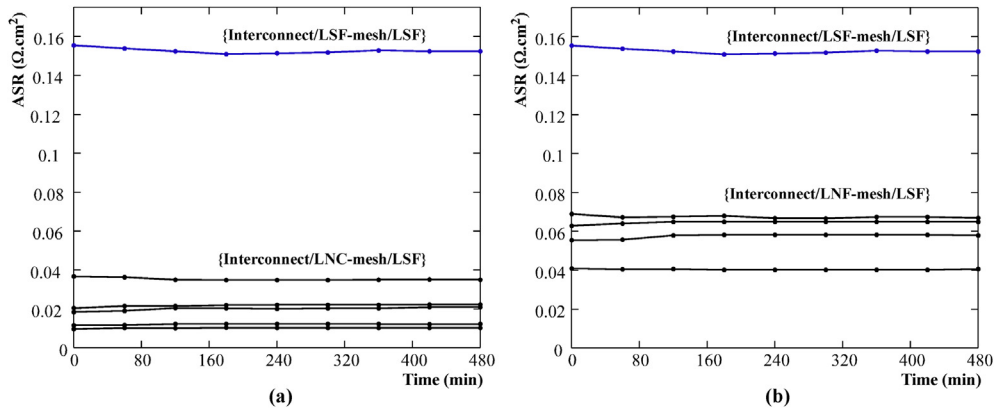

Fig. 2 – Area specific resistance values, at 800 °C in air, for different interfaces tested in the {interconnect/ablated LSF-mesh/cathode} structure as well as (a) {interconnect/ablated LNC-mesh/cathode} and (b) {interconnect/ablated LNF-mesh/cathode} systems, as a function of time.

homogenized for 5 h using a magnetic stirrer. The ceramic slurry composition employed were chosen in order to obtain dense contact layer. The obtained paste was then deposited on the preoxidized squared-meshes via controlled dipping at 4.5 mm s^{-1} speed. This step was repeated several times in order to achieve the required thickness. The interconnect was cut into square substrates measuring 10 mm × 10 mm with a thickness of 1 mm. The machined channels of substrate are 2 mm width, 0.5 mm depth, 10 mm length and the distance between neighboring is 2 mm. The obtained squared-steels were hand polished with 800 grit abrasive paper, cleaned with acetone in an ultrasonic bath and dried. All substrates were preoxidized at 800 °C for 100 h in air, to inhibit Fe and Cr transport from the alloys to the ceramic coating and to avoid the growth of the chromium based layer, which is known to increase the interfacial stress [19,20]. An additional layer of LNC or LNF was coated on the ribs of the interconnect substrate using wet colloidal spraying. The suspensions were made by mixing the powders, ethanol and ZrO_2 cylinders, as grinding media, in a ball mill for 1 h. The formed composite contact material was directly adhered to the interconnect and sintered at 1050 °C for 2 h, in air, to favour a dense ceramic coating. In order to achieve a better mechanical contact between the coated ribs of interconnect/composite interface, a weight load was placed on the top of the structure.

The laser set-up is described elsewhere [21]. Femtosecond laser pulses were generated by a Ti:Sapphire oscillator-regenerative amplifier system (1 kHz, 4.0 mJ, 40 fs pulses at 800 nm). The pulse energy was controlled by means of a variable neutral density filter, using 4000 pulses of 20 μJ. The light was focused onto the sample, which was mounted in a 3D translation stage (1 μm precision) at atmospheric pressure, using a fused silica lens (f = 100 mm). Matrixes of holes were machined with separation between drillings equal to 77 μm in both horizontal (x) and vertical (y) directions to complete the area of a channel of the interconnect, approximately 2 mm × 6 mm. Then, $La_{0.6}Sr_{0.4}FeO_3$ (LSF) cathode was spray deposited on the micromachined composite material, which was already connected with the channeled substrate, and heated at 950 °C for 2 h, in air, allowing a porous cathode morphology. These systems were then treated at 800 °C for 1000 h, in air.

Area Specific Resistance (ASR) measurements were performed using a DC four-probe method (the resistance value was estimated from the voltage value (Thurlby Thandar Instruments 1604 Digital Multimeter) measured on applying a current of 1 A (Thurlby Thandar Instruments PL300 current source)), on systems, which were prepared according to the geometries shown in Fig. 1. In order to check the reproducibility of the procedures described above, duplicate samples were prepared. Moreover, the electrical resistance of interconnect–cathode interface setup was also determined. Electrical contacts between samples and the external measuring circuit were made by pressing two Pt foils (99.95%, 0.0125-mm thick, Advent Research Materials Ltd. England/Oxford) against the sides of the interconnect as well as the surface of the composite contact material, in combination with a Pt paste.

Once the ASR tests were completed, the samples were epoxy-mounted, sectioned, and polished. Cross sections of the samples were analyzed using SEM/EDX system. Composition analysis was performed using back-scattered electrons (BSE) at 20 kV accelerating voltage and 5 10^{-9} A current. For EDX point analysis the live time was set to 100 s. EDX system calibration was performed measuring the beam current on pure element standards, allowing quantitative elemental

Table 2 – Area specific resistance values for different tested systems measured at 800 °C in air. ASR mean value for each system is included.

Replica	1	2	3	4	5	Mean
Cell-LNC ASR(Ω cm^2)	0.0201(9)	0.0122(3)	0.0219(5)	0.0353(7)	0.0103(2)	0.02(1)
Cell-LNF ASR(Ω cm^2)	0.0675(7)	0.0576(9)	0.0405(2)	0.0647(7)	–	0.06(1)

Please cite this article in press as: Morán-Ruiz A, et al., Laser machining of $LaNi_{0.6}M_{0.4}O_{3-\delta}$ (M: Co, Fe) dip-coated on a Fe–22Cr mesh material to obtain a new contact coating for SOFC: Interaction between Crofer22APU interconnect and $La_{0.6}Sr_{0.4}FeO_3$ cathode, International Journal of Hydrogen Energy (2015), http://dx.doi.org/10.1016/j.ijhydene.2015.04.134

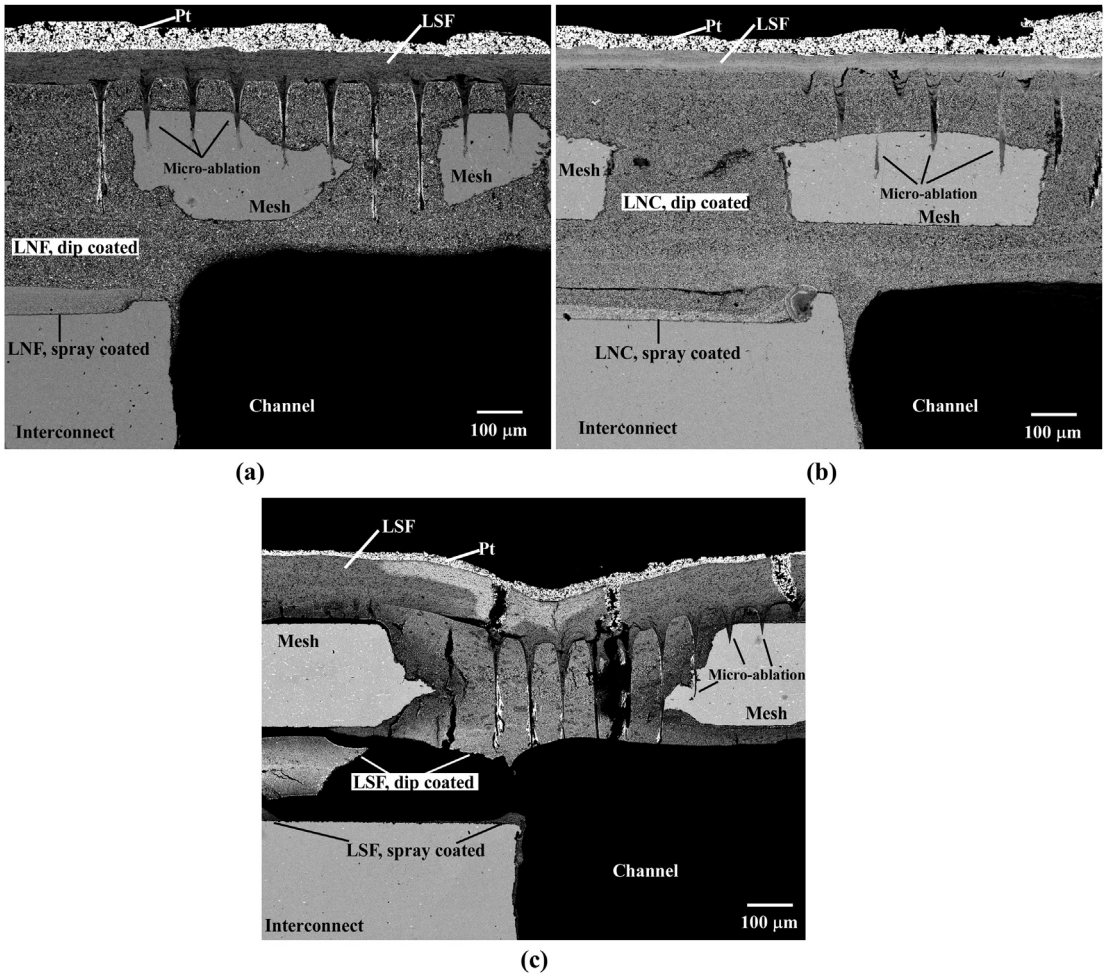

Fig. 3 – Cross-section microstructure images obtained by backscattered electrons signal (BSE) of (a) {interconnect/ablated LNF-mesh/cathode}, (b) {interconnect/ablated LNC-mesh/cathode} and (c) {interconnect/ablated LSF-mesh/cathode} structures after ASR measurements.

analyses. Moreover, EDX mapping was carried out using 13762.56 s (70 ms/pixel) as live time. The data processing was performed using Oxford INCA software. The characteristic emission lines used for the analysis were L_α for La and Nb, K_α for Co, Cr, Fe and Ni, and M_α for W.

Results and discussion

ASR measurements

Fig. 2 depicts the ASR values, as a function of time at 800 °C, for {interconnect/contact coating/cathode} structure composed of: channeled Crofer22APU interconnect adhered to the laser machined composite contact material, which is formed by LNC or LNF paste dip coated on a Fe-22Cr mesh, with an LSF top cathode coating. For comparison, the obtained ASR data, under similar conditions, for the {interconnect/ablated cathode-mesh layer/cathode} (interconnect/cathode) setup is also presented in Fig. 2.

In order to check the reproducibility of the process, at least four specimens were tested for each ceramic contact paste, and, Table 2 shows the average ASR value of the measured replicas. The results support the reproducibility for all the measured structures, indicating similar signal during the contact resistance tests.

However, the ASR of the {interconnect/cathode} system is higher than that of the {interconnect/contact material/cathode} structures, being 0.153 (1) Ω cm^2. The initial resistance value for {interconnect/contact material/cathode} structure depends on the electrical conductivity of the selected contact ceramic paste; ASR mean values for LNC and LNF are 0.02 (1) and 0.06 (1) Ω cm^2, respectively. These values are good enough for the performance of SOFC stack [22–25]. Taking into account the obtained results, the application of LNC and LNF perovskite as contact pastes results in a significant decrease in the contact resistance between the LSF cathode and the Crofer22APU interconnect. These results are in good agreement with the representative SEM images of the cross-section observed for each sample after ASR test (Fig. 3).

A good adherence between the composite contact material and the interconnect corroborates the adequate reproducibility of the process. In this context, a more efficient contact material microstructure is achieved for LNC

Please cite this article in press as: Morán-Ruiz A, et al., Laser machining of $LaNi_{0.6}M_{0.4}O_{3-\delta}$ (M: Co, Fe) dip-coated on a Fe–22Cr mesh material to obtain a new contact coating for SOFC: Interaction between Crofer22APU interconnect and $La_{0.6}Sr_{0.4}FeO_3$ cathode, International Journal of Hydrogen Energy (2015), http://dx.doi.org/10.1016/j.ijhydene.2015.04.134

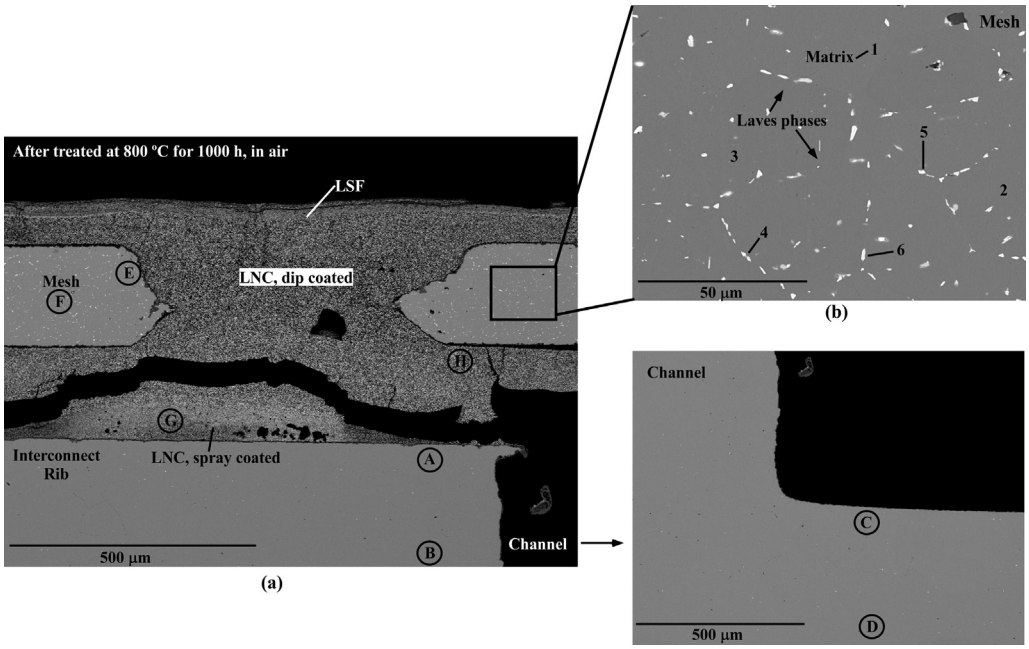

Fig. 4 – Cross-section view of (a) {interconnect/ablated LNC-mesh/cathode} sample, selecting the zone without evidence of laser ablation, after aging at 800 °C for 1000 h, in air. Capital letters indicate analysis areas shown in Table 3, (b) detail of Laves phase formation on the contact mesh during the long-term testing at 800 °C. Numbers indicate analysis areas shown in Table 5.

and LNF contact pastes, improving the adherence of the system. According to other authors and our previous studies [26–28] cathode compositions tend to react with Cr (VI, III) from the interconnect to form phases like $SrCrO_4$, while LNC and LNF materials often incorporate chromium forming Cr-containing perovskites. However, it is believed that the remarkable crack at the interface interconnect/cathode composite coating could have resulted from the infiltration of the sample with epoxy resin. Further, in our previous works [29] the cell were formed using multiple configurations, and different kinds of interconnect and protective materials, obtaining an average value of ~1.5 Ω cm^2 for each structure. Comparing these results with those listed in Table 2 (Fig. 2), the use of {channeled interconnect/ablated composite/cathode} setup significantly improves the performance of the cell.

The initial ASR values reported in previous studies based on {Crofer22APU interconnect sheet/$LaNi_{0.6}Fe_{0.4}O_3$ contact coating/$La_{0.8}Sr_{0.2}FeO_3$ cathode} and {Crofer22APU interconnect sheet/$MnCo_{1.9}Fe_{0.1}O_4$ protective layer/$La_{0.8}Sr_{0.2}Co_{0.75}Fe_{0.25}O_3$ contact coating/$La_{0.8}Sr_{0.2}FeO_3$ cathode} are 0.0864 and 0.0417 Ω cm^2, respectively, at 800 °C [30]. Moreover, other authors pointed out that the $Cu_{1.3}Mn_{1.7}O_4$ coated AISI 430 interconnect sheet steel shows an initial ASR value of 0.0151 Ω cm^2, at 750 °C [1]. Our previous studies indicated that for {Crofer22APU interconnect sheet/$LaNi_{0.6}Co_{0.4}O_{3-\delta}$ contact coating/$La_{0.8}Sr_{0.2}FeO_3$ cathode} and {Crofer22APU interconnect sheet/$LaNi_{0.6}Fe_{0.4}O_{3-\delta}$ contact coating/$La_{0.8}Sr_{0.2}FeO_3$ cathode} structures, the ASR values are 0.006 (1) and 0.010 (1) Ω·cm^2, respectively, at 800 °C after 16 h [13]. All of these values are of the same order of magnitude as those determined in the present study.

In this context, in order to understand the adherence between the metallic/ceramic contact composite and channeled steel interconnect, our previous work [28] has focused on characterizing the long-term stability and electrical performance of:$LaNi_{0.6}Co_{0.4}O_{3-\delta}$-mesh adhered to Crofer22APU, using the same processing conditions that are used in this paper. For this system, the obtained contact resistance value was 0.0054 (1) Ω cm^2, at 800 °C, which is lower than that produced by the proposed micromachined system. It is believed that the action of creating a line of craters on the sample might debilitate the adherence between ribs of the interconnect and composite, which could be the main factor influencing the initial contact resistance in this kind of system. The possible effect of using femtosecond irradiation on these systems in terms of long-term structural/chemical compatibility has been included in the following section.

Long-term stability of {Crofer22APU interconnect/ablated composite contact coating/$La_{0.6}Sr_{0.4}FeO_3$ cathode} system at 800 °C

Firstly, in our previous studies [28,31], the durability of LNC- and LNF-Fe22Cr mesh composites was tested. After they treated at 800 °C for 1000 h, in air, both materials presented an adequate mechanical integrity of ceramic/metallic interface. The long-term stability analysis of {Crofer22APU interconnect/ablated composite contact coating/$La_{0.6}Sr_{0.4}FeO_3$ cathode} structures is focused on the areas with and without craters. Figs. 4 and 5 show the cross-section view of the studied samples, selecting the zone without evidence of laser ablation.

A loss of adherence has been reported between LNC paste coating and substrate due to an insufficient match of the

Please cite this article in press as: Morán-Ruiz A, et al., Laser machining of $LaNi_{0.6}M_{0.4}O_{3-\delta}$ (M: Co, Fe) dip-coated on a Fe–22Cr mesh material to obtain a new contact coating for SOFC: Interaction between Crofer22APU interconnect and $La_{0.6}Sr_{0.4}FeO_3$ cathode, International Journal of Hydrogen Energy (2015), http://dx.doi.org/10.1016/j.ijhydene.2015.04.134

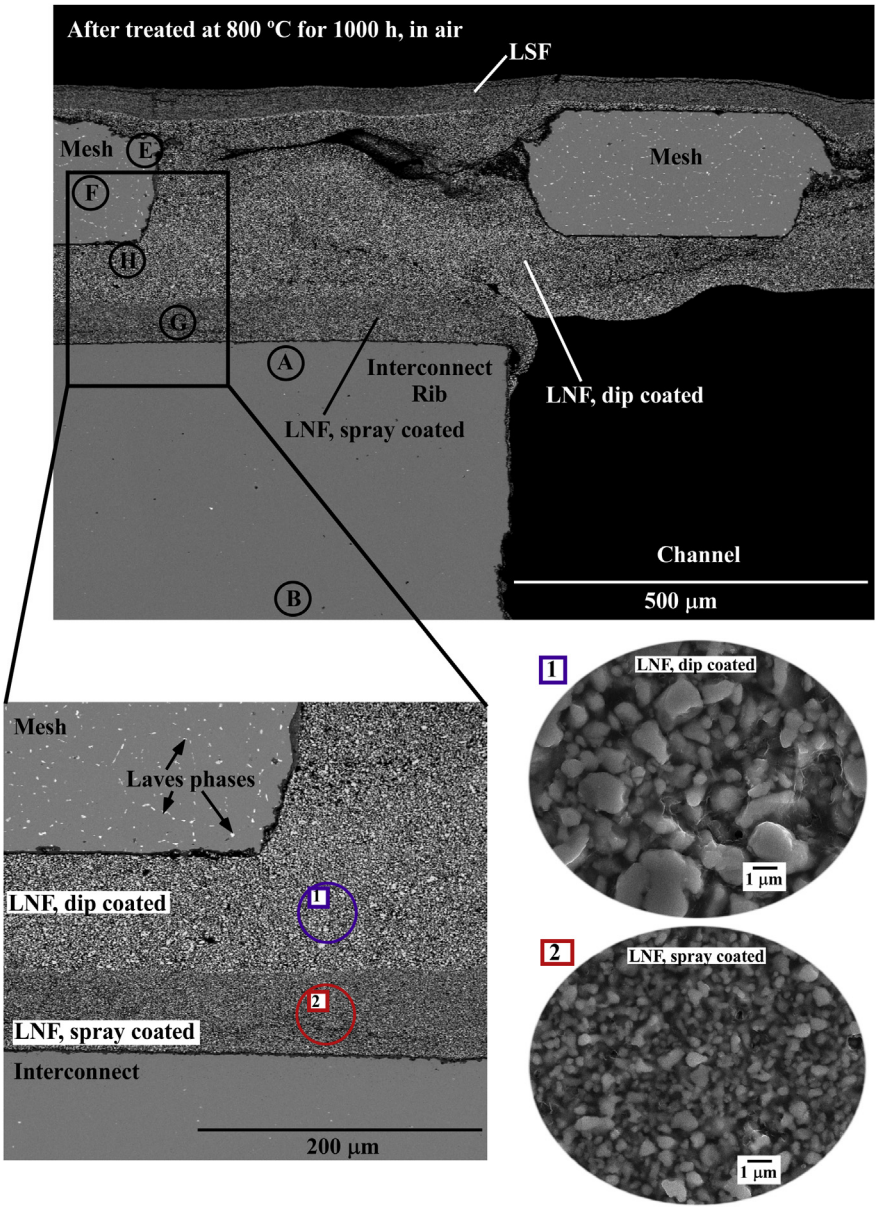

Fig. 5 – Cross-section image of {interconnect/ablated LNF-mesh/cathode} sample, selecting the zone without evidence of laser ablation, after aging at 800 °C for 1000 h, in air. Capital letters indicate analysis areas shown in Table 4. The microstructure of the LNF coatings formed by spraying and dipping are included.

corresponding thermal expansion coefficients (TECs). Moreover, the formation of the crack at the interface interconnect/LNC-mesh coating (Fig. 4) could also be due to the infiltration of the sample with epoxy resin. For both systems the EDX analyses (see Supplementary material; section A: Figs. S1 and S2, section B: Figs. S5 and S6) listed in Tables 3 and 4 and shown in Figs. 4 and 5, respectively, revealed a Cr content reduction on the outside area of the rib (zone A), channel (zone

Table 3 – Chemical composition in % wt. of points indicated in Fig. 4(a).

LNC	Zone	Cr	Fe	W	La	Ni	Co	O
Inter. Fe–Cr rib	(A) outside	22.4(1)	77.6(1)	–	–	–	–	–
	(B) inside	23.3(2)	76.7(2)	–	–	–	–	–
Inter. Fe–Cr channel	(C) outside	22.7(1)	77.3(1)	–	–	–	–	–
	(D) inside	23.5(1)	76.5(1)	–	–	–	–	–
Mesh Fe–Cr	(E) outside	19.3(4)	78.7(4)	2.0(1)	–	–	–	–
	(F) inside	22.6(2)	75.4(3)	2.0(1)	–	–	–	–
Ceramic material	(G) close to the rib	1.5(4)	–	–	55.0(3)	14.2(1)	9.4(3)	19.8(1)
	(H) close to the mesh	3.8(2)	–	–	53.3(2)	13.8(2)	8.9(1)	20.2(1)

Please cite this article in press as: Morán-Ruiz A, et al., Laser machining of $LaNi_{0.6}M_{0.4}O_{3-\delta}$ (M: Co, Fe) dip-coated on a Fe–22Cr mesh material to obtain a new contact coating for SOFC: Interaction between Crofer22APU interconnect and $La_{0.6}Sr_{0.4}FeO_3$ cathode, International Journal of Hydrogen Energy (2015), http://dx.doi.org/10.1016/j.ijhydene.2015.04.134

Table 4 – Chemical composition in % wt. of points indicated in Fig. 5.

LNF	Zone	Cr	Fe	W	La	Ni	O
Inter. Fe–Cr rib	(A) outside	22.2(3)	77.8(3)	–	–	–	–
	(B) inside	23.3(1)	76.7(1)	–	–	–	–
Inter. Fe–Cr channel	(C) outside	22.4(1)	77.6(1)	–	–	–	–
	(D) inside	23.2(1)	76.8(1)	–	–	–	–
Mesh Fe–Cr	(E) outside	20.8(10)	77.2(9)	2.1(2)	–	–	–
	(F) inside	23.3(1)	74.7(1)	2.0(1)	–	–	–
Ceramic material	(G) close to the rib	1.9(1)	9.0(3)	–	54.8(3)	14.3(4)	20.0(1)
	(H) close to the mesh	1.2(2)	9.1(3)	–	55.6(2)	14.2(2)	19.9(1)

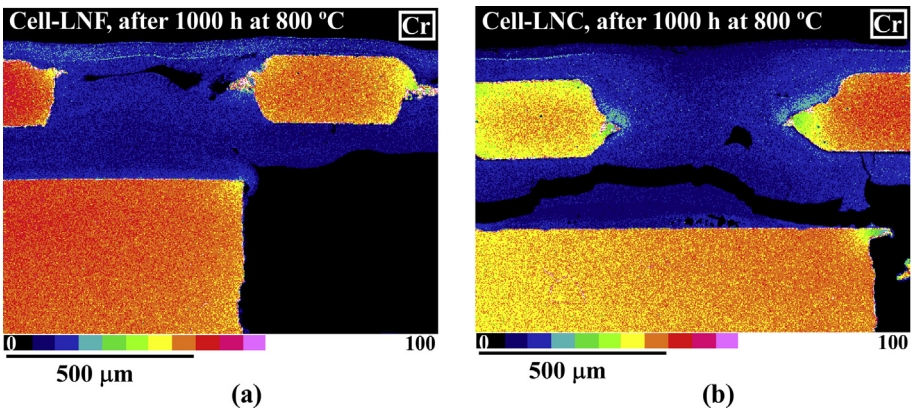

Fig. 6 – Cr-EDX mapping of the cross-section of (a) {interconnect/ablated LNF-mesh/cathode} and (b) {interconnect/ablated LNC-mesh/cathode} systems after heating at 800 °C for 1000 h, in air.

C) and contact mesh (zone E). In both systems, the ceramic material was also quantitatively analyzed, focusing on both the area close to the rib (zone G) and to the mesh (zone H) (see Supplementary material; section A: Fig. S3, section B: Fig. S7). Moreover, Cr enrichment was observed, in both LNC and LNF materials in addition to each contact paste elements (Tables 3 and 4), as was expected.

According to these results, the migration of chromium out of the steel to deposit into ceramic contact paste is demonstrated. Furthermore, this transportation or vaporization rate of Cr species (CrO_3 (g), $CrO_2(OH)_2$ (g)) is enhanced in the LNC composite material, which shows a more obvious Cr deposit ring along the edge of the mesh (Fig. 6).

As stated previously, the TEC mismatch between LNC and Fe–22Cr reduces their adherence, causing an increase in Cr (VI) species from steel. However, as observed in Fig. 6, for both systems, chromium enrichment is detected in areas close to the interconnect and mesh steels, as was expected [7,32,33]. In addition, a Cr rich interlayer is formed between the cathode and both contact pastes, probably due to the formation of $SrCrO_4$ [34].

Other authors have reported [35] that a ferritic type mesh steel possesses a higher creep strength than the Crofer22APU interconnect. Its higher strength is related to minor additions of Nb and W which result in a combination of solid-solution and precipitation strengthening by Laves phase formation, which have been analyzed after the steel was treated at 800 °C for 1000 h (Fig. 4). As was expected [36], stable precipitation composed of mixed (Fe,Cr) (Nb,W) elements is quantified (Table 5).

Table 5 – The average composition in % wt. of matrix and Laves phase indicated in Fig. 4(b).

Spectrum	Cr	Fe	Ni	Nb	W
Matrix: 1,2,3	22.8(4)	74.8(3)	0.4(1)	0.1(1)	1.9(1)
Laves phase: 4,5,6	10.7(2)	43.1(11)	0.4(1)	21.2(16)	24.6(28)

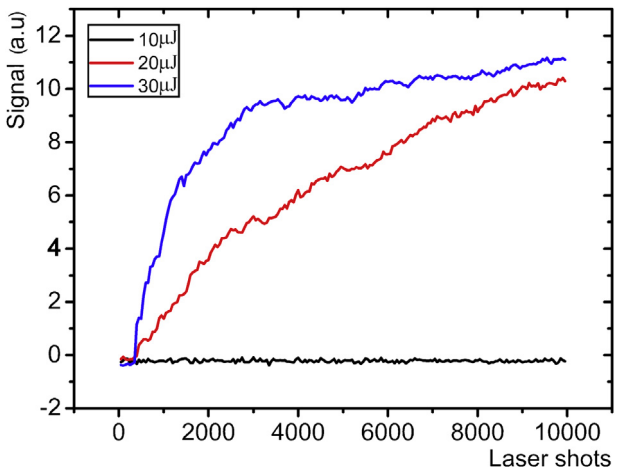

Fig. 7 – Laser intensity registered at the backside of the sample by means of a Si photodiode as a function of number of laser pulses applied.

Please cite this article in press as: Morán-Ruiz A, et al., Laser machining of $LaNi_{0.6}M_{0.4}O_{3-\delta}$ (M: Co, Fe) dip-coated on a Fe–22Cr mesh material to obtain a new contact coating for SOFC: Interaction between Crofer22APU interconnect and $La_{0.6}Sr_{0.4}FeO_3$ cathode, International Journal of Hydrogen Energy (2015), http://dx.doi.org/10.1016/j.ijhydene.2015.04.134

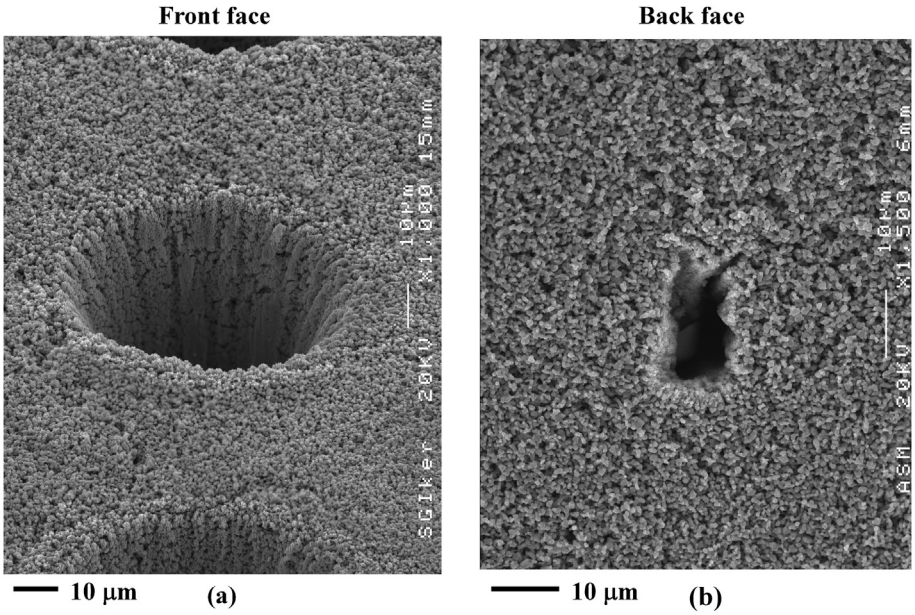

Fig. 8 – SEM surface images of (a) the front and (b) the back faces of the performed crater in $LaNi_{0.6}Co_{0.4}O_{3-\delta}$-Fe22Cr mesh composite. Laser parameters: wavelength 800 nm; pulse energy 20 μJ; pulse duration 40 fs; pulse repetition rate 1 kHz; number of pulses per hole 4000.

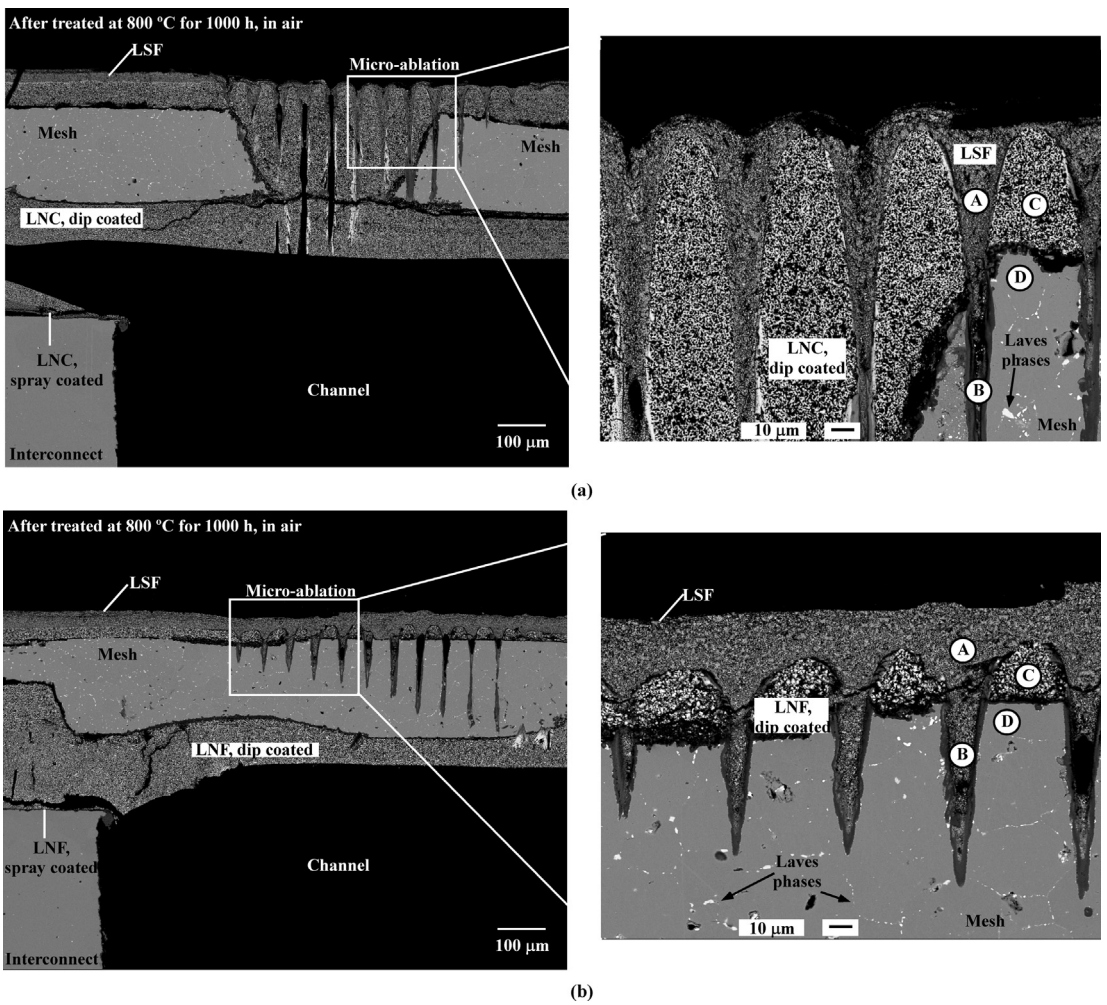

Fig. 9 – Cross-section views of (a) {interconnect/ablated LNC-mesh/cathode} and (b) {interconnect/ablated LNF-mesh/cathode} samples after long-term aging at 800 °C, selecting the ablation craters. Capital letters indicate analysis areas shown in Tables 6 and 7.

Please cite this article in press as: Morán-Ruiz A, et al., Laser machining of $LaNi_{0.6}M_{0.4}O_{3-\delta}$ (M: Co, Fe) dip-coated on a Fe–22Cr mesh material to obtain a new contact coating for SOFC: Interaction between Crofer22APU interconnect and $La_{0.6}Sr_{0.4}FeO_3$ cathode, International Journal of Hydrogen Energy (2015), http://dx.doi.org/10.1016/j.ijhydene.2015.04.134

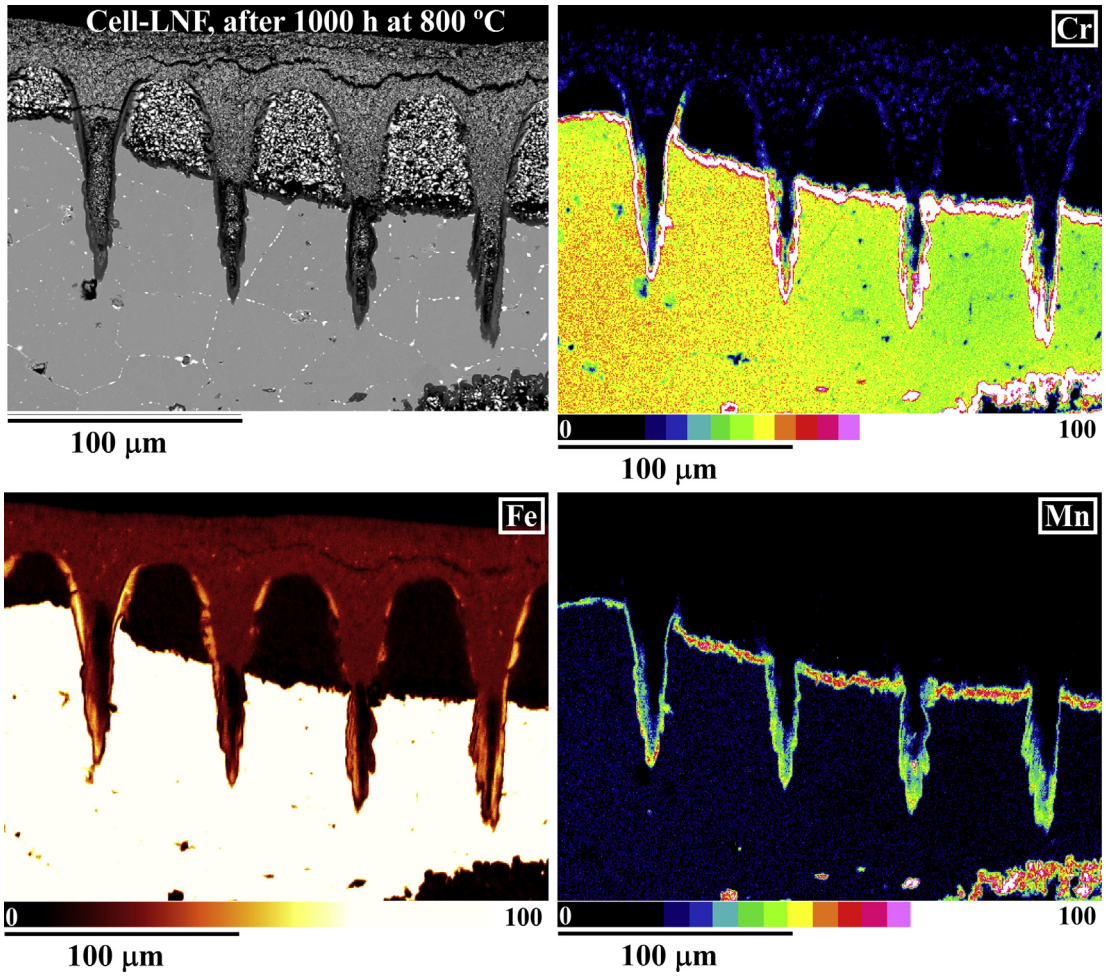

Fig. 10 – EDX mapping of the ablation cross-section of {interconnect/ablated LNF-mesh/cathode} sample after heating at 800 °C for 1000 h in air.

In order to check that after the laser ablation the holes penetrated through the whole ceramic coating layers, a Si photodiode was placed under each composite and the magnitude of their signal recorded with a digital oscilloscope as a function of the number of laser pulses applied, as shown in Fig. 7. The recorded curves correspond to different pulse energies 10, 20 and 30 μJ. In order to avoid reiteration, only results corresponding to LNC-mesh are presented since identical results were obtained in both composites.

Considering these results, 4000 pulses of 20 μJ was set as laser parameters to obtain a complete pore with the minimal damage in the adjacent material. This observation corroborated by the SEM surface images, in which the exit hole was observed (Fig. 8).

However, the morphology of the hole cross-sections depends on the cutting angle of the sample. Fig. 9 shows the cross-section of {Crofer22APU/LNC- and LNF-mesh/LSF} systems of laser ablated areas after long term heating at 800 °C, including EDX analysis zones (see Supplementary material; section A: Fig. S4, section B: Fig. S8).

In order to complement the quantitative results obtained, EDX mapping of both structures (Figs. 10 and 11) were also performed.

According to both analyses, when LNC paste is used the detected Cr content reduction in the contact mesh is higher than that observed in the mesh in contact with LNF (Tables 6 and 7). At the same time, Fe content reduction is also observed into LNC coated mesh, which could indicate that the formation of Fe-oxides in the border of the crater is favoured.

In good agreement with these results, the observed Mn content through the mesh is lower when LNC is applied. Thus, the detected high concentration of Cr in LNC coating indicated that the chromium concentration in the mesh is not enough to form a $(Mn,Cr)_3O_4$ spinel protective layer, which was observed using LNF, allowing an increase in Fe oxides formation [37,38]. Moreover, the Cr is mainly concentrated in the LSF cathode layer; this indicates that Sr dopant promotes the Cr deposition on the contact material surface, in good agreement with both other authors and our previous studies [13,26,34,39,40] and, consistent with the results obtained in ASR test (see Section 3.1).

It seems that the obtained data confirm that laser-metal interactions accelerate the oxidation of metallic chromium and iron, arising from the Fe–22Cr mesh, to deposit at the border of the craters as Fe–Cr oxides. However, EDX analyses performed on the crater environment confirm that the initial

Please cite this article in press as: Morán-Ruiz A, et al., Laser machining of $LaNi_{0.6}M_{0.4}O_{3-\delta}$ (M: Co, Fe) dip-coated on a Fe–22Cr mesh material to obtain a new contact coating for SOFC: Interaction between Crofer22APU interconnect and $La_{0.6}Sr_{0.4}FeO_3$ cathode, International Journal of Hydrogen Energy (2015), http://dx.doi.org/10.1016/j.ijhydene.2015.04.134

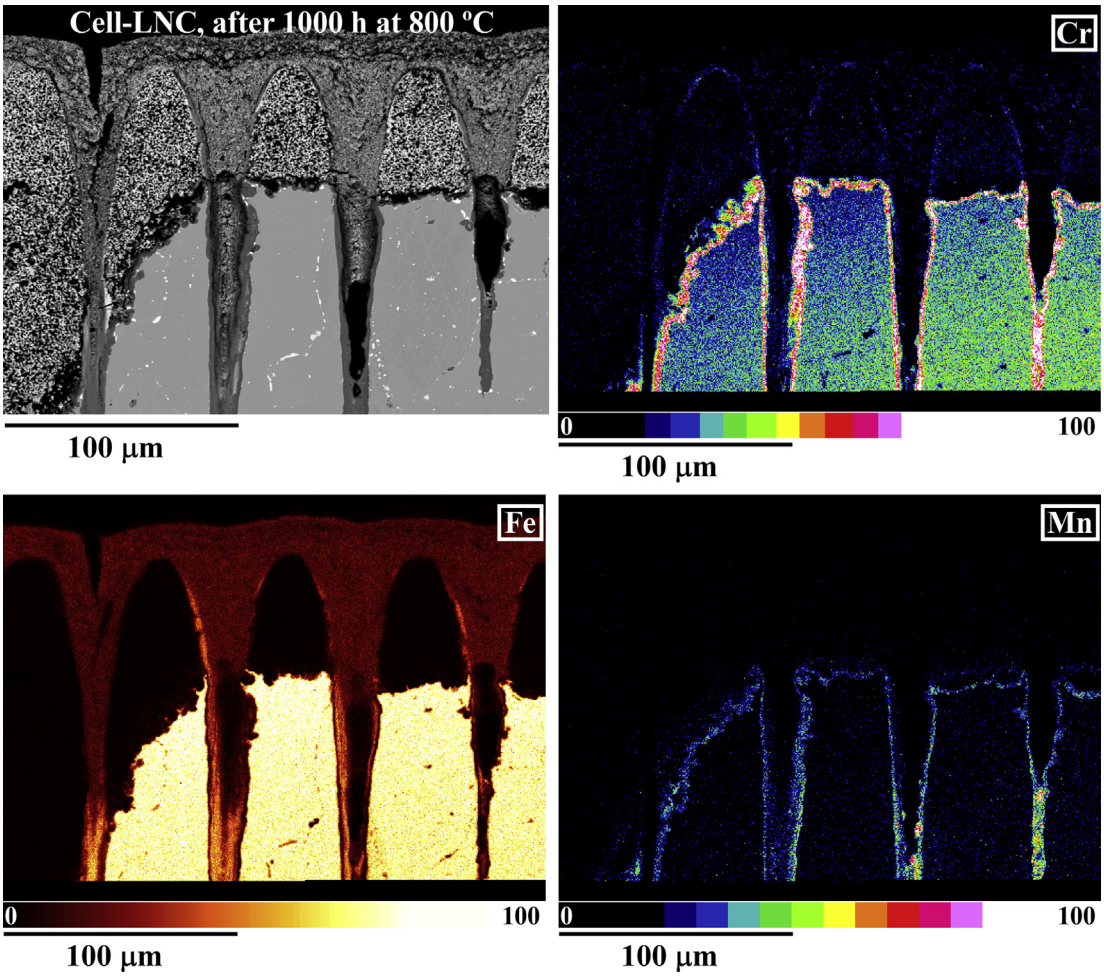

Fig. 11 – EDX mapping of the ablation cross-section of {interconnect/ablated LNC-mesh/cathode} sample after heating at 800 °C for 1000 h in air.

elemental composition, of each ceramic paste and metallic mesh, remains constant (Fig. 9, Tables 6 and 7). As a result, only very limited damage is observed in metal heat–affected zones.

Conclusions

Femtosecond laser machined micro-holes have been successfully achieved on LNC and LNF dip-coated on Fe–22Cr mesh material, obtaining a new contact composite. The initial ASR value of formed {interconnect/ablated contact layer/cathode} setup depends on the electrical conductivity of the ceramic contact coating. Multiple (four replicas) ASR testing for each system confirms the adequate reproducibility of the process.

However, the effectiveness of the contact composite over time depends on the adherence of the ceramic coating on the alloy material. A loss of adherence has been reported between LNC paste coating and interconnect due to an insufficient match of the corresponding thermal expansion coefficients (TECs), which favours the transport or vaporization rate of Cr species (CrO_3 (g), $CrO_2(OH)_2$ (g)). Furthermore, after 1000 h at 800 °C, the laser irradiated composite showed short-range damage, which was limited to the formation of iron and chromium oxides due to the evaporation and oxidation of the mesh. Considering these results, ablated LNF-mesh material

Table 6 – Chemical compositions in % wt. of points indicated in Fig. 9(a).

LNC	Cr	Fe	W	Mn	La	Sr	Ni	Co	O
(A) cathode LSF	6.2(2)	23.0(4)	–	–	34.6(1)	14.9(2)	–	–	21.4(1)
(B) cathode LSF	26.0(1)	23.4(1)	–	4.6(1)	17.7(1)	1.1(1)	–	–	27.3(1)
(C) contact LNC	5.2(4)	–	–	–	52.6(6)	–	13.1(3)	8.7(2)	20.4(1)
(D) mesh Fe–Cr	14.7(25)	82.6(25)	2.7(1)	–	–	–	–	–	–

Please cite this article in press as: Morán-Ruiz A, et al., Laser machining of $LaNi_{0.6}M_{0.4}O_{3-\delta}$ (M: Co, Fe) dip-coated on a Fe–22Cr mesh material to obtain a new contact coating for SOFC: Interaction between Crofer22APU interconnect and $La_{0.6}Sr_{0.4}FeO_3$ cathode, International Journal of Hydrogen Energy (2015), http://dx.doi.org/10.1016/j.ijhydene.2015.04.134

Table 7 – Chemical compositions in % wt. of points indicated in Fig. 9(b).

LNF	Cr	Fe	W	Mn	La	Sr	Ni	O
(A) cathode LSF	4.7(1)	23.6(1)	–	–	34.3(1)	14.2(1)	–	23.2(1)
(B) cathode LSF	24.3(1)	31.6(1)	–	5.2(1)	30.3(1)	1.2(1)	–	7.5(1)
(C) contact LNF	1.9(2)	9.8(4)	–	–	56.8(9)	–	12.6(7)	18.9(8)
(D) mesh Fe–Cr	18.7(2)	78.8(2)	2.5(1)	–	–	–	–	–

could be a good candidate to use as a contact coating between Crofer22APU channeled interconnect and LSF cathode.

Acknowledgments

This research has been funded by Ministerio de Economía y Competitividad (MAT2013-42092-R) and the Dpto. Educación, Política Lingüística y Cultura of the Basque Goverment (Research Group of the Basque University System IT-630-13). The authors wish to thank SGIker-UPV/EHU technical and human support. Dr. Sergio Fernandez Armas is acknowledged for useful scientific help in discussion of EDX measurements. The authors would also like to express their gratitude to Dr. Raúl Montero Santos for helping with femtosecond laser measurements. A. Morán-Ruiz thanks UPV/EHU for funding her PhD work.

Appendix A. Supplementary data

Supplementary data related to this article can be found at http://dx.doi.org/10.1016/j.ijhydene.2015.04.134.

REFERENCES

[1] Hosseini N, Abbasi MH, Karimzadeh F, Choi GM. Development of $Cu_{1.3}Mn_{1.7}O_4$ spinel coating on ferritic stainless steel for solid oxide fuel cell interconnects. J Power Sources 2015;273:1073–83.
[2] Shishkin M, Ziegler T. Direct modeling of the electrochemistry in the three-phase boundary of solid oxide fuel cell anodes by density functional theory: a critical overview. Phys Chem Chem Phys 2014;16:1798–808.
[3] Badwal SPS. Stability of solid oxide fuel cell components. Solid State Ionics 2001;143:39–46.
[4] Yokokawa H, Tu H, Iwanschitz B, Mai A. Fundamental mechanisms limiting solid oxide fuel cell durability. J Power Sources 2008;182:400–12.
[5] Barelli L, Barluzzi E, Bidini G. Diagnosis methodology and technique for solid oxide fuel cells: a review. Int J Hydrogen Energy 2013;38:5060–74.
[6] Guan WB, Jin L, Ma X, Wang WG. Investigation of impactors on cell degradation inside planar SOFC stacks. Fuel Cells 2012;12(6):1085–94.
[7] Jiang SP, Chen X. Chromium deposition and poisoning of cathodes of solid oxide fuel cells – a review. Int J Hydrogen Energy 2014;39(1):505–31.
[8] Ardigò MR, Perron A, Combemale L, Heintz O, Caboche G, Chevalier S. Interface reactivity study between $La_{0.6}Sr_{0.4}Co_{0.2}Fe_{0.8}O_{3-\delta}$ (LSCF) cathode material and metallic interconnect for fuel cell. J Power Sources 2011;196:2037–45.
[9] Kruk A, Stygar M, Brylewski T. Mn–Co spinel protective–conductive coating on AL453 ferritic stainless steel for IT-SOFC interconnect applications. J Solid State Electrochem 2013;17:993–1003.
[10] Liu Y, Chen DY. Protective coatings for Cr_2O_3-forming interconnects of solid oxide fuel cells. Int J Hydrogen Energy 2009;34:9220–6.
[11] Sung-Il L, Jongsup H, Hyoungchul K, Ji-Won S, Jong-Ho L, Byung-Kook K, et al. Highly dense Mn–Co spinel coating for protection of metallic interconnect of solid oxide fuel cells. J Electrochem Soc 2014;161(14):F1389–94.
[12] Guan WB, Zhai HJ, Jin L, Li TS, Wang WG. Effect of contact between electrode and interconnect on performance of SOFC stacks. Fuel Cells 2011;11(3):445–50.
[13] Morán-Ruiz A, Vidal K, Laguna-Bercero MA, Larrañaga A, Arriortua MI. Effects of using $(La_{0.8}Sr_{0.2})_{0.95}Fe_{0.6}Mn_{0.3}Co_{0.1}O_3$ (LSFMC), $LaNi_{0.6}Fe_{0.4}O_{3-\delta}$ (LNF) and $LaNi_{0.6}Co_{0.4}O_{3-\delta}$ (LNC) as contact materials on solid oxide fuel cells. J Power Sources 2014;248:1067–76.
[14] Yang Z, Xia G, Singh P, Stevenson JW. Electrical contacts between cathodes and metallic interconnects in solid oxide fuel cells. J Power Sources 2006;155:246–52.
[15] Tucker MC, Cheng L, DeJonghe LC. Selection of cathode contact materials for solid oxide fuel cells. J Power Sources 2011;196:8313–22.
[16] Vidal K, Morán-Ruiz A, Larrañaga A, Porras-Vázquez JM, Slater PR, Arriortua MI. Characterization of $LaNi_{0.6}Fe_{0.4}O_3$ perovskite synthesized by glycine-nitrate combustion method. Solid State Ionics 2015;269:24–9.
[17] Wu W, Guan W, Wang G, Liu W, Zhang Q, Chen T, et al. Evaluation of $Ni_{80}Cr_{20}/(La_{0.75}Sr_{0.25})_{0.95}MnO_3$ dual layer coating on SUS 430 stainless steel used as metallic interconnect for solid oxide fuel cells. Int J Hydrogen Energy 2014;39:996–1004.
[18] Yoon C. Computational design, fabrication, and characterization of microarchitectured solid oxide fuel cells with improved energy efficiency [Ph. D. thesis]. Georgia Institute of Technology; 2010.
[19] Hoyt KO, Gannon PE, White P, Tortop R, Ellingwood BJ, Khoshuei H. Oxidation behavior of $(Co,Mn)_3O_4$ coatings on preoxidized stainless steel for solid oxide fuel cell interconnects. Int J Hydrogen Energy 2012;37:518–29.
[20] Ou DR, Cheng M. Effect of pre-oxidation on the oxidation resistance of spinel-coated Fe–Cr ferritic alloy for solid oxide fuel cell applications. J Power Sources 2014;247:84–9.
[21] Di Maio Y, Colombier JP, Cazottes P, Audouard E. Ultrafast laser ablation characteristics of PZT ceramic: analysis methods and comparison with metals. Opt Laser Eng 2012;50:1582–91.
[22] Zhu WZ, Deevi SC. Development of interconnect materials for solid oxide fuel cells. Mat Sci Eng A-Struct 2003;348:227–43.
[23] Piccardo P, Gannon P, Chevalier S, Viviani M, Burbucci A, Caboche G, et al. ASR evaluation of different kinds of coatings on a ferritic stainless steel as SOFC interconnects. Surf Coat Tech 2007;202:1221–5.
[24] Shaigan N, Qu W, Douglas GI, Chen W. A review of recent progress in coatings, surface modifications and alloy developments for solid oxide fuel cell ferritic stainless steel interconnects. J Power Sources 2010;195:1529–42.

Please cite this article in press as: Morán-Ruiz A, et al., Laser machining of $LaNi_{0.6}M_{0.4}O_{3-\delta}$ (M: Co, Fe) dip-coated on a Fe–22Cr mesh material to obtain a new contact coating for SOFC: Interaction between Crofer22APU interconnect and $La_{0.6}Sr_{0.4}FeO_3$ cathode, International Journal of Hydrogen Energy (2015), http://dx.doi.org/10.1016/j.ijhydene.2015.04.134

[25] Da Conceiçao L, Dessemond L, Djurado E, Souza MMVM. $La_{0.7}Sr_{0.3}MnO_3$-coated SS444 alloy by dip-coating process for metallic interconnect supported solid oxide fuel cells. J Power Sources 2013;241:159–67.
[26] Menzler NH, Sebold D, Wessel E. Interaction of $La_{0.58}Sr_{0.40}Co_{0.20}Fe_{0.80}O_{3-\delta}$ cathode with volatile Cr in a stack test – scanning electron microscopy and transmission electron microscopy investigations. J Power Sources 2014;254:148–52.
[27] Morán-Ruiz A, Vidal K, Larrañaga A, Arriortua MI. Chemical compatibility and electrical contact of $LaNi_{0.6}Co_{0.4}O_{3-\delta}$ (LNC) between Crofer22APU interconnect and $La_{0.6}Sr_{0.4}FeO_3$ (LSF) cathode for IT-SOFC. Fuel Cells 2013;13(3):398–403.
[28] Morán-Ruiz A, Vidal K, Larrañaga A, Laguna-Bercero MA, Porras-Vázquez JM, Slater PR, et al. $LaNi_{0.6}Co_{0.4}O_{3-\delta}$ dip-coated on Fe-Cr mesh as a composite cathode contact material on intermediate solid oxide fuel cells. J Power Sources 2014;269:509–19.
[29] Miguel-Pérez V, Martínez-Amesti A, Nó ML, Larrañaga A, Arriortua MI. The effect of doping $(Mn,B)_3O_4$ materials as protective layers in different metallic interconnects for solid oxide fuel cells. J Power Sources 2013;243:419–30.
[30] Montero X, Tietz F, Stöver D, Cassir M, Villarreal I. Comparative study of perovskites as cathode contact materials between an $La_{0.8}Sr_{0.2}FeO_3$ cathode and a Crofer22APU interconnect in solid oxide fuel cells. J Power Sources 2009;188:148–55.
[31] Morán-Ruiz A, Vidal K, Larrañaga A, Porras-Vázquez JM, Slater PR, Arriortua MI. Evaluation of using protective/conductive coating on Fe-22Cr mesh as a composite cathode contact material for intermediate solid oxide fuel cells. Int J Hydrogen Energy 2015;40:4804–18.
[32] Chun-Lin C, Jian-Yih W, Shyong L. Effects of $La_{0.67}Sr_{0.33}MnO_3$ protective coating on SOFC interconnect by plasma-sputtering. Int J Hydrogen Energy 2008;33(10):2536–46.
[33] Stodolny MK. Cr-tolerance of the IT-SOFC La(Ni,Fe)O3 material [Ph.D. thesis]. University of Twente; 2012.
[34] Yokokawa H, Horita T, Sakai N, Yamaji K, Brito ME, Xiong YP, et al. Thermodynamic considerations on Cr poisoning in SOFC cathodes. Solid State Ionics 2006;117(35–36):3193–8.
[35] Kuhn B, Asensio-Jimenez C, Niewolak L, Hüttel T, Beck T, Hattendorf H, et al. Effect of Laves phase strengthening on the mechanical properties of high Cr ferritic steels for solid oxide fuel cell interconnect application. Mat Sci Eng A 2011;528:5888–99.
[36] Chiu YT, Lin CK. Effects of Nb and W additions on high-temperature creep properties of ferritic stainless steels for solid oxide fuel cell interconnect. J Power Sources 2012;198:149–57.
[37] Wang K, Liu Y, Fergus JW. Interactions between SOFC interconnect coating materials and chromia. J Am Ceram Soc 2011;94(12):4490–5.
[38] Essuman E, Meier GH, Zurek J, Hänsel M, Norby T, Singheiser L, et al. Protective and non-protective scale formation of NiCr alloys in water vapour containing high- and low-pO_2 gases. Corros Sci 2008;50(6):1753–60.
[39] Shong WJ, Liu CK, Chen CY, Peng CC, Tu HJ, Fey GTK, et al. Effects of lanthanum-based perovskite coatings on the formation of oxide scale for ferritic SOFC interconnect. Mater Chem Phys 2011;127:45–50.
[40] Miguel-Pérez V. Interconnectores metálicos y capas protectoras para su aplicación en pilas SOFC [Ph.D. thesis], UPV/EHU. 2013.

Please cite this article in press as: Morán-Ruiz A, et al., Laser machining of $LaNi_{0.6}M_{0.4}O_{3-\delta}$ (M: Co, Fe) dip-coated on a Fe–22Cr mesh material to obtain a new contact coating for SOFC: Interaction between Crofer22APU interconnect and $La_{0.6}Sr_{0.4}FeO_3$ cathode, International Journal of Hydrogen Energy (2015), http://dx.doi.org/10.1016/j.ijhydene.2015.04.134

Elsevier Editorial System(tm) for Journal of Power Sources
Manuscript Draft

Manuscript Number:

Title: Femtosecond laser micromachining of metallic/ceramic composite material for solid oxide fuel cell devices

Article Type: Research Paper

Keywords: Femtosecond laser; micromachining; metallic/ceramic composite; microstructure; solid oxide fuel cells.

Corresponding Author: Prof. Maribel Arriortua,

Corresponding Author's Institution:

First Author: Aroa Morán-Ruiz

Order of Authors: Aroa Morán-Ruiz; Karmele Vidal; Aitor Larrañaga; Raúl Montero; Maribel Arriortua

Manuscript Region of Origin: SPAIN

Abstract: The possible commercialization of solid oxide fuel cell (SOFC) devices depends on its long-term durability, being the contact resistance between interconnect/cathode a key factor. A Fe-22Cr mesh is dipped into a ceramic slurry to form a high electron conduction metallic/ceramic layer as contact material for SOFC, using three different ceramic compositions: LaNi0.6Co0.4O3-δ (LNC), LaNi0.6Fe0.4O3-δ (LNF) and (La0.8Sr0.2)0.95Fe0.6Mn0.3Co0.1O3 (LSFMC). The viability of drilling holes with minimal damage in these composites to enhance the transport of the gas has been evaluated. The diagnosis of laser damage has been determined using a scanning electron microscopy (SEM) equipped with an energy dispersive X-ray spectroscopy (EDX) system. Femtosecond laser ablation on the samples has been successfully performed; the results indicated that the effect of drilling on the initial elemental composition is very located, considering little to produce a significant alteration of the system performance.

Elsevier Editorial System(tm) for Materials Characterization
Manuscript Draft

Manuscript Number:

Title: Solid oxide fuel cell improvement using a ceramic contact material between Crofer22APU interconnect and La0.6Sr0.4FeO3 cathode

Article Type: Technical Paper

Keywords: SOFC; Cathode contact coating; Contact resistance; Chromium poisoning; Degradation.

Corresponding Author: Prof. Maribel Arriortua,

Corresponding Author's Institution: University of the Basque Country

First Author: Aroa Morán-Ruiz

Order of Authors: Aroa Morán-Ruiz; Karmele Vidal; Aitor Larrañaga; Maribel Arriortua

Abstract: LaNi0.6Co0.4O3-δ (LNC), LaNi0.6Fe0.4O3-δ (LNF) and (La0.8Sr0.2)0.95Fe0.6Mn0.3Co0.1O3 (LSFMC) were used as cathode contact coatings. The long-term stability of these materials was tested by X-ray diffraction (XRD). Thermo X-ray diffractometry (TDX) analyses revealed that the studied three perovskites present a reversible transition from rhombohedral to cubic structure with increasing temperature. X-ray photoelectron spectroscopy (XPS) indicated the presence of La2O3 and/or SrO as surface impurities on initial oxides. Long-term treatment at 800 ºC of powder mixtures of each contact material with La0.6Sr0.4FeO3 (LSF) cathode (1:1 wt.) allowed the formation of a complete solid solution of (LSF)x(LNC,LNF or LSFMC)1-x. The {Crofer22APU interconnect/contact coating} systems, were exposed at 800 ºC for 1000 h, showing a low degradation rate of contact coatings. XPS and XRD analyses performed on top of the three coated samples reveal the presence of Cr-perovskite when LNC and LNF are used. XRD, scanning electron microscopy with energy dispersive X-ray spectroscopy (SEM-EDX), and area specific resistance (ASR) measurements were used to evaluate the long-term behaviour of {interconnect/contact coating/cathode} structures, in presence and absence of contact coating. The contact resistance of cells decreases using contact layers; after 1300 h at 800 ºC the {Crofer22APU/ LNC/LSF} setup showed stable ASR value of 0.041(2) Ω*cm2.

Suggested Reviewers: Francisco Javier Belzunce Varela
Ciencia de los materiales e ingeniería metalúrgica, Escuela politécnica de ingeniería de Gijón, Universidad de Oviedo
belzunce@uniovi.es

Ángel Larrea Arbaizar
Ciencia y tecnología de materiales y fluidos, Instituto de Ciencia de Materiales de Aragón, CSIC-Universidad de Zaragoza
alarrea@unizar.es

José Manuel Porras Vázquez
Química Inorgánica, Universidad de Málaga
josema@uma.es

Xabier Montero Larrauri

High temperature materials, Dechema Forschungsinstitut
montero@dechema.de

eman ta zabal zazu

UPV EHU

Los materiales de contacto cátodo-interconector mejoran el flujo de electrones, siendo éste necesario en la generación de energía mediante celdas de combustible de óxido sólido (SOFC). El uso de aleaciones metálicas como material interconector, permite reducir la temperatura de funcionamiento de las celdas SOFC, aumentando así su durabilidad y aplicabilidad; sin embargo, el empleo de este tipo de materiales presenta como nuevo reto el desarrollo de materiales de contacto con microestructuras y propiedades óptimas.

Cathode-interconnect contact materials improve the electrons flow, which is an essential aspect for energy production in a solid oxide fuel cell (SOFC). The use of metallic alloys as interconnect material, reduces the operating temperature of SOFCs, increasing their durability and applicability. However, they present as a new challenge the development of contact materials with an adequate microstructure and properties.